

Dissertation zur Erlangung des Doktorgrades  
der Fakultät für Chemie und Pharmazie  
der Ludwig-Maximilians-Universität München

Text

Photoswitchable and non-photoswitchable tubulin inhibitors for  
applications in cell biology

Yvonne Kraus

aus

Friedberg (Bayern), Deutschland

2020

## Erklärung

Diese Dissertation wurde im Sinne von § 7 der Promotionsordnung vom 28. November 2011 von Herrn Dr. Oliver Thorn-Seshold betreut.

## Eidesstattliche Versicherung

Diese Dissertation wurde eigenständig und ohne unerlaubte Hilfe erarbeitet.

München, 15.12.2020

Yvonne Kraus

.....

Dissertation eingereicht am: 17.12.2020

1. Gutachter: Dr. Oliver Thorn-Seshold  
2. Gutachter: Prof. Dr. Stefan Zahler

Mündliche Prüfung am: 05.02.2021



## Publications from this Ph.D. thesis

[1] **Yvonne Kraus**<sup>+</sup>, Carina Glas<sup>+</sup>, Benedikt Melzer, Li Gao, Constanze Heise, Monique Preuße, Julia Ahlfeld, Franz Bracher, Oliver Thorn-Seshold; Isoquinoline-based biaryls as a robust scaffold for microtubule inhibitors

*European Journal of Medicinal Chemistry* **2020**, *186*, 111865.

[2] Alexander Sailer<sup>+</sup>, Franziska Ermer<sup>+</sup>, **Yvonne Kraus**<sup>+</sup>, Ferdinand Lutter, Carsten Donau, Maximilian Bremerich, Julia Ahlfeld, and Oliver Thorn-Seshold; Hemithioindigos for cellular photopharmacology: Desymmetrised molecular switch scaffolds enabling design control over the isomer-dependency of potent antimitotic bioactivity

*ChemBioChem* **2019**, *20*, 1305.

[3] Li Gao, Joyce Meiring, **Yvonne Kraus**, Maximilian Wranik, Tobias Weinert, Stefanie Pritzl, Rebekkah Bingham, Evangelia Ntoulidou, Klara Jansen, Natacha Olieric, Jörg Standfuss, Lukas Kapitein, Theobald Lohmüller, Julia Ahlfeld, Anna Akhmanova, Michel Steinmetz, and Oliver Thorn-Seshold; A robust, GFP-orthogonal photoswitchable inhibitor scaffold extends optical control over the microtubule cytoskeleton

*Cell Chemical Biology* **2021**, *28*, 1.

[4] Alexander Sailer, Fransika Ermer, **Yvonne Kraus**, Rebekkah Bingham, Ferdinand Lutter, Julia Ahlfeld, and Oliver Thorn-Seshold; Potent hemithioindigo-based antimitotics photocontrol the microtubule cytoskeleton in cellulo

*Beilstein Journal of Organic Chemistry* **2020**, *16*, 125.

[5] Adrian Müller-Deku, Joyce Meiring, Kristina Loy, **Yvonne Kraus**, Constanze Heise, Rebekkah Bingham, Julia Ahlfeld, Dirk Trauner & Oliver Thorn-Seshold; Photoswitchable paclitaxel-based microtubule stabilisers allow optical control over the microtubule cytoskeleton

*Nature Communications* **2020**, *11*, 4640.

[<sup>+</sup>]: These authors contributed equally to this work

## Abstract

The microtubule cytoskeleton performs a wide range of functions in all organisms, including in cell motility, cell division, intracellular transport, and mechanostasis. Microtubule targeting agents have been essential to study microtubule function in basic biological research. They also play a role in the treatment of cancer, either by direct cytotoxicity or by vascular disrupting activity.

In the first part of this thesis, I evaluate a new scaffold for microtubule depolymerisers, which provides enhanced metabolic stability to potential vascular disrupting agents. In the second part of this thesis, I evaluate new photoswitchable tubulin depolymerisers and stabilisers. The commonly known microtubule targeting agents lack spatiotemporal precision, which makes it difficult to use them in elucidating cytoskeleton-dependent processes that rely on precise control over biological timescales or at distinct locations. Photopharmacology can significantly enhance spatiotemporal control of drug activity by the use of photoswitchable molecules that can optically control microtubule dynamics. I present rationally designed microtubule destabiliser photopharmaceuticals based on relatively unexplored molecular scaffolds that can be applied to photocontrol microtubule dynamics. Our new photopharmaceuticals have significant advantages compared to azobenzene-based photopharmaceuticals. I also present the first photoswitchable microtubule stabilisers and analyse them with respect to their performance and weaknesses.

As a result, my research has made significant progress towards spatiotemporal control of microtubule dynamics and demonstrates that molecular “scaffold hopping” is an innovative and valuable concept for designing both pharmaceuticals and photopharmaceuticals.

## Zusammenfassung:

Das Mikrotubuli-Zytoskelett erfüllt umfassende Aufgaben in allen Organismen, einschließlich Zellfortbewegung, Zellteilung, intrazellulärem Transport und es vermittelt der Zelle Struktur und Stabilität. Wirkstoffe, die das Mikrotubuli-Zytoskelett beeinflussen, sind essenziell, um seine Funktion zu erforschen. Außerdem spielen sie ebenfalls eine Rolle in der Krebstherapie und entfalten ihre Wirkung entweder durch direkte Zytotoxizität oder durch ihren Effekt auf das vaskuläre System des Tumors.

Im ersten Teil meiner Dissertation untersuche ich ein neues molekulares Gerüst für depolymerisierende Mikrotubuli-Inhibitoren, das höhere Stabilität gegen die Abbaufunktionen des Organismus aufweist. Daher könnten diese Wirkstoffe einen Vorteil haben gegenüber herkömmlichen Wirkstoffen, die das vaskuläre System des Tumors angreifen und meist sehr schnell abgebaut werden.

Im zweiten Teil meiner Arbeit untersuche ich neue Wirkstoffe, die als Fotoschalter konzipiert sind und durch Bestrahlung mit Licht, Mikrotubuli entweder depolymerisieren oder stabilisieren können; beides hat einen negativen Effekt auf die Zellteilung. Herkömmliche Wirkstoffe, die das Mikrotubuli-Zytoskelett angreifen, können nicht zeitlich und räumlich kontrolliert werden, was es schwierig macht, biologische Prozesse zu untersuchen, die von präziser räumlicher und zeitlicher Kontrolle abhängen. Durch die Verwendung von Fotoschaltern, kann Fotopharmakologie diese Präzision erheblich verbessern, da das Mikrotubuli-Zytoskelett durch Licht kontrolliert werden kann. Ich präsentiere Fotoschalter, die auf der Basis neuer molekularer Gerüste beruhen und daher signifikante Vorteile gegenüber den bisherigen lichtsteuerbaren Molekülen haben, die Azobenzol-Gerüste haben.

Zusätzlich stelle ich die ersten lichtaktivierbaren Mikrotubuli-Stabilisatoren vor und bewerte ihre Wirkung und Schwächen. Daher ist meine Forschung ein signifikanter Fortschritt in der spatiotemporalen Kontrolle des Mikrotubuli-Zytoskeletts und zeigt, dass „scaffold-hopping“ (Austausch des molekularen Gerüsts) eine innovative und zukunftsweisende Strategie für die Herstellung von Pharmazeutika und Fotopharmazeutika ist.

## Table of Contents

Publications from this Ph.D. thesis.....	4
Abstract .....	5
Zusammenfassung: .....	6
1 Introduction.....	8
1.1 The eukaryotic cytoskeleton .....	8
1.2 History of cytoskeleton research.....	9
1.3 Microtubules .....	11
1.4 Other cytoskeleton proteins .....	17
1.5 Challenges and objectives of small-molecule cytoskeleton inhibitors.....	21
2 Aim of the Ph.D. thesis.....	23
3 Microtubule depolymerisers with potential VDA activity.....	24
4 Photopharmaceutical microtubule depolymerisers .....	36
4.1 Styrylbenzothiazole SBTubs.....	38
4.2 Hemithioindigo HOTubs.....	56
4.3 Hemithioindigo HITubs .....	68
5 Photopharmaceutical microtubule stabilisers .....	79
Discussion .....	94
Outlook.....	99
Acknowledgements.....	100
Appendix.....	101
List of Abbreviations .....	101
Bibliography .....	102
Supplementary Information .....	107

# 1 Introduction

## 1.1 The eukaryotic cytoskeleton

The eukaryotic cytoskeleton is a network of filamentous proteins that extends through the cytoplasm. It has to be both structurally stable and dynamic in its capability for rearrangement to perform its wide range of functions including the support of cell shape, cell migration, intracellular transport, positioning of organelles as well as cell division, cell-cell- and cell-matrix interactions through interaction with cadherins and integrins and cell polarity. Today, the term cytoskeleton usually describes three types of structures in the cell: Actin filaments (Fig. 1a), intermediate filaments (Fig. 1b) and microtubules (Fig. 1c). Lately, septins, as conserved GTP-binding proteins that act as a scaffold for protein recruitment at the plasma membrane have been recognized as another part of the cytoskeleton.<sup>1</sup>

All cytoskeleton proteins share common features such as their presence as linear polymers in cells and their ability to self-assemble into polymers *in vitro*.<sup>2</sup> The complexity of the network is controlled by several protein classes including nucleation-promoting factors for initiation of filament growth, capping factors for terminating growth, polymerases, depolymerising proteins and severing factors, which disassemble filaments, as well as crosslinkers and stabilising factors that assist in building higher-order structures.<sup>3</sup>

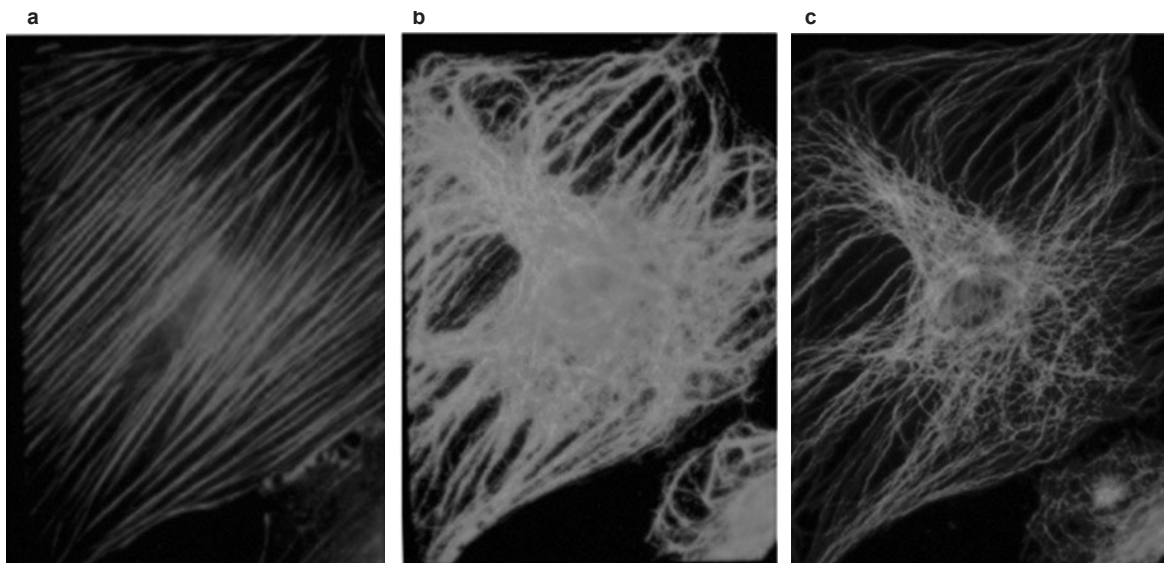


**Figure 1:** a: Actin filaments; b: Intermediate filaments (vimentin); c: Microtubules (adapted from Lodish et. al., 2000<sup>4</sup>)

There is a high demand for sophisticated research tools to study the role and importance of cytoskeleton structures and dynamics both in cells and *in vivo* because of their multiple functions in almost all cellular processes that are not sufficiently understood until now. Elucidating the role of cytoskeleton dynamics and function in key processes such as the cell cycle; morphogenesis, migration and clarifying the consequences of defects; and misregulation is a prerequisite for the development of drugs for many kinds of diseases such as cancer. The application of genetic approaches to study function and regulation of cytoskeletal proteins by using conditional mutations and genetic interaction studies in model



organisms such as yeast, *Dictyostelium*, *C. elegans*, *Drosophila* and mouse models is limited due to the wide range of functions of cytoskeleton proteins and the severe consequences of changing their structure by mutations, which often leads to embryonal lethality. These obstacles have resulted in insufficient comprehension of both cytoskeleton complexity and regulation.<sup>5</sup>

Therefore, small molecules that target the cytoskeleton have been essential for unravelling cellular processes involving the cytoskeleton. Their use in basic research has already led to the development of drugs to successfully treat gout and certain types of cancer. Available agents are operating either by direct cytotoxicity leading to disruption of the tubulin-microtubule equilibrium with microtubule depolymerising or stabilising capacity (most famously vinca alkaloids and taxanes, respectively) or as vascular disrupting agents (VDAs) most famously including Combretastatin A-4 (CA4), which has already proceeded into clinical trials<sup>6</sup>.

The structures of these small molecules, which are mainly isolated from natural sources or accessed semi-synthetically, build the basis to develop new and improved cytoskeleton modulators for research and clinical use. Over time, cytoskeleton research has developed from theoretical concepts over crude and basic methods into a large field of research driven by biochemical assays and benefiting from new developments in microscopy. The following short section provides an overview of cytoskeleton research history.

### **1.2 History of cytoskeleton research**

The concept of the cytoskeleton was already theorized in the first half of the 19<sup>th</sup> century (1835) by the French cytologist Dujardin, who made the important realization that the glutinous transparent substance, which he extracted from protozoa (and which he called “sarcode”), was involved in both cell shape and cell motility. This discovery was made with a simple microscope, micromanipulation and crude chemical extraction procedures.<sup>7</sup> From this first idea, it took until 1931 before the term cytoskeleton was introduced by the French embryologist Paul Wintrebert.<sup>8</sup> The development of electron microscopy in the 1950s revealed the structure of the axoneme, the structural component of cilia and flagella. In 1965, Gibbons and Rowe described the motor protein dynein<sup>9</sup> and its ATPase properties, which built the basis for the model of sliding tubes fuelled by ATP hydrolysis in flagella of sea urchins<sup>10</sup>.

Another process that had already fascinated Walther Flemming back in 1882 was the process of mitosis, which he analysed with fixed samples under a microscope. The limitations of fixed samples were later resolved when polarized light microscopy and live-cell imaging allowed direct observation of mitosis. Inoue and Sato introduced a model of mitotic spindle dynamics and its function in moving the chromosomes in their seminal paper in 1967 (Fig. 2a).<sup>11</sup> One of the most important discoveries in cytoskeleton research was the isolation of tubulin as a colchicine binding protein in 1968, which already anticipated the huge influence of small-molecule inhibitors in research. Weisenberg et al. described a procedure to isolate a protein dimer that binds one equivalent colchicine and two equivalents GTP with one component of

the dimer exchanging GTP in 15 min, while there was no exchange with the other part of the dimer. They claimed these dimers were the subunits of microtubules.<sup>12</sup>

In 1942, the discovery of actin was credited to the Hungarian biochemist Bruno Ferenc Straub, who developed a technique to isolate muscle proteins in the laboratory of Albert Szent-Györgyi by adding high salt concentrations to ground muscle. This led to the extraction of the lower viscosity protein myosin A, after 20 min, and the higher viscosity protein myosin B overnight. While the addition of Adenosine Triphosphate (ATP) to myosin B reduced its viscosity, myosin A was unaffected. Due to World War II, their findings were not published in English-language-journals until the end of the war.<sup>13</sup> In 1942, Needham et al. independently discovered the same effect.<sup>14</sup> In 1953, it was first described that cell-cell contacts can inhibit cell movements. In the 1970s, Abercrombie et al. published several papers describing different aspects of cell migration, which led to the theory that cells move by quick insertion of material on the leading edge.<sup>15</sup>

Another milestone, the model of sliding muscle filaments, was presented in 1954 by Huxley et al.<sup>16</sup> based on interference microscopy. In 1972, Schroeder described the actomyosin contractile ring in cytokinesis<sup>17</sup> (Fig. 2b). The discovery of the first non-conventional myosin in 1973 by Pollard and Korn<sup>18</sup> was followed by visualization of actin stress fibres by indirect immunofluorescence in 1974<sup>19</sup>.

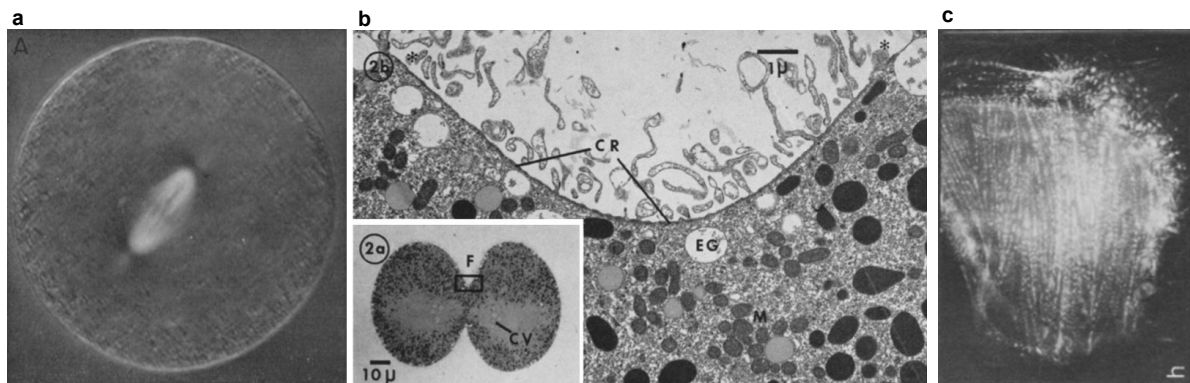


**Figure 2:** a: Mitotic spindle in arrested metaphase oocyte of *Pectinaria gouldi* (polarization microscopy) (adapted from <sup>11</sup>); b: Contractile ring in a half-cleaved egg of *Arbacia* (electron micrographs) (adapted from <sup>17</sup>); c: Tetramethylrhodamine isothiocyanate labelled  $\alpha$ -actinin, an actin-crosslinking protein, incorporated into a living gerbil fibroblast cell (phase micrographs) (adapted from Feramisco, 1979<sup>20</sup>)

Intermediate filaments were first discovered by Holzer et al. in developing muscles. In a key experiment, they used dividing cells with no notable actin filament content and treated them with mitotic inhibitors to break down the mitotic spindle. The remaining predominant fibre had a size of 10 nm diameter and was, therefore, named intermediate filaments.<sup>21</sup>

The field of cell biology and, especially, cytoskeleton research drastically changed when techniques to fluorescently label cellular components were developed. Taylor and Wang introduced a procedure using a fluorescent dye to label purified actin and then injecting it into cells.<sup>22</sup> The labelled actin behaved similar to unlabelled actin *in vitro* and *in vivo* with respect

to polymerisation, activation of myosin and incorporation into contracted pellets in motile cell extracts.<sup>23</sup> The same approach was applied with several fluorescent molecules<sup>24,20</sup> including the actin crosslinking protein  $\alpha$ -Actinin (Fig. 2c). This development led the way to sophisticated studies of cytoskeleton structure and dynamics in various models in a new era of cell biology shaped by new prospects in microscopy.

## 1.3 Microtubules

### 1.3.1 Microtubule structure and nucleation

Microtubules are dynamic polymers composed of  $\alpha/\beta$ -tubulin heterodimers that are essential for many cellular functions including cell division, intracellular transport and positioning of organelles. In purified tubulin solutions, tubulin is able to nucleate and elongate polymers in the presence of GTP.<sup>25</sup>  $\alpha$ - and  $\beta$ -tubulin subunits share 40% sequence identity, with identical core structures built of two  $\beta$ -sheets surrounded by  $\alpha$ -helices, as was determined by electron microscopy at 3.7 Å resolution.<sup>26</sup>  $\alpha$ - and  $\beta$ -tubulin assemble into heterodimers ("tubulin monomers") that are then polymerised into microtubules. Each tubulin monomer binds a guanine nucleotide, which can be exchanged when bound to the  $\beta$ -subunit and is non-exchangeable when bound to the  $\alpha$ -subunit.

The polymer structure of microtubules consists of 13 parallel protofilaments and builds one hollow microtubule that arises from tightly packed tubulin heterodimers (Fig. 3a and 3b). The tubular form is maintained by lateral and longitudinal interactions between the tubulin subunits. The head-to-tail arrangement of the  $\alpha$ - and  $\beta$ -tubulin subunits leads to the two microtubule ends—the  $\beta$ -exposed plus end and the  $\alpha$ -exposed minus end—having different properties. While the plus end can grow at high speed and reaches out into the cytoplasm and even to the plasma membrane, the minus end only grows slowly, frequently being integrated into the centrosome.

High-resolution maps show the differences between inside and outside of the microtubule with the outside surface being a shallow zigzag of density and the inside being rippled with connections between protofilaments lying close to the inner surface.<sup>27</sup> Microtubule growth occurs in two phases: nucleation and elongation. Nucleation requires a third type of tubulin,  $\gamma$ -tubulin, and takes place at the centrosome on the  $\gamma$ -tubulin ring complex.  $\gamma$ -tubulin concentration in the centrosome changes throughout the cell cycle and microtubule nucleation rate in anaphase and telophase increases up to seven-fold compared to interphase.<sup>28</sup> Microtubule nucleation is followed by elongation, the non-covalent addition of  $\alpha$ -/ $\beta$ -tubulin heterodimers. Populations of microtubules range between two extremes of stability: highly dynamic and short-lived populations serve for processes that need quick rearrangement such as mitosis, while fully stable microtubule-based structures are mostly found in non-dividing cells, which include axonemes in the flagellum of sperm and the marginal band in blood platelets.

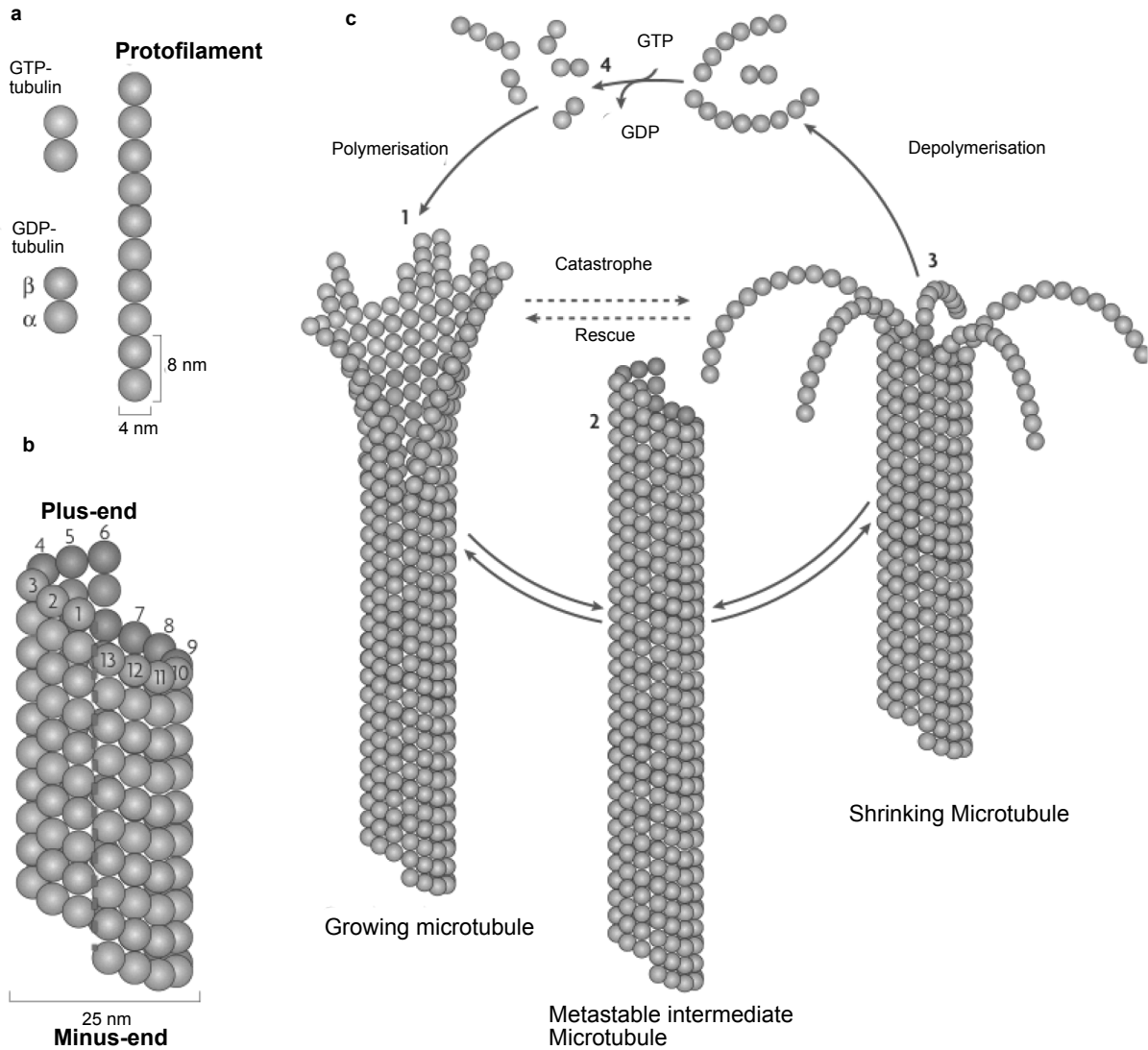


**Figure 3:** Microtubule structure and dynamic instability (Figure adapted from Akhmanova and Steinmetz, 2008<sup>29</sup>)

### 1.3.2 Microtubules and motor proteins

Microtubules give shape to cells and membranes. As structural elements of flagella and cilia, they take part in directed cell migration.<sup>30</sup> They form the mitotic spindle during cell division to precisely divide the genetic material into two identical daughter cells. In order to perform these tasks, microtubules serve as a platform for intracellular transport by providing tracks for kinesin and dynein family motor proteins.

These motor proteins move unidirectionally along the microtubules while hydrolysing ATP and fulfilling tasks that require intracellular transport. Thus, these motor proteins are essential for microtubule-dependent functions in mitosis, cargo transport and vesicle and organelle positioning. Kinesins are mostly plus-end directed motor proteins that move organelles, mitochondria and vesicles, initiate spindle bipolarity and arrange chromosomes between spindle poles.<sup>31</sup> Therefore, they play an important role in spindle assembly and chromosome segregation<sup>32</sup> in addition to their roles in intracellular transport. Dyneins are minus-end directed motor proteins and transport their cargos to the opposite minus end of microtubules.

Their role besides vesicular trafficking and intracellular transport of organelles<sup>33</sup> is contribution to the metaphase checkpoint, managing of spindle positioning and regulation of spindle length and focus<sup>31</sup>.

### 1.3.2 Dynamics in nucleated microtubules

GTP hydrolysis is the source of energy for the highly dynamic process of rearranging the cytoskeleton, which is a prerequisite for all microtubule functions including the extensive structural changes that are necessary to build the bipolar mitotic spindle. In the cell, microtubules undergo a phenomenon called dynamic instability (Fig. 3c) that connects the rate of microtubule growth and shortening, the rate of transitioning between a growing, paused or shrinking microtubule—which is rapid depolymerisation called microtubule “catastrophe”—and the change from the shrinking stage to regrowth (“rescue”) of the microtubule.

During microtubule growth, the growing plus end is protected by a GTP-cap with GTP being hydrolysed with a delay. Loss of the GTP cap leads to the microtubule catastrophe in a “peeling” measure.<sup>34</sup> GTP hydrolysis causes a conformational change resulting in a lower binding affinity between the subunits, which forces the microtubules in a curved state.<sup>35</sup> Another behaviour of microtubules, the so-called ‘treadmilling’, is also a phenomenon of dynamic instability. Microtubule subunits are added on the plus ends while they are released at the minus end at the same rate. Thus, the length of the polymer remains constant. The  $\alpha$ - $\beta$ -tubulin dimers move along the microtubule. This behaviour is often, but not exclusively, seen during metaphase and anaphase, and is thought to be necessary for intracellular signalling from the kinetochores to the poles.<sup>36</sup>

### 1.3.3 Biological regulation of microtubule stability and dynamics

In view of the fact that microtubules fulfil a huge range of functions in the cell, biological regulation is essential and is accomplished by several mechanisms. These mechanisms are based on interaction with various kinds of proteins, posttranslational modifications of tubulin and expression of different tubulin isotypes, as well as their dynamic structural reorganisation by de/polymerisation. Posttranslational modifications include polyamination, acetylation polyglutamylation, tryrosination,<sup>37</sup> phosphorylation and polyglycylation and can significantly change microtubule properties<sup>38</sup>. Additionally, both  $\alpha$ - and  $\beta$ -tubulin have several isotypes that emerge from the expression of alternative tubulin genes that are differently expressed in various cell types.<sup>39</sup> There are eight human  $\alpha$ -tubulin isoforms and seven human  $\beta$ -tubulin isoforms that show tissue-specific expression as well as variation of expression during different developmental stages.<sup>40</sup> In platelet microtubules, the  $\beta$ -tubulin isoform  $\beta$ VI (TUBB3) is essential for the formation of the marginal band that gives platelets their unique disc-like shape. A loss of this isoform leads to thrombocytopenia.<sup>38</sup>

Expression of different tubulin isotypes and posttranslational modifications have been named the “tubulin code”<sup>41</sup> (Fig. 4a), lead to an individual composition of microtubules that differs between cell types and species<sup>39</sup> and participate in the regulation of microtubule dynamics (Fig. 4b). Tubulin isoforms also play a role in drug resistance in chemotherapy and alterations are common in several kinds of cancer.

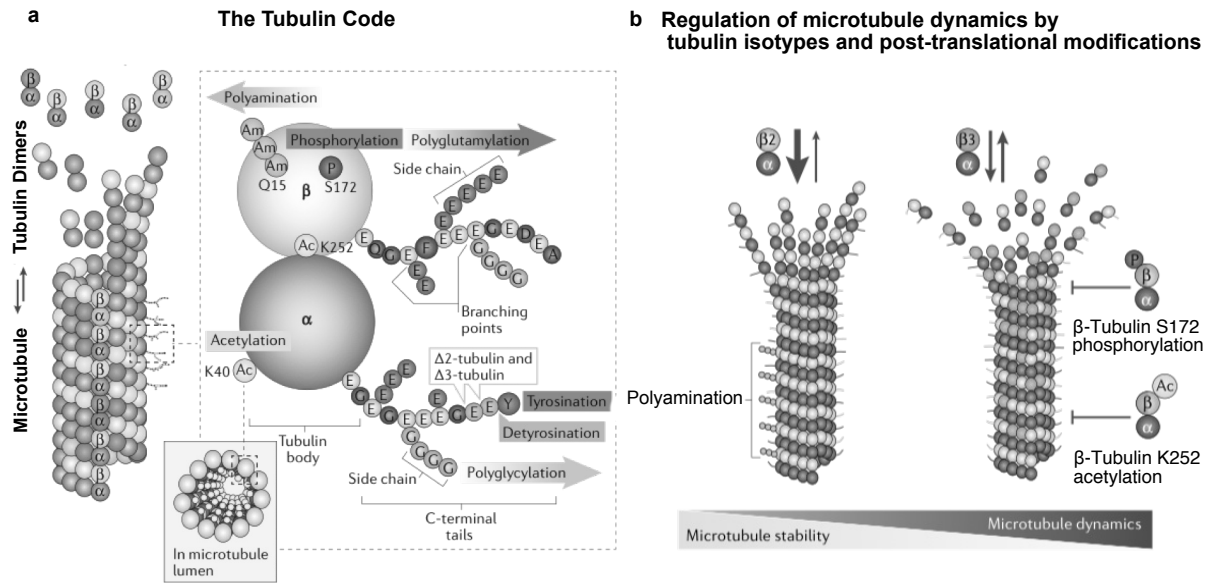


**Figure 4:** a: Elements of the Tubulin Code, b: Microtubule dynamics are regulated by tubulin isoforms and post-translational modifications (adapted from Janke and Mangiera, 2020<sup>39</sup>)

Besides the expression of isoforms and posttranslational modifications, microtubules are also regulated by microtubule-associated proteins (MAPs). Microtubule-associated proteins can modulate microtubule dynamics in the cell without the necessity of binding or hydrolysing GTP. While microtubule stabilising proteins can promote growth, prevent catastrophe, enhance stability and build connections and crosslinks, microtubule destabilising proteins can sever connections and promote depolymerisation by inducing catastrophes, preventing rescue or increasing shrinkage speed.<sup>35</sup>

Families of stabilising MAPs include MAP1, MAP2, MAP4 and tau. Tau is thought to stabilise microtubules in axons<sup>42</sup> and doublecortin, a unique MAP that can either stabilise or destabilise as well as regulating cellular dynamics or act as a linker between components of the cell<sup>43</sup>. Another very important class of microtubule stabilising proteins are the (+)TIP binding (microtubule-plus-end tracking proteins) proteins including EB1, which are known to preferentially bind the GTP-cap of growing microtubules to promote growth and provide a platform for further interaction partners such as the APC tumour suppressor protein.<sup>44</sup> Because of their selective binding to GTP-cap regions, end-binding proteins such as EB1 and EB3 can also be used as fluorescent fusion proteins to image microtubule polymerisation dynamics in living cells.<sup>45</sup> In addition, EB1 can convey interactions with the minus-end directed motor protein Ncd that focuses kinetochore microtubule bundles. They are subsequently transported to the centrosome by dynein during spindle formation.<sup>46</sup>

An opposing function is conducted by the microtubule-severing protein Katanin, which is an AAA ATPase that is targeted to the centrosome by a specialized targeting subunit and can disrupt contacts within the polymer lattice.<sup>47</sup> Along with its relative spastin, katanin seems to have an important function in the branch formation in neurons.<sup>48</sup> Further destabilising MAPs include nonmotile kinesins that have several modes of action including an ATP-dependent

catastrophe inducing mechanism and ATP-independent microtubule sequestration.<sup>49</sup> Other small proteins that negatively regulates microtubule stability are proteins of the oncoprotein18/stathmin family that can increase the rate of catastrophe by introducing a kink into the microtubule that mimics the peeling during microtubule catastrophe.<sup>50</sup> Microtubule regulating proteins will soon most likely receive even more attention as possible targets in cancer therapy as the family of microtubule associating proteins contains products of oncogenes, tumour suppressor genes and apoptosis promoting factors.<sup>51</sup>

### 1.3.4 Chemical regulation of microtubule stability and dynamics

Microtubule research has always been closely linked with the use of small-molecule drugs. The importance of drug binding sites on tubulin could already be presumed when the discovery of tubulin arose as a colchicine binding protein. Now, there are several drug binding sites known and intensely researched, not only to find small molecules as research tools to enlighten the nature of cellular processes that involve microtubules, but also for therapeutic applications to treat diseases linked to the cytoskeleton. Microtubule inhibitors can be classified into stabilisers that are taxanes, epothilones and laulimalide site interactors, and destabilisers, which are vinca alkaloids and colchicine site binding agents (Fig. 5a). Tubulin dimers have several known binding sites that are occupied by a variety of tubulin inhibitors (Fig. 5b).

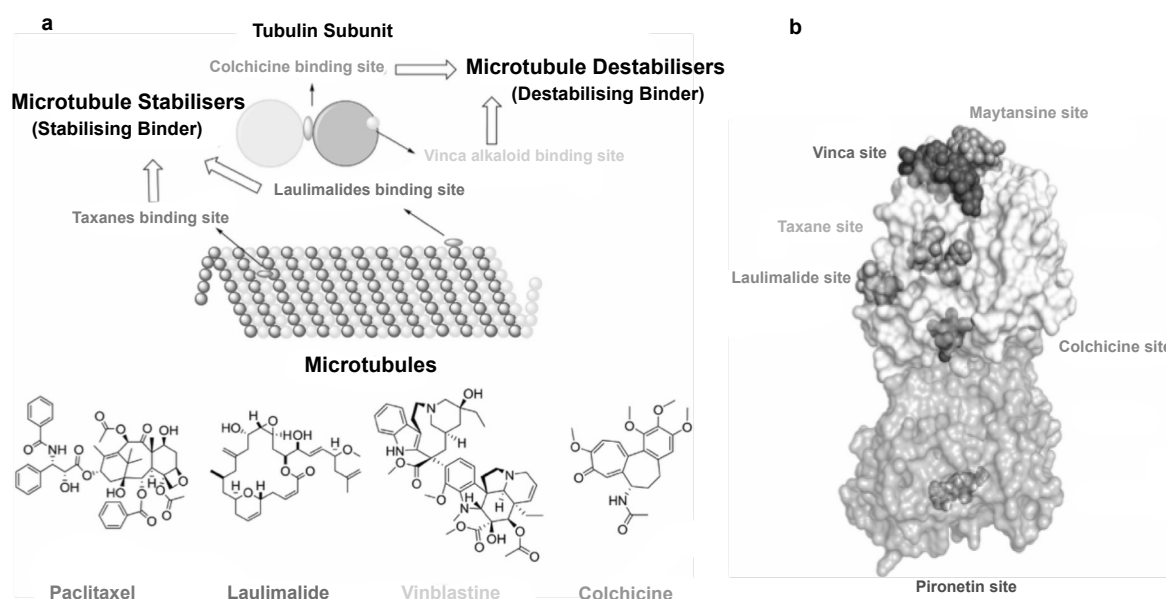


**Figure 5:** a: Schematic depiction of microtubule inhibitor binding sites and structures of famous microtubule inhibitors (adapted from Li et. al.,2018<sup>52</sup>), b: 3D-structure of a tubulin dimer with known drug binding sites (adapted from Steinmetz and Prota, 2018<sup>53</sup>)

Microtubule stabilising agents induce the formation of tubulin polymers without requiring GTP to bind to the E-site, which normally is the prerequisite for microtubule assembly.<sup>54</sup> Microtubule destabilising agents prevent assembly of microtubules by interrupting specific contacts.<sup>55</sup> Both classes of microtubule inhibitors are antimitotics and affect the rapid microtubule reorganisations needed to form and use the mitotic spindle during cell division.<sup>56</sup> This leads to blockage of mitosis in the G2/M stage in the cell cycle, activating cell cycle checkpoints and

eventually programmed cell death.<sup>57</sup> Agents binding at two particular sites, the colchicine binding site and the taxane binding site, will be the focus of this thesis.

The colchicine binding site is located in the intermediate domain of  $\beta$ -tubulin, close to the intradimer interface between the  $\alpha$ - and the  $\beta$ -subunit of tubulin. Binding of an inhibitor in this site leads to poorly reversible colchicine-tubulin complexes and prevents a curved-to-straight conformational change in the microtubule, which must occur for tubulin polymerisation.<sup>53</sup> The taxane binding site is characterized by hydrophobic residues and is localized on the luminal side of microtubules as a pocket in  $\beta$ -tubulin. Taxane site binding molecules seem to have a variety of mechanisms for interaction with subsites in the binding pocket<sup>53</sup> but, generally, promote stabilisation of GDP-bound tubulin and, therefore, prevent depolymerisation inhibiting microtubule rearrangement and dynamics. This blocks not only the formation of the mitotic spindle but also other cellular functions including transport as well.

### 1.3.5 The MT cytoskeleton as a therapeutic target

With an estimated expected number of 1,800,000 new cases of cancer in the United States in 2020<sup>58</sup>, the demand for new and improved treatment options for cancer is greater than ever. Cytoskeleton proteins are essential for almost all cellular processes including proliferation and migration. Therefore, alterations in their mode of action can result in cytoskeletal proteins aiding in the survival of tumour cells as well as tumour growth and invasion and makes them an attractive target for potential treatment options. Several classes of small-molecule antimetabolic agents are investigated for treatment options focusing on direct cytotoxicity or effects on tumour blood vessels (Table 1).

Some small molecules, developed to target the cytoskeleton, show either anti-angiogenic activity that can support treatment by preventing a tumour from building a vascular system to fulfil its nutritional needs or vascular disrupting activity such as combretastatin A4<sup>59</sup> that affects and destroys the already built vascular system of the tumour. This approach has plausible advantages for the number of cells that are targeted by the agent. Cytotoxic molecules target each cancer cell with severe side effects on healthy cells while vascular targeting molecules only attack vascular endothelial cells.<sup>60</sup> While CA4P has reached clinical trials, colchicine—another potentially powerful VDA—has proven to be too toxic in concentrations needed for its VD activity.

Colchicine's toxicity originates from its antimetabolic effects by binding tubulin—also in non-cancerous cells—and promoting GTPase activity and, therefore, loss of the GTP-cap independently from tubulin assembly. Disassembly of microtubules by colchicine is due to the disruption of lateral contacts needed for microtubule integrity.<sup>61</sup> Despite its severe cytotoxicity, colchicine is tremendously useful as a structural basis to develop new microtubule inhibitors that might have therapeutic potential. A variety of cancer types have been characterized with alterations in the microtubule cytoskeleton including expression changes of tubulin isoforms, altered posttranslational modifications and expression changes of microtubule-associated proteins. They are thought to have a great impact on resistance to chemotherapy, cell survival and tumour development.<sup>62</sup>



Tubulin inhibitors		
Tubulin destabilisers		Tubulin stabilisers
Vinca site binders	Colchicine site binders	Taxane site binders
vinblastine	colchicine	paclitaxel
vincristine	combretastatin	docetaxel
vinorelbine	podophyllotoxin	epothilones

**Table 1:** Classification of tubulin inhibitors and prominent representatives

## 1.4 Other cytoskeleton proteins

### 1.4.1 The actin cytoskeleton

Actin is the most abundant protein with most interaction partners and is able to transition between monomeric G-actin and filamentous F-actin states under the control of nucleotide hydrolysis. It is essential to cellular functions such as cell motility, adhesion, phagocytosis, protein sorting, maintenance of cell shape and polarity in the cytoplasm as well as forming the basis of muscle contraction together with the molecular motor myosin.<sup>63</sup> In the nucleus, actin plays an essential role in organizing chromatin remodelling complexes<sup>64</sup>, RNA processing or regulation of DNase I function<sup>65</sup>.

Actin in humans is encoded by six genes that express different isoforms and are highly conserved. There are four different isoforms of  $\alpha$ -actin in vertebrate muscle cells.  $\beta$ - and  $\gamma$ -actin in non-muscle cells only differ in four or five positions but still have different functions.<sup>66</sup> Actins also undergo posttranslational modifications that regulate their function.<sup>67</sup> The monomeric G-actin is separated into two lobes that are held together by ATP, which influences the conformation of the protein; without ADP or ATP-bound, the protein quickly denatures. Similar to microtubules, actin has structural and functional polarity with the ATP cleft being exposed at the minus end and covered by the next monomer at the plus end (Fig. 6a).

The polymerised actin filaments are commonly arranged into bundles or networks in the cell that have functionally the same role by providing support for the plasma membrane. In bundles, actin filaments are closely packed parallelly, while networks have a crisscross arrangement. This organisation is controlled by actin-crosslinking proteins that are able to bind to any kind of actin filament. Actin binding proteins include monomer binders such as profilin whose functions are nucleotide exchange, monomer capping, delivery and nucleation. Another class of proteins are filament binders that regulate bundling, crosslinking, membrane anchorage, branch formation, cytoskeletal linkers and there are capping and severing proteins.<sup>68</sup>

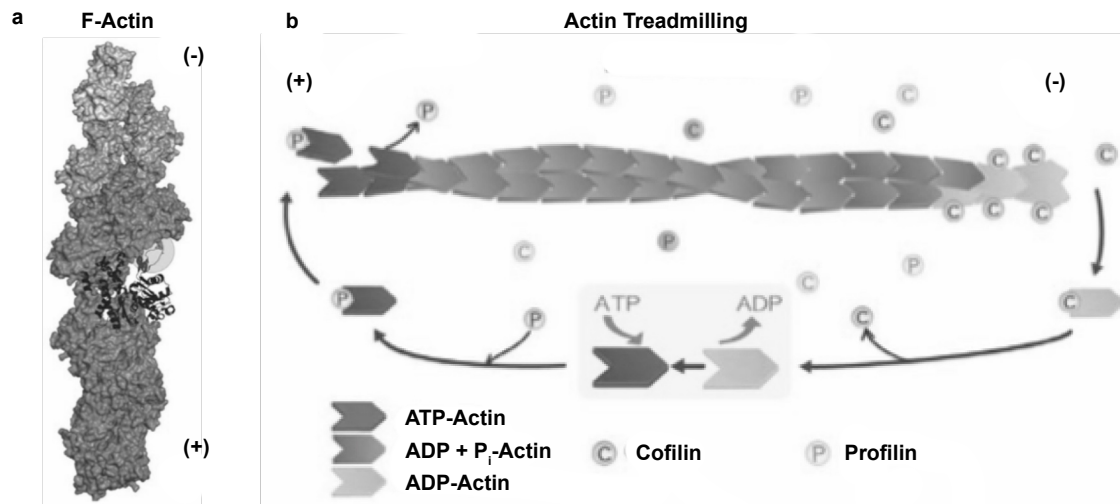


**Figure 6:** a: Actin structure; b: Actin treadmilling (adapted from Lee et al. <sup>69</sup>)

The actin richest area of a cell is the cortex that lies just below the plasma membrane and is linked to integral membrane proteins with a cell-type dependent structure. In platelets, cells have a discoid shape. After induction of blood clotting by clotting agents, the cells settle down and spread out several filopodia in a star-shaped manner, which needs extensive rearrangement of the actin cytoskeleton.<sup>70</sup> Actin shows a very distinct polymerisation behaviour divided into three steps. In the first period, the lag phase, G-actin aggregates into short, unstable oligomers until it reaches a certain length to provide a nucleus, which is rapidly elongated into a filament in the second phase. Actin monomers are added to both ends of the filament until it reaches a steady-state, which is an equilibrium between monomeric actin and filamentous actin (Actin “Treadmilling” Fig. 6b). Specialized actin-binding proteins regulate the assembly, length and stability of the actin filaments.<sup>68</sup>

The actin motor protein is myosin that couples ATP hydrolysis to conformational changes which allow movement of myosin and the actin filament relative to each other. Myosin II molecules gather into bipolar thick filaments that take part in muscle contraction, dependent on the Myosin II tail domain. Movement requires attachment of the actin filament to the Myosin II head, ATP-dependent bending of the head and detachment that results in movement between 5-25 nm.<sup>71</sup> Myosin cargos are vesicles, cell surface receptors, large protein complexes and organelles.<sup>72</sup>

Today, there is evidence that actin also has a major role in asymmetric cell division of human oocytes and actin-microtubule interplay is essential for bipolar spindle assembly and correct division of genetic material in human oocyte meiosis.<sup>73</sup> One additional role actin plays is executing apoptosis by inducing morphological changes such as cell rounding, blebbing and chromatin condensation.<sup>74</sup> The actin cytoskeleton can also play a role in promoting cancer. Oncogenic transformation often results in a decrease of focal adhesions and these changes in cell adhesion are one prerequisite of anchorage-independent growth and tumorigenesis.<sup>75</sup>

### 1.4.2. Intermediate Filaments

Another class of cytoskeleton proteins are intermediate filaments. They are composed of one or more members of a large family of proteins encoded by multiple genes<sup>76</sup> but their sequence similarity points to having one single ancestral gene<sup>77</sup>. Intermediate filaments are classified into six types: Types I and II are acidic and basic keratins, which have more than 15 isoforms and are mostly found in epithelial cells. Type III intermediate filaments include vimentin in the mesenchyme, desmin in muscle cells, peripherin in glial cells and astrocytes and glial fibrillary acidic protein in peripheral and central neurons. Type IV intermediate filaments are NF-L, NF-M and NF-H in mature neurons and internexin in the developing central nervous system. In lens fibre cells, the nonstandard Type IV intermediate filaments filensin and phakinin are found. Type V intermediate filaments are Lamins A, B and C that are found in the nucleus of all cell types.

Their main function is thought to be generating networks to shape cells, interactions with the extracellular matrix, cell type-specific functions and, even, gene expression.<sup>78</sup> All IF proteins share a conserved core domain consisting of a central  $\alpha$ -helical core flanked by globular N- and C-terminal domains. The core domain is a coiled-coil domain built from four long  $\alpha$ -helices and three nonhelical “spacers” with a conserved position and assembles through several intermediate structures that are built by lateral and end-to-end interactions.

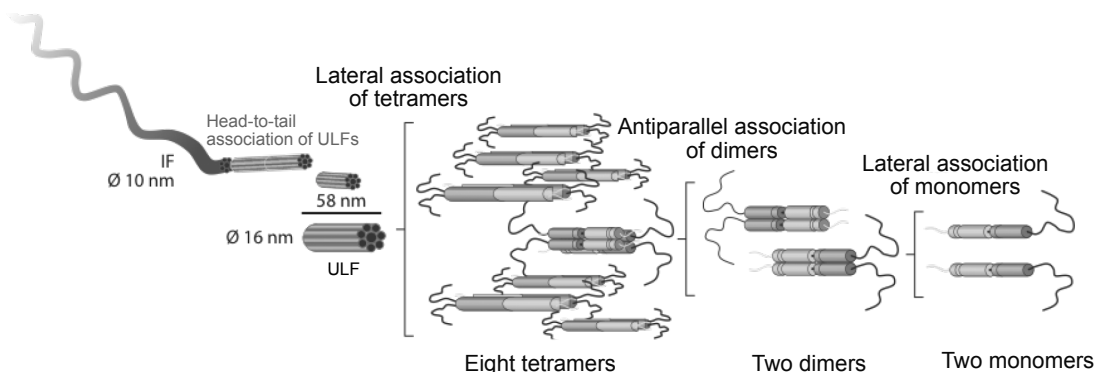


Figure 7: Structure and composition of intermediate filaments (adapted from Etienne-Manneville, 2018<sup>79</sup>)

Monomers assemble into dimers, which then associate in an antiparallel fashion into tetramers. Eight tetramers make up unit length filaments that are head-to-tail associated into the intermediate filaments<sup>79</sup> (Fig. 7). This assembly mechanism leads to filaments that are more flexible than actin and have the ability to highly stretch if necessary.<sup>80</sup> In contrast to microtubules and microfilaments, intermediate filaments are not polar, which means that their polymerisation and depolymerisation does not occur preferentially at one end. They do not need cofactors or hydrolysis of nucleoside triphosphates and are highly dynamic structures that can shorten, elongate and rearrange.<sup>81</sup> Intermediate filaments are regulated by post-translational modifications including farnesylation, phosphorylation, glycosylation and transglutamination as well as by associated proteins.<sup>82</sup> Mutations in intermediate filament genes can lead to severe pathologies including keratin diseases such as epidermolysis bullosa simplex, which can be fatal.<sup>83</sup> Expression of intermediated filament proteins can also be used to identify the tissue origin of poorly differentiated tumour cells.

### 1.4.3 Small-molecule inhibitors of the actin and IF cytoskeleton

The structural and molecular complexity of the actin cytoskeleton has made it difficult to shed light on how the actin cytoskeleton carries out its function and how it is regulated. One viable approach to study the function of the cytoskeleton is a pharmacological interference on the actin network. Similar to microtubule inhibitors, there are actin inhibitors that either disrupt the actin cytoskeleton or stabilise it and promote polymerisation. Actin interfering molecules conduct dramatic changes in actin driven processes including cell shape, cell motility, endo- and exocytosis and cell division and have played an extraordinary role in unravelling the biochemical properties of the actin cytoskeleton.

Cytochalasins are the best-known actin targeting molecules that bind and block the barbed end of actin filaments and prevent de/polymerisation similar to capping proteins and Cytochalasin D also influences the rate of ATP hydrolysis.<sup>84</sup> One setback in using Cytochalasins is the fact that they appear to have multiple effects on actin, which makes mechanistic studies challenging.<sup>85</sup> In recent years, it was possible to identify more actin targeted marine natural products including latrunculins, and jasplakinolides. Latrunculins, most famously Latrunculin A, inhibit actin polymerisation by binding monomeric actin and seem to have a simpler mode of action than Cytochalasins.<sup>86</sup> Studies have shown that Jasplakinolides induce growth inhibition and apoptosis in Jurkat T cells while murine thymocytes and spleen T cells seem to be resistant to Jasplakinolide-induced cell death. They seem to induce actin polymerisation similar to phalloidin—the most famous actin stabiliser—and compete with phalloidin for actin binding.<sup>87</sup> Further actin inhibitors currently under examination are swinholide A, misakinolide A, halichondramides and pectenotoxin II (Fenteany and Zhu 2003). Lately, the concept of photopharmacology has also reached actin cytoskeleton research by producing photoswitchable jasplakinolides called optojasps<sup>89</sup> that enhance spatiotemporal control for research applications including cell motility, viability and signalling.

Development of new improved modulators for the actin skeleton is one rate-limiting factor in cytoskeleton research and a challenge for chemical biology. Actin participates in a wide range of cellular processes is essential and can promote cancer, which makes it a theoretically possible therapeutic target. But using actin targeting molecules for therapeutic applications still bears the challenge of targeting actin without affecting skeletal and cardiac muscles<sup>90</sup>, which means it would be necessary to only attack distinct actin populations by targeting actin isoforms that are specifically upregulated in certain diseases such as cancer. (Some progress has been made with anti-tropomyosin compounds that reduce tumour cell growth without impairing cardiac structure and function<sup>91</sup> and Chondramin to inhibit actin in breast cancer cells<sup>92</sup>.)

Targeting the IF cytoskeleton chemically for research applications still trails far behind the other components of the cytoskeleton. So far, altered IF protein expression is mainly used for diagnostic and prognostic of certain types of cancer but chemical regulation for functional studies is vastly insufficient. The only molecule known so far targeting intermediate filaments is Whitakerin-A<sup>93</sup> that targets vimentin but with insufficient specificity.

## **1.5 Challenges and objectives of small-molecule cytoskeleton inhibitors**

All microtubule inhibitors as well as inhibitors of other cytoskeletal proteins have not only certain limitations including solubility issues, target specificity, and lack of spatiotemporal control in research applications, but also side effects due to toxicity, limitation of drug delivery methods, drug resistance and neuropathy in therapeutic settings. Despite the efforts to overcome these difficulties, there is a long way to go to produce improved microtubule targeting agents that are useful both as research tools and for therapeutic applications. The main prerequisite addressing such problems is the development of tools that enhance the basic understanding of the underlying cellular processes that involve the cytoskeleton and contribute to the development of cancer and other diseases. Furthermore, accessing information on the function and the consequences of disrupting cellular processes via small molecules can not only lead to a better understanding of the role of microtubules in interphase and during development but also, most importantly, during cell division (Fig. 8).

Profound knowledge of the consequences of modulating cytoskeleton dynamics in cell culture and *in vivo* can be achieved by evaluation of the effect of small-molecule cytoskeleton inhibitors on cellular processes in a spatiotemporal manner. To reach this goal, the development of new small molecules, less sensitive to the common obstacles of already known cytoskeleton inhibitors, should be expedited. Molecules that bear the prospect of advanced spatiotemporal control are of the essence to enlarge the biochemical toolbox for this important research topic. Not only is this important for basic research, but also in applied therapeutics research, since alterations in microtubule function and dynamics can lead to or exacerbate certain diseases, including cancer, gout and tubulinopathies.<sup>94</sup> These processes have to be known in detail to develop medical treatment options that are effective and have reduced and bearable side effects.

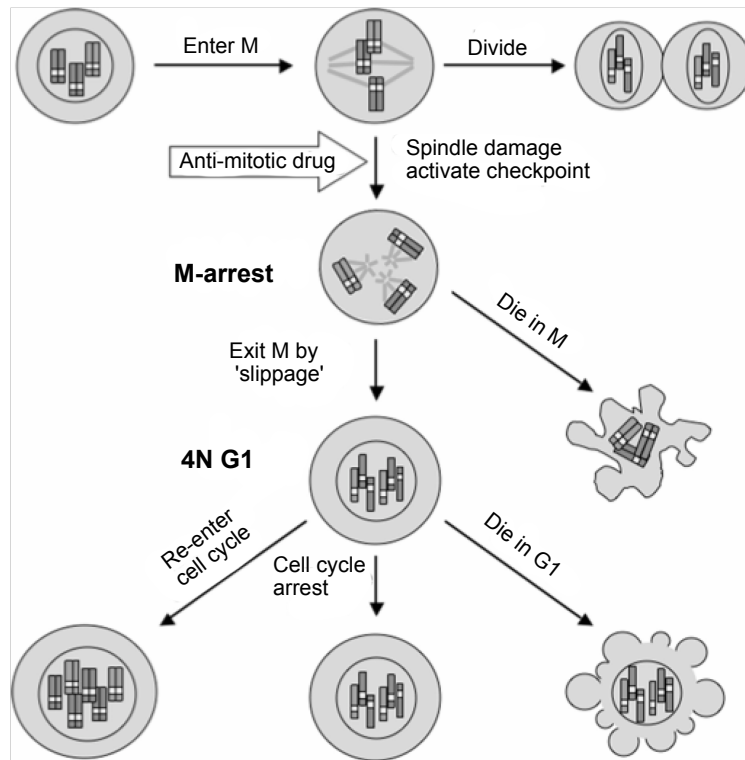


**Figure 8:** Anti-mitotic drug responses (adapted from Shi and Mitchison, 2017<sup>95</sup>)

## 2 Aim of the Ph.D. thesis

Unravelling microtubule function and regulation in various cellular processes is the main prerequisite for understanding their mechanisms as well as consequences of alterations in cells and *in vivo*. This is the central goal of this Ph.D. thesis. Since tubulin is hardly docile towards genetic tools, different approaches are necessary to access microtubule function. Another challenge is the vast amount of processes including cell motility, intracellular transport and organelle positioning, neurodegeneration and microtubule rearrangement during cell cycle phases that need to be analysed in a spatiotemporally controlled matter to get precise and useful insights in a biologically applicable time scale. Therefore, the enlargement and improvement of the small-molecule inhibitor toolbox that interacts with cytoskeleton proteins in general and microtubules in particular with the prospect of spatiotemporal control should be a primary objective in cytoskeleton basic research.

This thesis aims to explore and validate new photoswitchable microtubule targeting agents in cell culture and to assess their value as research tools for enhanced spatiotemporal control over microtubule function and dynamics. Therefore, photoswitches based on new molecular scaffolds were assessed to explore their validity regarding metabolic stability, tolerance towards imaging wavelengths, toxicity in the nanomolar range and solubility in aqueous environments. Another aim is to identify promising candidates for *in vivo* studies that can lead to improved microtubule-binding molecules for clinical approaches and as potential therapeutics. Non-photoswitchable molecules have been analysed regarding their potential to make more sophisticated vascular disrupting agents. In the following chapters, I present my research towards these aims, which has resulted in five published paper

### 3 Microtubule depolymerisers with potential VDA activity

This chapter is situated in the context of medicinal chemistry of tubulin-inhibiting agents.

#### **Background: tubulin inhibitors as vascular disrupting agents**

Small-molecule tubulin inhibitors have been developed predominantly as antimitotic/cytotoxic molecules that bind to the taxane or vinca site of tubulin and have been extensively used to treat various kinds of cancer.<sup>96</sup> Their main mode of action is to bind to tubulin and to inhibit tubulin de/polymerisation. The efficacy of destabilising microtubule inhibitors is based on their ability to disrupt the tubulin-microtubule equilibrium by the destruction of polymerised microtubules while the taxane-based inhibitors influence the equilibrium towards polymerised microtubules by stabilising GDP-bound microtubules. Both approaches have a negative effect on cell proliferation due to inhibition of the mitotic spindle and, therefore, cell division.

However, causing antimitotic effects in tumour cells by inhibiting their tubulin dynamics is not the only way that small-molecule tubulin inhibitors can be useful in basic research and in the fight against cancer. Another attractive option in cancer treatment is to employ tubulin inhibitors which can impair tumour blood flow. Tumours build their own system of blood vessels to fulfil their nutritional needs. However, the tumour blood vessel network is distinctly different from healthy vasculature because tumour blood vessels develop rapidly in response to overexpression of pro-angiogenic factors by neoplastic cells.

This abnormal growth results in immature and disorganized tumour blood vessel networks with little or no vessel hierarchy, and without typical structurally reinforcing layers of connective tissue and smooth muscle cells.<sup>97</sup> The lack of support makes the structural integrity of tumour vessels vulnerable towards mechanical stresses, such as to the rounding up of endothelial cells, which can be triggered by exposure to microtubule-depolymerising drugs.<sup>98</sup> Therefore, blood flow in tumour vessels is suppressed by these depolymerising agents, which are classed as "vascular disrupting agents" (VDAs). By impairing tumour blood flow, VDA treatment cuts off the supply of nutrients and oxygen needed for tumour survival, leading to necrosis of the tumour core (Fig. 9).<sup>99</sup>



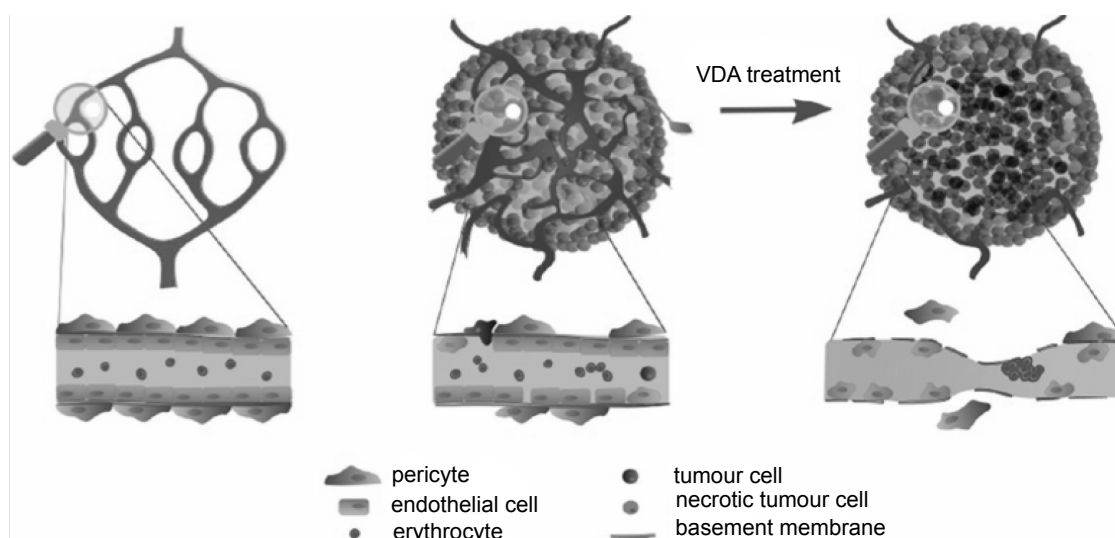


**Figure 9:** Schematic representation of VDA treatment on tumour vascularisation (adapted from Pérez-Pérez, 2016<sup>99</sup>).

### Properties of vascular disrupting agents: motivation for the work

A class of anti-tubulin agents that have promising properties as VDAs are the colchicine domain inhibitors (CDIs). These bind to the colchicine binding domain at the  $\alpha$ -/ $\beta$ -tubulin interface and inhibit tubulin polymerisation. Fortunately, in contrast to tubulin binders that target the vinca or taxol binding sites, CDIs seem to be indifferent to typical antimetabolic resistance mechanisms (overexpression of the  $\beta$ III-tubulin isotype, or the P-glycoprotein export pump<sup>100</sup>). Colchicine itself is not tolerated *in vivo* in a dosage that is sufficient for VDA activity, but other CDI analogues, including combretastatins, are. Structure-activity relationship (SAR) studies have shown that the CDI pharmacophore centres on two aryl-rings with distinct patterns of substituents.<sup>101</sup> Notably, the scaffold interior (nature of the aryl system) is variable and can ensure desirable tubulin-binding potency *in vitro* as long as the right arrangement of exterior substituents is chosen. However, the scaffold interior plays an essential role *in vivo* because it determines whether the molecule is metabolically stable towards cellular catabolic mechanisms. Enhancing overall robustness, especially, of the scaffold-dependent properties against metabolic processing such as ADME/PK parameters is highly desirable in a new generation of vascular disrupting agents that can be more useful therapeutic applications.

### Short summary of the IQTub work

We introduce a new class of colchicine domain tubulin inhibitors based on an isoquinoline-biaryl as a scaffold that addresses the current limitations of metabolic stability of colchicine tubulin inhibitors. The compounds have been rationally designed for tubulin binding potency by using substituent patterns similar to colchicine, but explore fully aromatic biaryls as a scaffold with the aim of being resistant towards *in vivo* inactivation and metabolic degradation mechanisms. Ensuring decent solubility was a priority, and inspiration was taken from designs of other CDIs, typically applied as soluble prodrugs that are cleaved and activated by cell-

surface or intracellular enzymes.<sup>99</sup> An inactively designed permutation control has also been used in the study, to prove the SAR-based design concept.

The mechanism of tubulin inhibition has been confirmed by antiproliferative assays, tubulin *in vitro* polymerisation, immunofluorescence of the microtubule cytoskeleton, cell cycle partition experiments and by directly visualizing the effect of the lead compound to polymerising microtubule assays by using an EB3-comet assay. The lead compound IQTub4 has been analysed regarding drug-relevant properties including metabolic stability, drug-drug interaction studies and assessment of tolerability towards future efficacy and mechanism studies in mouse was performed. The tolerability study showed that IQTub4 has good stability towards mouse and human liver microsomes and does not inhibit human cytochrome P450s. Furthermore, IQTub4 displayed no significant effect on the hERG channel at the highest tested concentration and showed an acceptable distribution coefficient logD at pH 7.4. These results are related to the (so far unevaluated) potential of IQTubs to be potent, metabolically stable and well-tolerated vascular disrupting agents. Therefore, they are excellent candidates for potential as drugs, which will be discussed further below (see Conclusions).

#### Authorial Contributions

I analysed these newly developed compounds in cells, confirming their bioactivity in anti-proliferation assays (Fig. 2a), and visualized their depolymerising effect on the tubulin cytoskeleton by immunofluorescence staining (Fig. 4). Furthermore, I explored their antimitotic effect by cell cycle analysis showing induction of G2/M arrest (Fig. 5a) (in collaboration with C. Heise and J. Ahlfeld), which supports their mechanism as microtubule inhibitors.<sup>59</sup> Additionally, I demonstrated the effect of our compounds on microtubule dynamics in living cells by an EB3-comet assay (Fig. 5c), using an EB3-GFP fusion protein in transiently transfected HeLa cells for live-cell imaging to visualize the growth of microtubules under a confocal microscope. Altogether, my analyses demonstrate that rationally designed active IQTubs have antiproliferative effects, which are most likely due to the interference with tubulin polymerisation due to G2/M arrest in cell cycle experiments, supported by visual tubulin depolymerisation in immunofluorescence samples and a visible effect on polymerising microtubules in live-cell imaging.



Contents lists available at ScienceDirect

European Journal of Medicinal Chemistry

journal homepage: <http://www.elsevier.com/locate/ejmech>

Research paper

## Isoquinoline-based biaryls as a robust scaffold for microtubule inhibitors



Yvonne Kraus<sup>1</sup>, Carina Glas<sup>1</sup>, Benedikt Melzer, Li Gao, Constanze Heise, Monique Preuße, Julia Ahlfeld, Franz Bracher, Oliver Thorn-Seshold\*

Department of Pharmacy – Center for Drug Research, Ludwig-Maximilians University of Munich, Butenandtstrasse 5-13, Munich, 81377, Germany

### ARTICLE INFO

#### Article history:

Received 9 August 2019  
 Received in revised form  
 8 October 2019  
 Accepted 6 November 2019  
 Available online 9 November 2019

#### Keywords:

Colchicine  
 Cytoskeleton  
 Isoquinoline  
 Microtubule dynamics  
 Tubulin polymerisation inhibitor

### ABSTRACT

We here report the discovery of isoquinoline-based biaryls as a new scaffold for colchicine domain tubulin inhibitors. Colchicinoid inhibitors offer highly desirable cytotoxic and vascular disrupting bioactivities, but their further development requires improving *in vivo* robustness and tolerability: properties that both depend on the scaffold structure employed. We have developed isoquinoline-based biaryls as a novel scaffold for high-potency tubulin inhibitors, with excellent robustness, druglikeness, and facile late-stage structural diversification, accessible through a tolerant synthetic route. We confirmed their bioactivity mechanism *in vitro*, developed soluble prodrugs, and established safe *in vivo* dosing in mice. By addressing several problems facing the current families of inhibitors, we expect that this new scaffold will find a range of *in vivo* applications towards translational use in cancer therapy.

© 2019 Elsevier Masson SAS. All rights reserved.

### 1. Introduction

The protein tubulin is a prime target for development of cancer therapeutic inhibitors, most famously since the microtubule cytoskeleton it forms plays a crucial role in mitosis, which is required for the progression of all cancer types [1,2]. Tubulin-inhibiting Antimitotic cytotoxins from the classes of taxanes and of vinca alkaloids have become blockbuster drugs, and have been used in the treatment of millions of patients [3]. A third class of tubulin inhibitors are the colchicine domain inhibitors (CDIs). CDIs with low or sub-nanomolar antiproliferative/cytotoxic activity *in cellulo* have been extensively developed. However, *in vivo* their main bioactive mechanism at tolerated doses is not cytotoxicity mediated through tubulin disruption in target (tumour) cells, but instead vascular disrupting agent (VDA) activity, mediated by disrupting microtubule integrity in the endothelial cells lining the vascular system. In the tumour neovascular network this disruption is poorly withstood, leading to stanching of tumoural blood flow and necrosis of the tumour interior [4]. VDA activity is thus highly desirable as a complementary mechanism to typical cytotoxins that usually

target the tumour exterior but are poorly effective in the interior [5].

The prototypical requirements for CDI bioactivity have been well studied [6]. CDIs typically display pharmacophore-relevant groups on two aryl rings, here denoted as north and south rings, that are usually twisted with respect to one another [7]. The south ring typically features a 3,4,5-trimethoxy substitution pattern and the north ring a monomethoxy substituent with a hydrogen or an optional small polar group (OH, NH<sub>2</sub>, F) in the *ortho* position [8,9]. These substituents ensure potent binding to tubulin when correctly arranged on the scaffold “exterior”. Combretastatin A-4 (**CA4**; Fig. 1a) [10] illustrates these features. It is a *Z*-stilbene that acts as a low nanomolar cytotoxin *in cellulo*, and its *E*-isomer - whose methoxy groups do not project in the correct directions - is several orders of magnitude less bioactive [11].

A crucial result observed during CDI development is that although *in cellulo* a broad range of scaffold “interiors” for CDIs can deliver good cytotoxic potency as long as the “exterior” substituents are correctly arranged, *in vivo* the scaffold choice often determines medicinal chemistry factors critical for therapeutic applications. For example, **CA4** reached Phase III clinical trials as a VDA in the form of its phosphate prodrug **CA4P**, while colchicine (which has a similar disposition of substituents and similar *in cellulo* potency) is not tolerated at the doses required for VDA activity (Fig. 1a) [12,13]. Typical scaffold-dependent factors decisive for

\* Corresponding author.

E-mail address: [oliver.thorn-seshold@cup.lmu.de](mailto:oliver.thorn-seshold@cup.lmu.de) (O. Thorn-Seshold).

<sup>1</sup> These authors contributed equally to this work.

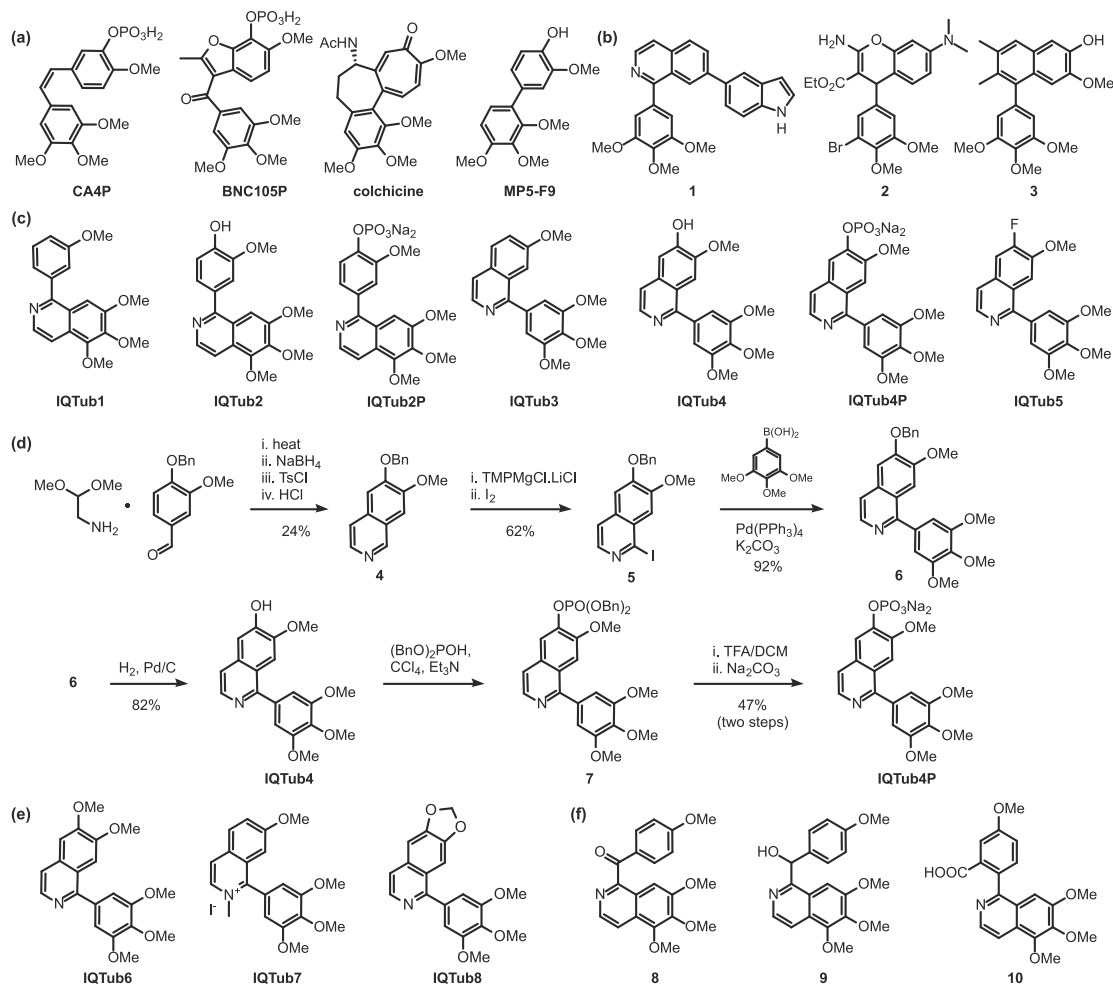


**Fig. 1.** (a) Archetypal literature-known CDIs. (b) Selected literature-reported biaryl-type CDIs. (c) IQTubs and their prodrugs. (d) Synthetic route to IQTubs, shown exemplarily for IQTub4 and IQTub4P. Ts: *para*-toluenesulfonyl, TMP: 2,2,6,6-tetramethylpiperidyl, Bn: benzyl, TFA: trifluoroacetic acid. (e,f) Control IQTubs, and other control compounds similar to IQTubs, used in this study (IQTub6[29], IQTub8[30], 8 and 9[31], and 10[32] were previously reported but not biologically evaluated).

*in vivo* use include robustness to spontaneous deactivation *in vivo* (e.g. stilbenes suffer *cis* to *trans* isomerisation [14]), as well as traditional ADME/PK parameters including metabolism (e.g. cytochrome degradation of, or inhibition by, the stilbene double bond [15,16], or metabolic processing of aryl aryl ketone bridges [17,18]) and overall plasma residence time [14], as well as their ease of synthetic access.

CA4-inspired CDIs with north and south rings held at a twist are the class of CDI VDAs which has progressed furthest in clinical trials, and these have been excellently reviewed [6,7,13]. A variety of such scaffolds have been tested, aiming to improve upon the *in vivo* properties of CA4P. Beyond stilbenes (like CA4P analogues CA1P [19] and AVE8062 [20]), colchicinoids such as ZD6126 [21], aryl aryl ketones such as BNC105P [22], and a range of other scaffolds have been used for CDIs, several of which feature *in vivo*-confirmed VDA activity (Fig. 1a) [4]. Other classes of CDIs, such as the quasi-planar

indanocine, plinabulin, nocodazole and indanorin [13], are less developed for *in vivo* applications and generally have not been confirmed to display VDA activity. Improved techniques for screening for VDA activity [23] are currently opening new perspectives for VDA development. While no CDIs have yet been approved as VDAs [24], the value of investigating new CDI scaffolds with potentially improved VDA activity has been elegantly stated by Fojo [25]; we here report our progress in this area [26].

## 2. Results

**Design and Synthesis.** We primarily desired to develop CA4-inspired CDIs with VDA potential, featuring a molecular scaffold that would be highly robust to *in vivo* inactivation and/or metabolic degradation mechanisms that affect the major VDA scaffolds in clinical trials (stilbenes and aryl aryl ketones). By contrast to the

range of twisted bis-aryl structures with one- or two-atom bridging groups between the rings (e.g. **BNC105P** or **CA4P**, respectively) and the CDIs with non-aromatic bicyclic rings (e.g. dihydronaphthalenes, benzosuberenes, benzodiazepines) [6,27,28], we found that fully aromatic biaryls are sparsely reported and underexplored as CDIs. This presented an opportunity, as a biaryl bond promises to be more metabolically resistant than other bridging bond types; biaryls can be druglike and do not require stereospecific synthesis; a biaryl is permanently in a ring-twisted state that is usually crucial for CDI bioactivity [6] (in contrast to stilbenes that can isomerise to a planar state); and biaryls can be constructed by easily diversifiable late-stage cross-couplings. Motivated by similar logic, a very limited number of CDI biphenyls such as **MP5-F9** [14] have previously been developed (Fig. 1a), but their potency was approximately 500-fold less than of the cognate stilbene-type CDIs and as far as we are aware they were unfavourable for further development. Alternatively, Miller et al. [17,18] reported a series of triaryl CDIs (e.g. **1**; Fig. 1b). However, we considered that triaryl designs introduce undesirable synthetic complexity and molecular weight, and they do not promise solubility high enough for *in vivo* application (typically, > 10 mM injection concentration in aqueous media for small animal studies). We therefore determined to explore biaryls that occupy similar space to colchicine itself, i.e. that feature one bicyclic and one monocyclic aromatic ring, in the hope that this would allow high potency, good solubilisation, and minimal complexity in our designs.

It was not obvious whether the north or the south ring inside the CDI pharmacophore would be more suitable for replacement by such a bicyclic aromatic ring. Cell-active CDIs with a large north ring are well attested (e.g. **2** and **3**; Fig. 1b) but the south ring has also been reported to tolerate replacement with bicyclics [13], which our recent experience [33–35] has supported. We therefore determined to synthesise and evaluate both “south” and “north” ring replacement types. We focused on isoquinolines as the bicyclic ring (rather than e.g. naphthalenes) due to isoquinolines’ straightforward and flexible retrosynthesis, as well as the solubility enhancement expected from including a ring nitrogen. Within the south and north sets we also wanted to explore both hydrogen and small polar group substituents at the variable position. This ligand-based design process yielded south ring replacements **IQTub1-2** and north ring replacements **IQTub3-5**. According to established SAR [7,13] we desired that **IQTub2** and/or **IQTub4** would prove the most potent members of their sets, according to preference of the isoquinoline for occupying the south or the north position. To render them potentially *in vivo* suitable we also designed their phosphate prodrugs **IQTub2P/IQTub4P** (Fig. 1c). The phenolic phosphate prodrug strategy has been particularly successful for CDI VDAs (**CA4P** and **CA1P** [36], **ZD6126** [21], **BNC105P**<sup>22</sup>) in conferring suitable water-solubility for *in vivo* application (allows i.v. injection at high concentration in aqueous media [22] and reduces plasma protein binding compared to the otherwise lipophilic phenols [21]) [13]. Although the phosphates are not cell permeable they can be efficiently and nonspecifically cleaved extracellularly by diverse phosphatases to liberate the active, membrane-permeable phenols which diffuse passively across membranes to exert bioactivity by binding to tubulin at the lipophilic colchicine binding domain [37].

Noting that a CDI’s bioactivity is typically abolished if its variable position is not occupied by small groups (but instead by OMe, Et, etc) [13], we designed *O*-methylated **IQTub6** in the hope it would be inactive (a “designed-inactive” control [33,34]). This probes whether **IQTubs** reproduce the general CDI structure-activity relationship (SAR): if so, it would support the conjecture that **IQTubs** are also CDIs. To explore other polarity-altering alkylations, we also designed *N*-methylated quaternary **IQTub7** and benzodioxolo **IQTub8**, to extend our SAR in case the north ring

replacements proved bioactive (Fig. 1e). Searching the literature across a similar scaffold space showed that only **IQTub6**, first reported in the 1930s [29] as a papaverine analogue, and **IQTub8**, reported by Reeve and Eareckson in 1950 [30] during a study towards di- and tetrahydroisoquinoline analogues of podophylotoxin, had previously been reported. However neither of these compounds had been evaluated for bioactivity nor were they used in SAR studies, so we determined to test them ourselves (see below and Supporting Information).

The isoquinoline building blocks were synthesised by a modified Pomeranz-Fritsch reaction according to Reimann [38]. These were directly metalated at C-1 using Knochel-Hauser base [39] similarly to a published procedure [31], and Suzuki coupled with appropriately-substituted phenylboronic esters [32], delivering the targets **IQTub1-5** and **IQTub8** after optional deprotection. Methylating **IQTub3** and **IQTub4** yielded **IQTub7** and **IQTub6** respectively. This synthetic protocol is tolerant to a range of substituents, and allows late-stage diversification from a given isoquinoline scaffold with high overall yields (Fig. 1d and Supporting Information). All **IQTubs** were then taken into cell biological testing for antiproliferative activity, using the resazurin viability assay in HeLa cervical cancer cell line [40].

**Structure-activity studies of IQTubs.** Neither of the south ring replacements showed strong cytotoxicity (apparent EC<sub>50</sub>: **IQTub1** ~ 15 μM, **IQTub2** ~ 50 μM). We controlled in two orthogonal ways whether re-orientation of the substituents could permit bioactivity while still retaining the south ring replacement strategy. Firstly, noting that ketone-bridged compounds such as **BNC105P** (Fig. 1a) and phenstatin [13] are potent CDIs, we slightly increased the flexibility between the aromatic rings by introducing a one-atom bridge to allow subtle changes in relative ring orientation while maintaining the positioning of all methoxy groups - an attested strategy in VDA development [6]. To this end we tested ketone bridged alkaloid thalimicrinone (**8**) as well as its sp<sup>3</sup>-configured carbinol synthetic precursor **9** [31] (Fig. 1e), however, neither was bioactive in our hands (EC<sub>50</sub> > 80 μM). Next, we reoriented the north ring methoxy group from the *meta* into the *para* position, in case a larger bite angle between the south and north ring methoxy substituents would be better accommodated. For this we examined oxoisoporphine precursor **10** from previous work [32] (Fig. 1e), but this too was inactive in our hands (EC<sub>50</sub> > 100 μM). We concluded that south ring replacement with the isoquinoline was not viable.

Pleasingly though, the designed-active north ring replacements **IQTub3-5** showed strong bioactivity with cellular cytotoxicity EC<sub>50</sub> values in the mid-nanomolar range (Fig. 2a). As hoped, the designed-inactive *O*-methylated control compound **IQTub6** was indeed inactive (EC<sub>50</sub> > 20 μM), suggesting that the north ring replacement **IQTubs** obey the SAR expected for colchicine site binders. We found no literature precedence for expecting either activity or inactivity of charged compound **IQTub7**, but in the event it was inactive (EC<sub>50</sub> > 30 μM). Previously reported structure **IQTub8** (see also discussion in Supporting Information) [30] featuring a benzodioxole north ring - which could be able to bind similarly to isovanillyl **IQTub4** according to literature SAR [13] - proved inactive in our hands (EC<sub>50</sub> > 20 μM; Fig. 2b).

However, as we observed turbidity while handling **IQTub8**, we assumed that its apparent cellular bioactivity could have been limited by poor solubility. We were therefore motivated to cross-check whether water-soluble prodrugs of both scaffold orientations would support our choice of the north ring strategy and confirm the inactivity of the south ring type. We synthesised phenolic phosphate prodrug **IQTub4P**, which was soluble in aqueous buffer to >10 mM (see Supporting Information). It displayed near-identical cytotoxicity in cell culture as its free phenol form **IQTub4** (Fig. 2) indicating that *O*-phosphorylation is reliable as a strategy for

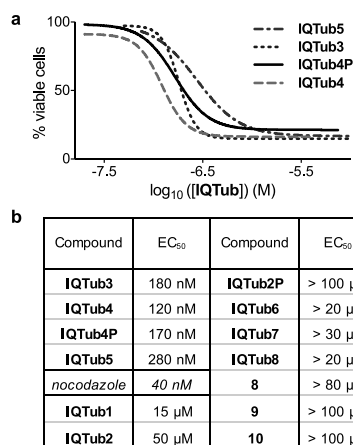


**Fig. 2.** Cell viability assessment of **IQTubs**. (a) Antiproliferation assays showed strong dose-dependent cytotoxicity for north ring designs **IQTub3**, **IQTub4**, **IQTub4P** and **IQTub5** (one representative experiment of three independent experiments shown). (b) EC<sub>50</sub> values for the bioactive compounds and permutation controls, as well as reference compound nocodazole. (HeLa cell line; 48 h incubation; resazurin assays; see also Supporting Information).

soluble prodrugs (see below); comparison of both compounds' cytotoxicities in a second cell line (HL-60 human leukaemia line) confirmed both their mid-nanomolar bioactivity and their close correspondence of potency (EC<sub>50</sub>s in HL-60: **IQTub4**: 340 nM, **IQTub4P**: 570 nM). To check whether **IQTub1-2**'s bioactivity could have been undercut by poor solubility, we synthesised phosphate prodrug **IQTub2P**, but its cytotoxic activity was not measurable (EC<sub>50</sub> >> 100 μM). We concluded that neither solubility nor substituent orientation effects had obscured the cytotoxicity of **IQTub1-2**, and that the isoquinoline is not well-tolerated as a south ring replacement. We attributed the weak apparent anti-proliferative activity of the "inactive" **IQTubs** (e.g. **IQTub1**, **IQTub6**) as tubulin-independent aggregation-dependent effects, known for similar motifs [9,33], and confirmed this in mechanistic studies (see below).

With their bioactivity matching our SAR understanding, we considered that north ring replacement **IQTubs** were a viable approach to a new scaffold for CDIs, and we determined to proceed with the potent and well-soluble **IQTub4P**.

**Drug-relevant properties of lead IQTub4/IQTub4P.** We then measured selected parameters of **IQTub4P** that would be relevant for *in vivo* applications of the isoquinoline-based biaryl (using **IQTub4** in these assays since it should be the *in situ*-dephosphorylated **IQTub4** that penetrates into cells to reach its site of action [13]). By examining its compound stability in the presence of mouse and human liver microsomes, we concluded that **IQTub4** has good metabolic stability (Fig. 3a). Studies with the five major human cytochrome P450s showed no significant inhibition of these CYPs by **IQTub4**, indicating that it may escape typical drug-drug interaction pathways (Fig. 3b). A fluorescence polarisation reporter assay for hERG channel inhibition showed no significant effect at the highest tested concentration (Fig. 3c). Lastly, we experimentally determined the distribution coefficient logD at pH 7.4 to be 2.18, which is within a range (1–3) considered optimum for general *in vivo* use [41]. These results suggested that **IQTub4** was suited for further pharmacological evaluation (see Supporting Information for further details and assay benchmarking).

**IQTubs inhibit microtubule structure and function.** We next

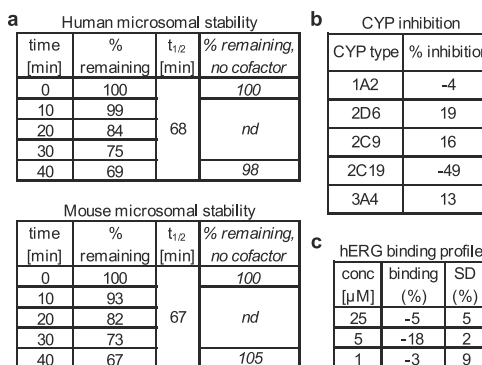


**Fig. 3.** Drug property assessments of **IQTub4**. (a) Metabolic stability against mouse and human liver microsomes (**IQTub4** at 2 μM). (b) Inhibition assay against five human cytochrome P450s (**IQTub4** at 10 μM). (c) hERG channel inhibition assay.

moved to confirm whether the cytotoxic **IQTubs**' mechanism of action was indeed inhibition of tubulin polymerisation. We first visualised their capacity for microtubule (MT) network perturbation in cell culture. Sustained tubulin polymerisation inhibition disorganises and ultimately depolymerises cellular MT networks. We observed dose-dependent MT network depolymerisation with the active **IQTubs** (Fig. 4a and b), and z-stack projection images additionally revealed that cells treated with low doses of active **IQTubs** already accumulated into rounded, mitotically arrested states with defective spindles and chromosome alignments (Fig. 4c). These are hallmarks of treatment with MT-depolymerising agents. In contrast, neither designed-inactive SAR control **IQTub6** (Fig. 4a) nor non-cytotoxic **IQTub7-8** (Fig. S5) gave any MT disorganisation in this assay even at the highest tested concentrations, suggesting that the bioactivity observed for **IQTubs** is tubulin-specific.

The cytotoxic effects of CDIs *in cellulo* typically arise due to interruption of tubulin reorganisation in the mitotic spindle, which blocks mitosis, ultimately triggering cell death (as observed under longer-term treatments in the viability assays). If **IQTubs** tubulin-disrupting effects were indeed the cause of their observed cytotoxicity, treated cells should be measurably arrested in G2/M-phase. We therefore used flow cytometry to perform cell cycle analysis of HeLa cells under **IQTub4P** treatment. Results indeed showed extensive G2/M-arrest from concentrations as low as 500 nM (Fig. 5a).

**IQTubs inhibit tubulin polymerisation dynamics.** Aiming to confirm the molecular mechanism of **IQTub** bioactivity as one of direct binding to tubulin (rather than binding to regulatory proteins or affecting signalling), we then tested for inhibition of tubulin polymerisation dynamics in cell-free settings using purified tubulin. We observed closely similar polymerisation inhibiting activity for **IQTubs** as for colchicine itself, which strongly supported the direct binding interpretation and the mechanistic classification of the **IQTubs** as microtubule depolymerisers (Fig. 5b).

Inhibition of tubulin polymerisation dynamics was then directly assayed *in cellulo* by live-cell confocal video microscopy in HeLa cells transfected to express EB3-YFP fusion protein. EB3-YFP is a fluorescent marker that selectively labels the growing tips of microtubules and manifests as moving "comets" when MTs are growing; the comets stop and disappear upon inhibition of tubulin polymerisation [9]. Within 2 min of applying prodrug **IQTub4P**, cellular EB3 comets stopped and vanished, indicating that extracellular dephosphorylation to **IQTub4** followed by internalisation

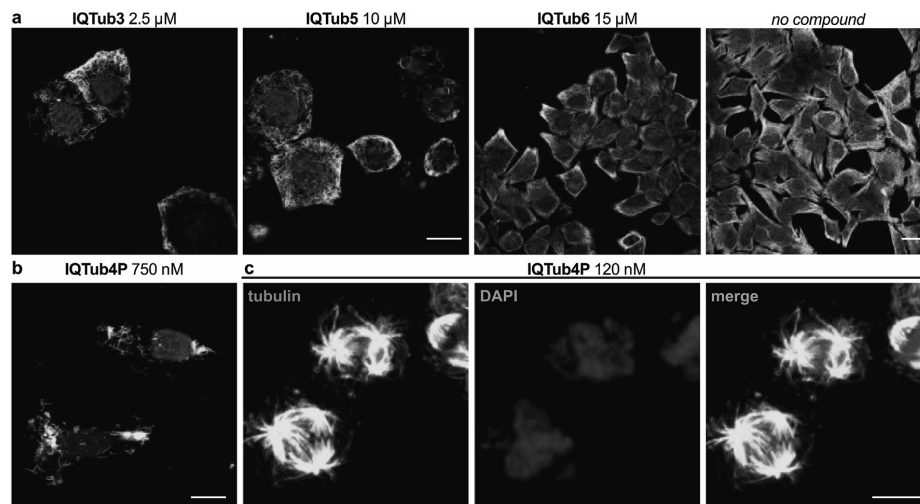


**Fig. 4.** Confocal microscopy assessment of cellular microtubule networks after treatment with **IQTubs**. (a) **IQTub3** and **IQTub5** induce MT network breakdown (panels on same scale) while SAR control **IQTub6** does not alter MT network integrity (compare to untreated control; panels on same scale). (b) Prodrug **IQTub4P** is active *in cellulo* at submicromolar doses. (c) 120 nM **IQTub4P** already leads to mitotic arrests and the formation of aberrant multipolar spindles (tubulin panel) with resulting unstructured chromosome alignment (DAPI panel). Maximum intensity projection along the z-axis of an image stack. (HeLa cells, 24 h treatment, green:  $\alpha$ -tubulin stain for microtubule polymer network, blue: DAPI nuclear counterstain, all scale bars 20  $\mu$ m; see also Fig. S5). (For interpretation of the references to colour in this figure legend, the reader is referred to the Web version of this article.)

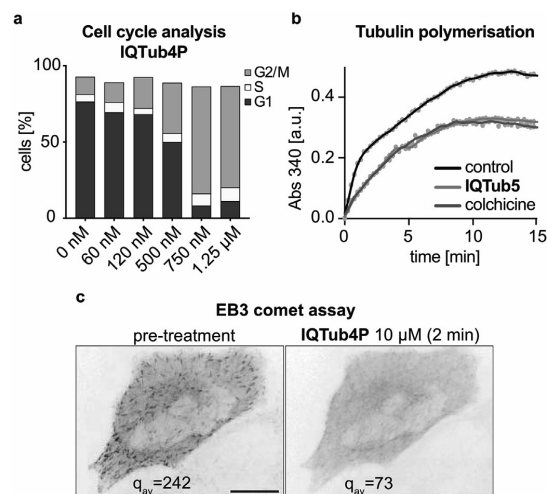


**Fig. 5.** (a) Cell cycle analysis of **IQTub4P**-treated cells shows potent induction of G2/M arrest. (b) **IQTub5** inhibits tubulin polymerisation (cell-free) with similar potency to the reference tubulin inhibitor colchicine (turbidimetric assay; **IQTub5** at 20  $\mu$ M, colchicine at 16  $\mu$ M). (c) Imaging of MT polymerisation dynamics in live HeLa cells transfected with EB3-YFP. EB3 comets were tracked, before and then 2 min after treatment with 10  $\mu$ M **IQTub4P** (comet tails tinged purple, tips shown black); EB3 comet count ( $q$ ) statistics were averaged over 7 cells (see Supporting Information for details).

rapidly gives potent inhibition of cellular tubulin polymerisation dynamics (Fig. 5c).

**IQTubs are well-tolerated *in vivo*.** These assays offered several independent indications that **IQTubs** are potent, robust

microtubule depolymerisers with SAR and performance matching expectations of CDIs. We considered this promising for their potential for *in vivo* performance, ultimately aiming at development of **IQTubs** as a new CDI VDA scaffold. To finish this early compound development study, we therefore assessed safe dosing parameters of **IQTub4P** *in vivo* in male and female Balb/c mice. Dose-escalation studies (i.p. and i.v. administration routes) established a single-administration maximal tolerated dose of 32 mg/kg (i.p.) and 50 mg/kg (i.v.). Repeated dosing (3 administrations, 48 h intervals) were conducted with 25 mg/kg for both i.v. and i.p. routes and were tolerated, thus **IQTubs** may avoid short-term cumulative toxicity, which is known for the most promising CDI VDAs. We consider these results favourable for further *in vivo* progress of this new scaffold; by comparison the archetypal CDI colchicine has a murine maximal tolerated dose around only 1 mg/kg [20].

### 3. Discussion and conclusion

The success of the taxanes and vinca alkaloids in clinical oncology has stimulated intense interest in novel tubulin inhibitors. Colchicine domain inhibitors offer a biological activity profile which not only includes the antimitotic and pro-apoptotic effects common to all tubulin inhibitors, but also vascular disrupting effects that are highly desirable for cancer treatment. This has stimulated much research and development of CDIs and several have reached late-stage clinical trials for cancer treatment, although none have yet reached clinical approval.

Here we have performed ligand-based design of isoquinoline-based biaryls – a simple and robust chemical backbone – as new scaffolds for potent CDIs. These **IQTubs** are easily accessible with straightforward late-stage diversification using short, high-yielding synthetic routes; and they have shown excellent performance in early measurements of *in vivo*-relevant druglike properties. They display high cellular potency in long-term cellular studies as well as in short-term live-cell imaging. They deliver robustness to the

scaffold-specific spontaneous deactivation mechanism affecting stilbene CDIs as well as metabolic liabilities of other major CDI families, thus offering potentially advantageous ADME/PK compared to the current CDIs. Through SAR studies as well as extensive cellular and cell-free assays, we have clarified and supported their mechanism of action, showing multiple proofs that their tubulin inhibition matches the bioactivity expected for CDIs. Lastly, we have determined the *in vivo* tolerability for the lead compound **IQTub4P** to be more than an order of magnitude higher than that of the archetypal CDI colchicine, which is promising for future research into the *in vivo* applications and VDA performance of this potent, biologically robust IQT scaffold.

It should also be noted that VDAs are typically designed for short plasma residence times (with high dose tolerance), enabling fast but transient dose delivery to vascular endothelial cells, aiming that in this way only the more susceptible tumour neovasculature should lose microtubule-based mechanostasis during the time of exposure, therefore giving tumour-selective vascular shutdown [24,42]. In this context, the speed of dephosphorylation-internalisation-inhibition observed with **IQTub4P** (Fig. 5c) is particularly encouraging.

The current **IQTubs** already feature satisfying cellular potency, but we fully expect that ongoing SAR studies will deliver analogues with higher potency and/or significantly tuned biochemical properties. Still, their therapeutic performance cannot yet be predicted since cellular potency is known not to be the limiting factor for CDI VDA activity *in vivo*. Cardiotoxicity is a major dose- and therapy-limiting parameter with CDIs, which is known to be scaffold-dependent in that it is strongly affected by ADME/PK as well as molecular structural parameters [24]. In this context, enabling exploration of a new scaffold class with the potential for strongly differentiated ADME/PK and scaffold-dependent tolerability is a valuable step for the development of CDI VDAs and investigations of these parameters are ongoing.

The ease and substituent tolerance of **IQTub** synthesis is another important feature of this work, comparing favourably with many CDI scaffold systems. However, more broadly, we consider that the design logic of scaffold hopping from stilbene to isoquinoline-based biaryl scaffolds to improve *in vivo*-relevant drug properties is an exciting advance, promising medicinal chemistry applications to targets well beyond the current CDIs.

In closing, we predict that by unlocking isoquinoline-based biaryl tubulin inhibitors, this research will open up new possibilities for refinement of tubulin inhibitors, for *in vivo* VDA development, and for broader applications of robust biaryl designs to other pharmacophores.

#### 4. Experimental section

Full and detailed chemical and biological protocols can be found in the Supporting Information.

**Compound synthesis and characterisation.** All reactions were performed with unpurified, undried, non-degassed solvents and reagents from commercial suppliers (Sigma-Aldrich, TCI Europe, Fisher Scientific etc.), used as obtained, under closed air atmosphere without special precautions, unless otherwise described. Manual flash column chromatography was performed on Merck silica gel Si-60 (40–63  $\mu\text{m}$ ). MPLC flash column chromatography was performed on a Biotage Isolera Spektra system, using Biotage prepacked silica cartridges. Thin-layer chromatography (TLC) was run on 0.25 mm Merck silica gel plates (60, F-254), with visualisation under UV light (254 nm and 365 nm). NMR characterisation was performed by  $^1\text{H}$  and  $^{13}\text{C}$  NMR spectra recorded on an Avance III HD 400 MHz Bruker BioSpin and Avance III HD 500 MHz Bruker BioSpin ( $^1\text{H}$ : 400 MHz and 500 MHz,  $^{13}\text{C}$ : 101 MHz and 126 MHz).

HRMS was performed by electron impact (EI) at 70 eV (Thermo Finnigan MAT 95 or Jeol GCmate II spectrometers) unless stated otherwise. HPLC-MS: Analytical measurements for determination of the purities of the final products were performed on an Agilent 1100 SL coupled HPLC-MS system with  $\text{H}_2\text{O}:\text{MeCN}$  eluent gradients through a Thermo Scientific Hypersil GOLD™ C18 column (1.9  $\mu\text{m}$ ; 3  $\times$  50 mm) maintained at 25 °C, detected on an Agilent 1100 series diode array detector and a Bruker Daltonics HCT-Ultra spectrometer (ESI mode, unit *m/z*). Full experimental details are given in the Supporting Information.

##### 4.1. Representative synthesis: **IQTub4**

**6-Benzyloxy-7-methoxyisoquinoline (4)** (first reported by a different procedure [43]). 4-Benzyloxy-3-methoxybenzaldehyde (4.99 g, 20.6 mmol) was dissolved in toluene (50 mL) and aminoacetaldehyde dimethyl acetal (2.38 g, 22.7 mmol) was added. Using a Dean-Stark apparatus the reaction mixture was heated to reflux for 16 h. After cooling to room temperature the volatiles were evaporated and the crude redissolved in MeOH (100 mL). The mixture was cooled to 0 °C and  $\text{NaBH}_4$  (1.56 g, 41.2 mmol) was added portionwise over 30 min, then the reaction mixture was warmed to room temperature and stirred for 4 h. The volatiles were evaporated and the crude taken up in water (100 mL) then extracted with DCM (3  $\times$  100 mL). The combined organic layers were dried over  $\text{Na}_2\text{SO}_4$ , filtered and concentrated. The crude product was redissolved in DCM (100 mL) and NaOH (1.40 g, 35.0 mmol) and tetrabutylammonium hydrogensulfate (0.490 g, 1.44 mmol) were added. After stirring for 10 min at room temperature a solution of *p*-toluenesulfonyl chloride (4.71 g, 24.7 mmol) in DCM (60 mL) was added dropwise over 1 h. The reaction mixture was stirred for an additional hour. Water (100 mL) was added, phases were separated, the organic phase washed with water (2  $\times$  100 mL) and brine (100 mL), dried over  $\text{Na}_2\text{SO}_4$  and concentrated. The resulting crude product was dissolved in 1,4-dioxane (150 mL), aq. 6 M HCl (30 mL) was added and the reaction mixture heated to reflux for 16 h. After cooling to room temperature, the solution was poured into water (150 mL) and washed with diethyl ether (2  $\times$  100 mL). Using a 6 M NaOH solution the aqueous phase was adjusted to pH > 9 and extracted with DCM (3  $\times$  150 mL). The combined organic layers were dried over  $\text{Na}_2\text{SO}_4$  and concentrated. The resulting crude product was purified by flash column chromatography (100% EtOAc) to give 6-benzyloxy-7-methoxyisoquinoline (**4**) as a white solid (1.29 g, 4.88 mmol, 24%). HRMS ( $\text{EI}^{+}$ ): 265.1103 calculated for  $\text{C}_{17}\text{H}_{15}\text{NO}_3^+$  [ $\text{M}]^{+}$ , 265.1110 found.  $^1\text{H}$  NMR (400 MHz,  $\text{CDCl}_3$ ):  $\delta$  (ppm) = 9.04 (s, 1H, 1-H), 8.36 (d,  $J$  = 5.6 Hz, 1H, 3-H), 7.51–7.47 (m, 2H, 2'-, 6'-H), 7.44 (d,  $J$  = 5.6 Hz, 1H, 4-H), 7.43–7.38 (m, 2H, 3'-, 5'-H), 7.36–7.31 (m, 1H, 4'-H), 7.21 (s, 1H, 8-H), 7.10 (s, 1H, 5-H), 5.29 (s, 2H,  $\text{CH}_2$ ), 4.03 (s, 3H,  $\text{OCH}_3$ ).  $^{13}\text{C}$  NMR (101 MHz,  $\text{CDCl}_3$ ):  $\delta$  (ppm) = 152.3 (C-6), 150.8 (C-7), 150.1 (C-1), 142.1 (C-3), 136.2 (C-1'), 132.5 (C-4a), 128.9 (2C, C-3',-5'), 128.3 (C-4'), 127.4 (2C, C-2',-6'), 125.0 (C-8a), 119.4 (C-4), 106.5 (C-5), 105.7 (C-8), 70.9 ( $\text{CH}_2$ ), 56.2 ( $\text{OCH}_3$ ).

**6-Benzyloxy-1-iodo-7-methoxyisoquinoline (5).** To a solution of 6-benzyloxy-7-methoxyisoquinoline (**4**) (531 mg, 2.00 mmol) in dry THF (8 mL) was slowly added  $\text{TMPMgCl}\cdot\text{LiCl}$  (1.0 M in THF/toluene; 3.00 mL, 3.00 mmol) dropwise at room temperature. After 4 h the reaction mixture was cooled to 0 °C, a solution of iodine (761 mg, 3.00 mmol) in dry THF (3 mL) was added dropwise and the resulting mixture stirred while warming to room temperature over 1 h. Sat. aq.  $\text{NH}_4\text{Cl}$  (4 mL) and sat. aq.  $\text{Na}_2\text{S}_2\text{O}_3$  (4 mL) were added and the organic materials extracted using DCM (3  $\times$  50 mL). The combined organic layers were dried over  $\text{Na}_2\text{SO}_4$  and concentrated *in vacuo*. The resulting crude product was purified by flash column chromatography (DCM/EtOAc 5:1) to give 6-benzyloxy-1-iodo-7-



methoxyisoquinoline (**5**) (0.482 g, 1.23 mmol, 62%) as a brown solid. HRMS ( $EI^{+}$ ): 391.0069 calculated for  $C_{17}H_{14}NO_3^{+}$  [ $M$ ] $^{+}$ , 391.0070 found.  $^1H$  NMR (400 MHz,  $CDCl_3$ ):  $\delta$  (ppm) = 8.09 (d,  $J$  = 5.4 Hz, 1H, 3-H), 7.50–7.46 (m, 2H, 2', 6'-H), 7.43–7.34 (m, 5H, 3', 4', 5', 4-, 8-H), 7.04 (s, 1H, 5-H), 5.30 (s, 2H,  $CH_2$ ), 4.08 (s, 3H,  $OCH_3$ ).  $^{13}C$  NMR (101 MHz,  $CDCl_3$ ):  $\delta$  (ppm) = 152.7 (C-6), 152.0 (C-7), 142.0 (C-3), 135.9 (C-1'), 132.5 (C-1), 128.9 (2C, C-3', -5'), 128.5 (C-4'), 128.3 (C-8a), 127.5 (2C, C-2', -6'), 124.9 (C-4a), 120.3 (C-4), 111.4 (C-8), 106.9 (C-5), 71.1 ( $CH_2$ ), 56.4 ( $OCH_3$ ).

**6-Benzyloxy-7-methoxy-1-(3,4,5-trimethoxyphenyl)isoquinoline (6).** To a solution of 6-benzyloxy-1-iodo-7-methoxyisoquinoline (**5**) (391 mg, 1.00 mmol) in THF (6 mL) was added 3,4,5-trimethoxyphenylboronic acid (254 mg, 1.20 mmol),  $Pd(PPh_3)_4$  (59.0 mg, 0.0500 mmol) and aq.  $K_2CO_3$  solution (1.0 M; 3.00 mL, 3.00 mmol). The reaction mixture was stirred in a sealed pressure tube under nitrogen at 90 °C for 16 h. After cooling to room temperature the mixture was poured into water (50 mL) and extracted with  $EtOAc$  ( $3 \times 50$  mL). The combined organic layers were dried over  $Na_2SO_4$  and concentrated in vacuo. The crude product was purified by flash column chromatography ( $EtOAc:DCM$  2:1) to give 6-benzyloxy-7-methoxy-1-(3,4,5-trimethoxyphenyl)isoquinoline (**6**) (395 mg, 0.915 mmol, 92%) as a yellow solid. HRMS ( $EI^{+}$ ): 431.1733 calculated for  $C_{26}H_{25}NO_5^{+}$  [ $M$ ] $^{+}$ , 431.1729 found.  $^1H$  NMR (400 MHz,  $CD_2Cl_2$ ):  $\delta$  (ppm) = 8.40 (d,  $J$  = 5.5 Hz, 1H, 3-H), 7.52–7.48 (m, 3H, 2', -6'', -4-H), 7.47 (s, 1H, 8-H), 7.46–7.41 (m, 2H, 3'', -5''-H), 7.40–7.35 (m, 1H, 4''-H), 7.23 (s, 1H, 5-H), 6.93 (s, 2H, 2', -6'-H), 5.24 (s, 2H,  $CH_2$ ), 3.88 (s, 6H, 3', -5'- $OCH_3$ ), 3.87 (s, 3H, 4'- $OCH_3$ ), 3.86 (s, 3H, 7'- $OCH_3$ ).  $^{13}C$  NMR (101 MHz,  $CD_2Cl_2$ ):  $\delta$  (ppm) = 158.5 (C-1), 153.8 (2C, C-3', -5'), 152.4 (C-6), 151.0 (C-7), 141.7 (C-3), 138.8 (C-4'), 136.7 (C-1''), 136.2 (C-1'), 134.2 (C-4a), 129.2 (2C, C-3'', -5''), 128.9 (C-4''), 128.5 (2C, C-2'', -6''), 123.0 (C-8a), 119.2 (C-4), 107.5 (2C, C-2', -6'), 107.0 (C-5), 106.3 (C-8), 71.3 ( $CH_2$ ), 61.1 (4'- $OCH_3$ ), 56.7 (2C, 3'', -5'- $OCH_3$ ), 56.4 (7'- $OCH_3$ ).

**7-Methoxy-1-(3,4,5-trimethoxyphenyl)isoquinolin-6-ol (IQTub4).** To a solution of 6-benzyloxy-7-methoxy-1-(3,4,5-trimethoxyphenyl)isoquinoline (**6**) (341 mg, 0.790 mmol) in MeOH (30 mL) was added  $Pd/C$  (10%, 100 mg). The mixture was stirred vigorously under an atmosphere of hydrogen at room temperature for 24 h, filtered through a pad of celite, and the filtrate concentrated in vacuo to give **IQTub4** (220 mg, 0.645 mmol, 82%) as a white solid. HRMS ( $EI^{+}$ ): 341.1263 calculated for  $C_{19}H_{19}NO_5^{+}$  [ $M$ ] $^{+}$ , 341.1256 found.  $^1H$  NMR (400 MHz,  $(CD_3)_2SO$ ):  $\delta$  (ppm) = 10.29 (s, 1H, OH), 8.31 (d,  $J$  = 5.6 Hz, 1H, 3-H), 7.53 (d,  $J$  = 5.6 Hz, 1H, 4-H), 7.44 (s, 1H, 8-H), 7.22 (s, 1H, 5-H), 6.99 (s, 2H, 2', -6'-H), 3.84 (s, 6H, 3', -5'- $OCH_3$ ), 3.82 (s, 3H, 7'- $OCH_3$ ), 3.76 (s, 3H, 4'- $OCH_3$ ).  $^{13}C$  NMR (101 MHz,  $(CD_3)_2SO$ ):  $\delta$  (ppm) = 156.9 (C-1), 152.7 (2C, C-3', -5'), 150.8 (C-6), 149.6 (C-7), 140.4 (C-3), 137.6 (C-4'), 135.3 (C-1'), 133.6 (C-4a), 121.1 (C-8a), 118.1 (C-4), 108.5 (C-5), 107.0 (2C, C-2', -6'), 105.3 (C-8), 60.1 (4'- $OCH_3$ ), 56.0 (2C, 3', -5'- $OCH_3$ ), 55.4 (7'- $OCH_3$ ). HPLC purity: >95%.

**Tubulin Polymerisation in vitro assay.** 99% purity tubulin from porcine brain was used in polymerisation assays run according to manufacturer's instructions (Cytoskeleton Inc., cat. #T240). Tubulin was pre-incubated for 10 min at 37 °C with either **IQTub5** (20  $\mu M$ ) or colchicine (16  $\mu M$ ) (in buffer (with 3% DMSO, 10% glycerol) as appropriate; at time zero, GTP (1 mM) was added and the absorbance at 340 nm was monitored over time at 37 °C [44].

**Cell Culture.** HeLa cells were maintained under standard cell culture conditions in Dulbecco's modified Eagle's medium supplemented with 10% fetal calf serum (FCS), 100 U/mL penicillin and 100 U/mL streptomycin, at 37 °C in a 5%  $CO_2$  atmosphere. HL-60 cells were cultured in RPMI 1640 medium with 10% FCS without antibiotics at 37 °C in a 5%  $CO_2$  atmosphere. Compounds and cosolvent (DMSO; 1% final concentration) were added via a D300e digital dispenser (Tecan).

**Antiproliferation Assays.** Mitochondrial diaphorase activity in HeLa cell line was quantified by spectrophotometrically measuring the reduction of resazurin (7-hydroxy-3H-phenoxazin-3-one-10-oxide) to resorufin. 5,000 cells/well were seeded on 96-well microtitre plates and treated with **IQTubs** 24 h later. Following 48 h of treatment, cells were incubated with 20  $\mu L$  of 0.15 mg/mL resazurin per well for 3 h at 37 °C. The resorufin fluorescence (excitation 544 nm, emission 590 nm) was then measured.

HL-60 cells were seeded in 96-well plates at 9,000 cells/well and incubated for 24 h before treatment with **IQTubs**. 24 h later, cells were treated with 0.5 mg/mL (3-(4,5-dimethylthiazol-2-yl)-2,5-diphenyltetrazolium bromide (MTT) for 2 h; the medium was aspirated and formazan crystals were re-dissolved in DMSO (190  $\mu L$ ) to measure their absorbance at 570 nm.

Fluorescence and absorbance were measured on a FLUOstar Omega microplate reader (BMG Labtech), averaged over the technical replicates and normalised as viability by reference to the cosolvent-only control set as 100%, and to cell-free (resazurin) or Triton-X®-100-treated (MTT) controls set as 0%. Results are means of at least three independent experiments.

**Cell cycle analysis.** **IQTubs** were added to HeLa cells in 24-well plates (seeding density: 50,000 cells/well) and incubated for 24 h. Cells were collected and stained with 2  $\mu g/mL$  propidium iodide (PI) at 4 °C for 30 min. Following PI staining, cells were analysed by flow cytometry using a BD LSR Fortessa flow cytometer (Becton Dickinson) run by BD FACSDiva software. 30,000 cells were measured per condition and the data were transferred to Flowing software for cell cycle analysis. Cells were sorted into sub-G1, G1, S and G2/M phase according to DNA content (PI signal).

**Immunofluorescence staining.** HeLa cells seeded on glass coverslips in 24-well plates (50,000 cells/well) were left to adhere for 18 h then treated for 24 h with **IQTubs**. Cover slips were washed then fixed with 0.5% glutaraldehyde, quenched with 0.1%  $NaBH_4$ , blocked with PBS +10% FCS, and treated with rabbit alpha-tubulin primary antibody (Abcam ab18251; 1:400 in PBS + 10% FCS) for 1 h; after washing with PBS, cells were incubated with goat-anti-rabbit Alexa fluor 488 secondary antibody (Abcam, ab150077; 1:400 in PBS + 10% FCS) for 1 h. After washing with PBS, coverslips were mounted onto glass slides using Roti-Mount FluorCare DAPI (Roth) and imaged with a Zeiss LSM Meta confocal microscope. Images were processed using Fiji software. For maximum intensity projections, images were recorded at different focal planes by incrementally stepping through the sample (step size 1–2  $\mu m$ ) and maximum intensity projections were obtained using Fiji.

**EB3 comet assay.** [45] HeLa cells (12,000 cells/well) were seeded on 8-well ibiTreat  $\mu$  slides (ibidi) 24 h prior to transfection. Cells were transiently transfected with EB3-YFP plasmid using jetPRIME reagent (Polyplus) according to the manufacturer's instructions. Cells were imaged 24 h later, under 37 °C and 5%  $CO_2$  atmosphere using an UltraVIEW Vox spinning disc confocal microscope (PerkinElmer) equipped with an EMCCD camera (Hamamatsu, Japan) and operated with Volocity software. After focussing on cells on the microscope stage, 5 imaging frames were acquired to set a reference measure for EB3 comet activity, then **IQTub4P** was added cautiously and cells incubated for 2 min before acquiring another 5 frames to quantify post-treatment EB3 comet activity. Cells were imaged at 514 nm (20% laser power, 300 ms exposure time, 45 frames/min). For EB3 comet statistics, 7 cells from three independent trials were taken. EB3 comets were counted with a Fiji plugin based on the "Find maxima" function from the NIH.

#### Author contributions

Y.K. performed immunofluorescence staining, live-cell microscopy and viability studies. C.G. performed synthesis and

coordinated chemical data assembly. B.M. and L.G. performed synthesis. C.H. and M.P. performed cell cycle analysis and viability studies. J.A. supervised biology, performed cell cycle analysis and viability studies, and coordinated biological data assembly. F.B. planned and supervised synthesis. O.T.-S. designed the study, supervised synthesis and biology, coordinated data assembly and wrote the manuscript.

#### Declaration of competing interest

The authors declare no conflict of interest.

#### Acknowledgments

This research was supported by funds from the German Research Foundation (DFG: SFB1032 Nanoagents for Spatiotemporal Control project B09 to O.T.-S.; SFB TRR 152 project P24 number 239283807 to O.T.-S.; and Emmy Noether grant to O.T.-S.) and the German Ministry of Education and Research (GO-Bio grant to O.T.-S.). We thank Rebekkah Bingham (LMU) for performing the tubulin polymerisation assay, Yuliia Holota (Bienta) for the *in vitro* ADME and *in vivo* tolerated dose assessments, Martina Stadler (LMU) for the HL-60 viability crosscheck, K. T. Wanner (LMU) for kind support and collegial discussions, and H. Harz and I. Solvei (LMU microscopy platform CALM) for microscopy support.

#### Appendix A. Supplementary data

Supplementary data to this article can be found online at <https://doi.org/10.1016/j.ejmech.2019.111865>.

#### References

- [1] T.J. Mitchison, The proliferation rate paradox in antimetabolic chemotherapy, *Mol. Biol. Cell* 23 (1) (2012) 1–6, <https://doi.org/10.1091/mbc.e10-04-0335>.
- [2] J.R. Peterson, T.J. Mitchison, Small molecules, big impact: a history of chemical inhibitors and the cytoskeleton, *Chem. Biol.* 9 (12) (2002) 1275–1285, [https://doi.org/10.1016/s1074-5521\(02\)00284-3](https://doi.org/10.1016/s1074-5521(02)00284-3).
- [3] D.G.L. Kingston, Taxol, a molecule for all seasons, *Chem. Commun.* 10 (2001) 867–880, <https://doi.org/10.1039/b100070p>.
- [4] D.W. Siemann, The unique characteristics of tumor vasculature and preclinical evidence for its selective disruption by tumor-vascular disrupting agents, *Cancer Treat. Rev.* 37 (1) (2011) 63–74, <https://doi.org/10.1016/j.ctrv.2010.05.001>.
- [5] G.M. Tozer, C. Kanthou, B.C. Baguley, Disrupting tumour blood vessels, *Nat. Rev. Cancer* 5 (6) (2005) 423–435, <https://doi.org/10.1038/nrc1628>.
- [6] K.G. Pinney, Molecular recognition of the colchicine binding site as a design paradigm for the discovery and development of vascular disrupting agents, in: *Vascular-Targeted Therapies in Oncology*, Wiley, 2006, pp. 95–121.
- [7] T.L. Nguyen, C. McGrath, A.R. Hermone, J.C. Burnett, D.W. Zaharevitz, B.W. Day, P. Wipf, E. Hamel, R. Gussio, A common pharmacophore for a diverse set of colchicine site inhibitors using a structure-based approach, *J. Med. Chem.* 48 (19) (2005) 6107–6116, <https://doi.org/10.1021/jm050502t>.
- [8] R. Gaspari, A.E. Prota, K. Bargsten, A. Cavalli, M.O. Steinmetz, Structural basis of *cis*- and *trans*-combrestatin binding to tubulin, *Chem* 2 (1) (2017) 102–113, <https://doi.org/10.1016/j.chempr.2016.12.005>.
- [9] M. Borowiak, W. Nahaboo, M. Reynders, K. Nekolla, P. Jalinet, J. Hasserodt, M. Rehberg, M. Delattre, S. Zahler, A. Vollmar, et al., Photoswitchable inhibitors of microtubule dynamics optically control mitosis and cell death, *Cell* 162 (2) (2015) 403–411, <https://doi.org/10.1016/j.cell.2015.06.049>.
- [10] G.R. Pettit, S.B. Singh, E. Hamel, C.M. Lin, D.S. Alberts, D. Garcia-Kendal, Isolation and structure of the strong cell growth and tubulin inhibitor combretastatin A-4, *Experientia* 45 (2) (1989) 209–211, <https://doi.org/10.1007/bf01954881>.
- [11] J.A. Woods, J.A. Hadfield, G.R. Pettit, B.W. Fox, A.T. McGown, The interaction with tubulin of a series of stilbenes based on combretastatin A-4, *Br. J. Canc.* 71 (4) (1995) 705–711, <https://doi.org/10.1038/bjc.1995.138>.
- [12] G.M. Tozer, C. Kanthou, C.S. Parkins, S.A. Hill, The biology of the combretastatins as tumour vascular targeting agents, *Int. J. Exp. Pathol.* 83 (1) (2002) 21–38, <https://doi.org/10.1046/j.1365-2613.2002.00211.x>.
- [13] G.C. Tron, T. Pirali, G. Sorba, F. Pagliari, S. Busacca, A.A. Genazzani, Medicinal chemistry of combretastatin A4: present and future directions, *J. Med. Chem.* 49 (11) (2006) 3033–3044, <https://doi.org/10.1021/jm0512903>.
- [14] D. Tarade, D. Ma, C. Pignanelli, F. Mansour, D. Simard, S. van den Berg, J. Gauld, J. McNulty, S. Pandey, Structurally simplified biphenyl combretastatin A4 derivatives retain *in vitro* anti-cancer activity dependent on mitotic arrest, *PLoS One* 12 (3) (2017), e0171806, <https://doi.org/10.1371/journal.pone.0171806>.
- [15] J. McNulty, S. van den Berg, D. Ma, D. Tarade, S. Joshi, J. Church, S. Pandey, Antimitotic activity of structurally simplified biaryl analogs of the anticancer agents colchicine and combretastatin A4, *Bioorg. Med. Chem. Lett.* 25 (1) (2015) 117–121, <https://doi.org/10.1016/j.bmcl.2014.10.090>.
- [16] S. Kim, H. Ko, J.E. Park, S. Jung, S.K. Lee, Y.-J. Chun, Design, synthesis, and discovery of novel *trans*-stilbene analogues as potent and selective human cytochrome P450 1B1 inhibitors, *J. Med. Chem.* 45 (1) (2002) 160–164, <https://doi.org/10.1021/jm010298j>.
- [17] D.-J. Hwang, J. Wang, W. Li, D.D. Miller, Structural optimization of indole derivatives acting at colchicine binding site as potential anticancer agents, *ACS Med. Chem. Lett.* 6 (9) (2015) 993–997, <https://doi.org/10.1021/acsmchemlett.5b00208>.
- [18] Y. Lu, J. Chen, J. Wang, C.-M. Li, S. Ahn, C.M. Barrett, J.T. Dalton, W. Li, D.D. Miller, Design, synthesis, and biological evaluation of stable colchicine binding site tubulin inhibitors as potential anticancer agents, *J. Med. Chem.* 57 (17) (2014) 7355–7366, <https://doi.org/10.1021/jm500764v>.
- [19] S.A. Hill, G.M. Tozer, G.R. Pettit, D.J. Chaplin, Preclinical evaluation of the antitumour activity of the novel vascular targeting agent oxi 4503, *Anticancer Res.* 22 (3) (2002) 1453–1458.
- [20] Y. Nihei, M. Suzuki, A. Okano, T. Tsuji, Y. Akiyama, T. Tsuruo, S. Saito, K. Hori, Y. Sato, Evaluation of antivascular and antimitotic effects of tubulin binding agents in solid tumor therapy, *Jpn. J. Cancer Res.* 90 (12) (1999) 1387–1395, <https://doi.org/10.1111/j.1349-7006.1999.tb00724.x>.
- [21] P.D. Davis, G.J. Dougherty, D.C. Blakey, S.M. Galbraith, G.M. Tozer, A.L. Holder, M.A. Naylor, J. Nolan, M.R.L. Stratford, D.J. Chaplin, et al., ZD6126: a novel vascular-targeting agent that causes selective destruction of tumor vasculature, *Cancer Res.* 62 (24) (2002) 7247–7253.
- [22] G. Kremmidiotis, A.F. Leske, T.C. Lavranos, D. Beaumont, J. Gasic, A. Hall, M. O'Callaghan, C.A. Matthews, B. Flynn, BNC105: a novel tubulin polymerization inhibitor that selectively disrupts tumor vasculature and displays single-agent antitumor efficacy, *Mol. Cancer Ther.* 9 (6) (2010) 1562, <https://doi.org/10.1158/1535-7163.mct-09-0815>.
- [23] R.P. Mason, D. Zhao, L. Liu, M.L. Trawick, K.G. Pinney, A perspective on vascular disrupting agents that interact with tubulin: preclinical tumor imaging and biological assessment, *Integr. Biol. (Camb)* 3 (4) (2011) 375–387, <https://doi.org/10.1039/c1ib00135j>.
- [24] J.H. Gill, K.L. Rockley, C. De Santis, A.K. Mohamed, Vascular disrupting agents in cancer treatment: cardiovascular toxicity and implications for co-administration with other cancer chemotherapeutics, *Pharmacol. Ther.* 202 (2019) 18–31, <https://doi.org/10.1016/j.pharmthera.2019.06.001>.
- [25] P. Giannakakou, D. Sackett, T. Fojo, Tubulin/microtubules: still a promising target for new chemotherapeutic agents, *J. Natl. Cancer Inst.* 92 (3) (2000) 182–183, <https://doi.org/10.1093/jnci/92.3.182>.
- [26] O. Thorn-Seshold, F. Bracher, B. Melzer, Isoquinoline Biaryl Compounds, 2018. EP18207030.
- [27] M. Sriram, J.J. Hall, N.C. Grohmann, T.E. Strecker, T. Wootton, A. Franken, M.L. Trawick, K.G. Pinney, Design, synthesis and biological evaluation of dihydronaphthalene and benzosuberene analogs of the combretastatins as inhibitors of tubulin polymerization in cancer chemotherapy, *Bioorg. Med. Chem.* 16 (17) (2008) 8161–8171, <https://doi.org/10.1016/j.bmc.2008.07.050>.
- [28] Y. Pang, H. Lin, C. Ou, Y. Cao, B. An, J. Yan, X. Li, Design, synthesis, and biological evaluation of novel benzodiazepine derivatives as anticancer agents through inhibition of tubulin polymerization *in vitro* and *in vivo*, *Eur. J. Med. Chem.* 182 (2019) 111670, <https://doi.org/10.1016/j.ejmech.2019.111670>.
- [29] Verfahren Zur Darstellung von 1-(3, 4, 5-Trialkoxyphenyl)-6, 7-Dialkoxisoquinolinen. DE614703.
- [30] W. Reeve, W.M. Eareckson, Synthesis of some isoquinoline derivatives related to podophyllotoxin, *J. Am. Chem. Soc.* 72 (11) (1950) 5195–5197, <https://doi.org/10.1021/ja01167a114>.
- [31] B. Melzer, F. Bracher, A divergent approach to benzyloisoquinoline-type and oxoaporphine alkaloids via regioselective direct ring metalation of alkoxy isoquinolines, *Org. Biomol. Chem.* 13 (28) (2015) 7664–7672, <https://doi.org/10.1039/c5ob00926j>.
- [32] B. Melzer, F. Bracher, A novel approach to oxoisoaporphine alkaloids via regioselective metalation of alkoxy isoquinolines, *Beilstein J. Org. Chem.* 13 (2017) 1564–1571, <https://doi.org/10.3762/bjoc.13.156>.
- [33] A. Sailer, F. Ermer, Y. Kraus, F. Lutter, C. Donau, M. Bremerich, J. Ahlfeld, O. Thorn-Seshold, Hemithioindigos as desymmetrised molecular switch scaffolds: design control over the isomer-dependency of potent photoswitchable antimitotic bioactivity in cellulose, *ChemBiochem* 20 (2019) 1305–1314, <https://doi.org/10.1002/cbic.201800752>.
- [34] L. Gao, Y. Kraus, M. Wranik, T. Weinert, S.D. Pritzl, J.C.M. Meiring, R. Bingham, N. Olieric, A. Akhmanova, T. Lohmüller, et al., Photoswitchable microtubule inhibitors enabling robust, GFP-orthogonal optical control over the tubulin cytoskeleton, 2019, p. 716233, <https://doi.org/10.1101/716233>, bioRxiv 2019.
- [35] A. Sailer, F. Ermer, Y. Kraus, R. Bingham, F.H. Lutter, J. Ahlfeld, O. Thorn-Seshold, Potent Hemithioindigo-Based Antimitotics Photocontrol the Microtubule Cytoskeleton in Cellulo, *ChemRxiv*, 2019, <https://doi.org/10.26434/chemrxiv.9176747.v1>.
- [36] K.G. Pinney, G.R. Pettit, M.L. Trawick, C. Jelinek, D.J. Chaplin, The discovery and development of the combretastatins, in: *Anticancer Agents from Natural Products*, CRC Press, Boca Raton, 2011, pp. 27–63.

- [37] National Cancer Institute, NCI Drug Dictionary: fosbretabulin disodium. <https://www.cancer.gov/publications/dictionaries/cancer-drug/def/fosbretabulin-disodium>.
- [38] E. Reimann, H. Renz, Protoberberine Aus Reissert-Verbindungen, 2. Mitt.: eine Neue Synthese von 8-Methyl-dibenzo[a,g]Chinolizidinen, *Arch. Pharm.* 326 (5) (1993) 253–258, <https://doi.org/10.1002/ardp.19933260502>.
- [39] A. Krasovskiy, V. Krasovskaya, P. Knochel, Mixed Mg/Li amides of the type  $R_2NMgCl \cdot LiCl$  as highly efficient bases for the regioselective generation of functionalized aryl and heteroaryl magnesium compounds, *Angew. Chem. Int. Ed.* 45 (18) (2006) 2958–2961, <https://doi.org/10.1002/anie.200504024>.
- [40] T.L. Riss, A.L. Niles, R.A. Moravec, *Cell Viability Assays*, 2013 May 1 [Updated 2016 Jul 1], <https://www.ncbi.nlm.nih.gov/books/NBK144065/>. (Accessed 8 May 2019).
- [41] M.J. Waring, Defining optimum lipophilicity and molecular weight ranges for drug candidates—molecular weight dependent lower LogD limits based on permeability, *Bioorg. Med. Chem. Lett* 19 (10) (2009) 2844–2851, <https://doi.org/10.1016/j.bmcl.2009.03.109>.
- [42] K.A. Monk, R. Siles, M.B. Hadimani, B.E. Mugabe, J.F. Ackley, S.W. Studerus, K. Edvardsen, M.L. Trawick, C.M. Garner, M.R. Rhodes, et al., Design, synthesis, and biological evaluation of combretastatin nitrogen-containing derivatives as inhibitors of tubulin assembly and vascular disrupting agents, *Bioorg. Med. Chem.* 14 (9) (2006) 3231–3244, <https://doi.org/10.1016/j.bmc.2005.12.033>.
- [43] A.R. Battersby, D.J. Le Count, S. Garratt, R.I. Thrift, Synthetic applications of 1,2-dihydroisoquinolines: synthesis of ( $\pm$ )-Coreximine, *Tetrahedron* 14 (1) (1961) 46–53, [https://doi.org/10.1016/0040-4020\(61\)80086-0](https://doi.org/10.1016/0040-4020(61)80086-0).
- [44] C.M. Lin, S.B. Singh, P.S. Chu, R.O. Dempcy, J.M. Schmidt, G.R. Pettit, E. Hamel, Interactions of tubulin with potent natural and synthetic analogs of the antimitotic agent combretastatin: a structure-activity study, *Mol. Pharmacol.* 34 (2) (1988) 200–208.
- [45] T. Kleele, P. Marinković, P.R. Williams, S. Stern, E.E. Weigand, P. Engerer, R. Naumann, J. Hartmann, R.M. Karl, F. Bradke, et al., An assay to image neuronal microtubule dynamics in mice, *Nat. Commun.* 5 (2014) 4827, <https://doi.org/10.1038/ncomms5827>.

## 4 Photopharmaceutical microtubule depolymerisers

This section is situated in the field of photopharmacology applied for cell biology research.

### **Background: photopharmaceutical inhibitors of tubulin**

Elucidating cellular processes executed by microtubules is an exceedingly important field of research and dominated by the use of small-molecule inhibitors. Because of the multitude of cellular functions accomplished by microtubules, it is challenging to precisely target any chosen process with ordinary microtubule targeting agents in an isolated manner. They cannot be applied with spatiotemporal specificity on the cellular level. One way to enhance spatiotemporal specificity is to use light for controlling bioactivity as light can be applied noninvasively with high spatiotemporal precision. This can, in principle, enable precise control over single cells rather than entire cell populations and tissues. Otherwise, this can allow bidirectionally switching between an active and an inactive isomer to pattern a specimen and perform inactivation and rescue microtubule function, which has been successfully applied to microtubule organisation in early mouse embryos.<sup>102</sup>

The advantages of using light to noninvasively control biological processes have already driven sophisticated insights in the field of optogenetics. Optogenetics uses genetically encoded photo-responsive protein domains to control protein function<sup>103</sup> and makes it possible to photocontrol cellular processes such as motility, proliferation or secretion. This results in a better understanding, especially, in neurobiology and muscle physiology.<sup>104</sup> Recently, this has been applied to execute control over microtubule end binding proteins.<sup>105</sup> While Optogenetics requires genetic engineering, which can be challenging or impossible for certain protein targets, photopharmacology is superior in many biological applications.

Photopharmacology, a combination of photochemistry and pharmacology, uses synthetically produced molecules whose bioactivity is affected by light. Photoactivatable or "photocaged / photo-uncageable" compounds that are irreversibly transformed or released upon application of light, which does not defy the diffusion of the active compound and therefore limits spatiotemporal control, are sometimes classed as photopharmaceuticals. In this work, I use photopharmacology to refer to photoswitchable compounds. Photoswitchable compounds are chemicals, with whom reversible switching between two isomers of a molecule by application of light—typically at two distinct wavelengths—can give access to photocontrol over biological systems. The concept has found a range of applications for different processes and has been used for targeting the proteasome<sup>106</sup>, RET kinases<sup>107</sup>, or depolarisation of neurons<sup>108</sup>.

In relation to the cytoskeleton, photopharmacology has been used to control microtubules by binding and releasing tubulin depending on the wavelength of illumination.<sup>109</sup> In the assessment of this concept, photoswitches that showed wavelength-dependent cytotoxicity were applied to living *C. elegans* embryos and single cells of the embryo were illuminated with either 405 nm light (toxic regimen) or 514 nm light (rescue protocol) to locally and reversibly inflict or release mitotic arrest on single-cell level, while neighbouring cells stayed unaffected. Application in living mouse tissue (cremaster muscle in C57/BL6 mice) led to the disruption of

microtubules under 390 nm light and no effect on the microtubule cytoskeleton was observed in the dark. Therefore, photoswitches are a valuable tool to address microtubule function during cellular processes in a spatiotemporal manner, as will be discussed in more detail below.

A common strategy to produce photoswitchable microtubule inhibitors is to use structural elements of already known microtubule binders. To make a photopharmaceutical, a small-molecule photoswitch can either be partially incorporated in a drug pharmacophore or attached without being a part of the pharmacophore.<sup>110</sup> These photoswitches should optimally be easily accessible on reliable synthetic routes and be thoroughly examined regarding biostability (metabolic degradation) and toxicity of both isomers *in vivo*, including the possibility of off-target effects.<sup>111</sup> The most commonly used photoswitches are azobenzenes that have been claimed to be well-characterized regarding the influence of the chemical structure on toxicity and stability under reducing conditions and degradation products,<sup>111</sup> although my research and that of others within and outside our research group disputes this claim<sup>112</sup>. Other photoswitches that have been accessed are stilbenes, spiropyran, diarylethenes, and thiophenefulgides. Until now, these molecules have seldom been applied as photoswitches in biology, and little knowledge about their biostability is available.

Prior research into photopharmaceuticals for the microtubule cytoskeleton has been essentially restricted to the azobenzene-based photostatins, which have been independently developed by several groups.<sup>109,113</sup> Photostatins (PSTs) were developed mimicking the structure of combretastatin, a stilbene-based microtubule depolymeriser that binds to the colchicine binding site of tubulin. In PSTs, the C=C double bond of combretastatin has been replaced with an N=N double bond, creating a photoswitchable azobenzene. Under illumination with violet light, the PST is isomerised into its active *cis* isomer which is more than two hundred times more toxic than the inactive *trans* isomer, and which can be switched back by either green light or thermal relaxation over time. Photostatins have been used in embryos of *C. elegans* for photocontrol of the microtubule skeleton on specific cells<sup>109</sup>, in embryos of *Drosophila* as part of studies on early wing epithelium development<sup>114</sup>, and in *D. rerio* embryos to study neuronal migration during development<sup>115</sup>.

However, the PSTs, such as azobenzenes, have certain limitations regarding metabolism, photoswitching wavelengths and performance, functional group toleration, and cellular potency. A consequence has been that *in vivo* applications in adult animals have not succeeded with PSTs despite years of (unpublished) research in our group. My research into novel photoswitchable systems was intended to develop photopharmaceuticals that addressed some of these limitations of PSTs.

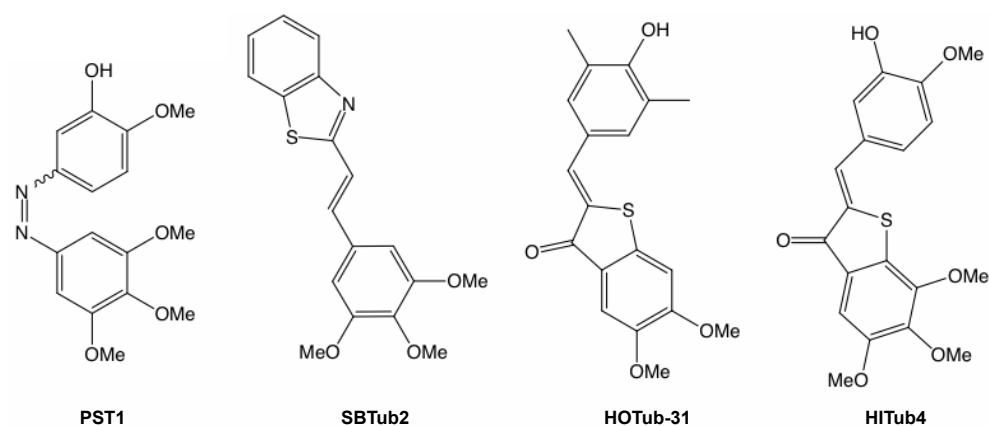


**Figure 10:** Structures of photoswitchable microtubule depolymerisers

PST1	SBTub2	HOTub-31	HITub-4
Bidirectionally switchable with low intensity visible light	GFP-orthogonal for imaging assays	Optical control of microtubule depolymerisation and cell death	10 times more potent than HOTubs
Control of mitosis with single cell precision	Biochemical and metabolic robustness,	Possible <i>a priori</i> design of dark active compounds	Reliable and robust visible light photoswitching
250-fold increase of cytotoxicity under blue light	Alternatively, tolerated range of substituents and relaxation rates	No off-target bioactivity	High fatigue resistance

**Table 2:** Overview of photoswitchable tubulin depolymerisers and their properties

## 4.1 Styrylbenzothiazole SBTubs

### Properties of photoswitchable reagents: motivation for this work

Although photostatins are a valuable tool to study microtubule activity locally, there are certain drawbacks that have their cause in the azobenzene scaffold. Biological assays to observe the role of microtubules in certain processes are often based on imaging applications. Because of their photo-response to common imaging wavelengths as GFP, YFP and RFP, it is not possible to use the full capacity of a photoswitchable molecule based on azobenzenes for these assays. The imaging wavelength can create a background activity in areas that are desired to be inactive and in illuminated areas of the specimen. The active isomer is created by the imaging wavelength in addition to the formation of the active isomer by photoswitching. Therefore, the PSTs' non-orthogonality to imaging limits their applications in biology.

Azobenzene-based photoswitches are also prone to degradation in the cellular environment after addition of cellular glutathione; after this addition, they lose their photoswitchability and potency and, in some cases, the degradation products are more bioactive than the starting compound.<sup>116</sup> Therefore, the sensitivity towards metabolic degradation limits their applications in biology. Finally, some azobenzene based photoswitches can undergo substituent-dependent, fast thermal relaxation in a  $\mu$ s-ms timescale. So, they would be dependent on a high photon flux to photo-pattern the specimen in some biological settings, which diminishes the free choice of photoswitches. Therefore, the requirement of high photon flux for some

photoswitches, which is unacceptable for biological specimen, limits their application in biology.

### Short summary of the SBTub work

In order to overcome these limitations, we chose to move forward with a styrylbenzothiazole scaffold to access a photoswitch based on a C=C double bond. We hoped that this would avoid problems such as fast metabolic degradation, non-orthogonality to common imaging wavelengths and would yield molecules with a longer half-life of the active isomer. Two potential SBT-scaffold microtubule inhibitors SBTub2 and SBTub3 were designed with the Z-isomer based on the structural requirements of colchicine site binding similar to bioactive *cis*-CA4 while the *E*-isomer mimics the inactive *trans*-CA4. We expected Z-SBTub-specific inhibition of microtubule dynamics. For validation and exclusion of artefacts, we also designed inactive permutation controls SBTub1 and SBTub4 in order to prove tubulin-specificity as well as Z-isomer specificity.

The SBTubs proved to be indifferent to changes in pH and environment, robust towards the addition of glutathione and metabolic degradation and showed no significant photobleaching. Active SBTubs in their "lit" state (Z-SBTub) were able to inhibit tubulin polymerisation in a cell-free assay with purified tubulin and showed similar behaviour as other colchicine site inhibitors while the inactive *E*-SBTubs showed no effect on tubulin *in vitro* polymerisation. The metastable Z-SBTubs showed no thermal relaxation after several hours at pH 7 but could be completely isomerised back into the thermodynamically stable *E*-state by warming them to 50°C overnight. To assess their biological value as research tools, we applied the SBTubs in several biological settings.

We analysed the antiproliferative effect of all SBTubs either with long term pulsing with light or one burst of light at the beginning of the experiment and were able to show that the actively designed compounds SBTub2 and SBTub3 indeed had antiproliferative effects in both illumination protocols while the designed inactive compounds SBTub1 and SBTub4 didn't show antiproliferative effects. Structural analysis of the microtubule cytoskeleton by immunofluorescence after treatment with SBTubs, under lit and dark conditions, showed microtubule perturbation for the designed active compounds in the lit state and no activity for the designed-inactive compounds either in dark or lit conditions. Projection along the Z-axis showed mitotic arrest under illuminated conditions, which has been confirmed by cell cycle analysis. Furthermore, we showed that SBTub3 can be used as GFP orthogonal tool for spatiotemporal control over polymerising microtubules in an EB3-comet assay and excluded any kind of artefacts by using the pre-lit compound in an additional experiment.

The major chemical drawback of the SBTubs is that one cannot directly photoswitch them from the bioactive *Z* back to the inactive *E* isomer at biologically compatible wavelengths (the details are discussed in the Conclusion). However, we developed a repeatable procedure to gain complete functional recovery of microtubule dynamics in a certain cell or region by rapid diffusion-based homogenisation of the active *Z*-isomer. Finally, we applied our lead compound

SBTub3 to subcellular control of microtubule dynamics in primary neurons with spatiotemporal control in single neurites.

#### Authorial Contributions

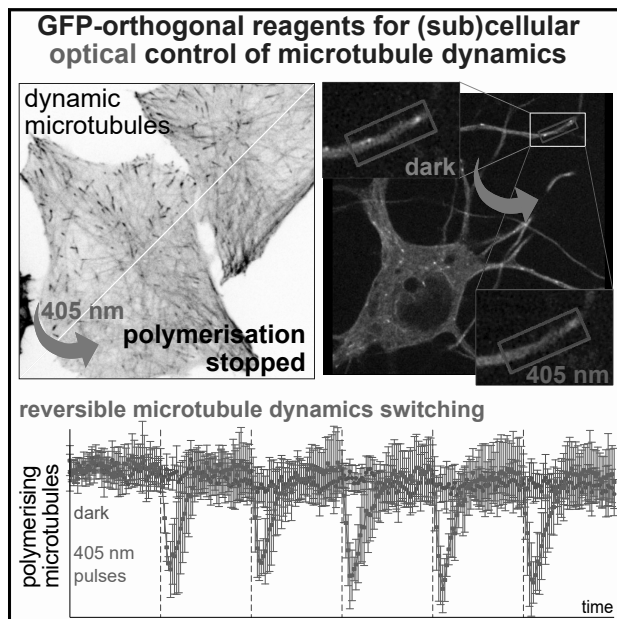
My part of this work was to analyse the effect of both active and designed inactive SBTubs in antiproliferation assays for cytotoxicity in their dark and lit state and to confirm their ability to interfere with the microtubule cytoskeleton by using immunofluorescence tubulin staining (Fig. 3H and 3I). I studied the effect of dark and lit SBTubs in a cell cycle assay (Fig. 3J) for their expected G2/M-phase cell cycle arrest<sup>59</sup> of the active SBTubs in their lit state. Furthermore, I transiently transfected HeLa cells with a fluorescently labelled tubulin end binding protein (EB3-GFP or EB3-YFP) to evaluate their superiority over azobenzene based photoswitches in imaging assays (GFP-orthogonality) (Fig. 4B), looked into inhibition of microtubule dynamics by activating the SBTubs during imaging and confirmed their mode of action by using pre-lit Z-SBTub (Fig. 4C), which built the basis for the development of a reversible control over microtubule dynamics and the spatiotemporally controlled microtubule inhibition in primary neurons that were performed by J. Meiring. In summation, the results show that we created GFP-orthogonal photoactivatable small-molecule microtubule destabilisers that are metabolically more stable than azobenzenes and demonstrated their mode of action and applied them to demonstrate their value as new improved research tools for cytoskeleton research.



## Cell Chemical Biology

# A Robust, GFP-Orthogonal Photoswitchable Inhibitor Scaffold Extends Optical Control over the Microtubule Cytoskeleton

### Graphical Abstract



### Authors

Li Gao, Joyce C.M. Meiring, ..., Julia Ahlfeld, Anna Akhmanova, Michel O. Steinmetz, Oliver Thorn-Seshold

### Correspondence

oliver.thorn-seshold@cup.lmu.de

### In Brief

Photocontrollable reagents have unique potential as high spatiotemporal precision modulators of biological systems. Here, Gao et al. demonstrate a GFP-orthogonal and metabolically stable photoswitch that allows optical control over microtubule dynamics and architecture with subcellular resolution. The photoswitch scaffold also offers new possibilities for photopharmaceutical design against other targets.

### Highlights

- SBTub3 photocontrols microtubule dynamics, organization, and dependent processes
- Microtubule photocontrol is cell and sub-cellularly precise and temporally reversible
- SBT photocontrol is orthogonal to GFP/YFP imaging and SBTs are metabolically stable
- The SBT scaffold is promising for photopharmaceuticals for other protein targets

Resource

# A Robust, GFP-Orthogonal Photoswitchable Inhibitor Scaffold Extends Optical Control over the Microtubule Cytoskeleton

Li Gao,<sup>1</sup> Joyce C.M. Meiring,<sup>2</sup> Yvonne Kraus,<sup>1</sup> Maximilian Wranik,<sup>3</sup> Tobias Weinert,<sup>3</sup> Stefanie D. Pritzl,<sup>4</sup> Rebekkah Bingham,<sup>1</sup> Evangelia Ntoulou,<sup>1</sup> Klara I. Jansen,<sup>2</sup> Natacha Olieric,<sup>3</sup> Jörg Standfuss,<sup>3</sup> Lukas C. Kapitein,<sup>2</sup> Theobald Lohmüller,<sup>4</sup> Julia Ahlfeld,<sup>1</sup> Anna Akhmanova,<sup>2</sup> Michel O. Steinmetz,<sup>3,5</sup> and Oliver Thorn-Seshold<sup>1,6,\*</sup>

<sup>1</sup>Department of Pharmacy, Ludwig-Maximilians University of Munich, Munich 81377, Germany

<sup>2</sup>Cell Biology, Neurobiology and Biophysics, Department of Biology, Faculty of Science, Utrecht University, Utrecht 3584, Netherlands

<sup>3</sup>Laboratory of Biomolecular Research, Division of Biology and Chemistry, Paul Scherrer Institut, Villigen 5232, Switzerland

<sup>4</sup>Chair for Photonics and Optoelectronics, Nano-Institute Munich, Department of Physics, Ludwig-Maximilians University of Munich, Munich 80539, Germany

<sup>5</sup>Biozentrum, University of Basel, Basel 4056, Switzerland

<sup>6</sup>Lead Contact

\*Correspondence: [oliver.thorn-seshold@cup.lmu.de](mailto:oliver.thorn-seshold@cup.lmu.de)

<https://doi.org/10.1016/j.chembiol.2020.11.007>

## SUMMARY

Optically controlled chemical reagents, termed “photopharmaceuticals,” are powerful tools for precise spatiotemporal control of proteins particularly when genetic methods, such as knockouts or optogenetics are not viable options. However, current photopharmaceutical scaffolds, such as azobenzenes are intolerant of GFP/YFP imaging and are metabolically labile, posing severe limitations for biological use. We rationally designed a photoswitchable “SBT” scaffold to overcome these problems, then derivatized it to create exceptionally metabolically robust and fully GFP/YFP-orthogonal “SBTub” photopharmaceutical tubulin inhibitors. Lead compound SBTub3 allows temporally reversible, cell-precise, and even subcellularly precise photomodulation of microtubule dynamics, organization, and microtubule-dependent processes. By overcoming the previous limitations of microtubule photopharmaceuticals, SBTubs offer powerful applications in cell biology, and their robustness and druglikeness are favorable for intracellular biological control in *in vivo* applications. We furthermore expect that the robustness and imaging orthogonality of the SBT scaffold will inspire other derivatizations directed at extending the photocontrol of a range of other biological targets.

## INTRODUCTION

The microtubule (MT) cytoskeleton supports an extraordinary range of cellular functions simultaneously, with central roles in nearly all directional processes, such as intracellular transport and cell motility; its crucial function in cell proliferation has also made it a prominent anticancer drug target (Dumontet and Jordan, 2010; Peterson and Mitchison, 2002). Although cytoskeleton research typically aims to study a subset of MT-dependent processes that are spatially and/or temporally localized, nearly all small-molecule inhibitors of MTs (drugs such as paclitaxel, colchicine, epothilone, etc.) cannot be spatiotemporally directed, so they inhibit MT dynamics throughout cells and systems to which they are applied (Janke and Steinmetz, 2015). For decades this restricted the scope of inhibition studies of MT biology.

Recently, the advent of optically targeted tools to manipulate biological systems with increased spatiotemporal precision has revolutionized diverse fields of biological research, particularly for temporally regulated and geometrically complex systems.

Optogenetics, photouncaging approaches, and photoswitchable small-molecule inhibitors or “photopharmaceuticals,” have all been developed as optically targeted tools, with distinct strengths and weaknesses (Wittmann et al., 2020). Photopharmaceuticals offer performance and applications that are quite distinct from the other methods. Unlike photouncaging, they feature near-instantaneous photoresponse without byproduct generation, and can offer reversible switching (Klían et al., 2013). As distinct from optogenetics, they possess the advantages of small-molecule inhibitors: they do not require genetic engineering; they can directly address critical proteins (such as tubulin), which due to their structure may not permit functional control through fusion to optogenetically active domains; they also offer easy transition between model systems as well as potential for therapeutic applications (Hüll et al., 2018; Zenker et al., 2017). Motivated by the spatiotemporal complexity and critical importance of MT cytoskeleton biology, the search for photopharmaceutical MT-modulating reagents has intensified in recent years (Castle and Odde, 2015).

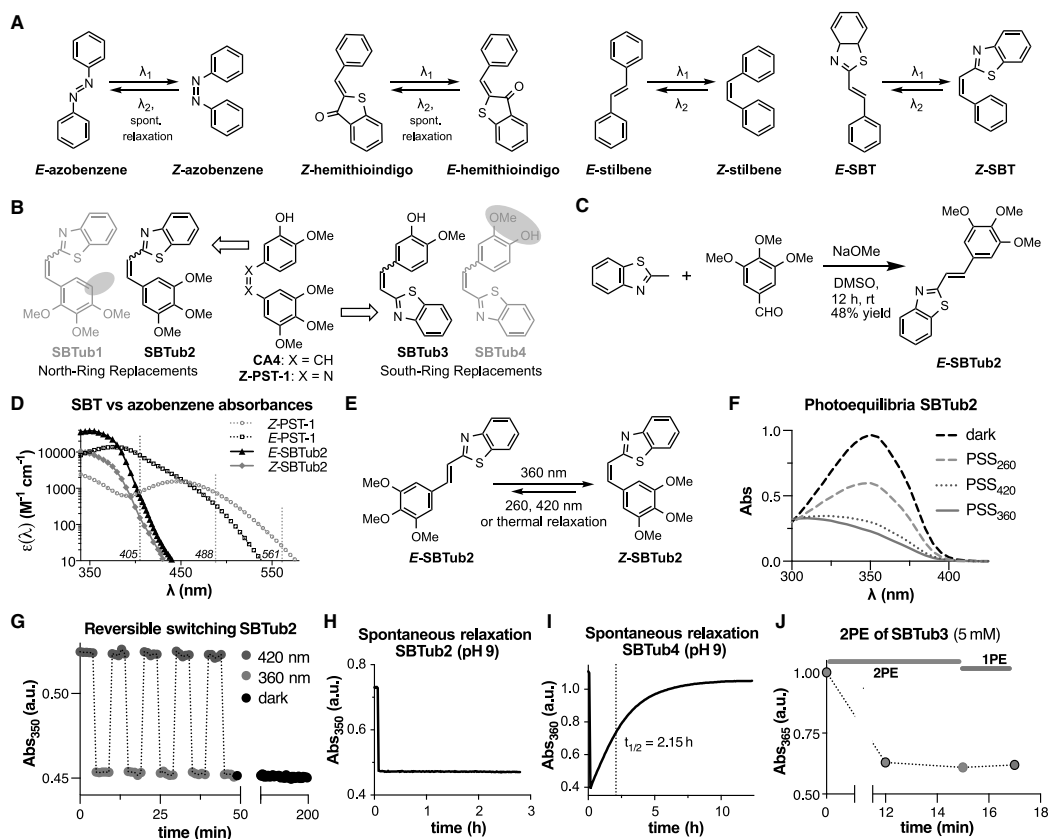


**Figure 1. Design, Synthesis and Photoswitching of SBTubs**

(A) Photoswitchable molecular scaffolds azobenzene, hemithioindigo, stilbene, and styrylbenzothiazole (SBT).  
 (B) SBTubs designed by derivatizing SBTs so that their Z isomers mimic (SBTub2/3) or mismatch (SBTub1/4) the tubulin-binding pharmacophore of combretastatin A-4 (CA4) and of azobenzene photopharmaceutical PST-1. Mismatches indicated by red shaded ovals.  
 (C) Synthesis of representative reagent, SBTub2.  
 (D) Comparison of absorbance spectra of representative SBT and azobenzene scaffolds illustrates the SBT's absorption cutoff above 410 nm, which suits it to orthogonality to GFP, YFP, and RFP imaging.  
 (E) SBTubs can be photoswitched from all-*E* to majority-*Z* using 360 nm, partially switched back with 420 or 260 nm light, and revert quantitatively to all-*E* by thermally driven spontaneous relaxation.  
 (F) Absorbance spectra of representative SBTub2 at various photostationary state (PSSs) equilibria.  
 (G) SBTubs can be photoswitched in aqueous medium under air over multiple cycles without degradation (see also [Figures S1B–S1J](#)). At pH ~7 they persist at PSS without appreciable spontaneous relaxation for hours when illumination is stopped.  
 (H and I) Spontaneous relaxation of (H) SBTub2 and (I) SBTub4 at pH ~9 shows the structure-dependent influence of solvent environment on relaxation rates (see also [Figure S1C](#)).  
 (J) SBTubs can be isomerized via two-photon excitation (2PE) reaching identical PSS as under single-photon excitation (1PE) (2PE at 780 nm, 1PE at 360 nm; compare [Figure S1D](#)).

The vast majority of photopharmaceuticals continue to be based on the reversibly photoswitchable azobenzene molecular scaffold, in which an abiotic N=N chromophore underlies photoswitching between the stable *E* and metastable *Z* isomers ([Figure 1A](#)) ([Broichhagen et al., 2015](#)). The most widely used photopharmaceuticals for optical MT control are also azobenzene based. These "photostatins" (PSTs) ([Figure 1B](#)) are analogs of

the tubulin depolymerizing agent combretastatin A-4 (CA4) ([Figure 1B](#)) ([Borowiak et al., 2015](#); [Engdahl et al., 2015](#); [Gaspari et al., 2017](#); [Sheldon et al., 2016](#)). Driven by illuminations with low-intensity visible light, PSTs undergo bidirectional photoswitching between the inactive *E* and the MT-inhibiting *Z* isomer. PST photoswitching has enabled noninvasive, reversible, cellularly resolved optical control over MT dynamics and network

structure in cell culture as well as *Drosophila melanogaster* (Singh et al., 2018), *Caenorhabditis elegans* (Borowiak et al., 2015), *Danio rerio* (Vandestadt et al., 2019), and mouse models (Zenker et al., 2017), helping to resolve questions in mammalian development and neuroscience (Eguchi et al., 2017; Zenker et al., 2018). These illustrate the power of photopharmacology to enable previously inaccessible studies of spatiotemporally complex processes. However, azobenzene-based approaches to photocontrol of intracellular biology in general incur three disadvantages.

Firstly, intracellular photopharmacology typically relies on imaging-based readouts, but azobenzenes usually feature such a strong uni- or bidirectional photoresponse to standard imaging wavelengths, that isomerization caused by imaging overrides their desired photoswitching (Borowiak et al., 2015; Hüll et al., 2018) and/or limits the scope of experiments. This photoresponse is due to the low-energy  $n \rightarrow \pi^*$  transitions of their N=N chromophore's lone pairs. Regardless of their starting isomer population, azobenzenes, such as PSTs, are rapidly switched to  $\sim 3:1$  E:Z under 488 nm (GFP/fluorescein imaging) and to  $\sim 4:1$  E:Z under 514 nm (YFP/Cy3); even 561 nm illumination noticeably affects isomer ratios on the confocal stage. Therefore, due to imaging, a background of Z-azobenzene is created in areas where isomerization away from the stable E isomer is not desired; and in areas where most Z isomer is generated (typically by photoswitching at 405 nm), each imaging frame instead increases the proportion of E isomer. By counteracting any spatiotemporally resolved isomer patterning throughout the sample, non-orthogonality to imaging wavelengths limits the azobenzene scaffold's potential for high-precision use in cell biology or transgenic animals (where the most common tags are GFP/YFP-based).

Secondly, azobenzene photopharmaceuticals for intracellular targets tend to lose performance when transitioning to cellular assays, which seems to be due to the cellular instability of their electrophilic and abiotic N=N chromophore (Schehr et al., 2019). The majority of azobenzenes can be degraded following the addition of cytoplasmic glutathione (GSH) (ca. 3–10 mM) to the N=N group, ultimately giving a range of non-photoswitchable byproducts of N=N bond degradation (Lei et al., 2019; Samanta et al., 2013a, 2013b; Sheldon et al., 2016). Cleavage byproducts may in many cases be *more* bioactive on target than the intact reagent, which blocks cellular photoswitchability of inhibition (Schehr et al., 2019). This is a major flaw of the prevailing design strategy of "azo-extension," which ensures that only half of the photoswitch is properly accommodated by the protein target, despite the known risks of scission. Even when cellularly photoswitchable reagents are designed by pharmacophore embedding, such that scission byproducts cannot be bioactive on target (such as PSTs), they typically feature losses of apparent potency that are presumably due to such degradation. For example, PSTs are  $\sim 2$  orders of magnitude less potent in cells than CA4, despite near-identical potency in cell-free assays. Potency loss and potentially problematic metabolites continue to obstruct robust applications of azobenzenes to intracellular targets, especially *in vivo* (Boulègue et al., 2007; Sheldon et al., 2016).

Thirdly, azobenzenes undergo spontaneous unidirectional Z  $\rightarrow$  E isomer relaxation, the rate of which depends on the substituents at the six *ortho* and *para* positions that interact strongly

with the N=N double bond. In particular, some of the most important functional groups for ligand-protein interactions (including hydroxy, amine, and thiol groups) cause fast relaxation in physiological aqueous medium if they substitute at any of these positions, typically giving  $\mu$ s–ms half-lives (Hüll et al., 2018; Samanta et al., 2013b). Fast-relaxing azobenzenes cannot practicably be photopatterned to address intracellular targets, since counteracting their uniform relaxation to the E isomer would require biologically unacceptable photon fluxes. Azobenzene photopharmacology is in general limited by the ranges of relaxation half-lives accessible to its tolerated substituent space, which also probably restricts its target scope.

These problems—non-orthogonality to standard imaging conditions, metabolic liabilities in intracellular settings, and strong substituent-dependent limits on thermal half-life—intrinsically derive from azobenzene's N=N double bond. We perceive that these problems have largely hindered the translation of azobenzene photopharmaceuticals for intracellular targets from cell-free to cell culture settings, and essentially block their applications from simple *in vivo* models to higher animals (for further discussion, see the Supplemental Information). Therefore, we were motivated to develop new photoswitchable scaffolds avoiding these three problems—both for the specific case of photoswitchable MT inhibitors, as well as for general applications to chemical biology—and to examine their performance features that could suit them to more robust, orthogonal, biological photocontrol in complex systems.

In light of these three problems, we here explored the almost-unstudied styrylbenzothiazole (SBT) molecular scaffold as an alternative photoswitch based on a C=C double bond that could avoid these three problems. We evaluated this scaffold for chemical biology by synthesizing a rationally designed series of SBT-based tubulin inhibitors (SBTubs) and assaying them for their performance as biochemically robust, GFP-orthogonal, photoswitchable analogs of CA4. We obtained ligand-protein crystal structures confirming the SBTubs' two modes of tubulin binding, then demonstrated their optical control over MT network integrity, cell division, and cell death. Finally, using their unique photoresponse characteristics, we demonstrate that they enable temporally reversible, optical modulation of MT dynamics independently of ongoing imaging, in live GFP-tagged cells, and demonstrate their capacity for subcellularly spatially resolved and temporally precise inhibition of endogenous MT dynamics in primary hippocampal neurons. This is to our knowledge the first use of SBTs as photopharmaceuticals in chemical biology, and highlights both SBTubs' and the SBT scaffold's promise for use in a range of high spatiotemporal precision biological studies.

## RESULTS

### Scaffold Selection

To avoid photoresponse to wavelengths above 460 nm, we chose a photoswitch based on a C=C double bond that has no chromophore lone pairs and so no  $n \rightarrow \pi^*$  bands (Horspool and Lenci, 2004), yet offers substantial geometric change upon isomerization so that bioactivity photoswitching could be possible. Hemithioindigo is the most widely used C=C-based photoswitch, but we excluded it because of its long-wavelength response even at 520 nm, due to the *ipso*-sulfur (Sailer et al.,

2020). Stilbenes are barely used in modern photopharmacology since they require UV light below 340 nm for photoswitching, which is not accessible on microscopes, and also degrade when illuminated in the presence of oxygen (Francioso et al., 2014). We instead selected the almost-unstudied SBT scaffold. SBT is a C=C double bond-based photoswitch whose planar *E* and bent *Z* isomers differ substantially in geometric fit and end-to-end distance. They have similar geometry as the azobenzene *E* and *Z* isomers, although they are larger on their benzothiazole side (Figure 1A). We expected that the non-electrophilic C=C double bond (Awad et al., 2013; Hofmann, 1880) would endow them with increased robustness toward GSH reduction as well as slower relaxation of the *Z* isomer, as compared with azobenzenes; while, as compared with stilbenes, the benzothiazole would redshift the  $\pi$ - $\pi^*$  band enough to be photoswitched with visible light (Mishra et al., 2013) while also blocking photochemical degradation (El-Hendawy et al., 2015).

#### Reagent Design and Synthesis

Searching for isomer-dependently bioactive tubulin inhibitors based on the SBT scaffold, we designed two SBTubs whose *Z* isomers could be closely isosteric replacements of the MT inhibitor CA4 and whose *E* isomers would mimic the inactive *trans*-CA4, so aiming at *Z*-SBTub-specific MT inhibition. These became SBTub2 (where the benzothiazole ring replaces the “north,” isovanillinyl ring of CA4), and SBTub3 (where the benzothiazole replaces the “south,” trimethoxyphenyl ring; Figure 1B). We expected that the benzothiazole would give similar space occupancy, geometry, and polarity intermediate as the replaced rings, and since the colchicine site is somewhat accommodating (Shan et al., 2011; Tron et al., 2006), we expected that both *Z*-SBTubs might bind despite sacrificing some potency-enhancing interactions.

As a key validation step, we also created permutation controls (designed-inactive compounds) to test the tubulin specificity and *Z* isomer specificity of SBTub bioactivity. Permutation controls contain the same number and types of functional groups, but swap the positions of key bioactivity-controlling substituents to intentionally mismatch requirements for target-specific binding. We have previously used this to distinguish effects of molecularly specific binding to the target protein (which should be a feature of the designed-active compounds only) versus “pan-assay interference compounds”-like nonspecific bioactive effects expected for typically hydrophobic photoswitch compounds (e.g., promiscuous binding to or aggregation on proteins, compound precipitation, membrane disruption [Baell and Nissink, 2018]) as well as nonspecific scaffold toxicity or phototoxicity under illumination, since any nonspecific bioactivity should be reproduced by permutation controls (Sailer et al., 2019). We permuted methoxy and hydro groups of SBTub2 to create control SBTub1, and permuted hydroxy and methoxy groups of SBTub3 to create control SBTub4 (Figure 1B). Reagents SBTub1–4 were synthesized in good yields by basic aldol condensations of 2-methylbenzothiazole with the corresponding aldehydes (Figure 1C; see the Supplemental Information).

#### SBTub Spectral Response in Cuvette Suggests Orthogonality to GFP Imaging

The spectral characteristics of SBTubs were similar, with  $\pi$ - $\pi^*$  absorption maxima for *E* (~360 nm) and *Z* isomers (~305 nm) be-

ing well separated, enabling directional photoisomerizations with LEDs at wavelengths  $\leq 425$  nm (Figures S1A–S1D). Pleasingly, both *E*- and *Z*-SBT isomers' absorptions drop sharply toward zero above 410 nm (Figure 1D). This is crucial for avoiding any *E*  $\leftrightarrow$  *Z* photoisomerization under 488 nm imaging with intense focused lasers (“GFP-orthogonality”) because absorption “tails” that extend far past absorbance maxima can cause substantial photoswitching in microscopy (e.g., 561 nm RFP imaging on the confocal microscope photoisomerizes the azobenzene Z-PST, although its absorbance maximum is at 445 nm). Our expectation was therefore, that the SBTubs' absorption cutoff is at the optimum position to permit rapid *E*  $\rightarrow$  *Z* photoswitching with the common 405 nm microscopy laser line, while potentially allowing GFP-orthogonality.

#### SBTub Photoswitching Is Robust across a Range of pH and Environments

Under physiological conditions, the SBTubs could be optimally *E*  $\rightarrow$  *Z* photoisomerized with 360 nm light, giving a photostationary state (PSS) equilibrium with a *Z*:*E* ratio of ~85:15. Applying shorter or longer wavelengths back-isomerized the SBTubs toward more *E*-enriched PSSs (Figures 1E and 1F). We selected “dark” (all-*E*) and “lit” (360 nm, mostly-*Z*) as default illumination conditions for further use (Berdnikova et al., 2012). Pleasingly for our aims, reversible photoisomerizations with high-power illuminations repeatedly traversing the biologically applicable range of 360–420 nm caused no detectable photodegradation under aerobic aqueous conditions (Figure 1G). The SBTub spectra and photoswitching properties were entirely robust to variations of pH and environment (Figures S1C and S1D). The functional performance of this first generation of slow-relaxing SBTubs is turn-on-only, due to the band overlap between *E* and *Z* isomers. However, the metastable *Z* isomers of all SBTubs could be quantitatively relaxed to *E* by warming to 50°C–60°C overnight, although at 25°C they showed no significant thermal relaxation after several hours at pH ~7 in physiological medium (Figure 1G). The *para*-hydroxy group unique to SBTub4 accelerated its relaxation in basic conditions (Figures 1H and 1I), but the stability of *Z*-SBTub4 against relaxation at pH ~7 contrasts favorably to both azobenzene and hemithioindigo photoswitches with *para*- (or *ortho*-) hydroxy or amino substituents that typically feature millisecond (azobenzene) to second (hemithioindigo) half-lives at these conditions. This underlines the broader chemocompatibility of SBTs as a photoswitch scaffold for these functional groups that are so important in ligand design (further discussion in the Supplemental Information).

#### SBTubs Can Undergo Two-Photon Photoswitching

We tested if SBTubs can be isomerized by two-photon excitation (2PE), which could increase spatial resolution compared with single-photon excitation (1PE) (Moreno et al., 2015). This may especially benefit high spatial precision cell-free studies, such as time-resolved studies of tubulin structural rearrangements following ligand isomerization inside a lattice. We used a mode-locked Ti:sapphire laser at 780 nm to bulk photoisomerize SBTub3 in concentrated (5 mM) DMSO solution, delivering 2PE inside a single voxel and relying on diffusion to establish *Z*/*E*-isomer equilibrium in the whole 8  $\mu$ L sample. After 12 min of 2PE the isomer equilibrium did not evolve either with additional 2PE or

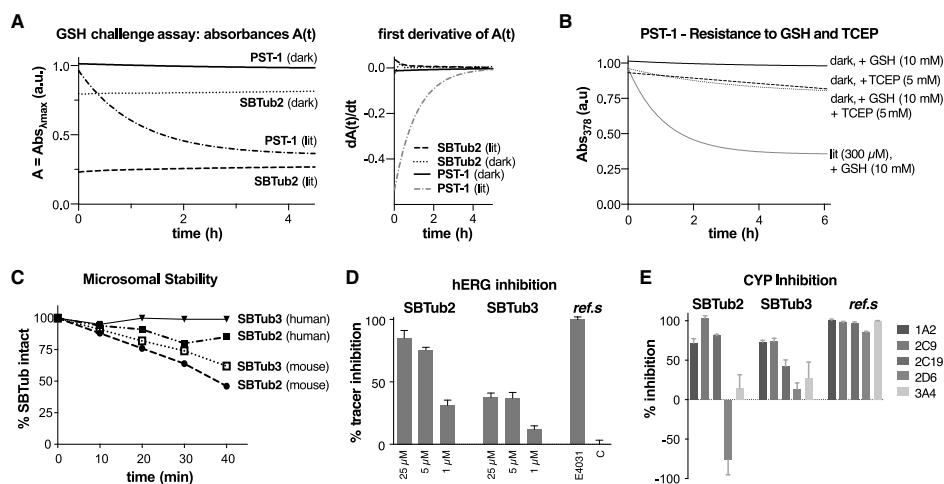


**Figure 2. Biochemistry of SBTubs**

(A and B) Glutathione (GSH) challenge assays under dark or lit conditions (A) monitoring the change of photoswitch absorbance during incubation with 10 mM GSH of SBT SBTub2 (25  $\mu$ M) and azobenzene PST-1 (50  $\mu$ M dark/300  $\mu$ M lit); decreases indicate molecular degradation. (B) The reducing agent TCEP degrades even the more resistant *E* isomer of PST-1, while Z-PST-1 is rapidly degraded by GSH (see also Figures S2A–S2F).

(C) SBTub2 and SBTub3 substantially resist metabolism by purified human and mouse liver microsomes (monitored by high-performance liquid chromatography).

(D) hERG binding by SBTub2 and SBTub3, referenced to positive control E4031 (30  $\mu$ M) and cosolvent-only negative control “C.” Data represented as mean with SE,  $n = 4$ .

(E) *E*-SBTubs (10  $\mu$ M) show moderate CYP450 inhibition.

See also Figure S2G.

with 1PE at 360 nm, indicating that 2PE can efficiently photo-switch *E*-SBTub to  $\sim$ 85% *Z* (Figure 1J).

### SBTubs Are Highly Robust to Glutathione, and Resist Photobleaching and Metabolism

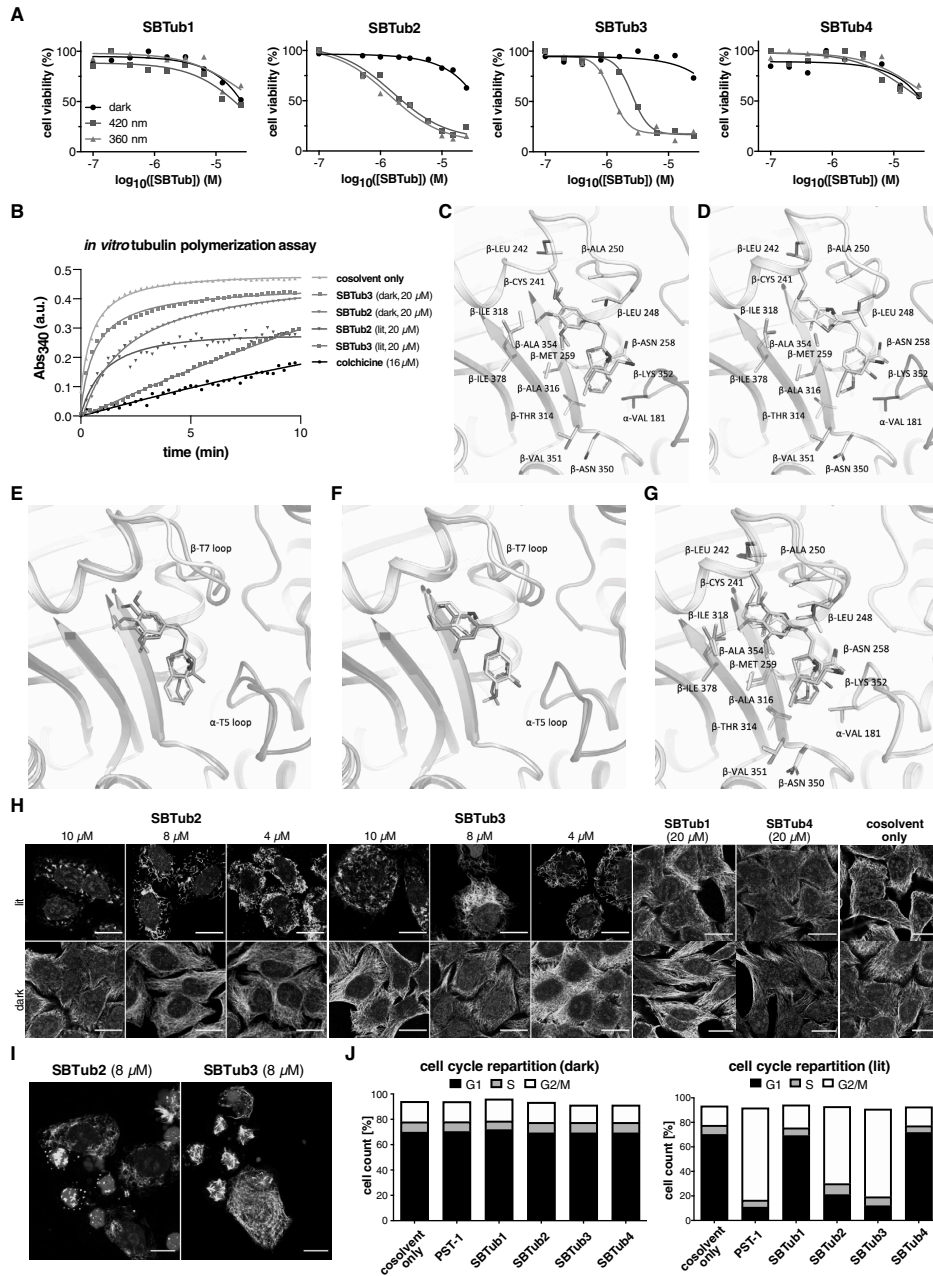
We next assessed the SBT scaffold’s photochemical and biochemical robustness. We monitored *E*- and *Z*-SBTubs under UV irradiation in a Rayonet photochemical reactor. We found them to be stable to 1 h of continuous high-power UV, indicating outstanding photochemical stability (Figures S1E and S1F). We assayed their sensitivity to cellular levels of GSH (10 mM) (Figures 2A and S2A), but detected no degradation, adduct formation, addition-elimination, reduction, or other loss mechanisms. This contrasts strongly to the GSH-mediated destruction of similarly substituted *Z*-azobenzenes, including PST-1 (Figures 2A, 2B, and S2B–S2F; see discussion in the Supplemental Information). We also performed an early *in vitro* metabolic assessment of SBTub2 and SBTub3 for their suitability *in vivo*, examining stability to processing by liver microsomes, inhibition of representative cytochromes, and hERG channel inhibition (Figures 2C–2E). Especially for SBTub3 these assays did not indicate typical drug development problems. As far as we know, only one report has ever considered these crucial biological stability aspects for photoswitches (Babii et al., 2020), and no data are reported for azobenzenes.

We consider the SBT’s performance as a photoswitch scaffold, as well as its improved stability and substituent tolerance

compared with azobenzenes, promising for further biological applications toward cellular and *in vivo* use. We thus began exploring its applicability as a photopharmaceutical scaffold for cell biology research, through the use of SBTubs as photo-switchable MT inhibitors.

### SBTubs Bind to Tubulin and Inhibit Tubulin Polymerization in Their “Lit” State

Since prolonged inhibition of cellular MT dynamics blocks cell proliferation and ultimately results in cell death, we first assayed SBTubs by examining their light-dependent antiproliferative effects on the HeLa cervical cancer cell line (incubation in “lit” conditions via pulsed illuminations with 360 or 420 nm light, or else “dark”). Both SBTub2 and SBTub3 were photoswitchably cytotoxic with  $\gg$ 20-fold cytotoxicity enhancement when lit at 360 nm (half maximal inhibitory concentration [ $IC_{50}$ ]  $\sim$ 1–2  $\mu$ M with  $\sim$ 85% *Z* isomer), as compared with the dark experiments ( $IC_{50} \gg$  20  $\mu$ M with  $\sim$ 100% *E* isomer). Crucially, neither permutation control SBTub1/4 displayed significant or light-dependent bioactivity. This supports the suitability of the SBT scaffold for long-term intracellular photopharmacology (Figure 3A). We attribute the weak antiproliferative activity of all SBTubs at high concentrations in the dark, equal to that of permutation controls SBTub1/4 under lit conditions, as aggregation-dependent effects from poor solubility of the compounds at high concentrations (known for similar species [Borowiak et al., 2015; Sailer et al., 2019], and examined further below). The light-dependent



(legend on next page)

activity of the designed-active SBTubs, and the low toxicity of their permutation controls, matched expectations that SBTub2/3's cellular antiproliferative potency should be based primarily on MT inhibition exerted only by the *in-situ*-photogenerated Z isomers binding to the colchicine site.

To examine their molecular mechanism of light-dependent cellular bioactivity, we first assayed the photoswitchably cytotoxic SBTub2/3 for light-dependent inhibition of polymerization of purified tubulin in a cell-free system. E-SBTub2/3 were essentially inactive, but their Z isomers generated in lit conditions (particularly Z-SBTub3) were inhibitors, as expected for colchicine-site ligands (Figure 3B).

Testing the assumption of Z isomer-specific tubulin binding at the colchicine site by SBTub2/3, we succeeded in crystallizing Z-SBTub2 and Z-SBTub3 in complex with the tubulin-DARPin D1 complex (Pecqueur et al., 2012) and solved the structures to 2.05 and 1.86 Å resolution by X-ray crystallography, respectively (Table S1). Both Z-SBTub2/3 bind to the colchicine site (at the interface of  $\alpha$ - and  $\beta$ -tubulin) (Figures 3C–3G and S3A–S3C). As designed in the ring replacement strategy, they bind with their benzothiazoles in opposite poses, despite contacting identical residues in the binding pocket. Z-SBTub2 places its trimethoxyphenyl ring in the "bottom" lobe of the pocket, which is characteristic of trimethoxyphenyl-bearing CA4 analogs (Tron et al., 2006), whereas Z-SBTub3 binds with its benzothiazole in the "bottom" lobe to maintain polar interactions at the top lobe with its isovanillyl ring (Figure S3D). The benzothiazole can therefore occupy the same space as either the trimethoxyphenyl or the isovanillyl unit of typical colchicine-site inhibitors (Gaspari et al., 2017). This intriguing top-versus-bottom desymmetrization should assist rational design of SBTub-based photopharmaceuticals that project substituents (e.g., functionally diverse side-chain reporters) outward from the colchicine-binding site.

#### SBTubs Light Dependently Inhibit MT Function in Cells

We began examining the cellular mechanism of isomer-dependent SBTub bioactivity by imaging the endogenous MT network architecture in cells incubated with E/Z-SBTubs. Dark assays with E-SBTub2/3 had no impact on MT network architecture, but SBTub2/3 lit at 360 nm (mostly-Z isomer) caused mitotic arrest and MT depolymerization, with similar dose dependency

as in the viability assays (Figure 3H). Z-stack images revealed substantial accumulation of rounded, mitotically arrested cells (Figure 3I). These are hallmarks of treatment with MT-inhibiting antimetotics, supporting the conjecture that SBTub2/3's strongly photoswitchable cytotoxicity arises from their Z isomers inhibiting MTs in cells. By contrast, the permutation controls SBTub1/4 showed no disruption of MT network architecture under dark or lit conditions, even at high concentrations which do exert antiproliferative effects (Figure 3H), further supporting that MT-inhibiting activity is specific to photoswitched Z-SBTub2/3 only. If their major cellular bioactivity mechanism is MT inhibition, Z-SBTub2/3 should induce light-dependent G<sub>2</sub>/M phase cell-cycle arrest (Tron et al., 2006), and using flow cytometric analysis we observed this for both Z-SBTub2 and 3, but not for their E isomers or for permutation controls E/Z-SBTub1/4 (Figure 3J). This further supports that all-E-SBTubs have negligible MT-inhibiting effects, while the appropriately substituted Z-SBTub2/3 potently inhibit MT function, suiting them to photoswitching-based control of MT-dependent processes. Observing that, from the two active compounds, SBTub3 was both more reliably soluble than SBTub2, and exhibited a sharper dose-response curve which makes it more suited to isomerization-based bioactivity switching, we selected SBTub3 as our preferred lead compound and performed all subsequent assays with it.

We next set out to test some conceptual advantages that the photophysical and biochemical properties of the SBT scaffold should endow upon the SBTubs, when compared with azobenzenes and other major photoswitch types, in their most likely biological applications.

#### A Single Isomerization of SBTub Enables Long-Term MT Photocontrol

Since Z-SBTubs are stable to cell-free biochemical challenge and to spontaneous relaxation (Figures 1 and 2), we first tested whether a single E→Z isomerization event could be used to induce long-term impact on cells, without requiring re-illuminations throughout the assay (as is necessary with faster-relaxing azobenzenes, e.g., PSTs) (Borowiak et al., 2015). We applied E-SBTub3 to cell culture, isomerized it *in situ* to a majority-Z population using 18 s of low-power LED illumination at 360 nm, then shielded the cells from outside light and observed cell viability

#### Figure 3. SBTubs' Bioactivity is Light Specific and Tubulin Mediated

(A) SBTub2/3 give strong light-specific antiproliferative effects, while controls SBTub1/4 give minor and light-independent effects (HeLa cells, 40 h incubation; all-E dark conditions versus mostly-Z lit conditions using low-power pulsed LED illuminations [75 ms per 15 s, <1 mW/cm<sup>2</sup>]; one representative experiment of three independent experiments shown).

(B) SBTub2/3 light dependently inhibit tubulin polymerization (turbidimetric *in vitro* polymerization assay; greater absorbance corresponds to a greater degree of polymerization).

(C–G) Close-up views at the colchicine-binding site of X-ray crystal structures of tubulin-Z-SBTub complexes (see also Figure S3). (C) Tubulin-Z-SBTub2 (PDB: 6ZWC) and (D) tubulin-Z-SBTub3 (PDB: 6ZWB) complexes (dark gray  $\alpha$ -tubulin and light gray  $\beta$ -tubulin in cartoon representation; ligands and interacting residues in stick representation with oxygens red, nitrogens blue, and ligand carbons green [SBTub2] or yellow [SBTub3]). (E–F) Superimpositions of tubulin-CA4 (orange carbons; PDB: 5LYJ) with (E) tubulin-SBTub2 (green carbons) and (F) tubulin-SBTub3 (yellow carbons) structures. (G) Superimposition of tubulin-SBTub2 (green carbons) and tubulin-SBTub3 (yellow carbons) structures.

(H) Immunofluorescence imaging of cells treated with SBTub2/3 shows breakdown of MT architecture under 360 nm pulsing ("lit") but no disorganization in the dark. Scaffold controls SBTub1/4 and cosolvent controls show no scaffold- or light-dependent confounding effects (HeLa cells, 20 h incubation;  $\alpha$ -tubulin in green, DNA stained with DAPI in blue). Scale bars, 20  $\mu$ m.

(I) Maximum intensity projections along the z axis of SBTub2/3 immunofluorescence image stacks show mitotic arrests in illuminated conditions; treatment as in (H).

(J) Cell-cycle analysis of cells treated with SBTub2/3 shows significant G<sub>2</sub>/M arrest under 360 nm pulsing ("lit") but not in the dark, as does reference PST-1. Controls SBTub1/4 and cosolvent show no cell-cycle effects (SBTubs at 20  $\mu$ M, PST-1 at 2.5  $\mu$ M).



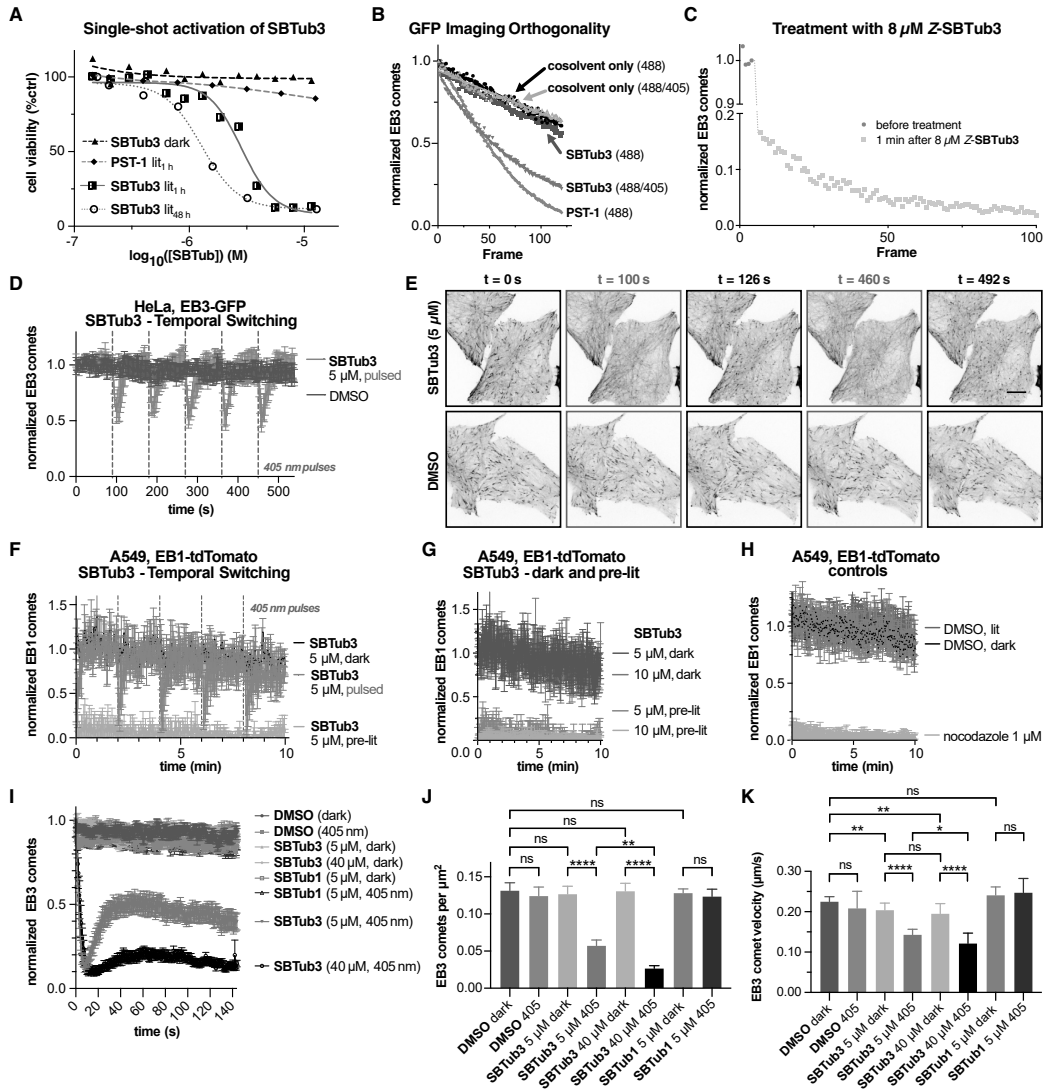


**Figure 4. SBTub3 is a GFP-Orthogonal Reagent that When Isomerized Causes Rapidly Reversible Inhibition of MT Dynamics in Live Cells**

(A) Antiproliferation assays with single-shot photoactivation ( $lit_{1h}$ ) versus with ongoing illumination ( $lit_{48h}$ ) show the SBT's sustained pharmacological activity compared with azobenzene PST-1 (HeLa cells, 48 h, pulsing as in Figure 3A; one representative experiment of three independent experiments shown). (B and C) Live-cell EB3-GFP "comet" counts during GFP imaging with 488 nm (HeLa cells). (B) Imaging in the presence of *E*-SBTub3 does not affect comets, whereas azobenzene PST-1 is isomerized by imaging and stops MT polymerization. Only with additional 405 nm pulses does *E*-SBTub3 isomerize to *Z*-SBTub3 and stop MT polymerization dynamics (10  $\mu$ M *E*-SBTub3 or *E*-PST-1). (C) Comet count before and after treatment with pre-lit (mostly-*Z*) SBTub3. (D and E) Data related to Video S1: EB3-GFP-transfected HeLa cells treated with/without SBTub3 were illuminated at 405 nm every 90 s; MT polymerization dynamics were quantified by imaging EB3 comets at 491 nm. (D) EB3 comet counts are reversibly modulated by 405 nm photoactivations with SBTub3 (red) but are unaffected in its absence (blue) (dotted lines indicate 405 nm pulses,  $n = 5$  movies per condition, mean with standard deviation). (E) Representative still images at baseline ( $t = 0$  s); at 10 s/36 s after the first photoactivation ( $t = 100$  s/126 s, comets vanished/recovered); and at 10 s/42 s after the fifth photoactivation ( $t = 460$  s/492 s, comets vanished/recovered). Scale bar, 10  $\mu$ m.

(legend continued on next page)

40 h later. Z-SBTub3's antiproliferative potency in this single-shot experiment (Figure 4A) nearly matched that observed under pulsed re-illuminations every 15 s, indicating the stability of the Z-SBTubs in cells in the long term (despite the presence of, e.g., cellular thiols). By comparison, azobenzene-based PST-1 was essentially inactive in this single-shot experiment, which was expected since degradative metabolism as well as thermal relaxation should deplete cellular Z-PST levels rapidly (reports suggest within an hour [Sheldon et al., 2016]).

#### SBTubs Enable Photocontrol of Cellular MT Dynamics Independently of GFP/YFP Imaging

To study SBTubs' ability to effect *in situ* photocontrol of MT dynamics in higher spatiotemporal resolution, we imaged live cells transfected with labeled end binding proteins (EBs). EBs, including EB1 and EB3, mark the GTP cap regions of polymerizing MTs. Imaging fluorescent EB fusion proteins by live-cell confocal microscopy reveals the plus ends of polymerizing MTs as dynamic comets (Merriam et al., 2013; Roostalu et al., 2020), and imaging during photoswitching is a spatiotemporally resolved readout for isomerization-dependent inhibition of MT dynamics by photoswitchable inhibitors (Borowiak et al., 2015; Müller-Deku et al., 2020).

We first tested whether SBTubs avoid any isomerization during imaging, which would make them suitable for fully orthogonal imaging and photocontrol: an important unsolved challenge for intracellular photopharmacology. We imaged MT dynamics using GFP-EB3 with excitation at 488 nm and YFP-EB3 with excitation at 514 nm by confocal microscopy. As hoped from their sharp absorption cutoff above 410 nm, neither GFP nor YFP imaging under treatment with E-SBTub3 caused inhibition of MT dynamics; but when 405 nm photoactivation pulses were additionally applied, MT dynamics were rapidly suppressed (Figure 4B). By imaging and photoactivation of cosolvent controls, and imaging under treatment with pre-activated Z-SBTub3, we showed that this suppression of MT dynamics is not due to photobleaching but is consistent with selective E→Z photoisomerization of SBTub3 under 405 nm only (Figures 4B and 4C). As treatment with Z-SBTub3 blocks MT dynamics throughout the imaging time course, this shows that both E→Z and Z→E-SBTub isomerization are fully orthogonal to typical imaging conditions (Figures 4C and S4A–S4C; see discussion in the Supplemental Information). We consider this a powerful demonstration that the SBT scaffold may more generally be well suited for use in photopharmaceuticals, against diverse targets, across many biological systems where GFP and YFP reporters are used.

#### SBTubs Enable Temporally Reversible MT Photocontrol in Cells that Are Orthogonal to Imaging

Achieving temporally reversible, spatially localized cellular applications of photoactivatable compounds is the major goal of both

photopharmacology and photouncaging. These first-generation SBTubs were designed for E→Z photoisomerization with high spatiotemporal precision. They cannot be substantially Z→E photoisomerized in cells, and they are too stable to undergo substantial spontaneous Z→E relaxation at physiological temperatures, so neither process can be relied upon to revert Z-SBTub to its bioinactive isomer. However, as in photouncaging, temporally reversible and spatially localized inhibition can still be achieved using spatiotemporally localized activating photoisomerization, if two conditions are met: (1) inhibitor-target dissociation and intracellular or transmembrane diffusion must quickly reduce the concentration of the photoactivated species below its inhibitory threshold and (2) protein function must be immediately restored upon inhibitor dissociation (true for colchicine domain inhibitors). If so, and particularly in systems with a highly nonlinear dose response (such as the MT cytoskeleton), localized photoactivation followed by diffusion-based depletion of the photogenerated bioactive isomer may give complete functional recovery in a single cell or region, on the compound's diffusion or transmembrane partitioning timescale. Z-SBTub3 did show fast membrane penetration kinetics, since its addition to cell bath solutions quickly stopped MT dynamics (Figure 4C). We therefore assayed the temporal reversibility of SBTub's cell-localized modulation of MT dynamics by an EB3-GFP imaging assay with pulses of 405 nm photoactivation. MT polymerization dynamics were repeatedly paused then rapidly recovered to normal, with quantifications aligning closely over many cells (Video S1; Figures 4D and 4E).

We performed a similar experiment while changing the cell line, biological label, and fluorescent marker, to test the SBTubs' broader applicability and the hypothesis that SBTubs generate readout in these assays by causatively modulating MT polymerization (rather than, e.g., by directly affecting EB3-GFP/YFP). We repeated the temporal reversibility experiments in A549 lung cancer cell line, transfected with the dsRed-derived tdTomato marker fused to the end binding protein EB1. We observed identical temporal modulation (Figures 4F–4K; Video S2), validated by benchmarking against non-405 nm illuminated cells treated with pre-lit Z-SBTub3 (Figures 4F and 4G). Comparing dark and pre-lit SBTub3 with DMSO-only controls and the positive control tubulin inhibitor nocodazole confirmed resistance to both E→Z and Z→E isomerization during imaging (Figures 4I–4K). SBTub photoswitching can therefore drive highly reproducible, GFP-orthogonal, temporally reversible modulation of MT polymerization in live cells, performance which no other tubulin photopharmaceutical has delivered.

#### SBTub Photoswitching Permits Subcellularly Resolved MT Inhibition in Primary Neurons

Rapid diffusion of small-molecule inhibitors within cells makes subcellular patterning of photopharmaceuticals against cytosolic

(F–H) Data related to Videos S1 and S2: EB1-tdTomato-transfected A549 cells treated with/without SBTub3 were imaged for EB1 comets at 561 nm. Cells exposed to SBTub3 and pulses of 405 nm show temporally precise suppressions of MT polymerization dynamics upon 405 nm applications that reach maximal inhibition similar to positive controls nocodazole or pre-lit SBTub3, but rapidly recovering to similar levels as non-pulsed SBTub3 or cosolvent controls.

(I–K) Controls related to (B–H). EB3-GFP-transfected HeLa cells were treated with SBTub3, scaffold control SBTub1, or DMSO solvent alone, then imaged directly after treatment, optionally with 405 illuminations interleaved. Movies were analyzed for (I) EB3 comet counts, (J) average EB3 comet density, and (K) average EB3 comet velocity. Data shown as mean ± standard deviation; \*p < 0.05, \*\*p < 0.01, \*\*\*p < 0.001, \*\*\*\*p < 0.0001; n.s., not significant; n = 10 cells per condition).

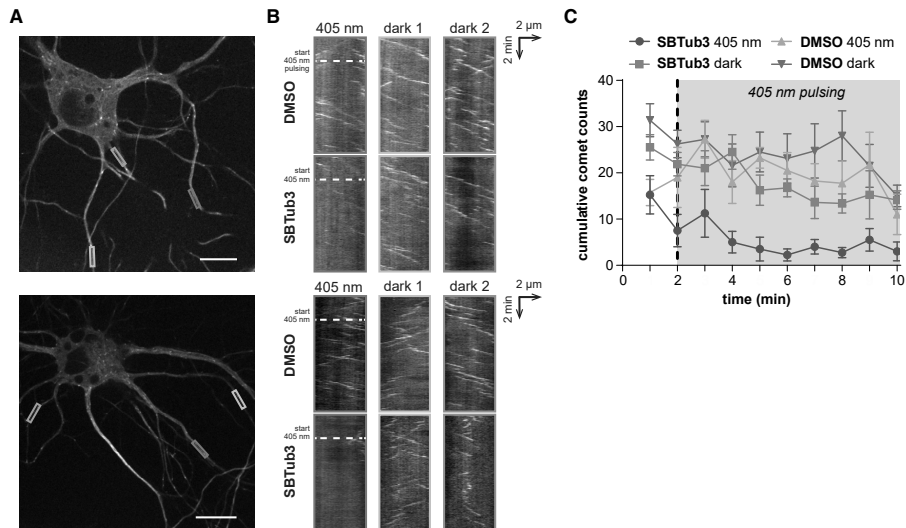


**Figure 5. Local SBTub Photoisomerization Inhibits MT Polymerization in Subcellular Regions of Primary Hippocampal Neurons**  
(A–C) Data related to [Video S3](#): cultured primary neurons (10 days *in vitro*) transfected with EB3-GFP and treated with 1% DMSO were imaged for EB3 for 10 min while an ROI (blue box) was pulsed with 405 nm commencing 2 min into the acquisition (indicated by dotted lines). Baseline EB3 dynamics in the cell and the ROI were shown to be light independent. The same neurons were then exposed to 1  $\mu$ M SBTub3 and immediately imaged for another 10 min; during this time the same ROI was again pulsed with 405 nm with 2 min onward. (A) Cell images with regions marked, and (B) EB3 kymographs of these regions. The ROI pulsed with 405 nm is boxed in blue; the regions not pulsed with 405 nm are boxed in orange and green. Scale bars, 10  $\mu$ m. (C) EB3 comet counts accumulated over 20 frame (1 min) intervals ( $\pm$ SEM) plotted over time, for regions treated with or without SBTub3 and 405 nm pulsing ( $n = 4$  cells).

targets challenging. However, large cells (e.g., embryonic systems) or irregularly shaped cells (e.g., neurons) are targets whose geometry and size may favor subcellular patterning. We cultured isolated primary rat hippocampal neurons until neurites developed, then transfected them with EB3-GFP for imaging ([Kapitein et al., 2010](#)). For each neuron, we selected several equal-sized areas along independent neurites and monitored the dynamics of EB3 comets before and during SBTub3 treatment, with repetitive ROI-localized 405 nm applications to one of the areas, aiming to locally block MT polymerization in the selected neuronal process area ([Figure 5](#); [Video S3](#)). For SBTub3-treated cells, kymographs of 405 nm illuminated neurites showed localized reductions in EB3 comet number and lifetime, while non-illuminated neurites showed no significant changes from baseline; and controls before/after SBTub3 application showed no photobleaching by 405 nm illumination ([Figure 5B](#)). Comet counts ([Figure 5C](#)) indicated likewise that SBTub3 photoswitching induces subcellularly localized inhibition of MT polymerization.

## DISCUSSION

Photopharmacological approaches to high spatiotemporal precision reagents for noninvasive studies of endogenous protein function have made significant progress in the last decade. From original applications in neuroscience ([Lester et al., 1980](#); [Volgraf et al., 2005](#)), they now impact membrane and cytoskeleton biology ([Borowiak et al., 2015, 2020](#); [Frank et al., 2016](#); [Ur-](#)

[ban et al., 2018](#)); and recent advances in long-wavelength photoswitches offer prospects for *in vivo* photopharmacology ([Bléger et al., 2012](#); [Konrad et al., 2016](#); [Samanta et al., 2013b](#)). However, the scope of targets and assays accessible to photopharmacology has been restricted by its chemistry. The overwhelming majority of photopharmaceutical designs employ azobenzenes as the photoswitch moiety and so inherit their functional limitations: (1) the diazene's nucleophilic and metabolic susceptibility is problematic for addressing intracellular targets or for long-term, systemic *in vivo* applications; (2) its  $n-\pi^*$  absorption in the blue-green spectral region is triggered by imaging standard biological tags (e.g., GFP/YFP); and (3) azobenzenes for cytosolic targets have restricted substituent scope since *ortho/para*-electron-donating groups that are key to strong ligand-protein interactions (OH, NH<sub>2</sub>, etc.) cause microsecond relaxation rates, so are not bulk photoisomerizable under physiological conditions. Only recently have non-azobenzene photoswitches, such as dithienylethenes and hemithioindigos, been used in bioactive pharmacophores ([Sailer et al., 2019](#); [Simeth et al., 2017](#)); and the development of novel photoswitch scaffolds is recognized as a valuable milestone even before reaching cellular applications ([Hoorens et al., 2019](#)).

Here, we have demonstrated the design and testing of a novel concept for a GFP-orthogonal metabolically resistant SBT photoswitch scaffold. The SBT scaffold has comparable chemical simplicity with that of azobenzene and delivers spatiotemporally precise photoswitching-based biological control, while also

addressing all three challenges by bringing: (1) biochemical/metabolic robustness; (2) orthogonality to common imaging conditions; and (3) an alternative range of isomerization-tolerant substituents (e.g., including *para*-OH). Thus, SBT expands the scope of intracellular targets and of biological assays (toward *in vivo* use) accessible to photopharmacology.

The reagents conceptually nearest to the SBTubs are the fully photoswitchable (but non-GFP-orthogonal and metabolically labile) PST-1, and (irreversibly) photouncageable inhibitors, such as nitrobenzylether-capped CA4 (Wuhr et al., 2010). A minor issue is that the potency of these SBTubs ( $IC_{50} \sim 1 \mu\text{M}$ ) is less than either previous system ( $IC_{50}$  PST-1  $\sim 0.5 \mu\text{M}$ , fully uncaged CA4  $\sim 20 \text{ nM}$ ); however, further structural tuning of SBTubs may improve potency. It is the different photoresponse of SBTubs that brings them more important advantages and disadvantages. In cells, azobenzenes can undergo  $Z \rightarrow E$  switching by illumination and  $Z \rightarrow E$  isomerization by spontaneous relaxation, whereas this first generation of SBTubs only allows cellular  $E \rightarrow Z$  switching (unidirectional activation). Spontaneous  $Z \rightarrow E$  relaxation could improve their performance in spatiotemporally localized activation assays, by passively counteracting the build-up of photoactivated but diffused reagent; and bidirectional  $Z \leftrightarrow E$  photoswitching would allow active control over the spatiotemporal localization of both  $E$  and  $Z$  isomers.

The unidirectional photoactivation of SBTubs is conceptually somewhat similar to that of photouncageable inhibitors; however, their performance differs in five respects (1) typical photocaging groups (e.g., *ortho*-nitrobenzyls) require hydrolysis before cargo release that can take seconds to minutes, which diminishes the spatiotemporal precision of photouncaging (off-to-on) and diffusion (on-to-off). Isomerization, as the SBTs use, is typically orders of magnitude faster ( $\ll \text{ns}$ ), and SBTubs give reproducibly high-precision biological control. (2) Photouncaging byproducts are often unspecifically toxic and may also be phototoxic (Klan et al., 2013), while SBTub's photochemically robust  $E \rightarrow Z$  isomerization allows cell-tolerated long-term experimentation. (3) Photouncaging strategies add significant molecular weight, which often penalizes bioavailability or biodistribution; they may suffer non-photolytic compound release (enzymatic or spontaneous hydrolysis); and they involve higher synthetic cost (Klan et al., 2013; Reefing and Szymanski, 2017). SBT inclusion in a pharmacophore does not add compound weight or complexity, and avoids any activation mechanisms except photoactivation. (4) The photocages that are orthogonal to 488 nm imaging (e.g., nitrobenzyls) have low uncaging yield at 405 nm and thus require high photon fluxes to uncage, which can cause phototoxicity problems and also photodegrade the released reagent; whereas SBT can efficiently exploit this common microscopy line with high yield and excellent photostability. (5) Photouncageable probes must be protected from irreversible ambient light-induced photodegradation during synthesis, storage, and use; SBTs are easier to handle and use because accidentally light-exposed stocks can be relaxed quantitatively back to the inactive  $E$  isomer by warming.

Taken together, these features set SBTs apart from photouncaging approaches and from azobenzene photoswitching, recommending them for reproducible, high-precision, "clean" photopharmacological control particularly in higher-complexity

biological systems. We therefore expect that the SBTubs may contribute to high-precision MT cytoskeleton studies and manipulation in neuroscience, motility, and embryology. If SBTubs can also be applied *in vivo* beyond small embryonic systems, it could offer exciting research potential. In larger animals, colchicine domain inhibitors are most often used as vascular disrupting agents and studied *in situ* by microscopy in one- or two-photon mode (Tozer et al., 2001). These are both feasible methods to isomerize SBTubs, and in superficial tissue settings the penetration of UV/violet light can be sufficient for photoswitching (Morstein et al., 2019). So far only one report of systemic pharmacokinetics of a photopharmaceutical has been published (Babii et al., 2020). If SBTubs or their derivatives do have favorable pharmacokinetics, their biochemical stability may enable powerful *in vivo* translation of MT photopharmacology.

We also believe that the development of the SBT scaffold itself is promising for photopharmaceutical development. The SBT scaffold unites photochemical and biochemical robustness with GFP-orthogonality, and tolerates drug-important polar functional groups. These characteristics recommend SBT for research applications that are inaccessible to current photopharmaceuticals, e.g., for intracellular photocontrol in embryos and primary cell isolates of GFP/YFP animal models, both of which are important in development and neurodegeneration. More broadly, it is significant that "scaffold hopping" from azobenzene (PST-1) to SBT (SBTub) has been successful. Novel photoswitches that can substitute typical azobenzenes without requiring total redesign, while offering new performance, are already impacting the hitherto azobenzene-based field of photopharmacology. In this context, diazocines (Reynders et al., 2020; Siewertsen et al., 2009), tetra-*ortho*-substitutions (Bleger et al., 2012), and azoniums (Samanta et al., 2013a) are rapidly garnering applications for spectral shifting. Our work suggests that SBT may be used more generally to substitute azobenzene in photopharmaceutical designs to improve performance on intracellular targets or for optically orthogonal use in live-imaging studies. SBT may thus drive the development of new generations of more powerful photopharmaceuticals against a broader range of biological targets.

## SIGNIFICANCE

**Photocontrollable reagents have unique potential as high spatiotemporal precision modulators of endogenous biological systems: in particular, systems—such as the microtubule cytoskeleton—where rapid dynamics and tight spatial organization are key to function. Lead compound SBTub3 provides spatiotemporally precise control over endogenous microtubule dynamics in live cells, to a level that has not previously been possible. Subcellularly localized SBTub3 photoswitching can even modulate MT polymerization dynamics in individual neurites: a level of precision manipulation that will motivate a range of highly resolved inhibition studies in neurobiology and beyond. More generally, the practical utility of SBTub3 and of SBT-based photoswitches in biological research is significantly greater than that of previous photopharmaceuticals based on azobenzenes, because the rational design of the SBT photoswitch scaffold solves the three outstanding problems**

hampering their biological use. Firstly, photocontrollable inhibitors must be light responsive, but not to the wavelengths used for imaging; the strong isomerization of the azobenzene scaffold under GFP and YFP (even RFP) excitation, can restrict the channels available for imaging and cause significant background activity. Secondly, azobenzenes can be metabolically unstable in the cytosol after illumination, and release intrinsically bioactive products upon degradation. Thirdly, azobenzenes have poor tolerance of key functional groups that drive ligand binding (OH, NH<sub>2</sub>, etc.). By contrast, the SBT scaffold's C=C double bond chromophore gives SBT-based photopharmaceuticals (such as SB<sub>3</sub>Tub3) outstanding performance in practical biological uses. SBTs are metabolically stable, allowing robust application to cytosolic targets; they tolerate tautomerizable groups without instability of the *cis* isomer; and they are orthogonal to GFP imaging, allowing background-free photoswitching and easy translation between models. Importantly, we show that azobenzene photopharmaceuticals can be redesigned into SBT photopharmaceuticals without losing their mechanism of action or their potency. SBTs are thus a promising advance for high-precision microtubule biology, and for the development of high-performance photopharmaceuticals against other protein targets.

#### STAR★METHODS

Detailed methods are provided in the online version of this paper and include the following:

- KEY RESOURCES TABLE
- RESOURCE AVAILABILITY
  - Lead Contact
  - Materials Availability
  - Data and Code Availability
- EXPERIMENTAL MODEL AND SUBJECT DETAILS
  - HeLa Human Cervical Carcinoma Cells
  - A549 Human Lung Cancer Cells
  - Rat Primary Hippocampal Neurons
  - Mouse Hepatic Microsomes
  - Human Hepatic Microsomes
  - Transfection
- METHODS DETAILS
  - Compound Synthesis and Characterisation
  - Photocharacterisation
  - Stability towards Glutathione (GSH)
  - Microsomal Stability, CYP Inhibition and hERG Inhibition
  - Tubulin Polymerisation *In Vitro*
  - Protein Production, Crystallisation and Soaking
  - X-ray Diffraction Data Collection, Processing and Refinement
  - MTT Antiproliferation Assay
  - Cell Cycle Analysis
  - Immunofluorescence Staining
  - EB1/EB3 Comet Assays with Whole-Sample Photoisomerisation
  - Quantification of the Impact of SB<sub>3</sub>Tub3 on Live Cell MT Dynamics

- EB3 Comet Assay with Cell-Specific Photoisomerisation
- EB3 Comet Assay in Rat Primary Hippocampal Neurons
- QUANTIFICATION AND STATISTICAL ANALYSIS

#### SUPPLEMENTAL INFORMATION

Supplemental Information can be found online at <https://doi.org/10.1016/j.chembiol.2020.11.007>.

#### ACKNOWLEDGMENTS

This research was supported by funds from the German Research Foundation (DFG: SFB1032 Nanoagents for Spatiotemporal Control project B09 to O.T.-S. and project A08 to T.L.; Emmy Noether grant no. 400324123, SFB TRR 152 project P24 no. 239283807, and SPP 1926 project no. 426018126 to O.T.-S.); the Swiss National Science Foundation (31003A\_166608 to M.O.S.); and the Munich Centre for NanoScience initiative (CeNS). J.C.M.M. acknowledges support from an EMBO Long-Term Fellowship. X-ray diffraction data were collected at the beamline X06SA at the Swiss Light Source (Paul Scherrer Institut, Villigen PSI, Switzerland). We thank S. Schmidt (LMU) for help with synthesis; K.T. Wanner (LMU) for collegial discussions; H. Harz, I. Solvei, and C. Jung (LMU microscopy platforms), K. Bartel, A. Vollmar, H. Leonhardt, and S. Zahler (LMU) for access to general biology and microscopy facilities; and D. Hörl (LMU) for measuring microscope laser power. We dedicate this paper to GFP's discoverer Osamu Shimomura, whose devoted research has made modern chemical biology possible.

#### AUTHOR CONTRIBUTIONS

L.G. performed synthesis, single-photon photocharacterization, *in vitro* studies, figure preparation, coordinated data assembly, and wrote the manuscript. J.C.M.M. performed characterization of EB3 dynamics, temporally reversible live-cell imaging studies, and subcellularly localized photoswitching. Y.K. performed *in vitro* studies. M.W. performed tubulin protein production, purification, crystallization, crystal handling, and X-ray data collection, processing, and refinement. T.W. performed tubulin crystal handling, data collection, and data processing and refinement. S.D.P. performed two-photon photocharacterization. R.B. performed cell-free tubulin polymerization assays. E.N. performed live-cell imaging on A549 cell lines. K.I.J. and L.C.K. performed primary neuron isolation and culture. N.O. performed tubulin protein production, purification, and crystallization. T.L. supervised two-photon photocharacterization. J.S. and M.O.S. supervised protein crystallography. A.A. supervised characterization of EB3 dynamics, temporally reversible cell imaging and subcellularly localized photoswitching. J.A. performed *in vitro* studies, coordinated data assembly and figure preparation, and supervised all other cell biology. O.T.-S. designed the concept and experiments, supervised all other experiments, coordinated data assembly, and wrote the manuscript with input from all authors.

#### DECLARATION OF INTERESTS

The authors declare no competing interests.

Received: October 21, 2020

Revised: November 10, 2020

Accepted: November 13, 2020

Published: February 18, 2021

#### REFERENCES

Adams, P.D., Afonine, P.V., Bunkoczi, G., Chen, V.B., Davis, I.W., Echols, N., Headd, J.J., Hung, L.-W., Kapral, G.J., Grosse-Kunstleve, R.W., et al. (2010). PHENIX: a comprehensive Python-based system for macromolecular structure solution. *Acta Crystallogr. Section D* 66, 213–221.

Please cite this article in press as: Gao et al., A Robust, GFP-Orthogonal Photoswitchable Inhibitor Scaffold Extends Optical Control over the Microtubule Cytoskeleton, *Cell Chemical Biology* (2020), <https://doi.org/10.1016/j.chembiol.2020.11.007>

## Cell Chemical Biology Resource



- Awad, M.K., El-Hendawy, M.M., Fayed, T.A., Etaiw, S.E.H., and English, N.J. (2013). Aromatic ring size effects on the photophysics and photochemistry of styrylbenzothiazole. *Photochem. Photobiol. Sci.* **12**, 1220–1231.
- Babii, O., Afonin, S., Schober, T., Garmanchuk, L.V., Ostapchenko, L.I., Yurchenko, V., Zozulya, S., Tarasov, O., Pishel, I., Ulrich, A.S., et al. (2020). Peptide drugs for photopharmacology: how much of a safety advantage can be gained by photocontrol? *Future Drug Discov.* **2**, FDD28.
- Baell, J.B., and Nissink, J.W.M. (2018). Seven year itch: pan-assay interference compounds (PAINS) in 2017—utility and limitations. *ACS Chem. Biol.* **13**, 36–44.
- Berdnikova, D., Fedorova, O., Gulakova, E., and Ihmels, H. (2012). Photoinduced in situ generation of a DNA-binding benzothiazoloquinolinium derivative. *Chem. Commun.* **48**, 4603–4605.
- Bléger, D., Schwarz, J., Brouwer, A.M., and Hecht, S. (2012). *o*-Fluoroazobenzenes as readily synthesized photoswitches offering nearly quantitative two-way isomerization with visible light. *J. Am. Chem. Soc.* **134**, 20597–20600.
- Borowiak, M., Küllmer, F., Gegenfurtner, F., Peil, S., Nasufovic, V., Zahler, S., Thorn-Seshold, O., Trauner, D., and Arndt, H.-D. (2020). Optical manipulation of F-actin with photoswitchable small molecules. *J. Am. Chem. Soc.* **142**, 9240–9249.
- Borowiak, M., Nahaboo, W., Reynders, M., Nekolla, K., Jalinet, P., Hasserodt, J., Rehberg, M., Delattre, M., Zahler, S., Vollmar, A., et al. (2015). Photoswitchable inhibitors of microtubule dynamics optically control mitosis and cell death. *Cell* **162**, 403–411.
- Boulègue, C., Löweneck, M., Renner, C., and Moroder, L. (2007). Redox potential of azobenzene as an amino acid residue in peptides. *ChemBioChem* **8**, 591–594.
- Broichhagen, J., Frank, J.A., and Trauner, D. (2015). A roadmap to success in photopharmacology. *Acc. Chem. Res.* **48**, 1947–1960.
- Castle, B.T., and Odde, D.J. (2015). Optical control of microtubule dynamics in time and space. *Cell* **162**, 243–245.
- Dumontet, C., and Jordan, M.A. (2010). Microtubule-binding agents: a dynamic field of cancer therapeutics. *Nat. Rev. Drug Discov.* **9**, 897.
- Eguchi, K., Taoufiq, Z., Thorn-Seshold, O., Trauner, D., Hasegawa, M., and Takahashi, T. (2017). Wild-type monomeric  $\alpha$ -synuclein can impair vesicle endocytosis and synaptic fidelity via tubulin polymerization at the calyx of Held. *J. Neurosci.* **37**, 6043–6052.
- El-Hendawy, M.M., Fayed, T.A., Awad, M.K., English, N.J., Etaiw, S.E.H., and Zaki, A.B. (2015). Photophysics, photochemistry and thermal stability of diarylethene-containing benzothiazolium species. *J. Photochem. Photobiol.* **307**, 20–31.
- Emsley, P., and Cowtan, K. (2004). Coot: model-building tools for molecular graphics. *Acta Crystallogr. Section D* **60**, 2126–2132.
- Engdahl, A.J., Torres, E.A., Lock, S.E., Engdahl, T.B., Mertz, P.S., and Streu, C.N. (2015). Synthesis, characterization, and bioactivity of the photoisomerizable tubulin polymerization inhibitor azo-combretastatin A4. *Org. Lett.* **17**, 4546–4549.
- Francioso, A., Boffi, A., Villani, C., Manzi, L., D'Erme, M., Macone, A., and Mosca, L. (2014). Isolation and identification of 2,4,6-trihydroxyphenanthrene as a byproduct of trans-resveratrol photochemical isomerization and electrocyclicization. *J. Org. Chem.* **79**, 9381–9384.
- Frank, J.A., Franquelim, H.G., Schwille, P., and Trauner, D. (2016). Optical control of lipid rafts with photoswitchable ceramides. *J. Am. Chem. Soc.* **138**, 12981–12986.
- Gaspari, R., Prota, A.E., Bargsten, K., Cavalli, A., and Steinmetz, M.O. (2017). Structural basis of *cis*- and *trans*-combretastatin binding to tubulin. *Chem* **2**, 102–113.
- Hofmann, A.W. (1880). Zimmtsäurederivat des Amidophenylmercaptans. *Chem. Ber.* **1235**–1238.
- Hoorens, M.W.H., Medved', M., Laurent, A.D., Di Donato, M., Fanetti, S., Slappendel, L., Hilbers, M., Feringa, B.L., Jan Buma, W., and Szymanski, W. (2019). Iminothioindoxyl as a molecular photoswitch with 100 nm band separation in the visible range. *Nat. Comm.* **10**, 2390.
- Horspool, W.M., and Lenci, F. (2004). *CRC Handbook of Organic Photochemistry and Photobiology*, 2nd ed. edn (CRC Press).
- Hüll, K., Morstein, J., and Trauner, D. (2018). In vivo photopharmacology. *Chem. Rev.* **118**, 10710–10747.
- Janke, C., and Steinmetz, M.O. (2015). Optochemistry to control the microtubule cytoskeleton. *EMBO J.* **34**, 2114–2116.
- Kabsch, W. (2010). XDS. *Acta Crystallographica Section D, Biol. Crystallogr.* **66**, 125–132.
- Kapitein, L.C., Yau, K.W., and Hoogenraad, C.C. (2010). Chapter 7. Microtubule dynamics in dendritic spines. In *Methods in Cell Biology*, L. Cassimeris and P. Tran, eds. (Academic Press), pp. 111–132.
- Klán, P., Šolomek, T., Bochet, C.G., Blanc, A., Givens, R., Rubina, M., Popik, V., Kostikov, A., and Wirz, J. (2013). Photoremovable protecting groups in chemistry and biology: reaction mechanisms and efficacy. *Chem. Rev.* **113**, 119–191.
- Kleele, T., Marinković, P., Williams, P.R., Stern, S., Weigand, E.E., Engerer, P., Naumann, R., Hartmann, J., Karl, R.M., Bradke, F., et al. (2014). An assay to image neuronal microtubule dynamics in mice. *Nat. Commun.* **5**, 4827.
- Konrad, D.B., Frank, J.A., and Trauner, D. (2016). Synthesis of redshifted azobenzene photoswitches by late-stage functionalization. *Chem. Eur. J.* **22**, 4364–4368.
- La Sala, G., Olieric, N., Sharma, A., Viti, F., de Asis Balaguer Perez, F., Huang, L., Tonra, J.R., Lloyd, G.K., Decherchi, S., Díaz, J.F., et al. (2019). Structure, thermodynamics, and kinetics of plinabulin binding to two tubulin isoforms. *Chem* **5**, 2969–2986.
- Lei, H., Mo, M., He, Y., Wu, Y., Zhu, W., and Wu, L. (2019). Bioactivatable reductive cleavage of azobenzene for controlling functional dumbbell oligodeoxynucleotides. *Bioorg. Chem.* **91**, 103106.
- Lester, H.A., Krouse, M.E., Nass, M.M., Wassermann, N.H., and Erlanger, B.F. (1980). A covalently bound photoisomerizable agonist: comparison with reversibly bound agonists at electrophorus electroplaques. *J. Gen. Physiol.* **75**, 207–232.
- Lin, C.M., Singh, S.B., Chu, P.S., Dempcy, R.O., Schmidt, J.M., Pettit, G.R., and Hamel, E. (1988). Interactions of tubulin with potent natural and synthetic analogs of the antimetabolic agent combretastatin: a structure-activity study. *Mol. Pharmacol.* **34**, 200–208.
- Meijering, E., Dzyubachyk, O., and Smal, I. (2012). Chapter 9. Methods for cell and particle tracking. In *Methods in Enzymology*, P.M. Conn, ed. (Academic Press), pp. 183–200.
- Merriam, E.B., Millette, M., Lombard, D.C., Saengsawang, W., Fothergill, T., Hu, X., Ferhat, L., and Dent, E.W. (2013). Synaptic regulation of microtubule dynamics in dendritic spines by calcium, F-actin, and drebrin. *J. Neurosci.* **33**, 16471.
- Mishra, A., Thangamani, A., Chatterjee, S., Chipem, F.A.S., and Krishnamoorthy, G. (2013). Photoisomerization of *trans*-2-[4'-(dimethylamino)styryl]benzothiazole. *Photochem. Photobiol.* **89**, 247–252.
- Moreno, J., Gerecke, M., Dobryakov, A.L., Ioffe, I.N., Granovsky, A.A., Bléger, D., Hecht, S., and Kovalenko, S.A. (2015). Two-photon-induced versus one-photon-induced isomerization dynamics of a bistable azobenzene derivative in solution. *J. Phys. Chem. B* **119**, 12281–12288.
- Morstein, J., Hill, R.Z., Novak, A.J.E., Feng, S., Norman, D.D., Donthamsetti, P.C., Frank, J.A., Harayama, T., Williams, B.M., Parrill, A.L., et al. (2019). Optical control of sphingosine-1-phosphate formation and function. *Nat. Chem. Biol.* **15**, 623–631.
- Müller-Deku, A., Meiring, J.C.M., Loy, K., Kraus, Y., Heise, C., Bingham, R., Jansen, K.I., Qu, X., Bartolini, F., Kapitein, L.C., et al. (2020). Photoswitchable paclitaxel-based microtubule stabilisers allow optical control over the microtubule cytoskeleton. *Nat Commun* **11**, 4640.
- Pecqueur, L., Duellberg, C., Dreier, B., Jiang, Q., Wang, C., Plüchthun, A., Surrey, T., Gigant, B., and Knossow, M. (2012). A designed ankyrin repeat protein selected to bind to tubulin caps the microtubule plus end. *Proc. Natl. Acad. Sci. U S A* **109**, 12011.
- Peterson, J.R., and Mitchison, T.J. (2002). Small molecules, big impact. *Chem. Biol.* **9**, 1275–1285.

- Reefling, F., and Szymanski, W. (2017). Beyond photodynamic therapy: light-activated cancer chemotherapy. *Curr. Med. Chem.* *24*, 4905–4950.
- Reynders, M., Matsuura, B.S., Bérouti, M., Simoneschi, D., Marzio, A., Pagano, M., and Trauner, D. (2020). PHOTACs enable optical control of protein degradation. *Sci. Adv.* *6*, eaay5064.
- Roostalu, J., Thomas, C., Cade, N.I., Kunzelmann, S., Taylor, I.A., and Surrey, T. (2020). The speed of GTP hydrolysis determines GTP cap size and controls microtubule stability. *eLife* *9*, e51992.
- Sailer, A., Ermer, F., Kraus, Y., Bingham, R., Lutter, F.H., Ahlfeld, J., and Thorn-Seshold, O. (2020). Potent hemithioindigo-based antimicrotubule photocontrol of the microtubule cytoskeleton in *cellulo*. *Beilstein J. Org. Chem.* *16*, 125–134.
- Sailer, A., Ermer, F., Kraus, Y., Lutter, F., Donau, C., Bremerich, M., Ahlfeld, J., and Thorn-Seshold, O. (2019). Hemithioindigos for cellular photopharmacology: desymmetrised molecular switch scaffolds enabling design control over the isomer-dependency of potent antimicrotubule bioactivity. *ChemBioChem* *20*, 1305–1314.
- Samanta, S., Babalhavaej, A., Dong, M.-x., and Woolley, G.A. (2013a). Photoswitching of ortho-substituted azonium ions by red light in whole blood. *Angew. Chem. Int. Ed.* *52*, 14127–14130.
- Samanta, S., Beharry, A.A., Sadowski, O., McCormick, T.M., Babalhavaej, A., Tropepe, V., and Woolley, G.A. (2013b). Photoswitching azo compounds in vivo with red light. *J. Am. Chem. Soc.* *135*, 9777–9784.
- Schehr, M., Ianes, C., Weisner, J., Heintze, L., Müller, M.P., Pichlo, C., Charl, J., Brunstein, E., Ewert, J., Lehr, M., et al. (2019). 2-Azo-, 2-diazocine-thiazoles and 2-azo-imidazoles as photoswitchable kinase inhibitors: limitations and pitfalls of the photoswitchable inhibitor approach. *Photochemical Photobiological Sci.* *18*, 1398–1407.
- Schindelin, J., Arganda-Carreras, I., Frise, E., Kaynig, V., Longair, M., Pietzsch, T., Preibisch, S., Rueden, C., Saalfeld, S., Schmid, B., et al. (2012). Fiji: an open-source platform for biological-image analysis. *Nat. Methods* *9*, 676–682.
- Shan, Y.S., Zhang, J., Liu, Z., Wang, M., and Dong, Y. (2011). Developments of combretastatin A-4 derivatives as anticancer agents. *Curr. Med. Chem.* *18*, 523–538.
- Sheldon, J.E., Dcona, M.M., Lyons, C.E., Hackett, J.C., and Hartman, M.C.T. (2016). Photoswitchable anticancer activity via *trans-cis* isomerization of a combretastatin A-4 analog. *Org. Biomol. Chem.* *14*, 40–49.
- Siewertsen, R., Neumann, H., Buchheim-Stehn, B., Herges, R., Näther, C., Renth, F., and Temps, F. (2009). Highly efficient reversible Z-E photoisomerization of a bridged azobenzene with visible light through resolved S1( $\pi\pi^*$ ) absorption bands. *J. Am. Chem. Soc.* *131*, 15594–15595.
- Simeth, N.A., Kneutlinger, A.C., Sterner, R., and König, B. (2017). Photochromic coenzyme Q derivatives: switching redox potentials with light. *Chem. Sci.* *8*, 6474–6483.
- Singh, A., Saha, T., Begemann, I., Ricker, A., Nüsse, H., Thorn-Seshold, O., Klingauf, J., Galic, M., and Matis, M. (2018). Polarized microtubule dynamics directs cell mechanics and coordinates forces during epithelial morphogenesis. *Nat. Cell Biol.* *20*, 1126–1133.
- Smart, O.S., Womack, T.O., Flensburg, C., Keller, P., Paciorek, W., Sharff, A., Vonrhein, C., and Bricogne, G. (2012). Exploiting structure similarity in refinement: automated NCS and target-structure restraints in BUSTER. *Acta Cryst. D* *68*, 368–380.
- Stepanova, T., Slemmer, J., Hoogenraad, C.C., Lansbergen, G., Dortland, B., De Zeeuw, C.I., Grosveld, F., van Cappellen, G., Akhmanova, A., and Galijart, N. (2003). Visualization of microtubule growth in cultured neurons via the use of eb3-GFP (end-binding protein 3-green fluorescent protein). *J. Neurosci.* *23*, 2655–2664.
- Strzyz, P.J., Lee, H.O., Sidhaye, J., Weber, I.P., Leung, L.C., and Norden, C. (2015). Interkinetic nuclear migration is centrosome independent and ensures apical cell division to maintain tissue integrity. *Dev. Cell* *32*, 203–219.
- Tickle, I.J., Flensburg, C., Keller, P., Paciorek, W., Sharff, A., Smart, O., Vonrhein, C., and Bricogne, G. (2018). STARANISO Anisotropy and Bayesian Estimation Server (Global Phasing Ltd).
- Tseng, Q., Duchemin-Pelletier, E., Deshiere, A., Bolland, M., Guillou, H., Filhol, O., and Thery, M. (2012). Spatial organization of the extracellular matrix regulates cell-cell junction positioning. *Proc. Natl. Acad. Sci. U S A* *109*, 1506–1511.
- Tozer, G.M., Prise, V.E., Wilson, J., Cemazar, M., Shan, S., Dewhurst, M.W., Barber, P.R., Vojnovic, B., and Chaplin, D.J. (2001). Mechanisms associated with tumor vascular shut-down induced by combretastatin A-4 phosphate: intravital microscopy and measurement of vascular permeability. *Cancer Res.* *61*, 6413–6422.
- Tron, G.C., Pirali, T., Sorba, G., Pagliari, F., Busacca, S., and Genazzani, A.A. (2006). Medicinal chemistry of combretastatin A4: present and future directions. *J. Med. Chem.* *49*, 3033–3044.
- Urban, P., Pritzl, S.D., Konrad, D.B., Frank, J.A., Pernpeintner, C., Roeske, C.R., Trauner, D., and Lohmüller, T. (2018). Light-controlled lipid interaction and membrane organization in photolipid bilayer vesicles. *Langmuir* *34*, 13368–13374.
- Vandestadt, C., Vanwalleghem, G.C., Castillo, H.A., Li, M., Schulze, K., Khabooshan, M., Don, E., Anko, M.-L., Scott, E.K., and Kaslin, J. (2019). Early migration of precursor neurons initiates cellular and functional regeneration after spinal cord injury in zebrafish. *bioRxiv*, 539940.
- Volgraf, M., Gorostiza, P., Numan, R., Kramer, R.H., Isacoff, E.Y., and Trauner, D. (2005). Allosteric control of an ionotropic glutamate receptor with an optical switch. *Nat. Chem. Biol.* *2*, 47.
- Weinert, T., Olieric, N., Cheng, R., Brünle, S., James, D., Ozerov, D., Gashi, D., Vera, L., Marsh, M., Jaeger, K., et al. (2017). Serial millisecond crystallography for routine room-temperature structure determination at synchrotrons. *Nat. Commun.* *8*, 542.
- Wittmann, T., Dema, A., and van Haren, J. (2020). Lights, cytoskeleton, action: optogenetic control of cell dynamics. *Curr. Opin. Cell Biol.* *66*, 1–10.
- Wuhr, M., Tan, E.S., Parker, S.K., Detrich, H.W., 3rd, and Mitchison, T.J. (2010). A model for cleavage plane determination in early amphibian and fish embryos. *Curr. Biol.* *20*, 2040–2045.
- Zenker, J., White, M.D., Gasnier, M., Alvarez, Y.D., Lim, H.Y.G., Bissiere, S., Biro, M., and Plachta, N. (2018). Expanding actin rings zipper the mouse embryo for blastocyst formation. *Cell* *173*, 776–791.
- Zenker, J., White, M.D., Templin, R.M., Parton, R.G., Thorn-Seshold, O., Bissiere, S., and Plachta, N. (2017). A microtubule-organizing center directing intracellular transport in the early mouse embryo. *Science* *357*, 925–928.

## 4.2 Hemithioindigo HOTubs

### Designing both "lit active" and "dark active" photoswitches: Motivation for this work

The most commonly used azobenzene photoswitches are severely limited with respect to their substituent pattern, which can also decrease relaxation half-lives. Another limitation of the concept of photoswitches is that, so far, there is no possibility to control if a photoswitchable molecule is more bioactive in its lit or its dark state because this is dictated by protein sterics that typically favour either a bent or a flat ligand (for azobenzenes, the *Z* or an *E* isomer) and it is improbable that re-ordering the substituent pattern in azobenzene photopharmaceuticals can switch between flat and bent-active compounds. We attempted to address this challenge by rationally designing photoswitchable molecules based on the hemithioindigo scaffold, in which both isomers are flat and therefore there should be no protein-based prejudice about the more active isomer.

Hemithioindigos are photoswitches with good photostability that can be bidirectionally photoswitched reversibly. They have been reviewed regarding their benefits compared to azobenzenes,<sup>117</sup> but in biology, they have so far been used mostly for lipid physical chemistry<sup>118</sup> and their potential for intracellular applications has not been determined yet. We designed substituent patterns to aim at both lit-active and dark-active compounds that target tubulin, and evaluated their use in biological settings in cells. The possibility of rationally designing photopharmaceuticals to be either "dark" or "lit" active would enlarge the toolbox of molecules that can be used in photopharmacology, and expand the range of applications in microtubule research.

### Short summary of the HOTub work

HOTubs (Hemithioindigo-cOlchicinoid Tubulin binders) were designed aiming at two potential dark-state active and two potential lit-state active reversibly photoswitchable tubulin binders and assessed for biological applications in cell culture. For these compounds, the photoswitch has been integrated into a methoxylation pattern that mimicked the structure of colchicine, either in the thermodynamically stable *Z* or metastable *E* isomer. This approach was expected to create a greater potency difference between the isomers than just adding a photoswitch on the periphery of an inhibitor. Corresponding to design goals we obtained a dark-active compound (HOTub-31) and a lit-active compound (HOTub-81) with photoswitchability of bioactivity that has been confirmed in anti-proliferative assays under dark and lit conditions. Designed inactive permutation controls showed little to no bioactivity both under dark and lit conditions.

Mechanistic confirmation of the mode of action was obtained with immunofluorescence staining of tubulin which displayed light or dark-dependent microtubule perturbation according to the designed activity profile of the compounds, and analysis of cell cycle repartition after treatment. These results demonstrate that drug-like HTI-based photopharmaceuticals, the HOTubs, can produce reliable and predictable cytotoxic effects on an intracellular protein target, and can be *a priori* designed into dark-active and lit-active compounds, which we



wanted to demonstrate. However, what we did not report was reversible switching or two wavelengths patterning in biological settings, which will be discussed further in the conclusions.

#### Authorial Contribution

My part of this project was the evaluation of these compounds in cell culture regarding cytotoxicity (Fig. 3a), disruption of tubulin structure by tubulin immunofluorescence staining and imaging (Fig. 4) and I supported our results by cell-cycle analysis in collaboration with F. Ermer revealing G2/M arrest for the active compounds as expected (Fig. 5). Taken together my results show that HTI-based HOTubs can be *a priori* designed with distinct photoswitchable activity profiles and are mechanistically most likely tubulin depolymerisers that are controllable by illumination.



# Hemithioindigos for Cellular Photopharmacology: Desymmetrised Molecular Switch Scaffolds Enabling Design Control over the Isomer-Dependency of Potent Antimitotic Bioactivity

Alexander Sailer<sup>+</sup>, Franziska Ermer<sup>+</sup>, Yvonne Kraus<sup>+</sup>, Ferdinand H. Lutter, Carsten Donau, Maximilian Bremerich, Julia Ahlfeld, and Oliver Thorn-Seshold<sup>\*[a]</sup>

Dedicated to G. R. "Bob" Pettit on the occasion of his 90th birthday

Druglike small molecules with photoswitchable bioactivity—photopharmaceuticals—allow biologists to perform studies with exquisitely precise and reversible, spatial and temporal control over critical biological systems inaccessible to genetic manipulation. The photoresponsive pharmacophores disclosed have been almost exclusively azobenzenes, which has limited the structural and substituent scope of photopharmacology. More detrimentally, for azobenzene reagents, it is not researchers' needs for adapted experimental tools, but rather protein binding site sterics, that typically force whether the *trans* (dark) or *cis* (lit) isomer is the more bioactive. We now present the ra-

tional design of HOTubs, the first hemithioindigo-based pharmacophores enabling photoswitchable control over endogenous biological activity in cellulose. HOTubs optically control microtubule depolymerisation and cell death in unmodified mammalian cells. Notably, we show how the asymmetry of hemithioindigos allows a priori design of either *Z*- or *E*- (dark- or lit)-toxic antimitotics, whereas the corresponding azobenzenes are exclusively lit-toxic. We thus demonstrate that hemithioindigos enable an important expansion of the substituent and design scope of photopharmacological interventions for biological systems.

## Introduction

Druglike small molecules with photoswitchable bioactivity—photopharmaceuticals—can deliver outstandingly precise spatial and temporal control over critically important biological systems.<sup>[1]</sup> Photopharmacology has been applied to a range of studies from cell-surface-acting ligands actuating ion channels<sup>[2]</sup> and GPCRs<sup>[3]</sup> in neuroscience, to intracellular ligands modulating metabolic<sup>[4]</sup> and epigenetic<sup>[5]</sup> enzymes, as well as the cytoskeletal scaffolding protein tubulin.<sup>[6]</sup> In all these applications, it is the ability to reversibly and noninvasively modulate biological functions independently of drug biodistribution and with high spatiotemporal precision, that brings the key conceptual advantages of photoswitch pharmacology, as against irreversible (uncaging) or slowly-reversible (wash-in/wash-out) methods.

Photopharmacology's most advanced applications are probably in transmembrane receptors, where photoswitches that trigger action potential firing upon photoisomerization to the metastable (lit) state, but relax rapidly to a non-triggering, thermodynamic (dark) state when illumination is removed, have been developed to photosensitise otherwise non-responsive neurons in the retina and restore visual response in blind animals.<sup>[7]</sup> The approximately millisecond timescale of these photoswitches' spontaneous relaxation perfectly matches the temporal scale of the desired biological control, so combatting spatial diffusion of the isomer patterning established by photoswitching is not needed and unidirectional photocontrol suffices for performance.

However, in intracellular applications, longer-timescale phenomena often associated to downstream pathways are more typically of interest, such as the biological consequences of enzymatic activity or protein relocalisation. Therefore, greater longevity of the metastable isomer is usually desirable to maintain isomer patterning over the experimental time course without repeated illuminations that cause intracellular photodamage to the system under study and/or imaging marker. The conceptually unique biological research applications of such photopharmaceuticals (especially in multicellular systems) then typically involve patterning the isomers in space and/or over time, by two-colour illuminations. Such spatiotemporally reversible two-colour patterning has notably allowed complex studies in em-

[a] A. Sailer,<sup>+</sup> F. Ermer,<sup>+</sup> Y. Kraus,<sup>+</sup> F. H. Lutter, C. Donau, M. Bremerich, Dr. J. Ahlfeld, Dr. O. Thorn-Seshold  
Department of Pharmacy, Ludwig-Maximilians University Munich  
Butenandtstrasse 5-13, Munich 81377 (Germany)  
E-mail: oliver.thorn-seshold@cup.lmu.de

[\*] These authors contributed equally to this work.

Supporting information and the ORCID identification numbers for the authors of this article can be found under <https://doi.org/10.1002/cbic.201800752>.

This article is part of the young researchers' issue ChemBioTalents. To view the complete issue, visit <http://chembiochem.org/chembiotalents>

bryology and development, where precise bidirectional switching was employed to subcellularly resolve the organisation of tubulin<sup>[8]</sup> and its interplay with the actin cytoskeleton<sup>[9]</sup> in early mouse embryos. In such bidirectional-switching applications, it is crucial for practical success that the metastable isomer be designed to be the more bioactive form, so that maintaining a “non-inhibited” background of activity in the organism does not require repeated illuminations scanning through the entire sample (but only localised illuminations in the area to be affected), and so that moderate spontaneous relaxation rates can help to suppress the accumulation of background levels of the active isomer.

However, no method yet exists for researchers to force the lit state of a photoswitchable ligand to be bioactive and avoid a background of bioactivity from its dark state, or vice versa, at will. We have addressed this conceptual gap by developing photopharmaceuticals around a relatively untried scaffold, with the purpose of delivering both dark- and lit-active compounds against the same protein target following rational design, and evaluating their photocontrol over endogenous biological function in cellulo.

The progress, and the definition, of photopharmacological research have expanded greatly in recent years and the field has been multiply reviewed.<sup>[10]</sup> In this work, we concentrate on photopharmacological design principles promoting translation through in cellulo to in vivo applications and enabling conceptually novel biological research on a range of extra- and intracellular targets. For this we define “narrow” photopharmacology as: druglike small molecules obeying the Lipinski rules, whose bioactivity can be reversibly modulated to a significant degree through bidirectionally photoreversible isomerisation. Although this definition excludes several noteworthy strategies, such as ligand bioactivity photoswitching that depends on modulating secondary structure elements in larger constructs,<sup>[11]</sup> we feel it usefully restricts the discussion to a major research area that faces common challenges.

Two main approaches have been used to deliver isomerically dependent changes of protein affinity in “narrow” photopharmacology: 1) The photoswitch is directly appended onto a druglike pharmacophore with the aim that isomerisation impacts the steric access of the pharmacophore to its binding

partner,<sup>[12]</sup> which in the context of azobenzenes is called “azo-extension”; 2) The photoswitch is embedded entirely inside the most critical part of the pharmacophore, which in the context of azobenzenes is called “azologization”.<sup>[1b]</sup> As far as possible, embedding approaches would seem the more rational design, and have been shown to deliver significant differences between the potencies of the more- and less-bioactive isomers (“photoswitchability of bioactivity”) in a variety of cellular and organism-based settings.<sup>[6]</sup>

The repertoire of molecular photoswitches is large, and many have been reported as photoswitch concepts (especially for cell-free in vitro studies); for example, photoswitch concepts depending on fulgides,<sup>[13]</sup> stilbenes,<sup>[14]</sup> and diarylethenes<sup>[15]</sup> have been reported for an interesting range of biological targets. However, azobenzenes remain essentially the only photoswitch to have been validated as a photopharmacological scaffold through multiple in cellulo to in vivo biological applications. The reasons for azobenzenes’ reliable performance are well known,<sup>[10]</sup> but the lack of alternative scaffolds has hampered progress in the field in several ways. Principally, although the large differences between *cis* and *trans* azobenzene sterics have allowed impressive photoswitchability of bioactivity in some endogenous cellular systems (up to >250-fold<sup>[6]</sup>), it also has the consequence that if a given binding site significantly better accommodates one isomer than the other, it is unlikely that redesigning the substituent pattern on the azobenzene will allow a reversal of isomer preference. Since the drugs that are basis scaffolds for azologization are often “med chem”-like substructures which mainly bind their targets in *trans*-like states (e.g., benzanilide, stilbene or benzyl phenyl ether-type scaffolds), many of the resulting azologues are therefore *trans*- (that is, dark-) active; and even azo-extension approaches often result in *trans*-active compounds.<sup>[16]</sup> Yet dark-active compounds face severe disadvantages as photopharmacological tools for intracellular research applications, principally due to their permanent background of activity despite partial photoswitching to the metastable state, as well as handling difficulties. Recently, ethylene-bridged azobenzenes (diazocines)<sup>[17]</sup> which feature a *cis*-like dark state and a *trans*-like lit state have made much synthetic progress; but while their potential to act as lit-active alternative scaffolds where linear azobenzenes are *trans*-active is tantalising, their cellular potential has not yet been demonstrated.

We reasoned that if a single isomerisable scaffold is intended to support the design of embedded-pharmacophore ligands with *either* lit- or dark-state bioactivity according to taste, its isomers must offer a nearly superimposable pattern of sites for attaching substituents, and so should be nearly flat in both isomeric states. We therefore selected the hemithioindigo (HTI) photoswitch as a robust, optically well-characterised, photostable and photoreversible molecular switch<sup>[18]</sup> in which the relative positions of the centroids of the two aryl rings are nearly identical in the *Z* (dark) and *E* (lit) isomers due to the near-planarity of both forms. HTIs bear four potential substituent sites on the thioindoxyl motif and five on the hemistilbene, so we considered it potentially adapted for pharmacophore embedding in most situations where azobenzenes also suc-

Oliver Thorn-Seshold studied chemistry at the University of Sydney and did his PhD in bioorganic chemistry of enzyme-responsive probes with Prof. Jens Hasserodt at the ENS Lyon. In 2013, he joined Prof. Dirk Trauner’s lab at LMU Munich where he developed azobenzene-based photoswitchable inhibitors for cytoskeleton research. Since 2016, he has been an independent research group leader at the LMU Munich. His research interests include cellular and in vivo applications of photopharmacology, and tools to study and respond to cellular redox biology.



ceed. Hemithioindigos oriented towards chemical biology applications (rather than in lipid physical chemistry<sup>[19]</sup>) have mainly been employed as photoswitchable bridges or cross-linkers for conformational photoswitching of peptides;<sup>[18,20]</sup> some designs for photoswitch-appended polypeptides have also been reported.<sup>[21]</sup> To our knowledge, only one druglike application of HTIs has been reported, where Kühn and co-workers<sup>[22]</sup> performed a short-term test comparison of the HPLC-separated *E* and *Z* isomers of a carboxylate-bearing HTI for their capacity to inhibit oxidation of linoleic acid in human monocytes transfected to express rabbit 12/15-lipoxygenase, with assays run over 15 min. Their reports showed an assay readout differential of about 1.3- to 1.7-fold between *E* and *Z* isomers, although the compound could not be applied above 4  $\mu\text{M}$ . We considered that this state of the art left much to be done towards the rational design and long-term, in situ-photoswitched biological evaluation of HTIs for cellular photopharmacology.

We therefore desired to test whether the hemithioindigo scaffold could be applied to create potent, reversibly photoswitchable, bioactive compounds for the challenging scenario of intracellular biological applications to endogenously expressed proteins, and we selected tubulin as our target. Cellular tubulin is in a constant state of flux, being continually (non-covalently) polymerised into and depolymerised from microtubules. These critical structures are tightly spatially and temporally coordinated, to drive a variety of anisotropic cellular scaffolding roles, from continual intracellular cargo trafficking, to cell migration in motile cells, through to separation of chromatids and daughter cells during cell division.<sup>[23]</sup> The requirement for correctly functional microtubule dynamics during mitosis has driven extensive work on targeted and selective microtubule-binding agents as “antimitotic” cancer chemotherapeutics, including paclitaxel, epothilone and vinca alkaloids.<sup>[24]</sup> In research, the sheer breadth and spatiotemporal complexity of microtubule-dependent biological roles presents an excellent opportunity for photopharmacological intervention, and microtubule-targeting photopharmaceuticals such as PST-1<sup>[6]</sup> have quickly moved on from chemical proof-of-concept<sup>[25]</sup> to find diverse cellular<sup>[26]</sup> and animal research applications.<sup>[8,9,27]</sup> Due to the massive clinical utility of microtubule-binding agents in cancer therapy, as well as the systemic side-effects of conventional antimitotics, it is also of extensive interest to find more potent photoswitchable microtubule inhibitors<sup>[28]</sup> and evaluate whether they can be guided by localised tumour illumination to act as tumour-specific antimitotics that spare healthy tissues from chemotherapeutic damage. Successful HTI-based antimitotics could therefore find applications as tools for the cytoskeleton research field, but the opportunity to scaffold-hop from known PST azobenzenes while retaining photoswitchable bioactivity was also of interest for translational applications.

## Results

### Design and rationale

Extensive structure–activity relationship (SAR) studies across a range of chemotypes<sup>[29]</sup> as well as recent progress in X-ray crystallography<sup>[30]</sup> have clarified the structural requirements for tubulin inhibitors binding at the colchicine site (Figure 1A), and this recommended it to us as a target for the development of HTI-based inhibitors. Prototypically, the important interactions of the colchicinoid pharmacophore (Figure 1B) are established from a trimethoxyphenyl “south” ring and a methoxyphenyl “north” ring; all contacts involve the  $\beta$ -tubulin subunit except for one contact from the north ring to flexible

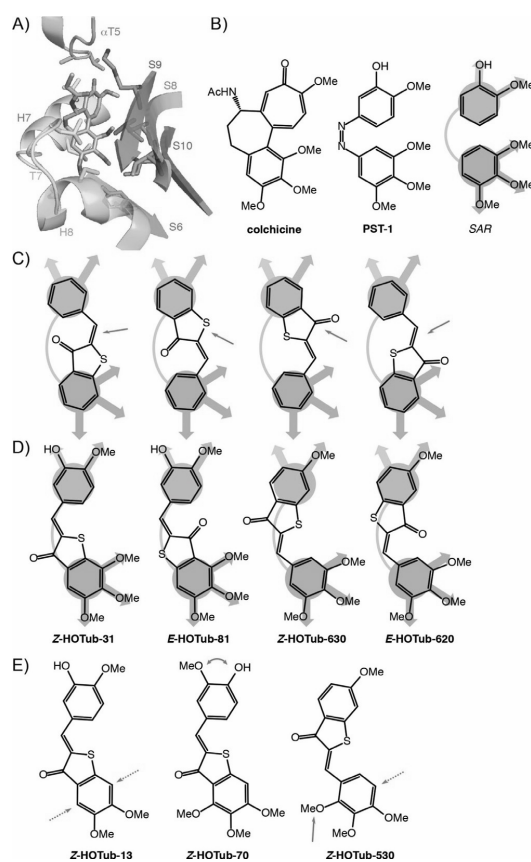


**Figure 1.** A) *N*-deacetyl-*N*-(2-mercaptoacetyl)-colchicine (DAMA-colchicine) in its binding site on  $\alpha\beta$ -tubulin with local secondary structure elements annotated and close-contact amino acids depicted (PDB ID: 1SA0<sup>[35]</sup>). B) Colchicine, PST-1, and a simplistic pharmacophore model. C) The four rejected orientations of HTI mapping onto the colchicine site pharmacophore, with red arrows highlighting the steric clashes anticipated to be detrimental for binding. D) The four HTI mappings remaining were decorated with substituents to match the SAR, giving HOTubs. E) Control structures designed to show no isomer-dependent binding (or no binding), with predicted detrimental groups indicated with red arrows.

loop T5 on the  $\alpha$ -subunit. Notably, for our designs the rings can be linked with molecular bridges ranging from the very short (biaryls like colchicine or single atom bridges such as a carbonyl group<sup>[31]</sup>) through to sizable *cis*-C=C double bonds<sup>[32]</sup> or even small heterocycles<sup>[29]</sup> without substantial impact on potency, as long as no atoms of the bridge abut the rigid wall formed by  $\beta$ -sheet strands S8/S9. The only general potency-enhancing substitution is to add a small electronegative substituent (OH, F, NH<sub>2</sub>) in *ortho* to the methoxy group on the north ring, pointing away from the S8/S9 wall. Noteworthy, the south ring tolerates neither the introduction, removal, nor permutation of a substituent from the 3,4,5-trisubstituted template; the north ring is slightly more tolerant of changes but introducing groups abutting into S8/S9 essentially abolishes binding. This preferred substituent pattern for close colchicine analogues is shown simplified in Figure 1B; but the binding domain is highly plastic, and accommodates a surprising range of structurally distinct small molecules whose interactions can be difficult to predict.<sup>[33]</sup> Colchicine domain binders display a limited range of tubulin-disrupting IC<sub>50</sub> values as determined against purified enzyme *in vitro*, with only around a fivefold difference apparent between potent binders such as combretastatin A-4 (CA4, IC<sub>50</sub> ~2  $\mu$ M) and binders considered weak; yet their EC<sub>50</sub> values for antiproliferative/cytotoxic activity in cell culture span many orders of magnitude (typically ~10 nM for CA4 and up to 5  $\mu$ M for colchicine in the same human cell line).<sup>[29]</sup> A likely explanation is that, as is known for CA4, variable but potentially strong cellular bioconcentration from the extracellular medium as well as sensitive biolocalisation effects within the cell, are substantially more important for observed cell culture potencies in these agents than their K<sub>i</sub> against purified enzyme.<sup>[34]</sup>

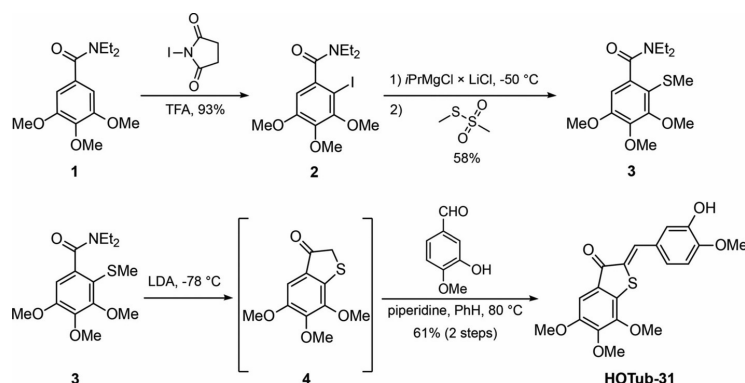
To embed HTIs into this pharmacophore, we hypothesised that the relatively long “bridge” between the two phenyl rings would be accepted if the substituent pattern SAR for colchicinoid binders was respected. Without using exact bond geometries, we naively examined the eight potential mappings of the HTI scaffold's lit and dark isomers onto this pattern, and eliminated those which projected the bridging double bond towards the S8/S9 wall and/or did not allow us to map the correct trisubstituted geometry on the south ring (Figure 1C). This left two mappings in the *E* state and two in the *Z* state: that is, two potential lit-state and two potential dark-state bioactives, of which one each was in the “top-down” and one each in the “bottom-up” configuration. We named these HOTubs (Hemithioindigo-cOlcichinoid Tubulin binders).

We expected that orienting the carbonyl group towards the S8/S9 wall (e.g., *E*-HOTub-81) might slightly reduce potency compared to orienting it away (*Z*-HOTub-31), but were hopeful of observing bioactivity nonetheless. We considered the “bottom-up” orientation fixing the hemistilbene motif (easier to diversify) as the north ring (more tolerant) to be particularly desirable for synthesis. For the initial study, we decided to simplify the “top-down” scaffolds by deleting the optional hydroxy group on the north ring, since we anticipated that the relatively vigorous conditions needed for ring closure of the thioindoxyl, plus the sensitivity of HTIs towards nucleophilic attack,

would otherwise make the choice of a protecting group to carry through the synthesis difficult. This simplified the “top-down” targets to HOTub-620 and HOTub-630; the “bottom-up” targets HOTub-31 and HOTub-81 were retained with the OH group in the expectation of improved water solubility and potency (Figure 1D). We also designed three “intentional negative control” compounds by molecularly small permutations which according to our SAR understanding ought to abolish specific on-target bioactivity (Figure 1E). We believe this is a valuable general concept for reliable photopharmacology. In the case of HOTubs, as tubulin is critical for cell survival it is impossible to create a “tubulin knock-out” with which to confirm that photoswitching in the absence of the intended target has no biological effect. We instead wished to use these negative control compounds to estimate whether our SAR understanding was correct, in that these key substituent changes would abolish tubulin-specific bioactivity; if so, it would also support that our rational design approach is valid for installing tubulin-specificity. It is important that the changes are small—ideally only regioisomeric permutations—since the resulting close regioisomers could then be expected to show near-identical cellular accumulation and biolocalisation. In this way, the control can then be used as a quick assessment for whether aggregation, membrane-modulation, phototoxicity inside cellular reservoirs where the compounds can be expected to accumulate (e.g., in lipid vesicles), or other confounding effects (such as CALI-type photodamage<sup>[36]</sup>) are potential problems. Accordingly, HOTub-13 was designed relative to HOTub-31 and HOTub-81 by removing one of the three south ring methoxy groups we estimated necessary for potent binding, which still could permit docking of the compound and then photoreactivity with the protein if that were problematic. HOTub-530 was designed as a single permutation regioisomer of HOTub-630 and a double permutation regioisomer of HOTub-620, allowing it to have similar solubility and biodistribution but intended to abolish tubulin binding; we viewed HOTub-70 not only as a regioisomer of HOTub-31 but also as a control that the orientation in which we mapped the HTI scaffold was appropriate.

### Synthesis and photocharacterisations

HTIs are conveniently synthesised by aldol condensation of the corresponding thioindoxyls and benzaldehydes.<sup>[37]</sup> We first explored the synthesis of our thioindoxyls by intramolecular acylation of the phenyl ring in 2-(phenylthio)acetic acid derivatives. Although preparation of 2-(phenylthio)acetic acids is facile, common cyclisation methods (Friedel–Crafts acylation of the acid chloride, or dehydrative cyclisation with Eaton's reagent) gave only poor yields in our hands. We therefore explored thioindoxyl synthesis by deprotonation of the acidic 5-methyl group in methyl phenyl sulfides bearing *ortho*-carboxylate derivatives by using lithium diisopropylamide (LDA) followed by intramolecular acylation of the carbanion,<sup>[38]</sup> which we found to give drastically better yields and easier workup. We typically synthesised the deprotonation–cyclisation precursors by magnesium–halogen exchange on iodophenyl deriva-



Scheme 1. Synthesis of representative compound HOTub-31 (see also Supporting Information).

tives with Turbo-Grignard,<sup>[39]</sup> followed by electrophilic quenching with methyl chloroformate (for *ortho*-iodophenyl methyl sulfides) or with MeSSO<sub>2</sub>Me (for *ortho*-iodobenzoic acid derivatives).

We tested several condensation reaction conditions, including 1) condensation with amphoteric dehydrating catalysis using aluminium oxide in dry chlorinated solvents, 2) condensation in dry refluxing benzene with piperidine catalysis, and 3) condensation in refluxing NaOH/*t*BuOH.<sup>[37]</sup> Of these, the benzene/piperidine conditions typically gave the highest isolated yields. Some HTIs decomposed on silica, but we found their relatively low water solubility could be harnessed for purification, by precipitating them from DMSO solutions of crude material. All HOTubs were reached typically on 100 mg scale (see the Supporting Information); a representative synthesis is shown in Scheme 1.

The typical photochemical behaviour of hemithioindigos has been reviewed by Dube and co-workers.<sup>[18]</sup> We did not expect unusual performance for the polymethoxylated HOTubs so we photocharacterised them pragmatically to qualitatively estimate parameters for later biological applications. Primarily we wished to determine their photostationary state (PSS) compositions—the equilibrium proportion of *E* and *Z* isomers established under saturating illumination at specified wavelengths—to select optimal switching wavelengths for cellular work. For PSS quantification, we initially illuminated samples at various wavelengths then separated the *E* and *Z* isomers by analytical HPLC, quantifying their proportions with an inline diode array detection at an isobestic point wavelength. However, we determined that UV/Vis spectrophotometry was substantially more accurate in repeatably (<1% deviation) determining small changes to the *E/Z* ratios in samples. Determining PSS by spectrophotometry required HOTub solution concentrations well above their aqueous solubility limit (as do NMR measurements), so we constrained our measurements to water-cosolvent mixtures. We do not assume that the average cellular PSS or relaxation rates for HTIs will be identical to those determined in cuvette measurements, as in cellular HTIs will be in heterogeneous environments depending on cellular localisation

(e.g., into lipid membranes or aqueous cytosol) and the absorption band intensities and positions, quantum yields of photoisomerisations, and the thermal *E* to *Z* relaxation rate are all known to be solvent dependent.<sup>[40]</sup> However, we expected that the trends of PSS wavelength dependency as measured in UV/Vis would reasonably correspond to those in the cellular context. We therefore acquired PSS spectra by UV/Vis spectrophotometry (Figure 2A), and using NMR reference measurements we calibrated and compared PSSs in the visible region

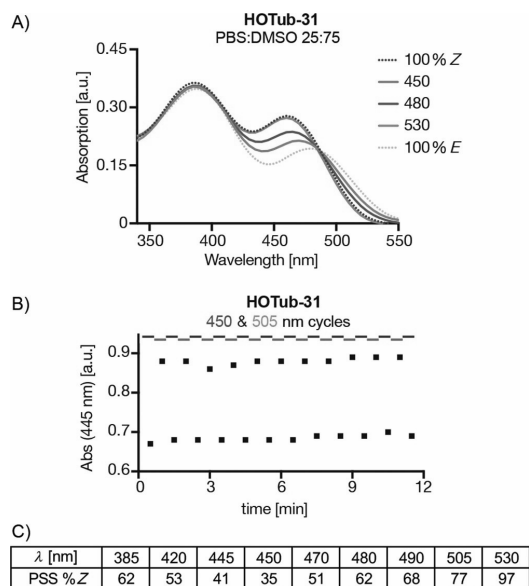


Figure 2. A) Typical PSS spectra of HOTub-31 measured in PBS:DMSO 25:75, under saturating 450 nm, 480 nm, and 530 nm illumination, with back-inferred 100% *Z* and 100% *E* spectra. B) Photoreversible switching measured by UV/Vis spectrophotometry, under alternating 450 nm and 505 nm illuminations. No photobleaching was observed after 285 switching cycles. C) Measured PSSs over 385–530 nm, in PBS/DMSO 25:75.

(420–530 nm) to find optimal wavelengths for biological photoswitching applications (Figure 2C).

Rather than highly monochromatic light, we used LEDs with about 15 nm FWHM emission bandwidth for these measurements, similarly to how we intended to perform long-term biological assays. The ratio of the two isomers' photoisomerisation quantum yields,  $\Phi$ , depends on which band is excited, and rough calculations from PSS spectra show that in the  $S_0 \rightarrow S_1$  band (covering ~430–540 nm) the ratio  $\Phi_{E \rightarrow Z} / \Phi_{Z \rightarrow E}$  is approximately 1.6, and in the  $S_0 \rightarrow S_2$  band (~340–430 nm) the  $\Phi_{E \rightarrow Z} / \Phi_{Z \rightarrow E}$  ratio is about 0.9. According to calculations from the 75:25 DMSO/PBS solution measurements (Figure 2A), illumination with 450 nm gave the highest PSS content of metastable *E* isomer (65% *E*) and illumination at 530 nm reached a PSS of ~97% *Z*, both within 30 s illumination. In this solvent mix at 37 °C, the spontaneous relaxation half life of *E*-HOTub-31 was approximately 30 min. We also performed extended tests of photoreversible photoswitching in 75:25 DMSO/PBS in a non-degassed solution open to air, as one method to examine whether photodegradation could be problematic for in cellulo biology. Under these conditions we observed highly repeatable photoreversible switching (Figure 2B) that encouraged us to begin cell culture photoswitching applications.

#### Photoswitchability of bioactivity in cellulo

Inhibitors of tubulin dynamics act as antimetabolic cytotoxins in cell culture, allowing cell viability to serve as a proxy readout for their antitubulin potency in the cellular context. To evaluate the isomer dependency of in cellulo bioactivity of HOTubs we therefore began by assaying their cellular antiproliferative activity, under repeated in situ photoswitching conditions. We used HeLa cervical cancer cells as a cell line representative of the general responses of mammalian cells to tubulin inhibitors. We used self-built arrays of low-intensity LEDs<sup>61</sup> to deliver illuminations with relatively narrow spectral bandwidth, pulsing them once per minute during the entire experimental timeframe to maintain PSS equilibria in cellulo. We initially compared illumination responses under a range of wavelengths from 380–530 nm and dark conditions, and observed that, as expected from the PSS determinations, 450 nm and dark (or, equivalently, 530 nm) illuminations delivered the greatest differences in potency. We therefore concentrated on comparing 450 nm and dark results. We were delighted to observe that the "bottom-up" oriented, hydroxyl-bearing HOTub-31 and HOTub-81 showed potent and repeatable cellular cytotoxicity well below their precipitation threshold, but with sign inversion: HOTub-31 was "dark-toxic" with fourfold photoswitchability of bioactivity (Figure 3A) while HOTub-81 was "lit-toxic", which matched our molecular design goals. Importantly, the permutation control compound HOTub-70 was completely inactive below 20  $\mu\text{M}$  under 450 nm and dark conditions, suggesting that the scaffold design has no significant nonspecific toxic effects as either isomer or in response to illumination. The methoxy-group deletion control compound HOTub-13 was observed to aggregate out of solution at 10  $\mu\text{M}$ , and showed an only gently sloping cytotoxic response (low Hill coefficient)

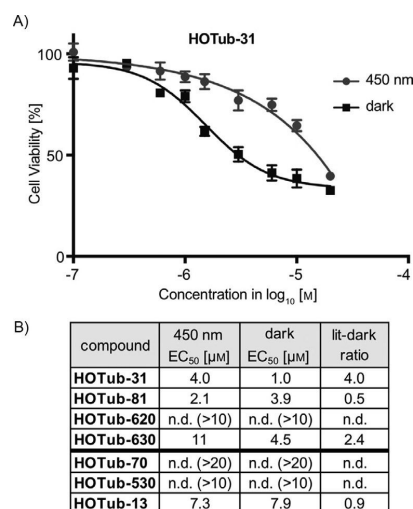


**Figure 3.** A) Representative MTT antiproliferation assay in HeLa cell line, for HOTub-31, showing the strong difference between antimetabolic potencies under 450 nm and dark conditions. B) Cellular antiproliferation EC<sub>50</sub> values for the HOTubs under 450 nm and dark conditions, with the ratio of lit to dark EC<sub>50</sub> values calculated, to highlight the fold change of photoswitchable bioactivity.

at higher concentrations which we suggest is due to aggregation toxicity not specific binding; we have previously observed that, as compared to 1,2-dimethoxy or 1,2,4-trimethoxy motifs, 1,2,3-trimethoxyaryl compounds have surprisingly greater aqueous solubility, which may be attributed to the out-of-plane orientation of the middle methoxy group that disrupts  $\pi$ -stacking.

Some abrogation of potency had been expected for HOTub-620 and HOTub-630 due to the absence of an orienting hydroxyl group, and they did not prove as potent as the hydroxylated "bottom-up" compounds. Despite showing a lower potency than HOTub-31, we were pleased to observe that "top-down" HOTub-630 also gave the dark-specificity for which it was designed. However, HOTub-620 did not display strong antiproliferative effects below 10  $\mu\text{M}$  under either illumination condition. Again, the permutation control HOTub-530 displayed only weak antiproliferative effects and these were entirely independent of illumination conditions (see the Supporting Information for full data).

We found many aspects of these results exciting. The minimal-permutation controls showed substantially weaker as well as totally non-photoswitchable toxicity, thus suggesting that HTI photoswitches with appropriate properties (especially solubility) can be cellularly tolerated at mid-micromolar concentrations and do not necessarily cause phototoxicity under repeated illumination conditions. This opens broader opportunities for their photopharmaceutical exploitation; and is particularly pleasing because the possibility to near-quantitatively photoisomerise HTIs from the metastable to the stable isomer (here,

~97%) differentiates them from the performance of the azobenzene scaffold, where the typically far less complete nature of this photoprocess (~80%) depresses the maximum achievable dynamic range of photoswitching. The robust and repeatable cytotoxicity of the active compounds represents the first demonstration of HTI-based “narrow” (druglike) photopharmaceuticals designed for an endogenous protein target, and an intracellular target at that. Most pleasingly, the rationally designed isomer-specific cytotoxicity in the active compounds supported that our design procedure for “mapping” the *E*- or *Z*-state HTI isomers into the colchicinoid pharmacophore to create lit- or dark-state toxins at will, despite potential preferences of the protein binding site, could indeed be robustly achieved on the desymmetrised HTI scaffold, in accordance with our design aims.

However, cytotoxicity assays do not provide mechanistic information about the most relevant in cellulo target or targets of a compound over a long-term assay (neither do in vitro assays against purified enzyme). Therefore, we wished to answer the question of whether isomer-dependent modulation of tubulin polymerisation dynamics is the major in cellulo bioactivity mechanism of the HOTubs, across both lit- and dark-active designs. We focussed on “bottom-up” HOTub-31 and HOTub-81, anticipating that their greater solubility compared to the non-hydroxylated “top-down” compounds would deliver a cleaner pharmacological profile.

Firstly, we examined directly their capacity to photomodulate microtubule network structure within cells in long-term illuminations. The direct mechanism of action of colchicine-site binding drugs is to reduce tubulin polymerisation dynamics, but after long-term exposure to the more potent inhibitors in this class, microtubule network structures become disorganised and then progressively depolymerised (although effective inhibitors of polymerisation dynamics that produce antimetabolic effects but do not reduce polymer mass are also known<sup>[41]</sup>). We accordingly performed immunofluorescence staining and confocal microscopy of the polymer microtubule network of cells treated for 24 h (Figure 4).

Dark-toxic HOTub-31 gave strong photoswitchability of microtubule structure disruption, with the greatest difference in effect visible around 1.5  $\mu\text{M}$ . At this concentration, lit cells featured nearly normal microtubule networks whereas dark-treated cells had almost entirely depolymerised structures. Incubations at higher concentrations confirmed the dark-toxicity of this compound (Figure S5). Lit-toxic HOTub-81 required higher concentrations to see substantial effects, but whereas lit cells treated at 10  $\mu\text{M}$  were substantially found in an entirely microtubule-depolymerised state, cells could be treated at up to 20  $\mu\text{M}$  under dark conditions with only a smaller fraction of cells (that were apparently arrested in mitosis, when cells have preemptively depolymerised most of their microtubules) showing substantial network depolymerisation. Although there is residual disruption of microtubule structure and mass with both compounds in their less active states (compare to negative control image), our strategy towards forcing both isomer specificities of microtubule disrupting activity seemed supported by this direct biological visualisation (Figure 4).

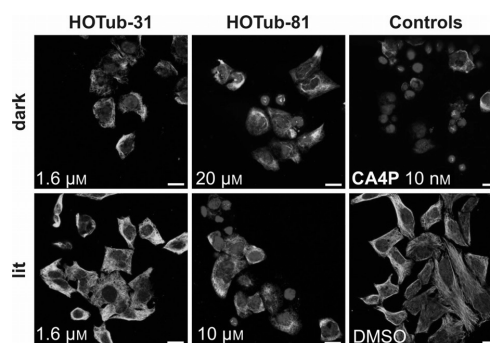


**Figure 4.** Confocal microscopy of immunofluorescently stained microtubule networks after 24 h lit- or dark-treatment with HOTubs shows illumination-specific antimicrotubule effects that match the sign and the potency of their cellular cytotoxicity. HOTub-31 at 1.6  $\mu\text{M}$ , with the lit treatment at 410 nm; HOTub-81 at 10  $\mu\text{M}$  under the lit treatment (450 nm) but 20  $\mu\text{M}$  under dark treatment; negative control image: 1% DMSO cosolvent-treated cells under 450 nm; positive control image: CA4 phosphate (MTT  $\text{EC}_{50}$  = 5 nM) at 10 nM. Scale bars: 20  $\mu\text{m}$ . DAPI nuclear stain shown in blue, immunostained tubulin shown in green; for details, see the Supporting Information and Figure S5.

Lastly, we analysed cell cycle perturbation, as an orthogonal method to test whether tubulin binding in cellulo is the likely long-term mechanism of action of these compounds. Tubulin-binding agents, whose major cellular mechanism of toxicity is the disruption of microtubule dynamics or structure, should show cell cycle arrest in  $G_2/M$  phase.<sup>[24b]</sup> Compounds with other toxic mechanisms, such as nonspecific photodamage, should not significantly impact the cell cycle; and even cell-cycle-affecting compounds that may confound immunofluorescence assessment of microtubule polymer structure can be filtered out if they have a different profile of cell cycle effects (e.g., doxorubicin can reduce microtubules seen in microscopy, but does not cause  $G_2/M$  arrest). We therefore used flow cytometry to analyse cell cycle repartition in cells treated for 24 h. HOTub-31 showed strongly illumination-dependent bioactivity, provoking almost total  $G_2/M$  arrest at 3  $\mu\text{M}$  under dark conditions, but with no visible cell cycle perturbation at this concentration under 450 nm illumination (Figure 5).

## Discussion

Taken together, our biological cross-evaluations support that the HOTubs' relevant cellular target is tubulin, that the hemithioindigo scaffold can serve as a basis for cell-compatible and potent photopharmaceuticals according to the “narrow” druglike definition, and that the molecular asymmetry of the HTI can be used to rationally design photopharmaceuticals that, according to taste, feature either lit-activity or dark-activity against the same endogenous intracellular target protein.

That HOTubs could successfully be designed for tubulin offers several perspectives for their unique, practical applications. Tubulin is one of many survival-critical intracellular proteins whose activity it has not been possible to regulate directly by genetic methods, such as by the creation of optogenetic tubulin constructs, that would give the experimenter biologi-



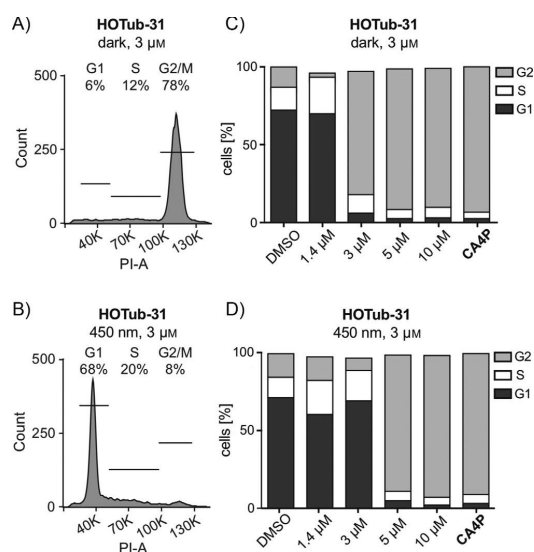


**Figure 5.** Cell cycle analysis of HOTub-31-treated cells. A, B) Representative histograms showing light-dependency of cell cycle arrest, with population binning indicated. C, D) HOTub-31 causes dose- and light-dependent cell cycle arrest. All experiments contained DMSO at 1% v/v; CA4P was used at 10 nM (further details in Supporting Information).

cally meaningful (spatiotemporally precise) control over microtubule structure and biology. In this context, by enabling such previously impossible studies, the azobenzene-based photopharmaceutical PST-1 (azocombretastatin) has already achieved significant applications, leveraging the spatially and temporally precise photoreversible switching of its bioactivity.<sup>[8,9,27]</sup> Alternative photoswitchable scaffolds for tubulin photocontrol that could expand the chemical substituent tolerance of practical tubulin photopharmaceuticals, as well as enable the opposite photoresponse (dark-active) from PST-1 and so access conceptually distinct applications, would also be of extensive interest to the cytoskeleton research community.

Towards more general photopharmaceutical applications of HTIs, it is noteworthy that the metastable isomers of HTIs bearing mesomerically stabilising or tautomerisable substituents in *para* on the hemistilbene are not necessarily “fast-relaxing” (half-lives below ~1 ms) in aqueous environments, unlike what is seen for azobenzenes (probably the same is true on all positions of the thioindoxyl, explorations are ongoing by other groups<sup>[42]</sup>). Azobenzenes face other common challenges in cellular environments, including thiol addition into the photoswitchable N=N double bond that can lead to compound degradation, sequestration, or off-target effects; we expect that the C=C photoswitchable bond in HTIs will have a different and overall diminished profile of thiol sensitivity. The cellular applicability we now show for “narrow” HTI photopharmaceuticals (where the ability to decorate the photoswitch with arbitrary substituents is particularly important) argues this photoswitch scaffold may now prove important in opening new chemical space in photopharmacology.

The cytotoxic potencies of HOTub-31 (ca. fourfold change between dark and 450 nm treatments) suggest that the PSS values measurable in DMSO or 75:25 DMSO/PBS do not apply to the “average” PSS established in the cellular situation. Even were its *E* isomer essentially inactive, the change of potency to be expected between dark and lit treatments in the MTT assay would otherwise be only threefold (35% Z at 450 nm) according to the PSS in 75:25 DMSO/PBS. We believe that one factor behind this observation will prove to be that the relatively lipophilic HOTubs might be extensively localised in lipid environments (potentially with different partition coefficients in the Z and *E* forms), and that this modifies the effective cellular PSSs. While in the case of HOTub-31 this may work in favour of the photoswitchability of its apparent potency, we anticipate that installing still better aqueous solubility in HTIs will prove important for their reliability in general cellular applications, for predictability of photoswitching and biodistribution as well as to avoid potential [2+2] photocycloadditions<sup>[43]</sup> in aggregated HTIs (we also believe the importance of solubility is reflected in the weaker photoswitchability of potency of the non-hydroxylated HOTubs). Current advances in HTI photoswitch design are also leading to photoswitches with extremely high photoswitchability of isomer ratios,<sup>[44]</sup> which if applied to HOTub derivatives could offer perspectives for even dark-state-active HTIs to be photopatterned with yet higher photoswitchability of bioactivity.

## Conclusions

This study has demonstrated the first uses of pharmacophore-embedded hemithioindigos as cell-compatible photopharmaceuticals enabling long-term in situ photocontrol of an endogenous intracellular biological target. The match of our compounds’ photodependent bioactivities to the predictions from SAR mapping, as well as the inactivity of the intentional negative controls, argues that off-target bioactivity including aggregation toxicity and photodamage effects are not problematic with the scaffolds and concentrations employed. In particular, we consider the ability to rationally embed the HTI scaffold in such a way as to show either lit- or dark-state bioactivity, to hold much potential for photopharmacology applications, where typically lit-active compounds are desirable. In the present case, we have shown the ability of the HTI scaffold to be used as an effective asymmetric mimic for a pharmacophore mapping onto a *cis*-azobenzene, which due to the difference in torsion angles (~60° for *cis*-azobenzene and nearly planar for either HTI isomer) was not immediately obvious, but which probably relies on binding site plasticity. We fully expect however that the HTI can also be mapped asymmetrically onto (geometrically more similar) *trans*-azobenzene-like pharmacophores, and that HTIs can therefore be used to “rework” especially dark-active azobenzene photopharmaceuticals into conceptually more valuable lit-active HTI analogues (or, also, dark-actives if so desired).

Despite the attractiveness of tubulin as a target for continued development of in cellulo- (and ultimately in vivo-) appropriate photopharmaceuticals with diverse properties, we now

believe that the most straightforwardly rewarding applications of such molecular reworking will be in the creation of lit-active HTI-type photopharmaceuticals for situations where azobenzene reagents have hitherto been *trans*-active. By “inverting the sign” of photoresponse, such reagents could avoid the major problems associated with *trans*-active azobenzenes, that is, spontaneous generation of, and incomplete photoisomerisation away from, the more bioactive isomer. These problems typically act in concert to limit the photoswitchability of bioactivity that can be applied in cellular contexts. We therefore hope that, by enabling free design of lit- or dark-state activity, the present work will open new horizons for robust photopharmacological applications against a variety of targets.

## Experimental Section

**Materials:** Chemistry building blocks and biology reagents were obtained from commercial sources as described in the Supporting Information.

**General synthesis:** Typical synthetic strategies are summarised as follows. Hemithioindigos were synthesised by aldol condensation of the corresponding thioindoxyls and benzaldehydes. Diverse condensation reaction conditions were trialled, including 1) room temperature condensation on neutral, basic, or acidic aluminium oxide under dry chlorinated solvents, 2) condensation in dry refluxing benzene with piperidine catalysis, and 3) condensation in refluxing NaOH/*t*BuOH; of these, the benzene/piperidine conditions typically gave highest isolated yields. One-pot procedures without intermediate purification of the thioindoxyls typically resulted in tedious workups and low yields. In our hands, some hemithioindigos decomposed significantly during normal phase silica gel column chromatography despite precautions to deactivate the gel, generating a plethora of decomposition products. Purification through precipitating the hemithioindigo out of concentrated DMSO solution by adding water, often proved a better alternative. Thioindoxyls were synthesised by intramolecular cyclisation, either of the 2-(phenylthio)acetyl chloride with AlCl<sub>3</sub> in chlorinated solvents, of the 2-(phenylthio)acetic acid with Eaton's reagent, or with exposure of 2-(methylthio)benzoic esters or amides to LDA in THF; of these, the LDA/THF conditions typically gave highest isolated yields when alternative routes could practicably be compared. Despite literature reports of the instability of thioindoxyls, in our hands these electron-rich thioindoxyls showed no significant degradation upon long-term storage at -20 °C, and generally tolerated workups and ordinary bench handling without decomposition (high pH should be avoided however). Towards 2-(methylthio)benzoate derivatives, we first attempted directed *ortho*-metalations of, for example, methyl(3,4,5-trimethoxyphenyl)sulfide with *s*BuLi/TMEDA, but this instead deprotonated the *S*-methyl group, leading to undesired 2-(3,4,5-trimethoxyphenylthio)acetic acids upon quenching with CO<sub>2</sub>. The cyclisation precursors were therefore typically synthesised by magnesium-halogen exchange on *ortho*-iodobenzene derivatives with turbo-Grignard,<sup>[39]</sup> followed by electrophilic quenching with methyl chloroformate (for phenyl methyl thioethers) or with MeSSO<sub>2</sub>Me (for benzoate derivatives). All syntheses are fully described in the Supporting Information.

**Photoisomerisation:** reference photostationary states were determined by NMR spectroscopy of DMSO solutions of HOTubs at 1 mM, that had been 1) kept dark at 60 °C overnight (all-*Z*), or else 2) irradiated with a 3 W Epistar LED driven at 350 mA and placed directly under a stirred vial of HOTub solution (1 cm diameter,

height < 0.4 cm) for 2 min and for 5 min before solution transfer to the NMR tube and its loading into the spectrometer were performed rapidly under dark conditions. NMR acquisition was started immediately (total delay time ~ 1 min). That PSS had been reached was confirmed by the equivalence of the 2 min and 5 min illumination measured PSSs; that thermal relaxation during delay time did not significantly affect the measured PSSs was confirmed by the equivalence of a single representative PSS measurement with an analogous measurement where an additional 20 min delay was introduced. These were taken to define the PSSs of 100 μM HOTub solutions in 75:25 DMSO/PBS mixture at 25 °C that had been photoequilibrated with the same LEDs, the absorption spectra of which were measured by UV/Vis spectroscopy. UV/Vis was then used to scan sequentially through a range of PSSs established under varying LED wavelengths, to show the repeatability of photoswitching as well as to characterise intermediate PSSs between the reference PSSs determined from NMR spectroscopy (450 nm and dark (all-*Z*) conditions as cross-checked to 505 nm). Full descriptions are given in the Supporting Information.

**Cell biology:** studies were performed as previously described.<sup>[6]</sup> In brief, HeLa human cervical cancer cell line sourced from the ATCC was used for all studies; all treatments were performed in triplicate; results are only reported when three independent experiments returned quantitatively similar results within acceptable error ranges; experiments were typically conducted using combretastatin A-4 phosphate as a highly potent, positive control reference compound with the same binding site and bioactivity as was desired to for the HOTubs. Antiproliferative or cytotoxic potencies were determined by MTT assay of cells seeded at ~5000 cells/well in 96-well microtitre plates and left to adhere for 24 h before treatment with HOTub for 48 h, under pulsed *in situ* illuminations typically at 450 nm (typical timing: 100 ms ON per 60 s OFF) delivered from self-built LED plates containing ~10 mW LEDs (Roithner Lasertechnik) as compared to cells incubated under dark conditions, as previously described.<sup>[6]</sup> Immunofluorescence staining of cellular microtubule networks was performed after 24 h treatment of cells with HOTubs under pulse-illuminated or dark conditions; removal of monomeric tubulin with extraction buffer was followed by fixation with methanol or glutaraldehyde, and immunostaining using rabbit anti- $\alpha$ -tubulin primary antibody and donkey anti-rabbit Alexa Fluor 488 secondary antibody, mounted in presence of DAPI nuclear stain; imaging was typically conducted on a Zeiss LSM710 confocal microscope (Zen Black software 2009) and images were processed with Fiji/ImageJ software (NIH); for full details see the Supporting Information. Flow cytometric cell cycle analysis was performed after 24 h of HOTub treatments as per previous experiments, with cell permeabilization then chromatin staining using propidium iodide (both in fixed and in non-fixed cells, identical results were observed by these methods); flow cytometric analysis for cell cycle repartition was conducted with standard gating for intact PI-positive cells, partitioning events into sub-G<sub>1</sub>, G<sub>1</sub>, S, or G<sub>2</sub>/M bins by using either FlowJo or FlowingSoftware (with qualitatively identical results). See the Supporting Information for full details.

## Acknowledgements

This project was funded by the Deutsche Forschungsgemeinschaft (DFG, German Research Foundation) (SFB 1032 project B09; TRR 152, project P24 number 239283807; and Emmy Noether grant TH 2231/1-1). We thank Irina Solovei (CALM microscopy platform,

LMU) and Christophe Jung (Gene Centre, LMU) for access to and assistance with confocal imaging; Neda Tadrishi for access to and assistance with FACS (FACS Core Facility, Gene Centre, LMU Munich); Luis de la Osa de la Rosa, Malgorzata Borowiak, Ruben Sachse and Niklas Peters for trialling cellular toxicity assay parameters; Herbert Bachmeier and Axel Gersdorf for LED arrays (LMU); Peter Gänzheimer, Patricia Schuerle and Sophia Schwarz for advice on synthetic routes; and colleagues at the International Symposia on Photopharmacology for productive discussions.

### Conflict of Interest

The authors declare no conflict of interest.

**Keywords:** antiproliferation · cytoskeleton · drug design · hemithioindigo · photochromism · photopharmacology

- [1] a) A. A. Beharry, G. A. Woolley, *Chem. Soc. Rev.* **2011**, *40*, 4422–4437; b) K. Hüll, J. Morstein, D. Trauner, *Chem. Rev.* **2018**, *118*, 10710–10747; c) W. A. Velema, W. Szymanski, B. L. Feringa, *J. Am. Chem. Soc.* **2014**, *136*, 2178–2191.
- [2] A. Bautista-Barrufet, M. Izquierdo-Serra, P. Gorostiza, in *Novel Approaches for Single Molecule Activation and Detection* (Eds.: F. Benfenati, E. Di Fabrizio, V. Torre), Springer, Berlin, **2014**, pp. 169–188.
- [3] a) A. Rullo, A. Reiner, A. Reiter, D. Trauner, E. Y. Isacoff, G. A. Woolley, *Chem. Commun.* **2014**, *50*, 14613–14615; b) X. Gómez-Santacana, S. Pitolo, X. Rovira, M. Lopez, C. Zussy, J. A. R. Dalton, A. Faucherre, C. Jopling, J.-P. Pin, F. Ciruela, C. Goudet, J. Giraldo, P. Gorostiza, A. Llebaria, *ACS Cent. Sci.* **2017**, *3*, 81–91.
- [4] W. A. Velema, J. P. van der Berg, M. J. Hansen, W. Szymanski, A. J. M. Driessen, B. L. Feringa, *Nat. Chem.* **2013**, *5*, 924–928.
- [5] W. Szymanski, M. E. Ouralidou, W. A. Velema, F. J. Dekker, B. L. Feringa, *Chem. Eur. J.* **2015**, *21*, 16517–16524.
- [6] M. Borowiak, W. Nahaboo, M. Reyniers, K. Nekolla, P. Jalinot, J. Hasseroth, M. Rehberg, M. Delattre, S. Zahler, A. Vollmar, D. Trauner, O. Thorn-Seshold, *Cell* **2015**, *162*, 403–411.
- [7] A. Polosukhina, J. Litt, I. Tochitsky, J. Nemargut, Y. Sychev, I. De Kouchkovsky, T. Huang, K. Borges, D. Trauner, R. N. Van Gelder, R. H. Kramer, *Neuron* **2012**, *75*, 271–282.
- [8] J. Zenker, M. D. White, R. M. Templin, R. G. Parton, O. Thorn-Seshold, S. Bissiere, N. Plachta, *Science* **2017**, *357*, 925–928.
- [9] J. Zenker, M. D. White, M. Gasnier, Y. D. Alvarez, H. Y. G. Lim, S. Bissiere, M. Biro, N. Plachta, *Cell* **2018**, *173*, 776–791.
- [10] M. M. Lerch, M. J. Hansen, G. M. van Dam, W. Szymanski, B. L. Feringa, *Angew. Chem. Int. Ed.* **2016**, *55*, 10978–10999; *Angew. Chem.* **2016**, *128*, 11140–11163.
- [11] a) O. Babii, S. Afonin, M. Berditsch, S. Reißer, P. K. Mykhailiuk, V. S. Kubyshkin, T. Steinbrecher, A. S. Ulrich, I. V. Komarov, *Angew. Chem. Int. Ed.* **2014**, *53*, 3392–3395; *Angew. Chem.* **2014**, *126*, 3460–3463; b) C. J. Stankovic, S. H. Heinemann, S. L. Schreiber, *Biochim. Biophys. Acta* **1991**, *1061*, 163–170.
- [12] a) W. A. Velema, M. J. Hansen, M. M. Lerch, A. J. M. Driessen, W. Szymanski, B. L. Feringa, *Bioconjugate Chem.* **2015**, *26*, 2592–2597; b) M. Wegener, M. J. Hansen, A. J. M. Driessen, W. Szymanski, B. L. Feringa, *J. Am. Chem. Soc.* **2017**, *139*, 17979–17986.
- [13] D. Lachmann, C. Studte, B. Männel, H. Hübner, P. Gmeiner, B. König, *Chem. Eur. J.* **2017**, *23*, 13423–13434.
- [14] D. Schmidt, T. Rodat, L. Heintze, J. Weber, R. Horbert, U. Girreser, T. Raeker, L. Bußmann, M. Kriegs, B. Hartke, C. Peifer, *ChemMedChem* **2018**, *13*, 2415–2426.
- [15] a) D. Wilson, J. W. Li, N. R. Branda, *ChemMedChem* **2017**, *12*, 284–287; b) N. A. Simeth, A. C. Kneutinger, R. Sterner, B. König, *Chem. Sci.* **2017**, *8*, 6474–6483.
- [16] a) A. Mourot, T. Fehrentz, Y. Le Feuvre, C. M. Smith, C. Herold, D. Dalkara, F. Nagy, D. Trauner, R. H. Kramer, *Nat. Methods* **2012**, *9*, 396; b) B. Eisel, F. W. W. Hartrampf, T. Meier, D. Trauner, *FEBS Lett.* **2018**, *592*, 343–355.
- [17] a) M. Schehr, D. Hugenbusch, T. Moje, C. Näther, R. Herges, *Beilstein J. Org. Chem.* **2018**, *14*, 2799–2804; b) R. Siewertsen, H. Neumann, B. Buchheim-Stehn, R. Herges, C. Näther, F. Renth, F. Temps, *J. Am. Chem. Soc.* **2009**, *131*, 15594–15595.
- [18] S. Wiedbrauk, H. Dube, *Tetrahedron Lett.* **2015**, *56*, 4266–4274.
- [19] a) T. Seki, T. Tamaki, T. Yamaguchi, K. Ichimura, *Bull. Chem. Soc. Jpn.* **1992**, *65*, 657–663; b) K. Eggers, T. M. Fyles, P. J. Montoya-Pelaez, *J. Org. Chem.* **2001**, *66*, 2966–2977.
- [20] N. Regner, T. T. Herzog, K. Hauser, C. Hoppmann, M. Beyermann, J. Sauermann, M. Engelhard, T. Cordes, K. Rück-Braun, W. Zinth, *J. Phys. Chem. B* **2012**, *116*, 4181–4191.
- [21] T. Loughheed, V. Borisenko, T. Hennig, K. Rück-Braun, G. A. Woolley, *Org. Biomol. Chem.* **2004**, *2*, 2798–2801.
- [22] S. Herre, T. Schadendorf, I. Ivanov, C. Herrberger, W. Steinle, K. Rück-Braun, R. Preissner, H. Kuhn, *ChemBioChem* **2006**, *7*, 1089–1095.
- [23] C. Dumontet, M. A. Jordan, *Nat. Rev. Drug Discovery* **2010**, *9*, 790–803.
- [24] a) T. J. Mitchison, *Mol. Biol. Cell* **2012**, *23*, 1–6; b) J. R. Peterson, T. J. Mitchison, *Chem. Biol.* **2002**, *9*, 1275–1285.
- [25] a) J. E. Sheldon, M. M. Dcona, C. E. Lyons, J. C. Hackett, M. C. T. Hartman, *Org. Biomol. Chem.* **2016**, *14*, 40–49; b) A. J. Engdahl, E. A. Torres, S. E. Lock, T. B. Engdahl, P. S. Mertz, C. N. Streu, *Org. Lett.* **2015**, *17*, 4546–4549.
- [26] K. Eguchi, Z. Taoufiq, O. Thorn-Seshold, D. Trauner, M. Hasegawa, T. Takahashi, *J. Neurosci.* **2017**, *37*, 6043–6052.
- [27] A. Singh, T. Saha, I. Begemann, A. Ricker, H. Nüsse, O. Thorn-Seshold, J. Klingauf, M. Galic, M. Matis, *Nat. Cell Biol.* **2018**, *20*, 1126–1133.
- [28] S. K. Rastogi, Z. Zhao, S. L. Barrett, S. D. Shelton, M. Zafferani, H. E. Anderson, M. O. Blumenthal, L. R. Jones, L. Wang, X. Li, C. N. Streu, L. Du, W. J. Brittain, *Eur. J. Med. Chem.* **2018**, *143*, 1–7.
- [29] G. C. Tron, T. Pirali, G. Sorba, F. Pagliai, S. Busacca, A. A. Genazzani, *J. Med. Chem.* **2006**, *49*, 3033–3044.
- [30] R. Gaspari, A. E. Prota, K. Bargsten, A. Cavalli, M. O. Steinmetz, *Chem.* **2017**, *2*, 102–113.
- [31] G. R. Pettit, B. Toki, D. L. Herald, P. Verdier-Pinard, M. R. Boyd, E. Hamel, R. K. Pettit, *J. Med. Chem.* **1998**, *41*, 1688–1695.
- [32] G. R. Pettit, S. B. Singh, E. Hamel, C. M. Lin, D. S. Alberts, D. Garcia-Kendal, *Experientia* **1989**, *45*, 209–211.
- [33] Y. Wang, H. Zhang, B. Gigant, Y. Yu, Y. Wu, X. Chen, Q. Lai, Z. Yang, Q. Chen, J. Yang, *FEBS J.* **2016**, *283*, 102–111.
- [34] R. H. Bisby, S. W. Botchway, J. A. Hadfield, A. T. McGown, A. W. Parker, K. M. Scherer, *Eur. J. Cancer* **2012**, *48*, 1896–1903.
- [35] R. B. Ravelli, B. Gigant, P. A. Curmi, I. Jourdain, S. Lachkar, A. Sobel, M. Knossow, *Nature* **2004**, *428*, 198–202.
- [36] K. Jacobson, Z. Rajfur, E. Vitriol, K. Hahn, *Trends Cell Biol.* **2008**, *18*, 443–450.
- [37] M. T. Konieczny, W. Konieczny, S. Okabe, H. Tsujimoto, Y. Suda, K. Wierzbak, *Chem. Pharm. Bull.* **2006**, *54*, 350–353.
- [38] C. Mukherjee, S. Kamila, A. De, *Tetrahedron* **2003**, *59*, 4767–4774.
- [39] A. Krasovskiy, P. Knochel, *Angew. Chem. Int. Ed.* **2004**, *43*, 3333–3336; *Angew. Chem.* **2004**, *116*, 3396–3399.
- [40] J. Wang, K. Rueck-Braun, *ChemPhotoChem* **2017**, *1*, 493–498.
- [41] J. Zhou, D. Panda, J. W. Landen, L. Wilson, H. C. Joshi, *J. Biol. Chem.* **2002**, *277*, 17200–17208.
- [42] F. Kink, M. P. Collado, S. Wiedbrauk, P. Mayer, H. Dube, *Chem. Eur. J.* **2017**, *23*, 6237–6243.
- [43] J. D. Harris, M. J. Moran, I. Aprahamian, *Proc. Natl. Acad. Sci. USA* **2018**, *115*, 9414.
- [44] J. E. Zweig, T. R. Newhouse, *J. Am. Chem. Soc.* **2017**, *139*, 10956–10959.

Manuscript received: November 30, 2018

Accepted manuscript online: January 11, 2019

Version of record online: April 12, 2019

## 4.3 Hemithioindigo HITubs

### Motivation for this work

With the development of HOTubs as hemithioindigo-based photoswitches, we showed that the pseudosymmetry of hemithioindigo scaffold can be used for *a priori* design of pharmacophores that inhibit tubulin in a light-dependent manner within a micromolar concentration range and can be either dark or lit-active depending on the arrangement of substituents<sup>119</sup>.

Nevertheless, we thought that the improvement of potency of hemithioindigo based tubulin depolymerisers would be desirable without sacrificing the photo-response advantages of the HTI scaffold.

### Short summary of the HITub work

In order to achieve the goal of more potent hemithioindigo-based photopharmaceuticals, we decided to move away from a substituent pattern structurally similar to colchicine and instead focus on indanocine's substituent pattern. Indanocine is also a CDI, with nanomolar range potency and features a substituent pattern that we thought to be suitable to fit onto a hemithioindigo core. This resulted in the lead-structure for the HITubs (hemithioindigo-based indanone-like tubulin inhibitors). This strategy allowed for potent photo-controllable tubulin inhibitors that can harbour a hydroxyhemistilbene motif, which is not possible for azobenzene based molecules due to negligible short lifetimes of their metastable *Z*-isomers. We tested 7 HTI-based compounds to confirm our rational on SAR for changes on key substituents and respective north and south-rings. We showed that para-hydroxy HTIs that have not been reported before, exhibit robust and photoswitchable bioactivity on the microtubule cytoskeleton in cells with a significant improvement of potency compared to our previously designed HOTubs. Furthermore, our results are indicative for the *E*-isomers of our HITs being virtually inactive in biological settings, which could be ground-breaking to more sophisticated photopharmaceuticals with unique abilities as will be discussed in the conclusions.

### Authorial Contributions

After the compounds were analysed by R. Bingham for their ability to inhibit tubulin polymerisation *in vitro* under a lighting regime, my part of this work was to verify antiproliferative effects of the HITubs under dark and lit conditions (Fig. 4 in collaboration with F. Ermer) as well as using immunofluorescence and confocal imaging to directly visualize the effects of the compounds towards the microtubule cytoskeleton (Fig. 5). Furthermore, I confirmed the mechanism in collaboration with F. Ermer and J. Ahlfeld by cell cycle analysis that revealed a significant G2/M arrest (Fig. 6).



## Potent hemithioindigo-based antimetotics photocontrol the microtubule cytoskeleton in cellulo

Alexander Sailer, Franziska Ermer, Yvonne Kraus, Rebekkah Bingham, Ferdinand H. Lutter, Julia Ahlfeld and Oliver Thorn-Seshold\*

### Full Research Paper

[Open Access](#)

Address:  
Department of Pharmacy, Ludwig Maximilian University of Munich,  
Butenandtstraße 5-13, Munich 81377, Germany

Email:  
Oliver Thorn-Seshold\* - oliver.thorn-seshold@cup.lmu.de

\* Corresponding author

Keywords:  
antimetotics; cytoskeleton; hemithioindigo; photopharmacology;  
photoswitch

*Beilstein J. Org. Chem.* **2020**, *16*, 125–134.  
doi:10.3762/bjoc.16.14

Received: 31 July 2019  
Accepted: 13 November 2019  
Published: 27 January 2020

This article is part of the thematic issue "Molecular switches".

Guest Editor: W. Szymanski

© 2020 Sailer et al.; licensee Beilstein-Institut.  
License and terms: see end of document.

### Abstract

**Background:** Hemithioindigo is a promising molecular photoswitch that has only recently been applied as a photoswitchable pharmacophore for control over bioactivity in cellulo. Uniquely, in contrast to other photoswitches that have been applied to biology, the pseudosymmetric hemithioindigo scaffold has allowed the creation of both dark-active and lit-active photopharmaceuticals for the same binding site by a priori design. However, the potency of previous hemithioindigo photopharmaceuticals has not been optimal for their translation to other biological models.

**Results:** Inspired by the structure of tubulin-inhibiting indanones, we created hemithioindigo-based indanone-like tubulin inhibitors (**HITubs**) and optimised their cellular potency as antimetotic photopharmaceuticals. These **HITubs** feature reliable and robust visible-light photoswitching and high fatigue resistance. The use of the hemithioindigo scaffold also permitted us to employ a *para*-hydroxyhemistilbene motif, a structural feature which is denied to most azobenzenes due to the negligibly short lifetimes of their metastable *Z*-isomers, which proved crucial to enhancing the potency and photoswitchability. The **HITubs** were ten times more potent than previously reported hemithioindigo photopharmaceutical antimetotics in a series of cell-free and cellular assays, and allowed robust photocontrol over tubulin polymerisation, microtubule (MT) network structure, cell cycle, and cell survival.

**Conclusions:** **HITubs** represent a powerful addition to the growing toolbox of photopharmaceutical reagents for MT cytoskeleton research. Additionally, as the hemithioindigo scaffold allows photoswitchable bioactivity for substituent patterns inaccessible to the majority of current photopharmaceuticals, wider adoption of the hemithioindigo scaffold may significantly expand the scope of cellular and in vivo targets addressable by photopharmacology.

## Introduction

The cytoskeletal scaffolding protein tubulin, a heterodimer consisting of  $\alpha$  and  $\beta$  subunits, each of various isotypes, reversibly assembles into giant non-covalent polymeric microtubules (MTs), which play a pivotal role as a dynamic scaffold for a multitude of cellular processes. These include mechanostasis, the completion of mitosis, cell motility, and cargo trafficking in all cell types, as well as cell-type-specific roles, such as polarization, cargo sorting, and trafficking in neurons; the regulation and functioning of these processes is still not satisfactorily understood [1–4]. The MT cytoskeleton is a finely tuned complex system that is highly conserved through evolution. Direct genetic modifications of tubulin that affect its functions risk causing a diversity of effects, due to its many survival-critical roles, as well as non-functionality of the modified tubulin product. For example, knockout approaches have only been described for single isoforms of  $\alpha/\beta$ -tubulin, and these cannot deliver the dynamic reversibility and effect-specificity that is required for understanding MT biology; and optogenetic modifications of tubulin have never succeeded. Instead, studies of the roles of MTs in these processes overwhelmingly rely on small molecule tubulin inhibitors [1].

Due to the non-invasiveness and high spatiotemporal precision with which optical stimulation can be applied, photopharmacology has drawn great interest for studies of crucial biological processes in a range of fields, from neuroscience [5,6] and G-protein-coupled receptor (GPCR) function [7,8] to antibiotic research [9]. Particularly in the context of MT biology, photopharmacology is an attractive development beyond classical small molecule inhibitors; since the spatiotemporal complexity inherent to the diversity of tubulin-dependent cellular processes may finally yield to studies that can leverage high-spatiotemporal-specificity optical control to deliver cell-specific, time-reversible modulation of native cytoskeleton function.

We and others have reported on photoswitchable azobenzene-based inhibitors of tubulin polymerisation [10–13] that have since been used in studies of neuronal trafficking [14] and embryonic development [15,16], and we have recently reported biologically robust heterostilbenes that deliver green fluorescent protein (GFP)-orthogonal MT photocontrol [17]. However, in both azobenzene and heterostilbene scaffolds, the steric properties of the *E*- and *Z*-isomer are so different that the protein binding site shape determines that the *Z*-isomer (the lit-form) is the more bioactive one, without the possibility of sign inversion by substituent shifts. To overcome this conceptual limitation, we recently reported on the first use of hemithioindigos (HTIs) as photoswitchable pharmacophores for optical control of tubulin dynamics in vitro (cell-free) and MT-dependent processes in cellulo [18]. We showed for the first time that the

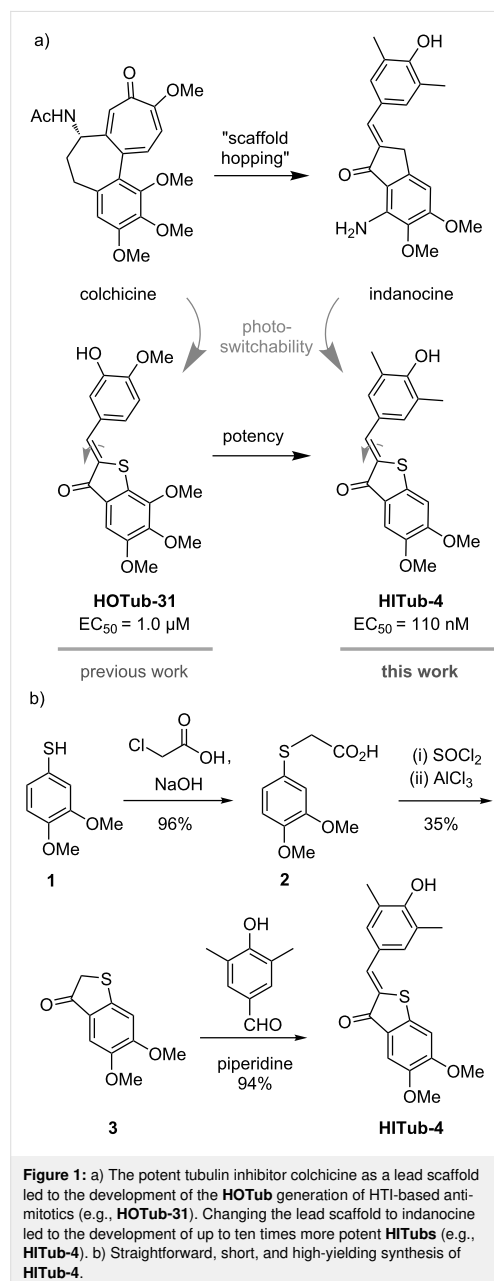


**Figure 1:** a) The potent tubulin inhibitor colchicine as a lead scaffold led to the development of the **HOTub** generation of HTI-based anti-mitotics (e.g., **HOTub-31**). Changing the lead scaffold to indanocine led to the development of up to ten times more potent **HITubs** (e.g., **HITub-4**). b) Straightforward, short, and high-yielding synthesis of **HITub-4**.

pseudosymmetry of hemithioindigos can be used to enable a priori design of HTI-based pharmacophores for a single binding site, with higher bioactivity as either the lit-form *E*- or the dark-

form *Z*-isomer, just by changing substituent patterns, and developed HTI-based antimetabolites with cytotoxic potencies in the low micromolar range (Figure 1a) [18].

In this work, we wished to enhance the bioactivity of the distinctive dark-active HTI-based tubulin-binding antimetabolites while retaining the benefits of the HTI scaffold, namely robust, fatigue-resistant, all-visible-light photoswitching.

## Results and Discussion

### Design strategy for HTIs

The HTI-based colchicinoid **HOTubs** (e.g., **HOTub-31**) that we previously explored had the HTI photoswitch embedded inside a methoxylation pattern, such that one isomer obeyed the structure–activity relationship (SAR) of colchicine or its analogue combretastatin A-4 and was bioactive, while the other isomer clashed with their SAR and was less active [18]. That approach of directly embedding a photoswitch motif inside the pharmacophore seemed to be more promising for photopharmacology than the synthetically more straightforward attachment of photoswitches on the pharmacophore periphery. We expected that embedding (which is referred to as azologization in the case of azobenzene-based photopharmaceuticals [19]) should in general lead to more significant alterations of the binding-relevant structure, and increase the differential potency between isomers of the resulting photopharmaceutical, than peripheral attachment (referred to as azo-extension in the case of azobenzenes [18]). We therefore desired to maintain the embedding strategy, yet to improve potency we chose to break with substitution patterns strictly based on colchicine. It is not the case that colchicine (or any other small-molecule inhibitor) represents an ideal structure that colchicine domain inhibitors (CDIs) should reproduce. Thus, our design focus was to introduce reversible photoresponse to a CDI rather than developing compounds with high similarity to colchicine *per se*, aiming at compounds where one isomer would be almost biologically inactive such that light can be used to effect a photoisomerisation-based switch-on/switch-off of bioactivity. The end-to-end distance of the HTI scaffold is significantly longer than that in either the biaryl colchicine or the stilbene combretastatin, and the torsion angle between the aryl blades of the HTI is nearly planar (up to 4°), while that between the rings of (*Z*)-combretastatin or colchicine is approximately 50–60° [20]. Thus, we assumed that the length and the near-planarity of the HTI could suit it to different substituent patterns to those of colchicine, and attempted to rationally determine these.

Firstly, since the HTI scaffold is longer than a biaryl motif but should occupy a similar volume in the pocket, we assumed that we would have to reduce the substituent bulk present on

colchicine/combretastatin A-4. The middle methoxy group of colchicine's trimethoxy-substituted "south ring" (Figure 1a) makes a beneficial polar contact in the binding pocket via the oxygen atom, but upon demethylation, the potency is much reduced, presumably from insufficient desolvation in the colchicine site (which is known from work on podophyllotoxin derivatives [20]). We therefore chose to keep that methoxy group intact. However, colchicine's methoxy group on the "north ring" establishes a non-polar spacefilling interaction, which can be replaced equipotently by an ethyl group. Thus, we considered that the HTI scaffold could best be reduced in volume by "shortening" this substituent, maintaining the above-mentioned non-polar interaction.

Secondly, since the torsion angle of the HTI is far lower than that of (*Z*)-stilbenes or biaryl compounds, we considered that even with shortening, their SARs might not directly match. Mainly, we assumed that re-orientation of the substituent pattern on one or both rings (e.g., re-orientation of the archetypal 3,4,5-trimethoxyphenyl south ring pattern to a 4,5,6-trimethoxyaryl pattern) might be needed to occupy a similar space.

A wealth of CDIs have been reported, including scaffolds such as aurones that apparently reproduce the substituent pattern SAR of combretastatins [21] while having closely similar scaffold steric properties to HTIs. However, in light of the considerations above, we rather selected indanocine as a starting point for alternative substituent patterning (Figure 1a). Indanocine is a cytotoxic indanone-based CDI ( $EC_{50} \approx 10\text{--}40\text{ nM}$ ) [22] with similar cell culture potency to colchicine ( $EC_{50} \approx 3\text{--}20\text{ nM}$ ) [23] that likewise disrupts MTs, arrests cells in the G2/M phase, and induces apoptosis. Although the size and geometry of thioindoxyl and indanone rings differ because of the S/CH<sub>2</sub> replacement, we assumed that "mapping" the substitution pattern of indanocine onto a hemithioindigo core should result in a lead structure for tubulin-binding (*Z*)-HTIs, namely the class of **HITubs**.

The *para*-hydroxy substitution of indanocine suggested that HTI might be a more desirable photopharmaceutical scaffold than the widely used azobenzene motif. While *para*-hydroxyazobenzenes feature negligibly short *cis*-to-*trans* thermal relaxation half-lives in aqueous media in the range of  $\mu\text{s}$  [24,25], probably making them unsuitable for robust photoswitching applications against intracellular targets, data for *para*-hydroxy HTIs have not been reported so far. We considered that if the *para*-hydroxy-**HITubs** featured photoswitchable bioactivity in cellulo, implying suitable (*E*)-HTI stability under cellular conditions, this would more generally commend them as a scaffold of choice for cellular photo-

pharmaceutical use with strong electron-donating substituents, such as amino or hydroxy groups in *ortho*- or *para*-position, aiming at intracellular targets. This is an important scope of substituents to address, since these small polar groups often establish high-affinity ligand–target interactions, but otherwise represent an obstacle to photoswitchability with azobenzene compounds.

### Preview: design of target HITubs

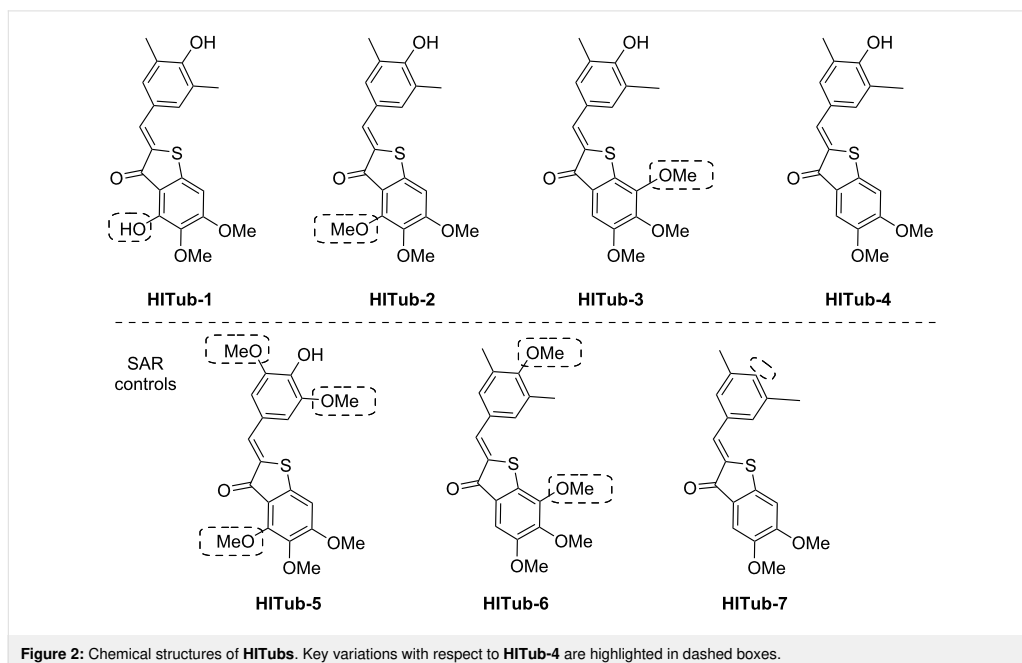
Our SAR-driven compound development path is described in full later in the section on bioactivity, but in brief, we began the series of indanocine-inspired HTI designs by replacing the south ring amino unit of indanocine (which is attached in *ortho*-position to the key south ring methoxy group) by a hydroxy function, giving **HITub-1** (Figure 2).

When **HITub-1** later proved less bioactive than we had wished, we explored steric and polarity changes to this south ring hydroxy group by methylation (**HITub-2**), methylation and shifting on the ring (**HITub-3**), or even its removal (**HITub-4**). We additionally controlled against our design logic of north ring substituent shortening (**HITub-5**). We also controlled for the SAR observation that CDIs should not tolerate a non-polar central north ring substituent (**HITub-6**), but can support removal of this substituent altogether, with only small potency loss (**HITub-7**) [20]. The progression and results of

this SAR study are explained below in the section on bioactivity.

### General synthetic access

Synthetic routes to HTIs are well established [26] and typically involve aldol condensation of benzaldehyde onto thioindoxyls. However, the key step is the formation (and where necessary, isolation) of the thioindoxyl species. In our studies, the electron-rich dimethoxy- and trimethoxy-substituted thioindoxyls were noted to be unstable to air, base, and silica gel during chromatography, so it was sought to minimise their exposure to these conditions during synthesis. In the end, we used two routes to the thioindoxyls: either Friedel–Crafts acylation of  $\alpha$ -phenylthioacetic acids (which are easily accessible from thiophenols by alkylation using 2-chloroacetic acid, Figure 1b) or else, lithium diisopropylamide (LDA)-mediated cyclisation of 2-(methylthio)benzamides, which were obtained by directed *ortho*-metalation of the respective benzamides followed by quenching with dimethyl disulfide [27] (Supporting Information File 1, Scheme S1). In general, we found the LDA-mediated cyclisation more convenient, as it generated fewer side products and enabled faster, easier workup and purification. We used these routes to synthesise the **HITubs** typically in good (32% for **HITub-4**, Figure 1b) to excellent (93% for **HITub-7**, Scheme S5) overall yields from commercial building blocks (see Supporting Information File 1).



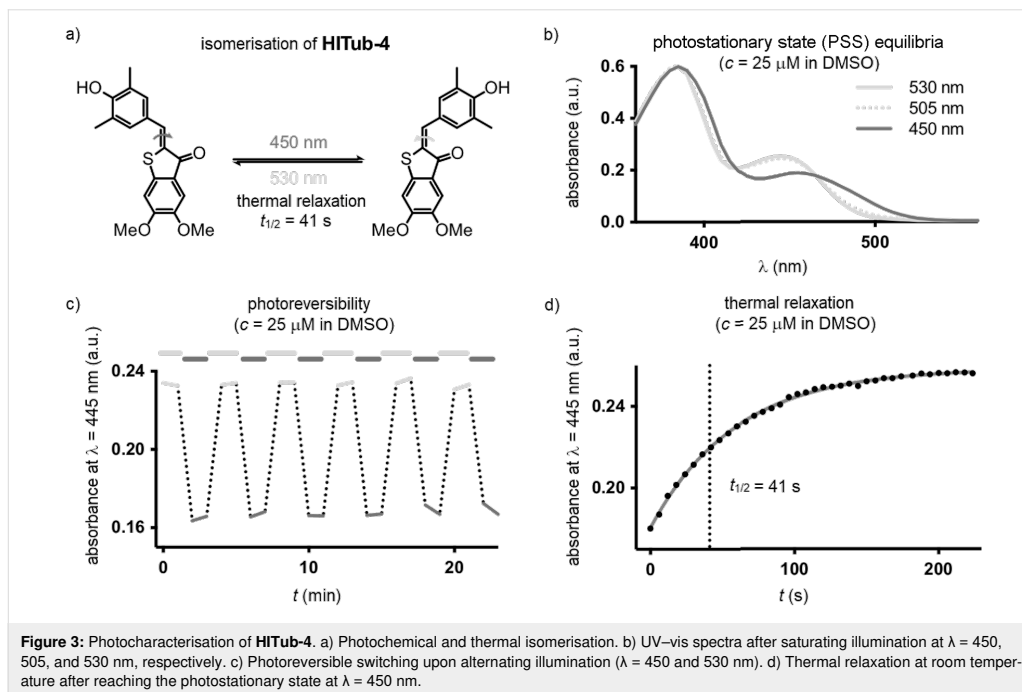


## Photocharacterisation

Although some *para*-hydroxy-substituted HTIs have been described [28,29], we are unaware of any report of the solvent- and pH-dependency of their photochromism and thermal relaxation. Dube and co-workers have reported that in general, increasing the electron-donating strength of groups in the hemistilbene *para*-position of HTIs correlates to (a) a bathochromic shift of the  $S_0 \rightarrow S_1$  absorption band (up to  $\lambda_{\max} \approx 500$  nm with julolidine substitution) and (b) decreased thermal stability of the metastable *E*-isomer, i.e., faster thermal relaxation [30]. However, they also reported that introducing electron-donating groups (methoxy, dimethylamino) in *para*-position to the thioindoxyl sulfur atom restored *E*-stability while maintaining red-shifted absorption maxima. This *para*-position was occupied by the key methoxy group in all our **HITub** designs. With scant information available, we could not predict the thermal stability of (*E*)-**HITubs** in cellular conditions, so we turned to experimental measurement.

Since we found no substantial differences between the photochemical properties of the *para*-hydroxylated compounds (Figure 3 and Supporting Information File 1, Figure S1), we here describe the photocharacterisation of **HITub-4** as a representative example of the photoswitchable bioactive compounds

(for more detailed analysis see Supporting Information File 1). In polar aprotic solvents, the **HITub-4** *Z*-isomer ( $\lambda_{\max} \approx 380$ , 460 nm) showed robust, reliable, and fully reversible photoswitching ( $\lambda = 450$  nm for *Z*  $\rightarrow$  *E* and 530 nm for *E*  $\rightarrow$  *Z* switching), with the high fatigue resistance characteristic of HTIs. The *E*-isomer's thermal half-life in EtOAc or DMSO was ca. 40 s (Figure 3 and Supporting Information File 1, Figure S3). Its absorption spectra and photoswitchability were unaltered by the addition of acid, however, addition of base led to a remarkable bathochromic and hyperchromic shifts of the absorption band at ca. 550 nm, and no observed photoswitchability (Supporting Information File 1, Figure S2). We assumed that this spectrum resulted from a quinoidal structure, formed after deprotonation of the hydroxy group, and that the lack of observable photoswitchability arose due to fast free rotation around the C–C single bond connecting the thioindigo and hemistilbene motifs. Interestingly, in neutral or acidic aqueous media where the quinoidal structure is not present ( $\lambda_{\max}$  ca. 370, 480 nm), photoswitching could not be observed either, which we presumed to be due to fast thermal relaxation. However, noting that typical CDIs are substantially biolocalised into lipid environments within cells [31], we decided to explore photoswitching-based cellular assays with these compounds nonetheless (further discussion in Supporting Information File 1).



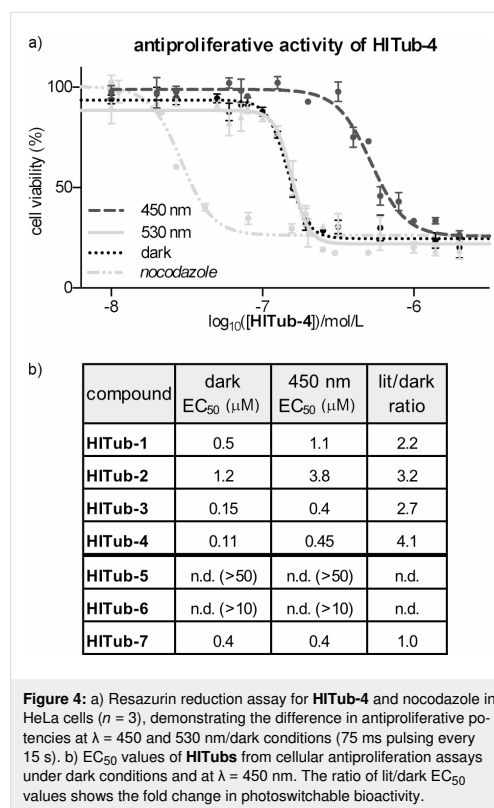
We found that the photochemical properties of the non-*para*-hydroxylated control **HITub-6** were similar to those of previously reported non-*para*-hydroxylated **HOTubs** [18], with satisfactory photoswitching in both DMSO and phosphate-buffered saline (PBS)/DMSO mixtures (Figure S1f,g in Supporting Information File 1).

### Bioactivity: SAR study of **HITubs** in cellulo

To begin evaluating the isomer-dependent bioactivity of **HITub** photopharmaceuticals in cellulo, we first performed resazurin (resorufin *N*-oxide) antiproliferation assays under different lighting conditions (Figure 4). Inhibitors of tubulin polymerisation act as antimitotic cytotoxins in cell culture by preventing formation of a functional mitotic spindle, resulting in mitotic arrest and eventually cell death. The reduction of resazurin by viable cells serves as a fluorogenic proxy readout for antimitotic potency in cellulo, since the degree of resazurin turnover scales to the number of cells still viable after compound treatment, although the mechanism behind antiproliferative activity must later be determined using more specific assays. We used the HeLa human cervical cancer cell line to assess the biological activity of **HITubs** in all cellular experiments shown in this work. Since tubulin is a highly conserved protein target critical for survival in all cell types, we expected that, as for other colchicine domain tubulin inhibitors, trends in potency and in photoswitchability of potency determined in this representative mammalian cell line can be translated to other cell types, although their specific response (e.g., EC<sub>50</sub> values) would need individual determination. Nocodazole was used as a benchmarking reference and mechanistic positive control in all in cellulo assays since it is a potent inhibitor of the colchicine binding site (EC<sub>50</sub> ≈ 40 nM) with both appropriate solubility and straightforward handling.

Self-made low-intensity LED arrays with relatively narrow bandwidth were used for illumination of cells during assays, with a pulsing regime of 75 ms every 15 s to maintain photostationary state equilibria in cellulo [10]. We cross-checked different illumination wavelengths in cellular toxicity assays; in accordance with the DMSO photoswitching studies, we observed that 530 nm (ca. 97% *Z*-configuration, but additionally controls for non-specific phototoxicity) delivered results equivalent to dark conditions (exclusively *Z*-configuration), to which 450 nm (lit conditions, ca. 70% *E*-configuration) gave the greatest difference in antiproliferative potencies.

We began our studies with **HITub-1**. This is a HTI analogue of indanocine in which the indanocine amino function (in *ortho*-position to the key south ring methoxy group) has been replaced by a synthetically more accessible hydroxy group (delivered via demethylation of a trimethoxy precursor through BB<sub>R</sub><sub>3</sub>). The



hydroxy and amino groups have similar size and polarity, and can both act as H-bond donors or acceptors. Therefore, we expected **HITub-1** to allow reliable evaluation of the indanocine substituent pattern. (*Z*)-**HITub-1** was already strongly bioactive (EC<sub>50</sub> ≈ 500 nM, Figure 4b), although one order of magnitude less so than indanocine (EC<sub>50</sub> ≈ 10–40 nM, depending on the cell line). Pleasingly, although we had not observed its photoswitching in pure aqueous media, in the heterogeneous cellular environment, we found that its overall toxicity under lit conditions was reliably and reproducibly halved.

We then explored changes to the substituent pattern to determine whether we could improve both *Z*-isomer potency in an absolute sense and the overall photoswitchability of potency comparing *E*- and *Z*-isomers. We began by methylating the south ring hydroxy group (**HITub-2**) to see how changes in size and polarity affect the bioactivity; surprisingly, the potency loss was not dramatic (indicating that this position is not a key determinant of bioactivity), but the photoswitchability increased substantially (3-fold with regard to the lit/dark ratio). We took this as an encouraging indicator of the overall polarity

required for binding, and now examined re-orienting the south ring substituents by shifting the trimethoxy pattern on the ring (**HITub-3**), which improved the potency dramatically ( $EC_{50} \approx 150$  nM for the *Z*-isomer) while retaining the 3-fold photoswitchability of bioactivity.

Since comparison of **HITub-2** and **HITub-3** showed that the potency can be retained without substituents in *ortho*-position to either the carbonyl group or the sulfur atom, for maximal simplicity, we tested whether both substituents could be deleted simultaneously (**HITub-4**). This proved to be the strongest-performing compound of our studies, with the *Z*-isomer possessing an  $EC_{50}$  value of ca. 110 nM and a 4-fold difference of bioactivity between lit and dark conditions ( $\lambda = 450$  nm). This difference was surprisingly high, given that even in aprotic media (e.g., lipid environment reservoirs within cells), there should be ca. 30% residual *Z*-isomer at photoequilibrium [18], and we had expected that any (*E*)-**HITub** entering the cytosol (aqueous environment) would quickly relax to its more bioactive *Z*-isomer before encountering its cytosolic protein target. We theorised that fast cytosolic relaxation of the *para*-hydroxy **HITubs** to their bioactive *Z*-isomer may actually be a decisive factor in preventing the simple equilibration of the extracellular **HITub** concentration (exclusively *Z*-configuration due to fast relaxation, irrespective of illumination conditions) with the cytosolic (*Z*)-**HITub** concentration available to bind to tubulin (and which all experiments show is reduced under  $\lambda = 450$  nm illumination). Examining this in detail is beyond the scope of this study, however, see Supporting Information File 1 for a discussion on isomer-dependent subcellular biolocalisation effects.

We first controlled against our design logic of north ring substituent shortening by changing the north ring apolar-contact methyl groups to methoxy groups (**HITub-5**), and were satisfied when this abolished bioactivity. We also controlled for the result, known from extensive SAR work at the colchicine site [18,32], that CDIs should not tolerate a non-polar central north ring substituent (**HITub-6**) but can support removal of this substituent altogether, with only small potency loss (**HITub-7**). We considered that if the screened compounds obeyed this principle, it would reinforce our mechanistic understanding of them as CDIs. Indeed, **HITub-6** proved inactive until it reached its solubility limit, but (*Z*)-**HITub-7** was relatively potent and featured an only 4-fold reduction of bioactivity as compared to its hydroxylated parent (*Z*)-**HITub-4**. Interestingly, however, **HITub-7** displayed no difference between dark (all-*Z*) and lit (mostly *E*) conditions, and we were unable to rationalise this with reference to either polarity or structure, in light of our prior work on apolar **HOTubs** [18] (see also Supporting Information File 1). We were, however, overall satisfied by these findings

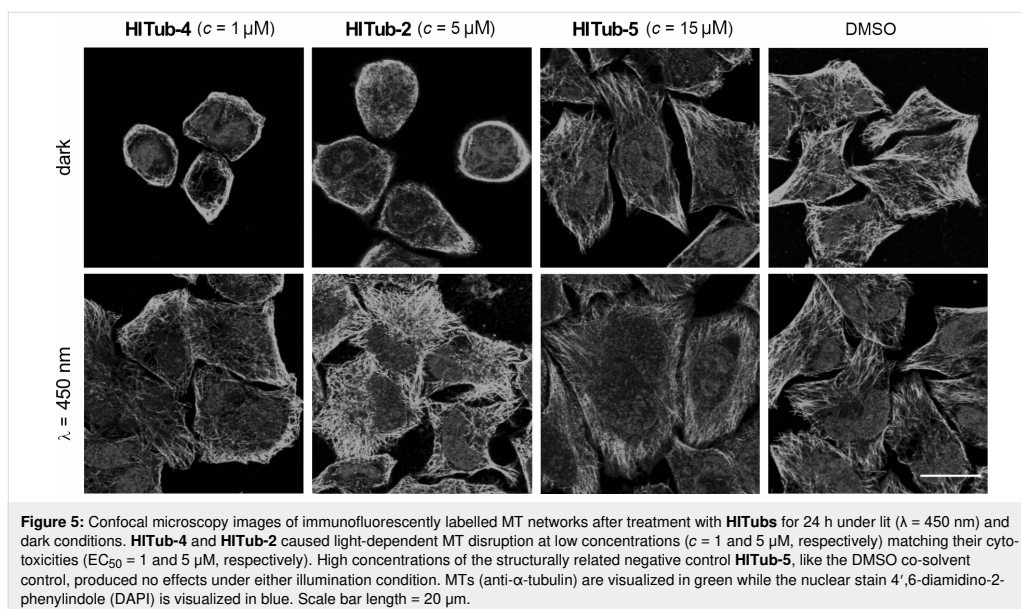
(Supporting Information File 1, Figure S4), especially by the potency and photoswitchability of **HITub-4**.

These results indicated that indanocine-inspired HTI-based reagents are a potent, cellularly bioactive class of photoswitchably antiproliferative agents, with the most potent light-controlled antimetabolic bioactivity reported for photoswitches designed for tubulin: 10-fold enhancement compared to the predecessor HTI generation **HOTubs** [18] and styrylbenzothiazole-based **SBTubs** [17], and 5-fold superior to azocombretastatins [10–12]. In view of the generally limited solubility of photopharmaceuticals (associated with their extended flat aromatic structures), this increase in potency renders the **HITub** compound class a promising addition to the toolbox of photoswitchable antimetotics, which might prove valuable for future *in vivo* studies.

We also noted that the *para*-hydroxy **HITubs** featured ca. 30% residual (*Z*)-**HITub** at PSS  $\lambda = 450$  nm in cell-free measurements, and that for **HITub-2-4**, the PSS isomer mixture's cellular cytotoxicity at that wavelength was on average 3.3-fold lower than the cytotoxicity of the corresponding (*Z*)-**HITub** (Figure 4). This can be interpreted as indicative that the *E*-isomers are essentially biologically inactive, similar to what has been observed for heterostilbene **SBTubs** [17] and azobenzene photostatsins (**PSTs**) [10]. If substantiated, HTI-like analogues for which photostationary state (PSS) with enhanced proportions of *E*-isomer can be photogenerated would represent an exciting advance: they could, in contrast to the other photoswitch types, allow all-visible, photoreversible, high-potency switching while reproducing similarly beneficial photoswitchability of bioactivity.

### Mechanistic assessment of **HITub** action

We now determined to confirm the mechanism of action of the **HITub** compounds. To evaluate the biological mechanism of action behind the **HITubs'** photoswitchable antimetabolic activity, we first checked their inhibition of polymerisation of purified tubulin in a cell-free assay. The results showed almost identical inhibition potency for **HITub-4** at  $c = 10$   $\mu$ M as for the archetypal CDI colchicine at  $c = 20$   $\mu$ M (Figure S5, Supporting Information File 1), which we took to indicate that (*Z*)-**HITub-4** exerted its bioactivity by specifically binding to tubulin directly in the cell-free system. This suggests that the same specific direct action can be reproduced in cellulo, and that effects on auxiliary cellular systems dependent upon the MT cytoskeleton can likely be downstream effects of MT depolymerisation. We next investigated the **HITubs'** isomer-dependent effects on the MT network inside cells, focusing on the active analogues **HITub-4** and **HITub-2** in comparison with inactive **HITub-5** as a control (Figure 5). By reducing tubulin polymerisation dy-



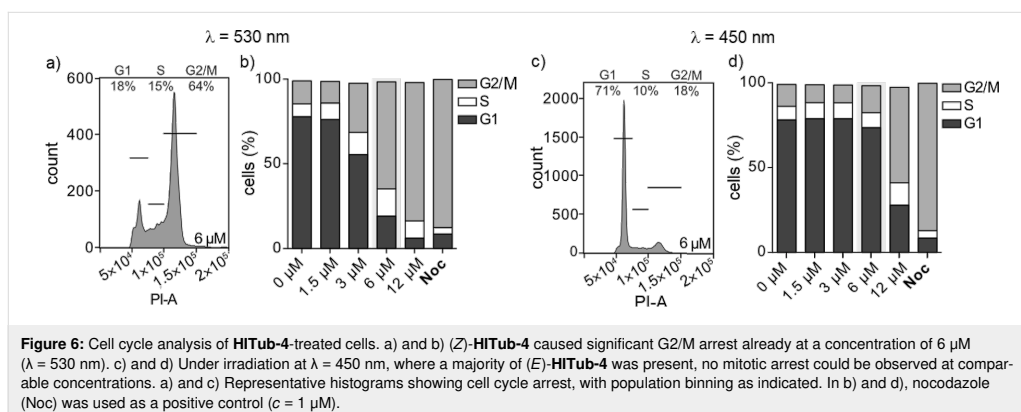
namics, CDI treatment should first disorganise and then depolymerise the cellular MT network. We performed immunofluorescence staining of the MT network within cells treated with **HITubs** and documented the resulting disruption of the physiological MT network integrity, and consequently also changes in cell morphology by confocal microscopy. Cells exposed to **HITub-4** ( $1$   $\mu\text{M}$ ) in the dark or under  $\lambda = 530$  nm illumination (to maintain exclusively Z-configuration) show near-complete disruption of MT structures after 24 h, while treatment with  $\lambda = 450$  nm illumination caused no significant disruption of the MT network compared to an untreated dark control (Figure 5). Less potent **HITub-2** also showed similar light dependency of its biological effects at higher concentrations (Supporting Information File 1, Figure S6). Pleasingly, SAR control **HITub-5** showed no impact on MT integrity at the highest tested concentration under lit or dark conditions, which we took as a promising indication for the absence of phototoxicity or of other effects non-specific to tubulin disruption.

Lastly, to substantiate the causative link between the observations on MT disruption and cellular toxicity, we examined the impacts of **HITub-4** on the cell cycle. Tubulin-binding agents whose major cellular mechanism of toxic action is the disruption of MT dynamics or structure should cause cell cycle arrest in the G2/M phase by preventing the completion of mitosis [1]. We examined cell cycle repartition by quantification of cellular DNA content via propidium iodide (PI) incorporation, which was analysed by flow cytometry (Supporting Information

File 1, Figure S7). HeLa cells were treated for 24 h with **HITub-4** under  $\lambda = 530$  and  $450$  nm irradiation, respectively, with the synthetic tubulin-binding agent nocodazole (Noc) used as a reference. As expected, **HITub-4** showed highly light-dependent bioactivity with near-complete G2/M phase arrest at a concentration of  $6$   $\mu\text{M}$  and  $\lambda = 530$  nm irradiation (Figure 6a and Figure 6b), but nearly no cell cycle interference at the same concentration and  $\lambda = 450$  nm irradiation (Figure 6c and Figure 6d).

## Conclusion

Taken together, these results indicate that the **HITubs** had achieved their design aims, being a rationally-designed, potency-enhanced set of HTI-based tubulin-inhibiting photopharmaceuticals with photoswitchable bioactivity across cell biology assays, allowing reliable photocontrol over tubulin polymerisation, MT network structure, cell cycle, and cell survival. They feature mid-nanomolar potency in cellulo, the highest yet reported for photopharmaceutical tubulin inhibitors, as well as satisfactory photoswitchability of potency. We expect that due to the **HITubs**' potency of tubulin inhibition, they will prove a powerful reagent system for biological studies on MT, especially where dark-isomer activity (compared to the currently known, lit-active azobenzenes or styrylbenzothiazoles) is desirable, in particular for cell-free mechanistic studies [33]. More broadly, this work also shows that the HTI scaffold robustly enables the photoswitchable use of resonance-capable substituents that can establish high-affinity interactions (such as *para*-



hydroxy groups), which are otherwise problematic for current photopharmaceutical scaffolds to tolerate without loss of photoswitchability. In the broader sense, this is of interest for cell biology and further highlights the potential of HTIs as a pharmacophore scaffold for expanding the scope of cellular photopharmacology.

## Supporting Information

### Supporting Information File 1

Full experimental protocols for chemical syntheses, photocharacterisation, biochemistry, and cell biology, including NMR spectra.

[<https://www.beilstein-journals.org/bjoc/content/supplementary/1860-5397-16-14-S1.pdf>]

## Acknowledgements

This research was supported by funds from the German Research Foundation (DFG: SFB1032 *Nanoagents for Spatiotemporal Control* project B09, SFB TRR 152 project P24 number 239283807, and an Emmy Noether grant) and the Munich Centre for Nanoscience (CeNS) to O.T.-S. A.S. particularly thanks Linda Pettersson for her great assistance during photocharacterisation.

## ORCID® iDs

Alexander Sailer - <https://orcid.org/0000-0003-4140-9956>

Rebekkah Bingham - <https://orcid.org/0000-0001-5740-0353>

Julia Ahlfeld - <https://orcid.org/0000-0002-4879-4159>

Oliver Thorn-Seshold - <https://orcid.org/0000-0003-3981-651X>

## Preprint

A non-peer-reviewed version of this article has been previously published as a preprint doi:[10.26434/chemrxiv.9176747](https://doi.org/10.26434/chemrxiv.9176747)

## References

- Peterson, J. R.; Mitchison, T. J. *Chem. Biol.* **2002**, *9*, 1275–1285. doi:10.1016/s1074-5521(02)00284-3
- Guedes-Dias, P.; Nirschl, J. J.; Abreu, N.; Tokito, M. K.; Janke, C.; Magiera, M. M.; Holzbaur, E. L. F. *Curr. Biol.* **2019**, *29*, 268–282.e8. doi:10.1016/j.cub.2018.11.065
- Armstrong, M. T.; Armstrong, P. B. *Exp. Cell Res.* **1979**, *120*, 359–364. doi:10.1016/0014-4827(79)90395-1
- Kelliher, M. T.; Saunders, H. A.; Wildonger, J. *Curr. Opin. Neurobiol.* **2019**, *57*, 39–45. doi:10.1016/j.conb.2019.01.003
- Banghart, M.; Borges, K.; Isacoff, E.; Trauner, D.; Kramer, R. H. *Nat. Neurosci.* **2004**, *7*, 1381–1386. doi:10.1038/nn1356
- Caporale, N.; Kolstad, K. D.; Lee, T.; Tochitsky, I.; Dalkara, D.; Trauner, D.; Kramer, R.; Dan, Y.; Isacoff, E. Y.; Flannery, J. G. *Mol. Ther.* **2011**, *19*, 1212–1219. doi:10.1038/mt.2011.103
- Riefolo, F.; Matera, C.; Garrido-Charles, A.; Gomila, A. M. J.; Sortino, R.; Agnetta, L.; Claro, E.; Masgrau, R.; Holzgrabe, U.; Battie, M.; Decker, M.; Guasch, E.; Gorostiza, P. *J. Am. Chem. Soc.* **2019**, *141*, 7628–7636. doi:10.1021/jacs.9b03505
- Agnetta, L.; Kauk, M.; Canizal, M. C. A.; Messerer, R.; Holzgrabe, U.; Hoffmann, C.; Decker, M. *Angew. Chem., Int. Ed.* **2017**, *56*, 7282–7287. doi:10.1002/anie.201701524
- Velema, W. A.; van der Berg, J. P.; Hansen, M. J.; Szymanski, W.; Driessen, A. J. M.; Feringa, B. L. *Nat. Chem.* **2013**, *5*, 924–928. doi:10.1038/nchem.1750
- Borowiak, M.; Nahaboo, W.; Reynders, M.; Nekolla, K.; Jalinet, P.; Hasserodt, J.; Rehberg, M.; Delattre, M.; Zahler, S.; Vollmar, A.; Trauner, D.; Thorn-Seshold, O. *Cell* **2015**, *162*, 403–411. doi:10.1016/j.cell.2015.06.049
- Engdahl, A. J.; Torres, E. A.; Lock, S. E.; Engdahl, T. B.; Mertz, P. S.; Streu, C. N. *Org. Lett.* **2015**, *17*, 4546–4549. doi:10.1021/acs.orglett.5b02262
- Sheldon, J. E.; Dcona, M. M.; Lyons, C. E.; Hackett, J. C.; Hartman, M. C. T. *Org. Biomol. Chem.* **2016**, *14*, 40–49. doi:10.1039/c5ob02005k
- Müller-Deku, A.; Loy, K.; Kraus, Y.; Heise, C.; Bingham, R.; Ahlfeld, J.; Trauner, D.; Thorn-Seshold, O. *bioRxiv* **2019**, No. 778993. doi:10.1101/778993
- Eguchi, K.; Taoufiq, Z.; Thorn-Seshold, O.; Trauner, D.; Hasegawa, M.; Takahashi, T. *J. Neurosci.* **2017**, *37*, 6043–6052. doi:10.1523/jneurosci.0179-17.2017

15. Zenker, J.; White, M. D.; Templin, R. M.; Parton, R. G.; Thorn-Seshold, O.; Bissiere, S.; Plachta, N. *Science* **2017**, *357*, 925–928. doi:10.1126/science.aam9335
16. Singh, A.; Saha, T.; Begemann, I.; Ricker, A.; Nüsse, H.; Thorn-Seshold, O.; Klingauf, J.; Galic, M.; Matis, M. *Nat. Cell Biol.* **2018**, *20*, 1126–1133. doi:10.1038/s41556-018-0193-1
17. Gao, L.; Kraus, Y.; Wranik, M.; Weinert, T.; Pritzl, S. D.; Meiring, J. C. M.; Bingham, R.; Olieric, N.; Akhmanova, A.; Lohmüller, T.; Steinmetz, M. O.; Thorn-Seshold, O. *bioRxiv* **2019**, No. 716233. doi:10.1101/716233
18. Sailer, A.; Ermer, F.; Kraus, Y.; Lutter, F. H.; Donau, C.; Bremerich, M.; Ahlfeld, J.; Thorn-Seshold, O. *ChemBioChem* **2019**, *20*, 1305–1314. doi:10.1002/cbic.201800752
19. Hüll, K.; Morstein, J.; Trauner, D. *Chem. Rev.* **2018**, *118*, 10710–10747. doi:10.1021/acs.chemrev.8b00037
20. Tron, G. C.; Pirali, T.; Sorba, G.; Pagliai, F.; Busacca, S.; Genazzani, A. A. *J. Med. Chem.* **2006**, *49*, 3033–3044. doi:10.1021/jm0512903
21. Lawrence, N. J.; Rennison, D.; McGown, A. T.; Hadfield, J. A. *Bioorg. Med. Chem. Lett.* **2003**, *13*, 3759–3763. doi:10.1016/j.bmcl.2003.07.003
22. Leoni, L. M.; Hamel, E.; Genini, D.; Shih, H.; Carrera, C. J.; Cottam, H. B.; Carson, D. A. *J. Natl. Cancer Inst.* **2000**, *92*, 217–224. doi:10.1093/jnci/92.3.217
23. Dose Response Curves for NSC 757. National Cancer Institute - Developmental Therapeutics Program: Rockville, MD, <https://dtp.cancer.gov/services/nci60data/coloradoseresponse/pdf/757> (accessed Nov 6, 2019).
24. Garcia-Amorós, J.; Sánchez-Ferrer, A.; Massad, W. A.; Nonell, S.; Velasco, D. *Phys. Chem. Chem. Phys.* **2010**, *12*, 13238–13242. doi:10.1039/c004340k
25. Dunn, N. J.; Humphries, W. H., IV; Offenbacher, A. R.; King, T. L.; Gray, J. A. *J. Phys. Chem. A* **2009**, *113*, 13144–13151. doi:10.1021/jp903102u
26. Wiedbrauk, S.; Dube, H. *Tetrahedron Lett.* **2015**, *56*, 4266–4274. doi:10.1016/j.tetlet.2015.05.022
27. Mukherjee, C.; De, A. *Synlett* **2002**, 325–327. doi:10.1055/s-2002-19752
28. Takeo, Y.; Takahiro, S.; Takashi, T.; Kunihiro, I. *Bull. Chem. Soc. Jpn.* **1992**, *65*, 649–656. doi:10.1246/bcsj.65.649
29. Eggers, K.; Fyles, T. M.; Montoya-Pelaez, P. J. *J. Org. Chem.* **2001**, *66*, 2966–2977. doi:10.1021/jo0056848
30. Kink, F.; Collado, M. P.; Wiedbrauk, S.; Mayer, P.; Dube, H. *Chem. – Eur. J.* **2017**, *23*, 6237–6243. doi:10.1002/chem.201700826
31. Bisby, R. H.; Botchway, S. W.; Hadfield, J. A.; McGown, A. T.; Parker, A. W.; Scherer, K. M. *Eur. J. Cancer* **2012**, *48*, 1896–1903. doi:10.1016/j.ejca.2011.11.025
32. Nguyen, T. L.; McGrath, C.; Hermone, A. R.; Burnett, J. C.; Zaharevitz, D. W.; Day, B. W.; Wipf, P.; Hamel, E.; Gussio, R. *J. Med. Chem.* **2005**, *48*, 6107–6116. doi:10.1021/jm050502t
33. Gaspari, R.; Prota, A. E.; Bargsten, K.; Cavalli, A.; Steinmetz, M. O. *Chem* **2017**, *2*, 102–113. doi:10.1016/j.chempr.2016.12.005

## License and Terms

This is an Open Access article under the terms of the Creative Commons Attribution License (<https://creativecommons.org/licenses/by/4.0>). Please note that the reuse, redistribution and reproduction in particular requires that the authors and source are credited.

The license is subject to the *Beilstein Journal of Organic Chemistry* terms and conditions: (<https://www.beilstein-journals.org/bjoc>)

The definitive version of this article is the electronic one which can be found at:  
doi:10.3762/bjoc.16.14

## 5 Photopharmaceutical microtubule stabilisers

This work is situated in the context of spatiotemporally controllable microtubule stabilisers.

### Background to microtubule stabilisers

Microtubule stabilisers, most famously paclitaxel (Fig. 10a) and docetaxel (Fig. 10b), are biologically different than microtubule destabilisers and besides their extensive use as cancer treatment, they can be used for unique purposes in research settings. For example, it has been shown that low concentrations of microtubule stabilisers can create aneuploidy through the formation of multipolar spindles leading to a different kind of mitotic block when compared to microtubule destabilising agents.<sup>120</sup> There is no need of exogenous GTP, organic buffers or microtubule-binding proteins for microtubule polymerisation in the presence of paclitaxel, and microtubules are both stabilised *in vitro* and in cells.<sup>121</sup> Microtubule stabilisers have been used to uncover the role of microtubule polymerisation in axon formation during development<sup>122</sup> and for recovery after spinal cord injury.<sup>123</sup>

This makes microtubule stabilisers a unique class of microtubule modulating agents that have a huge potential, besides their current use in therapeutic settings, which is of immense interest to enlighten processes such as the formation of neural networks including potentially reversing the effects of neuronal injuries. Another aspect would be the role of microtubules in cell division during the development of zebrafish embryos, which has proven to be quite differently organised than in adult organisms.<sup>115</sup> This has been partially uncovered by the use of photoswitchable microtubule depolymerisers (Photostatins as described before). Photoswitchable stabilisers that have not been available before, will be able to prevent microtubule depolymerising with spatiotemporal control and, therefore, will give new insights into processes that are dependent on microtubule depolymerisation at a certain time.

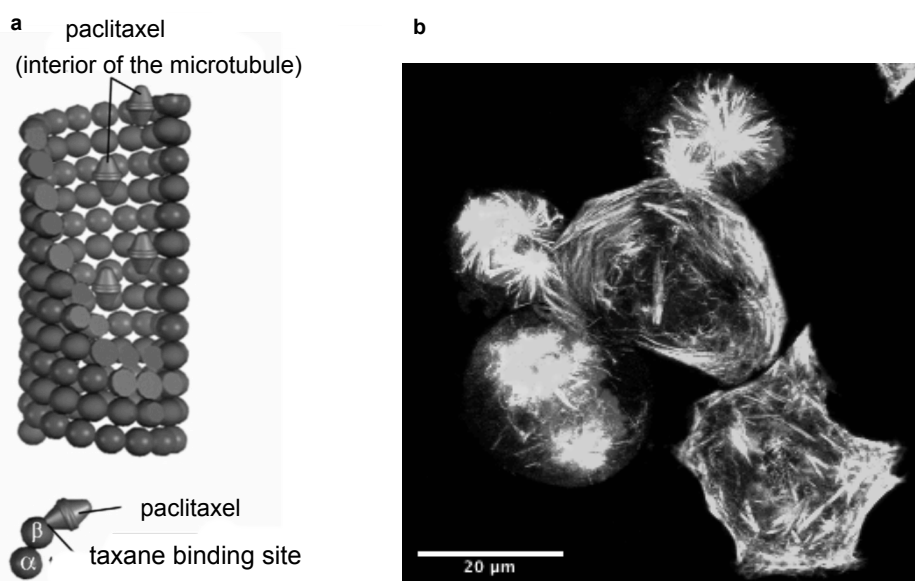


**Figure 10:** a: Schematic of microtubule stabilisation with paclitaxel (adapted from Dcona, 2012<sup>124</sup>) b: Z-Maximum projection of HeLa cells treated with 1  $\mu$ M docetaxel for 24 hours and then stained for tubulin (green) and DNA (blue) (Y. Kraus, unpublished data)

## **Photopharmaceutical Performance: motivation for this work**

Similar to conventional microtubule destabilisers, the known microtubule stabilisers cannot be applied to the microtubule cytoskeleton with spatiotemporal precision, although microtubule stabilisers are commonly used for cancer treatment. Their low water solubility and lack of target specificity have been challenging and many attempts have been made to enhance performance and spatiotemporal control of paclitaxel. One approach was the development of photocaged compounds.<sup>125</sup> Photocaged compounds have masked activity until they are activated by light, which irreversibly frees the linked targeting agent. Taxol is one microtubule stabiliser that has been modified into a “photo-uncageable drug”.<sup>126</sup>

Unfortunately, photocaged taxols have severe disadvantages:

- (1) designing prodrugs with better water solubility and similar potency has been shown to be challenging<sup>127</sup>,
- (2) the need for prolonged intense illumination with mid-UV light can cause phototoxicity<sup>128</sup>,
- (3) the uncaging process requires hydrolysis and is rather slow, which partially revokes temporal control of compound release<sup>127</sup>,
- (4) caging strategies often enlarge molecular weight, which can limit biodistribution and bioavailability<sup>128</sup> and
- (5) finally, the released photocage byproducts can cause severe damage in the organism.<sup>129</sup>

Photoswitching would be an attractive alternative since rational design can be applied to enhance water solubility, the activation can be reversible, there is no need for enhancing molecular weight that can restrict bioavailability, metabolically stable photoswitches would not produce toxic by-products and, depending on the photoswitch, the illumination protocol can be less aggressive. While there are recent successes with photoswitchable microtubule destabilisers, photoswitchable microtubule stabilisers are so far lacking.

Our goal was to develop a photoswitchable microtubule stabiliser that is easily accessible by simple synthetic routes, that shows a significant difference in bioactivity between the two isomers, that has the desired microtubule-stabilising activity, and that is most preferable in the nano- to micromolar concentration range while the other isomer is not active/toxic. The optimal relaxation half-life would lie in the hundreds of microseconds till second range to address short-term assays and be able to undergo several cycles of fully reversible photoactivation/photodeactivation that would allow repeated photoswitching in cells.

## **Short summary of the AzTax work**

We created photoswitchable paclitaxel analogues by growing an azobenzene photoswitch out from the taxane core structure, then we evaluated the photoswitchable performance of our compounds in various cell-biological assays. We showed a light-dependent antiproliferative effect in cell viability assays as well as inhibition of tubulin polymerisation in cell-free assays, which confirms that our drug is water-soluble and shows a significant difference in bioactivity upon treatment with light. We confirmed an expected G2/M arrest due to the microtubule stabilising effect and inhibition of cell division in cell cycle partition experiments. We visualized the effect of our compounds towards microtubule structure in immunofluorescence imaging of the microtubule cytoskeleton and showed precisely the reversible spatiotemporal control of









microtubule dynamics in HeLa cells, transfected with EB3-tdTomato as well as manipulation of microtubule polymerisation dynamics subcellularly in rat primary hippocampal neurons.

Therefore, we created the first tubulin hyperpolymerising agent that can be activated by light with cellular precision, that shows similar biological effects as taxane and that gives spatiotemporal control over the microtubule network down to the subcellular level. We recognize that the completeness in  $E \rightarrow Z$  photoswitchability does not transfer to photoswitchability of bioactivity, the difference fold in potency between the isomers is narrow and we do not report reversible photoswitching of bioactivity in cells by light, which will be discussed later.

#### Authorial Contribution

My part of this study was analysis effects of our compounds towards the microtubule network in long term treatment by immunofluorescence and confocal imaging (Fig. 3a) and performance of initial live-cell imaging (unpublished data). My results show light-dependent disruption of the microtubule network as well as cells in mitotic arrest harbouring multiple spindles and early apoptotic cells, which is a hallmark for treatment with microtubule stabilisers and shows isomer-specific cytotoxicity of our lead compound AzTax3MP.

# Photoswitchable paclitaxel-based microtubule stabilisers allow optical control over the microtubule cytoskeleton

Adrian Müller-Deku <sup>1</sup>, Joyce C. M. Meiring <sup>2</sup>, Kristina Loy<sup>1</sup>, Yvonne Kraus<sup>1</sup>, Constanze Heise<sup>1</sup>, Rebekkah Bingham<sup>1</sup>, Klara I. Jansen<sup>2</sup>, Xiaoyi Qu<sup>3</sup>, Francesca Bartolini<sup>3</sup>, Lukas C. Kapitein<sup>2</sup>, Anna Akhmanova <sup>2</sup>, Julia Ahlfeld <sup>1</sup>, Dirk Trauner <sup>4,5</sup> & Oliver Thorn-Seshold <sup>1,5</sup>✉

Small molecule inhibitors are prime reagents for studies in microtubule cytoskeleton research, being applicable across a range of biological models and not requiring genetic engineering. However, traditional chemical inhibitors cannot be experimentally applied with spatiotemporal precision suiting the length and time scales inherent to microtubule-dependent cellular processes. We have synthesised photoswitchable paclitaxel-based microtubule stabilisers, whose binding is induced by photoisomerisation to their metastable state. Photoisomerising these reagents in living cells allows optical control over microtubule network integrity and dynamics, cell division and survival, with biological response on the timescale of seconds and spatial precision to the level of individual cells within a population. In primary neurons, they enable regulation of microtubule dynamics resolved to subcellular regions within individual neurites. These azobenzene-based microtubule stabilisers thus enable non-invasive, spatiotemporally precise modulation of the microtubule cytoskeleton in living cells, and promise new possibilities for studying intracellular transport, cell motility, and neuronal physiology.

<sup>1</sup>Department of Pharmacy, Ludwig-Maximilians University, Butenandtstrasse 5-13, Munich 81377, Germany. <sup>2</sup>Cell Biology, Neurobiology and Biophysics, Department of Biology, Faculty of Science, Utrecht University, Padualaan 8, 3584 Utrecht, The Netherlands. <sup>3</sup>Department of Pathology & Cell Biology, Columbia University Medical Center, New York, NY 10032, USA. <sup>4</sup>Department of Chemistry, New York University, 100 Washington Square East, New York, NY 10003, USA. <sup>5</sup>These authors jointly supervised this work: Dirk Trauner, Oliver Thorn-Seshold. ✉email: [oliver.thorn-seshold@cup.lmu.de](mailto:oliver.thorn-seshold@cup.lmu.de)

The cytoskeleton serves as the scaffold for critical biological processes ranging from signalling and cargo trafficking, to cell shape maintenance and cell division. Most of the cytoskeleton's myriad of biological roles are inherently spatially and temporally differentiated, although they all rely on the same protein scaffold structures. Studying these cytoskeleton-dependent processes with the spatiotemporal resolution necessary to understand and exploit these individual biological functions is an important challenge. Accordingly, in recent years, a number of approaches towards photocontrol over cytoskeletal or cytoskeleton-associated proteins have been made, aiming to allow their spatiotemporally precise optical manipulation<sup>1–3</sup>. Nevertheless, much remains to be done before generally applicable tool systems can be developed.

We here focus on the microtubule (MT) cytoskeleton. MTs play particularly important roles in intracellular transport, cell motility and morphological plasticity, and there is a conspicuous need to achieve a better understanding of how these many functions are implemented and regulated<sup>4,5</sup>. The role of MT dynamics during cell proliferation has also made them a major anticancer target, for which several outstanding drugs (taxanes, epothilones and vinca alkaloids) have been developed<sup>6–8</sup>. These drugs and other small molecule modulators (e.g., nocodazole, combretastatin and peloruside) remain the most general tools for MT cytoskeleton research. However, these inhibitors simultaneously suppress all MT-dependent functions spatially indiscriminately. Therefore, they do not allow spatiotemporally precise MT inhibition on the length or time scales appropriate for selectively studying MT-dependent processes. This restricts their scope of applications and their utility for selective research into MT cytoskeleton biology<sup>9</sup>.

Deeper insights could be gained from inhibitors that allow spatiotemporally specific MT manipulation. In this regard, optogenetic approaches to MT regulation have advanced greatly in recent years. In one example, a photo-inactivatable variant of the MT plus tip adaptor protein EB1 was engineered, which upon illumination lost its ability to bind other plus-end-tracking proteins, thus optically inhibiting MT growth and allowing spatiotemporally resolved modulation of directional cell migration<sup>10</sup>. Another domain of research has focused on optogenetic switches tethered to kinesins and compartment identity markers, to manipulate the transport of vesicles and organelles. With such methods, it is possible to photomodulate the association of motor proteins to cargos, to investigate the role of MTs in specific transport processes<sup>11,12</sup>.

However, while optogenetics has succeeded in providing motors and scaffold-associated proteins that are responsive to externally controlled stimuli, no optogenetic variants of the basic cytoskeleton scaffold proteins actin and tubulin have been achieved. An exogenously controllable system for directly patterning cytoskeleton scaffold dynamics and structure with spatiotemporal resolution would however be highly desirable, since it would allow researchers to modulate any of the cytoskeleton-dependent functions. For this purpose, pharmacological interventions that directly address the stability and dynamics of the cytoskeleton scaffold remain the methods of choice. For example, photouncageable versions of MT inhibitors, particularly of the blockbuster drug paclitaxel, have been used for localised photoactivatable inhibition of MT dynamics in several studies<sup>13,14</sup>. Yet despite their ability to modulate the cytoskeleton directly, photouncaging approaches suffer disadvantages, such as irreversibility of inhibition, the intense and phototoxic mid-UV illumination typically needed for uncaging, the often slow and rate-limiting intermediate hydrolysis that diminishes their precision of temporal control, their release of nonspecifically toxic and also phototoxic photouncaging byproducts, background

activity through enzymatic hydrolysis, and increased molecular weight that can cause biodistribution problems<sup>15</sup>.

Against this background, photopharmaceuticals—photoswitchably potent exogenous small molecule inhibitors—have been extensively developed in recent years<sup>16–19</sup>. Photopharmaceuticals conceptually enable studies not otherwise accessible to biology, marrying the spatiotemporal precision of light application known from optogenetics, to the flexibility and system-independence of exogenous small molecule inhibitors. This combination is favourable for non-invasive studies of temporally regulated, spatially anisotropic biological systems—such as the MT cytoskeleton<sup>16,19,20</sup>. Photopharmaceuticals have succeeded in delivering a measure of optical control over a broad range of biochemical and biological phenomena, with early cell-free studies now supplanted by applications in cultured cells and recently in vivo in embryonic and adult animals<sup>21–24</sup>.

In the cytoskeleton field, several photopharmaceutical MT destabilisers were recently developed, to begin addressing the need for spatiotemporally precise MT cytoskeleton studies. The azobenzene-based Photostatins (PSTs), which can be reversibly photoswitched by low-intensity visible light between their biologically inactive *E*-isomers and their MT-destabilising colchicine-like *Z*-isomers, were first developed in 2014<sup>16,25–27</sup>. MT-destabilising photopharmaceuticals based on two different families of molecular photoswitch—styrylbenzothiazoles (SBTubs)<sup>28</sup> and hemithioindigos (bi-active HOTubs<sup>29</sup> and dark-active HITubs<sup>30</sup>)—have since been developed, delivering increased metabolic robustness in the intracellular environment and alternative optical switching profiles (all-visible switching with hemithioindigos, GFP-orthogonal switching with SBTubs). All three reagent families have enabled spatiotemporally precise optical control over endogenous MT network integrity, MT polymerisation dynamics, cell division and cell death. PSTs have already been used in animals to tackle unsolved questions in mammalian development<sup>21,22</sup> and neuroscience<sup>31</sup>. These applications illustrate the power of photopharmacology to enable previously inaccessible studies of spatiotemporally anisotropic cytoskeletal processes without genetic engineering.

With the optically precise destabilisation of MTs addressed by a range of agents, we desired to develop photopharmaceutical MT stabilisers as conceptually novel tools with an alternative spectrum of biological research applications. While both MT destabilisers and MT stabilisers can be used to suppress MT polymerisation dynamics in cell culture, stabilisers have enabled a variety of research and human therapeutic applications which are inaccessible to destabilisers<sup>14,32,33</sup>, due to their differing pharmacology, stoichiometry and spectrum of biological effects. Since the biological functions of the MT cytoskeleton are primarily dependent on the localisation of stabilised or growing MTs themselves, we reasoned that optically controlled tools modulating MT network stability could allow spatiotemporally precise stimulation of a range of these MT-dependent functions, in ways not otherwise amenable to control.

We therefore chose to develop light-responsive paclitaxel analogues as optically controlled MT stabilisers for in situ spatiotemporally precise photocontrol of cellular MT network architecture, dynamics and MT-dependent functions. We now report our development of these reagents.

## Results

**Design and synthesis.** We chose the azobenzene photoswitch for installing photoswitchable potency onto the taxane core. This photoswitch offers a substantial geometric change upon isomerisation, which we hoped would differentiate the isomers' binding constants, and it allows reliable, high-quantum-yield,

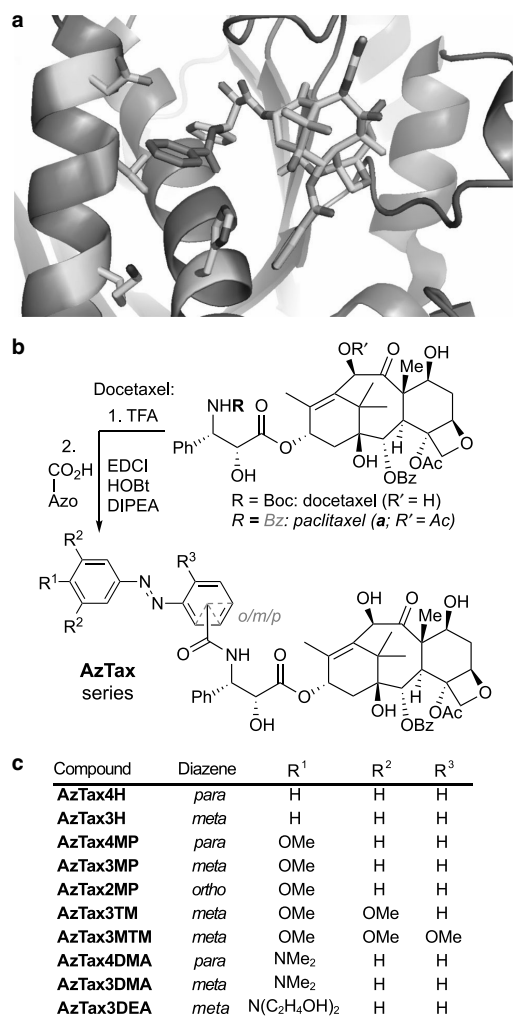


**Fig. 1** Design and synthesis of AzTax. **a** Paclitaxel:tubulin structure (PDB: 3J6G<sup>36</sup>) with the benzamide indicated in pink. **b** Synthesis of AzTax from docetaxel. **c** Panel of AzTax examined in this study.

near-UV/visible-light-mediated, highly robust  $E \leftrightarrow Z$  photoisomerisability, which enables repeated photoswitching in situ in living cells. Taxanes feature a number of chemically modifiable positions; we chose to focus on sites where substituents can be tolerated, but where their geometric changes might impact binding potency through steric interactions or by modulating the orientation of key interacting groups nearby. Potent taxanes feature a side-chain 3'-amine acylated/substituted with mid-size hydrophobic groups (e.g., Boc group in docetaxel and Bz in paclitaxel)<sup>8,34</sup> which about the tubulin protein surface yet are projected away from the protein interior (Fig. 1a, highlighted in pink); the other side-chain positions (e.g., the 3'-phenyl or 2'-hydroxyl) offer less tolerance for substitution as they project into the protein<sup>8</sup>. The 3'-amine also tolerates the attachment of somewhat polar cargos such as the large silarhodamine fluorophore, as long as they are attached via a long spacer, with only

moderate potency loss<sup>35</sup>, making it desirable for photopharmaceutical tuning as it might tolerate azobenzenes with a range of structural characteristics. However, we anticipated that attenuating the high potency of paclitaxel itself (low nM range) might be required, in order that the relatively small structural change of a  $E/Z$  isomerisation at the molecular periphery could substantially modify the overall potency.

We accordingly designed a panel of 3'-azobenzamide-taxanes (AzTax) for biological testing. As taxanes have famously poor aqueous solubility (still worsened by attaching an azobenzene), we initially determined to focus on compounds displaying satisfactory potency at concentrations substantially below their solubility limit. This avoids the case that the compounds' apparent potencies would be dictated by solubility effects, and so should enable robust use as reagents across a variety of systems and settings. Theorising that the sterics around the azobenzene phenyl ring proximal to the taxane core would be the greatest potency-affecting factor, we first focussed on testing which orientations of photoswitch would be best tolerated. We therefore scanned orientations of the diazene in *ortho*, *meta* and *para* relative to the amide (AzTax2/3/4 compound sets, Fig. 1b, c), and when early cellular testing showed that the AzTax2 set had the lowest potency, we abandoned it at this stage.

Next, examination of the published tubulin:paclitaxel cryo-EM structures (Fig. 1a)<sup>36,37</sup> indicated that the azobenzene's distal ring can project freely away from the protein. Therefore, we hypothesised that steric variation to the distal ring would not greatly impact binding potency of either isomer, but could be used orthogonally to tune their photochemical properties, by substitutions in *para* to the diazene that chiefly mesomerically affect the photochemistry of the N=N double bond. We accordingly synthesised unsubstituted ("H"), *para*-methoxy ("MP") and *para*-dimethylamino ("DMA") derivatives of the AzTax3/4 sets. These were chosen to vary the photochemical properties of most relevance to photopharmacology: the completeness of the  $E \rightarrow Z$  and the  $Z \rightarrow E$  photoisomerisations at fixed wavelengths, which dictate the dynamic range of isomer photoswitchability, and  $\tau$  (the half-life of the spontaneous unidirectional  $Z \rightarrow E$  relaxation). Lastly, when the AzTax3 set proved promising in early studies, we also examined installing an electron-donating 3,4,5-trimethoxy motif on the distal ring (AzTax3TM) as well as an additional R<sup>3</sup> methoxy group to reduce the rotatability of the proximal ring in case this could amplify the difference between isomer potencies (AzTax3MTM), and we controlled for solubility effects by exchanging the dimethylamino substituent for a more soluble diethanolamino ("DEA") group (AzTax3DEA). The target AzTax were synthesised by degradation of commercial docetaxel followed by amide couplings to various azobenzenecarboxylic acids in moderate yields (Fig. 1b, c and Supplementary Note 1).

**Photochemical characterisation.** The AzTax all displayed robust and repeatable  $E \leftrightarrow Z$  photoswitching under near-UV/visible illuminations, as expected from the literature<sup>19</sup> (Supplementary Fig. 1). Since their protein target is located in the cytosol, we first wished to evaluate their photoswitching in physiological aqueous media. Since taxanes are too poorly water-soluble to perform reliable photoswitching studies easily by UV-Vis spectroscopy, we synthesised fully water-soluble diethanolamides of all the azobenzenecarboxylic acids and used them in aqueous photoswitching tests (see Supplementary Note 2). The photochemical properties within each substituent set were similar. The unsubstituted (H) compounds displayed a 3-fold dynamic range of  $Z$ -isomer photoswitchability between the photostationary states (PSSs) at 375 nm (80%  $Z$ ) and 410 nm (26%  $Z$ ), and had

substantially slower relaxation than biological timescales ( $\tau$  ca. 50 days). The methoxylated compounds (MP, TM and MTM) had been chosen to improve the dynamic range of isomer photoswitching by relative shifting of the isomers' absorption bands<sup>16</sup> (Supplementary Fig. 2). Indeed, they delivered a ca. 9-fold dynamic range of *Z*-isomer photoswitchability (375 nm: 96% *Z*; 530 nm: 11% *Z*), and their relaxation remained substantially slower than biological timescales ( $\tau$  ca. 24 h).

Advantageously for practical work, the metastable *Z*-isomers of all **AzTax**s could be quantitatively relaxed to *E* by warming DMSO stocks to 60 °C overnight (which increases the practical ease-of-use of these reagents as compared to irreversibly photouncaged reagents). The *para*-amino (DMA and DEA) compounds featured  $\tau$  values too small to observe bulk photoswitching in aqueous media under biologically applicable conditions. Yet, since less water-solvated environments such as lipid vesicles, membranes, or protein-adsorbed states are likely intracellular localisations for hydrophobic taxane conjugates, we then determined their photochemistry in moderately polar aprotic media (EtOAc). Here, they were easily bulk-switchable ( $\tau$  ca. 11 min), giving a 4-fold dynamic range of *Z*-isomer photoswitchability (410 nm: 91% *Z*; 530 nm: 21% *Z*) (further detail in Supplementary Note 2). As the **AzTax** reagents were intended for use with microscopy, we also examined photoswitching of all compounds over a broader range of wavelengths, to determine what dynamic range of isomer photoswitchability would be accessible in practice, with standard (405, 488 and 514 nm) or more exotic (380, 440 and 532 nm) microscopy laser wavelengths (Fig. 2a, Supplementary Fig. 2 and Supplementary Table 1).

We then proceeded to explore the biological applicability of **AzTax** as photoswitchable MT stabilisers in living cells. Since near-UV illumination gave PSSs with high-*Z* populations for all photoswitches, while thermal relaxation and maintenance in the dark returned the *E*-isomer quantitatively, we began by comparing all-*E* "dark" conditions (all-*E* stock applied, then maintained dark) with mostly *Z* "360 nm" lit conditions (all-*E* stock applied, then photoisomerised *in situ* by pulsed illuminations with low-power 360 nm LED light, giving a mostly-*Z* PSS), to determine which structures allowed the highest fold difference of bioactivity.

**AzTax display photocontrolled bioactivity in living cells.** Since stabilisation of MTs in cells over a prolonged period blocks cell proliferation and ultimately causes cell death<sup>8</sup>, we first assayed the **AzTax** for light-dependent cellular activity by the resazurin cell proliferation/viability assay. Viability dose-response curves under dark or UV conditions were assessed in the HeLa cervical cancer cell line (Fig. 2b, c). All compounds displayed dose-response curves with similar Hill coefficients as the parent drug docetaxel (Supplementary Fig. 3), which is in line with the conjecture that they act through the same mechanism, albeit with different potency. All compounds except the fast-relaxing **AzTax3DMA** had *Z*-isomers that were more potent, or else equipotent, to the *E*-isomers, suggesting that this trend in isomer-dependent cellular bioactivity across several photoswitch types has robust significance. *E*-**AzTax2MP** had the poorest overall potency ( $EC_{50}$  ca. 7  $\mu$ M, all-*E*), which we took as indicating the unsuitability of *ortho* substitutions that likely project the azobenzene into solution (c.f. Fig. 1a) where its hydrophobicity could interfere with binding stability. By contrast, the **AzTax4** set featured compounds up to 100 times more potent, and structure-dependently covered a 40-fold potency range. However, despite the good isomeric photoswitchability of e.g., **AzTax4MP**, none of the **AzTax4** set displayed substantial photoswitchability of bioactivity (fold difference between the 360 nm and the dark bioactivity). We

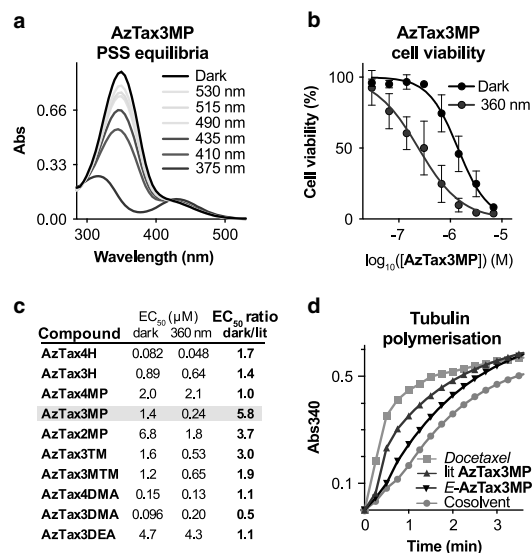


**Fig. 2** Photoswitchable performance of **AzTax**. **a** Photostationary state UV-Vis absorption spectra of **AzTax3MP** under a range of cell-compatible wavelengths similar to microscopy laser lines. **b, c** Resazurin antiproliferation assays of **AzTax** highlight their structure- and light-dependent cell cytotoxicity. HeLa cells, 40 h incubation in dark conditions (all-*E*) or under pulsed illuminations with low-power LEDs (75 ms per 15 s near-UV at  $<1$  mW cm<sup>-2</sup>; lit = -80% *Z*) (dose-response curves are fitted to the means (shown with s.d.) of 3 independent biological experiments). **d** A cell-free assay for polymerisation of purified tubulin comparing the MT stabilisation activity of docetaxel, all-*E*- and 360 nm-lit-**AzTax3MP** (all 10  $\mu$ M) shows light-specific promotion of polymerisation by *Z*-**AzTax3MP**, matching the trend observed in cellular assays.

interpreted this substitution-independent result as an indication that the distal ring may project too far from the protein contact surface, in both *E*- and *Z*-isomers, for the **AzTax4** isomer state to substantially affect binding.

In contrast, members of the **AzTax3** series all showed photoswitchability of bioactivity. **AzTax3MP** featured a nearly 6-fold difference between the more-toxic *Z* and less-toxic *E*-isomers' bioactivity, over the 48 h experimental time course (Fig. 2b). Adding more methoxy groups to the scaffold decreased the *Z*-isomer's cytotoxicity without greatly affecting that of the *E*-isomer (**AzTax3TM**, **AzTax3MTM**), and deleting the methoxy group also decreased the *Z*-isomer's cytotoxicity (**AzTax3H**), which we took as a sign that balancing the polarity of the photoswitch was important for maximising bioactivity. In line with this interpretation, the potencies of **AzTax3DMA** were similar to **AzTax4DMA** while the more hydrophilic **AzTax3DEA** showed a 40-fold loss of potency. Despite the potential for photoswitching the *para*-amino **AzTax** inside lipid environments, they should only reach their cytosolic target tubulin as the *E*-isomers due to fast aqueous relaxation. Surprisingly, **AzTax3DMA** appeared slightly more bioactive as the unilluminated *E*-isomer, although as expected **AzTax4DMA** and **AzTax3DEA** both showed no illumination-dependency of bioactivity; and controls under 410 nm illumination (to establish the optimum PSS for the *para*-amino compounds) showed no different result to those obtained with UV illumination (Fig. 2). The apparent cytotoxicity differential seen for **AzTax3DMA** might reflect reduced availability to the cytosol rather than

differential binding of the isomers<sup>30</sup> although these results do not allow further conjecture.

To continue the study, we therefore selected **AzTax3MP**, due to its photoswitchability of bioactivity (6-fold when under optimum illumination conditions), satisfactory potency ( $EC_{50} = 0.24 \mu\text{M}$  when UV illuminated), bidirectional photoswitchability (optimum 9-fold-change of concentration of the more bioactive Z-isomer), and reproducibly photoswitchable cellular performance across assays with different illumination conditions, to proceed with further mechanistic biological evaluations.

**Photocontrol of tubulin polymerisation and cell cycle.** To examine the molecular mechanism of **AzTax** isomer-dependent cellular bioactivity, we first assayed the potency of **AzTax3MP** for promoting tubulin polymerisation in cell-free assays using purified tubulin. The majority-Z 360 nm-lit state gave a ca. 60% enhancement of polymerisation over control (benchmarked to docetaxel at 100%), while all-*E*-**AzTax3MP** gave only ca. 30% polymerisation enhancement (Fig. 2d and Supplementary Note 2). Note that the enhancements seen in this cell-free assay are not predictive of the relative cellular potencies, but it clarifies the mechanism of action of **AzTax** as MT stabilisers, like their parent taxanes. We next studied the direct effects of in situ-photoisomerised **AzTax** upon cellular MT organisation and MT-dependent processes. Immunofluorescence imaging of cells after 24 h of exposure revealed that **AzTax3MP** light-dependently disrupts MT network architecture. As **AzTax** concentration increases, MTs first become disorganised, then mitotic spindle defects that result in multinucleated cells are seen, and finally mitotically arrested and early apoptotic cells with fragmented nuclei dominate; the effective concentrations needed to achieve these effects are substantially lower for lit **AzTax** than under all-*E* dark conditions (Fig. 3, further detail in Supplementary Note 4). The best window for visualising this isomer-dependent bioactivity lay around 0.3–1  $\mu\text{M}$ . Both the mitotic arrest, and the nuclear defects of cells that escape arrest, are hallmarks of MT stabiliser treatment<sup>38</sup>, arguing that the isomer-dependent cytotoxicity of **AzTax3MP** arises from MT stabilisation preferentially by its Z-isomer.

The presence of multinucleated cells indicated that **AzTax** also inhibit MT-dependent functions such as successful completion of mitosis. To quantify this we examined cell-cycle repartition after **AzTax** treatment by flow cytometry, expecting to observe G<sub>2</sub>/M-phase cell-cycle arrest<sup>39</sup>. G<sub>2</sub>/M-arrest was observed with approximate  $EC_{50}$  around 1.5  $\mu\text{M}$  after 24 h incubation with the lit **AzTax3MP**. This was twice as potent as *E*-**AzTax** (Fig. 4a–c) and mimicked the effect of docetaxel although with lower potency (Supplementary Fig. 4). As a control for illumination/photoswitch-dependent off-target effects, we also examined the non-photoswitchably bioactive but potent **AzTax4DMA**, which reproduced the effects of docetaxel independent of illumination conditions indicating no significant assay complications (Supplementary Fig. 4). This further supported the notion that **AzTax3MP** acts across a range of assays and readouts as a light-modulated taxane, with reproducible photocontrol over the isomers' bioactivity, allowing effective inhibition both of MTs and of MT-dependent processes.

**AzTax enable spatiotemporally specific MT control in cells.** With their photoisomerisation-dependent bioactivity shown in long-term experiments (days), we next tested one of the key conceptual advantages that photoswitchable MT stabilisers should enable: real-time in situ optical control of the MT cytoskeleton with single-cell spatial specificity and high temporal precision.

We transfected HeLa cells to express the EB3-tdTomato fluorescent reporter, that selectively labels GTP:tubulin-rich regions of MTs. In ordinary conditions this is a marker for the GTP cap region of polymerising MTs, thus selectively revealing polymerising MTs as comets moving towards the cell periphery<sup>40</sup>. As taxane treatment suppresses MT polymerisation dynamics<sup>41</sup>, we imaged EB3-tdTomato dynamics using live cell confocal microscopy, as a spatiotemporally resolved readout for MT inhibition by **AzTax**.

We applied **AzTax3MP** globally to these cells at 1  $\mu\text{M}$ , and targeted single cells with low-intensity illuminations at 405 nm, hoping to achieve precisely temporally resolved control of MT dynamics in those single cells only, by selectively isomerising **AzTax3MP** inside them. In targeted cells, EB3 comet counts were halved upon 405 nm illuminations, recovering almost completely within 80 s after 405 nm illumination was stopped (Fig. 5a), while surrounding cells as well as non-treated controls were unaffected (Fig. 5b); and the process could be repeated over several cycles (Supplementary Movies 1 and 2, Supplementary Note 4 and Supplementary Discussion). Thus, **AzTax** can indeed be used to reversibly inhibit MT dynamics of target cells with temporal precision on the scale of seconds and spatial precision on the level of tens of microns. To examine *E*-**AzTax3MP** (dark state) for residual effects on MT dynamics, we also quantified other parameters of EB3 motility. *E*-**AzTax3MP** caused only a slight decrease in EB3 comet velocities (Fig. 5c), and an insignificant decrease in EB3 comet density (Fig. 5d). By comparison, in photoswitched cells, so few comets remain that meaningful velocity quantification was not possible (Fig. 5c, d). It can be concluded that working concentrations can be appropriately chosen such that **AzTax3MP** does not hinder MT polymerisation in the absence of illumination, but does so strongly when illuminated.

Finally, to study the entire cellular MT population and not only the actively polymerising fraction of MTs, HeLa cells transfected to express mCherry- $\alpha$ -tubulin were imaged to quantify total MT density under **AzTax3MP** treatment (Supplementary Movies 3 and 4). No change in MT density was observed during treatment or photoswitching (Supplementary Fig. 5). Taken together, this argues that, as expected, **AzTax** do not act by reducing the overall number of MTs, but rather by suppressing MT polymerisation dynamics.

**AzTax allow subcellular photocontrol of neuronal MT dynamics.** Having demonstrated MT control with spatial resolution to single cells, we now wished to examine the performance of **AzTax** as applied to subcellular resolution. Small molecule inhibitors diffuse rapidly within cells, so using them to achieve sustained subcellular patterning of biological effects is challenging. Yet, for potential applications in neurobiology, the highly polarised, elongated neuronal cell shape should restrict diffusion and favour subcellular resolution. We used mature cultured rat hippocampal neurons with well-developed dendrites, and transfected these cells with EB3-tdTomato for imaging. For each neuron, we selected equal-sized areas along independent processes, and monitored their EB3 dynamics before and during **AzTax3MP** treatment, with ROI-localised 405 nm application to one area (Fig. 6 and Supplementary Movies 5–8).

Kymographs of these areas reveal localised reductions in MT polymerisation dynamics in 405 nm-illuminated ROIs in the presence of **AzTax3MP**, while no significant changes are seen in other dendritic processes; and internal controls before/after **AzTax** application confirmed that no significant photobleaching is caused by 405 nm illumination before **AzTax** application (Fig. 6a). The induction of inhibition in the ROI was typically

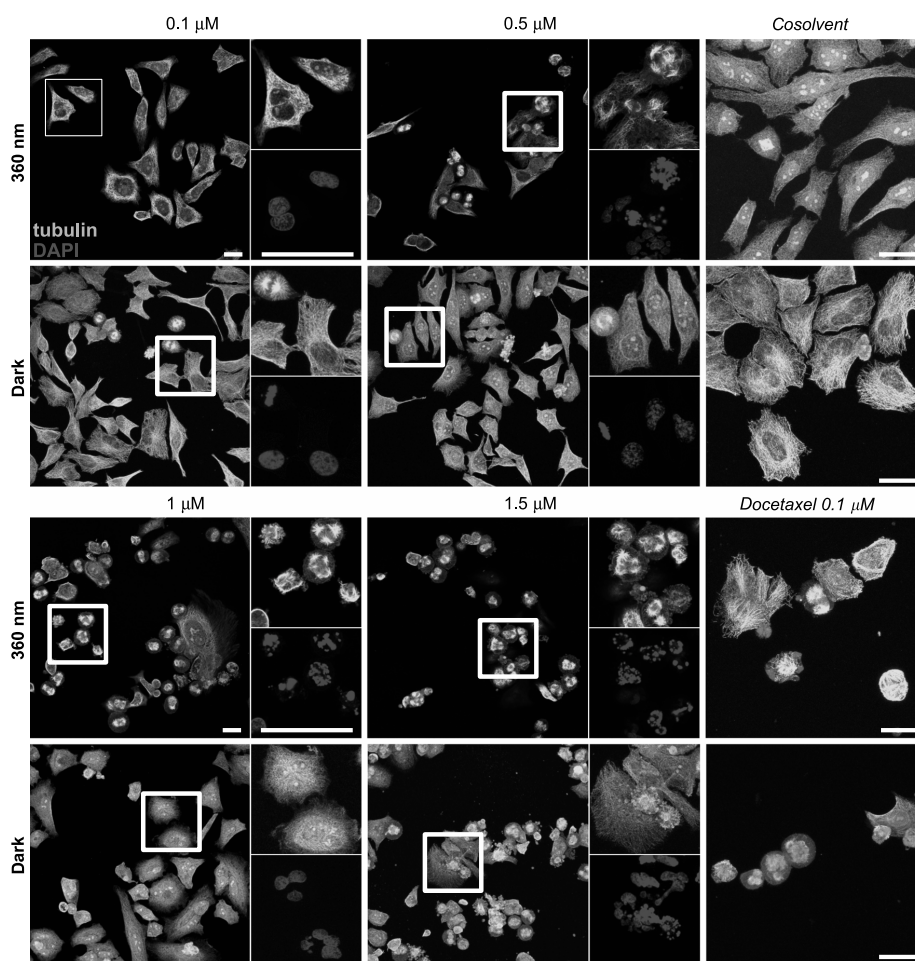


**Fig. 3** **AzTax3MP** light-dependently disrupts MTs in cultured cells. Immunofluorescence staining indicates dose- and light-dependent disruption of MT organisation, mitotic completion, and cell viability. HeLa cells treated with **AzTax3MP**, docetaxel, or DMSO cosolvent only for 24 h;  $\alpha$ -tubulin in green, DNA in blue; docetaxel positive control at 0.1  $\mu$ M; DMSO cosolvent at 1% in all conditions; scale bars 25  $\mu$ m (staining was repeated twice after two independent experiments and evaluated each time by at least two scientists independently).

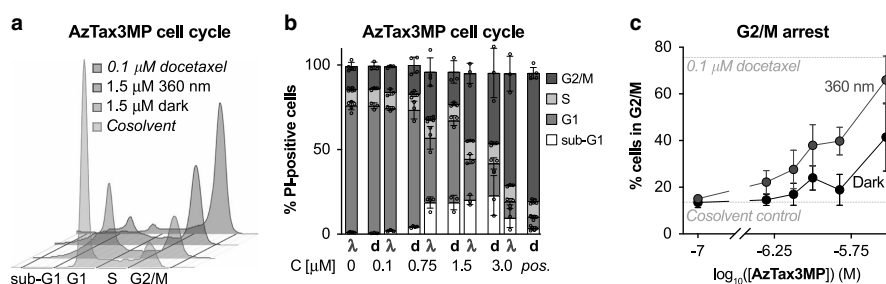


**Fig. 4** **AzTax3MP** leads to dose- and light-dependent cell-cycle arrest. **a** Flow cytometry analysis of cell-cycle repartition shows that **AzTax3MP** leads to a light-dependent shift of living cells towards  $G_2/M$  phase. **b**, **c** The cell-cycle distribution of **AzTax**-treated cells approaches that of docetaxel-treated cells in a dose- and light-dependent manner. HeLa cells treated under light/dark conditions for 24 h (**d** indicates dark and  $\lambda$  indicates lit conditions; *pos.* indicates docetaxel control at 0.1  $\mu$ M;  $n = 3$  biologically independent experiments, except  $n = 4$  for 0.75  $\mu$ M **AzTax3MP** and  $n = 5$  for cosolvent and docetaxel controls; data shown as mean with s.d.).

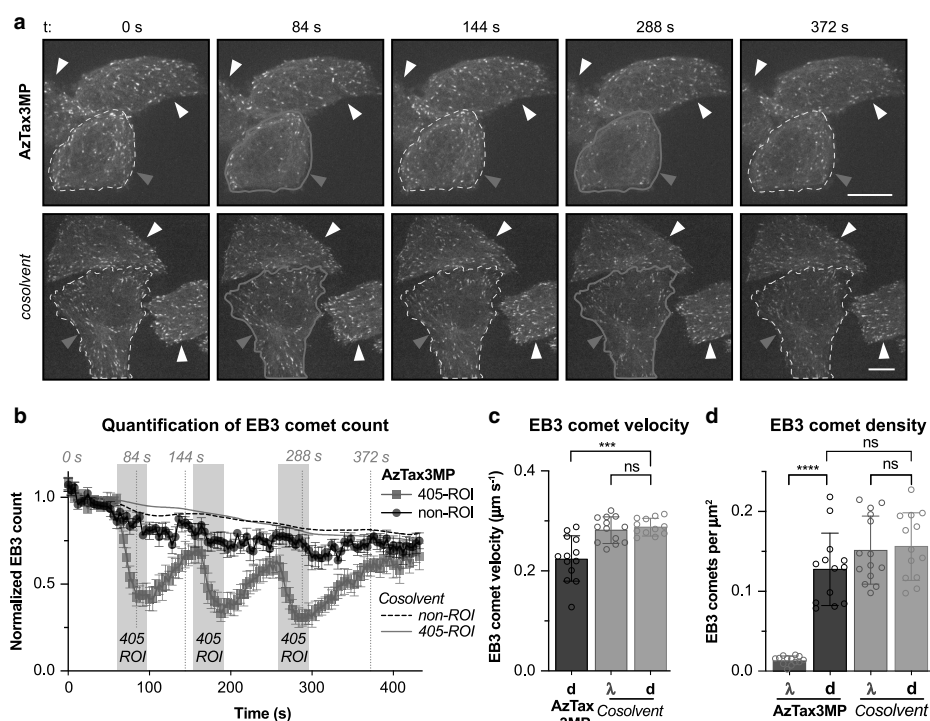


**Fig. 5** **AzTax** photoswitching allows cell-precise, temporally reversible inhibition of MT polymerisation dynamics. Data related to Supplementary Movies 1 and 2. HeLa cells transfected with EB3-tdTomato treated with 1% DMSO cosolvent with or without 1  $\mu\text{M}$  **AzTax3MP**. **a**, **b** Target cells (violet arrowheads) were selectively illuminated with 405 nm in bursts, and EB3 tracking in defined regions of interest (ROIs) performed. **a** Target ROIs in frames acquired immediately after 405 nm illumination are outlined in violet, target ROIs in  $t_0$  and post-recovery frames (ca. 80 s after 405 nm illumination periods) are outlined in dotted white; nontarget cells are indicated with white arrowheads; scale bars indicate 10  $\mu\text{m}$ . **b** Quantification of EB3 comet counts (averages over  $n = 7$  cells per treatment group across 3 experiments, each cell's EB3 comet count time course was normalised to the average of the first ten frames) in target ROI and in non-illuminated cells. Periods of ROI illumination with 405 nm are shaded in violet; times of frames from the representative movies shown in (**a**) are indicated with dotted lines annotated with the times, data shown as group-average of EB3 comet count time course (normalised to initial count) with s.e.m. For clarity, data for cosolvent-only areas are shown with LOWESS fits. **c**, **d** HeLa cells transfected with EB3-tdTomato were treated with either 1  $\mu\text{M}$  **AzTax3MP** or DMSO cosolvent only, and imaged directly after drug application for 2.4 min with 405 nm illumination (signified by " $\lambda$ ") or without (signified by " $d$ "). Supplementary Movies were analysed for **c** EB3 comet velocity ( $n = 12$  cells for **AzTax3MP**;  $n = 13$  cells for cosolvent conditions), and **d** EB3 comet counts, normalised to cell surface area ( $n = 13$  cells for **AzTax3MP** lit and both cosolvent conditions;  $n = 14$  cells for **AzTax3MP** dark condition). EB3 comet velocity could not be meaningfully analysed in **AzTax3MP**-treated cells under 405 nm illumination due to the strong loss of EB3 comets and is therefore not represented. Data are shown as mean with s.d. Unpaired, two-tailed  $t$  test: \*\*\* $P = 0.001$  (95% CI 0.035–0.093), \*\*\*\* $P < 0.0001$  (95% CI 0.089–0.14), ns denotes not significant, no adjustments for multiple comparisons.

clear within ca. 1–3 min, which is approximately one order of magnitude slower than in the whole-cell photoswitching experiments of Fig. 5, and which may partially reflect the lower **AzTax** concentration that was selected to avoid complications with the more sensitive neurons. Statistics collected over multiple cells highlighted the reproducibility of using ROI-localised **AzTax3MP** illumination to deliver subcellularly localised MT polymerisation inhibition in this system (Fig. 6b).

Collectively, these results demonstrate the use of **AzTax3MP** as a powerful tool to directly optically modulate endogenous MT network architecture, polymerisation dynamics and MT-dependent functions in live cells with excellent spatiotemporal control.

## Discussion

Photocontrol over protein function is an attractive method to study anisotropic, multifunctional cellular systems, since it can

deliver the spatiotemporal specificity required to focus on specific roles or aspects within these complex biological systems. Small molecule photopharmaceuticals have already proven valuable photocontrol tools because of their ability to address such targets that are not directly accessible to optogenetics, such as the MT cytoskeleton (for which a range of photoswitchable depolymerising agents have recently been reported<sup>16,28,30</sup>). Here we have expanded the scope of photopharmaceutical MT reagents to demonstrate the first photoswitchable MT stabilising agents. Through structure-photochemistry/activity-relationship studies, we have selected a lead compound **AzTax3MP** that gives robust, in situ photoswitchable MT stabilising activity in cell-free and cellular assays, and can light-dependently reproduce key direct as well as downstream biological effects of the taxanes but with excellent spatiotemporal control down to the subcellular level. While this is a promising starting point for further reagent optimisation, we believe that **AzTax3MP** itself will already find a



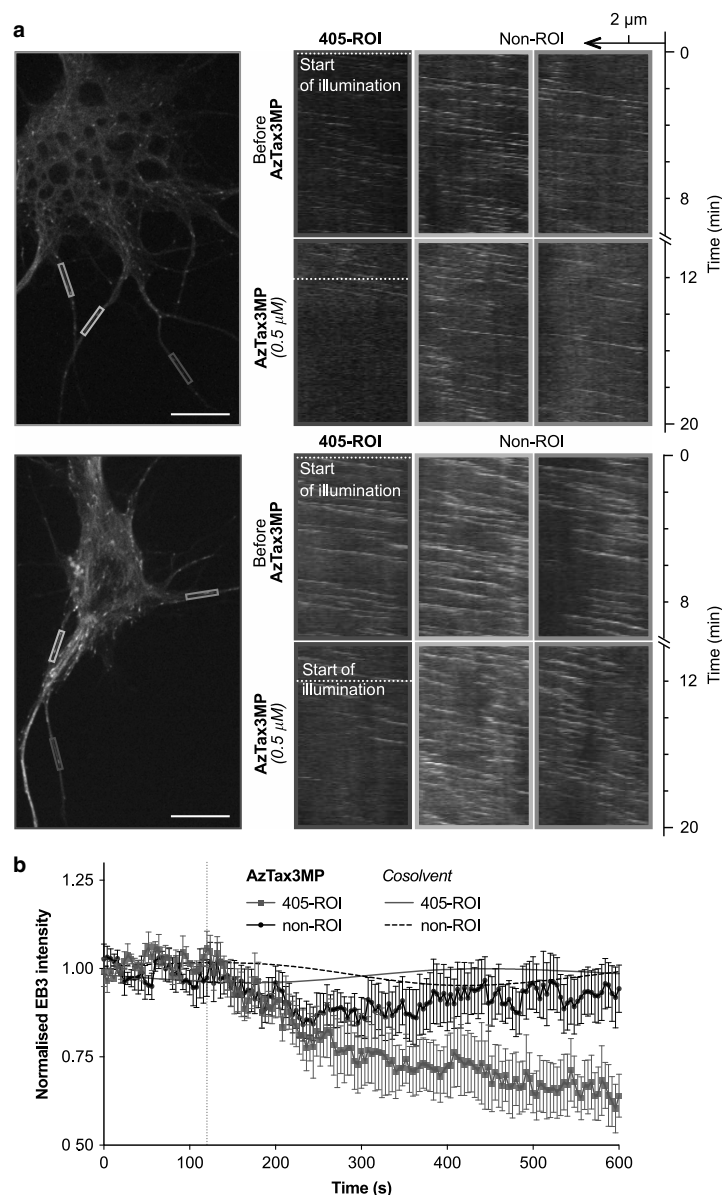


**Fig. 6 Manipulation of MT polymerisation dynamics in subcellular ROIs of rat primary hippocampal neurons using AzTax3MP.** Data related to Supplementary Movies 5–8. **a**, **b** Cultured primary neurons (9 days in vitro) transfected with EB3-tdTomato treated with 1% DMSO were initially imaged for EB3 for 10 min while a ROI (violet box) was pulsed with 405 nm light, establishing baselines for EB3 activity in the cell and in the ROI, which were demonstrated to be light-independent. The same neurons were then exposed to 0.5  $\mu$ M AzTax3MP and immediately imaged for another 10 min; during this time the same ROI (violet box) was pulsed with 405 nm light beginning at 2 min into the acquisition (indicated by dotted lines). **a** Cell images with areas marked, and corresponding kymographs of these areas. The ROI pulsed with 405 nm is boxed in violet, the non-ROI areas (not pulsed with 405 nm) are boxed in orange and green. Scale bars indicate 10  $\mu$ m. **b** Normalised area-average pixel EB3 intensities (with s.e.m.), for areas treated with or without AzTax3MP and 405 nm pulsing ( $n = 4$  cells). For clarity, data for cosolvent-only areas are shown as spline fits; see Supplementary Note 4 for further details.

range of applications particularly in embryology, neuroscience and studies of cell motility and polarity, where its spatiotemporally specific bioactivity will enable studies not previously possible.

Liu et al. also recently reported photoswitchable MT stabilisation, using a photoswitchable supramolecular host-guest system intended to crosslink cellular MTs<sup>42</sup>. However, these effects were also reproduced when the tubulin stabilisation motif was deleted<sup>43</sup>, and it remains unclear if the host-guest system could perform specific tubulin binding<sup>44</sup>. The druglike reagents developed in this work, offering robust and structurally rationalisable performance, may therefore be valuable to address still-unmet needs.

If **AzTax** reagents with still greater bioactivity differentials could be accessed, this would improve reagent performance with respect to several limitations of the current best candidate **AzTax3MP**. This reagent's dynamic range of bioactivity photoswitching is between two- and six-fold, depending on the assay readout. Thus, relatively precise concentration tuning is needed to find the best working concentration, and background activity before photoactivation may be observed depending on the assay and conditions. Determining the sources of the differential bioactivity between **AzTax** isomers in living cells is therefore key for reagent optimisation. Since modifying polarity at a distal site that should not clash sterically with the protein gave a 40-fold change of apparent potency (**AzTax3DEA** compared to **AzTax3DMA**), we believe that the sterics of the **AzTax** isomers are not necessarily the sole determinant of cellular bioactivity. Yet, polarity-dependent cellular biolocalisation or penetration cannot entirely explain the photoswitchable activity of **AzTax3MP** since it shows isomer-dependent activity in cell-free assays also, so the azobenzene must significantly impact protein-ligand affinity. Therefore, we conclude that maximising the bioactivity difference between isomers will require photoswitches with isomer-dependency both of sterics and of polarity. We note too that the completeness of the *E*→*Z* photoswitchability of the azobenzene was not correlated to the photoswitchability of biological activity (c.f. **AzTax3MTM**, **AzTax4MP**). Since the *Z*-**AzTax** were typically the more-active isomers, we conclude that further defavouring the binding of the *E*-isomer while allowing the *Z*-isomer to retain bioactivity, e.g. by tuning sterics and polarity, is likely the best way to maximise the photocontrol over inhibition. Research in these directions is underway.

Reducing the half-life of spontaneous relaxation of an **AzTax** to its less-binding isomer, could also offer perspectives for improving the ease of cellularly or subcellularly specific photocontrol. Faster relaxation could reduce the biological effects of a photoactivated isomer diffusing away from a desired spatial and temporal locality, and so improve spatiotemporal precision. However, if relaxation becomes too fast, the requirements for repeated localised illuminations may become the limiting factor for compound utility. We estimate that relaxation on the scale of seconds, or hundreds of microseconds, would best address most desirable short-term assays. While the relaxation speed of **AzTax3MP** was in this respect too slow, and that of **AzTax3DMA** was too fast, it is likely that by electronic tuning of the azobenzene's distal phenyl ring, more useful derivatives with intermediate relaxation rates can be obtained. Research in this direction is ongoing.

Photopharmacology studies often assume that increasing the dynamic range of isomeric photoswitchability under a freely available choice of illumination conditions, and red-shifting overall absorption wavelengths, are required for improved biological performance. However, in the case of the current or any potentially tuned future **AzTax** stabilisers, as elsewhere, probably neither is true:

First, after *Z*-**AzTax** induces increased MT rescues, which alter MT dynamics and network architecture, the downstream MT-dependent biology probably cannot be rapidly returned to its usual state even if the stabiliser would be totally removed (e.g., by complete back-isomerisation to a hypothetically non-binding state). This is because any **AzTax**-stabilised MTs are likely to be organised abnormally, and will presumably require time to break down and return tubulin monomer to the cytoplasmic pool so that a functional, directional MT network can be rebuilt. Therefore, there is probably a limit to the temporal resolution of *true* biological reversibility that any photoswitchable stabiliser can display, even if selected readouts (such as speed of polymerisation of individual MTs) recover more quickly. With this consideration in mind, we do not believe that improving the completeness of bidirectional isomeric photoswitchability<sup>45</sup> will be as important for **AzTax** development as for other classes of inhibitors that can feature instantaneous downstream biological response.

Second, red-shifting photoswitch absorption wavelengths is also likely to be counterproductive for microscopy, since there are few fluorescent proteins with significant excitation efficiency at laser lines above 561 nm (typically the next wavelength available is 647 nm). Therefore, maintaining orthogonality to the widest possible range of imaging wavelengths by blue-shifting is in our opinion and experience more advantageous, since it can keep other imaging channels vacant for multiparameter, photo-orthogonal studies<sup>28</sup>. However, a key property that should be readily tunable to the advantage of this system is the *E*→*Z* photoisomerisation efficiency at 405 nm, which is usually the only microscopy laser available in the 350–440 nm range. Here we consider that improved performance for **AzTax**-like reagents will depend on optimising photoconversion at the wavelength/s that will in practice be used for their photocontrol. Developing a set of standard photoswitches with better 405 nm *E*→*Z* photoconversion than these *para*-alkoxyazobenzenes (~46% *Z*) yet with similar polarity and substantial stability against thermal relaxation, is a nontrivial goal of our ongoing research.

From a biological perspective, while **AzTax** have reproduced the effects expected for taxanes across these studies, comparing their mechanism more deeply remains to be addressed. Given the structural overlap of the binding pharmacophores (Fig. 1; ca. 215 Å<sup>2</sup> of paclitaxel's total polar surface area (221 Å<sup>2</sup>) overlaps with that of **AzTax3MP** (249 Å<sup>2</sup>)) we consider it likely that their effects will prove similar in a variety of settings. This would open up possibilities towards e.g., time-resolved studies of the effects of taxane binding relying on these photoswitchable analogues.

The **AzTax** photoswitchable MT stabilisers can be used in conjunction with long term, *in situ* photoswitching in live cells to control critical biology from cytoskeleton architecture to cell survival. In short-term experiments, they can reliably apply cell-specific and temporally reversible MT inhibition under straightforward optical control, and have allowed subcellularly resolved inhibition in primary cells with unusual geometry. By complementing the existing MT-depolymerising photopharmaceuticals, the development of **AzTax** now brings both principal modes of pharmacological MT modulation under optical control.

**AzTax** reagents open up a multitude of possibilities for high-precision biological studies not possible with previous methods. They may contribute to studies across a variety of settings where temporally, cell- or subcellularly specific roles of MTs either are unclear, or else determine downstream biology that is itself of interest. For example, cell specific, temporally precise modulation of MT stability and dynamics may be particularly useful for studies of rapid coordinated processes such as mitotic progression, transport, migration and immune cell response, even in complex environments. **AzTax** may also find particular utility in

neurobiology, for example in exploring the recently discovered important roles of MTs in developing and regenerating neurons. Although MT stabilisation during development was shown to determine axonal identity and remodelling, MT stabilisation in mature neurons seems to promote axonal regeneration by reducing the formation of retraction bulbs and modulating glial scar formation after spinal cord injury<sup>14,32,46–48</sup>. However, the temporal characteristics of these phenomena are unclear, and the roles of MT stabilisation in surrounding glia and immune cells rather than in damaged neurons themselves have not yet been resolved. Photopharmaceutical stabilisers could shed new light on this field by stimulating the phenomena with high enough spatiotemporal resolution to clarify the primary processes responsible<sup>32,33</sup>.

In the field of pharmacology, it is still to a large degree unclear<sup>38</sup> how the blockbuster taxane drugs exert their cellular/tissue-level effects *in vivo*. This provides enormous clinically driven interest in increasing the understanding of taxane pharmacology: both towards improved paclitaxel-site antimetabolic therapeutics, and towards designing better combination treatment regimens involving these broad-spectrum cancer chemotherapeutics. Against this backdrop too, **AzTax** offer an intriguing method for precise studies, that may clarify the spatiotemporal dependency of biological action of the parent taxanes.

Beyond the first generation of **AzTax** reagents, we have also identified perspectives for further improving **AzTax**'s photocontrol of biological function through structure-photochemistry/activity-relationship studies. This opens up several avenues for applying fundamental research in the rapidly evolving field of chemical photoswitches to generate specialty MT stabiliser photopharmaceuticals for cell-free mechanistic studies, cell biology, and towards *in vivo* use. More broadly, this work will also guide and encourage further photopharmaceutical reagent development for other proteins inaccessible to direct optogenetics, including the actin cytoskeleton.

In conclusion, we believe that the **AzTax** will prove useful in studies from intracellular transport, cell division and cell motility, to neurobiology; and that this first demonstration of photo-switchable MT stabilisers is a substantial step towards high-spatiotemporal-precision studies of a range of critical processes in cell biology.

## Methods

Full and detailed experimental protocols can be found in the Supplementary Information.

**Compound synthesis and characterisation.** Reactions and characterisations were performed by default with non-degassed solvents and reagents (Sigma-Aldrich, TCI Europe, Fisher Scientific), used as obtained, under closed air atmosphere without special precautions. Manual flash column chromatography was performed on Merck silica gel Si-60 (40–63  $\mu\text{m}$ ). MPLC flash column chromatography was performed on a Biotage Isolera Spektra, using Biotage prepacked silica cartridges. Thin-layer chromatography was run on 0.25 mm Merck silica gel plates (60, F-254), with UV light (254 and 365 nm) for visualisation. NMR characterisation was performed on Bruker 400 or 500 MHz spectrometers. HRMS was performed by electron impact at 70 eV with Thermo Finnigan MAT 95 or Jeol GCmate II spectrometers; or by electrospray ionisation with a Thermo Finnigan LTQ FT Ultra Fourier Transform Ion Cyclotron resonance spectrometer. Analytical HPLC-MS was performed on an Agilent 1100 SL HPLC with  $\text{H}_2\text{O}:\text{MeCN}$  eluent gradients, a Thermo Scientific Hypersil GOLD<sup>®</sup> C18 column (1.9  $\mu\text{m}$ ; 3  $\times$  50 mm) maintained at 25  $^\circ\text{C}$ , detected on an Agilent 1100 series diode array detector (DAD) and a Bruker Daltonics HCT-Ultra mass spectrometer.

**Photocharacterisation.** UV-Vis-based studies (determination of absorption spectra, photostationary states, reversibility of photoisomerisation, and *Z* to *E* relaxation) were performed on a Varian CaryScan 60 (1 cm pathlength) at room temperature with model photoswitches that were water-soluble analogues of the **AzTax** species, since reliable UV-Vis studies require compound concentrations around 25–50  $\mu\text{M}$ , while the **AzTax** compounds are only reliably molecularly soluble at such concentrations with high cosolvent percentages (e.g., 50%

DMSO) that do not reflect the intracellular environment and also alter the isomers' spectra, quantum yields, and relaxation times. We synthesised and used di(2-ethanol)amine carboxamides as water-soluble analogues of the taxane carboxamide **AzTax** (see Supplementary Information) enabling measurements in PBS at pH ~7.4 with only 1% of DMSO as cosolvent, thus matching the intracellular environment around the **AzTax** protein target, tubulin. Star model 3W LEDs (360–530 nm, each FWHM ~25 nm, Roithner Lasertechnik) were used for photoisomerisations in cuvette that were thus predictive of what would be obtained in the cytosol during LED-illuminated cell culture. Spectra of pure *E*- and *Z*-isomers were acquired from the HPLC's inline Agilent 1100 series DAD over the range 200–550 nm, manually baselining across each elution peak of interest to correct for eluent composition.

**Tubulin polymerisation *in vitro*.** In total, 99% purity tubulin from porcine brain was obtained from Cytoskeleton Inc. (cat. #T240) and polymerisation assays run according to manufacturer's instructions. Tubulin was incubated at 37  $^\circ\text{C}$  with lit- or dark-**AzTax** (10  $\mu\text{M}$ ) in buffer (with 3% DMSO, 10% glycerol) and GTP (1 mM), and the change in absorbance at 340 nm was monitored over 15 min at 37  $^\circ\text{C}$ <sup>49</sup>.

**Standard cell culture.** HeLa (ATCC CCL-2) and COS-7 (ATCC CRL-1651) cells were maintained under standard cell culture conditions in Dulbecco's modified Eagle's medium supplemented with 10% foetal calf serum (FCS), 100 U mL<sup>-1</sup> penicillin and 100  $\mu\text{g mL}^{-1}$  streptomycin, at 37  $^\circ\text{C}$  in a 5%  $\text{CO}_2$  atmosphere (see also Supplementary Information for protocols for other cell types). For long-term assays under photoswitching, HeLa cells were transferred to phenol red free medium prior to assays. Compounds (in the all-*E* state) and cosolvent (DMSO; 1% final concentration) were added via a D300e digital dispenser (Tecan). Treated cells were then incubated under dark (light excluded) or lit conditions (where 75 ms illumination pulses were applied to microtiter plates every 15 s by self-built wavelength-specific multi-LED arrays, to create and maintain the wavelength-dependent photostationary state isomer ratios throughout the experiment<sup>10</sup>).

**Antiproliferation assay.** As a proxy readout for viable cells, mitochondrial diaphorase activity in HeLa cell line was quantified by measuring the reduction of resazurin (7-hydroxy-3H-phenoxazin-3-one 10-oxide) to resorufin. 5000 cells per well were seeded on 96-well plates. After 24 h, cells were treated with *E*-**AzTax**, shielded from ambient light with light-proof boxes, and exposed to the appropriate light regimes. Following 48 h of treatment, cells were incubated with 20  $\mu\text{L}$  of 0.15 mg mL<sup>-1</sup> resazurin per well for 3 h at 37  $^\circ\text{C}$ . The resorufin fluorescence (excitation 544 nm, emission 590 nm) was measured using a FLUOstar Omega microplate reader (BMG Labtech). Results are represented as percent of DMSO-treated control (reading zero was assumed to correspond to zero viable cells) and represented as mean of at least three independent experiments with s.d.

**Cell-cycle analysis.** *E*-**AzTax** were added to HeLa cells in 6-well plates (seeding density: 300,000 cells per well) and incubated under dark or lit conditions for 24 h. Cells were harvested and fixed in ice-cold 70% ethanol then stained with propidium iodide (PI, 200  $\mu\text{g mL}^{-1}$  in 0.1% Triton X-100 containing 200  $\mu\text{g mL}^{-1}$  DNase-free RNase (Thermo Fischer Scientific EN0531) for 30 min at 37  $^\circ\text{C}$ . Following PI staining, cells were analysed by flow cytometry using an LSR Fortessa (Becton Dickinson) run by BD FACSDiva 8.0.1 software. The cell-cycle analysis was subsequently performed using FlowJo-V10 software (Tree Star Inc.). Cells were sorted into sub-G1, G1, S and G<sub>2</sub>/M phase according to DNA content (PI signal). Quantification from gating on the respective histograms is shown as percent of live/singlet/PI-positive parent population per cell-cycle phase across different concentrations of the compound. Every experiment was performed in technical triplicates, at least three times independently, with a minimum of 10,000 (mean: 14,000) PI-positive singlet cells analysed per replicate.

**Immunofluorescence staining.** HeLa cells seeded on glass coverslips in 24-well plates (50,000 cells per well) were left to adhere for 24 h then treated for 24 h with **AzTax** under dark or lit conditions. Cover slips were washed then fixed with 0.5% glutaraldehyde, quenched with 0.1%  $\text{NaBH}_4$ , blocked with PBS + 10% FCS, treated with rabbit alpha-tubulin primary antibody (ab18251, abcam), washed, and incubated with donkey-anti-rabbit Alexa fluor 488 secondary antibody (A-21206, Invitrogen). After washing with PBS, coverslips were mounted onto glass slides using Roti-Mount FluorCare DAPI (Roth) and imaged with a Leica SP8 confocal microscope with a 63  $\times$  glycerol objective (DAPI: 405 nm, tubulin: 488 nm). *Z*-stacks (step size: 0.33  $\mu\text{m}$ ) were projected using Fiji and gamma values adjusted for visualisation.

**EB3 imaging with cell-specific photoisomerisation.** HeLa cells were transiently transfected with EB3-tdTomato (gift from Erik Dent; Addgene #50708) using FuGENE 6 (Promega) according to manufacturer's instructions (see Supplementary Information for all other imaging protocols). Cells were imaged on a Nikon Eclipse Ti microscope equipped with a perfect focus system (Nikon), a spinning disk-based confocal scanner unit (CSU-X1-A1, Yokogawa) and an Evolve 512 EMCCD camera (Photometrics) with a stage top incubator INUBG2E-ZILCS

(Tokai Hit) and lens heating calibrated for incubation at 37 °C with 5% CO<sub>2</sub>. Cells were incubated in standard cell culture medium with 0.5% DMSO cosolvent, with or without *E-AzTax3MP*, for 10 min before microscope image acquisition using MetaMorph 7.7 was begun, with EB3-tdTomato imaging performed at 561 nm (0.17 mW, 300 ms every 4 s). Periods of intracellular-ROI-localised 405 nm illuminations (10 μW, 1 scan every 4 s during 24 s periods) were applied during imaging. Acquisition used a Plan Apo VC 60 × NA 1.4 oil objective. Comet count analysis was performed in ImageJ using the ComDet plugin (E. Katrukha, University of Utrecht, <https://github.com/ekatrakha/ComDet>).

**Subcellular MT manipulation in primary hippocampal neurons.** Mouse primary hippocampal neurons were derived from hippocampi of embryonic day 18 pups and plated on poly-L-lysine (Sigma-Aldrich) and laminin (Roche) coated coverslips. Primary neurons were cultured in Neurobasal medium (NB) supplemented with 2% B27 (Gibco), 0.5 mM glutamine (Gibco), 15.6 μM glutamate (Sigma-Aldrich) and 1% penicillin/streptomycin (Gibco) at 37 °C and 5% CO<sub>2</sub>. Neurons were transfected with EB3-tdTomato on the 7th day in vitro (DIV 7) using Lipofectamine 2000 (Invitrogen) and were imaged at DIV 9. Neurons were imaged on the same system used for cell-specific-photoisomerisation experiments (described above). Neurons were first immersed in conditioned NB with 1% DMSO. EB3-tdTomato was imaged at 561 nm (0.1 mW, 400 ms every 4 s), while a ROI (violet box) was pulsed with 405 nm light (0.2 mW, 8 ms per trace) tracing over the ROI four times every 4 s with imaging frames interleaved. The same neurons were then immersed in conditioned NB with 1% DMSO and 0.5 μM *AzTax3MP* and immediately imaged for another 10 min; during this time the same ROI (violet box) was pulsed with 405 nm light (same protocol) starting 2 min into the acquisition.

**Statistics.** If not indicated otherwise all statistical analyses are unpaired, two-tailed Student's *t* test conducted with GraphPad Prism for Mac 8.4. *P* values below 0.05 were considered significant.

**Reporting summary.** Further information on research design is available in the Nature Research Reporting Summary linked to this article.

#### Data availability

All data generated or analysed during this study are included in this published article and its Supplementary Information files, including the Source Data file provided (raw data for Figs. 2–5 and Supplementary Figs. 1–5). This and all data of the study can also be obtained from the authors upon request. None of these datasets are resources of public interest and therefore are not archived publicly in other forms. All materials are available from the Corresponding Author upon request. Source data are provided with this paper.

Received: 14 November 2019; Accepted: 19 August 2020;

Published online: 15 September 2020

#### References

- Wu, Y. I. et al. A genetically encoded photoactivatable Rac controls the motility of living cells. *Nature* **461**, 104–108 (2009).
- Tas, R. P. et al. Guided by light: optical control of microtubule gliding assays. *Nano Lett.* **18**, 7524–7528 (2018).
- Adikes, R. C., Hallett, R. A., Saway, B. F., Kuhlman, B. & Slep, K. C. Control of microtubule dynamics using an optogenetic microtubule plus end-F-actin cross-linker. *J. Cell Biol.* **217**, 779–793 (2018).
- Bruce, A. et al. *Molecular Biology of the Cell*. (Garland Science, 2007).
- Kopf, A. et al. Microtubules control cellular shape and coherence in amoeboid migrating cells. *J. Cell Biol.* **219**, e201907154 (2020).
- Dumontet, C. & Jordan, M. A. Microtubule-binding agents: a dynamic field of cancer therapeutics. *Nat. Rev. Drug Discov.* **9**, 790–803 (2010).
- Peterson, J. R. & Mitchison, T. J. Small molecules, big impact: a history of chemical inhibitors and the cytoskeleton. *Chem. Biol.* **9**, 1275–1285 (2002).
- Kingston, D. G. I. Taxol, a molecule for all seasons. *Chem. Commun.* 867–880. <https://doi.org/10.1039/b100070p> (2001).
- Castle, B. T. & Odde, D. J. Optical control of microtubule dynamics in time and space. *Cell* **162**, 243–245 (2015).
- van Haren, J. et al. Local control of intracellular microtubule dynamics by EB1 photodissociation. *Nat. Cell Biol.* **20**, 252–261 (2018).
- Nijenhuis, W., van Grinsven, M. M. P. & Kapitein, L. C. An optimized toolbox for the optogenetic control of intracellular transport. *J. Cell Biol.* **219**, e201907149 (2020).
- van Bergwijk, P., Adrian, M., Hoogenraad, C. C. & Kapitein, L. C. Optogenetic control of organelle transport and positioning. *Nature* **518**, 111–114 (2015).
- Buck, K. B. & Zheng, J. Q. Growth cone turning induced by direct local modification of microtubule dynamics. *J. Neurosci.* **22**, 9358–9367 (2002).
- Witte, H., Neukirchen, D. & Bradke, F. Microtubule stabilization specifies initial neuronal polarization. *J. Cell Biol.* **180**, 619–632 (2008).
- Klän, P. et al. Photoremovable protecting groups in chemistry and biology: reaction mechanisms and efficacy. *Chem. Rev.* **113**, 119–191 (2013).
- Borowiak, M. et al. Photoswitchable inhibitors of microtubule dynamics optically control mitosis and cell death. *Cell* **162**, 403–411 (2015).
- Rastogi, S. K. et al. Photoresponsive azo-combretastatin A-4 analogues. *Eur. J. Med. Chem.* **143**, 1–7 (2018).
- Borowiak, M. et al. Optical manipulation of F-actin with photoswitchable small molecules. *J. Am. Chem. Soc.* **142**, 9240–9249 (2020).
- Hüll, K., Morstein, J. & Trauner, D. In vivo photopharmacology. *Chem. Rev.* **118**, 10710–10747 (2018).
- Zenker, J. et al. Expanding actin rings zipper the mouse embryo for blastocyst formation. *Cell* **173**, 776–791 (2018).
- Zenker, J. et al. A microtubule-organizing center directing intracellular transport in the early mouse embryo. *Science* **357**, 925–928 (2017).
- Singh, A. et al. Polarized microtubule dynamics directs cell mechanics and coordinates forces during epithelial morphogenesis. *Nat. Cell Biol.* **20**, 1126–1133 (2018).
- Morstein, J. et al. Optical control of sphingosine-1-phosphate formation and function. *Nat. Chem. Biol.* **15**, 623–631 (2019).
- Laprell, L. et al. Photopharmacological control of bipolar cells restores visual function in blind mice. *J. Clin. Investig.* **127**, 2598–2611 (2017).
- Thorn-Seshold, O., Borowiak, M., Trauner, D. & Hasserodt, J. Azoaryls as reversibly modulatable tubulin inhibitors. WO2015166295A1. <https://worldwide.espacenet.com/patent/search/family/051263438/publication/WO2015166295A1?q=prn%3DWO2015166295A1> (2014).
- Engdahl, A. J. et al. Synthesis, characterization, and bioactivity of the photoisomerizable tubulin polymerization inhibitor azo-combretastatin A4. *Org. Lett.* **17**, 4546–4549 (2015).
- Sheldon, J. E., Dcona, M. M., Lyons, C. E., Hackett, J. C. & Hartman, M. C. T. Photoswitchable anticancer activity via trans-cis isomerization of a combretastatin A-4 analog. *Org. Biomol. Chem.* **14**, 40–49 (2016).
- Gao, L. et al. Photoswitchable microtubule inhibitors enabling robust, GFP-orthogonal optical control over the tubulin cytoskeleton. Preprint at <https://www.biorxiv.org/content/10.1101/716233v1> (2019).
- Sailer, A. et al. Hemithioindigos as desymmetrised molecular switch scaffolds: design control over the isomer-dependency of potent photoswitchable antimetabolic bioactivity in cellulo. *ChemBioChem* **20**, 1305–1314 (2019).
- Sailer, A. et al. Potent hemithioindigo-based antimetotics photocontrol the microtubule cytoskeleton in cellulo. *Beilstein J. Org. Chem.* **16**, 125–134 (2020).
- Vandestadt, C. et al. Early migration of precursor neurons initiates cellular and functional regeneration after spinal cord injury in zebrafish. Preprint at <https://www.biorxiv.org/content/10.1101/539940v1> (2019).
- Hellal, F. et al. Microtubule stabilization reduces scarring and causes axon regeneration after spinal cord injury. *Science* **331**, 928–931 (2011).
- Sengottuvel, V., Leibinger, M., Pfreimer, M., Andreadaki, A. & Fischer, D. Taxol facilitates axon regeneration in the mature CNS. *J. Neurosci.* **31**, 2688–2699 (2011).
- Kingston, D. G. I. The chemistry of taxol. *Pharmacol. Therapeutics* **52**, 1–34 (1991).
- Lukinavicius, G. et al. Fluorogenic probes for live-cell imaging of the cytoskeleton. *Nat. Meth.* **11**, 731–733 (2014).
- Alushin, G. M. et al. High-resolution microtubule structures reveal the structural transitions in αβ-tubulin upon GTP hydrolysis. *Cell* **157**, 1117–1129 (2014).
- Löwe, J., Li, H., Downing, K. H. & Nogales, E. Refined structure of αβ-tubulin at 3.5 Å resolution. *J. Mol. Biol.* **313**, 1045–1057 (2001).
- Mitchison, T. J. The proliferation rate paradox in antimetabolic chemotherapy. *Mol. Biol. Cell* **23**, 1–6 (2012).
- Das, G. C., Holiday, D., Gallardo, R. & Haas, C. Taxol-induced cell cycle arrest and apoptosis: dose-response relationship in lung cancer cells of different wild-type p53 status and under isogenic condition. *Cancer Lett.* **165**, 147–153 (2001).
- Merriam, E. B. et al. Synaptic regulation of microtubule dynamics in dendritic spines by calcium, F-actin, and drebrin. *J. Neurosci.* **33**, 16471–16482 (2013).
- Gonçalves, A. et al. Resistance to taxol in lung cancer cells associated with increased microtubule dynamics. *Proc. Natl Acad. Sci. USA* **98**, 11737–11742 (2001).
- Zhang, Y.-M., Zhang, N.-Y., Xiao, K., Yu, Q. & Liu, Y. Photo-controlled reversible microtubule assembly mediated by paclitaxel-modified cyclodextrin. *Angew. Chem. Int. Ed.* **57**, 8649–8653 (2018).
- Zhang, Y.-M., Liu, J.-H., Yu, Q., Wen, X. & Liu, Y. Targeted polypeptide-microtubule aggregation with cucurbit[8]uril for enhanced cell apoptosis. *Angew. Chem. Int. Ed.* **58**, 10553–10557 (2019).

44. Thorn-Seshold, O. Comment on "Photo-Controlled Reversible Microtubule Assembly Mediated by Paclitaxel-Modified Cyclodextrin". *Angew. Chem. Int. Ed.* **59**, 7652–7654 (2020).
45. Weston, C. E., Richardson, R. D., Haycock, P. R., White, A. J. P. & Fuchter, M. J. Arylazopyrazoles: azoheteroarene photoswitches offering quantitative isomerization and long thermal half-lives. *J. Am. Chem. Soc.* **136**, 11878–11881 (2014).
46. Brill, M. S. et al. Branch-specific microtubule destabilization mediates axon branch loss during neuromuscular synapse elimination. *Neuron* **92**, 845–856 (2016).
47. Ertürk, A., Hellal, F., Enes, J. & Bradke, F. Disorganized microtubules underlie the formation of retraction bulbs and the failure of axonal regeneration. *J. Neurosci.* **27**, 9169–9180 (2007).
48. Ruschel, J. et al. Axonal regeneration. Systemic administration of epothilone B promotes axon regeneration after spinal cord injury. *Science* **348**, 347–352 (2015).
49. Lin, C. M. et al. Interactions of tubulin with potent natural and synthetic analogs of the antimetabolic agent combretastatin: a structure-activity study. *Mol. Pharmacol.* **34**, 200–208 (1988).

### Acknowledgements

This research was supported by funds from the German Research Foundation (DFG: SFB1032 Nanoagents for Spatiotemporal Control project B09 to D.T. and O.T.-S.; SFB TRR 152 project P24 number 239283807, Emmy Noether grant TH2231/1-1, and SPP 1926 project number 426018126 to O.T.-S.); the NIH (Grant R01GM126228 to D.T.; RO1AG050658 to F.B.); and the Thompson Family Foundation (TFFI to F.B.). We thank P.A.S. (LMU) for initial synthesis, F. Ermer and M. Borowiak (LMU) for initial MTT viability assays, H. Harz for microscopy access (LMU microscopy platform CALM), and CeNS (LMU) for support. We thank Natalia Marahori and Thomas Misgeld for valuable experimental feedback on **AzTax3MP**; and Maximilian Wranik, Michel Steinmetz, and the members of the Steinmetz group for work towards obtaining crystal structures of **AzTax**s bound to tubulin. We are indebted to Tim Mitchison for his contributions to small molecule inhibitors in MT research.

### Author contributions

A.M.-D. performed synthesis, photocharacterisation, and coordinated chemical data assembly. J.C.M.M. performed temporally reversible live cell imaging studies. K.L. and Y.K. performed cell biology. C.H. performed flow cytometry. R.B. performed in vitro tubulin polymerisation assays. K.I.J. and L.C.K. performed primary neuron isolation and culture. X.Q. and F.B. conducted early cell experimentation. A.A. supervised temporally

reversible cell studies. J.A. performed and supervised cell biology, and coordinated biological data assembly. D.T. designed the concept and supervised initial synthesis. O.T.-S. designed the study, performed and supervised synthesis, supervised all other experiments, coordinated data assembly and wrote the paper with input from all authors.

### Funding

Open Access funding provided by Projekt DEAL.

### Competing interests

The authors declare no competing interests.

### Additional information

**Supplementary information** is available for this paper at <https://doi.org/10.1038/s41467-020-18389-6>.

**Correspondence** and requests for materials should be addressed to O.T.-S.

**Peer review information** *Nature Communications* thanks Craig Streu and the other, anonymous, reviewer(s) for their contribution to the peer review of this work. Peer reviewer reports are available.

**Reprints and permission information** is available at <http://www.nature.com/reprints>

**Publisher's note** Springer Nature remains neutral with regard to jurisdictional claims in published maps and institutional affiliations.



**Open Access** This article is licensed under a Creative Commons Attribution 4.0 International License, which permits use, sharing, adaptation, distribution and reproduction in any medium or format, as long as you give appropriate credit to the original author(s) and the source, provide a link to the Creative Commons license, and indicate if changes were made. The images or other third party material in this article are included in the article's Creative Commons license, unless indicated otherwise in a credit line to the material. If material is not included in the article's Creative Commons license and your intended use is not permitted by statutory regulation or exceeds the permitted use, you will need to obtain permission directly from the copyright holder. To view a copy of this license, visit <http://creativecommons.org/licenses/by/4.0/>.

© The Author(s) 2020

## Discussion

In this section, I discuss the results of my published work and its prospects for the future.

**(1) CDIs:** I explored new CDIs to test their usefulness as possible improved vascular disrupting agents. While colchicine site inhibitors often show enticing properties including high cytotoxicity *in vitro* and vascular disruption *in vivo*, they regularly fall short regarding robustness to metabolic processes and general tolerability *in vivo*, which we attribute to their molecular scaffolds. In my first paper, we presented isoquinoline-based biaryls as a new molecular scaffold for colchicinoid inhibitors based on a reasonable synthetic route with the possibility of structure diversification in a late stage. Therefore, after I confirmed cytotoxicity for our active designed compounds and confirmed their mode of action in various assays, we chose a lead compound, IQTub4, and its phosphorylated prodrug, IQTub4P, for further testing *in vitro* and *in vivo* towards applicability as an improved vascular disrupting agent. IQTub4 is metabolically stable (microsome assay), avoids common drug-drug interaction issues (CYP inhibition assays), has good distribution coefficient (logD) for *in vivo* bioavailability (as IQTub4), and does not interfere with the hERG channel. Furthermore, the phosphorylated prodrug IQTub4P that we used for *in vivo* dosage studies is well-tolerated at moderate doses.

However, the potential of IQTub4/4P as a VDA has not been evaluated, and this should be tested in the next steps.

(a) A neovasculature network disruption assay can reveal VD activity. A Matrigel plug containing bFGF is implanted subcutaneously into mice, and vessels are left to grow for typically 7 days. Administration of the supposed VDA is performed in different dosages. After 1-3 hours, the vasculature can be perfused with FITC dextran; a decrease in blood vessels in newly grown vessels indicates VD activity.

(b) One crucial aspect is whether the vascular disruption activity is specific to tumour blood vessels and does not severely affect non-tumour blood vessels. A blood perfusion test can measure the blood flow into the tumour and other tissues by uptake of radiolabelled IAP (iodo-antipyrine). In case there is VD activity, the blood flow to tumours should be drastically reduced (reduced IAP accumulation). If this VD activity is not specific to tumours, lack of accumulation of IAP in normal tissue would show which tissues are sensitive to the supposed VDA. The optimal result would be almost no blood flow (no IAP) in the tumour while other tissues would remain unaffected.

In case these experiments succeed, IQTub4 would be the first, potent tubulin-binding VDA based on an isoquinoline biaryl scaffold, with enhanced metabolic stability and good *in vivo* tolerability, which can be highly relevant as cardiotoxicity is scaffold-dependent.<sup>130</sup> This could be a great success and the compound might proceed towards further trials. Regardless of whether IQTub4 shows VDA activity or not, the most valuable insight of this project is that “scaffold hopping” from stilbene to biaryl has been successful and is a reasonable method to **change drug attributes for *in vivo* applications**. I proved that the metabolic stability of small-molecule tubulin depolymerisers can be modulated by using a different chemical scaffold. Changing a scaffold to improve drug properties for *in vivo* applications is a highly

valuable step, and here it can advance the design and development of VDAs/ tubulin inhibitors. The simplicity of synthesis and high substituent tolerability of the biaryl scaffold will open new possibilities not only to MTAs but also to inhibitors for a range of target proteins.

**(2)** The major goal of my PhD thesis has been to investigate new photoswitchable destabilisers and stabilisers for the microtubule cytoskeleton and to reveal their strengths and weaknesses regarding their performance as tools for microtubule-related research.

**2A:** In my second paper, I evaluated SBTubs, a new class of SBT-based photoswitches, regarding their value and applicability in research settings, with the aim of testing the SBT as the basis for photopharmaceuticals that avoid the weaknesses of azobenzenes. We developed SBTubs as new photoswitchable microtubule depolymerisers to prove that the SBT scaffold, which hasn't been explored for its use as photopharmaceuticals yet, can feature potent photocontrol over microtubule cytoskeleton function while avoiding many drawbacks that common photoswitches hold. I confirmed their rational design and tubulin depolymerising bioactivity in several assays including immunofluorescence imaging of the microtubule cytoskeleton, analysis of cell cycle repartition, and imaging effects on microtubule dynamics in live cells under photoswitching.

My research demonstrates that SBTubs are superior to PSTs, the most commonly used photoswitchable compounds based on azobenzene, in several aspects. SBTubs are more amicable towards alternative ranges of substituents, which makes them amenable in their relaxation rates. PSTs react to imaging wavelengths including 488 nm (GFP), 514 nm (YFP) and even 561 nm (RFP), which drastically limits their applicability in imaging assays. In contrast to PSTs, SBTubs are completely indifferent to the most commonly used imaging wavelengths, especially towards 488 nm, which is overwhelmingly used for GFP-tagged reporter proteins in biological experiments. Finally, SBTubs show enhanced stability towards glutathione addition and therefore are a preferable choice for intracellular experiments and for proceeding into *in vivo* applications.

**Critical comment on the results so far:** The major chemical drawback of the SBTubs is that they cannot directly be photoswitched from the bioactive *Z* back to the inactive *E* isomer at biologically compatible wavelengths. While this seems like a disadvantage compared to PSTs, which can be bidirectionally switched with visible light, the fact that SBTubs can be activated by a flash of light and then stay active without re-applying light continuously might be preferable for imaging assays that depend on a longer timescale because it can avoid bleaching of the reporter fluorophores and endangering the specimen. Additionally, we developed a protocol that allowed a quick, diffusion-based homogenisation of the active *Z*-isomer in cell regions or whole cells, which made it possible to do repeated switching under live cell conditions.

Taken together my work on SBTubs proves that the SBT scaffold makes an enticing addition to the toolbox of photoswitchable tubulin inhibitors and the range of biological assays I performed lead to the next steps that now can be taken.

- (1) Since SBTubs are orthogonal to GFP-imaging, this opens the opportunity of multicolour imaging assays while simultaneously photo-targeting microtubule inhibition. Initiation of axon collateral branches is regulated by drebrin, a protein that simultaneously interacts with actin and the tips of microtubules.<sup>131</sup> By using cells co-transfected with both fluorescently labelled microtubules and drebrin and additional staining with SiR-actin, it will be possible to depolymerise microtubules by using SBTubs and light, while studying the consequences of microtubule loss during axon collateral branch formation. Following actin and drebrin behaviour at the same time during microtubule loss and the possible reorganisation of the system after diffusion of the active compound will give new insights on axon branch formation.
- (2) Because SBTubs can be applied in primary neurons with subcellular activation, explanted slices from fluorescently-tagged animal models can be used with high-precision inhibition of microtubule dynamics to examine the effects of this on downstream processes such as apoptotic pathways.
- (3) So far, photoswitchable control of microtubules has proved impossible to transfer into adult animals with the PSTs primarily due to the lack of metabolic stability. Because of their enhanced stability of the C=C double bond towards glutathione addition, another promising avenue would be to analyse the SBTubs' *in vivo* ADME-PK to test if their biochemical stability would allow them to be transferred into higher animal models.
- (4) From a chemical point of view, I believe unlocking the SBT scaffold, which permits polar functional substituents for drug-like structures together with enhanced biochemical stability, is highly valuable for progress in photopharmacology and can replace azobenzene-based photoswitches that have conceptual disadvantages as discussed before. This may influence not only research on microtubules but also on other high-value targets: for example, actin that recently has been addressed by photoswitches for the first time, although these are still based on less favourable azobenzenes.<sup>89</sup>

**2B:** In my third and fourth, papers we presented photoswitchable microtubule depolymerisers that are based on a hemithioindigo scaffold. We aimed to demonstrate that the unique features of the hemithioindigo scaffold, mainly the ability to accommodate a different range of substituent patterns, would allow *a priori* design of dark and lit-active compounds that can be directionally photoswitched. We modelled the HOTubs's substituent pattern to colchicine and for the HITubs we took indanocine as a template. During photocharacterisation we resolved the PSS (photostationary state), which specifies the equilibrium proportions of E and Z isomer at a certain wavelength. We successfully demonstrated that the HOTubs and HITubs indeed followed their predicted activity either as dark-active or lit-active compounds with the HITubs being 10 times more potent and we performed antiproliferative studies as well as immunofluorescence and cell cycle repartition experiments to make their microtubule depolymerising activity evident.

Despite the fact that we were able to reversibly photoswitch the compounds during photocharacterisation in a cuvette, we did not show reversible photoswitching of bioactivity in cells. As bidirectional photoswitching has already been achieved by the development of PSTs based on azobenzene, we decided to move our focus for the hemithioindigo-based photoswitches away from patterning a specimen with two different wavelengths and moved it



towards alternative substituent tolerance and inversed photo-response (dark-active), which is not possible for azobenzenes, to broaden the possible applications of photoswitches.

(1) Having worked with two different CDIs as templates, it is already benefiting our mechanistic studies of what the molecular basis for bioactivity/potency differences is, and will lead to more sophisticated structure-guided photopharmaceutical design.

(2) There may be only a few applications that can actually benefit from a dark active HTI-based compound, compared to a lit-active photoswitch. The main value of that part of the project, in my opinion, lies in showing that HTI-based photoswitches can, in general, be used as drug-like pharmacophores with free design control over the lit or dark-activity. This suggests that lit-active (planar) HTI-based photopharmaceuticals can be designed to replace (planar) trans-active azobenzenes, to avoid the drawbacks that azobenzene photoisomerization from trans to cis is incomplete and that the trans-isomer is continually regenerated by relaxation.

(3) As with the SBTs, we expect the C=C double bond to be more stable in the cellular environment than the N=N double bond of azobenzenes. So, HTIs may also suffer less compound degradation and fewer off-target effects, which is favourable for general biological use.

(4) One application for dark active compounds could be microtubule nucleation studies. Microtubules have an important role in cell polarization and it has been reported that asymmetrical nucleation is taking place on alternative MTOCs such as the Golgi.<sup>132</sup> Microtubule depolymerisation by application of a microtubule depolymeriser is a key step in these assays. Then, microtubule re-nucleation and rebuilding the microtubule network in the cell can be visualized by fluorescently labelled EB-proteins<sup>133</sup> after washout of the compound. Using dark active photoswitches would make the washout step redundant and by applying light to only an ROI in the cell, re-initialisation of microtubule nucleation can be spatiotemporally controlled to a cell region or compartment. This can be especially superior for the use in embryos during *in vivo* applications as the compound can be precisely deactivated in single cells by application of light, which could give insight in the role of microtubules during asymmetric cell division and cell fate determination in early embryogenesis.

**2C:** In my fifth paper, I analysed photoswitchable MT stabilisers for application in biological assays. Our goal was to develop and characterize these tools to make one crucial step towards progress in microtubule research with the use of light-controlled microtubule stabilisers. Microtubule stabilisers play an important role in microtubule research and in therapeutic settings. The different mode of action of microtubule stabilisers allows to shed light on variable research questions that cannot be approached with microtubule depolymerisers. Photoswitchable microtubule stabilisers permit optical control over microtubule dynamics and I applied them in biological assays to demonstrate their performance and conceptual advantages compared to classic microtubule stabilisers. We created AzTaxes by adding an azobenzene photoswitch to a taxane core, photocharacterised them, and tested them in biological assays including antiproliferation tests, cell cycle perturbation, tubulin immunofluorescence and performance in live-cell imaging of microtubule dynamics, which all

confirmed hallmarks of treatment with microtubule stabilisers with two to six-fold potency differences upon exposure to light.

**Critical comment on the results so far:** The rather small potency difference that limits the concentration range applicable to cells, and their too slow relaxation speed, are both challenges that need to be addressed in later generations of AzTax compounds. It was not possible to completely block or revert AzTax bioactivity by applying light of a certain wavelength *in situ*. Full and direct deactivation of the compound by light is desirable and will be the subject of later compound improvement. So far, the inhibition of microtubule polymerisation dynamics by AzTax3MP and the reduction in the number of EB3-comets, is only partially reversibly by diffusion of the active compound.

In conclusion, we reached our goal to produce the first photoswitchable microtubule stabilisers with taxane bioactivity. Generally, I believe that AzTax molecules will play an important role in unravelling processes that depend on spatial and temporal control of microtubules to take place, including mitosis, motility and neurobiology. Therefore, many next important steps can be made to employ and/or improve this tool.

(1) Progress has been made in resolving the formation of neurons in development by using microtubule stabilisers,<sup>122</sup> and they have also been used in elucidating nerve regeneration after injury, which includes reducing retraction bulbs,<sup>134</sup> and in reducing glial scarring after spinal cord injury.<sup>123</sup> With AzTax compounds, it will not only be possible to resolve these processes more precisely in time but also to get insight in the roles of glia and immune cells in close proximity to the injured nerve cells with single-cell spatial precision, which could not be done before.

(2) If AzTax-like photoswitchable stabilisers can be made with a different photoswitch scaffold providing better metabolic stability, it will vastly benefit studies of neuronal function and nerve regeneration. In the case of a metabolically stable, photocontrollable microtubule stabiliser can be developed; employing an SBT or HTI photoswitch, I believe it might revolutionize *in vivo* studies in adult animals. Neuroscience applications such as studies on nerve regeneration and spinal cord injuries could be moved from cell culture into adult *in vivo* models such as fluorescent microtubule reporter mice.<sup>135</sup>

## Outlook

The development of new and improved pharmaceuticals is indispensable for both basic research and for therapeutic medicine. Resolving processes accomplished by proteins that are not easy to control precisely by genetic engineering, which is the case for cytoskeleton proteins, is dependent on these new developments. In my work, I chose the microtubule cytoskeleton as a valuable target for small-molecule inhibitors. The major challenge in studying microtubule function and dynamics is the lack of spatiotemporal control of common tubulin inhibitors. In my studies, I show how newly designed photopharmaceuticals can exhibit optical control reversibly over microtubule dynamics through the application of light. These photoswitchable tubulin inhibitors allow manipulation of microtubules with spatiotemporal precision, which bears great potential for gaining insights into microtubule function in physiology and disease. For example, the development of a light-responsive analogue of the anticancer drug paclitaxel will allow analysing its action in detail, to resolve how the antitumor effect and the common severe side effects such as neurotoxicity arise, which can be key to developing drugs with reduced side effects. I have also shown how the rational choice of chemical scaffold and substituent patterns can modulate bioactivity and biostability of photoswitchable and non-photoswitchable tubulin inhibitors. Enhanced metabolic stability is a prerequisite for applying microtubule inhibitors *in vivo* and is necessary for moving photopharmacology from cell culture and small embryonic models into *in vivo* applications in adult animals, which has not been accomplished before. This will be a valuable second area of application for the pharmaceuticals developed through this work. Finally, in this work I have analysed a variety of rationally designed small-molecule pharmaceuticals that allow a wide range of polar substituents, different possibilities to tune cytotoxicity, and alternative relaxation rates and photoresponse compared to standard photoswitches. This new spectrum of possibilities will certainly inspire new ideas and opportunities for progress in the design and application of photoswitchable drugs looking beyond the field of microtubule inhibitors.

## Acknowledgements

I would like to thank Dr. Oliver Thorn-Seshold for the opportunity to work on my Ph.D. in his lab, his great supervision and insight and his outstanding support for me even in very challenging times. I also would like to thank Prof. Stefan Zahler for his supervision in the first year and his kind encouragement and support. Further thanks go to my family, who supported me on every step of the process as well as to my best friend Ellen Weber for lively discussions and great support. I also want to thank the whole Thorn-Seshold group for providing a great working environment, fruitful collaboration and an awesome time. Finally, I want to thank my boyfriend Benni Kaltschmidt, who has been standing adamantly at my side over the last months and significantly contributed to this thesis by cheering me up when everything seemed so dark.

## Appendix

### List of Abbreviations

ADME/PK:	Absorption, distribution, metabolism, excretion/ pharmacokinetics
ADP:	Adenosine diphosphate
ATP:	Adenosine triphosphate
CDI:	Colchicine domain inhibitor
GDP:	Guanosine diphosphate
GFP:	Green fluorescent protein
GTP:	Guanosine triphosphate
HTI:	Hemithioindigo
IF:	Intermediate filaments
MAP:	Microtubule associated protein
MT:	Microtubule
MTA:	Microtubule targeting agent
MTOCs:	Microtubule organizing centres
PST:	Photostatin
RFP:	Red fluorescent protein
ROI:	Region of interest
SAR:	Structure activity relationship
SBT:	Styrylbenzothiazole
VDA:	Vascular disrupting agent
YFP:	Yellow fluorescent protein

## Bibliography

1. Mostowy S, Cossart P. Septins: the fourth component of the cytoskeleton. *Nat Rev Mol Cell Biol.* 2012;13(3):183-194. doi:10.1038/nrm3284
2. Moseley J. An expanded view of the eukaryotic cytoskeleton. *Mol Biol Cell.* 2013;24(11):1615-1618. doi:10.1091/mbc.E12-10-0732
3. Fletcher D, Mullins RD. Cell mechanics and the cytoskeleton. *Nature.* 2010;463(7280):485-492. doi:10.1038/nature08908
4. Lodish H, Berk A, Zipursky SL, Matsudaira P, Baltimore D, Darnell J. *Molecular Cell Biology.* 4th ed. W. H. Freeman; 2000.
5. Sutherland JD, Witke W. Molecular genetic approaches to understanding the actin cytoskeleton. *Curr Opin Cell Biol.* 1999;11(1):142-151. doi:10.1016/S0955-0674(99)80018-0
6. Tozer GM, Akerman S, Cross NA, et al. Blood Vessel Maturation and Response to Vascular-Disrupting Therapy in Single Vascular Endothelial Growth Factor-A Isoform-Producing Tumors. *Cancer Res.* 2008;68(7):2301-2311. doi:10.1158/0008-5472.CAN-07-2011
7. Pollard T. Cytoskeletal functions of cytoplasmic contractile proteins. *J Supramol Struct.* 1976;5(3):317-334. doi:10.1002/jss.400050306
8. Wintrebert P. La rotation immédiate de l'oeuf pondu et la rotation d'activation chez *Discoglossus pictus*. *Oth CR Soc Biol.* 1931;106:439-442.
9. Gibbons IR, Rowe AJ. Dynein: A Protein with Adenosine Triphosphatase Activity from Cilia. *Science.* 1965;149(3682):424-426. doi:10.1126/science.149.3682.424
10. Summers KE, Gibbons IR. Adenosine triphosphate-induced sliding of tubules in trypsin-treated flagella of sea-urchin sperm. *Proc Natl Acad Sci U S A.* 1971;68(12):3092-3096. doi:10.1073/pnas.68.12.3092
11. Inoué S, Sato H. Cell motility by labile association of molecules. The nature of mitotic spindle fibers and their role in chromosome movement. *J Gen Physiol.* 1967;50(6):Suppl:259-292. <https://www.ncbi.nlm.nih.gov/emedien.ub.uni-muenchen.de/pmc/articles/PMC2225745/>
12. Weisenberg RC, Broisy GG, Taylor EWilliam. Colchicine-binding protein of mammalian brain and its relation to microtubules. *Biochemistry.* 1968;7(12):4466-4479. doi:10.1021/bi00852a043
13. Perry SV. When was actin first extracted from muscle? *J Muscle Res Cell Motil.* 2003;24(8):597-599. doi:10.1023/B:JURE.0000009917.02874.b0
14. Needham J, Kleinzeller A, Miall M, Dainty M, Needham M, Lawrence ASC. Is Muscle Contraction Essentially an Enzyme-Substrate Combination? *Nature.* 1942;150(3793):46-49. doi:10.1038/150046a0
15. Abercrombie M, Heaysman JE, Pegrum SM. The locomotion of fibroblasts in culture. I. Movements of the leading edge. *Exp Cell Res.* 1970;59(3):393-398. doi:10.1016/0014-4827(70)90646-4
16. Huxley AF, Niedergerke R. Structural changes in muscle during contraction; interference microscopy of living muscle fibres. *Nature.* 1954;173(4412):971-973. doi:10.1038/173971a0
17. Schroeder TE. The contractile ring. II. Determining its brief existence, volumetric changes, and vital role in cleaving *Arbacia* eggs. *J Cell Biol.* 1972;53(2):419-434. doi:10.1083/jcb.53.2.419
18. Pollard T, Korn E. *Acanthamoeba* myosin. I. Isolation from *Acanthamoeba castellanii* of an enzyme similar to muscle myosin. *J Biol Chem.* 1973;248(13):4682-4690.
19. Lazarides E, Weber K. Actin antibody: the specific visualization of actin filaments in non-muscle cells. *Proc Natl Acad Sci U S A.* 1974;71(6):2268-2272. doi:10.1073/pnas.71.6.2268
20. Feramisco JR. Microinjection of fluorescently labeled  $\alpha$ -actinin into living fibroblasts. *Proc Natl Acad Sci.* 1979;76(8):3967-3971. doi:10.1073/pnas.76.8.3967
21. Ishikawa H, Bischoff R, Holtzer H. Mitosis and intermediate-sized filaments in developing skeletal muscle. *J Cell Biol.* 1968;38(3):538-555. doi:10.1083/jcb.38.3.538
22. Taylor DL, Wang YL. Molecular cytochemistry: incorporation of fluorescently labeled actin into living cells. *Proc Natl Acad Sci U S A.* 1978;75(2):857-861. doi:10.1073/pnas.75.2.857
23. Baumann K. Milestones timeline : Nature Milestones in Cytoskeleton. Published 2008. Accessed July 7, 2020. <https://www.nature.com/milestones/milecyto/timeline.html>
24. Taylor DL, Wang Y-L. Fluorescently labelled molecules as probes of the structure and function of living cells. *Nature.* 1980;284(5755):405-410. doi:10.1038/284405a0
25. Johnson KA, Borisy GG. Kinetic analysis of microtubule self-assembly in vitro. *J Mol Biol.* 1977;117(1):1-31. doi:10.1016/0022-2836(77)90020-1
26. Nogales E, Wolf SG, Downing KH. Structure of the  $\alpha\beta$  tubulin dimer by electron crystallography. *Nature.* 1998;391(6663):199-203. doi:10.1038/34465
27. Nogales E, Whittaker M, Milligan RA, Downing KH. High-Resolution Model of the Microtubule. *Cell.* 1999;96(1):79-88. doi:10.1016/S0092-8674(00)80961-7
28. Piehl M, Tulu US, Wadsworth P, Cassimeris L. Centrosome maturation: Measurement of microtubule nucleation throughout the cell cycle by using GFP-tagged EB1. *Proc Natl Acad Sci.* 2004;101(6):1584-1588. doi:10.1073/pnas.0308205100

29. Akhmanova A, Steinmetz MO. Tracking the ends: a dynamic protein network controls the fate of microtubule tips. *Nat Rev Mol Cell Biol.* 2008;9(4):309-322. doi:10.1038/nrm2369
30. Etienne-Manneville S. Microtubules in cell migration. *Annu Rev Cell Dev Biol.* 2013;29:471-499. doi:https://doi.org/10.1146/annurev-cellbio-101011-155711
31. Titus J, Wadsworth P. Mitotic Spindle Assembly: The Role of Motor Proteins. In: *ELS.* American Cancer Society; 2012. doi:10.1002/9780470015902.a0022519
32. She Z-Y, Yang W-X. Molecular mechanisms of kinesin-14 motors in spindle assembly and chromosome segregation. *J Cell Sci.* 2017;130(13):2097-2110. doi:10.1242/jcs.200261
33. Goldstein L, Yang Z. Microtubule-Based Transport Systems in Neurons: The Roles of Kinesins and Dyneins. *Annu Rev Neurosci.* 2000;23(1):39-71. doi:10.1146/annurev.neuro.23.1.39
34. Mitchison T, Kirschner M. Dynamic instability of microtubule growth. *Nature.* 1984;312(5991):237-242. doi:10.1038/312237a0
35. Stanton RA, Gernert KM, Nettles JH, Aneja R. Drugs that target dynamic microtubules: A new molecular perspective. *Med Res Rev.* 2011;31(3):443-481. doi:10.1002/med.20242
36. McIntosh JR, Grishchuk EL, West RR. Chromosome-Microtubule Interactions During Mitosis. *Annu Rev Cell Dev Biol.* 2002;18(1):193-219. doi:10.1146/annurev.cellbio.18.032002.132412
37. Song Y, Brady ST. Post-translational modifications of tubulin: pathways to functional diversity of microtubules. *Trends Cell Biol.* 2015;25(3):125-136. doi:10.1016/j.tcb.2014.10.004
38. Roll-Mecak A. How cells exploit tubulin diversity to build functional cellular microtubule mosaics. *Curr Opin Cell Biol.* 2019;56:102-108. doi:10.1016/j.ceb.2018.10.009
39. Janke C, Magiera MM. The tubulin code and its role in controlling microtubule properties and functions. *Nat Rev Mol Cell Biol.* Published online February 27, 2020. doi:10.1038/s41580-020-0214-3
40. Parker AL, Teo WS, McCarroll JA, Kavallaris M. An Emerging Role for Tubulin Isoforms in Modulating Cancer Biology and Chemotherapy Resistance. *Int J Mol Sci.* 2017;18(7):1434. doi:10.3390/ijms18071434
41. Janke C. The tubulin code: Molecular components, readout mechanisms, and functions. *J Cell Biol.* 2014;206(4):461-472. doi:10.1083/jcb.201406055
42. Mandelkow E, Mandelkow E-M. Microtubules and microtubule-associated proteins. *Curr Opin Cell Biol.* 1995;7(1):72-81. doi:10.1016/0955-0674(95)80047-6
43. Ayanlaja AA, Xiong Y, Gao Y, Ji G, Tang CT. Distinct Features of Doublecortin as a Marker of Neuronal Migration and Its Implications in Cancer Cell Mobility. *Front Mol Neurosci.* 2017;10. doi:10.3389/fnmol.2017.00199
44. Fodde R, Kuipers J, Rosenberg C, et al. Mutations in the APC tumour suppressor gene cause chromosomal instability. *Nat Cell Biol.* 2001;3(4):433-438. doi:10.1038/35070129
45. Gierke S, Kumar P, Wittmann T. Analysis of microtubule polymerization dynamics in live cells. *Methods Cell Biol.* 2010;97:15-33. doi:10.1016/S0091-679X(10)97002-7
46. Goshima G, Nédélec F, Vale R. Mechanisms for focusing mitotic spindle poles by minus end-directed motor proteins. *J Cell Biol.* 2005;171(2):229-240. doi:10.1083/jcb.200505107
47. Hartman JJ, Mahr J, McNally K, et al. Katanin, a Microtubule-Severing Protein, Is a Novel AAA ATPase that Targets to the Centrosome Using a WD40-Containing Subunit. *Cell.* 1998;93(2):277-287. doi:10.1016/S0092-8674(00)81578-0
48. Yu W, Qiang L, Solowska JM, Karabay A, Korulu S, Baas PW. The Microtubule-severing Proteins Spastin and Katanin Participate Differently in the Formation of Axonal Branches. *Mol Biol Cell.* 2008;19(4):1485-1498. doi:10.1091/mbc.E07-09-0878
49. Newton C, Wagenbach M, Ovechkina Y, Wordeman L, Wilson L. MCAK, a Kin I kinesin, increases the catastrophe frequency of steady-state HeLa cell microtubules in an ATP-dependent manner in vitro. *FEBS Lett.* 2004;572(1-3):80-84. doi:10.1016/j.febslet.2004.06.093
50. Steinmetz M, Kammerer R, Jahnke W, Goldie K, Lustig A, van Oostrum J. Op18/stathmin caps a kinked protofilament-like tubulin tetramer. *EMBO J.* 2000;19(4):572-580. doi:10.1093/emboj/19.4.572
51. Bhat K, Setaluri V. Microtubule-Associated Proteins as Targets in Cancer Chemotherapy. *Clin Cancer Res.* 2007;13(10):2849-2854. doi:10.1158/1078-0432.CCR-06-3040
52. Li L, Jiang S, Li X, Liu Y, Su J, Chen J. Recent advances in trimethoxyphenyl (TMP) based tubulin inhibitors targeting the colchicine binding site. *Eur J Med Chem.* 2018;151:482-494. doi:10.1016/j.ejmech.2018.04.011
53. Steinmetz M, Prota A. Microtubule-Targeting Agents: Strategies To Hijack the Cytoskeleton. *Trends Cell Biol.* 2018;28(10):776-792. doi:10.1016/j.tcb.2018.05.001
54. Field JJ, Díaz JF, Miller JH. The Binding Sites of Microtubule-Stabilizing Agents. *Chem Biol.* 2013;20(3):301-315. doi:10.1016/j.chembiol.2013.01.014
55. Gigant B, Cormier A, Dorléans A, Ravelli RBG, Knossow M. Microtubule-Destabilizing Agents: Structural and Mechanistic Insights from the Interaction of Colchicine and Vinblastine with Tubulin. In: *Tubulin-Binding Agents: Synthetic, Structural and Mechanistic Insights.* Topics in Current Chemistry. Springer; 2009:259-278. doi:10.1007/128\_2008\_11

56. Seligmann J, Twelves C. Tubulin: an example of targeted chemotherapy. *Future Med Chem.* 2013;5(3):339-352. doi:10.4155/fmc.12.217
57. Cao Y-N, Zheng L-L, Wang D, Liang X-X, Gao F, Zhou X-L. Recent advances in microtubule-stabilizing agents. *Eur J Med Chem.* 2018;143:806-828. doi:10.1016/j.ejmech.2017.11.062
58. Siegel RL, Miller KD, Jemal A. Cancer statistics, 2020. *CA Cancer J Clin.* 2020;70(1):7-30. doi:10.3322/caac.21590
59. Tron GC, Pirali T, Sorba G, Pagliai F, Busacca S, Genazzani AA. Medicinal Chemistry of Combretastatin A4: Present and Future Directions. *J Med Chem.* 2006;49(11):3033-3044. doi:10.1021/jm0512903
60. Ji Y-T, Liu Y-N, Liu Z-P. Tubulin Colchicine Binding Site Inhibitors as Vascular Disrupting Agents in Clinical Developments. *Current Medicinal Chemistry.* Published March 31, 2015. Accessed August 5, 2020. <http://www.eurekaselect.com/127664/article>
61. McLoughlin EC, O'Boyle NM. Colchicine-Binding Site Inhibitors from Chemistry to Clinic: A Review. *Pharmaceuticals.* 2020;13(1):8. doi:10.3390/ph13010008
62. Parker AL, Kavallaris M, McCarroll JA. Microtubules and Their Role in Cellular Stress in Cancer. *Front Oncol.* 2014;4. doi:10.3389/fonc.2014.00153
63. Dominguez R, Holmes KC. Actin Structure and Function. *Annu Rev Biophys.* 2011;40:169-186. doi:https://doi.org/10.1146/annurev-biophys-042910-155359
64. Olave IA, Reck-Peterson SL, Crabtree GR. Nuclear actin and actin-related proteins in chromatin remodeling. *Annu Rev Biochem.* 2002;71:755-781. doi:10.1146/annurev.biochem.71.110601.135507
65. Chhabra D, Bao S, Remedios CG. The distribution of cofilin and DNase I in vivo. *Cell Res.* 2002;12(3):207-214. doi:10.1038/sj.cr.7290126
66. Herman IM. Actin isoforms. *Curr Opin Cell Biol.* 1993;5(1):48-55. doi:10.1016/S0955-0674(05)80007-9
67. Varland S, Vandekerckhove J, Drazic A. Actin Post-translational Modifications: The Cinderella of Cytoskeletal Control. *Trends Biochem Sci.* 2019;44(6):502-516. doi:10.1016/j.tibs.2018.11.010
68. Winder SJ, Ayscough KR. Actin-binding proteins. *J Cell Sci.* 2005;118(4):651-654. doi:10.1242/jcs.01670
69. Lee SH, Dominguez R. Regulation of Actin Cytoskeleton Dynamics in Cells. *Mol Cells.* 2010;29(4):311-325. Accessed July 7, 2020. <https://www.ncbi.nlm.nih.gov/pmc/articles/PMC3910092/>
70. Bearer EL, Prakash JM, Li Z. Actin Dynamics in Platelets. *Int Rev Cytol.* 2002;217:137-182. doi:https://doi.org/10.1016/s0074-7696(02)17014-8
71. Titus J. Myosins. *Curr Opin Cell Biol.* 1993;5(1):77-81. doi:10.1016/S0955-0674(05)80011-0
72. Hartman MA, Spudich JA. The myosin superfamily at a glance. *J Cell Sci.* 2012;125(7):1627-1632. doi:10.1242/jcs.094300
73. Roesles J, Tsiavalariis G. Actin-microtubule interplay coordinates spindle assembly in human oocytes. *Nat Commun.* 2019;10(1):1-10. doi:10.1038/s41467-019-12674-9
74. Mills JC, Stone NL, Pittman RN. Extranuclear apoptosis. The role of the cytoplasm in the execution phase. *J Cell Biol.* 1999;146(4):703-708. doi:10.1083/jcb.146.4.703
75. Pawlak G, Helfman DM. Cytoskeletal changes in cell transformation and tumorigenesis. *Curr Opin Genet Dev.* 2001;11(1):41-47. doi:10.1016/S0959-437X(00)00154-4
76. Hesse M, Magin TM, Weber K. Genes for intermediate filament proteins and the draft sequence of the human genome: novel keratin genes and a surprisingly high number of pseudogenes related to keratin genes 8 and 18. *J Cell Sci.* 2001;114(14):2569-2575. Accessed March 26, 2020. <https://jcs.biologists.org/content/114/14/2569>
77. Abercrombie M, Gao J, Humbert J, et al. The importance of intermediate filaments in the adaptation of tissues to mechanical stress: Evidence from gene knockout studies. *Biol Cell.* 1997;89(2):85-97. doi:10.1016/S0248-4900(99)80068-9
78. Herrmann H, Bär H, Kreplak L, Strelkov SV, Aebi U. Intermediate filaments: from cell architecture to nanomechanics. *Nat Rev Mol Cell Biol.* 2007;8(7):562-573. doi:10.1038/nrm2197
79. Etienne-Manneville S. Cytoplasmic Intermediate Filaments in Cell Biology. *Annu Rev Cell Dev Biol.* 2018;34(1):1-28. doi:10.1146/annurev-cellbio-100617-062534
80. Kreplak L, Bär H, Leterrier JF, Herrmann H, Aebi U. Exploring the Mechanical Behavior of Single Intermediate Filaments. *J Mol Biol.* 2005;354(3):569-577. doi:10.1016/j.jmb.2005.09.092
81. Etienne-Manneville. Cytoplasmic Intermediate Filaments in Cell Biology. *Annu Rev Cell Dev Biol.* 2018;34(1):1-28. doi:https://doi.org/10.1146/annurev-cellbio-100617-062534
82. Omary MB, Coulombe PA, McLean WHI. Intermediate Filament Proteins and Their Associated Diseases. *N Engl J Med.* 2004;351(20):2087-2100. doi:10.1056/NEJMra040319
83. Steinert PM. Intermediate filaments in health and disease. *Exp Mol Med.* 1996;28(2):55-63. doi:10.1038/emm.1996.9
84. Brenner SL, Korn ED. The effects of cytochalasins on actin polymerization and actin ATPase provide insights into the mechanism of polymerization. *J Biol Chem.* 1980;255(3):841-844. doi:https://pubmed.ncbi.nlm.nih.gov/emedien.ub.uni-muenchen.de/6444302/



85. Fenteany G, Zhu S. Small-Molecule Inhibitors of Actin Dynamics and Cell Motility. *Curr Top Med Chem.* 2003;3(6):593-616. doi:https://doi.org/10.2174/1568026033452348
86. Coué M, Brenner SL, Spector I, Korn ED. Inhibition of actin polymerization by latrunculin A. *FEBS Lett.* 1987;213(2):316-318. doi:10.1016/0014-5793(87)81513-2
87. Bubb MR, Senderowicz AMJ, Sausville EA, Duncan LK, Korn ED. Jasplakinolide, a cytotoxic natural product, induces actin polymerization and competitively inhibits the binding of phalloidin to F-actin. *J Biol Chem.* 1994;269(21):14869-14871. doi:https://pubmed.ncbi.nlm.nih.gov/emedien.uni-muenchen.de/8195116/
88. Spector I, Braet F, Shochet NR, Bubb MR. New anti-actin drugs in the study of the organization and function of the actin cytoskeleton. *Microsc Res Tech.* 1999;47(1):18-37. doi:10.1002/(SICI)1097-0029(19991001)47:1<18::AID-JEMT3>3.0.CO;2-E
89. Borowiak M, Küllmer F, Gegenfurtner F, et al. Optical Manipulation of F-Actin with Photoswitchable Small Molecules. *J Am Chem Soc.* 2020;142(20):9240-9249. doi:10.1021/jacs.9b12898
90. Bonello TT, Stehn JR, Gunning PW. New approaches to targeting the actin cytoskeleton for chemotherapy. *Future Med Chem.* 2009;1(7):1311-1331. doi:10.4155/fmc.09.99
91. Stehn JR, Haass NK, Bonello T, et al. A Novel Class of Anticancer Compounds Targets the Actin Cytoskeleton in Tumor Cells. *Cancer Res.* 2013;73(16):5169-5182. doi:10.1158/0008-5472.CAN-12-4501
92. Foerster F, Braig S, Moser C, et al. Targeting the actin cytoskeleton: selective antitumor action via trapping PKC  $\epsilon$ . *Cell Death Dis.* 2014;5(8):e1398-e1398. doi:10.1038/cddis.2014.363
93. Satelli A, Li S. Vimentin as a potential molecular target in cancer therapy Or Vimentin, an overview and its potential as a molecular target for cancer therapy. *Cell Mol Life Sci CMLS.* 2011;68(18):3033-3046. doi:10.1007/s00018-011-0735-1
94. Aiken J, Buscaglia G, Aiken AS, Moore JK, Bates EA. Tubulin mutations in brain development disorders: Why haploinsufficiency does not explain TUBA1A tubulinopathies. *Cytoskeleton.* 2020;77(3-4):40-54. doi:10.1002/cm.21567
95. Shi J, Mitchison TJ. Cell death response to anti-mitotic drug treatment in cell culture, mouse tumor model and the clinic. *Endocr Relat Cancer.* 2017;24(9):T83-T96. doi:10.1530/ERC-17-0003
96. Kingston DGI. Taxol, a molecule for all seasons. *Chem Commun.* 2001;(10):867-880. doi:10.1039/B100070P
97. Siemann DW. The Unique Characteristics of Tumor Vasculature and Preclinical Evidence for its Selective Disruption by Tumor-Vascular Disrupting Agents. *Cancer Treat Rev.* 2011;37(1):63-74. doi:10.1016/j.ctrv.2010.05.001
98. Hadfield JA, Ducki S, Hirst N, McGown AT. Tubulin and microtubules as targets for anticancer drugs. *Prog Cell Cycle Res.* 2003;5:19.
99. Pérez-Pérez M-J, Priego E-M, Bueno O, Martins MS, Canela M-D, Liekens S. Blocking Blood Flow to Solid Tumors by Destabilizing Tubulin: An Approach to Targeting Tumor Growth. *J Med Chem.* 2016;59(19):8685-8711. doi:10.1021/acs.jmedchem.6b00463
100. Greene LM, Meegan MJ, Zisterer DM. Combretastatins: More Than Just Vascular Targeting Agents? *J Pharmacol Exp Ther.* 2015;355(2):212-227. doi:10.1124/jpet.115.226225
101. Nguyen TL, McGrath C, Hermone AR, et al. A Common Pharmacophore for a Diverse Set of Colchicine Site Inhibitors Using a Structure-Based Approach. *J Med Chem.* 2005;48(19):6107-6116. doi:10.1021/jm050502t
102. Zenker J, White MD, Templin RM, et al. A microtubule-organizing center directing intracellular transport in the early mouse embryo. *Science.* 2017;357(6354):925-928. doi:10.1126/science.aam9335
103. Ferenczi EA, Tan X, Huang CL-H. Principles of Optogenetic Methods and Their Application to Cardiac Experimental Systems. *Front Physiol.* 2019;10. doi:https://doi.org/10.3389/fphys.2019.01096
104. Bamberg E, Gärtner W, Trauner D. Introduction: Optogenetics and Photopharmacology. *Chem Rev.* 2018;118(21):10627-10628. doi:10.1021/acs.chemrev.8b00483
105. van Haren J, Charafeddine RA, Ettinger A, Wang H, Hahn KM, Wittmann T. Local control of intracellular microtubule dynamics by EB1 photodissociation. *Nat Cell Biol.* 2018;20(3):252-261. doi:10.1038/s41556-017-0028-5
106. Hansen MJ, Velema WA, de Bruin G, Overkleeft HS, Szymanski W, Feringa BL. Proteasome Inhibitors with Photocontrolled Activity. *ChemBioChem.* 2014;15(14):2053-2057. doi:10.1002/cbic.201402237
107. Ferreira R, Nilsson JR, Solano C, Andréasson J, Grøtli M. Design, Synthesis and Inhibitory Activity of Photoswitchable RET Kinase Inhibitors. *Sci Rep.* 2015;5. doi:https://doi.org/10.1038/srep09769
108. Chambers JJ, Banghart MR, Trauner D, Kramer RH. Light-Induced Depolarization of Neurons Using a Modified Shaker K<sup>+</sup> Channel and a Molecular Photoswitch. *J Neurophysiol.* 2006;96(5):2792-2796. doi:10.1152/jn.00318.2006
109. Borowiak M, Nahaboo W, Reynders M, et al. Photoswitchable Inhibitors of Microtubule Dynamics Optically Control Mitosis and Cell Death. *Cell.* 2015;162(2):403-411. doi:10.1016/j.cell.2015.06.049
110. Velema WA, Szymanski W, Feringa BL. Photopharmacology: Beyond Proof of Principle. *J Am Chem Soc.* 2014;136(6):2178-2191. doi:10.1021/ja413063e

111. Lerch MM, Hansen MJ, van Dam GM, Szymanski W, Feringa BL. Emerging Targets in Photopharmacology. *Angew Chem Int Ed*. 2016;55(37):10978-10999. doi:10.1002/anie.201601931
112. Gao. A Robust, GFP-Orthogonal Photoswitchable Inhibitor Scaffold Extends Optical Control over the Microtubule Cytoskeleton. *Cell Chem Biol*. 2021;28:1. doi:https://doi.org/10.1016/j.chembiol.2020.11.007
113. Zhu M, Zhou H. Azobenzene-based small molecular photoswitches for protein modulation. *Org Biomol Chem*. 2018;16(44):8434-8445. doi:10.1039/C8OB02157K
114. Singh A, Saha T, Begemann I, et al. Polarized microtubule dynamics directs cell mechanics and coordinates forces during epithelial morphogenesis. *Nat Cell Biol*. 2018;20(10):1126-1133. doi:10.1038/s41556-018-0193-1
115. Theisen U, Ernst AU, Heyne RLS, Ring TP, Thorn-Seshold O, Köster RW. Microtubules and motor proteins support zebrafish neuronal migration by directing cargo. *J Cell Biol*. 2020;219(10):e201908040. doi:10.1083/jcb.201908040
116. Schehr M, Ianes C, Weisner J, et al. 2-Azo-, 2-diazocine-thiazols and 2-azo-imidazoles as photoswitchable kinase inhibitors: limitations and pitfalls of the photoswitchable inhibitor approach. *Photochem Photobiol Sci*. 2019;18(6):1398-1407. doi:10.1039/C9PP00010K
117. Wiedbrauk S, Dube H. Hemithioindigo—an emerging photoswitch. *Tetrahedron Lett*. 2015;56(29):4266-4274. doi:10.1016/j.tetlet.2015.05.022
118. Yamaguchi T, Seki T, Tamaki T, Ichimura K. Photochromism of Hemithioindigo Derivatives. I. Preparation and Photochromic Properties in Organic Solvents. *Bull Chem Soc Jpn*. 1992;65(3):649-656. doi:10.1246/bcsj.65.649
119. Sailer A, Ermer F, Kraus Y, et al. Hemithioindigos for Cellular Photopharmacology: Desymmetrised Molecular Switch Scaffolds Enabling Design Control over the Isomer-Dependency of Potent Antimitotic Bioactivity. *ChemBiochem Eur J Chem Biol*. 2019;20(10):1305-1314. doi:10.1002/cbic.201800752
120. Chen J-G, Horwitz SB. Differential Mitotic Responses to Microtubule-stabilizing and -destabilizing Drugs. *Cancer Res*. 2002;62(7):1935-1938. doi:https://doi.org/10.4161/cc.7.4.5313.
121. Schiff PB, Horwitz SB. Taxol assembles tubulin in the absence of exogenous guanosine 5'-triphosphate or microtubule-associated proteins. *Biochemistry*. 1981;20(11):3247-3252. doi:10.1021/bi00514a041
122. Witte H, Neukirchen D, Bradke F. Microtubule stabilization specifies initial neuronal polarization. *J Cell Biol*. 2008;180(3):619-632. doi:10.1083/jcb.200707042
123. Hellal F, Hurtado A, Ruschel J, et al. Microtubule stabilization reduces scarring and causes axon regeneration after spinal cord injury. *Science*. 2011;331(6019):928-931. doi:10.1126/science.1201148
124. McGrogan BT, Gilmartin B, Carney DN, McCann A. Taxanes, microtubules and chemoresistant breast cancer. *Biochim Biophys Acta*. 2008;1785(2):37. doi:https://doi.org/doi: 10.1016/j.bbcan.2007.10.004.
125. Dcona MM, Mitra D, Goehle RW, Gewirtz DA, Lebman DA, Hartman MCT. Photocaged permeability: a new strategy for controlled drug release. *Chem Commun*. 2012;48(39):4755. doi:10.1039/c2cc30819c
126. Wong PT, Tang S, Cannon J, et al. A Thioacetal Photocage Designed for Dual Release: Application in the Quantitation of Therapeutic Release via Synchronous Reporter Decaging. *ChemBiochem Eur J Chem Biol*. 2017;18(1):126-135. doi:10.1002/cbic.201600494
127. Reeßing F, Szymanski W. Beyond Photodynamic Therapy: Light-Activated Cancer Chemotherapy. *Curr Med Chem*. 2018;24(42). doi:10.2174/0929867323666160906103223
128. Klán P, Šolomek T, Bochet CG, et al. Photoremovable Protecting Groups in Chemistry and Biology: Reaction Mechanisms and Efficacy. *Chem Rev*. 2013;113(1):119-191. doi:10.1021/cr300177k
129. Noguchi M, Skwarczynski M, Prakash H, et al. Development of novel water-soluble photocleavable protective group and its application for design of photoresponsive paclitaxel prodrugs. *Bioorg Med Chem*. 2008;16(10):5389-5397. doi:10.1016/j.bmc.2008.04.022
130. Gill JH, Rockley KL, De Santis C, Mohamed AK. Vascular Disrupting Agents in cancer treatment: Cardiovascular toxicity and implications for co-administration with other cancer chemotherapeutics. *Pharmacol Ther*. 2019;202:18-31. doi:10.1016/j.pharmthera.2019.06.001
131. Ketschek A, Spillane M, Dun X-P, Hardy H, Chilton J, Gallo G. Drebrin Coordinates the Actin and Microtubule Cytoskeleton During the Initiation of Axon Collateral Branches. *Dev Neurobiol*. 2016;76(10):1092-1110. doi:10.1002/dneu.22377
132. Zhu X, Kaverina I. Golgi as an MTOC: making microtubules for its own good. *Histochem Cell Biol*. 2013;140(3):361-367. doi:10.1007/s00418-013-1119-4
133. Zhu X, Kaverina I. Quantification of asymmetric microtubule nucleation at sub-cellular structures. *Methods Mol Biol Clifton Nj*. 2011;777:235-244. doi:10.1007/978-1-61779-252-6\_17
134. Ertürk A, Hellal F, Enes J, Bradke F. Disorganized Microtubules Underlie the Formation of Retraction Bulbs and the Failure of Axonal Regeneration. *J Neurosci*. 2007;27(34):9169-9180. doi:https://doi.org/10.1523/JNEUROSCI.0612-07.2007
135. Kleele T, Marinković P, Williams PR, et al. An assay to image neuronal microtubule dynamics in mice. *Nat Commun*. 2014;5(1):1-10. doi:10.1038/ncomms5827

## Supplementary Information

### **Supplementary Information Chapter 3: Microtubule depolymerisers with potential VDA activity**

License

Reprinted with permission from: Yvonne Kraus, Carina Glas, Benedikt Melzer, Constanze Heise, Monique Preuße, Franz Bracher, Oliver Thorn-Seshold, Isoquiniline-based biaryls as a robust scaffold for microtubule inhibitors, *European Journal of Medicinal Chemistry* **2020**, *186*, 111865. Copyright 2019 Elsevier Masson SAS.

## Supporting Information

# Isoquinoline-based biaryls as a robust scaffold for microtubule inhibitors

Yvonne Kraus<sup>1,#</sup>, Carina Glas<sup>1,#</sup>, Benedikt Melzer<sup>1</sup>, Li Gao<sup>1</sup>, Constanze Heise<sup>1</sup>,  
Monique Preusse<sup>1</sup>, Julia Ahlfeld<sup>1</sup>, Franz Bracher<sup>1</sup>, Oliver Thorn-Seshold<sup>1,\*</sup>

1: Department of Pharmacy – Center for Drug Research, Ludwig-Maximilians University,  
Butenandtstraße 5-13, Munich 81377, Germany

# These authors contributed equally to this work.

ORCIDs C.G. 0000-0002-5014-4921; J.A. 0000-0002-4879-4159; F.B. 0000-0003-0009-8629;

O.T.-S. 0000-0003-3981-651X

\*Correspondence to O.T.-S. ([oliver.thorn-seshold@cup.lmu.de](mailto:oliver.thorn-seshold@cup.lmu.de))

### **Table of Contents**

<b>Part A: Chemical Synthesis .....</b>	<b>2</b>
Conventions.....	2
Synthesis procedures .....	4
<b>Part B: Biochemistry <i>in vitro</i>.....</b>	<b>16</b>
Tubulin polymerisation <i>in vitro</i> .....	16
Metabolic stability.....	16
CYP450 inhibition .....	18
hERG inhibition.....	19
Determination of distribution coefficient (logD, pH 7.4).....	20
Solubility determination of IQTub4P .....	20
<b>Part C: Biological Data .....</b>	<b>21</b>
Cell assay methods.....	21
Immunofluorescence imaging of microtubule networks.....	23
Determination of safe <i>in vivo</i> dosing parameters.....	23
<b>Supplementary Information Bibliography.....</b>	<b>24</b>
<b>Part D: Selected NMR spectra.....</b>	<b>25</b>

## Part A: Chemical Synthesis

### Conventions

Abbreviations: The following abbreviations are used: hexanes – distilled isohexanes, EtOAc – ethyl acetate, Me – methyl, MeCN – acetonitrile, DCM – dichloromethane, DMSO – dimethylsulfoxide, PBS – phosphate-buffered saline aqueous buffer, THF – tetrahydrofuran.

Safety Hazards: no unusual safety hazards were encountered.

Reagents and Conditions: Unless stated otherwise, (1) all reactions and purifications were performed with unpurified, undried, non-degassed solvents and reagents, used as obtained, under closed air atmosphere without special precautions, unless stated otherwise; (2) “hexane” used for chromatography was distilled from commercial crude isohexane fraction by rotary evaporation; (3) “column” and “chromatography” refer to manual flash column chromatography on Merck silica gel Si-60 (40–63  $\mu\text{m}$ ); (4) “MPLC” refers to flash column chromatography purification on a Biotage Isolera Spektra system, using prepacked silica cartridges purchased from Biotage; (5) procedures and yields are mostly unoptimised; (6) yields refer to isolated chromatographically and spectroscopically pure materials; (7) all eluent and solvent mixtures are given as volume ratios unless otherwise specified; (8) for chromatography eluents e.g. “3:1  $\rightarrow$  1:1” indicates a stepwise or continual gradient of eluent composition.

Thin-layer chromatography: (TLC) was run on 0.25 mm Merck silica gel plates (60, F-254). Plates were visualised using UV light (254 nm or 365 nm) or staining with 1% aq.  $\text{KMnO}_4$  or CAM (ceric ammonium molybdate).

NMR: Standard NMR characterisation was performed by  $^1\text{H}$ - and  $^{13}\text{C}$ -NMR spectra recorded on an Avance III HD 400 MHz Bruker BioSpin and Avance III HD 500 MHz Bruker BioSpin ( $^1\text{H}$ : 400 MHz and 500 MHz,  $^{13}\text{C}$ : 101 MHz and 126 MHz) using the deuterated solvent stated. Chemical shifts ( $\delta$ ) are reported in ppm calibrated to residual non-perdeuterated solvent as an internal reference<sup>1</sup>. Peak descriptions singlet (s), doublet (d), triplet (t), and multiplet (m) are used. Coupling constants  $J$  are given in Hz. NMR spectra are given in Part D.

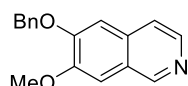
HRMS: High-resolution mass spectrometry (HRMS) was carried out by the Zentrale Analytik of the Faculty of Chemistry and Pharmacy of the LMU Munich (electron impact (EI) at 70 eV with a Thermo Finnigan MAT 95 or a Jeol GCmate II spectrometer; electrospray ionization (ESI) with a Thermo Finnigan LTQ FT Ultra Fourier Transform Ion Cyclotron resonance mass spectrometer) in positive or negative mode as stated.

**HPLC-MS:** Analytical measurements for determination of the purities of the final products were performed on an Agilent 1100 SL coupled HPLC-MS system with H<sub>2</sub>O:MeCN eluent gradients through a Thermo Scientific Hypersil GOLD™ C18 column (1.9 μm; 3×50 mm) maintained at 25°C, detected on an Agilent 1100 series diode array detector and a Bruker Daltonics HCT-Ultra spectrometer (ESI mode, unit m/z).

## Synthesis procedures

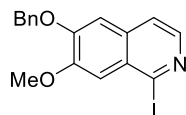
### 6-(Benzyloxy)-7-methoxyisoquinoline (4)

6-(benzyloxy)-7-methoxyisoquinoline (**4**) was first described in 1961 by Battersby et. al.<sup>2</sup> in the context of a synthetic protocol towards (±)-coreximine using a different synthetic procedure.



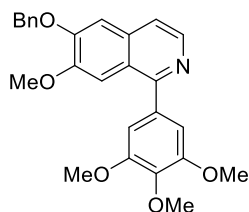
4-benzyloxy-3-methoxybenzaldehyde (4.99 g, 20.6 mmol) was dissolved in toluene (50 mL) and aminoacetaldehyde dimethyl acetal (2.38 g, 22.7 mmol) was added. Using a Dean-Stark apparatus the reaction mixture was heated to reflux for 16 h. After cooling to room temperature the volatiles were evaporated and the crude redissolved in MeOH (100 mL). The mixture was cooled to 0°C and NaBH<sub>4</sub> (1.56 g, 41.2 mmol) was added portion-wise over 30 min, then the reaction mixture was warmed to room temperature and stirred for 4 h. The volatiles were evaporated and the crude taken up in water (100 mL) then extracted with DCM (3 × 100 mL). The combined organic layers were dried over Na<sub>2</sub>SO<sub>4</sub>, filtered and concentrated. The crude product was redissolved in DCM (100 mL) and NaOH (1.40 g, 35.0 mmol) and tetrabutylammonium hydrogensulfate (0.490 g, 1.44 mmol) were added. After stirring for 10 min at room temperature a solution of *p*-toluenesulfonyl chloride (4.71 g, 24.7 mmol) in DCM (60 mL) was added dropwise over 1 h. The reaction mixture was stirred for an additional hour. Water (100 mL) was added, phases were separated, the organic phase washed with water (2 x 100 mL) and brine (100 mL), dried over Na<sub>2</sub>SO<sub>4</sub> and concentrated. The resulting crude product was dissolved in 1,4-dioxane (150 mL), aq. 6 M HCl (30 mL) was added and the reaction mixture heated to reflux for 16 h. After cooling to room temperature, the solution was poured into water (150 mL) and washed with diethyl ether (2 x 100 mL). Using a 6 M NaOH solution the aqueous phase was adjusted to pH > 9 and extracted with DCM (3 x 150 mL). The combined organic layers were dried over Na<sub>2</sub>SO<sub>4</sub> and concentrated *in vacuo*. The resulting crude product was purified by flash column chromatography (100% EtOAc) to give 6-(benzyloxy)-7-methoxyisoquinoline (**4**) as a white solid (1.29 g, 4.88 mmol, 24%).

**HRMS (EI<sup>+</sup>):** 265.1103 calculated for C<sub>17</sub>H<sub>15</sub>NO<sub>2</sub><sup>+</sup> [M]<sup>+</sup>, 265.1110 found. **<sup>1</sup>H NMR (400 MHz, CDCl<sub>3</sub>):** δ (ppm) = 9.04 (s, 1H, 1-H), 8.36 (d, *J* = 5.6 Hz, 1H, 3-H), 7.51 – 7.47 (m, 2H, 2', 6'-H), 7.44 (d, *J* = 5.6 Hz, 1H, 4-H), 7.43 – 7.38 (m, 2H, 3', 5'-H), 7.36 – 7.31 (m, 1H, 4'-H), 7.21 (s, 1H, 8-H), 7.10 (s, 1H, 5-H), 5.29 (s, 2H, CH<sub>2</sub>), 4.03 (s, 3H, OCH<sub>3</sub>). **<sup>13</sup>C NMR (101 MHz, CDCl<sub>3</sub>):** δ (ppm) = 152.3 (C-6), 150.8 (C-7), 150.1 (C-1), 142.1 (C-3), 136.2 (C-1'), 132.5 (C-4a), 128.9 (2C, C-3' and C-5'), 128.3 (C-4'), 127.4 (2C, C-2' and C-6'), 125.0 (C-8a), 119.4 (C-4), 106.5 (C-5), 105.7 (C-8), 70.9 (CH<sub>2</sub>), 56.2 (OCH<sub>3</sub>).

**6-(Benzyloxy)-1-iodo-7-methoxyisoquinoline (5)**

To a solution of 6-benzyloxy-7-methoxyisoquinoline (**4**) (531 mg, 2.00 mmol) in dry THF (8 mL) was slowly added TMPMgCl·LiCl (1.0 M in THF/toluene; 3.00 mL, 3.00 mmol) dropwise at room temperature. After 4 h the reaction mixture was cooled to 0°C, a solution of iodine (761 mg, 3.00 mmol) in dry THF (3 mL) was added dropwise and the resulting mixture stirred while warming to room temperature over 1 h. Sat. aq. NH<sub>4</sub>Cl (4 mL) and sat. aq. Na<sub>2</sub>S<sub>2</sub>O<sub>3</sub> (4 mL) were added and the organic materials extracted using DCM (3 x 50 mL). The combined organic layers were dried over Na<sub>2</sub>SO<sub>4</sub> and concentrated *in vacuo*. The resulting crude product was purified by flash column chromatography (DCM/EtOAc 5:1) to give 6-benzyloxy-1-iodo-7-methoxyisoquinoline (**5**) (0.482 g, 1.23 mmol, 62%) as a brown solid.

**HRMS (EI<sup>+</sup>):** 391.0069 calculated for C<sub>17</sub>H<sub>14</sub>INO<sub>2</sub><sup>+</sup> [M]<sup>+</sup>, 391.0070 found. **<sup>1</sup>H NMR (400 MHz, CDCl<sub>3</sub>):** δ (ppm) = 8.09 (d, *J* = 5.4 Hz, 1H, 3-H), 7.50 – 7.46 (m, 2H, 2',-6'-H), 7.43 – 7.34 (m, 5H, 3',-4',-5',-4-, 8-H), 7.04 (s, 1H, 5-H), 5.30 (s, 2H, CH<sub>2</sub>), 4.08 (s, 3H, OCH<sub>3</sub>). **<sup>13</sup>C NMR (101 MHz, CDCl<sub>3</sub>):** δ (ppm) = 152.7 (C-6), 152.0 (C-7), 142.0 (C-3), 135.9 (C-1'), 132.5 (C-1), 128.9 (2C, C-3' and C-5'), 128.5 (C-4'), 128.3 (C-8a), 127.5 (2C, C-2' and C-6'), 124.9 (C-4a), 120.3 (C-4), 111.4 (C-8), 106.9 (C-5), 71.1 (CH<sub>2</sub>), 56.4 (OCH<sub>3</sub>).

**6-(Benzyloxy)-7-methoxy-1-(3,4,5-trimethoxyphenyl)isoquinoline (6)**

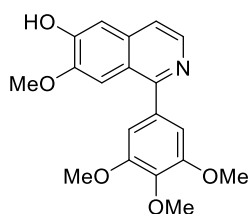
To a solution of 6-benzyloxy-1-iodo-7-methoxyisoquinoline (**5**) (391 mg, 1.00 mmol) in THF (6 mL) was added 3,4,5-trimethoxyphenylboronic acid (254 mg, 1.20 mmol). After addition of Pd(PPh<sub>3</sub>)<sub>4</sub> (59.0 mg, 0.0500 mmol) and aq. K<sub>2</sub>CO<sub>3</sub> solution (1.0 M; 3.00 mL, 3.00 mmol) the reaction mixture was stirred in a sealed pressure tube under nitrogen atmosphere at 90°C for 16 h. After cooling to room temperature the mixture was poured into water (50 mL) and extracted with EtOAc (3 x 50 mL). The combined organic layers were dried over Na<sub>2</sub>SO<sub>4</sub> and concentrated *in vacuo*. The crude product was purified by flash column chromatography



(EtOAc/DCM 2:1) to give 6-benzyloxy-7-methoxy-1-(3,4,5-trimethoxyphenyl)isoquinoline (**6**) (395 mg, 0.915 mmol, 92%) as a yellow solid.

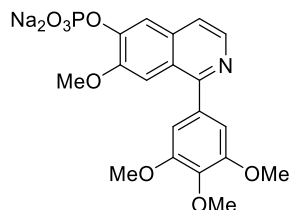
**HRMS (EI<sup>+</sup>):** 431.1733 calculated for C<sub>26</sub>H<sub>25</sub>NO<sub>5</sub><sup>+</sup> [M]<sup>+</sup>, 431.1729 found. **<sup>1</sup>H NMR (400 MHz, CD<sub>2</sub>Cl<sub>2</sub>):**  $\delta$  (ppm) = 8.40 (d,  $J$  = 5.5 Hz, 1H, 3-H), 7.52 – 7.48 (m, 3H, 2''-, 6''-, 4-H), 7.47 (s, 1H, 8-H), 7.46 – 7.41 (m, 2H, 3''-, 5''-H), 7.40 – 7.35 (m, 1H, 4''-H), 7.23 (s, 1H, 5-H), 6.93 (s, 2H, 2'-, 6'-H), 5.24 (s, 2H, CH<sub>2</sub>), 3.88 (s, 6H, 3'-, 5'-OCH<sub>3</sub>), 3.87 (s, 3H, 4'-OCH<sub>3</sub>), 3.86 (s, 3H, 7-OCH<sub>3</sub>). **<sup>13</sup>C NMR (101 MHz, CD<sub>2</sub>Cl<sub>2</sub>):**  $\delta$  (ppm) = 158.5 (C-1), 153.8 (2C, C-3' and C-5'), 152.4 (C-6), 151.0 (C-7), 141.7 (C-3), 138.8 (C-4'), 136.7 (C-1''), 136.2 (C-1'), 134.2 (C-4a), 129.2 (2C, C-3'' and C-5''), 128.9 (C-4''), 128.5 (2C, C-2'' and C-6''), 123.0 (C-8a), 119.2 (C-4), 107.5 (2C, C-2' and C-6'), 107.0 (C-5), 106.3 (C-8), 71.3 (CH<sub>2</sub>), 61.1 (4'-OCH<sub>3</sub>), 56.7 (2C, 3'- and 5'-OCH<sub>3</sub>), 56.4 (7-OCH<sub>3</sub>).

#### **7-Methoxy-1-(3,4,5-trimethoxyphenyl)isoquinolin-6-ol (IQTub4)**



To a solution of 6-benzyloxy-7-methoxy-1-(3,4,5-trimethoxyphenyl)isoquinoline (**6**) (341 mg, 0.790 mmol) in MeOH (30 mL) was added Pd/C (10%, 100 mg). The reaction mixture was stirred vigorously under an atmosphere of hydrogen at room temperature for 24 h. The mixture was filtered through a pad of celite and the filtrate concentrated *in vacuo* to give **IQTub4** (220 mg, 0.645 mmol, 82%) as a white solid.

**HRMS (EI<sup>+</sup>):** 341.1263 calculated for C<sub>19</sub>H<sub>19</sub>NO<sub>5</sub><sup>+</sup> [M]<sup>+</sup>, 341.1256 found. **<sup>1</sup>H NMR (400 MHz, (CD<sub>3</sub>)<sub>2</sub>SO):**  $\delta$  (ppm) = 10.29 (s, 1H, OH), 8.31 (d,  $J$  = 5.6 Hz, 1H, 3-H), 7.53 (d,  $J$  = 5.6 Hz, 1H, 4-H), 7.44 (s, 1H, 8-H), 7.22 (s, 1H, 5-H), 6.99 (s, 2H, 2'-, 6'-H), 3.84 (s, 6H, 3'-, 5'-OCH<sub>3</sub>), 3.82 (s, 3H, 7-OCH<sub>3</sub>), 3.76 (s, 3H, 4'-OCH<sub>3</sub>). **<sup>13</sup>C NMR (101 MHz, (CD<sub>3</sub>)<sub>2</sub>SO):**  $\delta$  (ppm) = 156.9 (C-1), 152.7 (2C, C-3' and C-5'), 150.8 (C-6), 149.6 (C-7), 140.4 (C-3), 137.6 (C-4'), 135.3 (C-1'), 133.6 (C-4a), 121.1 (C-8a), 118.1 (C-4), 108.5 (C-5), 107.0 (2C, C-2' and C-6'), 105.3 (C-8), 60.1 (4'-OCH<sub>3</sub>), 56.0 (2C, 3'- and 5'-OCH<sub>3</sub>), 55.4 (7-OCH<sub>3</sub>). **HPLC purity:** >95 %.

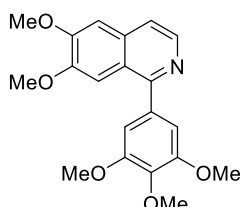
**Sodium 7-methoxy-1-(3,4,5-trimethoxyphenyl)isoquinolin-6-yl phosphate (IQTub4P)**

To a solution of **IQTub4** (3.30 g, 9.67 mmol), Et<sub>3</sub>N (2.69 mL, 19.3 mmol), and CCl<sub>4</sub> (4.66 mL, 48.3 mmol) in dry MeCN (30 mL) at 0°C was added dropwise a solution of dibenzyl phosphite (3.55 g, 13.5 mmol) in dry MeCN (41 mL), and the resulting mixture stirred while warming to room temperature over 2 h. The volatiles were evaporated and the crude partitioned between water and EtOAc; the organic layer was dried over Na<sub>2</sub>SO<sub>4</sub> and filtered. The filtrate was concentrated, then dissolved in a 1:1 TFA:DCM mixture (75 mL) and stirred overnight, capped under nitrogen. The volatiles were evaporated and phosphate buffer (pH ~7, 50 mL) was added. The aqueous phase was washed with 1:1 hexanes:EtOAc (3 x 50 mL). The aqueous layer was then adjusted to pH 4-5 with KHSO<sub>4</sub> and the organic materials extracted using EtOAc (3 x 50 mL). The organic layer was dried over Na<sub>2</sub>SO<sub>4</sub>, filtered and concentrated. The residue was dissolved in MeOH (50 mL) and NaHCO<sub>3</sub> (1.79 g, 21.3 mmol) was added. The mixture was stirred for one hour. The solvent was removed *in vacuo*, the crude product redissolved in MeOH (30 mL) and RP-silica was added. After evaporation of the volatiles, reversed-phase column chromatography (MeCN/water 99:1) gave **IQTub4P** (2.10 g, 4.52 mmol, 47%) as a yellow solid.

**HRMS (ESI<sup>+</sup>):** 422.0999 calculated for C<sub>19</sub>H<sub>21</sub>NO<sub>8</sub>P<sup>+</sup> [M+H]<sup>+</sup>, 422.0996 found. **<sup>1</sup>H NMR (500 MHz, MeOD):** δ (ppm) = 8.23 (d, *J* = 5.7 Hz, 1H, 3-H), 8.14 (s, 1H, 5-H), 7.64 (d, *J* = 5.7 Hz, 1H, 4-H), 7.39 (s, 1H, 8-H), 6.95 (s, 2H, 2'-, 6'-H), 3.89 (s, 6H, 3'-, 5'-OCH<sub>3</sub>), 3.87 (s, 3H, 4'-OCH<sub>3</sub>), 3.83 (s, 3H, 7-OCH<sub>3</sub>). **<sup>13</sup>C NMR (126 MHz, MeOD):** δ (ppm) = 158.9 (C-1), 154.5 (2C, C-3' and C-5'), 153.4 (C-7), 150.3 (C-6), 140.1 (C-3), 139.6 (C-4'), 136.6 (C-1'), 135.7 (C-4a), 124.1 (C-8a), 121.0 (C-4), 115.1 (C-5), 108.3 (2C, C-2' and C-6'), 106.4 (C-8), 61.2 (4'-OCH<sub>3</sub>), 56.8 (2 C, 3'-OCH<sub>3</sub> and 5'-OCH<sub>3</sub>), 56.2 (7-OCH<sub>3</sub>). **NMR purity:** > 97%.

**6,7-Dimethoxy-1-(3,4,5-trimethoxyphenyl)isoquinoline (IQTub6)**

**IQTub6**, first reported in 1930s as a papaverine analogue<sup>3</sup>, then again by Hati and Sen<sup>4</sup> during a study of an dehydrogenative aromatization reaction, where it was delivered as a reaction product (compound **4h**) illustrating scope of the methodology, but bioactivity was not proposed.

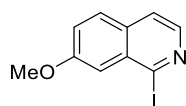


**IQTub4** (61.5 mg, 0.180 mmol) was dissolved in DMF (2 mL).  $K_2CO_3$  (27.4 mg, 0.198 mmol) and iodomethane (38.4 mg, 0.270 mmol) were added and the mixture stirred, capped, at room temperature for 16 h. Water (10 mL) was added and the organic material extracted with EtOAc (3 x 15 mL). The combined organic phases were washed with water (2 x 10 mL), dried over  $Na_2SO_4$  and the solvent was removed *in vacuo*. Column chromatography (hexane/EtOAc 5:1→1:3) returned **IQTub6** (24.0 mg, 0.0675 mmol, 38%) as a yellowish solid.

**HRMS (ESI<sup>+</sup>)**: 356.1492 calculated for  $C_{20}H_{22}NO_5^+$   $[M+H]^+$ , 356.1492 found. **<sup>1</sup>H NMR (500 MHz, MeOD)**:  $\delta$  (ppm) = 8.27 (d,  $J$  = 5.7 Hz, 1H, 3-H), 7.66 – 7.63 (m, 1H, 4-H), 7.38 (s, 1H, 5-H), 7.30 (s, 1H, 8-H), 6.95 (s, 2H, 2'-, 6'-H), 3.98 (s, 3H, 7-OCH<sub>3</sub>), 3.89 (s, 6H, 3'-, 5'-OCH<sub>3</sub>), 3.87 (s, 3H, 4'-OCH<sub>3</sub>), 3.82 (s, 3H, 6'-OCH<sub>3</sub>). **<sup>13</sup>C NMR (126 MHz, MeOD)**:  $\delta$  (ppm) = 159.0 (C-1), 154.9 (C-6 or C-7), 154.6 (2C, C-3' and C-5'), 152.0 (C-6 or C-7), 140.6 (C-3), 139.8 (C-4'), 136.1 (C-1'), 135.8 (C-4a), 123.8 (C-8a), 120.8 (C-4), 108.3 (2C, C-2' and C-6'), 106.5 (C-5 or C-8), 106.4 (C-5 or C-8), 61.2 (4'-OCH<sub>3</sub>), 56.8 (2C, 3'-OCH<sub>3</sub> and 5'-OCH<sub>3</sub>), 56.5 (7-OCH<sub>3</sub>), 56.3 (6-OCH<sub>3</sub>). **HPLC purity**: >95 %.

**1-Iodo-7-methoxyisoquinoline (S1)**

5-Iodo-[1,3]dioxolo[4,5-g]isoquinoline (**S3**) was first described in 2013 by Chuang et. al.<sup>5</sup> as an intermediate towards tetracyclic alkaloids using a different synthetic procedure.

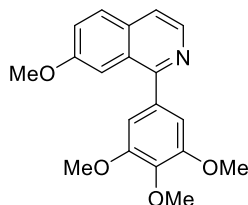


TMPMgCl·LiCl (1.0 M in THF/toluene; 5.65 mL, 5.65 mmol) was added dropwise at room temperature to a solution of 7-methoxyisoquinoline (600 mg, 3.77 mmol) in dry THF (11 mL). After 4 h the reaction mixture was cooled to 0°C, a solution of iodine (1.43 g, 5.65 mmol) in dry THF (6.65 mL) was added dropwise and the resulting mixture stirred while warming to

room temperature over 1 h. Sat. aq.  $\text{NH}_4\text{Cl}$  (6 mL) and sat. aq.  $\text{Na}_2\text{S}_2\text{O}_3$  (6 mL) were added and the organic materials extracted using DCM (3 x 50 mL). The combined organic layers were dried over  $\text{Na}_2\text{SO}_4$  and concentrated *in vacuo*. The resulting crude product was purified by flash column chromatography (EtOAc/hexanes 1:9) to give 1-iodo-7-methoxyisoquinoline (**S1**) (469 mg, 1.64 mmol, 44%) as a yellowish solid.

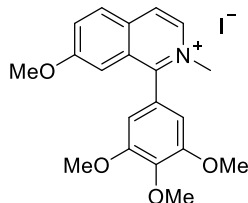
**HRMS (ESI<sup>+</sup>):** 285.9723 calculated for  $\text{C}_{10}\text{H}_9\text{INO}^+$   $[\text{M}+\text{H}]^+$ , 285.9722 found. **<sup>1</sup>H NMR (500 MHz,  $\text{CDCl}_3$ ):**  $\delta$  (ppm) = 8.16 (d,  $J$  = 5.5 Hz, 1H, 3-H), 7.67 – 7.63 (m, 1H, 6-H), 7.51 (dd,  $J$  = 5.5, 0.7 Hz, 1H, 4-H), 7.37 (m, 1H, 8-H), 7.38 – 7.34 (m, 1H, 5-H), 4.00 (s, 3H, 7-OCH<sub>3</sub>). **<sup>13</sup>C NMR (126 MHz,  $\text{CDCl}_3$ ):**  $\delta$  (ppm) = 160.0 (C-7), 141.5 (C-3), 133.5 (C-4a), 131.8 (C-8a), 129.1 (C-4), 125.9 (C-1), 124.3 (C-5), 121.2 (C-6), 110.6 (C-8), 55.8 (7-OCH<sub>3</sub>).

### **7-Methoxy-1-(3,4,5-trimethoxyphenyl)isoquinoline (IQTub3)**



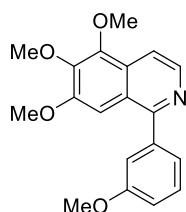
3,4,5-Trimethoxyphenylboronic acid (254 mg, 1.20 mmol) was added to a solution of 1-iodo-7-methoxyisoquinoline (**S1**) (400 mg, 1.40 mmol) in THF (8 mL). After addition of  $\text{Pd}(\text{PPh}_3)_4$  (81.0 mg, 0.0700 mmol) and an aq.  $\text{K}_2\text{CO}_3$  solution (1.0 M in  $\text{H}_2\text{O}$ ; 4.20 mL, 4.20 mmol) the reaction mixture was stirred under nitrogen at 90°C for 16 h. After cooling to room temperature the mixture was poured into water (30 mL) and extracted with EtOAc (3 x 50 mL). The combined organic layers were dried over  $\text{Na}_2\text{SO}_4$  and concentrated *in vacuo*. The crude product was purified by flash column chromatography (EtOAc/hexanes 1:1) to give **IQTub3** (377 mg, 1.16 mmol, 83%) as a yellowish solid.

**HRMS (ESI<sup>+</sup>):** 326.1389 calculated for  $\text{C}_{19}\text{H}_{20}\text{NO}_4^+$   $[\text{M}+\text{H}]^+$ , 326.1385 found. **<sup>1</sup>H NMR (500 MHz,  $\text{CDCl}_3$ ):**  $\delta$  (ppm) = 8.49 (d,  $J$  = 5.6 Hz, 1H, 3-H), 7.80 (d,  $J$  = 8.9 Hz, 1H, 5-H), 7.59 (dd,  $J$  = 5.6, 0.9 Hz, 1H, 4-H), 7.46 (d,  $J$  = 2.5 Hz, 1H, 8-H), 7.37 (dd,  $J$  = 8.9, 2.5 Hz, 1H, 6-H), 6.95 (s, 2H, 2'-H and 6'-H), 3.94 (s, 3H, 4'-OCH<sub>3</sub>), 3.91 (s, 6H, 3'-OCH<sub>3</sub> and 5'-OCH<sub>3</sub>), 3.83 (s, 3H, 7-OCH<sub>3</sub>). **<sup>13</sup>C NMR (126 MHz,  $\text{CDCl}_3$ ):**  $\delta$  (ppm) = 159.0 (C-1), 158.5 (C-7), 153.4 (2C, C-3' and C-5'), 140.4 (C-3), 138.5 (C-4'), 135.4 (C-1'), 132.7 (C-4a), 128.8 (C-5), 127.9 (C-8a), 123.3 (C-6), 119.9 (C-4), 107.1 (2C, C-2' and C-6'), 105.2 (C-8), 61.1 (4'-OCH<sub>3</sub>), 56.4 (2C, 3'-OCH<sub>3</sub> and (5'-OCH<sub>3</sub>), 55.6 (7-OCH<sub>3</sub>). **HPLC purity:** >95 %.

**7-Methoxy-2-methyl-1-(3,4,5-trimethoxyphenyl)isoquinolinium iodide (IQTub7)**

**IQTub3** (200 mg, 0.615 mmol) was added to a pressure tube and dissolved in toluene (3 mL). MeI (57.4  $\mu$ L, 0.922 mmol) was added, the vessel sealed, and the reaction was heated to 115°C for 7 h. After cooling to room temperature the resulting precipitate was collected, washed with toluene (3 x 10 mL) and dried under reduced pressure to give the desired product **IQTub7** (224 mg, 0.479 mmol, 78%) as a yellow solid.

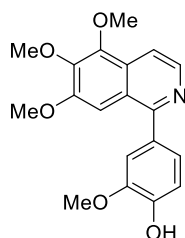
**HRMS (ESI<sup>+</sup>):** 340.1543 calculated for C<sub>20</sub>H<sub>22</sub>NO<sub>4</sub><sup>+</sup> [M+H]<sup>+</sup>, 340.1541 found. **<sup>1</sup>H NMR (500 MHz, (CD<sub>3</sub>)<sub>2</sub>SO):**  $\delta$  (ppm) = 8.80 (d,  $J$  = 6.7 Hz, 1H, 3-H), 8.57 (d,  $J$  = 6.7 Hz, 1H, 4-H), 8.35 (d,  $J$  = 9.0 Hz, 1H, 5-H), 7.92 (dd,  $J$  = 9.0, 2.5 Hz, 1H, 6-H), 7.07 (s, 2H, 2'-H and 6'-H), 6.95 (d,  $J$  = 2.5 Hz, 1H, 8-H), 4.14 (s, 3H, NCH<sub>3</sub>), 3.83 (s, 3H, 4'-OCH<sub>3</sub>), 3.82 (s, 6H, 3'-OCH<sub>3</sub> and 5'-OCH<sub>3</sub>), 3.80 (s, 3H, 7-OCH<sub>3</sub>). **<sup>13</sup>C NMR (126 MHz, (CD<sub>3</sub>)<sub>2</sub>SO):**  $\delta$  (ppm) = 160.3 (C-7), 156.5 (C-1), 153.5 (2C, C-3' and C-5'), 139.0 (C-4'), 134.8 (C-3), 133.2 (C-4a), 129.7 (C-8a), 129.4 (C-5), 128.3 (C-6), 124.7, 124.7, 107.2 (C-8), 106.7 (2C, C-2' and C-6'), 60.3 (4'-OCH<sub>3</sub>), 56.3 (2C, 3'-OCH<sub>3</sub> and 5'-OCH<sub>3</sub>), 55.9 (7-OCH<sub>3</sub>), 47.4 (NCH<sub>3</sub>). **HPLC purity:** >95 %.

**5,6,7-Trimethoxy-1-(3-methoxyphenyl)isoquinoline (IQTub1)**

2-(3-Methoxyphenyl)-4,4,5,5-tetramethyl-1,3,2-dioxaborolane<sup>6</sup> (84.0 mg, 0.360 mmol) was added to a solution of 1-iodo-5,6,7-trimethoxyisoquinoline<sup>7</sup> (104 mg, 0.300 mmol) in THF (2 mL). After addition of Pd(PPh<sub>3</sub>)<sub>4</sub> (17.0 mg, 0.015 mmol) and an aq. K<sub>2</sub>CO<sub>3</sub> solution (1.0 M; 900  $\mu$ L, 0.900 mmol) the reaction mixture was stirred under nitrogen at 85°C for 16 h in a pressure tube. After cooling to room temperature the solution was poured into water (20 mL) and extracted with EtOAc (4 x 20 mL). The combined organic layers were dried over Na<sub>2</sub>SO<sub>4</sub> and concentrated *in vacuo*. The crude product was purified by flash column chromatography (EtOAc/hexanes 1:1) to give **IQTub1** (59.0 mg, 0.181 mmol, 60%) as a light yellow solid.

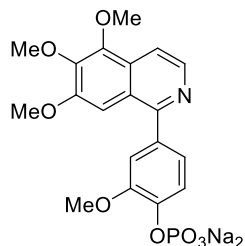
**HRMS (EI<sup>+</sup>):** 325.1314 calculated for C<sub>19</sub>H<sub>19</sub>NO<sub>4</sub><sup>+</sup> [M]<sup>+</sup>, 325.1325 found. **<sup>1</sup>H NMR (400 MHz, CD<sub>2</sub>Cl<sub>2</sub>):** δ (ppm) = 8.45 (d, *J* = 5.7 Hz, 1H, 3-H), 7.83 (dd, *J* = 5.7, 0.8 Hz, 1H, 4-H), 7.43 (t, *J* = 7.9 Hz, 1H, 5'-H), 7.25 (dt, *J* = 7.5, 1.2 Hz, 1H, 6-H), 7.23 – 7.21 (m, 2H, 8-, 2'-H), 7.03 (ddd, *J* = 8.3, 2.6, 1.0 Hz, 1H, 4-H), 4.06 (s, 3H, 6-OCH<sub>3</sub>), 3.99 (s, 3H, 7-OCH<sub>3</sub>), 3.86 (s, 3H, 5-OCH<sub>3</sub>), 3.82 (s, 3H, 3'-OCH<sub>3</sub>). **<sup>13</sup>C NMR (101 MHz, CD<sub>2</sub>Cl<sub>2</sub>):** δ (ppm) = 160.3 (C-3'), 158.7 (C-1), 154.2 (C-7), 147.3 (C-6), 144.4 (C-5), 142.1 (C-1'), 141.2 (C-3), 129.8 (C-5'), 129.4 (C-4a), 124.3 (C-8a), 122.5 (C-6'), 115.4 (C-2'), 114.9 (C-4'), 114.4 (C-4), 102.4 (C-8), 62.1 (6-OCH<sub>3</sub>), 61.5 (7-OCH<sub>3</sub>), 56.3 (3'-OCH<sub>3</sub>), 55.9 (5-OCH<sub>3</sub>). **HPLC purity:** >95 %.

**2-Methoxy-4-(5,6,7-trimethoxyisoquinolin-1-yl)phenol (IQTub2)**



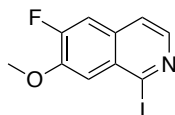
2-Methoxy-4-(4,4,5,5-tetramethyl-1,3,2-dioxaborolan-2-yl)phenol<sup>8</sup> (120 mg, 0.480 mmol) was added to a solution of 1-iodo-5,6,7-trimethoxyisoquinoline (**S2**) (138 mg, 0.400 mmol) in THF (2.5 mL). After addition of Pd(PPh<sub>3</sub>)<sub>4</sub> (23.0 mg, 0.0200 mmol) and an aq. K<sub>2</sub>CO<sub>3</sub> solution (1.0 M; 1.20 mL, 1.20 mmol) the reaction mixture was stirred under nitrogen at 85°C for 16 h in a pressure tube. After cooling to room temperature the solution was poured into water (20 mL) and extracted with EtOAc (4 × 20 mL). The combined organic layers were dried over Na<sub>2</sub>SO<sub>4</sub> and concentrated *in vacuo*. The crude product was purified by flash column chromatography (EtOAc/hexanes 1:1) to give **IQTub2** (0.0530 g, 0.155 mmol, 39%) as a yellow solid.

**HRMS (EI<sup>+</sup>):** 341.1263 calculated for C<sub>19</sub>H<sub>19</sub>NO<sub>5</sub><sup>+</sup> [M]<sup>+</sup>, 341.1276 found. **<sup>1</sup>H NMR (400 MHz, CD<sub>2</sub>Cl<sub>2</sub>):** δ (ppm) = 8.43 (d, *J* = 5.7 Hz, 1H, 3'-H), 7.79 (dd, *J* = 5.7, 0.8 Hz, 1H, 4'-H), 7.27 (s, 1H, 8'-H), 7.26 (d, *J* = 1.9 Hz, 1H, 3-H), 7.19 (dd, *J* = 8.1, 1.9 Hz, 1H, 5-H), 7.01 (d, *J* = 8.1 Hz, 1H, 6-H), 6.20 (s, 1H, OH), 4.05 (s, 3H, 2-OCH<sub>3</sub>), 3.99 (s, 3H, 5'-OCH<sub>3</sub>), 3.92 (s, 3H, 6'-OCH<sub>3</sub>), 3.84 (s, 3H, 7'-OCH<sub>3</sub>). **<sup>13</sup>C NMR (101 MHz, CD<sub>2</sub>Cl<sub>2</sub>):** δ (ppm) = 158.7 (C-1'), 154.1 (C-7'), 147.4 (C-5'), 147.3 (C-2), 146.8 (C-1), 144.3 (C-6'), 141.1 (C-3'), 132.8 (C-4), 129.4 (C-4a'), 124.3 (C-8a'), 123.4 (C-5), 114.5 (C-6), 114.0 (C-4'), 113.1 (C-3), 102.6 (C-8'), 62.1 (2-OCH<sub>3</sub>), 61.5 (6'-OCH<sub>3</sub>), 56.6 (5'-OCH<sub>3</sub>), 56.3 (7'-OCH<sub>3</sub>). **HPLC purity:** >95 %.

**Sodium 2-methoxy-4-(5,6,7-trimethoxyisoquinolin-1-yl)phenyl phosphate (IQTub2P)**

To a solution of  $\text{POCl}_3$  (115 mg, 0.750 mmol) in dry DCM (1 mL) in a flame dried Schlenk tube was added a solution of **IQTub2** (85.0 mg, 0.249 mmol) in dry DCM (1 mL) at  $0^\circ\text{C}$  under  $\text{N}_2$  atmosphere. A solution of dry triethylamine (114 mg, 1.13 mmol) in dry DCM (1 mL) was added dropwise and stirring continued for 10 min at  $0^\circ\text{C}$ . After addition of water (5 mL) phases were separated and the aqueous phase extracted with DCM (3 x 10 mL). The combined organic layers were dried over  $\text{Na}_2\text{SO}_4$  and concentrated *in vacuo*. The resulting crude product was resuspended in water (5 mL) and the pH adjusted to pH ~10 using 0.5 M aq. NaOH solution. After stirring at  $70^\circ\text{C}$  for 8 h the mixture was filtered and the filtrate washed with EtOAc (3 x 10 mL). The aqueous layer was concentrated *in vacuo* repeatedly to remove water. The resulting crude product was purified by reversed-phase column chromatography (water/MeOH 100:0  $\rightarrow$  0:100) to give **IQTub2P** (48.0 mg, 0.103 mmol, 41%) as a beige solid.

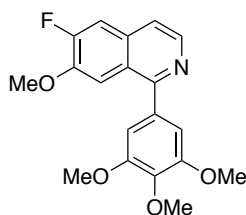
**HRMS (ESI<sup>-</sup>):** 420.08538 calculated for  $\text{C}_{19}\text{H}_{19}\text{NO}_8\text{P}^-$  [M-H]<sup>-</sup>, 420.08597 found. **<sup>1</sup>H NMR (500 MHz, D<sub>2</sub>O):**  $\delta$  (ppm) = 8.22 (d,  $J$  = 5.9 Hz, 1H, 3'-H), 7.79 (d,  $J$  = 5.9 Hz, 1H, 4'-H), 7.59 (d,  $J$  = 8.2 Hz, 1H, 6-H), 7.25 – 7.20 (m, 1H, 3-H), 7.17 (s, 1H, 8'-H), 7.15 – 7.09 (m, 1H, 5-H), 3.98 (s, 3H, 7'-OCH<sub>3</sub>), 3.95 (s, 3H, 5'-OCH<sub>3</sub>), 3.91 (s, 3H, 2-OCH<sub>3</sub>), 3.79 (s, 3H, 6'-OCH<sub>3</sub>). **<sup>13</sup>C NMR (126 MHz, D<sub>2</sub>O):**  $\delta$  (ppm) = 157.3 (C-1'), 152.9 (C-6'), 149.9 (d,  $J_{\text{C-P}}$  = 6.1 Hz, C-2), 145.4 (C-5'), 144.2 (~d,  $J_{\text{C-P}}$  = 5.6 Hz, C-1), 144.1 (C-7'), 137.8 (C-3'), 131.5 (C-4), 129.0 (C-4a'), 123.3 (C-8a'), 122.7 (C-5), 120.2 (d,  $J_{\text{C-P}}$  = 1.8 Hz, C-6), 114.4 (C-4'), 114.1 (C-3), 103.0 (C-8'), 61.9 (7'-OCH<sub>3</sub>), 61.2 (5'-OCH<sub>3</sub>), 56.2 (2-OCH<sub>3</sub>), 55.8 (6'-OCH<sub>3</sub>). **NMR purity:** >96%.

**6-Fluoro-1-iodo-7-methoxyisoquinoline (S2)**

To a solution of 6-fluoro-7-methoxyisoquinoline<sup>9</sup> (677 mg, 3.82 mmol) in dry THF (18 mL) was slowly added  $\text{TMPMgCl}\cdot\text{LiCl}$  (1.0 M in THF/toluene; 12.8 mL, 12.8 mmol) dropwise at  $0^\circ\text{C}$ . The reaction mixture was stirred at room temperature for 5 h. The reaction mixture was cooled to  $0^\circ\text{C}$ , a solution of iodine (1.45 mg, 5.73 mmol) in dry THF (3 mL) was added dropwise and the

resulting mixture was allowed to warm up to room temperature. After stirring for 2 h. sat. aq.  $\text{NH}_4\text{Cl}$  (3 mL) and sat. aq.  $\text{Na}_2\text{S}_2\text{O}_3$  (3 mL) were added and the organic materials were extracted with DCM (3 x 50 mL). The combined organic layers were dried over  $\text{Na}_2\text{SO}_4$  and concentrated *in vacuo*. The resulting crude product was purified by flash column chromatography (EtOAc:Hex, 2:8  $\rightarrow$  3:8) to give 6-fluoro-1-iodo-7-methoxyisoquinoline (**S2**) (600 mg, 1.98 mmol, 52%) as a colourless powder. **HRMS (ESI<sup>+</sup>)**: 303.96291 calculated for  $\text{C}_{10}\text{H}_8\text{FINO}^+$ , 303.96294 found. **<sup>1</sup>H NMR (400 MHz, (CD<sub>3</sub>)<sub>2</sub>SO)**:  $\delta$  (ppm) = 8.17 (d,  $J$  = 5.5 Hz, 1H, 3-H), 7.88 (d,  $J$  = 11.7 Hz, 1H, 5-H), 7.75 (d,  $J$  = 5.5 Hz, 1H, 4-H), 7.45 (d,  $J$  = 8.3 Hz, 1H, 8-H), 4.04 (s, 3H, 7-OCH<sub>3</sub>). **<sup>13</sup>C NMR (100 MHz, (CD<sub>3</sub>)<sub>2</sub>SO)**:  $\delta$  (ppm) = 155.1 (d,  $J$  = 255.9 Hz, C-6), 149.8 (d,  $J$  = 13.4 Hz, C-7), 142.7 (C-3), 131.4 (d,  $J$  = 10.2 Hz, C-4a), 129.7 (C-8a), 125.6 (d,  $J$  = 1.4 Hz, C-1), 121.3 (d,  $J$  = 5.0 Hz, C-4), 113.1 (d,  $J$  = 3.0 Hz, C-8), 112.5 (d,  $J$  = 18.8 Hz, C-5), 56.7 (7-OCH<sub>3</sub>).

**6-Fluoro-7-methoxy-1-(3,4,5-trimethoxyphenyl)isoquinoline (IQTub5)**



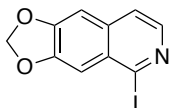
3,4,5-Trimethoxyphenylboronic acid (364 mg, 1.24 mmol) was added to a solution of **S2** (300 mg, 1.0 mmol) in THF (5 mL). After addition of  $\text{Pd}(\text{PPh}_3)_4$  (57 mg, 5 mol%) and aq.  $\text{K}_2\text{CO}_3$  solution (2 M; 1.5 mL, 3.0 mmol) the reaction mixture was stirred under nitrogen at 90°C for 16 h. After cooling to room temperature water (40 mL) was added and the mixture extracted with EtOAc (3 x 50 mL). The combined organic layers were dried over  $\text{Na}_2\text{SO}_4$  and concentrated *in vacuo*. The crude product was purified by flash column chromatography (EtOAc/hexanes 3:7 $\rightarrow$ 1:1) to give **IQTub5** (232 mg, 0.68 mmol, 68%) as a colourless solid.

**HRMS (ESI<sup>+</sup>)**: 344.1293 calculated for  $\text{C}_{19}\text{H}_{19}\text{FNO}_4^+$  [M+H]<sup>+</sup>, 344.1291 found. **<sup>1</sup>H NMR (400 MHz, (CD<sub>3</sub>)<sub>2</sub>SO)**:  $\delta$  (ppm) = 8.48 (d,  $J$  = 5.5 Hz, 1H, 3-H), 7.89 (d,  $J$  = 11.9 Hz, 1H, 5-H), 7.74 (d,  $J$  = 5.6 Hz, 1H, 4-H), 7.63 (d,  $J$  = 8.6 Hz, 1H, 8-H), 7.02 (s, 2H, 2'-H and 6'-H), 3.89 (s, 3H, 7'-OCH<sub>3</sub>), 3.84 (s, 6H, 3'-OCH<sub>3</sub> and 5'-OCH<sub>3</sub>), 3.77 (s, 3H, 4'-OCH<sub>3</sub>). **<sup>13</sup>C NMR (100 MHz, (CD<sub>3</sub>)<sub>2</sub>SO)**:  $\delta$  (ppm) = 157.6 (d,  $J$  = 1.2 Hz, C-1), 154.1 (d,  $J$  = 254.3 Hz, C-6), 152.8 (2C, C-3' and C-5'), 147.8 (d,  $J$  = 13.2 Hz, C-7), 141.1 (C-3), 137.9 (C-4'), 134.7 (C-1'), 132.4 (d,  $J$  = 9.8 Hz, C-4a), 123.6 (C-8a), 119.3 (d,  $J$  = 4.8 Hz, C-4), 111.6 (d,  $J$  = 18.2 Hz, C-5), 107.7 (d,  $J$  = 2.9 Hz, C-4), 107.1 (2C, C-2' and C-6'), 60.2 (7-OCH<sub>3</sub>), 56.1 (2C, 3'-OCH<sub>3</sub> and 5'-OCH<sub>3</sub>), 55.9 (4'-OCH<sub>3</sub>). **HPLC purity**: >95 %.



**5-Iodo-[1,3]dioxolo[4,5-g]isoquinoline (S3)**

5-Iodo-[1,3]dioxolo[4,5-g]isoquinoline (**S3**) was first described in 2013 by Chuang et. al.<sup>5</sup> as an intermediate towards tetracyclic alkaloids using a different synthetic procedure.

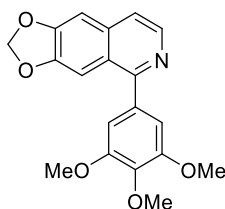


To a solution of [1,3]dioxolo[4,5-g]isoquinoline<sup>10</sup> (561 mg, 3.24 mmol) in dry THF (18 mL) was slowly added TMPMgCl·LiCl (1.0 M in THF/toluene; 10.9 mL, 10.9 mmol) dropwise at 0°C. The reaction mixture was stirred at room temperature for 5 h. The reaction mixture was cooled to 0°C, a solution of iodine (1.23 mg, 4.86 mmol) in dry THF (3 mL) was added dropwise and the resulting mixture was allowed to warm up to room temperature. After stirring for 2 h. sat. aq. NH<sub>4</sub>Cl (3 mL) and sat. aq. Na<sub>2</sub>S<sub>2</sub>O<sub>3</sub> (3 mL) were added and the organic materials were extracted with DCM (3 x 50 mL). The combined organic layers were dried over Na<sub>2</sub>SO<sub>4</sub> and concentrated *in vacuo*. The resulting crude product was purified by flash column chromatography (EtOAc:Hex, 4:6 → 9:1) to give 5-iodo-[1,3]dioxolo[4,5-g]isoquinoline (**S3**) (526 mg, 1.76 mmol, 54%) as a beige solid.

**HRMS (ESI<sup>+</sup>):** 299.95160 calculated for C<sub>10</sub>H<sub>7</sub>INO<sub>2</sub><sup>+</sup>, 299.95149 found. **<sup>1</sup>H NMR (400 MHz, (CD<sub>3</sub>)<sub>2</sub>SO):** δ (ppm) = 8.99 (s, 1H, 8-H), 8.39 (d, *J* = 5.5 Hz, 1H, 3-H), 7.58 (dd, *J* = 5.6, 0.8 Hz, 1H, 4-H), 7.31 (s, 1H, 5-H), 6.28 (s, 2H, CH<sub>2</sub>). **<sup>13</sup>C NMR (100 MHz, (CD<sub>3</sub>)<sub>2</sub>SO):** δ (ppm) = 152.7 (C-8), 151.5 (C-6), 149.4 (C-7), 143.3 (C-3), 135.6 (C4a), 125.3 (8a), 120.4 (C-4), 102.9 (C-5), 102.1 (CH<sub>2</sub>), 70.8 (C-1).

**5-(3,4,5-Trimethoxyphenyl)-[1,3]dioxolo[4,5-g]isoquinoline (IQTub8)**

**IQTub8** was first described in 1950 by Reeve et. al. as compound **10**<sup>11</sup>, an isoquinoline derivative related to the tubulin depolymerizing agent podophyllotoxin, *en route* to di- and tetrahydroisoquinolines that Reeve *et al.* assumed might also possess the tumor damaging properties of podophyllotoxin. However, their potential pharmacological effects were not investigated.



3,4,5-Trimethoxyphenylboronic acid (430 mg, 1.46 mmol) was added to a solution of **S3** (350 mg, 1.17 mmol) in THF (5 mL). After addition of Pd(PPh<sub>3</sub>)<sub>4</sub> (68 mg, 5 mol%) and aq.

K<sub>2</sub>CO<sub>3</sub> solution (2 M; 1.76 mL, 3.52 mmol) the reaction mixture was stirred under nitrogen at 90°C for 16 h. After cooling to room temperature and addition of water (50 mL) the mixture was extracted with EtOAc (3 × 50 mL). The combined organic layers were dried over Na<sub>2</sub>SO<sub>4</sub> and concentrated *in vacuo*. The crude product was purified by flash column chromatography (EtOAc/hexanes 3:7) to give **IQTub8** (207 mg, 0.61 mmol, 52%) as a colourless solid.

**HRMS (ESI<sup>+</sup>):** 340.1180 calculated for C<sub>19</sub>H<sub>18</sub>NO<sub>5</sub><sup>+</sup> [M+H]<sup>+</sup>, 340.1177 found. **<sup>1</sup>H NMR (400 MHz, (CD<sub>3</sub>)<sub>2</sub>SO):** δ (ppm) = 8.85 (s, 1H, 8-H), 8.34 (d, *J* = 5.6 Hz, 1H, 3-H), 7.70 (d, *J* = 5.5 Hz, 1H, 4-H), 7.38 (s, 1H, 5-H), 6.81 (s, 2H, 2'-H and 6'-H), 6.19 (s, 2H, CH<sub>2</sub>), 3.79 (s, 6H, 3'-OCH<sub>3</sub> and 5'-OCH<sub>3</sub>), 3.76 (s, 3H, 4'-OCH<sub>3</sub>). **<sup>13</sup>C NMR (100 MHz, (CD<sub>3</sub>)<sub>2</sub>SO):** δ (ppm) = 153.5 (C-3' and C-5'), 150.6 (C-6), 148.3 (C-8), 145.8 (C-7), 142.3 (C-3), 137.9 (C-4'), 134.6 (C-1), 127.8 (C-1'), 124.7 (C-8a), 120.7 (C-4a), 117.2 (C-4), 108.3 (C-2' and C-6'), 102.4 (CH<sub>2</sub>), 102.2 (C-5), 60.6 (4'-OCH<sub>3</sub>), 56.6 (3'-OCH<sub>3</sub> and 5'OCH<sub>3</sub>). *This compound appears as a mixture of atropisomers in NMR characterization.* **HPLC purity:** >95 %.

## Part B: Biochemistry *in vitro*

### Tubulin polymerisation *in vitro*

99% tubulin from porcine brain was obtained from Cytoskeleton Inc. (cat. #T240). The polymerisation reaction was performed at 5 mg/mL tubulin, in polymerisation buffer BRB80 (80 mM piperazine-N,N'-bis(2-ethanesulfonic acid) (PIPES) pH = 6.9; 0.5 mM EGTA; 2 mM MgCl<sub>2</sub>), in a cuvette (120 µL final volume, 1 cm path length) in a Varian CaryScan 60 with Peltier cell temperature control unit maintained at 37°C; with glycerol (10 µL). Tubulin was first incubated for 10 min at 37°C with **IQTub5** (20 µM) or colchicine (16 µM) in buffer with 3% DMSO, without GTP. Then GTP was added to achieve final GTP concentration 1 mM (with mixing), and the change in absorbance at 340 nm was monitored for 15 min, scanning at 15 s intervals;<sup>12</sup> greater absorbance (= turbidity) corresponds to a greater degree of polymerization (Figure 5b). **IQTub5** showed noticeable slowdown of polymerisation kinetics, nearly identical to that with the reference microtubule inhibitor colchicine.

### Metabolic stability

Metabolic stability of **IQTub4** in the presence of mouse and human liver microsomes, at 2 µM, was assayed by Bienta Biology Services (Kiev, Ukraine) over a 40 min timecourse at 37°C as is standard practice<sup>13</sup> (Figure S1). Mouse hepatic microsomes were isolated according to a standard protocol; human hepatic microsomes were supplied by XenoTech. Microsomal incubations were performed in duplicates and control incubations were performed replacing the NADPH-cofactor system with PBS. Supernatants were analyzed using HPLC system coupled with tandem mass spectrometer. The elimination constant ( $k_{el}$ ), half-life ( $t_{1/2}$ ) and intrinsic clearance ( $Cl_{int}$ ) were determined in plot of  $\ln(AUC)$  versus time, using linear regression analysis. Reference compounds were imipramine, caffeine and propranolol.

<b>a Human microsomal stability</b>			
<b>IQTub4</b>			
time [min]	% remaining	t <sub>1/2</sub> [min]	% remaining without cofactor
0	100	68	100
10	99		nd
20	84		nd
30	75		nd
40	69		98
<b>Caffeine</b>			
time [min]	% remaining	t <sub>1/2</sub> [min]	% remaining without cofactor
0	100	206	100
10	99		nd
20	96		nd
30	91		nd
40	88		105
<b>Imipramine</b>			
time [min]	% remaining	t <sub>1/2</sub> [min]	% remaining without cofactor
0	100	77	100
10	91		nd
20	81		nd
30	77		nd
40	69		94

<b>b Mouse microsomal stability</b>			
<b>IQTub4</b>			
time [min]	% remaining	t <sub>1/2</sub> [min]	% remaining without cofactor
0	100	68	100
10	99		nd
20	84		nd
30	75		nd
40	69		98
<b>Propranolol</b>			
time [min]	% remaining	t <sub>1/2</sub> [min]	% remaining without cofactor
0	100	54	100
10	74		nd
20	69		nd
30	61		nd
40	58		94
<b>Imipramine</b>			
time [min]	% remaining	t <sub>1/2</sub> [min]	% remaining without cofactor
0	100	8	100
10	49		nd
20	23		nd
30	8		nd
40	3		94

Figure S1: Metabolic stability of **IQTub4** and given reference compounds in the presence of **a** human and **b** mouse liver microsomes.

In human microsomes, the degradation rate of **IQTub4** was identical to reference compound imipramine (31% over 40 min), under conditions where second reference compound caffeine was <10% metabolised. In mouse microsomes, imipramine was >90% degraded after 30 minutes but **IQTub4** had only 33% degradation over 40 min, demonstrating high stability. The result may be very favourably compared to that of isoquinoline triaryl compound **2** from Hwang *et al.*<sup>13</sup> which had a half-life of 39 min in human microsomes and only 2 min in mouse microsomes under the same assay conditions. Therefore we conclude that **IQTubs** are substantially metabolically stable, suiting them for further pharmacological evaluation. “No cofactor” control data indicate that the observed compound conversion is primarily determined by CYP450 activity.

### CYP450 inhibition

The potential for CYP450 inhibition was assessed by *in vitro* inhibition studies using fluorogenic CYP450 substrates with the corresponding CYP450 enzymes (CYP2D6, CYP2C9, CYP3A4, CYP2C19, CYP1A2) and NADPH regeneration system (Vivid CYP450 Screening Kits) with some minor changes to the manufacturer's protocols, performed by Bienta Biology Services (Figure S2). The fluorescent signal produced from reaction is directly proportional to the cytochrome P450 activity. In the cases when tested compounds interfere with the CYP450 enzyme-substrate reaction, the fluorescent signal decreases.

In brief, the tested compound was first dissolved in DMSO at 1 mM, then diluted in aqueous assay buffer to 25  $\mu$ M, then the dilute solutions were mixed with a pre-mix consisting of the human CYP450 with an NADP<sup>+</sup> regeneration system (glucose-6-phosphate and glucose-6-phosphate dehydrogenase). After 10 min pre-incubation, the enzymatic reaction was initiated by the addition of a mix of NADPH and the appropriate CYP450 substrates yielding a test compound concentration of 10  $\mu$ M. The reaction was incubated for the desired reaction time (25 min for CYP1A2, CYP2C9, CYP2D6, and CYP3A4, 60 min for CYP2C19) after which Stop Reagent was added and fluorescence measured using SpectraMax Paradigm Multi-Mode Microplate Reader. All test points were performed in quadruplicates at concentration 10  $\mu$ M (1% DMSO). Reference compounds used to benchmark the CYP inhibition under these conditions are listed in Figure S2.

CYP inhibition profile for IQTub4 [10 $\mu$ M] and reference compounds					
CYP	% inhibition by IQTub4 (n = 4)	SD (%)	reference inhibitor	ref. inhibitor conc. [ $\mu$ M]	% inhibition by ref. inhib.
1A2	-4	3	$\alpha$ -naphthoflavone	0.4	100
2D6	19	4	sulfaphenazole	5	85
2C9	16	4	ticlopidine	5	93
2C19	-49	6	quinidine	0.5	78
3A4	13	5	koconazole	0.4	85

Figure S2: Summary of CYP450 inhibition assay by IQTub4 at 10  $\mu$ M and the stated reference compounds used.

At 10  $\mu$ M **IQTub4** showed only from 13-19% inhibition for CYP2D6, CYP2C9 and CYP3A4; CYP1A2 showed zero inhibition, and CYP2C19 showed an apparent enhancement of 50% activity. Therefore, we conclude that no significant inhibition of these CYP enzymes is caused by **IQTub4**, indicating that it may escape typical drug-drug interaction pathways.

### hERG inhibition

hERG inhibition experiments were performed by Bienta Biology Services using Invitrogen Predictor™ hERG Fluorescence Polarisation Assay in accordance with the manufacturer's protocol (Protocol PV5365). In brief, a fluorescent tracer was incubated with **IQTub4** and membranes bearing hERG channel for 2–4 h in the solution and the polarisation of fluorescence emission (higher when bound to hERG, lower in solution due to free tumbling) is assayed with reference to control inhibitor E-4031 to validate assay performance. **IQTub4** was tested in quadruplicates at 1  $\mu$ M, 5  $\mu$ M and 25  $\mu$ M with reference to a positive control (only tracer, fluorescence polarisation is maximal when nothing interferes with the reaction of the tracer and hERG membranes - minimal tracer rotation) and a negative control (30  $\mu$ M of E-4031, i.e. 100% tracer displacement and minimum assay polarisation value, due to tested compound competing with the tracer for the hERG channel, the polarization of emitted light) (Figure S3).

hERG binding profile for IQTub4 and reference E4031			
Compound	conc [ $\mu$ M]	mean binding % (n = 4)	SD (%)
IQTub4	25	-5	5
	5	-19	2
	1	-3	9
E4031	30	100	0
no cpd		0	2

Figure S3: Inhibition of tracer binding to hERG by **IQTub4** alongside negative control (30  $\mu$ M of E4031) and positive control (cosolvent only). The data are represented as mean with SD, n=4.

**IQTub4** showed no inhibition of fluorescent tracer binding, implying no hERG inhibition liability. Note that **IQTub4** was used in this assay, although (unlike in the microsomal stability and CYP inhibition assays) it is, in theory, possible that the transmembrane hERG channel could also be exposed to the extracellular form of this drug, i.e. **IQTub4P**, by diffusion into the open channel space. The reason for this choice is that the hERG channel liabilities are known to stem from exposure to lipophilic compounds, while the prodrug form **IQTub4P** is strongly hydrophilic due to the phosphate ester, therefore we expected no hERG liability from it (this would match our unpublished data on other phosphate prodrugs).

### Determination of distribution coefficient (logD, pH 7.4)

Distribution coefficient logD was assessed experimentally by Bienta Biology Systems using the octanol/water shake-flask method (Figure S4). In brief, **IQTub4** DMSO stock was added to a mixture of PBS buffer and *n*-octanol, the mixture equilibrated by mixing in a rotor for 1 h, and phase separation then performed by centrifugation. Both phases were then analysed using HPLC system coupled with tandem mass spectrometer. Mebendazole was used as a reference compound.

#### Experimental logD (pH 7.4) data for reference compound Mebendazole and IQTub4

Compound	Incubation	logD (pH 7.4)	
<b>Mebendazole</b>	1	2.82	<b>2.90</b>
	2	2.93	
	3	2.93	
<b>IQTub4</b>	1	2.19	<b>2.18</b>
	2	2.18	
	3	2.18	

Figure S4: Experimental assessment of logD at pH 7.4 for reference compound mebendazole and **IQTub4**.

The logD at pH 7.4 for **IQTub4** was determined to be 2.18, with reference to control compound mebendazole showing a logD of 2.9 under the same conditions. Therefore, we conclude that the logD of **IQTub4** is within a range (1-3) considered optimum for general *in vivo* use<sup>14</sup>.

### Solubility determination of IQTub4P

**IQTub4P** was dissolved in (a) standard 0.9% NaCl solution to a concentration of 10 mM, with 4  $\mu$ L/mL of sat. aq. Na<sub>2</sub>CO<sub>3</sub> added to maintain pH, then subsequent filtration; or else (b) DMSO. Both solutions were then diluted into DMSO to reach concentrations 200  $\mu$ M, 100  $\mu$ M, 75  $\mu$ M and 50  $\mu$ M (2% - 0.05% water in DMSO respectively for NaCl dilutions); UV-Vis spectra between 360-400 nm were then acquired. Average absolute values of deviations between corresponding concentrations' absorptivities A( $\lambda$ ) were determined and were averaged yielding <15%, which indicates satisfactorily comparable solubility at 10 mM in aq. solution at tested pH (in mildly acidic solution, the solubility decreases as expected).

## Part C: Biological Data

### Cell assay methods

#### General cell culture

HeLa cells were maintained under standard cell culture conditions in Dulbecco's modified Eagle's medium (DMEM; PAN-Biotech: P04-035550) supplemented with 10% fetal calf serum (FCS), 100 U/mL penicillin and 100 U/mL streptomycin. HL-60 cells were maintained under standard cell culture conditions in RPMI 1640 medium (PAA Laboratories) supplemented with 10% FCS, without the addition of antibiotics. Cells were grown and incubated at 37°C in a 5% CO<sub>2</sub> atmosphere. Substrates and cosolvent (DMSO; 1% final concentration) were added *via* a D300e digital dispenser (Tecan) for resazurin assays and manually for MTT assays.

#### Resazurin antiproliferation assay

HeLa cells were seeded in 96-well plates at 5,000 cells/well and left to adhere for 24 h before treating with **IQTubs** for 48 h with a final well volume of 100  $\mu$ L, 1% DMSO; three technical replicates; the cosolvent control was treated with 1% DMSO only. Resazurin (7-hydroxy-3H-phenoxazin-3-one-10-oxide) was added to the cells for 3 h. Absorbance of the resazurin-metabolite resorufin was measured at 590 nm (excitation 544 nm) using a FLUOstar Omega microplate reader (BMG Labtech). Absorbance data was averaged over the technical replicates, then normalised to viable cell count from the cosolvent control cells (% control) as 100%, where 0% viability was assumed to correspond to absorbance zero. Data were plotted against the log of **IQTub** concentration ( $\log_{10}([\text{IQTub}] \text{ (M)})$ ).

#### MTT antiproliferation assay

HL-60 cells were seeded in 96-well plates at 9,000 cells/well and left for 24 h before treating with **IQTubs** for 24 h (1% DMSO; three technical replicates); the cosolvent control (maximum viability) was treated with 1% DMSO only and Triton-X® 100 was used as a positive control (0% viability). Cells were then treated with 0.5 mg/mL (3-(4,5-dimethylthiazol-2-yl)-2,5-diphenyl tetrazolium bromide (**MTT**) for 2 h, the medium was aspirated, and formazan crystals were re-dissolved in DMSO (100  $\mu$ L); absorbance was measured at 570 nm using a FLUOstar Omega microplate reader (BMG Labtech). Absorbance data was averaged over the technical replicates, then normalized with cosolvent control absorbance as 100% and Triton positive control absorbance as 0%. Data were plotted and analysed in GraphPad Prism.

#### Cell cycle analysis

**IQTubs** were added to HeLa cells in 24-well plates (50,000 cells/well; three technical replicates, three biological replicates) and incubated for 24 h. Cells were collected, permeabilised, treated with RNase (20  $\mu$ g/mL) and stained with 2  $\mu$ g/mL propidium iodide (PI)



in HFS buffer (PBS, 0.1% Triton X-100, 0.1% sodium citrate) at 4°C for 30 min then analysed by flow cytometry using a BD LSR Fortessa flow cytometer (Becton Dickinson) run by BD FACSDiva software<sup>15</sup>. 30,000 events per technical replicate were analysed; the PI signal per event (corresponding to cellular DNA content) was measured and cells were binned into G1, S and G2 phase according to DNA content using *Flowing* software. Results (means of three technical replicates) from one experiment of three independent trials are shown.

#### **Immunofluorescence staining**

HeLa cells were seeded on glass coverslips in 24-well plates (50,000 cells/well), left to adhere for 16 h, then treated for 24 h with **IQTubs**. Cells were washed with pre-warmed (37°C) MTSB buffer (80 mM PIPES, 1 mM MgCl<sub>2</sub>, 5 mM EGTA adjusted to pH ~6.8 with 0.5% Triton X-100, see Cramer and Desai<sup>16</sup>) for 30 s then fixed with 0.5% glutaraldehyde for 10 min. After quenching with 0.1% NaBH<sub>4</sub> (7 min), samples were blocked in PBS + 10% FCS (30 min). The cells were treated with primary antibody (1:400 rabbit alpha-tubulin; Abcam ab18251) in blocking buffer for 1 h and then washed with PBS. Cells were incubated with secondary antibody (1:400 goat anti-rabbit Alexa fluor 488; Abcam ab150077) in blocking buffer for 1 h. After washing with PBS, the coverslips were mounted onto glass slides using Roti-Mount FluorCare DAPI (Roth) and imaged with a Zeiss LSM Meta confocal microscope (CALM platform, LMU). Images were processed using the free Fiji software<sup>17</sup>. Postprocessing was only performed to improve visibility. For maximum intensity projections, images were recorded at different focal planes incrementally stepping through the sample (step size 1–2 μm) and maximum intensity projections were obtained using Fiji software.

#### **EB3-comet live-cell assay**

HeLa cells (12,000 cells/well) were seeded on 8-well ibiTreat μ ibidi slides (ibidi, Martinsried, Germany) 24 h prior to transfection. Cells were transiently transfected with *EB3-YFP* plasmid using jetPRIME reagent (Polyplus) according to the manufacturer's instructions. Cells were imaged 24 h later, at 37°C under 5% CO<sub>2</sub> atmosphere, using an UltraVIEW Vox spinning disc confocal microscope (PerkinElmer) operated with *VLOCITY* software equipped with an EMCCD camera (Hamamatsu, Japan), and an environmental chamber kept at 37°C and 5% CO<sub>2</sub> using a 63×, 1.4 NA Plan-Apochromat oil-immersion objective (Zeiss). Cells were left to equilibrate on the stage for 10 min before acquiring uninhibited cellular EB3 comet images at timepoint  $t_{ref}$ , imaging at 514 nm (45 frames/min). **IQTub4P** (10 μM) was then added, cells were incubated for a further 2 minutes (for dephosphorylation and cell penetration), then imaged again (timepoint  $t_2$ ). For analysis, 7 cells were chosen from three independent trials. The EB3-comets were counted and each cell's comet count value at  $t_{ref}$  or  $t_2$  was set as the average from 5 frames taken at  $t_{ref}$  or  $t_2$ . EB3-comets<sup>18</sup> were counted with highly conservative

parametrisation using a plugin for *Fiji* software based on the “Find maxima” function from the NIH (<https://imagej.nih.gov/ij/macros/FindStackMaxima.txt>).

### Immunofluorescence imaging of microtubule networks

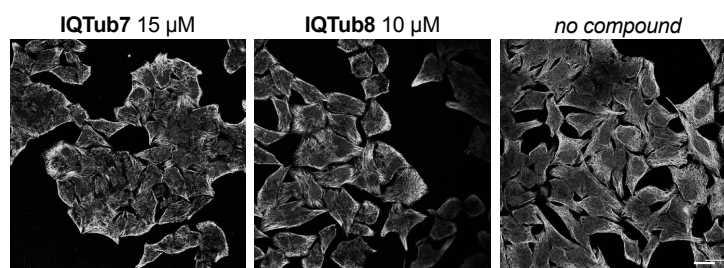


Figure S5: Immunofluorescence imaging of microtubules in cells treated for 24 h with **IQTub7** and **IQTub8** show no disruption of microtubule network structure even at high concentrations, with reference to cosolvent control. (Cosolvent control panel was also shown in Figure 4; HeLa cells; MTs immunostained with anti- $\alpha$ -tubulin (green); nuclei stained with DAPI (blue); scale bar = 20  $\mu$ m).

### Determination of safe *in vivo* dosing parameters

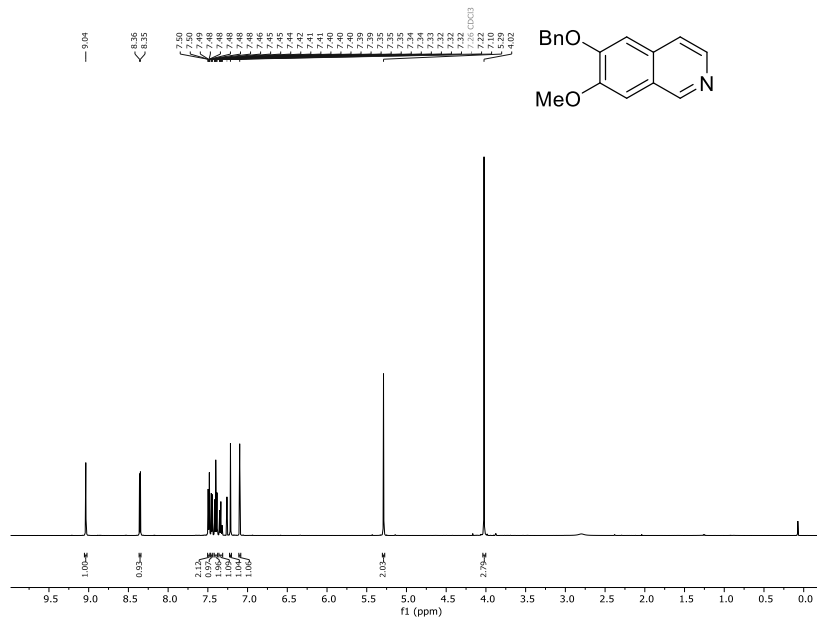
Safe dosing parameters of **IQTub4**'s fully water-soluble prodrug **IQTub4P** (as disodium salt) were determined *in vivo* in male and female Balb/c mice by standard methods (LASA NC3Rs) following *i.v.* and *i.p.* compound administration; all animal experiments performed were conducted in compliance with institutional guidelines (Bienta Biology Services). Single dosage of 50 mg/kg *i.v.* or below was tolerated, with piloerection in one mouse observed on days 2 and 3 after injection corresponding to body weight loss but other mice experiencing steady body weight (from -2% to +8% over 7 days). Single dosage of 31.5 mg/kg *i.p.* was tolerated by all mice tested with no observable effects and average body weight change -0.1% over 7 days. Repeated dosage studies were conducted at dosage of 25 mg/kg (delivered by injection at 100  $\mu$ L total volume, ie. 12.5 mM compound concentration in phosphate-buffered saline at injection) both *i.v.* (n = 5F, 5M; PBS control 2F, 2M) and *i.p.* (n = 6F, 6M; PBS control 3F, 3M) with 3 administrations at 48 h intervals and 20 monitoring timepoints. One *i.v.* injection male mouse was removed from study on day 2 due to bodyweight loss, the other 9 mice of the *i.v.* study showed good appearance with no piloerection observed, there was one timepoint of inactivity in one mouse in each of the control and the test groups and both recovered before the next timepoint. In the *i.p.* injection set, two mice experienced transient piloerection which disappeared after the two next monitoring points; other mice had good appearance. Note that this requirement for a high injection concentration in aqueous media underscores the emphasis placed on water solubility for practical application *in vivo*.

## Supplementary Information Bibliography

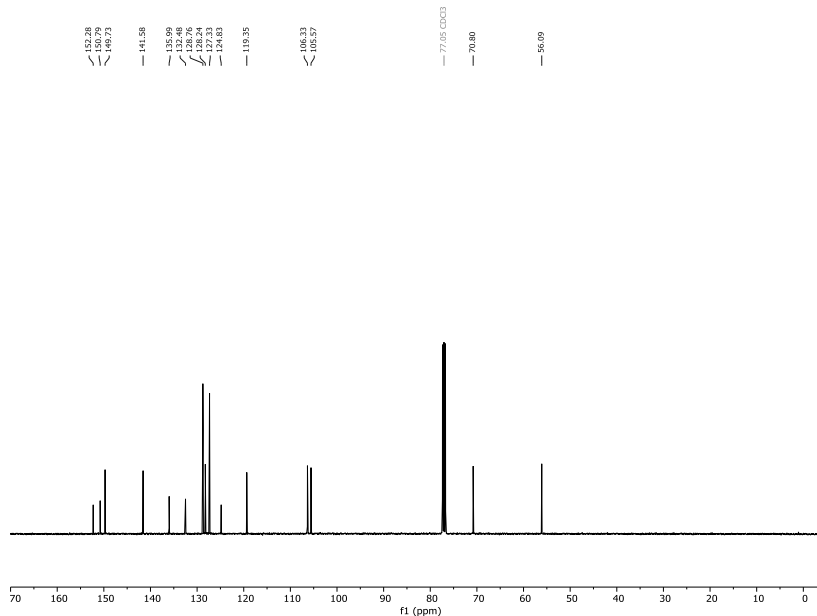
- Gottlieb, H. E.; Kotlyar, V.; Nudelman, A., NMR Chemical Shifts of Common Laboratory Solvents as Trace Impurities. *The Journal of Organic Chemistry* **1997**, *62* (21), 7512-7515, doi: 10.1021/jo971176v.
- Battersby, A. R.; Le Count, D. J.; Garratt, S.; Thrift, R. L., Synthetic applications of 1,2-dihydroisoquinolines: Synthesis of ( $\pm$ )-coreximine. *Tetrahedron* **1961**, *14* (1), 46-53, doi: 10.1016/0040-4020(61)80086-0.
- Fabrik, A. A. A.-G. C. Verfahren zur Darstellung von 1-(3,4,5-Trialkoxyphenyl)-6,7-dialkoxyisochinolininen. DE614703C, **1932**.
- Hati, S.; Sen, S., Cerium Chloride Catalyzed, 2-Iodoxybenzoic Acid Mediated Oxidative Dehydrogenation of Multiple Heterocycles at Room Temperature. *European Journal of Organic Chemistry* **2017**, *2017* (9), 1277-1280, doi: 10.1002/ejoc.201601419.
- Chuang, T.-H.; Li, C.-F.; Lee, H.-Z.; Wen, Y.-C., Direct Conversion of 1-(2-Bromobenzoyl)isoquinolines to Dibenz[de,g]quinolin-7-ones via Reductive Photocyclization. *The Journal of Organic Chemistry* **2013**, *78* (10), 4974-4984, doi: 10.1021/jo400645g.
- Robbins, J. S.; Schmid, K. M.; Phillips, S. T., Effects of Electronics, Aromaticity, and Solvent Polarity on the Rate of Azaquinone–Methide-Mediated Depolymerization of Aromatic Carbamate Oligomers. *The Journal of Organic Chemistry* **2013**, *78* (7), 3159-3169, doi: 10.1021/jo400105m.
- Melzer, B. C.; Bracher, F., A novel approach to oxoisoaporphine alkaloids via regioselective metalation of alkoxy isoquinolines. *Beilstein J. Org. Chem.* **2017**, *13*, 1564-1571, doi: 10.3762/bjoc.13.156.
- Tong, Q.; Schwebel, N.; Brocke, C.; Deing, K. C.; Vogt, J.; Meyer, E. Polymerizable Compounds And The Use Thereof in Liquid-Crystal Displays. US2016362606 (A1), **2016**.
- Pettersson, M.; Johnson, D. S.; Subramanyam, C.; Bales, K. R.; am Ende, C. W.; Fish, B. A.; Green, M. E.; Kauffman, G. W.; Mullins, P. B.; Navaratnam, T.; Sakya, S. M.; Stiff, C. M.; Tran, T. P.; Xie, L.; Zhang, L.; Pustilnik, L. R.; Vetelino, B. C.; Wood, K. M.; Pozdnyakov, N.; Verhoest, P. R.; O'Donnell, C. J., Design, Synthesis, and Pharmacological Evaluation of a Novel Series of Pyridopyrazine-1,6-dione  $\gamma$ -Secretase Modulators. *Journal of Medicinal Chemistry* **2014**, *57* (3), 1046-1062, doi: 10.1021/jm401782h.
- Birch, A. J.; Jackson, A. H.; Shannon, P. V. R., A new modification of the pomeranz–fritsch isoquinoline synthesis. *Journal of the Chemical Society, Perkin Transactions 1* **1974**, (0), 2185-2190, doi: 10.1039/P19740002185.
- Reeve, W.; Eareckson, W. M., Synthesis of Some Isoquinoline Derivatives Related to Podophyllotoxin. *Journal of the American Chemical Society* **1950**, *72* (11), 5195-5197, doi: 10.1021/ja01167a114.
- Lin, C. M.; Singh, S. B.; Chu, P. S.; Dempcy, R. O.; Schmidt, J. M.; Pettit, G. R.; Hamel, E., Interactions of tubulin with potent natural and synthetic analogs of the antimitotic agent combretastatin: a structure-activity study. *Molecular Pharmacology* **1988**, *34* (2), 200-8, doi: 10.1021/ja01167a114.
- Hwang, D.-J.; Wang, J.; Li, W.; Miller, D. D., Structural Optimization of Indole Derivatives Acting at Colchicine Binding Site as Potential Anticancer Agents. *ACS Medicinal Chemistry Letters* **2015**, *6* (9), 993-997, doi: 10.1021/acsmchemlett.5b00208.
- Waring, M. J., Defining optimum lipophilicity and molecular weight ranges for drug candidates—Molecular weight dependent lower logD limits based on permeability. *Bioorganic & Medicinal Chemistry Letters* **2009**, *19* (10), 2844-2851, doi: 10.1016/j.bmcl.2009.03.109.
- Borowiak, M.; Nahaboo, W.; Reynders, M.; Nekkolla, K.; Jalinet, P.; Hasserodt, J.; Rehberg, M.; Delattre, M.; Zahler, S.; Vollmar, A.; Trauner, D.; Thorn-Seshold, O., Photoswitchable Inhibitors of Microtubule Dynamics Optically Control Mitosis and Cell Death. *Cell* **2015**, *162* (2), 403-411, doi: 10.1016/j.cell.2015.06.049.
- Desai, A.; Cramer, L.; Mitchison, T., Fluorescence Procedures for the Actin and Tubulin Cytoskeleton in Fixed Cells. **2012**, <<<http://mitchison.med.harvard.edu/protocols.html>>>, doi: <http://mitchison.med.harvard.edu/protocols/>.
- Schindelin, J.; Arganda-Carreras, I.; Frise, E.; Kaynig, V.; Longair, M.; Pietzsch, T.; Preibisch, S.; Rueden, C.; Saalfeld, S.; Schmid, B.; Tinevez, J.-Y.; White, D. J.; Hartenstein, V.; Eliceiri, K.; Tomancak, P.; Cardona, A., Fiji: an open-source platform for biological-image analysis. *Nature Methods* **2012**, *9*, 676, doi: 10.1038/nmeth.2019.
- Kleele, T.; Marinković, P.; Williams, P. R.; Stern, S.; Weigand, E. E.; Engerer, P.; Naumann, R.; Hartmann, J.; Karl, R. M.; Bradke, F.; Bishop, D.; Herms, J.; Konnerth, A.; Kerschensteiner, M.; Godinho, L.; Misgeld, T., An assay to image neuronal microtubule dynamics in mice. *Nat Commun* **2014**, *5*, 4827-4827, doi: 10.1038/ncomms5827.

**Part D: Selected NMR spectra**  
**6-(Benzyloxy)-7-methoxyisoquinoline (4)**

**<sup>1</sup>H-NMR:**



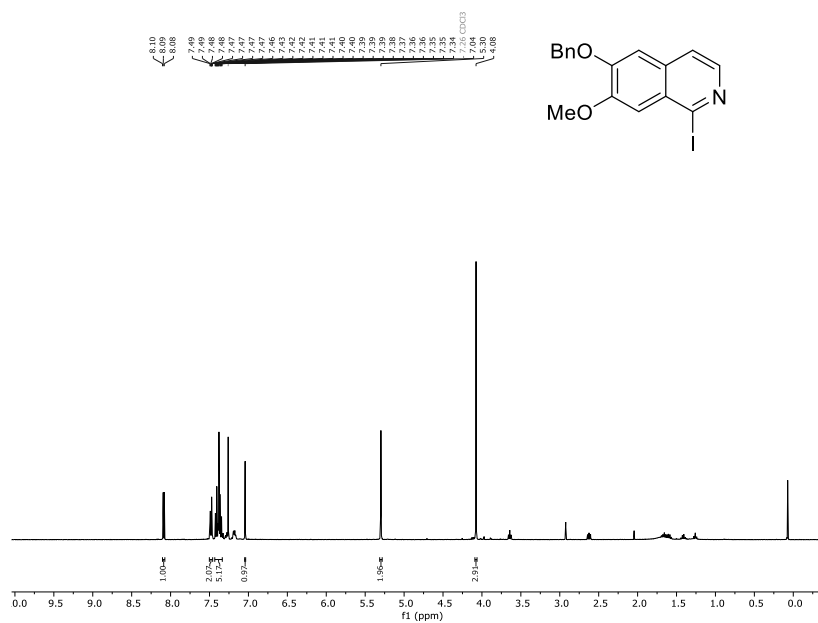
**<sup>13</sup>C-NMR:**



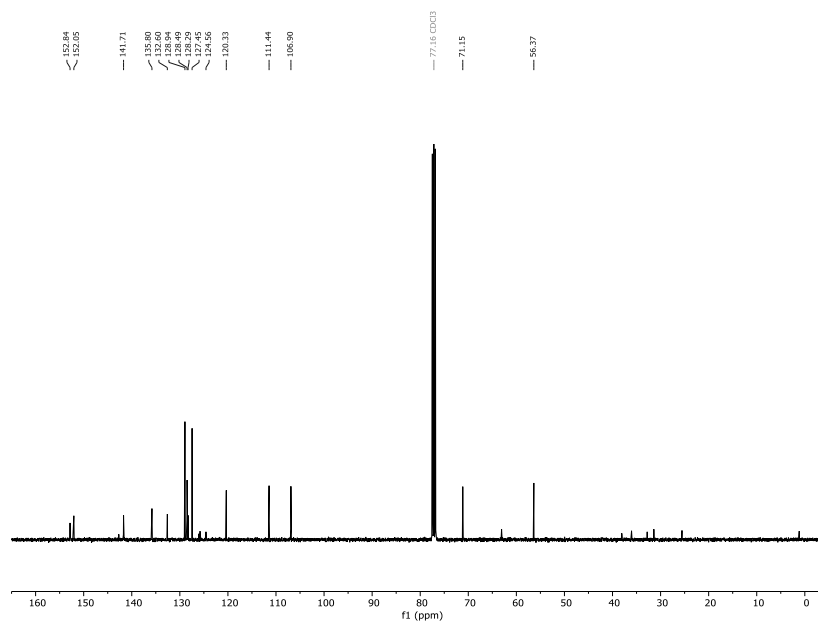
S26

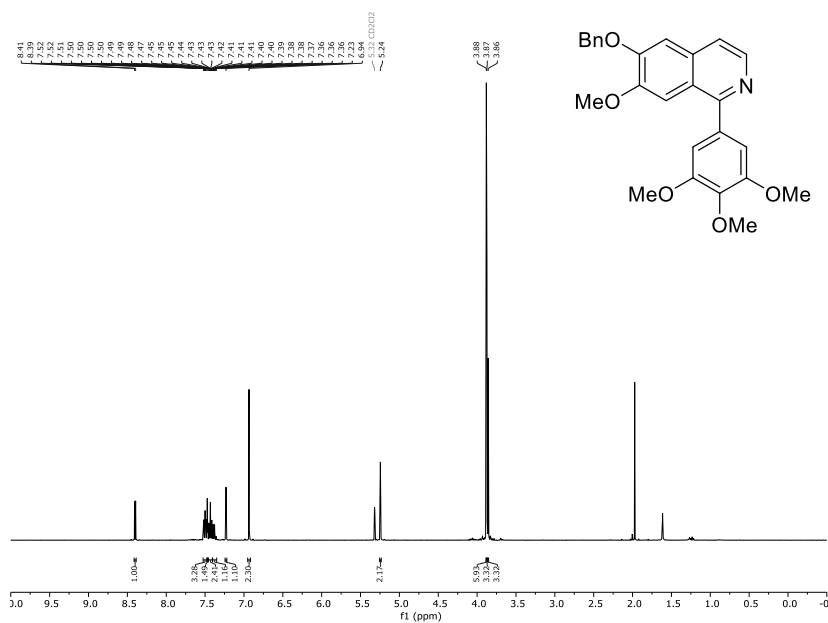
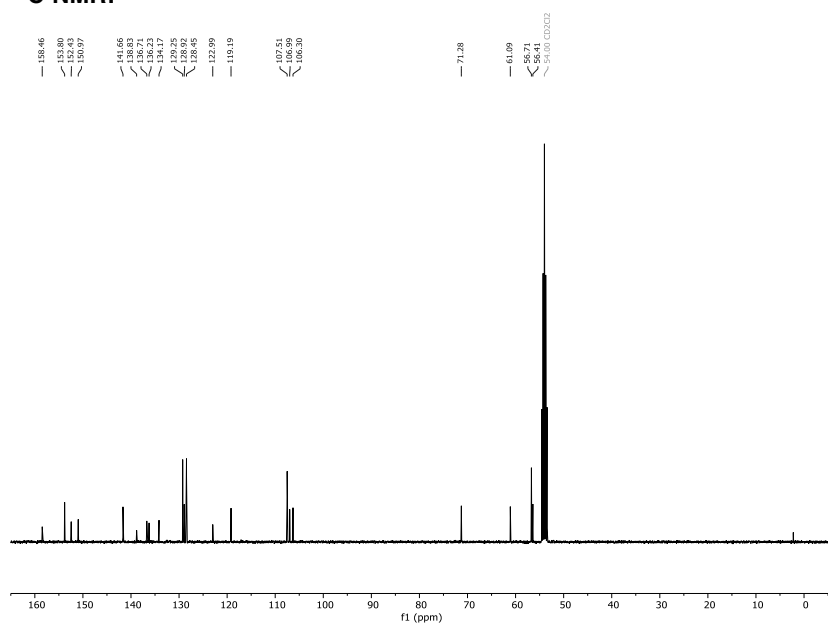
**6-(Benzyloxy)-1-iodo-7-methoxyisoquinoline (5)**

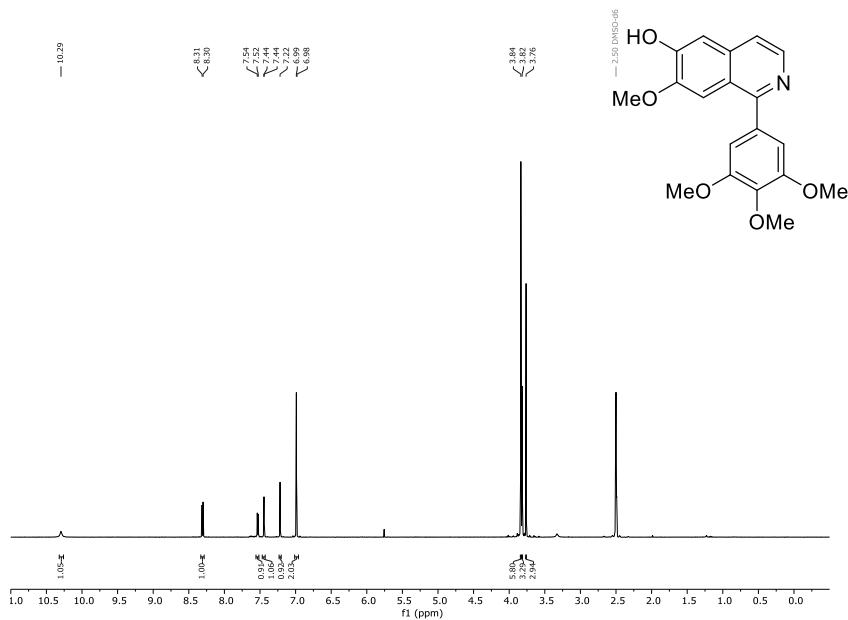
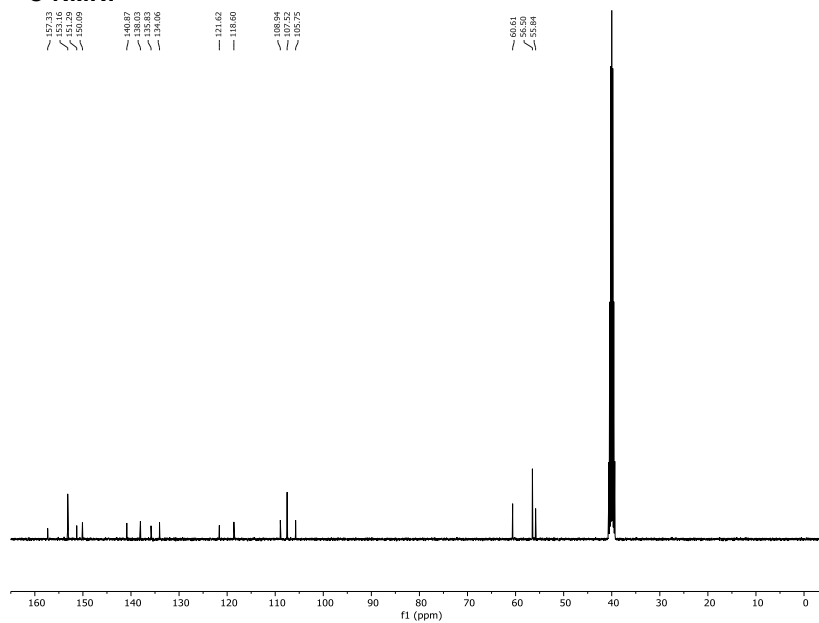
**<sup>1</sup>H-NMR:**

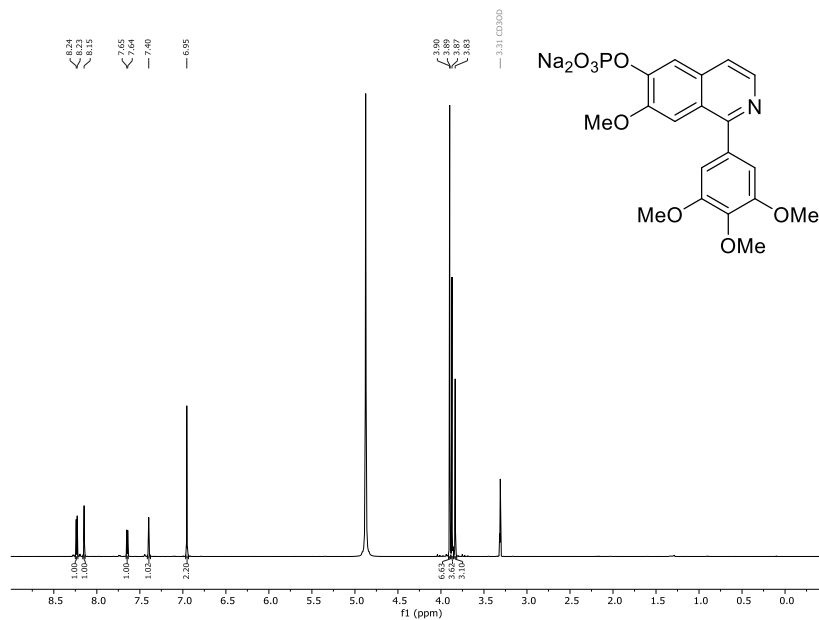
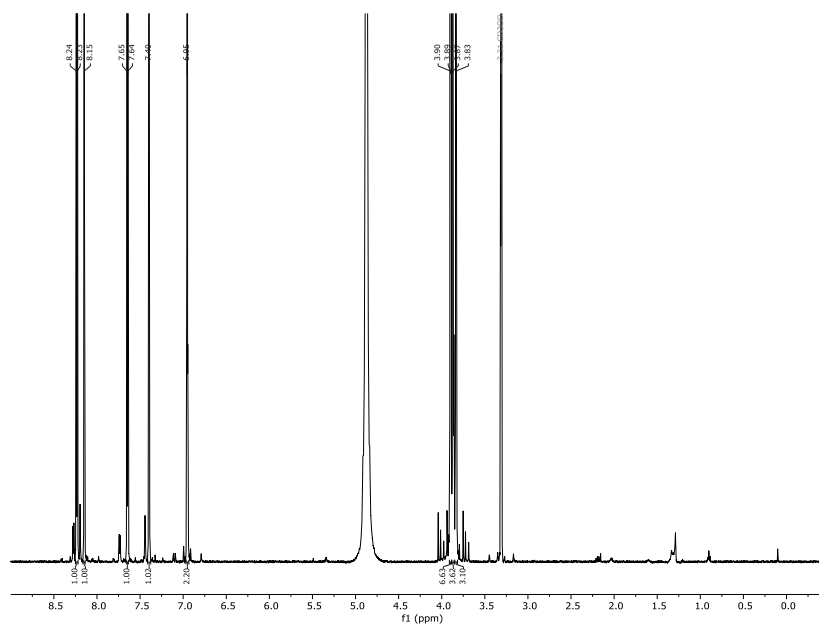


**<sup>13</sup>C-NMR:**



**6-(Benzyloxy)-7-methoxy-1-(3,4,5-trimethoxyphenyl)isoquinoline (6)****<sup>1</sup>H-NMR:****<sup>13</sup>C-NMR:**

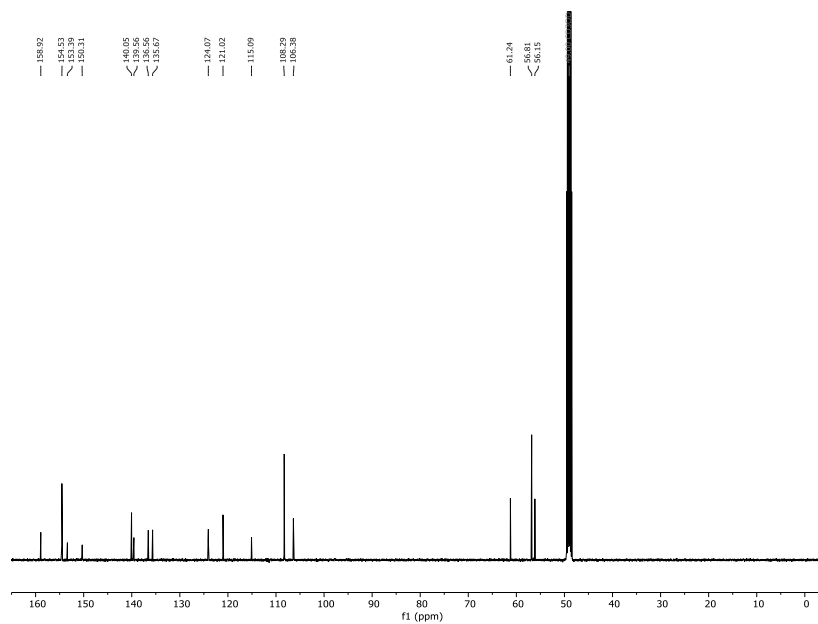
**7-Methoxy-1-(3,4,5-trimethoxyphenyl)isoquinolin-6-ol (IQTub4)****<sup>1</sup>H-NMR:****<sup>13</sup>C-NMR:**

**Sodium 7-methoxy-1-(3,4,5-trimethoxyphenyl)isoquinolin-6-yl phosphate (IQTub4P)****<sup>1</sup>H-NMR:****Enlargement, <sup>1</sup>H-NMR:**



S30

<sup>13</sup>C-NMR:



## **Supplementary Information Chapter 4: Photopharmaceutical microtubule depolymerisers**

### Chapter 4.1 Styrylbenzothiazole SBTubs

Licence

Reprinted with permission from: Li Gao, Joyce Meiring, Yvonne Kraus, Maximilian Wranik, Tobias Weinert, Stefanie Pritzl, Rebekkah Bingham, Evangelia Ntoliou, Klara Jansen, Natacha Olieric, Jörg Standfuss, Lukas Kapitein, Theobald Lohmüller, Julia Ahlfeld, Anna Akhmanova, Michel Steinmetz and Oliver Thorn-Seshold, A robust, GFP-orthogonal photoswitchable inhibitor scaffold extends optical control over the microtubule cytoskeleton, *Cell Chemical Biology* **2021**, 28, 1. Copyright 2020 Elsevier Ltd.

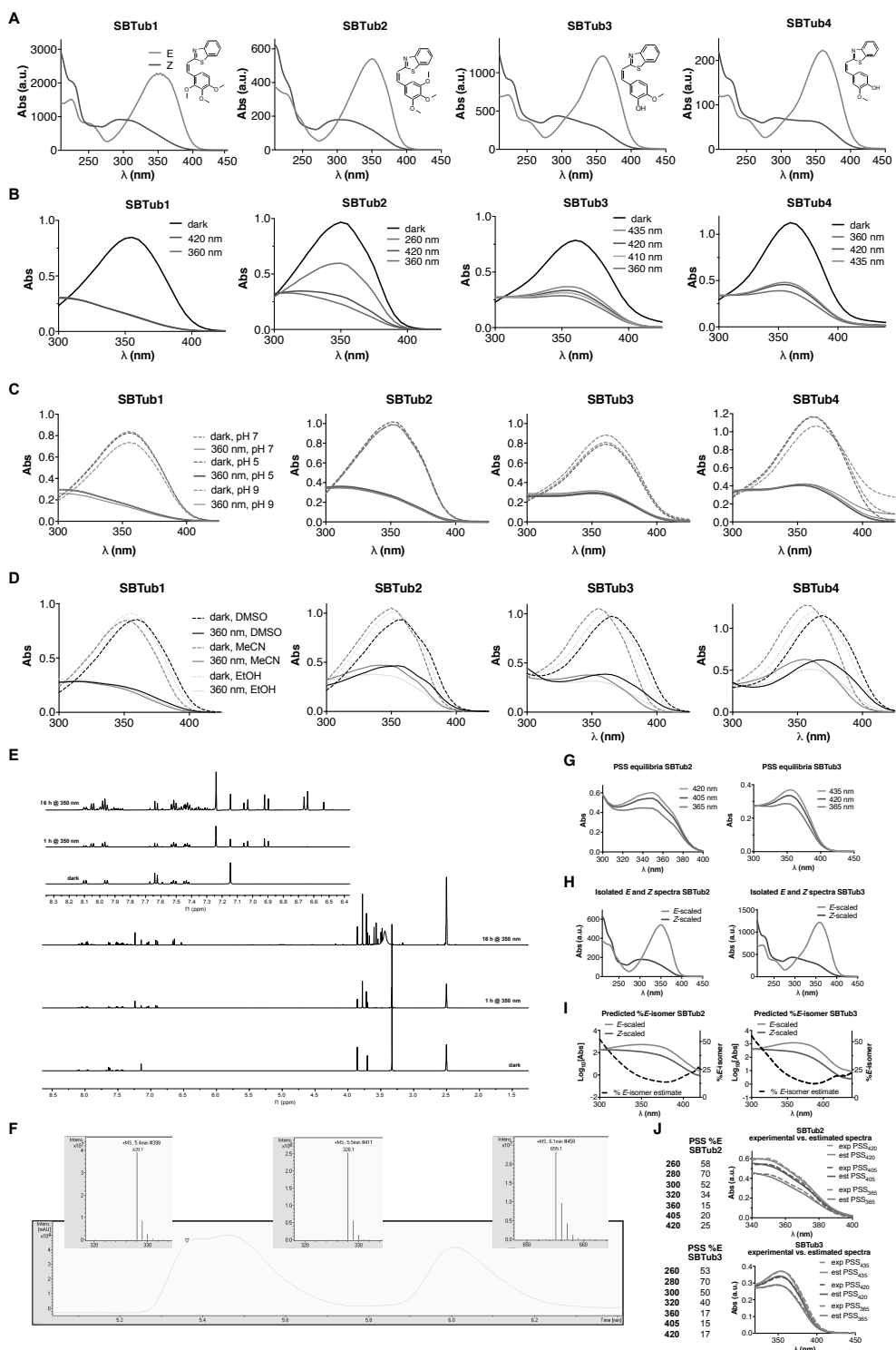


**Figure S1. Photoswitching of SBTubs, Related to Figure 1**

(A) all-*E* and all-*Z* spectra of SBTub1-4 from inline HPLC-DAD. (B) Absorption spectra of SBTub samples under saturating illumination at different wavelengths generating the given photostationary state (PSS) equilibria for SBTub1-4, from UV-Vis spectrophotometry, in 90% PBS:10% DMSO (SBTubs at 25  $\mu$ M).

(C-D) Absorption spectra of SBTub1-4 (25  $\mu$ M) in the dark (dashed lines) and at 360 nm PSS (solid lines), in (C) 90% PBS+10% DMSO at different buffer pH values and (D) different solvent environments.

(E) H-NMR spectra of SBTub2 in the dark (all-trans) and after exposure to 350 nm UV in Rayonet photoreactor for 1 h / 16 h, with zoom-ins on the aromatic region that illustrates isomerisation/cycloaddition.

(F) HPLC-MS trace of SBTub2 after irradiation with 350 nm in the UV photoreactor for 16 h displaying all three major peaks, with zoom panels showing mass spectra at 5.4 min (*Z*-SBTub2), 5.5 min (*E*-SBTub2), and 6.1 min (the [2+2] cycloaddition product).

(G-J) Procedure for determining PSS composition (see details in Supplemental Information): (G) PSS absorption spectra acquired in biological media are used to scale (H) HPLC spectra of pure *E* and *Z* isomers, which are then used to calculate (I) predicted *E*-isomer percentages at PSS under a range of illumination wavelengths (black dotted line scaling to the right axis, and accompanying tables). (J) The correspondence of simulated PSS ("est. PSS") to measured PSS ("exp. PSS") absorption spectra is checked, to confirm whether PSS interpolation is valid. PSS interpolation is shown to be closely valid for SBTub2 and SBTub3.

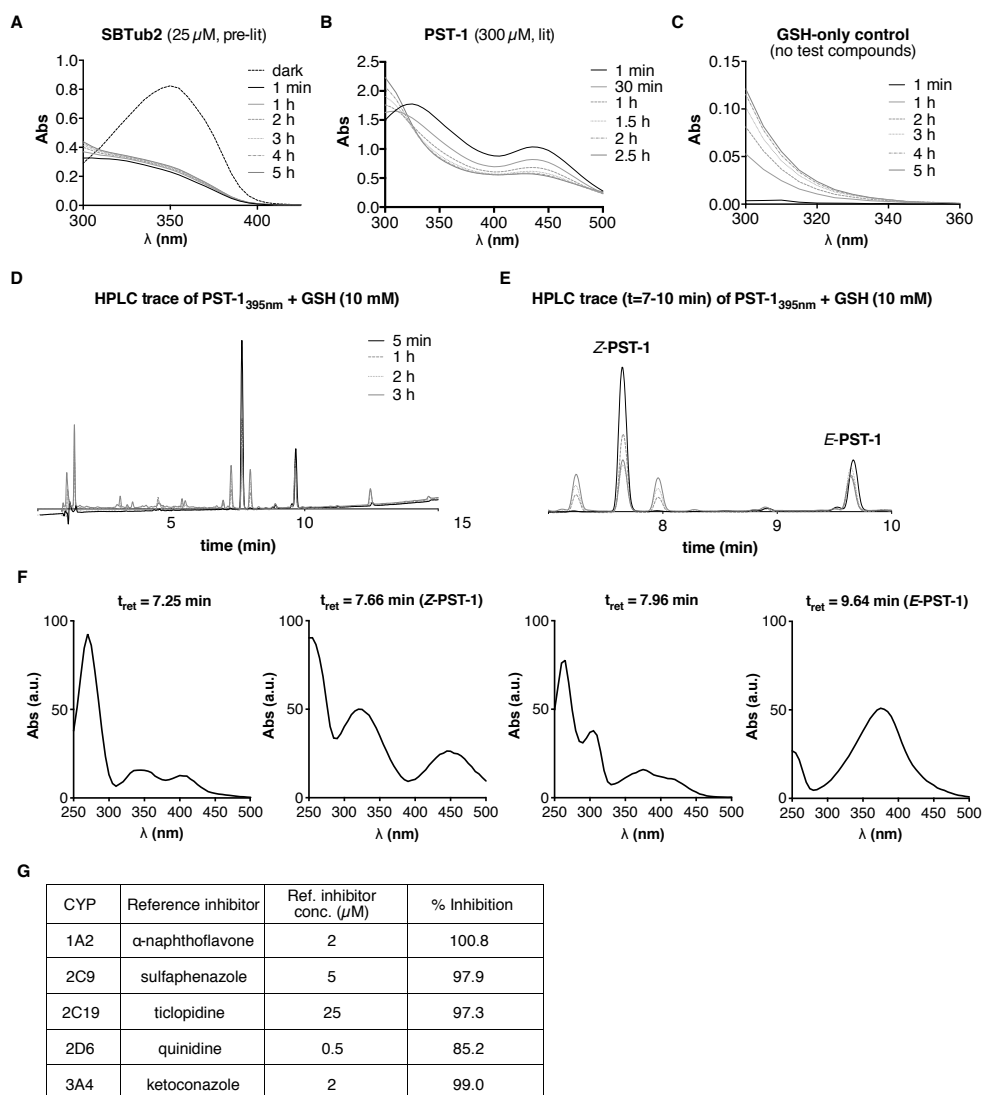


**Figure S2. Biochemistry of SBTubs, Related to Figure 2**

(A-F) GSH resistance assays, incubating test compounds with 10 mM GSH, data corresponding to Figure 2A. (A-B) Absorbance spectra of SBTub2 and PST-1 over time during GSH challenge. (C) Absorption spectrum of no-compound control sample (dark, 10 mM GSH only) presumably showing disulfide-formation-based absorption change underlying the profile changes in Figure S2A-B, which does not substantially affect results when taking the intercept at 360 nm or above. (D-E) 254 nm HPLC trace timecourse of PST-1 (0.5 mM) incubated with 10 mM GSH, with (D) the full-scale panel also shown as (E) zoom on the region of interest from  $t_{ret}$  = 7–10 min, showing Z-PST-1 ( $t_{ret}$  7.66 min), E-PST-1 ( $t_{ret}$  9.64 min) and the two new unidentified signals that increase over time ( $t_{ret}$  7.25 min and  $t_{ret}$  7.96 min). (F) DAD absorption spectra at the four major peaks. (All assays conducted with 10% DMSO for solubilisation). (G) Reference compounds used to benchmark CYP inhibition (see Figure 2E).

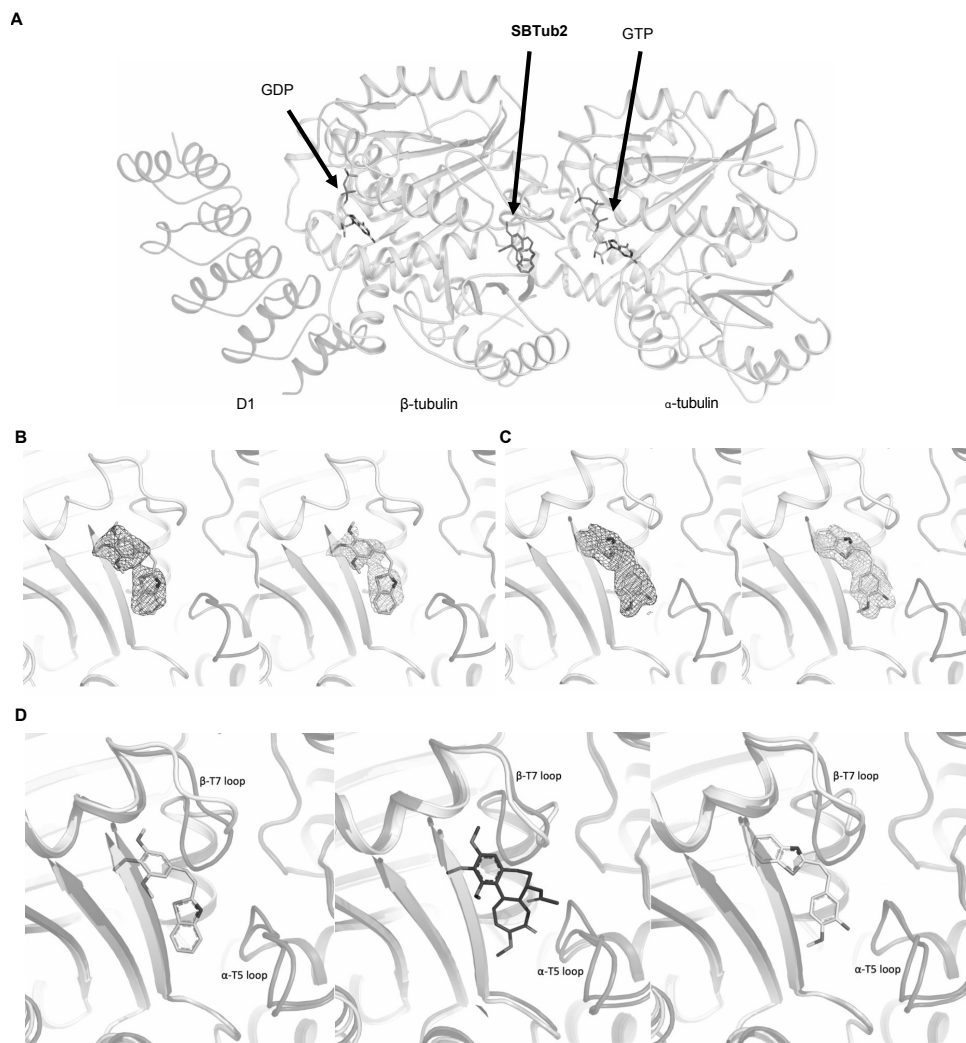


**Figure S3. Cell-Free Crystal Structures of Tubulin-SBTub Complexes Support Their Light-Specific Tubulin-Mediated Mechanism of Action, Related to Figure 3**

(A) Overall view of the TD1-Z-SBTub2 complex structure shown in cartoon representation with the different ligands shown in sticks representation.

(B) Colchicine site of tubulin-Z-SBTub2 with 2FoFc map contoured at 1 $\sigma$  shown in blue (left) and simulated annealing omit map at 2.5 $\sigma$  shown in green (right) mesh representation.

(C) Colchicine site of tubulin-Z-SBTub3 with 2FoFc map contoured at 1 $\sigma$  shown in blue (left) and simulated annealing omit map at 2.5 $\sigma$  shown in green (right) mesh representation.

(D) Side-by-side comparison of the colchicine sites of the tubulin-colchicine (middle; PDB ID 5NM5), tubulin-Z-SBTub2 (left) and tubulin-Z-SBTub3 (right) complex structures. On each structure, the ligand-free protein structure (PDB ID 5NQT) has been superimposed (shown in pink), to highlight structural rearrangements induced upon complexation.

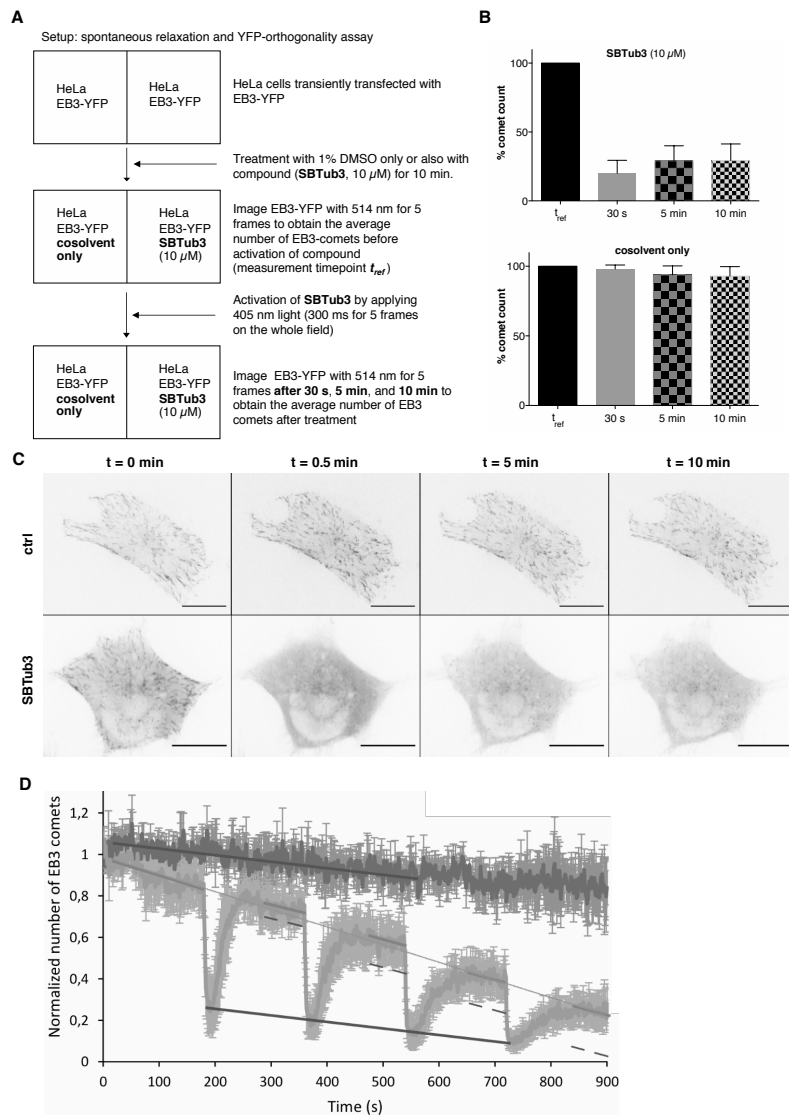


**Figure S4. EB imaging protocol and troubleshooting, Related to Figure 4**

(A) Experimental setup for photoswitching during live cell imaging of SBTub3 to evaluate orthogonality to YFP imaging (similar protocol used for evaluating GFP orthogonality) and resistance to relaxation on the stage.

(B) Quantification of EB3-YFP comets at different timepoints upon photoswitching during live cell imaging, normalised relative to comet count at  $t_{ref}$ .

(C) Stills of SBTub3 live cell imaging experiment corresponding to Figure S4B. (Cells have similar surface areas but stills are differently scaled in order to fill the fields of view; an inverted color scheme is used (black=bright signal, white=no signal) to highlight EB3 comets, which here appear as black dots; scale bar represents 20  $\mu$ m).

(D) Example EB3-imaging experiment where the starting choice of imaging parameters did not allow temporally reversible MT control and also caused fluorescent protein marker (FP) photobleaching. Blue statistics: DMSO control. Orange statistics: an SBTub-treated sample (40  $\mu$ M) where 405 nm photoactivation was applied for ca. 5 seconds every 180 seconds. Dotted purple and solid blue, red and pink fitlines are discussed in the Practical User Guide section of the Supplemental Information.

**Table S1. Crystallographic Data for Z-SBTub2 bound to tubulin-DARPin D1 (TD1) complex and for Z-SBTub3 bound to TD1 complex, Related to Star Methods X-ray diffraction data collection, processing and refinement.**

Data Statistics	TD1-Z-SBTub2	TD1-Z-SBTub3
Space group	P 2 <sub>1</sub>	P 2 <sub>1</sub>
Unit cell (a; b; c; $\beta$ )	73.90 91.85 82.81 96.58	73.87 91.72 83.00 97.06
Wavelength (Å)	1.0	1.0
Resolution (Å)	45.18 – 2.05 (2.33 – 2.05)	45.85 – 1.86
R <sub>pim</sub> (%)	7.4 (59.1)	5.5 (50.0)
I/ $\sigma$ I	7.1 (1.6)	9.3 (1.7)
Spherical completeness (%)	59.5 (9.3)	68.4 (12.9)
Ellipsoidal completeness (%)	88.2 (53.1)	91.2 (59.9)
Ellipsoidal truncation resolution limits (Å)	2.04, 2.50, 2.55	1.84, 2.23, 2,12
Multiplicity	4.1 (4.7)	4.2 (4.3)
CC <sub>1/2</sub>	0.992 (0.951)	0.997 (0.526)
<b>Refinement Statistics</b>		
Resolution	45.18 – 2.05	45.04 – 1.75
No. reflections	40926	68146
R <sub>work</sub> / R <sub>free</sub>	22.5 / 28.1	18.5 / 23.3
Ramachandran favoured	94.98%	97.15%
Ramachandran outliers	0.79%	0.1%
R.m.s.d. bond length (Å)	0.002	0.003
R.m.s.d. bond angles (°)	0.463	0.627
PDB code	6ZWC	6ZWB



## **Data S1. Detailed information on synthesis, characterization, handling and usage of photoswitchable SBTubs, Related to STAR Methods**

### **Part A: Practical User Guide**

- SBTub - User Introduction
- Storage Notes
- SBTub - Photoisomerisation: How to do it
- SBTub - Recovering the inactive state by relaxation and/or diffusion
- Generic Details
- Frequently Asked Questions (FAQ)
- Worked example of tuning parameters for cell assay

### **Part B: Photo/Chemical Design**

- Molecular photoswitches for biology reagents and MTs - chemical background
- Design problems of current photoswitchable reagents that SBTs may solve

### **Part C: Chemical Synthesis**

- Conventions
- Synthesis procedures

### **Part D: Photocharacterisation in vitro**

- HPLC for UV-Vis spectroscopy on separated isomers
- UV-Vis spectrophotometry of bulk samples
- E- and Z-isomers' absorption spectra and photostationary state equilibria
- SBTubs' absorption spectra and photostationary states
- Thermal relaxation of p-hydroxy SBTub4 differs from non-p-hydroxy SBTubs
- Complementary relaxation performance of SBTubs compared to azobenzenes
- Photostability of SBTubs – isomerisation and cycloaddition
- PSS measurements and their comparison to simulated PSS( $\lambda$ )
- Two-photon excitation

### **Part E: Biochemistry**

- Stability towards glutathione – comparison to an azobenzene photoswitch
- Further exploration of glutathione-induced Z-azobenzene degradation
- Microsomal Stability
- hERG Inhibition
- CYP450 inhibition
- SBTubs show light specific inhibition of tubulin polymerisation in vitro

### **Part F: Protein Crystallisation**

- Protein crystallisation materials and methods
- X-ray structural analysis

### **Part G: Biological Data**

- Cell assay methods
- FACS cell cycle analysis
- Immunofluorescence imaging of microtubule network structure
- Live cell imaging: GFP/YFP orthogonality via EB3 comet assay
- Live cell imaging on A549 lung cancer cell line
- Detailed quantification of the impact of SBTub3 on live cell MT dynamics

## Part H: NMR Spectra

### Supplementary Information Bibliography

## Part A: Practical User Guide

### **SBTub - User Introduction**

- **SBTubs** are light-triggered tubulin depolymerisers. They can be used to switch cells and organisms from a state of ordinary MT polymerisation dynamics to an inhibited state.
- Light illumination changes **SBTubs** from their inactive *trans* [E] to their bioactive *cis* [Z] isomer. Upon reaching a **threshold concentration of the *cis* state** inside a cell, tubulin polymerisation will slow then stop (and microtubules start to depolymerise); when the *cis* concentration drops below this threshold, tubulin polymerisation restarts. The threshold is usually reached at an applied extracellular *cis*-concentration of  $\sim 2\text{-}4\ \mu\text{M}$ .
- The **SBTubs'** *cis* state has similar biological effects to known tubulin inhibitors colchicine, combretastatin or nocodazole but is somewhat less potent than these inhibitors, so **SBTubs** have to be used at higher concentrations to achieve comparable biological effects. Titrate for your system! The **SBTubs'** inactive *trans* state does not affect tubulin at all.
- The inhibitory threshold concentration of *cis*-**SBTub** may typically be reached by applying a low concentration of **SBTub** and converting most of it to *cis* using light: e.g. converting 85% of a total dose of  $2\text{-}4\ \mu\text{M}$  **SBTub3** to *cis* by applying light at any wavelengths from 360 to 405 nm (aiming to arrest tubulin polymerisation dynamics).

### **Storage Notes**

For **SBTub2**, **SBTub3** (or controls like **PST-1**): stocks (as powder or as 100%-DMSO stocks) can be stored at room temperature (shielded from light in a cardboard box or wrapped in aluminum foil) or at 4°C; freeze-thaw cycles are no problem. Warm up any cold DMSO stock to room temp before using; there should be no solids and the solutions should be optically clear (otherwise sonicate). Adjust your pure-DMSO stocks to 100X and then dilute them straight into buffer for assays (see cosolvent instructions below). **Do not cold store diluted samples in buffer-DMSO mixtures** as the compounds will precipitate out of solution and won't redissolve – keep any buffer-DMSO samples at room temperature or at 37°C, shielded from light. Ideally, only store DMSO/powder stocks and make all working dilutions fresh. Compound lifetime > 2 years.

### **SBTub - Photoisomerisation: How to do it**

- Short answer: Applying UV/violet light isomerises the **SBTub** to its bioactive isomer.
- **Illumination** with a given wavelength of light shifts the balance between *cis* and *trans* forms toward a "photoequilibrium ratio" that is dictated by the wavelength used. Relatively low light intensities are sufficient, even unfocussed LEDs; lasers are NOT required. Slow isomerisation under light that has a UV/blue component (e.g. sunlight) takes place when the compound is in solution; stocks should therefore always be stored protected from light and/or in brown glass vials if you want to keep them as *E*-isomer (inactive isomer), e.g. to establish baseline behaviour before local switching.
- The equilibrium percentage of *cis* and *trans* that illumination eventually establishes at photoequilibrium [the "PSS"] depends on what wavelength is used for illumination. **When the equilibrium ratio has been reached in a certain location or sample** (by passing enough

photons through that location/sample), **then applying any more light to that location/sample will not change the *cis/trans* ratio in that location/sample any more** (i.e. no further activation will be achieved). This is very different performance to “photouncageable” compounds such as photocaged Taxol or combretastatin.

- After photoisomerisations that push the **SBTub** population mainly into the bioactive *Z* isomer state, the typical **SBTubs can not be substantially photoreverted** back towards the *trans* isomer with biologically acceptable light wavelengths (>300 nm). Spontaneous relaxation (unidirectional spontaneous process, from *cis* to all-*trans*) is the only way this can be achieved (see below). Consequence: **photopatterned SBTubs can be imaged with any wavelengths of light above 470 nm without optically disrupting the photopattern of MT inhibition**. That offers different performance compared to our previous light-responsive tubulin polymerisation inhibitors the “photostatins” [PSTs].

### ***SBTub - Recovering the inactive state by relaxation and/or diffusion***

- **SBTub** molecules that have been illuminated into the *cis* state show **negligible spontaneous change** [“relaxation”] back towards the all-*trans* (inactive) state under standard usage conditions [<38°C, DMSO or DMSO-water solvent systems]. Therefore a cell that has been exposed to enough **SBTub** with enough illumination *applied throughout the whole well* such that MT dynamics slow/stop, will remain with slowed/stopped MT dynamics for >24 h (one-shot activation). If a whole tissue has been illuminated, then MT dynamics will not recover until the *cis*-**SBTub** inside the cells of that tissue diffuse out into naïve or fresh surrounding media. **However, if only a single cell within a larger well or tissue has been illuminated** by photoisomerising UV light, this diffusion can be extremely rapid (“diffusion-based temporal reversibility”) - **it is typically complete within much less than 60 s**, and diffusion-based reversibility kinetics can be substantially tuned by choice of concentration, photoisomerisation ROI, photoisomerisation pulse photon flux, etc. These are all different performance features compared to **PSTs** [**PSTs** do spontaneously relax back to the non-inhibiting state with half-lives of minutes to hours].
- Under standard *biological usage* conditions there is <1% relaxation after 24 h, but **SBTub** relaxation does however occur. Its relaxation half-life  $\tau$  depends strongly on the temperature, and also on the compound used, the pH, the solvent, etc.
- **In case of unwanted photoactivation of a SBTub stock solution**, one can exploit relaxation to recover a stock of **SBTub** into its fully bioinactive state before an assay by storing it (capped tightly) overnight in an oven set to 60 °C. This speeds up relaxation of the *cis* form to the *trans* form, reaching ~100%-*trans* (with first-order kinetics) typically after 12 h, which we call a “fully dark” stock. An experiment run with a fully dark stock under dark or redlight conditions will therefore contain 100% of the biologically inactive *trans* form and should show no MT inhibition (*cis* compound control experiment). This recoverability is another difference to photouncageable compounds.

### ***Generic Details***

- **SBTub3** (M = 283 g/mol) is usually provided as a **10 mM stock in DMSO**, or can be sent as a solid to be dissolved in any other polar organic solvent if needed (MeOH, EtOH, MeCN, DMF, EtOAc, CH<sub>2</sub>Cl<sub>2</sub>). **SBTub3 is not soluble** in pure aqueous buffers.

- For biological testing, it should be assumed that **SBTub3** is *irreversibly activated*, once exposed to near-UV light. However see the note about recovering unwanted photoactivation of a stock (above).
- A final factor to consider in choosing a **SBTub** is its solubility. Most **SBTubs** are almost insoluble in pure media/buffers, unless a cosolvent is used. A good cosolvent stops compound invisibly precipitating/aggregating out of solution and allows to perform experiments reliably. Typical good cosolvent choices are preferably 1% DMSO (this is usually acceptable for cell culture and is recommended for all cell extract work); ethanol or DMSO, *at least* 0.1% are required. We recommend to spike directly from a 100% DMSO solution adjusted to 100X concentration, into the aqueous media of the test well. **Some SBTubs** are being formulated (ongoing work) as fully water-soluble prodrugs that require no cosolvent and are highly *in vivo* compatible, however the **prodrugs are unsuitable for cell-free use** and may be poorly effective in short-term experiments (<10 min) where cell penetration speed is important. For prodrug formulations of **SBTubs** (experimental) and for reference prodrugs: store the compounds (powder or aqueous stocks) at 20°C. Do not use DMSO cosolvent with the formulations; they are only soluble in buffer. Freeze-thaw cycles are no problem. Store diluted samples frozen. Warm frozen stocks/samples to room temp or 37°C before using; there should be no solids & the solutions should be optically clear (otherwise sonicate). Compound lifetime ~1 year. Contact us for more information.
- **SBTubs** require much less illumination than **PSTs** to show a cytotoxic effect since they only need to be illuminated once to provide a long-term effect. This ‘single-shot activation’ allows easier illumination setups especially for moving cells or animals, since no repetitive re-illuminations or cell/tissue tracking is required. It is also more ‘forgiving’ in case that illumination is accidentally stopped at some point during the setup, or when model system is not fixed to one location – floating / moving around.

### **Frequently Asked Questions (FAQ)**

#### **When do I need to use an SBTub instead of a PST for MT photocontrol?**

**SBTub** is a highly photostable and much more biostable analogue of **PST**. It showcases longer thermal halflife and total resistance against glutathione (GSH) and has no effects caused by imaging at >450 nm.

We recommend using **SBTubs (a)** in **long-term in vivo** experiments to reduce the **PSTs’** complications (**PSTs** need repeated illuminations & there is GSH/metabolic depletion of *cis-PST*); **(b)** when controlling MTs while **imaging GFP or fluorescein** to avoid worrying about unwanted photoisomerization (full GFP-orthogonality). **SBTubs** switch on best with 360 nm but if working on the microscope, 405 nm also does the job.

How easily are SBTubs activated with ambient room light (e.g. computer monitor light, DIC light used to typically find sample focus, etc.)?

(1) The danger of activation by ambient room light at usual intensities on the work surface (in the era of LEDs and fluorescent lamps, which barely emit below 410 nm) is far lower for **SBTubs** (absorption cutoff: 410 nm) than for their azobenzene counterparts such as **PSTs** (absorption cutoff: 490-530 nm, depending on isomer). (2) Monitor light is of too low intensity and has too little UV component to affect **SBTubs** at all, though should not greatly affect **PSTs** either. (3) For **PSTs** white DIC light on the microscope causes strong isomerisation that has repeatedly complicated

experiments in our and other labs. However under white DIC light conditions we did not observe any induction of inhibitory effects with **SBTubs**. (4) Since we always ship **SBTub** stocks in brown glass vials and since bio/microscope labs are “closed” systems, daylight activation of **SBTubs** should not be expected under ordinary handling. **SBTubs** can be pipetted and handled with ambient light without compound activation. By comparison, **PST** users are advised to keep **PST** in the dark and pipette under redlight.

#### **My dark experiment shows the same (or more!) MT inhibition as my lit experiment!**

The stock may have been **accidentally photoactivated**. In this case store an all-DMSO stock solution overnight in a 60°C oven to thermally relax 100% of the compound to the trans form. Redo the experiment using this “baked” stock making sure that there is minimal UV, white light or sunlight applied during the dark experiment (red light work; store in dark box, etc).

#### **Should I expect the same results for a SBTub and its prodrug?**

In cells/animals, yes. Any differences are most likely due to different solubility in aqueous media. Prodrugs are more reliably soluble; **SBTubs** require cosolvents (e.g. DMSO), which is not always tolerated by the model system (e.g. zebrafish in our hands go up to 1% DMSO).

#### **How should I store SBTub?**

See Storage Note at start of this doc! For **SBTub3** powders and DMSO stocks, you can store them at room temperature prior to diluting them with buffer for your assays. Don't store the diluted samples at 4°C as the compound can crash out of solution and it can't go back in solution. For long-term storage, the DMSO stocks/powders can be stored at –20°C.

#### **I have no way to do 360 nm illumination, is 400 nm or 420 nm also ok?**

Any UV wavelength or violet light up to 420 nm still gives satisfactory photoactivation compared to the dark experiment. “UV Blacklight” LEDs or LED-strip-lights can be bought on Amazon and these work fine. We can also provide LED-arrays or single LEDs if needed. *Or we can send a build guide for making a 20€ UV illumination array for cell culture microplates based on sticking together 120 LEDs/m UV Blacklight strip lighting off Amazon, together with a pulse timer that costs 8€.*

#### **Worked example of tuning parameters for cell assay**

Figure S4D shows an EB3-imaging experiment where conditions for imaging while photoswitching **SBTub3** (40 μM) did not allow temporally reversible MT control and also caused fluorescent protein marker (FP) photobleaching. This highlights several problems which can be individually tuned by better choice of experimental settings, to allow temporally-reversible **SBTub**-based photocontrol of MT dynamics, as follows:

**Problem 1.** FP-imaging protocol used (a) directly bleaches 20% of comets in DMSO control over 900 s (blue solid fit line to blue DMSO dataset); and (b) is also making a *cis*-**SBTub** background throughout the cell & relevant-surrounding-volume (e.g. in first 180s cycle, already lost 20% of comets in the orange **SBTub** dataset; the extra **SBTub** background is visible in that the pink solid fit line to the tops of the **SBTub**-data decreases faster than the blue fit line to DMSO, indicating slow buildup of *cis*-**SBTub**).

**Diagnosis 1:** imaging photon flux is far too high for this high concentration of **SBTub** applied!

**Solutions 1a:** slow down imaging frame acquisition rate 5-fold and also make each imaging pulse 1/4 of the current acquisition time. This reduces imaging photon flux 20-fold. So you should now see

20-fold less direct photobleaching in the DMSO control; *and* 20-fold less background activation to *cis*-**SBTub** which means better - **more frequent, more complete, and faster** - recoveries.

Theoretically you can also reduce the laser intensity for imaging, so that photon flux per imaging frame is further reduced. But **we do not recommend this** since in many microscopes the photon flux is not linear with "laser power %" over the full range, whereas imaging frame acquisition time is definitely linear to flux, so there you know what you are dealing with. (Or, you could theoretically increase the pixel size, but there can be other pixel size effects, as well as loss of resolution, too so we also do not recommend this).

Check 1: Now retry imaging, with same concentration of **SBTub** for 600 s. How many comets are lost over time in DMSO control? Further reduce flux until it's acceptable.

Check 2: How about (pink) comet loss fit line for the **SBTub**-treated case? Better?

**Solutions 1b:** If there is still significant loss of comets, **adjust SBTub concentration down** (e.g. to 10  $\mu$ M) and compare. Keep titrating **SBTub** concentrations such that the 405 nm flash still gets to a desired level of EB inhibition, but there's less *trans*-**SBTub** present in the whole well to get background activated (better recoveries). There will be a concentration that doesn't show significant comet reduction over time.

**Observation 2:** Comet count at the peak of the 405 nm periods (blue fit to orange data) decreases at same rate as does comet direct FP bleaching by FP imaging, seen in DMSO control, i.e. the *max-cis*-**SBTub** in cell seems not to increase with 405 nm pulsing; conclude: we reach the same concentration of *cis*-**SBTub** during each 405 nm pulse (just we have some comets getting bleached) despite the fact that there is a background level of *cis*-**SBTub** which is increasing over time in the whole sample (see Problem 1).

**Diagnosis 2a:** The 405 flash photon flux being used must be "overkill" since the cell already experiences the highest possible concentration of *cis*-**SBTub** during the first 405 nm flash, despite the low background level of *cis*-**SBTub**. The aim in such an experiment is however not to isomerise all **SBTub** inside the cell (and in the conical light path through the well), but *just enough* of the **SBTub** in the cell to get a substantial block of EB comets. So all that extra 405 nm photon flux can be causing too much off-target photobleaching or photoisomerisation when experiments get more complex.

**Solution 2a:** Minimise the 405 nm flux before starting difficult experiments. This can make a **faster recovery halflife** too. Modify 405 nm frame flux (total time per 405 nm period), and see if results look similar. If similar, keep halving flux until the inhibition reached is no longer good enough; stop there and use whatever was still OK - the true minimum 405 nm flux.

**Diagnosis 2b:** There is no significant contribution from 405 nm in-cell isomerisations to the loss of comets over time (if there were, the recovered comet count timecourse would "step" down (dotted purple lines) instead of going smoothly down (red lines) and recovery time kinetics of ~80 s would also lengthen. So if needed, can do at least double the time-density of 405 nm isomerisations eg. one every 90 s (adjust according to the recovery times after all previous improvements).

**Ideas:** (3) Apply FP imaging to a smaller field of view, to reduce background SBT isomerisation in the whole sample? Assuming the aperture has already been adjusted to minimum! (4) Compare to **PST-1** active photoswitching under similar conditions.

## Part B: Photo/Chemical Design

This section is expanded from the main text of the manuscript to provide a more comprehensive introduction to the design motivations behind the development of the **SBTubs**.

### ***Molecular photoswitches for biology reagents and MTs - chemical background***

Molecular photoswitches have been used to install optical control over a broad range of phenomena, with applications from material sciences<sup>[1,2]</sup> through to reversible photocontrol of ligand binding affinities<sup>[3]</sup> and manipulation of diverse cellular processes in chemical biology<sup>[4,5]</sup>. For studies of temporally-regulated and spatially anisotropic biological systems, particularly those that simultaneously support several cellular functions, photoswitchable inhibitors ("photopharmaceuticals") conceptually enable a range of powerful studies not accessible with other tool systems.<sup>[6-8]</sup>

The microtubule (MT) cytoskeleton is a prime example of such a spatiotemporally regulated, multifunctional system where photoswitchable inhibitors have the potential to enable conceptually important and unique studies. Whereas cytoskeleton research typically aims to study a subset of MT-dependent processes that are spatially and/or temporally localised, nearly all MT inhibitors reported as tool compounds for biological research are drugs that are active wherever they are distributed, including at sites and at times where drug activity is not desired.<sup>[9]</sup> This restricts the scope of applications and utility of these inhibitors for selective research into the various, highly dynamic, anisotropic processes dependent on MTs.<sup>[10]</sup>

The structure of the colchicine site MT inhibitor combretastatin A-4 (**CA4**; Figure 1B)<sup>[11]</sup> has recently inspired photoswitchable solutions to the problem of achieving spatiotemporal control over MT inhibition. **CA4** is a stilbene whose *Z*-isomer (*cis*) binds tubulin, acts as a low nanomolar cytotoxin *in cellulo*, and reached Phase III trials as an anticancer drug.<sup>[12,13]</sup> Crucially, its *E*-isomer (*trans*) is several orders of magnitude less bioactive.<sup>[14]</sup> An approach to microtubule photocontrol *via* photoisomerisation of its bridging C=C bond has been proposed, whereby bioactive *Z*-combretastatins should be generated *in situ* from inactive *E*-precursors, allowing spatially and temporally precise application of antimitotic bioactivity.<sup>[15]</sup> However, to the best of our knowledge this concept has not been realised in biology, hindered by the bio-incompatible short-wavelength illumination required ( $\lambda_{\text{max}} \sim 300 \text{ nm}$ ) and the irreversible photochemical degradations that stilbenes undergo in aerobic conditions (e.g. oxidative 6 $\pi$ -electrocyclisation).<sup>[16]</sup>

Instead, designing **CA4** analogues incorporating the synthetic azobenzene photoswitch scaffold inside their pharmacophore - a design strategy known as "azologisation"<sup>[17]</sup> - delivered the biocompatibly-switchable, azobenzene-based Photostatins (**PSTs**; Figure 1B)<sup>[6,18-20]</sup>, which undergo optically reversible, bidirectional photoswitching between inactive *E* and MT-inhibiting *Z* isomers using low-intensity visible light. The **PSTs** have enabled specific optical control over MT structure and dynamics in live cells as well as *D. melanogaster*<sup>[21]</sup>, *C. elegans*<sup>[6]</sup>, zebrafish<sup>[22]</sup>, and mouse<sup>[7]</sup> and have been used to resolve key biological questions in mammalian development and in neuroscience.<sup>[8,23]</sup> These applications illustrate the power of photopharmacology to enable previously inaccessible studies of spatiotemporally anisotropic processes without genetic engineering, which is particularly important for studies of cytoskeletal scaffold proteins, since no optogenetic methods have yet been developed that can control their structure-dependent functions.<sup>[7,8,21,24]</sup>

### ***Design problems of current photoswitchable reagents that SBTs may solve***

Photopharmacology in general has been extensively reviewed in the chemical literature,<sup>[25-28]</sup> from which it is apparent that (a) the vast majority of all photopharmaceuticals reported are based on the azobenzene photoswitch scaffold, (b) many photopharmaceuticals have a poor dynamic range of photoswitchability (less than 10-fold difference between on-target bioactivities of their "best on-state PSS" and "best off-state PSS" photogenerated equilibrium populations; see also below); (c) most compounds reported as photopharmaceuticals have not been shown to succeed except in cell-free systems, and of those that have been applied to cells the majority act on membrane-bound extracellularly-accessible targets; (d) azobenzene photopharmaceuticals only rarely perform well enough against protein targets in intracellular environments to be serious candidates for research uses (e.g. satisfactory cellular potency of the more-bioactive photogenerated population, >10-fold reduction of potency of the less-active photogenerated population).

In addition to the discussion in the main text, we particularly note the following problems of design and performance:

(1) Though "normal" azobenzenes are not orthogonal to GFP/YFP imaging, the current focus in azobenzene spectral shifting research is actually on "red-shifting" photoresponse spectra to still-longer wavelengths. Since "red-shifting strategies" almost always shift the photoresponse spectra of *both* isomers, the result of these is that bidirectional photoswitching continues to be stimulated by imaging fluorescent proteins: extending their non-orthogonality with GFP/YFP now strongly to RFP/mCherry imaging too and making the problem worse.

(2) almost all azobenzene photopharmaceuticals which display photoswitchable bioactivity on intracellular targets in cell assays, have very poor potency as compared to their parent inhibitor compounds. For example, cellularly photoswitchable **PSTs** are ~2 orders of magnitude less potent in cells than **CA4**, despite almost identical potency in cell-free assays; other azobenzenes retain potency but are no longer photoswitchable. The reasons have barely been investigated, but it is known that the majority of azobenzenes can be sequestered and degraded following the addition of cytoplasmic glutathione (GSH; ca. 3-10 mM) to the electrophilic and abiotic N=N group<sup>[29-31]</sup>, which initiates rapid destruction particularly of electron-rich systems<sup>[32]</sup>. Although other mechanisms are also likely to be relevant, this is sufficient to understand the performance loss described above. For those few "azo-inclusion" designs (such as **PSTs**) where the azobenzene must be intact for binding to occur, only the undegraded fraction of reagent is available for binding, so an apparent potency loss may be seen due to sequestration/degradation of a fraction of the applied azobenzene. More commonly, particularly for "azo-extension" designs, the products of cleavage of the N=N bond (such as anilines, which also incur toxicity risks, e.g. carcinogenicity risks through nitrosobenzene intermediates) can often be predicted to be potent on-target binders, yet these will no longer be photoswitchable; therefore cellular metabolic products from a degraded azobenzene may deliver potent *though non-photoswitchable* on-target bioactivity which blocks the utility of the compound. Potency loss and/or problematic metabolites obstruct robust applications of azobenzenes to intracellular targets in general; and especially so *in vivo* where high doses may be required due to partial degradation, so that by-products have to be evaluated, so their toxicity risks are likely to be particularly problematic<sup>[19,33]</sup>.

(3) Azobenzene relaxation halfives span more than 13 orders of magnitude, and compared to timescales of typical biological experiments (seconds to hours) these mainly fall into two clusters: either fast-relaxing (aqueous halfives from microseconds up to 1 second) or slow-relaxing (longer



than 24 h). Fast-relaxing azobenzenes (aqueous half-lives from microseconds up to 1 second) typically arise when any of several common polar functional groups (OH, NHR, NH<sub>2</sub>, etc: which are often vital in establishing ligand-protein interactions) are used in any of the six *ortho* or *para* positions. These half-lives are far too short for reliable isomerisation-based photopatterning in the aqueous intracellular environment, leaving only the four *meta* positions available for these functional groups. The water-solubilisable **PST** derivatives **PST-1** and **PST-2** place these polar groups in *meta* and so did attain favourable half-lives for cellular applications (in the range 1 - 60 min), but even this was not optimal for *in vivo* use: they would require re-illuminations during longer *in vivo* studies which are problematic to deliver with spatial precision in motile embryos or animals, and re-illuminations can also cause photobleaching of fluorescent labels on target proteins<sup>[6]</sup> as well as nonspecific photodamage. (**PST-1** is solubilisable as the phosphorylated **PST-1P**, and **PST-2** as the serinylated **PST-2S**). In comparison, SBT bioactivity persists in the long term after switching on by a single illumination (see Fig 4A). This can reduce both the overall photon flux needed for SBT operation as well as the requirements for repeating illuminations, which can be experimentally problematic, and which more rapidly-relaxing or isomer-dependently metabolically labile photopharmaceutical scaffolds such as azobenzenes require. The SBTs' violet-light operation and their extreme photochemical robustness under biological conditions also differentiates them from previously proposed but still not *in situ*-demonstrated deep-UV-operated stilbene-based probes<sup>[15]</sup> which are likely to suffer electrocyclisation-oxidation degradation<sup>[34]</sup>.

We perceived however that these three key problems intrinsically associated to the azobenzene's N=N double bond (non-orthogonality to standard GFP / YFP imaging conditions, cellular/metabolic liabilities in intracellular settings, and substituent-dependent limits on thermal half-life scope) which reduce the success of translation of azobenzene photopharmaceuticals for intracellular targets from cell-free into cell culture and thence *in vivo* research applications, could be addressed by moving instead to new photoswitchable scaffolds that avoiding these three chemistry-based problems – both for the specific case of photoswitchable MT inhibitors, as well as for other applications in chemical biology.

**Opportunities for SBT photopharmaceuticals:** The current vogue of shifting isomerisation wavelengths towards the red wavelengths is intended to allow photopharmaceuticals to be photoswitched *in vivo* in animals, by light sources external to the organism (since red light penetrates biological tissue much deeper because it is not absorbed by chromophores such as hemoglobin; which also raises the problem that non-absorbed light actually loses spatial specificity due to its penetration completely through a subject). However, our ongoing results as well as published reports (Morstein et al., 2019) have shown successful subcutaneous isomerisation of photoswitches even with simple transdermal 360 nm LED illumination. Indeed, *in vivo*, colchicine domain inhibitors are often used as vascular disrupting agents and studied *in situ* in surface tissues using one- and two-photon microscopy (Tozer et al., 2001): which are both feasible approaches to also photoswitch **SBTubs**. In these superficial tissue settings, the penetration of violet light required for single-photon **SBTub** isomerisation is unlikely to be problematic. Rather than light accessibility for tissues, we consider that two compound-specific factors are likely to determine the success of *in situ*-actuated photoswitches for intracellular targets reaching *in vivo* applications. One is systemic pharmacokinetics. Only one pharmacokinetic study of a photopharmaceutical has been published (Babii et al., 2020), and no data are known for azobenzenes; yet the metabolic stability and druglikeness the SBTs feature are positive early signs. The second is the ability to robustly photomodulate intracellular biology, which relies on the intracellular biochemical stability of the

bioactive isomer, and in this respect SBTs show superior performance compared to the cognate azobenzenes. We therefore consider the **SBTubs** to offer exciting potential for *in vivo* translation within the context of MT photopharmacology.

## Part C: Chemical Synthesis

### **Conventions**

**Abbreviations:** The following abbreviations are used: Hex – distilled isohexanes, EA – ethyl acetate, Me – methyl, MeCN – acetonitrile, DMSO – dimethylsulfoxide, PBS – phosphate buffered saline aqueous buffer.

**Safety Hazards:** no remarkable safety hazards were encountered.

**Reagents and Conditions:** Unless stated otherwise, (1) all reactions and characterisations were performed with unpurified, undried, non-degassed solvents and reagents, used as obtained, under closed air atmosphere without special precautions; (2) “hexane” used for chromatography was distilled from commercial crude isohexane fraction by rotary evaporation; (3) “column” and “chromatography” refer to manual flash column chromatography on Merck silica gel Si-60 (40–63  $\mu\text{m}$ ); (4) “MPLC” refers to flash column chromatography purification on a Biotage Isolera Spektra system, using prepacked silica cartridges purchased from Biotage; (5) procedures and yields are unoptimised; (6) yields refer to isolated chromatographically and spectroscopically pure materials; (7) all eluent and solvent mixtures are given as volume ratios unless otherwise specified, thus “1:1 Hex:EA” indicates a 1:1 mixture (by volume) of hexanes and ethyl acetate; (8) chromatography eluents e.g. “3:1  $\rightarrow$  1:1” indicate a stepwise or continual gradient of eluent composition.

**Thin-layer chromatography** (TLC) was run on 0.25 mm Merck silica gel plates (60, F-254), typically with Hex:EA eluents. UV light (254 nm) was used as a visualising agent, with cross-checking by 365 nm UV lamp for **SBTub** fluorescence. TLC characterisations are abbreviated as  $R_f = 0.64$  (UV 254 nm, EA:Hex = 1:1).

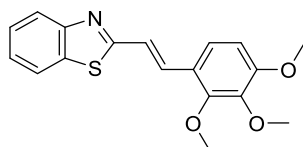
**NMR:** Standard NMR characterisation was by  $^1\text{H}$ - and  $^{13}\text{C}$ -NMR spectra on a Bruker Ascend 400 (400 MHz & 100 MHz for  $^1\text{H}$  and  $^{13}\text{C}$  respectively). Chemical shifts ( $\delta$ ) are reported in ppm calibrated to residual non-perdeuterated solvent as an internal reference<sup>[35]</sup>. Peak descriptions singlet (s), doublet (d), triplet (t), and multiplet (m) are used. NMR spectra are given in Part H.

**HRMS:** High resolution mass spectrometry (HRMS) was carried out by the Zentrale Analytik of the LMU Munich using ESI ionisation in the positive mode.

**IR Spectroscopy:** IR spectra were recorded on a PerkinElmer Spectrum BX II FT-IR system. Both solids and liquids were directly applied as thin films of neat substance on the ATR unit. The measured wavenumbers are reported with relative intensities, abbreviated by s (strong), m (medium) and w (weak).

## Synthesis procedures

### 2-(2,3,4-trimethoxystyryl)benzothiazole (SBTub1)



2-methylbenzothiazole (0.12 mL, 1 mmol) and 2,3,4-trimethoxybenzaldehyde (196 mg, 1 mmol, 1 eq) were dissolved in DMSO (2 mL). NaOMe (5.4 M in MeOH, 185  $\mu$ L, 1 mmol, 1 eq) was added and the reaction was stirred overnight. H<sub>2</sub>O (10 mL) was added. The mixture was extracted with ethyl acetate (3  $\times$  15 mL). The combined organic layers were washed with brine (10 mL) and dried over MgSO<sub>4</sub>. Flash column purification of the crude material (EA:Hex = 3:7) yielded **SBTub1** as light yellowish solid (298 mg, 0.91 mmol, 91%).

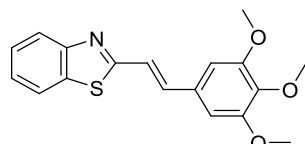
$R_f$  = 0.64 (UV 254 nm, EA:Hex = 1:1). **HRMS (ESI<sup>+</sup>)**: 328.10002 calculated for C<sub>18</sub>H<sub>18</sub>NO<sub>3</sub>S<sup>+</sup> [M+H]<sup>+</sup>, 328.10003 found. **<sup>1</sup>H-NMR (400 MHz, CDCl<sub>3</sub>)**:  $\delta$  = 7.98 (d,  $J$  = 8.1 Hz, 1H), 7.84 (d,  $J$  = 8.0 Hz, 1H), 7.71 (d,  $J$  = 16.4 Hz, 1H), 7.45 (t,  $J$  = 8.3 Hz, 1H), 7.41 (d,  $J$  = 16.4 Hz, 1H), 7.35 (t,  $J$  = 8.2 Hz, 1H), 7.35 (d,  $J$  = 8.8 Hz, 1H), 6.73 (d,  $J$  = 8.8 Hz, 1H), 3.98 (s, 3H), 3.91 (s, 3H), 3.90 (s, 3H) ppm. **<sup>13</sup>C-NMR (100 MHz, CDCl<sub>3</sub>)**:  $\delta$  = 168.2, 155.0, 154.0, 152.8, 142.5, 134.3, 132.9, 126.4, 125.3, 122.9, 122.6, 122.4, 121.6, 121.5, 108.0, 61.6, 61.1, 56.2 ppm. **IR (FT, ATR)**:  $\tilde{\nu}$  = 2946 (w), 2835 (w), 1619 (w), 1588 (m), 1497 (m), 1455 (m), 1435 (m), 1412 (m), 1288 (s), 1254 (m), 1195 (m), 1093 (s), 1042 (m), 1014 (m), 968 (m), 945 (m), 914 (w), 851 (w), 798 (m), 754 (m) cm<sup>-1</sup>.

### 2-(3,4,5-trimethoxystyryl)benzothiazole (SBTub2)

Note that this compound was reported - although only in the *trans* state - as a cytotoxic resveratrol analogue targeting tubulin, in 2014-2015 by Penthala *et al.*, as "Example Compound 4 (Formula (I)(d))" in their patent WO2014/172363<sup>[36]</sup> and as compound 13 in their paper<sup>[37]</sup>. In these reports it was synthesised and biologically evaluated for antiproliferative activity in 2D cell culture (patent Table 1, showing growth inhibition GI<sub>50</sub> < 1  $\mu$ M in almost all reported cell lines (NCI60 panel), down to GI<sub>50</sub> = 40 nM. Its *trans* (*E*)-geometry was established explicitly and extensive docking simulations were performed to rationalise observed activity<sup>[36,37]</sup>, docking the *trans*-state to the colchicine site of tubulin using Sybyl software. The authors conclude, "[compound 13] exhibited significant growth inhibition against most of the human cancer cells in the 60-cell panel, and the results from the molecular modeling studies are consistent with the *in vitro* anti-cancer activit[y] ...being mediated via binding to the colchicine binding site on tubulin... [it was] considered as [an] important lead compound for further development as [an] anti-cancer drug". The authors implicitly argue against the widely-reported requirement<sup>[14,38]</sup> for colchicine-site binders of this type to be *cisoid* isomers, which has been structurally rationalised by us<sup>[39]</sup>. We decided therefore to pursue our paper's design logic paying particular attention to experimentally verify the isomer status and binding mode of the compound.

Penthala *et al*'s prior reports of **SBTub2** properties also argue directly against our experience<sup>[6,39,40]</sup> and literature understanding<sup>[13]</sup> of the requirements of the colchicine binding site, as well as our present cellular bioactivity assays and our experimental ligand:protein crystallisation results, in which we show that *trans*-**SBTub2** has no specific cytotoxicity whereas *cis*-**SBTub2** is strongly bioactive. We consider that Penthala *et al* may initially have synthesised **SBTub2** purely as its *trans*-isomer, but that the possibility of its photoisomerisation-dependent bioactivity (which has not been reported

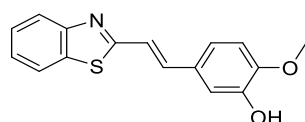
before our current work) escaped their attention. This may have led them to perform bioactivity tests without rigorous certainty of what isomer was being tested in what situation; that would nullify the predictive value of their reports and cast doubt on the validity of the docking. We consider that their work has therefore, from conceptual grounds, not delivered an understanding of these compounds' bioactivity, so we here wish to report upon the **SBTub** independently of Penthala *et al.*'s reported cellular activities and docking study, by careful and rationalised studies controlling for isomerisation and experimentally verifying the docking mode of these ligands.



2-methylbenzothiazole (0.12 mL, 1 mmol) and 3,4,5-trimethoxybenzaldehyde (196 mg, 1 mmol, 1 eq) were dissolved in DMSO (2 mL). NaOMe (5.4 M in MeOH, 185  $\mu$ L, 1 mmol, 1 eq) was added and the reaction mixture was stirred overnight. H<sub>2</sub>O (10 mL) was added and the mixture was extracted with ethyl acetate (3  $\times$  15 mL). The combined organic layers were washed with brine (10 mL) and dried over MgSO<sub>4</sub>. Flash column purification of the crude material (EA:Hex = 3:7) yielded **SBTub2** as faint-yellow solid (158 mg, 0.48 mmol, 48%).

$R_f$  = 0.68 (UV 254 nm, EA:Hex = 1:1). **HRMS (ESI<sup>+</sup>)**: 328.10002 calculated for C<sub>18</sub>H<sub>18</sub>NO<sub>3</sub>S<sup>+</sup> [M+H]<sup>+</sup>, 328.10002 found. **<sup>1</sup>H-NMR (400 MHz, CDCl<sub>3</sub>)**:  $\delta$  = 7.99 (d,  $J$  = 8.1 Hz, 1H), 7.86 (d,  $J$  = 8.0 Hz, 1H), 7.47 (t,  $J$  = 7.1 Hz, 1H), 7.45 (d,  $J$  = 16.1 Hz, 1H), 7.38 (t,  $J$  = 7.0 Hz, 1H), 7.33 (d,  $J$  = 16.1 Hz, 1H), 6.82 (s, 2H), 3.92 (s, 6H), 3.90 (s, 3H) ppm. **<sup>13</sup>C-NMR (100 MHz, CDCl<sub>3</sub>)**:  $\delta$  = 167.0, 153.9, 153.7, 139.6, 137.7, 134.4, 131.1, 126.5, 125.5, 123.0, 121.7, 121.7, 104.6, 61.1, 56.3 ppm. **IR (FT, ATR)**:  $\tilde{\nu}$  = 2997 (w), 2966 (w), 2934 (w), 2833 (w), 1626 (w), 1581 (m), 1504 (m), 1452 (m), 1417 (m), 1329 (m), 1240 (m), 1202 (w), 1155 (w), 1126 (s), 1005 (m), 983 (w), 964 (m), 812 (m), 758 (m), 729 (m) cm<sup>-1</sup>.

#### **5-(2-(benzothiazol-2-yl)vinyl)-2-methoxyphenol (SBTub3)**



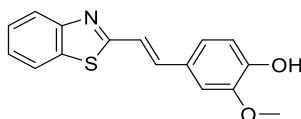
2-methylbenzothiazole (0.25 mL, 2 mmol), 3-hydroxy-4-methoxybenzaldehyde (304 mg, 2 mmol, 1 eq) were dissolved in DMSO (4 mL). NaOMe (5.4 M in MeOH, 741  $\mu$ L, 4 mmol, 2 eq) was added. After stirring overnight sat. aq. NH<sub>4</sub>Cl solution (30 mL) was added and the reaction mixture was extracted with EA (3  $\times$  20 mL). The combined organic layers were washed with water (20 mL), brine (20 mL) and dried over MgSO<sub>4</sub>. The crude material was purified by normal phase MPLC using gradient elution (EA:Hex = 0:100  $\rightarrow$  100:0) to yield **SBTub3** as slightly yellowish solid (502 mg, 1.77 mmol, 89%).

$R_f$  = 0.55 (UV 254 nm, EA:Hex = 1:1). **HRMS (ESI<sup>+</sup>)**: 284.07398 calculated for C<sub>16</sub>H<sub>14</sub>NO<sub>2</sub>S<sup>+</sup> [M+H]<sup>+</sup>, 284.07384 found. **<sup>1</sup>H-NMR (400 MHz, CDCl<sub>3</sub>)**:  $\delta$  = 7.98 (d,  $J$  = 8.1 Hz, 1H), 7.85 (d,  $J$  = 8.0 Hz, 1H), 7.46 (t,  $J$  = 7.1 Hz, 1H), 7.44 (d,  $J$  = 16.2 Hz, 1H), 7.36 (t,  $J$  = 7.0 Hz, 1H), 7.26 (d,  $J$  = 16.1 Hz, 1H), 7.20 (d,  $J$  = 2.1 Hz, 1H), 7.09 (dd,  $J$  = 8.3, 2.1 Hz, 1H), 6.88 (d,  $J$  = 8.3 Hz, 1H), 5.73 (s, 1H, OH), 3.93 (s, 3H) ppm. **<sup>13</sup>C-NMR (100 MHz, CDCl<sub>3</sub>)**:  $\delta$  = 167.5, 153.9, 148.1, 146.1, 137.7, 134.4, 129.2, 126.4, 125.3, 122.9, 121.6, 120.9, 120.5, 112.7, 110.8, 56.2 ppm. **IR (FT, ATR)**:  $\tilde{\nu}$  = 3053 (w), 2846

(w), 1626 (w), 1598 (w), 1585 (w), 1522 (m), 1483 (w), 1435 (s), 1358 (w), 1308 (w), 1293 (m), 1245 (m), 1231 (m), 1199 (s), 1164 (s), 1123 (s), 1026 (m), 981 (w), 946 (s), 923 (w), 838 (w), 797 (s), 765 (s), 731 (m)  $\text{cm}^{-1}$ .

#### **4-(2-(benzothiazol-2-yl)vinyl)-2-methoxyphenol (SBTub4)**<sup>[41]</sup>

*E*-**SBTub4** has also previously been synthesised in the context of ligands for platinum complexes<sup>[41]</sup>, although its isomerisation to *Z* was not considered. It was reported in the *trans* state by Lozano *et al.* as compound **1i**<sup>[41]</sup>, where it was used as a monodentate ligand in a tribromo platinum(II) complex (**2i**). In that report it was assessed for cytotoxicity as a free ligand and also when complexed, in both cases only in *trans* and without consideration of isomerisation. In this work its role was to serve as a designed inactive biological control compound *in the cis state*, being a permutation control of **SBTub3** that is designed to be *cis*-active. Here we require it specifically as a *Z*-isomeric control and accordingly we pursued its synthesis and biological characterisation ourselves, paying particular attention to the isomer state.



2-methylbenzothiazole (0.41 mL, 3.3 mmol), 4-hydroxy-3-methoxybenzaldehyde (0.5 g, 3.3 mmol, 1.0 eq) and NaOMe (5.4 M solution in MeOH, 1.2 mL, 6.5 mmol, 2 eq) were dissolved in DMSO (6.5 mL). After stirring overnight, sat. aq.  $\text{NH}_4\text{Cl}$  solution (30 mL) was added and the reaction mixture was extracted with EA (3  $\times$  20 mL). The combined organic layers were washed with water (20 mL), brine (20 mL) and dried over  $\text{MgSO}_4$ . The crude material was purified by normal phase MPLC using gradient elution (EA:Hex = 0:100  $\rightarrow$  100:0) and  $\lambda_{\text{collect}} = 360 \text{ nm}$  to yield **SBTub4** as a yellow solid (256 mg, 0.9 mmol, 28%).

$R_f = 0.6$  (UV 254 nm, EA:Hex = 1:1). **HRMS (ESI<sup>+</sup>)**: 284.07398 calculated for  $\text{C}_{16}\text{H}_{14}\text{NO}_2\text{S}^+$  [M+H]<sup>+</sup>, 284.07385 found. **<sup>1</sup>H-NMR (400 MHz,  $\text{CDCl}_3$ )**:  $\delta = 7.98$  (d,  $J = 8.1 \text{ Hz}$ , 1H), 7.85 (d,  $J = 7.9 \text{ Hz}$ , 1H), 7.46 (t,  $J = 7.1 \text{ Hz}$ , 1H), 7.45 (d,  $J = 15.7 \text{ Hz}$ , 1H), 7.36 (t,  $J = 7.1 \text{ Hz}$ , 1H), 7.27 (d,  $J = 16.1 \text{ Hz}$ , 1H), 7.13 – 7.07 (m, 2H), 6.95 (d,  $J = 8.7 \text{ Hz}$ , 1H), 6.02 (s, 1H, OH), 3.94 (s, 3H) ppm. **<sup>13</sup>C-NMR (100 MHz,  $\text{CDCl}_3$ )**:  $\delta = 167.5, 153.9, 147.5, 147.1, 138.0, 134.3, 128.1, 126.4, 125.3, 122.9, 122.4, 121.6, 120.0, 115.0, 108.8, 56.1$  ppm. **IR (FT, ATR)**:  $\tilde{\nu} = 3004$  (w), 2829 (w), 2643 (w), 1623 (m), 1587 (s), 1518 (s), 1456 (m), 1431 (m), 1399 (m), 1338 (w), 1308 (m), 1286 (s), 1254 (s), 1220 (m), 1197 (w), 1169 (w), 1138 (m), 1112 (s), 1064 (w), 1037 (m), 1014 (w), 967 (m), 922 (w), 908 (w), 829 (m), 802 (m), 781 (w), 751 (s), 722 (m)  $\text{cm}^{-1}$ .

## **Part D: Photocharacterisation in vitro**

### ***HPLC for UV-Vis spectroscopy on separated isomers***

Analytical high-performance liquid chromatography (HPLC) was performed on an Agilent 1100 SL coupled HPLC system with (a) a binary pump to deliver  $\text{H}_2\text{O}:\text{MeCN}$  eluent mixtures containing 0.1% formic acid at a 0.4 mL/min flow rate, (b) Thermo Scientific Hypersil GOLD™ C18 column (1.9  $\mu\text{m}$ ; 3  $\times$  50 mm) maintained at 25°C, whereby the solvent front eluted at  $t_{\text{ret}} = 0.5 \text{ min}$ , (c) an Agilent 1100 series diode array detector, which was used to acquire peak spectra of separated compound isomers in the range 200–550 nm after manually baselining across each elution peak of interest to correct

for eluent composition effects. Run conditions were a linear gradient of H<sub>2</sub>O:MeCN eluent composition from 90:10 through to 1:99, applied during the separation phase (first 5 min), then 0:100 for 2 min for flushing; the column was (re)equilibrated with 90:10 eluent mixture for 2 min before each run.

### ***UV-Vis spectrophotometry of bulk samples***

Absorption spectra in cuvette (“UV-Vis”) were acquired on a Agilent CaryScan 60 (1 cm pathlength). For photoisomerisation measurements, Hellma microcuvettes (108-002-10-40) taking 500  $\mu$ L volume to top of optical window were used with test solution such that the vertical pathlength of the isomerization light is less than 7 mm to the bottom of the cuvette, with the default test solution concentrations of 25  $\mu$ M. Measurements were performed by default in PBS at pH  $\sim$ 7.4 with 10–20% of DMSO. Photoisomerisations and relaxation rate measurements were performed at room temperature. “Star” LEDs (H2A1-models spanning 360–435 nm from Roithner Lasertechnik and a 260 nm HP-LED from Sahlmann Photochemical Solutions) were used for photoisomerisations in the cuvette that were also predictive of what would be obtained in LED-illuminated cell culture.

### ***E- and Z-isomers’ absorption spectra and photostationary state equilibria***

Pure *E* and *Z* isomer spectra of **SBTubs** (Figure S1A) were obtained on the HPLC DAD as outlined in *HPLC*. Whole-sample absorption spectra of **SBTubs** at different photostationary state equilibria (Figure S1B) were measured as outlined in *Spectrophotometry*. This illustrates the efficient photoswitching to nearly-all-*Z* that may be achieved by a range of violet/near-UV wavelengths.

### ***SBTubs’ absorption spectra and photostationary states***

**SBTubs** feature substantially solvent- and pH-independent absorption spectra and photostationary states (Figure S1C-D). This outlines their robustness of photoresponse with respect to variations of local conditions as may be encountered in biology, with e.g. localisation into different cellular compartments or changes of environmental dielectric constant during partitioning. We feel that this particularly recommends the SBT scaffold as a reproducible photoswitch for biology use.

### ***Thermal relaxation of p-hydroxy SBTub4 differs from non-p-hydroxy SBTubs***

*para*-hydroxy **SBTub4** was the only **SBTub** to show appreciable spontaneous *Z*→*E* isomerization at 25°C in aqueous media (Figure 1I), and this only under basic aqueous conditions (pH  $\sim$ 9): the non-*para*-hydroxy **SBTubs** did not show relaxation under these conditions (Figure 1H). We presume **SBTub4**’s pH-dependent relaxation rate acceleration results from resonance between the phenolate form (where the bridging bond is a C=C double bond) and its quinoidal form (bridging C-C single bond, for which free rotation to the thermodynamically more stable *transoid* conformation could occur).

In azobenzenes the choice of substituents in *ortho* or *para* to the diazene is restricted, if photoswitching is to be performed in predominantly aqueous environments (e.g. in the cytosol in biological systems) since *o/p*-hydroxyl, -thiol or -amine groups give fast thermal relaxation, often complete in under a second, and in many cases their *Z* states cannot even be observed in aqueous environments.<sup>[42,43]</sup> However these groups are powerful interaction points for docking to proteins, which it would be desirable to be able to place freely around the azobenzene scaffold while maintaining reliable photoswitchability. This can be achieved using SBTs, which we feel is a particular advantage for SBTs as a new photoswitch scaffold for chemical biology.

### **Complementary relaxation performance of SBTubs compared to azobenzenes**

In summary, the metastable *Z*-isomers of all **SBTubs** could be quantitatively relaxed to *E* by warming to 50-60°C in DMSO overnight, although at 25°C they showed no significant thermal relaxation within hours at pH~7 in aqueous media (Figure 1G-H). However, *para*-hydroxy **SBTub4** thermally relaxed at pH~9 with a half-life around 2 h (Figure 1I). This offers two opportunities for future applications of styrylbenzothiazole photopharmaceuticals. Firstly, the *Z*-stability of *para*-hydroxy **SBTub4**'s *Z* isomer at pH~7 contrasts to both azobenzene and hemithioindigo photoswitches with *para*- (or *ortho*-) hydroxy or aniline substituents, that typically feature millisecond (azobenzene) to second (hemithioindigo) aqueous relaxation half-lives even at pH~7. This underlines the broader chemocompatibility of styrylbenzothiazoles as a photoswitch scaffold for these functional groups, that are highly prevalent in bioactive molecules for many biological targets due to e.g. their importance in creating high-affinity ligand-protein interactions. Secondly, the pH-sensitivity of *para*-hydroxy **SBTub4**'s relaxation rate suggests that pK<sub>a</sub>-modulation could deliver styrylbenzothiazoles relaxing on a second or minute timescale at pH~7, such that local *E*→*Z* photoswitching could be combined with sample-wide thermal relaxation to improve spatiotemporal localisation of the *Z*-isomer.

### **Photostability of SBTubs – isomerisation and cycloaddition**

To examine whether degradative photochemical side reactions (e.g. 6- $\pi$  electrocycloisomerisation, [2+2] cycloaddition, etc.) could affect the **SBTubs** during chemical biology use, a sample of **SBTub2** (3.3 mg) in *d*<sub>6</sub>-DMSO (0.5 mL) in a quartz NMR tube capped under air, was irradiated with 350 nm UV within a Rayonet RPR-200 photochemistry reactor (Rayonet RPR-3500A lamps, air cooled with a cooling fan). The NMR tube was mounted to an RMA-500 Merry Go-Round unit to maintain an approximate distance of 2 cm from the UV-lamps. An NMR was taken before and after constant irradiation for 1 h, showing exclusively a mixture of *E*- and *Z*-isomers (no photodegradation or cycloaddition). During standard biological assays, illuminations are conducted with far lower photon fluxes (e.g. < 1 mW/cm<sup>2</sup> pulses from low-power LEDs for total <1 min illuminated time over long-term viability experiments), therefore it can be assumed that negligible photodegradation of the **SBTubs** should occur. Only after constant Rayonet reactor irradiation overnight, was photodegradation (primarily [2+2] cycloaddition product) evidenced by NMR and LC-MS analysis (detected by HPLC coupled to a Bruker Daltonics HCT-Ultra spectrometer used in ESI mode, unit *m/z*) although the major compound present was still the **SBTub** (as a mixture of *E*- and *Z*-isomers) (Figure S1E-F).

### **PSS measurements and their comparison to simulated PSS( $\lambda$ )**

For photopharmaceutical assays in biology it is helpful to straightforwardly estimate the *E/Z* ratio at any wavelength's photostationary state (PSS), to choose optimal wavelength conditions for illumination during biological assays or to understand the limits of what is possible on a given setup. The absorption spectrum of a bulk sample at a certain PSS is a linear combination of spectra of the constituent *E* and *Z*-isomers. Therefore we compared experimentally measured UV-spectra from different PSS equilibria, with calculated PSS spectra obtained by assuming (1) that quantum yields for *E*→*Z* and *Z*→*E* isomerisations are approximately equal over the measured photoisomerisation region (which is experimentally verifiable by confirming that illumination at the isosbestic point gives an *E/Z* ratio approximately 1:1), and that (2) the isomer spectra measured inline in HPLC are approximately identical to those that underlie UV-Vis measurements in biological media in cuvette

(which we verified by solvent independency measurements, as shown in Figure S1C-D, comparing HPLC eluent solvent to biological media): these assumptions allow us to simulate PSS spectra on the basis of HPLC traces as follows (see also Figure S1G-J):

- Taking experimental PSS absorption spectra on a UV-Vis spectrometer under different illumination wavelengths, thus also determining the isosbestic point  $\lambda_{\text{iso}}$ .
- Obtaining absorption spectra  $\epsilon E(\lambda)$  and  $\epsilon Z(\lambda)$  of the pure *E* and *Z*-isomers from an inline diode array detector (DAD) of an HPLC system. Absorption spectra of both isomers are scaled by multiplication in order to cross at  $\lambda_{\text{iso}}$ , generating data  $\epsilon' E(\lambda)$  and  $\epsilon' Z(\lambda)$  in arbitrary units, such that  $\epsilon' E(\lambda) / \epsilon' Z(\lambda) = \epsilon E(\lambda) / \epsilon Z(\lambda)$  across all wavelengths.
- Estimation of  $\text{Frac}[E]_{\text{PSS}}(\lambda)$ , the fraction of *E*-isomer that should be generated at photostationary state illumination at wavelength  $\lambda$  (assumes identical quantum yields for  $E \rightarrow Z$  and  $Z \rightarrow E$  isomerisations) via

$$\text{Frac}[E]_{\text{PSS}}(\lambda) = \frac{\epsilon' Z(\lambda)}{\epsilon' Z(\lambda) + \epsilon' E(\lambda)}$$

- Simulating absorption spectra in arbitrary units via

$$\text{Abs}_{\text{SIM}}(\lambda) = \text{Frac}[E]_{\text{PSS}}(\lambda) \times \epsilon' E(\lambda) + (1 - \text{Frac}[E]_{\text{PSS}}(\lambda)) \times \epsilon' Z(\lambda)$$

and comparing the predicted-PSS *curve shape* to that of experimental data (more important than comparing single absolute absorption values since more robust to variation). When the curve shapes match across a range of PSS wavelengths, we assume that we can interpolate other PSS *E/Z* ratios under any bracketed illumination wavelength, from the measured isolated-isomer spectra (HPLC). This was found to be exquisitely accurate for **SBTubs**.

### **Two-photon excitation**

Two-photon excitation of **SBTub3** (5 mM in DMSO) was performed using a mode-locked Ti-Sapphire Laser operating at 780 nm (Spectra Physics, Tsunami) with a pulse repetition frequency of 80 MHz (pulse width <100 fs) and an output power of 0.65 W. The laser was coupled into an upright Microscope (Zeiss AxioTech 100) and focused with a 40× reflective objective (**Thorlabs, LMM-40X-UVV**) onto the sample. Transmittance through the sample was measured using a HAL 100 illuminator (Carl Zeiss) and a SP300i spectrograph equipped with a MicroMAX CCD camera for signal recording (both Princeton Instruments), between 360 nm and 380 nm. This spectral range was chosen to be around the absorbance maximum of **SBTub3** in DMSO (~366 nm Figure S1D). Spectra were recorded with low intensity incident light, and an exposure time of only 1 s to prevent any unintended photoisomerization of the molecules during the measurement (and as a control, 12 min of continuous spectral recording produced an *E* to *Z* isomerisation of only 4%). The sample was measured in a home-made microcuvette with optical path length  $d=0.1$  mm and volume ~7.8  $\mu\text{L}$ . Photoisomerization was analyzed by measuring the change in light intensity across the spectral range 360-380 nm (0.5 nm increments) after passing through the sample ( $I_{\text{SBTub3}}$ ) in relation to light passing through a reference sample of only DMSO ( $I_{\text{DMSO}}$ ), smoothing the spectra (Savitsky-Golay) confirming the overlap of the spectra with those acquired under dilute conditions on the UV-Vis (50  $\mu\text{M}$ , 1 cm path length) to rule out concentration-dependent effects on spectra or photoisomerisation, then taking a representative intercept to the smoothed spectra and calculating absorbance of the sample as **A =  $-\log_{10}(I_{\text{SBTub3}} / I_{\text{DMSO}}$ )**.



## Part E: Biochemistry

### ***Stability towards glutathione – comparison to an azobenzene photoswitch***

In summary, we monitored **SBTub** changes due to GSH adduct formation, thiol addition-elimination (that should return *E*-**SBTub** due to the  $sp^3$  intermediate), reductive degradation (involving a second equivalent of GSH) or other compound loss mechanisms by UV-Vis and HPLC-UV-MS, yet no such changes were observed. This contrasts markedly to the instability in our hands of similar *Z*-azobenzenes when challenged by GSH, including **PST-1** (note however that our GSH challenge assay, which avoided the biologically irrelevant exogenous phosphine nucleophile TCEP, resulted in substantially less adduct formation/photoswitch destruction than literature methods<sup>[19]</sup> despite using a vast excess of reduced GSH which is elsewhere incorrectly reported as though it were the only active species in GSH+TCEP mixtures; compare also Figure 2B).

Stability towards glutathione (GSH) of samples of both all-*E* (“dark”) and mostly-*Z* (“pre-lit”) **SBTub2** (Figure 2A) was determined similarly to published methods, and compared to that of **PST-1** (all-*E* “dark”, and mostly-*Z* “lit”).<sup>[19]</sup> All solutions were prepared in PBS pH ~7.4 with 10% DMSO, containing GSH (10 mM), in UV-Vis cuvettes that were sealed under air atmosphere (gas head volume <2 mL) with parafilm and maintained at 37°C, during absorbance measurements over several hours in a Agilent Cary 60 spectrophotometer. “Dark” assays were performed with the *E*-isomers of the test compounds; “pre-lit” **SBTub2** (note: relaxation far slower than experiment time) had been pre-illuminated to reach PSS under 360 nm light; while “lit” **PST-1** (note: relaxation faster than experiment time) was maintained under continuous illumination from above with a 390 nm LED to maintain undegraded **PST-1** in a mostly-*cis* state. The  $\pi \rightarrow \pi^*$  transition was monitored for dark **PST-1** and lit/dark **SBTub2**, (**SBTub2** at 345 nm, **PST-1** at 378 nm) while for lit **PST-1**, its stronger  $n \rightarrow \pi^*$  band at 440 nm was followed instead for more accurate readout (Figure 2A-B). This is because **SBTub2** has a large enough  $\pi \rightarrow \pi^*$  absorbance coefficient to be reliably measured at 25  $\mu$ M in both dark and lit experiments; the smaller absorbance coefficient of *trans*-**PST-1** encouraged us to use it at 50  $\mu$ M for the dark assay, while we performed the crucial lit assay of **PST-1** (*Z* isomer absorbance ca. 6 times lower still) at 300  $\mu$ M. The full absorbance spectra and those of a no-compound GSH-only control are shown in Figure S2A-C.

**SBTub2** was stable against GSH addition and/or GSH-dependent reduction of the chromophore (which should both decrease its  $\pi \rightarrow \pi^*$  absorbance at 345 nm towards zero) in both all-*E* and mostly-*Z* assays. *Z*-**SBTub2** did not appear susceptible to significant *Z* to *E* isomerisation catalysed by reversible GSH addition-elimination since if this had continued to completion it would increase the  $\pi \rightarrow \pi^*$  absorbance for the “lit” solution by a factor of 3; we instead assign the slight absorbance increase at short wavelengths (Figure S2A) primarily to GSH oxidation to GSSG (Figure S2C) with almost negligible thermal relaxation of *Z*-**SBTub2** over the experimental time course.

We compared the SBT scaffold’s GSH stability to that of the widely used photopharmaceutical scaffold azobenzene, using similarly-decorated azobenzene **PST-1** as a comparison.

In our hands *E*-**PST-1** (50  $\mu$ M) was stable to the GSH challenge (Figure 2A-B) which does not match the “GSH/reductive susceptibility” described in the literature for this as well as other azobenzenes.<sup>[19]</sup> However, we trust our result to replicate the average cellular situation, and ascribe the discrepancy to literature use of co-reductants such as phosphines which we feel do not well predict the cellular situation. Those literature assays are typically performed with a powerful co-reductant such as TCEP, that is intended to keep GSH in its reduced form, with the non-explicit assumption that the

phosphine should not perform Mitsunobu-type addition to the diazene or otherwise affect the reaction paths available to the photoswitch. When we tested for degradative effects due to 5 mM TCEP (with and without GSH) we found that TCEP alone caused appreciable *E*-**PST-1** degradation, and to an identical degree as the TCEP + GSH combination (Figure 2B). This suggests that TCEP (not GSH) is the agent responsible for degradation of *E*-**PST-1** in such literature “GSH assays”, arguing more generally for caution in interpreting prior *in vitro* assessments of azobenzene “bioinstability” against cellular thiol concentrations if non-innocent co-reductants were employed. In our opinion, limiting the amount of oxygen available to a sample (e.g. capping a vial/cuvette under air with a negligible headspace volume) should be sufficient for running such assays reliably: since it seems to us that applying an approx. 10 mM concentration of GSH (i.e. at least 30-fold excess), should allow enough GSH to persist in the reduced state throughout an assay lifetime, despite potential oxidation from dissolved oxygen or from air in the headspace, such that large excesses (with respect to test compound) of additional reductants of a chemically different nature (especially those that are not physiological in nature or in concentration) can be productively avoided. Certainly, a less risky approach to test whether autoxidative GSSG formation precludes biochemically relevant compound reduction in the assay lifetime would be to vary the concentration and/or equivalents of GSH applied.

However, we observed unequivocally that *Z*-**PST-1** (300  $\mu$ M) evolved rapidly in the absence of TCEP, indicating near-stoichiometric degradation by GSH (Figure 2B, Figure S2B-F). We ruled out addition-elimination-catalysed *Z* to *E* isomerisation as the *major* mechanism of absorbance evolution, since complete *Z* to *E* isomerisation would increase the assay absorbance reading from the starting value of ca. 1 to ca. 6, whereas in fact the absorbance decreases to 0.40 at plateau<sup>[6]</sup> (Figure 2B). We presumed at this stage that GSH adduct formation, and/or reduction through to the hydrazine or still further to the anilines, is the major cause of loss of absorbance, and explored this in more detail with HPLC as detailed below.

### ***Further exploration of glutathione-induced Z-azobenzene degradation***

To further examine the degradation of *Z*-azobenzene by GSH, a timecourse of HPLC analyses of a similar “lit” sample of **PST-1** (0.5 mM, lit at 395 nm) with 10 mM GSH in PBS + 10% DMSO was performed following our standard HPLC conditions (Figure S2D-F). The results showed progressive formation of two major UV-active impurities, which because of their retention time shifts and their *Z*- and *E*-azobenzene-like UV spectra (Figure S2F) it could be tempting to assign as e.g. *ortho*-SG adducts on north and south aryl rings; however we were not able to observe interpretable signals in MS perhaps due to fragmentation in the spray.

The greater susceptibility of *Z*-**PST-1** was to be expected from the literature-known faster kinetics of nucleophile addition to *Z*-azobenzenes, as well as their greater oxidising potential, as compared to the *E* isomers.<sup>[33]</sup> The stoichiometry and the limiting amount of reduction in the presence of physiological concentrations of thiol reductant can however be questioned; and we prefer not to conclude broadly about the final fate of azobenzenes in cells, nor about the completeness of adduct formation or reduction in general, since while the cell-free model gives a clear result of *Z*-azobenzene degradation with GSH, this is not equivalent to showing *cellular* degradation: (1) Cells are not homogenous aqueous cosolvent environments but have complex compartmentalisation effects controlling compound distribution as well as redox environments<sup>[44]</sup>, e.g. that lipid-environment-bound azobenzenes could very reasonably be expected to be protected from reaction with cytosolic GSH; (2) cellular, embryonic and adult animal assays<sup>[7,21,24]</sup> have robustly shown photoreversible switching with **PST-1**; and this implies that cells maintain a cellularly-available pool of freely

photoisomerisable, non-adduct-state *E*- and **Z-PST-1** at a basal concentration that is above the inhibitory threshold, hence that reduction is by no means complete in the cellular context and certainly does not impact the cellular utility of this cytosol-active azobenzene; (3) the survival of cells treated briefly with high **Z-PST-1** concentrations (see one-time-activation assay Figure 4A) argues strongly against cellularly-relevant stoichiometric disturbance of the thiol pool or of thiol-based enzymes through poorly-reversible adduct formation and/or reduction through to the hydrazine and beyond; (4) our results do not exclude a non-innocent role for the dimethylsulfoxide cosolvent which is present at very high equivalence (or its potential contaminants) in modifying the **PSTs**' apparent GSH stability. Addressing these azobenzene-centric issues is beyond the scope of this study into styrylbenzothiazoles and will be tackled elsewhere.

### **Microsomal Stability**

The **SBTubs**' stability to degradation by liver microsomes was assessed by *in vitro* studies using isolated mouse and human liver microsomes, performed by Bienta Biology Services (Kiev, Ukraine) over a 40 min timecourse at 37°C following standard practice. Mouse hepatic microsomes were isolated according to a standard protocol; human hepatic microsomes were supplied by XenoTech. Microsomal incubations were performed in duplicates and control incubations were performed replacing the NADPH-cofactor system with PBS. Supernatants were analyzed using HPLC-MS. **SBTub2** and **SBTub3** showed good microsomal stability (Figure 2C).

### **hERG Inhibition**

hERG inhibition experiments were performed by Bienta Biology Services using Invitrogen Predictor™ hERG Fluorescence Polarization Assay in accordance with the manufacturer's protocol (Protocol PV5365). In brief, a fluorescent tracer is incubated with **SBTub** and membranes bearing hERG channel for 2–4 hours in the solution and the polarization of fluorescence emission (higher when bound to hERG, lower in solution due to free tumbling) is assayed with reference to control inhibitor E-4031 to validate assay performance. **SBTubs** were tested in quadruplicates at 1 µM, 5 µM and 25 µM with reference to a positive control (only tracer, fluorescence polarization is maximal when nothing interferes with the reaction of the tracer and hERG membranes - minimal tracer rotation) and a negative control (30 µM of E-4031, i.e. 100% tracer displacement and minimum assay polarization value, due to tested compound competing with the tracer for the hERG channel, the polarization of emitted light).

**SBTub2** showed strong and dose dependent hERG binding, while **SBTub3** showed moderate and dose dependent hERG binding (Figure 2D). However, tracer inhibition can be exaggerated if low compound solubility or if promiscuous protein binding are issues. Further evaluations in more sophisticated models are ongoing.

### **CYP450 inhibition**

The potential for CYP450 inhibition was assessed by *in vitro* inhibition studies using fluorogenic CYP450 substrates with the corresponding CYP450 enzymes and NADPH regeneration system (Vivid CYP450 Screening Kits) with some minor changes to the manufacturer's protocols, performed by Bienta Biology Services. The fluorescent signal produced from reaction is directly proportional to the cytochrome P450 activity. In the cases when tested compounds interfere with the CYP450 enzyme-substrate reaction, the fluorescent signal decreases.

In brief, the tested compounds were first dissolved in DMSO at 1 mM, then diluted in aqueous assay buffer to 25  $\mu$ M, then the dilute solutions were mixed with a pre-mix consisting of human CYP450 + oxidoreductase and NADP<sup>+</sup> regeneration system (glucose-6-phosphate and glucose-6-phosphate dehydrogenase). After 10 min pre-incubation, the enzymatic reaction was initiated by the addition of a mix of NADPH and the appropriate CYP450 substrates yielding a test compound concentration of 10  $\mu$ M. The reaction was incubated for the desired reaction time (25 min for CYP1A2, CYP2C9, CYP2D6, and CYP3A4, 60 min for CYP2C19) after which Stop Reagent was added and fluorescence measured using SpectraMax Paradigm Multi-Mode Microplate Reader. All test points were performed in quadruplicates at concentration 10  $\mu$ M (1% DMSO). Reference compounds used to benchmark the CYP inhibition under these conditions are listed in Figure S2G.

At 10  $\mu$ M, **SBTub2** and **SBTub3** showed strong inhibition of 1A2, 2C9 and 2C19 CYP isoforms (Figure 2E). *Higher* fluorescence was detected after incubation of **SBTub2** with CYP2D6 comparing to positive control, which resulted in negative value of inhibition, but we assign that result to assay interference. Further evaluations are ongoing.

### ***SBTubs show light specific inhibition of tubulin polymerisation in vitro***

99% tubulin from porcine brain was obtained from Cytoskeleton Inc. (cat. #T240). The polymerisation reaction was performed at 5 mg/mL tubulin, in polymerisation buffer BRB80 (80 mM piperazine-N,N'-bis(2-ethanesulfonic acid) (PIPES) pH = 6.9; 0.5 mM EGTA; 2 mM MgCl<sub>2</sub>), in a cuvette (120  $\mu$ L final volume, 1 cm path length) in a Agilent CaryScan 60 with Peltier cell temperature control unit maintained at 37°C; with glycerol (10  $\mu$ L). Tubulin was first incubated for 10 min at 37°C with "lit"- (360 nm-pre-illuminated; mostly-Z<sup>-</sup>) or dark- (all-E) **SBTub** (final **SBTub** concentration 20  $\mu$ M) in buffer with 3% DMSO, without GTP. Then GTP was added to achieve final GTP concentration 1 mM (with mixing), and the change in absorbance at 340 nm was monitored for 15 min, scanning at 15 s intervals<sup>[45]</sup>. While **SBTub2** and **SBTub3** in the "dark"-state (20  $\mu$ M) displayed almost similar MT growth dynamics as the cosolvent-only control, "lit" **SBTub2** and **SBTub3** (20  $\mu$ M) showed noticeable slowdown of polymerisation kinetics, similar to known microtubule inhibitors such as colchicine (assayed at 16  $\mu$ M) (Figure 3B). Designed-inactive **SBTub1** and **SBTub4** were not tested for cell-free tubulin polymerization inhibition since they robustly showed no MT inhibiting effects (cytotoxicity, G2/M arrest, MT breakdown in IF) in any other experiments.

## **Part F: Protein Crystallisation**

### ***Protein crystallisation materials and methods***

#### **Protein production, crystallization and soaking.**

The DARPin D1 was prepared as previously described<sup>[46]</sup>. Tubulin from bovine brain was purchased from the Centro de Investigaciones Biológicas (Microtubule Stabilizing Agents Group), CSIC, Madrid, Spain.

The tubulin-DARPin D1 (TD1) complex was formed by mixing the respective components in a 1:1.1 molar ratio. The TD1 complex was crystallized overnight by the hanging drop vapor diffusion method (drop size 2  $\mu$ L, drop ratio 1:1) at a concentration of 15.9 mg/mL and at 20°C with a precipitant solution containing 18% PEG 3350, 0.2 M ammonium sulfate and 0.1 M bis-tris methane, pH 5.5. All drops were subsequently hair-seeded with crystalline material obtained in previous PEG-screening, which resulted in single and large (0.5  $\mu$ m) TD1 complex crystals. The crystals were

fished and transferred into new precipitant solution drops containing 10% DMSO and respective compounds (**SBTub2**/**SBTub3**) at a final concentration of 2 mM and were pre-switched with 360 nm LEDs for 5 min. After 4 h of soaking in the dark, the **SBTub**:tubulin crystals were mounted for X-ray diffraction data collection.

#### **Data Collection, processing and refinement.**

Data were collected at beamline X06SA at the Swiss Light Source (Paul Scherrer Institute, Villigen, Switzerland). The beam was focused to 30 x 30  $\mu\text{m}$ , the flux was  $3 \times 10^{10}$  photons/ s and the data collection speed was  $2^\circ/\text{s}$  at an oscillation range of  $0.2^\circ$  per frame (see Table S1). For TD1-**SBTub2** and TD1-**SBTub3**,  $210^\circ$  and  $220^\circ$  of data were collected, respectively. Data processing was done with XDS<sup>[47]</sup>. Due to anisotropy, the data were corrected using the Staraniso server (<http://staraniso.globalphasing.org/>). The structures were solved by molecular replacement using PDB ID 5NQT as a search model<sup>[48]</sup>. The ligands and restraints were generated with the grade server (<http://grade.globalphasing.org/>) using their SMILES annotation. The structures were then refined iteratively in PHENIX<sup>[49]</sup> with manual editing cycles in COOT<sup>[50]</sup>.

#### **X-ray structural analysis**

Both ligands, *Z*-**SBTub2** and *Z*-**SBTub3**, bind to the colchicine site at the interface of  $\alpha$ - and  $\beta$ -tubulin (Figure 3C-G, Figure S3A-D; PDB: 6ZWC and 6ZWB respectively). The two ligands bind in exactly opposite poses despite interacting with identical residues in the binding pocket, matching the design goal of this study whereby the poses should be defined by the specific part of the ligand inherited from the combretastatin-A4 archetype (trimethoxyphenyl in case of **SBTub2** and isovanillyl in case of **SBTub3**). The benzothiazole group is able to bind in both orientations (Figure 3E-F).<sup>[39]</sup> The  $\beta$ -T7 loop is not well ordered in both tubulin-**SBTub2** and tubulin-**SBTub3** structures, likely due to the influence of the ligands. Despite the weak density for some parts of the loop, it is apparent that the larger trimethoxyphenyl-ring of **SBTub2** occupies more space and pushes  $\beta$ -Leu-248 and the  $\beta$ -T7 loop further out than the smaller flat benzothiazole group in **SBTub3** (Figure 3E-F).

The hydrophilic OH-group at the isovanillyl-ring of **SBTub3** (which binds in the “top-down” pose) appears to stabilize the  $\alpha$ -T5 loop in the conformation the ligand-free structure displays (Figure S3D). **SBTub2** binds in the “bottom-up” pose and the  $\alpha$ -T5 loop displays an altered conformation similar to that seen with colchicine (Figure S3D). While both ligands, being colchicine site binders, likely interfere with the “curved-to-straight” conformational transition of tubulin during the formation of microtubules<sup>[51,52]</sup>, their difference in disturbing the  $\alpha$ -T5 loop conformation may be of pharmacological relevance, given that the archetypical colchicine disturbs the  $\alpha$ -T5 loop, while the vascular disrupting agent combretastatin A4 does not.<sup>[39]</sup>

## **Part G: Biological Data**

### **Cell assay methods**

#### **General cell culture**

HeLa and A549 cells were maintained under standard cell culture conditions in Dulbecco's modified Eagle's medium (DMEM; PAN-Biotech: P04-035550) supplemented with 10% fetal calf serum (FCS), 100 U/mL penicillin and 100 U/mL streptomycin. Cells were grown and incubated at  $37^\circ\text{C}$  in a 5%  $\text{CO}_2$  atmosphere. Cells were typically transferred to phenol red free medium prior to assays (DMEM; PAN-Biotech: P04-03591). Substrates and cosolvent (DMSO; 1% final concentration) were

added *via* a D300e digital dispenser (Tecan). Cells were either incubated under “lit” or “dark” conditions; “lit” indicates a pulsed illumination protocol was applied by multi-LED arrays to create the *Z*-isomers of the compounds *in situ* in cells and then maintain the wavelength-dependent PSS isomer ratio throughout the experiment, as described previously.<sup>[6]</sup> Typical “lit” timing conditions were 75 ms pulses of  $\sim 1$  mW/cm<sup>2</sup> applied every 15 s. “Dark” indicates that compounds were set to the all-*trans* state by thermal relaxation of the DMSO stocks at 60°C overnight, applied while working under red-light conditions, and cells were then incubated in light-proof boxes to shield from ambient light, thereby maintaining the all-*E*-isomer population throughout the experiment. *Single shot activation* (lit<sub>1h</sub>) indicates, that cells are treated with *E*-**SBTubs** and illuminated *in situ* for a short time (75 ms every 15 s during the first hour only; total illumination time 18 s) before stopping illuminations and incubating for the remaining 47 h without any further illumination.

### MTT antiproliferation assay

Cells were seeded in 96-well plates at 5,000 cells/well and left to adhere for 24 h before treating with test compounds. *E*-**SBTubs** were added under the indicated lighting conditions for 48 h (final well volume 100  $\mu$ L, 1% DMSO; six technical replicates); the “cosolvent control” (“ctrl”) indicates treatment with DMSO only. Cells were then treated with 0.5 mg/mL (3-(4,5-dimethylthiazol-2-yl)-2,5-diphenyl tetrazolium bromide (**MTT**)) for 3 h. The medium was aspirated and formazan crystals were re-dissolved in DMSO (100  $\mu$ L); absorbance was measured at 550 nm (Abs<sub>550</sub>) using a FLUOstar Omega microplate reader (BMG Labtech). Absorbance data was averaged over the technical replicates, then normalized to viable cell count from the cosolvent control cells (%control) as 100%, where 0% viability was assumed to correspond to absorbance zero. Three independent experiments were performed; data are shown from a single representative experiment, as indicated; data were plotted against the log of **SBTub** concentration (log<sub>10</sub>([**SBTub**]) (M)).

### Cell cycle analysis

*E*-**SBTubs** were added to HeLa cells in 24-well plates (50,000 cells/well; three technical replicates, three biological replicates) and incubated under “dark” or “lit” conditions for 24 h. Cells were collected, permeabilised and stained with 2  $\mu$ g/mL propidium iodide (PI) in HFS buffer (PBS, 0.1% Triton X-100, 0.1% sodium citrate) at 4°C for 30 min then analysed by flow cytometry using a FACS Canto II flow cytometer (Becton Dickinson) run by BD FACSDiva software. 30,000 events per technical replicate were analysed; the PI signal per event (corresponding to cellular DNA content) was measured and cells were binned into sub-G1, G1, S and G2 phase according to DNA content using *Flowing* software. Results (means of three technical replicates) from one experiment of three independent trials are shown.

### Immunofluorescence staining

HeLa cells were seeded on glass coverslips in 24-well plates (50,000 cells/well) and treated with **SBTubs** the next day under “dark” or “lit” conditions for 24 h. Cells were washed with pre-warmed (37°C) MTSB buffer (80 mM PIPES pH 6.8; 1 mM MgCl<sub>2</sub>, 5 mM ethylene glycol tetraacetic acid (EGTA) dipotassium salt; 0.5% Triton X-100) for 30 s then fixed with 0.5% glutaraldehyde for 10 min. After quenching with 0.1% NaBH<sub>4</sub> (7 min), samples were blocked with PBS + 10% FCS (30 min). The cells were treated with primary antibody (1:400 rabbit alpha-tubulin; Abcam ab18251) in PBS containing 10% FCS for 1 h and then washed with PBS. Cells were incubated with secondary antibody (1:400 goat-anti-rabbit Alexa fluor 488; Abcam ab150077) in PBS containing 10% FCS for 1 h. After washing with PBS, the coverslips were mounted onto glass slides using Roti-Mount FluorCare DAPI (Roth) and imaged with a Zeiss LSM Meta confocal microscope (CALM platform,

LMU). Images were processed using the free Fiji software. Postprocessing was only performed to improve visibility. For maximum intensity projections, images were recorded at different focal planes incrementally stepping through the sample (step size 1–2  $\mu\text{m}$ ) and maximum intensity projections were obtained using Fiji software.

### **EB3-comet live cell assays in HeLa cell line: general procedure**

HeLa cells (12,000 cells/well) were seeded on 8-well ibiTreat  $\mu$  ibidi slides (ibidi, Martinsried) 24 h prior to transfection. Cells were transiently transfected with *EB3-GFP* or *EB3-YFP* plasmids using jetPRIME reagent (Polyplus) according to the manufacturer's instructions. Cells were imaged 24 h later, at 37°C under 5% CO<sub>2</sub> atmosphere, using an UltraVIEW Vox spinning disc confocal microscope (PerkinElmer) operated with *Volocity* software equipped with an EMCCD camera (Hamamatsu, Japan), and an environmental chamber kept at 37°C and 5% CO<sub>2</sub> using a 63 × 1.4 NA Plan-Apochromat oil-immersion objective (Zeiss), while applying the specified illumination conditions. EB3-comets<sup>[53]</sup> were counted with a plugin for the *Fiji* software, based on the "Find maxima" function from the NIH (<https://imagej.nih.gov/ij/macros/FindStackMaxima.txt>).

### **Live cell imaging for photobleaching/wavelength orthogonality**

For photobleaching/wavelength orthogonality experiments, a suitable focus plane was first chosen on the microscope (white light for focusing). **SBTub** was then added *cautiously* while the cells were still on the microscope stage, and cells incubated for 10 min before imaging. This protocol avoids exposure of the **SBTub** to white focusing light, preventing unwanted isomerization prior to imaging which could falsify results when testing for GFP/YFP orthogonality. Cells were imaged either at 488 nm (GFP; 23% laser power, 400 ms exposure time, 45 frames/min) or 514 nm (YFP; similar parameters; data not shown since GFP orthogonality implies YFP orthogonality); cells were optionally additionally exposed to interleaved dummy frames of **SBTub**-isomerizing 405 nm light for compound activation (250 ms exposure time, 45 frames/min). For analysis statistics, 6 cells per condition from three independent trials were taken. First-order exponential decay curves were fitted to each cell's data with their comet counts normalized to 100% at time zero, enabling intercomparison of cells with different starting comet counts (depending on their size, the position of the focal plane, etc.).

### **Treatment of live cells with Z-SBTub3 under GFP imaging**

To show the effect of photoisomerized **Z-SBTub3** (as a control for the orthogonality experiment), a suitable focus plane was first chosen on the microscope (white light for focusing) and 5 frames were acquired at 488 nm, to set a reference for basal comet count. An **SBTub3** stock that had been isomerized to PSS with 360 nm was carefully applied on the stage, and after one minute incubation time, 180 frames were taken at 488 nm (400 ms exposure time, 23% laser power, 60 frames/min). The number of remaining comets per frame after treatment was counted and expressed as percentage of the starting reference timepoint.

### **Temporally reversible MT dynamics modulation with GFP-orthogonality**

HeLa cells were transfected with EB3-GFP using FuGENE 6 (Promega) according to manufacturer's instructions. Experiments were imaged on a Nikon Eclipse Ti microscope equipped with a perfect focus system (Nikon), a spinning disk-based confocal scanner unit (CSU-X1-A1, Yokogawa), an Evolve 512 EMCCD camera (Photometrics) attached to a 2.0x intermediate lens (Edmund Optics), a Roper Scientific custom-made set of Stradus 405 nm (100 mW, Vortran) and Calypso 491 nm (100 mW, Cobolt) lasers, a set of ET-BFP2 and ET-GFP filters (Chroma), a motorized stage MS-

2000-XYZ, a stage top incubator INUBG2E-ZILCS (Tokai Hit) and lens heating calibrated for incubation at 37°C with 5% CO<sub>2</sub>. Microscope image acquisition was controlled using MetaMorph 7.7 and images were acquired using a Plan Apo VC 60× NA 1.4 oil objective. Comet count analysis was performed in ImageJ using the ComDet plugin (E. Katrukha, University of Utrecht, Netherlands, <https://github.com/ekatrukha/ComDet>). GFP imaging was performed at 491 nm (0.17 mW; 300 ms every 2 s). In-frame **SBTub** photoactivation was performed at 405 nm (77 μW; 100 ms every 90 s; cell of interest plus in-frame surrounding area). Results were presented in the main text and correspond to Movie M1.

### **Temporally reversible MT modulation through EB1-comet assays in A549 cell line**

A549 cells (40,000 cells/well) were seeded on 8-well ibiTreat μ slides (ibidi) 24 h prior to transfection. Cells were transiently transfected with *EB1-tdTomato* plasmid using jetPRIME reagent (Polyplus) according to the manufacturer's instructions. Cells were imaged 24 h later, under 37°C and 5% CO<sub>2</sub> atmosphere, using a Nikon TiE microscope equipped with a Yokogawa CSU-W1 spinning disk confocal unit (50 μm pinhole size), an Andor Borealis illumination unit, Andor ALC600 laser beam combiner (405/488/561/640 nm), Andor IXON 888 Ultra EMCCD camera, and a Nikon 100× NA 1.45 oil immersion objective. The microscope was controlled by Nikon NIS Elements software (v.5.02.00). Cells were pre-incubated with the indicated compound or cosolvent conditions in the dark for 5 min before acquisition through imaging at 561 nm (20% laser power, 300 ms exposure time, 30 frames/min). Optionally 405 nm illuminations (10% laser power, 175 μs pixel dwell time) were re-applied at 2 min intervals during acquisition as indicated. 3 cells per condition from three independent trials were taken for statistics. EB1 comets were counted in ImageJ using the ComDet plugin (E. Katrukha, University of Utrecht, <https://github.com/ekatrukha/ComDet>). EB1 count values were normalised to 100% at time zero or else normalised to 100% at the first return to plateau (pulsing experiments) as appropriate; this enables intercomparison of cells with different starting comet counts (depending on their size, the position of the focal plane, etc). Data are represented as mean comet count over time, with standard deviation; scalebars in EB1 movies (Movies M2-M7) are 10 μm.

### **Live Cell Imaging of EB3 in primary neuronal cultures**

Animals: All animal experiments were performed in accordance with Dutch law (Wet op de Dierproeven, 1996) and European regulations (Directive 2010/63/EU) under animal licence AVD1080020173404. All animal experiments were approved by the Dutch Animal Experiments Committee (DEC, Dier Experimenten Commissie) and were in line with the institutional guidelines of Utrecht University. Pregnant Wistar rats (Janvier), which were at least 10 weeks of age and not involved in any previous experiments, were used in this study.

Primary neuronal cultures and transfections: Primary hippocampal neurons were derived from hippocampi of embryonic day 18 pups (male and female). Hippocampi were dissociated into single cells by a combination of enzymatic and mechanical dissociation, as described.<sup>[54]</sup> After dissociation, neurons were plated in 12-well plates at a density of 100,000 cells per well on coverslips coated with poly-L-lysine (37.5 μg/mL, Sigma-Aldrich) and laminin (1.25 μg/mL, Roche). The primary hippocampal cultures were kept at 37°C and 5% CO<sub>2</sub> in Neurobasal medium (NB, Gibco) supplemented with 2% B27 (Gibco), 0.5 mM glutamine (Gibco), 15.6 μM glutamate (Sigma-Aldrich) and 1% penicillin/streptomycin (Gibco). Neurons were transfected at the 7th day *in vitro* (DIV 7) using Lipofectamine 2000 (Invitrogen) and were imaged at DIV 10. Briefly, for the transfection of each coverslip, 1.8 μg of total DNA (0.4 μg EB3-GFP, 0.2 μg RFP, 1.2 μg empty backbone) was mixed with 3.3 μL of Lipofectamine 2000 in 200 μL non-supplemented NB and incubated for 30 min



at 20°C. Before the DNA/Lipofectamine mix was added to the neurons, half of the volume of supplemented NB in which the neurons had been growing (conditioned NB) was transferred to a new 12-well plate and replaced by NB supplemented with 0.5 mM glutamine. Then, the DNA/Lipofectamine mix was added to the neurons and incubated for 1 h at 37°C and 5% CO<sub>2</sub>. After transfection, neurons were rinsed by dipping the coverslips into pre-warmed non-supplemented NB and placed back in conditioned NB that was mixed 50/50 with fresh, supplemented NB.

Live neuronal imaging: Neurons were immersed in conditioned NB with 1% DMSO cosolvent. Cells were imaged similarly to the conditions for **Temporally reversible MT dynamics modulation with GFP-orthogonality**, except in that GFP was imaged at 491 nm (0.1 mW, 500 ms every 3 s). Neurons were initially imaged for EB3 for 10 min while a ROI (blue box) was pulsed with 405 nm light commencing 2 min into the acquisition, establishing baselines for EB3 activity in the cell and in the ROI (areas not pulsed with 405 nm but analysed in kymographs are boxed in orange and green); the ROI-pulsing protocol was to illuminate the ROI at 405 nm (95 μW, 7 ms per trace) tracing over the ROI 5 times every 3 s with imaging frames interleaved. The same neurons were then exposed to **SBTub3** and immediately imaged for another 10 min using the same protocol.

### **FACS cell cycle analysis**

Results (Figure 3J) show full photoswitching-based control of G2/M-phase cell cycle arresting properties of **SBTub2** and **SBTub3**. Under dark (all-*E*) conditions they give no change of cell cycle repartition while under lit conditions (mostly-*Z*) they show strong G2/M-phase arrest similar to that of the proven photoswitchable colchicine site tubulin inhibitor **PST-1**. Crucially, neither isomer of the permutation control compounds **SBTub1** and **SBTub4** has effects on cell cycle repartition despite low antiproliferative effects at this concentration (see Figure 3A).

### **Immunofluorescence imaging of microtubule network structure**

The results in Figure 3H-I show light- and dose- dependent depolymerisation of microtubule structure by **SBTub2** and **SBTub3**, while **SBTub1** and **SBTub4** have no effect on MT structure under dark and illuminated conditions even at high concentrations of 20 μM. The maximum intensity projection (along the z-axis) of cells treated for 24 h with lit **SBTub2** or lit **SBTub3** shows that most treated cells have been arrested in mitosis and display severe MT depolymerisation and organisational defects, while only a minor population of adherent cells persists albeit with disorganized microtubule networks.

### **Live cell imaging: GFP/YFP orthogonality via EB3 comet assay**

**SBTub2** and **SBTub3** inhibit tubulin polymerisation upon photoswitching to their *Z*-isomers; note that this does not imply that they should depolymerise existing microtubule polymer immediately upon photoswitching (and, at cellularly relevant concentrations over short assay timescales < 30 min, they will not do so). Live cell imaging of EB3-GFP/YFP is a standard assay to monitor microtubule growth dynamics<sup>[55]</sup> and was therefore used as a readout of in situ generation and cellular retention of these **SBTubs'** bioactive *Z*-isomers.

Two assays were used, such that taken together, the results show orthogonality of both *E*- and *Z*-**SBTubs** to GFP/YFP imaging.

Firstly: stability of the *Z*-**SBTub** against *Z*-to-*E* isomerisation under GFP/YFP imaging was assessed. As per the “live cell imaging” methods section, cells were pre-incubated with all-*E* **SBTub3** (10 μM) or with cosolvent only (ctrl) in the dark for 10 min before acquiring uninhibited cellular EB3 comet

count statistics at timepoint  $t_{ref}$ . **SBTub3** was then isomerized substantially to *Z* by whole-field illumination at 405 nm ( $5 \times 300$  ms) and 5 GFP/YFP imaging frames at time points 30 s, 5 min and 10 min later were acquired (Figure S4A). Three independent trials were performed. For analysis, 8 cells per condition were chosen from the three independent trials. The EB3-comets were counted and each time point's comet count value was set as the average from those of its 5 frames. Each cell's comet counts were normalised with the average of its  $t = 0$  s imaging frames being set to 1. The number of comets at the following timepoints are expressed as fraction or percentage of the initial pre-treatment comet numbers and are represented as mean with SD (Figure S4B).

Comet counts were abruptly and, in this experiment permanently reduced, upon the first global **SBTub3** activation with 405 nm while the cosolvent control showed no effect from this photoswitching, indicating the photostability of the bioactive *Z*-**SBTub3** (Figure S4C).

Secondly: evaluation of *E*-**SBTubs**' photostability ability to effect *in situ* photocontrol over protein dynamics while avoiding interference from the imaging wavelengths of common fluorescent labels GFP and YFP was performed by comparing the EB3 comet count under different lighting and compound conditions (Figure 4B-C). Figure 4B shows the following conditions and conclusions:

**neg ctrl**: cosolvent-only controls (DMSO) imaged under 488 nm only, or under alternating 488/405 nm lighting protocol as used for **SBTub** photoactivation, are identical, showing the timecourse of "normal" reduction of EB3 comets due to photobleaching only (i.e. in this setup 405 nm pulsing does not result in photobleaching).

**SBTub3<sub>488</sub>** (red squares): cells treated with **SBTub3** ( $10 \mu\text{M}$ ) and imaged at 488 nm only: reduction of EB3 comets was comparable to those of both **neg ctrls**, indicating that **SBTub3** is not photoactivated by 488 nm light.

**SBTub3<sub>405</sub>** (blue triangles): cells treated with **SBTub3** ( $8 \mu\text{M}$ ) and imaged with 488 nm frames with interleaved 405 nm frames to induce **SBTub** activation. These show a faster decrease of EB3 comet count than of both **neg ctrls** and of **SBTub3<sub>488</sub>**; decrease is comparable to that of **pos ctrl PST-1** imaged at 488 nm, suggesting comparable inhibition of MT polymerisation.

**pos ctrl**: known azobenzene based MT depolymerizer **PST-1** ( $8 \mu\text{M}$ , non-GFP orthogonal) was imaged at 488 nm, causing compound activation and fast reduction of EB3 comet count (beyond the photobleaching rate).

Additionally, cells were treated with pre-illuminated *Z*-**SBTub3** enriched stock solutions and incubated for 1 min before imaging at 488 nm (Figure 4C). This experimental setup rules out a reduction of EB3 comets due to photobleaching, while also showing that reduction of EB3 comets is caused by exposing cells to *Z*-**SBTub3**.

Taken together, these results show the full orthogonality of both *E*- and *Z*-**SBTubs** to GFP/YFP imaging.

### **Live cell imaging on A549 lung cancer cell line**

To prove a potential broader use for cell biological investigations we assayed the temporal reversibility of **SBTub3**'s cell-localised modulation of MT dynamics using a different cell line, biological label, and fluorescent marker: i.e. performing an EB1-tdTomato "comet" assay on the A549 cell line. A549 cells with or without **SBTub3** were exposed to single pulses of 405 nm every 120 s while imaging EB1-tdTomato comets at 561 nm as described in the main text, achieving temporally reversible MT modulation (Video S1 part B and Figure 4F-H) similar to the results seen in HeLa cells

(Video S1 part A and Figure 4D-E). Particularly, MT polymerisation dynamics were reversibly modulated by cell-localised photoactivations with **SBTub3** (Figure 4F, red trace) but unaffected in the absence of **SBTub3** (Figure 4H, blue trace); MT polymerisation dynamics are not inhibited by unactivated **SBTub3** at 5 and 10  $\mu\text{M}$  (Figure 4G, blue and purple traces), whereas pre-lit **SBTub3** stops MT polymerisation dynamics upon treatment at both concentrations (Figure 4G, red and green traces); and DMSO cosolvent controls under dark and lit regimes (Figure 4H, black and blue traces) show no decrease in comet count, while the positive control colchicine binding site inhibitor nocodazole stops MT polymerisation dynamics at 1  $\mu\text{M}$  (Figure 4H, green trace). See also Video S2 as a representative example of these treatments.

Note that during recovery phases the EB3-GFP “comets” appear to reform and continue their trajectories from their stop positions, which is congruent to the **SBTubs**' design rationale (and results showing) that **Z-SBTub** is tubulin-specific and does not directly inhibit EB3.

### ***Detailed quantification of the impact of SBTub3 on live cell MT dynamics***

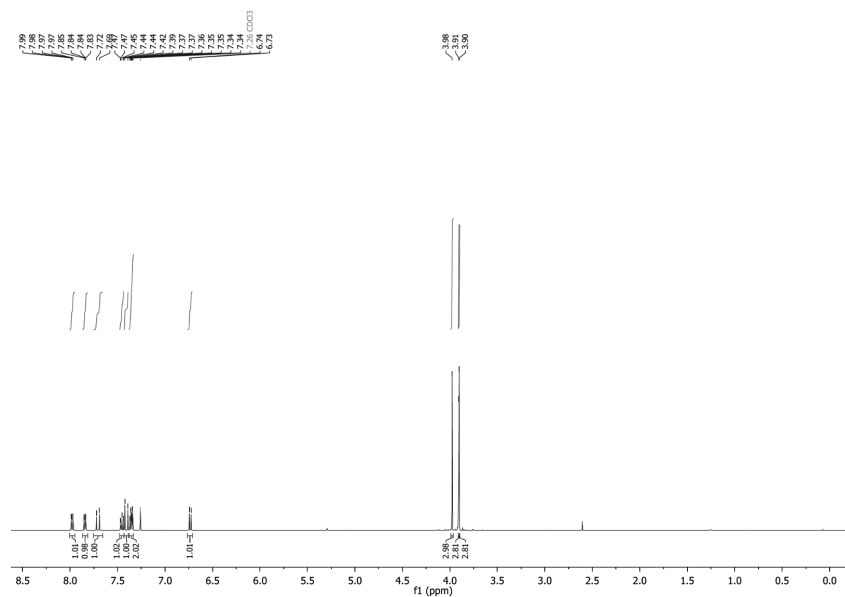
In order to study MT dynamics we used fluorescently labelled EB3 as a marker for the GTP cap of polymerizing microtubules. HeLa cells were transfected with EB3-GFP using FuGENE 6 (Promega) according to manufacturer's instructions. Cells were imaged similarly to the conditions for **Temporally reversible MT dynamics modulation with GFP-orthogonality**, except here GFP was imaged at 491 nm (0.2 mW, 100 ms every 0.6 s) and full frame SBTub3 photoactivation was performed using 405 nm (0.1 mW, 100ms every 1.2 s). Comet count analysis was performed in ImageJ using the ComDet plugin (E. Katrukha, University of Utrecht, Netherlands, <https://github.com/ekatrunkha/ComDet>). Velocity analysis was performed in Image J using the MTrackJ plugin.<sup>[56]</sup>

As expected, 405 nm light, **SBTub3** without 405 nm activation, and **SBTub1** inactive control all had no significant impact on EB3 comet numbers or density (Figure 4I-K). However, **SBTub3** with 405 nm activation showed a 90-95% reduction in EB3 comets within the first 5-10 s of 405 nm activation, which subsequently recovered to an equilibrium at ~50% or ~20% of the original comet count for 5  $\mu\text{M}$  or 40  $\mu\text{M}$  of **SBTub3** respectively. It is unclear to us what the cause for this dipped curve is, in particular whether this is an effect resulting from the rate of drug exchange between the inside and outside of the cell or whether this is occurring at the MT level. However, elucidating this mechanism goes beyond the scope of this paper. As expected based on the difference in comet count curves, 40  $\mu\text{M}$  **SBTub3** with 405 nm activation also had a significantly lower EB3 comet density than 405 nm activated 5  $\mu\text{M}$  **SBTub3**. EB3 comet velocities were already very slightly reduced in the **SBTub3** treated cells, prior to photoactivation with 405, though there was no significant difference between 5  $\mu\text{M}$  and 40  $\mu\text{M}$  treated cells. However, activation of **SBTub3** with 405 nm caused a further 30% or 38% decrease in velocity of persisting EB3 comets for 5  $\mu\text{M}$  and 40  $\mu\text{M}$  **SBTub3** respectively (Figure 4K). As expected the permutation control **SBTub1** had no impact on EB3 comet velocity (Figure 4K). We conclude that **SBTub3** can be used effectively in live cells to disrupt MT dynamics in a temporally controlled manner, and that **SBTub3** concentration can be modulated to calibrate the desired level of impact.

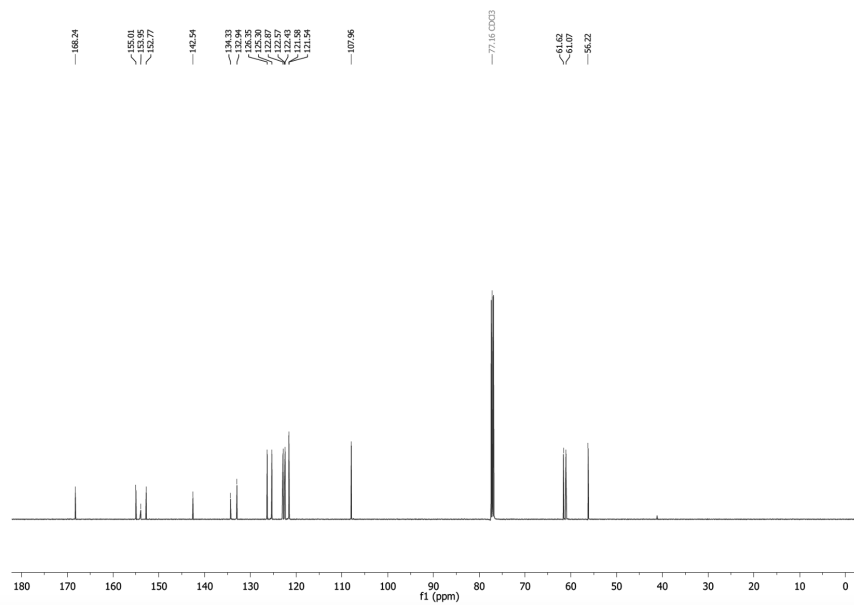
## Part H: NMR Spectra

### 2-(2,3,4-trimethoxystyryl)benzothiazole (SBTub1)

<sup>1</sup>H-NMR:

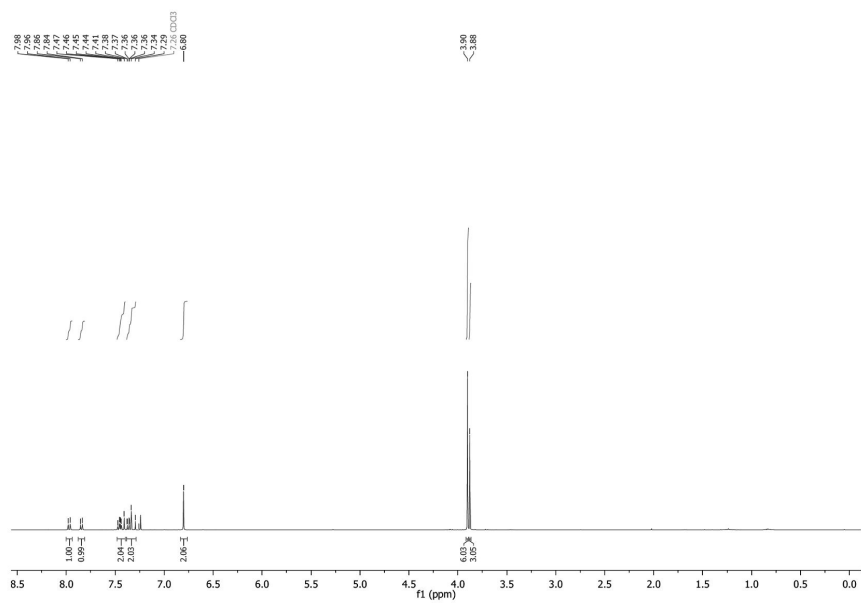


<sup>13</sup>C-NMR:

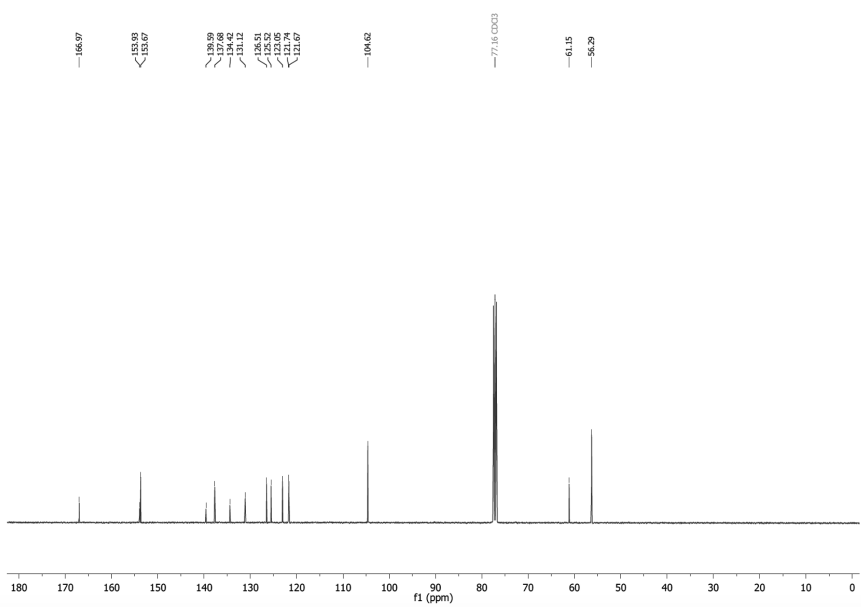


## 2-(3,4,5-trimethoxystyryl)benzothiazole (SBTub2)

<sup>1</sup>H-NMR:

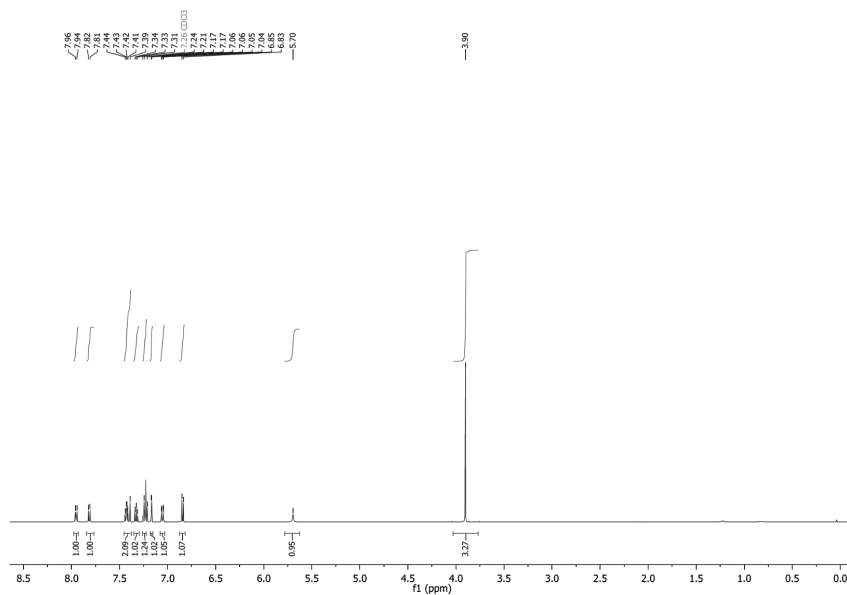


<sup>13</sup>C-NMR:

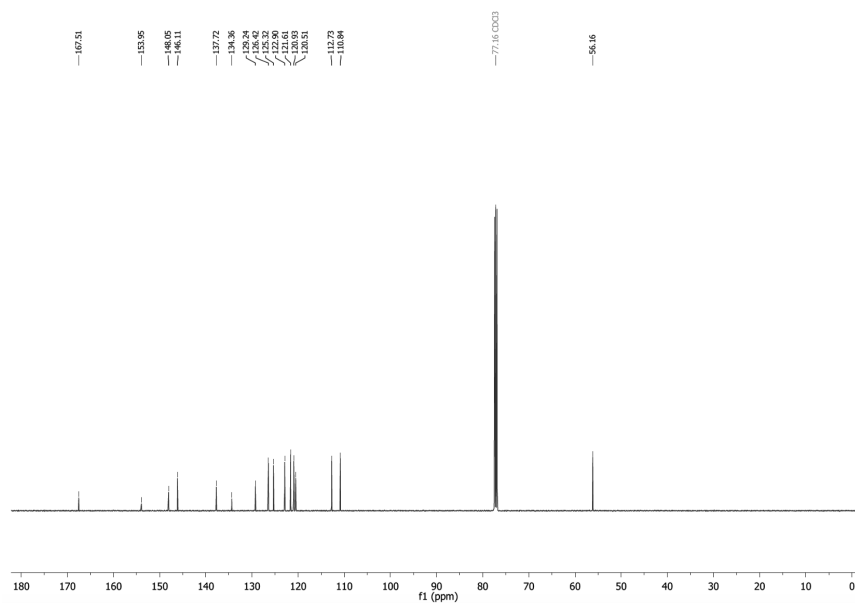


### 5-(2-(benzothiazol-2-yl)vinyl)-2-methoxyphenol (SBTub3)

<sup>1</sup>H-NMR:

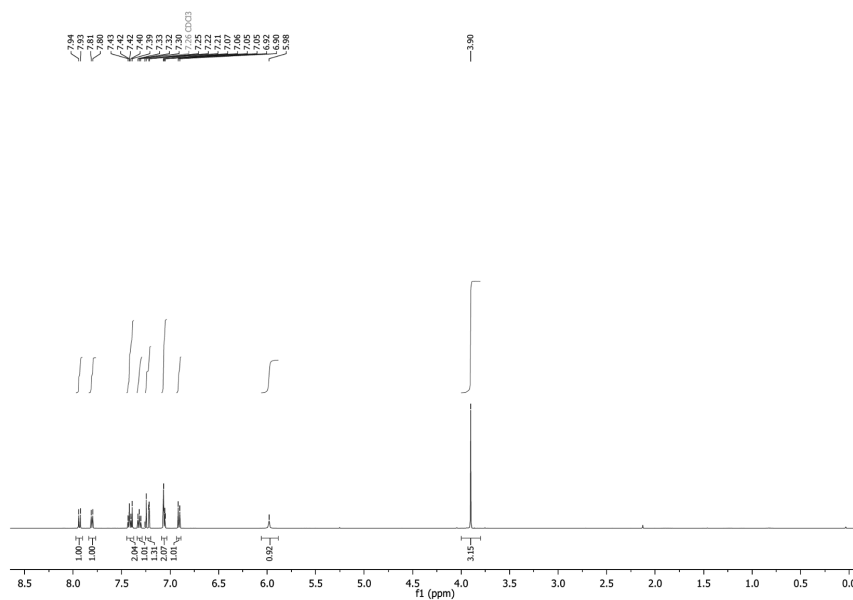


<sup>13</sup>C-NMR:

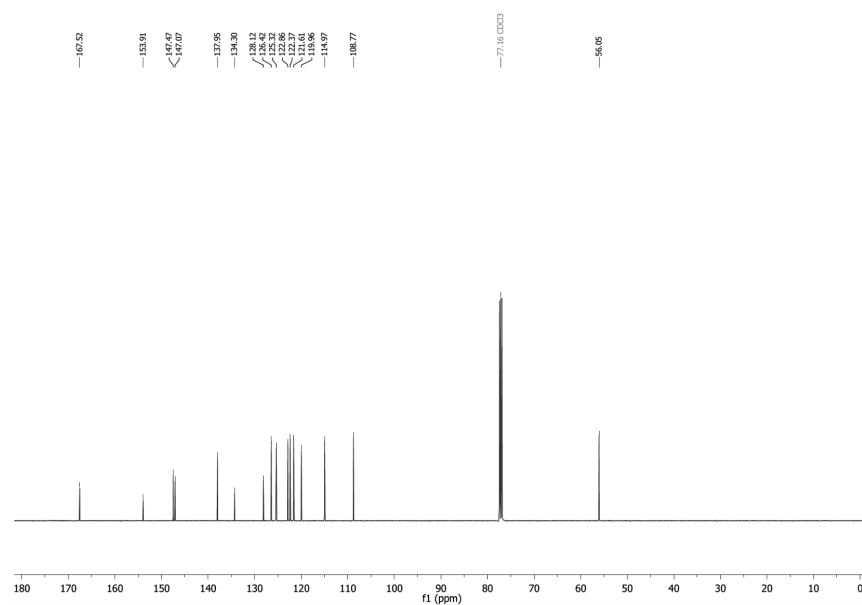


### 4-(2-(benzothiazol-2-yl)vinyl)-2-methoxyphenol (SBTub4)

<sup>1</sup>H-NMR:



<sup>13</sup>C-NMR:



## Supplementary Information Bibliography

- [1] H. Zhou, C. Xue, P. Weis, Y. Suzuki, S. Huang, K. Koynov, G. K. Auernhammer, R. Berger, H.-J. Butt, S. Wu; *Nat. Chem.* **2017**, *9*, 145 (10.1038/nchem.2625).
- [2] G. S. Kumar, D. C. Neckers; *Chem. Rev.* **1989**, *89*, 1915–1925 (10.1021/cr00098a012).
- [3] W. A. Velema, J. P. van der Berg, W. Szymanski, A. J. M. Driessen, B. L. Feringa; *ACS Chem. Biol.* **2014**, *9*, 1969–1974 (10.1021/cb500313f).
- [4] K. Hüll, J. Morstein, D. Trauner; *Chem. Rev.* **2018**, *118*, 10710–10747 (10.1021/acs.chemrev.8b00037).
- [5] M. Dong, A. Babalhavaeji, S. Samanta, A. A. Beharry, G. A. Woolley; *Acc. Chem. Res.* **2015**, *48*, 2662–2670 (10.1021/acs.accounts.5b00270).
- [6] M. Borowiak, W. Nahaboo, M. Reynders, K. Nekolla, P. Jalinot, J. Hasserodt, M. Rehberg, M. Delattre, S. Zahler, A. Vollmar, D. Trauner, O. Thorn-Seshold; *Cell* **2015**, *162*, 403–411 (10.1016/j.cell.2015.06.049).
- [7] J. Zenker, M. D. White, R. M. Templin, R. G. Parton, O. Thorn-Seshold, S. Bissiere, N. Plachta; *Science* **2017**, *357*, 925–928 (10.1126/science.aam9335).
- [8] J. Zenker, M. D. White, M. Gasnier, Y. D. Alvarez, H. Y. G. Lim, S. Bissiere, M. Biro, N. Plachta; *Cell* **2018**, *173*, 776–791 (10.1016/j.cell.2018.02.035).
- [9] C. Janke, M. O. Steinmetz; *EMBO J.* **2015**, *34*, 2114–2116 (10.15252/embj.201592415).
- [10] B. T. Castle, D. J. Odde; *Cell* **2015**, *162*, 243–245 (10.1016/j.cell.2015.06.064).
- [11] G. R. Pettit, S. B. Singh, E. Hamel, C. M. Lin, D. S. Alberts, D. Garcia-Kendall; *Experientia* **1989**, *45*, 209–211.
- [12] G. M. Tozer, Kanthou, C., Parkins, C.S., Hill, S.A.; *Int. J. Exp. Pathol.* **2002**, *83*, 21–38 (10.1046/j.1365-2613.2002.00211.x).
- [13] G. C. Tron, T. Pirali, G. Sorba, F. Pagliai, S. Busacca, A. A. Genazzani; *J. Med. Chem.* **2006**, *49*, 3033–3044 (10.1021/jm0512903).
- [14] J. A. Woods, J. A. Hadfield, G. R. Pettit, B. W. Fox, A. T. McGown; *Br. J. Cancer* **1995**, *71*, 705–711 (10.1038/bjc.1995.138).
- [15] K. M. Scherer, R. H. Bisby, S. W. Botchway, J. A. Hadfield, A. W. Parker; *J. Biomed. Opt.* **2015**, *20*, 051004 (10.1117/1.Jbo.20.5.051004).
- [16] K. B. Jørgensen; *Molecules* **2010**, *15*, 4334–4358 (10.3390/molecules15064334).
- [17] J. Morstein, M. Awale, J.-L. Reymond, D. Trauner; *ACS Central Science* **2019**, (10.1021/acscentsci.8b00881).
- [18] A. J. Engdahl, E. A. Torres, S. E. Lock, T. B. Engdahl, P. S. Mertz, C. N. Streu; *Org. Lett.* **2015**, *17*, 4546–4549 (10.1021/acs.orglett.5b02262).
- [19] J. E. Sheldon, M. M. Dcona, C. E. Lyons, J. C. Hackett, M. C. T. Hartman; *Org. Biomol. Chem.* **2016**, *14*, 40–49 (10.1039/c5ob02005k).
- [20] S. K. Rastogi, Z. Zhao, S. L. Barrett, S. D. Shelton, M. Zafferani, H. E. Anderson, M. O. Blumenthal, L. R. Jones, L. Wang, X. Li, C. N. Streu, L. Du, W. J. Brittain; *Eur. J. Med. Chem.* **2018**, *143*, 1–7 (10.1016/j.ejmech.2017.11.012).
- [21] A. Singh, T. Saha, I. Begemann, A. Ricker, H. Nüsse, O. Thorn-Seshold, J. Klingauf, M. Galic, M. Matis; *Nat. Cell Biol.* **2018**, *20*, 1126–1133 (10.1038/s41556-018-0193-1).
- [22] C. Vandestadt, G. C. Vanwalleghem, H. A. Castillo, M. Li, K. Schulze, M. Khabooshan, E. Don, M.-L. Anko, E. K. Scott, J. Kaslin; *bioRxiv* **2019**, 539940 (10.1101/539940).
- [23] K. Eguchi, Z. Taoufiq, O. Thorn-Seshold, D. Trauner, M. Hasegawa, T. Takahashi; *J. Neurosci.* **2017**, *37*, 6043–6052 (10.1523/jneurosci.0179-17.2017).
- [24] K. Eguchi, Z. Taoufiq, O. Thorn-Seshold, D. Trauner, M. Hasegawa, T. Takahashi; *J. Neurosci.* **2017**, *37*, 6043–6052 (10.1523/jneurosci.0179-17.2017).
- [25] J. Broichhagen, J. A. Frank, D. Trauner; *Acc. Chem. Res.* **2015**, *48*, 1947–1960 (10.1021/acs.accounts.5b00129).
- [26] W. A. Velema, W. Szymanski, B. L. Feringa; *J. Am. Chem. Soc.* **2014**, *136*, 2178–2191 (10.1021/ja413063e).
- [27] S. Samanta, A. A. Beharry, O. Sadovski, T. M. McCormick, A. Babalhavaeji, V. Tropepe, G. A. Woolley; *J. Am. Chem. Soc.* **2013**, *135*, 9777–9784 (10.1021/ja402220t).
- [28] R. Friederike, S. Wiktor; *Curr. Med. Chem.* **2017**, *24*, 4905–4950 (10.2174/0929867323666160906103223).
- [29] S. Samanta, A. A. Beharry, O. Sadovski, T. M. McCormick, A. Babalhavaeji, V. Tropepe, G. A. Woolley; *J. Am. Chem. Soc.* **2013**, *135*, 9777–9784 (10.1021/ja402220t).
- [30] J. E. Sheldon, M. M. Dcona, C. E. Lyons, J. C. Hackett, M. C. T. Hartman; *Org. Biomol. Chem.* **2016**, *14*, 40–49 (10.1039/c5ob02005k).
- [31] S. Samanta, A. Babalhavaeji, M.-x. Dong, G. A. Woolley; *Angew. Chem., Int. Ed.* **2013**, *52*, 14127–14130 (10.1002/anie.201306352).
- [32] H. Lei, M. Mo, Y. He, Y. Wu, W. Zhu, L. Wu; *Bioorg. Chem.* **2019**, 103106 (10.1016/j.bioorg.2019.103106).
- [33] C. Boulègue, M. Löweneck, C. Renner, L. Moroder; *ChemBioChem* **2007**, *8*, 591–594 (10.1002/cbic.200600495).
- [34] A. Gilbert; *ChemInform* **2004**, *35*, (10.1002/chin.200418261).
- [35] H. E. Gottlieb, V. Kotlyar, A. Nudelman; *J. Org. Chem.* **1997**, *62*, 7512–7515 (10.1021/jo971176v).



- [36] N. R. Penthala, P. Crooks, V. Sonar; *Combretastatin analogs (US20160068506A1)*, **2016**.
- [37] N. R. Penthala, S. Thakkar, P. A. Crooks; *Bioorg. Med. Chem. Lett.* **2015**, *25*, 2763-2767 (10.1016/j.bmcl.2015.05.019).
- [38] G. C. Tron, T. Pirali, G. Sorba, F. Pagliai, S. Busacca, A. A. Genazzani; *J. Med. Chem.* **2006**, *49*, 3033-3044 (10.1021/jm0512903).
- [39] R. Gaspari, A. E. Prota, K. Bargsten, A. Cavalli, M. O. Steinmetz; *Chem* **2017**, *2*, 102-113 (10.1016/j.chempr.2016.12.005).
- [40] A. Sailer, F. Ermer, Y. Kraus, F. Lutter, C. Donau, M. Bremerich, J. Ahlfeld, O. Thorn-Seshold; *ChemBioChem* **2019**, *20*, 1305-1314 (10.1002/cbic.201800752).
- [41] C. M. Lozano, O. Cox, M. M. Muir, J. D. Morales, J. L. Rodríguez-Cabán, P. E. Vivas-Mejía, F. A. Gonzalez; *Inorganica Chimica Acta* **1998**, *271*, 137-144 (doi.org/10.1016/S0020-1693(97)05952-5).
- [42] A. M. Sanchez, M. Barra, R. H. d. Rossi; *J. Org. Chem.* **1999**, *64*, 1604-1609 (10.1021/jo982069j).
- [43] N. J. Dunn, W. H. Humphries, A. R. Offenbacher, T. L. King, J. A. Gray; *J. Phys. Chem. A* **2009**, *113*, 13144-13151 (10.1021/jp903102u).
- [44] C. A. Kulkarni, P. Brookes; *Antioxid Redox Signal* **2019**, (10.1089/ars.2018.7722).
- [45] C. M. Lin, S. B. Singh, P. S. Chu, R. O. Dempcy, J. M. Schmidt, G. R. Pettit, E. Hamel; *Molecular Pharmacology* **1988**, *34*, 200-208.
- [46] L. Pecqueur, C. Duellberg, B. Dreier, Q. Jiang, C. Wang, A. Plücker, T. Surrey, B. Gigant, M. Knossow; *Proceedings of the National Academy of Sciences* **2012**, *109*, 12011 (10.1073/pnas.1204129109).
- [47] W. Kabsch; *Acta crystallographica. Section D, Biological crystallography* **2010**, *66*, 125-132 (10.1107/S0907444909047337).
- [48] T. Weinert, N. Olieric, R. Cheng, S. Brünle, D. James, D. Ozerov, D. Gashi, L. Vera, M. Marsh, K. Jaeger, F. Dworkowski, E. Panepucci, S. Basu, P. Skopintsev, A. S. Doré, T. Geng, R. M. Cooke, M. Liang, A. E. Prota, V. Panneels, P. Nogly, U. Ermler, G. Schertler, M. Hennig, M. O. Steinmetz, M. Wang, J. Standfuss; *Nature Communications* **2017**, *8*, 542 (10.1038/s41467-017-00630-4).
- [49] P. D. Adams, P. V. Afonine, G. Bunkoczi, V. B. Chen, I. W. Davis, N. Echols, J. J. Headd, L.-W. Hung, G. J. Kapral, R. W. Grosse-Kunstleve, A. J. McCoy, N. W. Moriarty, R. Oeffner, R. J. Read, D. C. Richardson, J. S. Richardson, T. C. Terwilliger, P. H. Zwart; *Acta Crystallographica Section D* **2010**, *66*, 213-221 (doi:10.1107/S0907444909052925).
- [50] P. Emsley, K. Cowtan; *Acta Crystallographica Section D* **2004**, *60*, 2126-2132 (doi:10.1107/S0907444904019158).
- [51] M. O. Steinmetz, A. E. Prota; *Trends in Cell Biology* **2018**, *28*, 776-792 (10.1016/j.tcb.2018.05.001).
- [52] R. B. G. Ravelli, B. Gigant, P. A. Curmi, I. Jourdain, S. Lachkar, A. Sobel, M. Knossow; *Nature* **2004**, *428*, 198-202 (10.1038/nature02393).
- [53] T. Kleele, P. Marinković, P. R. Williams, S. Stern, E. E. Weigand, P. Engerer, R. Naumann, J. Hartmann, R. M. Karl, F. Bradke, D. Bishop, J. Herms, A. Konnerth, M. Kerschensteiner, L. Godinho, T. Misgeld; *Nat. Commun.* **2014**, *5*, 4827 (10.1038/ncomms5827).
- [54] L. C. Kapitein, K. W. Yau, C. C. Hoogenraad; in *Methods in Cell Biology*, (Vol. 97), (Eds.: L. Cassimeris and P. Tran), Academic Press, **2010**, pp. 111-132.
- [55] T. Stepanova, J. Slemmer, C. C. Hoogenraad, G. Lansbergen, B. Dortland, C. I. De Zeeuw, F. Grosveld, G. van Cappellen, A. Akhmanova, N. Galjart; *The Journal of Neuroscience* **2003**, *23*, 2655 (10.1523/JNEUROSCI.23-07-02655.2003).
- [56] E. Meijering, O. Dzyubachyk, I. Smal; in *Methods in Enzymology*, (Vol. 504), (Ed. P. M. conn), Academic Press, **2012**, pp. 183-200.

## Chapter 4.2 Hemithioindigo HOTubs

### Licence

Reprinted with permission from: Alexander Sailer, Franziska Ermer, Yvonne Kraus, Ferdinand Lutter, Carsten Donau, Maximilian Bremerich, Dr. Julia Ahlfeld, Dr. Oliver Thorn-Seshold, Hemithioindigos for cellular photopharmacology: Desymmetrised molecular switch scaffolds enabling design control over the isomer-dependency of potent antimitotic bioactivity, *ChemBioChem* **2019**, *20*, 1305. Copyright Wiley-VCH Verlag GmbH & Co. KGaA, Weinheim.

Supporting Information

**Hemithioindigos for Cellular Photopharmacology:  
Desymmetrised Molecular Switch Scaffolds Enabling  
Design Control over the Isomer-Dependency of Potent  
Antimitotic Bioactivity**

Alexander Sailer<sup>†</sup>, Franziska Ermer<sup>†</sup>, Yvonne Kraus<sup>†</sup>, Ferdinand H. Lutter, Carsten Donau,  
Maximilian Bremerich, Julia Ahlfeld, and Oliver Thorn-Seshold<sup>\*[a]</sup>

cbic\_201800752\_sm\_miscellaneous\_information.pdf

### **Author Contributions**

*Following ICMJE guidelines, the authors declare their roles as follows: AS: performed chemical synthesis and photocharacterisations; FE: performed viability screening, immunostaining, and cell cycle analysis; YK: performed viability screening and immunostaining; FHL, CD, MB: performed chemical synthesis; JA: performed confocal imaging, cell cycle analysis, and data analysis; OTS: conceived and supervised the study, wrote the manuscript with support from all authors.*

## Table of Contents

Conventions .....	3
Standard Procedures .....	4
Synthesis of <b>HOTub-13</b> .....	4
Synthesis of <b>HOTub-31</b> .....	6
Synthesis of <b>HOTub-620</b> .....	9
Synthesis of <b>HOTub-630</b> .....	11
Synthesis of 4,5,6-trimethoxybenzo[ <i>b</i> ]thiophen-3(2 <i>H</i> )-one ( <b>S15</b> ) .....	13
Synthesis of <b>HOTub-70</b> .....	17
Synthesis of <b>HOTub-81</b> .....	17
Determination of the E/Z-ratio in the photostationary state .....	18
<i>in cellulo</i> biology assays .....	20
Supplemental References .....	23
NMR spectra .....	23

## Conventions

Hemithioindigo geometry and nomenclature: Hemithioindigos (HTIs) are drawn by default in their Z-isomeric form, however, both E & Z forms will constitute a given sample depending on light exposure so they are named without E/Z-designations.

Abbreviations: The following abbreviations are used: Hex – distilled isohexanes, cHex – cyclohexane, EA – ethyl acetate, HRMS – high-resolution mass spectrometry, DCM – dichloromethane, LDA – lithium diisopropylamide, TFA – 2,2,2-trifluoroacetic acid, THF – tetrahydrofuran, Me – methyl, Et – ethyl, MeCN – acetonitrile, MS – molecular sieves, *i*Pr – isopropyl, Bu – butyl.

Reagents and Conditions: Unless stated otherwise: (1) all reactions and characterisations were performed with unpurified, undried, non-degassed solvents and reagents, used as obtained, under closed air atmosphere without special precautions; (2) “hexane” used for chromatography was distilled from commercial crude isohexane fraction on rotavap; (3) when not specified, “column” and “chromatography” refer to flash column chromatography performed on Merck silica gel Si-60 (40-63  $\mu\text{m}$ ); (4) procedures and yields are unoptimised; (5) yields refer to isolated spectroscopically pure materials, corrected for residual solvent content; (6) all eluent and solvent mixtures are given as volume ratios unless otherwise specified, thus “1:1 EA:Hex” indicates a 1:1 mixture (by volume) of ethyl acetate and hexanes.

Thin-layer chromatography (TLC) was run on 0.25 mm Merck silica gel plates (60, F-254). UV light (254 nm) was used as a visualising agent.  $R_f$  values were usually determined in ethyl acetate : hexane (EA:Hex) eluents. TLC characterisations are thus abbreviated as per ( $R_f$  = 0.09 on 6:1 EA:Hex).

NMR: Standard NMR characterisation was by 1D  $^1\text{H}$ - and  $^{13}\text{C}$ -NMR spectra, with COSY, HSQC, HMBC or heteronuclear NMR performed as needed. Known compounds were checked against literature data and their spectral analysis is not detailed unless necessary. The default spectrometer used was a Bruker Ascend 400 (400 MHz & 100 MHz for  $^1\text{H}$  and  $^{13}\text{C}$  respectively); NMR solvents are given individually for each compound. For determination of the composition of the photostationary states (450 and 505 nm), a Bruker Avance III HD (500 MHz) equipped with CryoProbe™ Prodigy broadband probe was used. Chemical shifts ( $\delta$ ) are reported in ppm calibrated to residual non-perdeuterated solvent as an internal reference<sup>[1]</sup>. The following peak descriptions are used: singlet (s), doublet (d), triplet (t), quartet (q), multiplet (m), broad (br) and doublet of doublets (dd).

Mass Spectra: HRMS was carried out by the Zentrale Analytik of the LMU, Munich using ESI or EI ionisation as specified.

UV-Vis Spectra: UV-vis spectra were recorded on an Agilent Cary 60 UV-vis spectrophotometer.

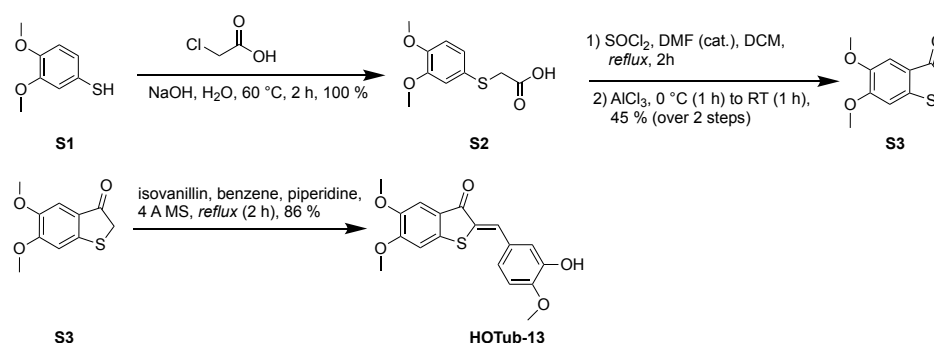
## Standard Procedures

Where Standard Procedures were used in synthesis, unless stated otherwise, the amounts of reactants/reagents employed were implicitly adjusted to maintain the same molar ratios as in the given Procedure, and no other alterations from the Standard Procedure (eg. reaction time, extraction solvent, temperature) were made, unless stated otherwise.

### Standard Procedure: Formation of HTIs via Piperidine Catalysed Aldol Condensations

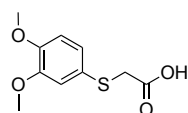
An oven dried Schlenk flask was charged with the thioindoxyl (1.00 eq.), the aldehyde (equivalents are given individually) and molecular sieves (4 Å) under an atmosphere of nitrogen. Dry benzene (5 – 10 mL) and piperidine (0.1 mL) were added and the solution was heated to reflux for the time indicated individually. After cooling to room temperature, a saturated aqueous solution of NH<sub>4</sub>Cl (5 – 15 mL) was added, the phases were separated and the aqueous layer was extracted with DCM (3 x 50 mL), dried over Na<sub>2</sub>SO<sub>4</sub> or MgSO<sub>4</sub> and evaporated. Purification was accomplished as indicated individually.

## Synthesis of HOTub-13



Scheme S1: Synthesis of HOTub-13

### 2-((3,4-dimethoxyphenyl)thio)acetic acid (S2)

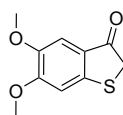


To a suspension of 3,4-dimethoxythiophenol (1.97 g, 11.6 mmol, 1.00 eq) in an aqueous sodium hydroxide solution (2 M, 46 mL) was added a solution of chloroacetic acid (1.27 g, 13.4 mmol, 1.16 eq) in water (8 mL) at room temperature. The resulting reaction mixture was heated to 60 °C for 2 h. Concentrated hydrochloric acid was added to the clear solution until

pH = 1. The yellow suspension was extracted with ethyl acetate (3 × 15 mL) and the combined organic extracts were washed with brine and dried over Na<sub>2</sub>SO<sub>4</sub>. The solvent was removed under reduced pressure affording **S2** as a pale yellow solid (2.64 g, 11.6 mmol, 100 %).

**<sup>1</sup>H-NMR** (DMSO-d<sub>6</sub>, 400 MHz): δ (ppm) = 12.67 (s, 1H), 7.00 (d, *J* = 1.7 Hz, 1H), 6.94 (dd, *J* = 1.7 / 8.3 Hz, 1H), 6.90 (d, *J* = 8.3 Hz, 1H), 3.74 (s, 3H), 3.73 (s, 3H), 3.67 (s, 2H); **<sup>13</sup>C-NMR** (DMSO-d<sub>6</sub>, 100 MHz): δ (ppm) = 161.3, 139.2, 138.5, 116.2, 112.9, 104.2, 102.6, 45.9, 45.8, 27.3; **HRMS** (ESI<sup>-</sup>) for C<sub>10</sub>H<sub>11</sub>O<sub>4</sub>S<sup>-</sup> [M-H<sup>+</sup>]: calcd. *m/z* 227.03780, found *m/z* 227.03844.

### 5,6-Dimethoxybenzo[*b*]thiophen-3(2*H*)-one (**S3**)

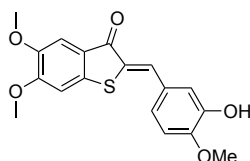


To a solution of **S2** (500 mg, 2.19 mmol, 1.00 eq.) in dry DCM (10 mL) was added SOCl<sub>2</sub> (339 mg, 2.85 mmol, 0.21 mL, 1.30 eq.) and dry DMF (0.1 mL) and the reaction mixture was heated to reflux for 2 h after which time the volatiles were removed *in vacuo* using an external cooling trap. The remaining orange crude product was dissolved in dry DCM (10 mL), cooled to 0 °C and AlCl<sub>3</sub> (730 mg, 5.48 mmol, 2.50 eq.) was carefully added portion wise under a stream of nitrogen. The solution was stirred at 0 °C for 30 min, then allowed to reach room temperature and stirred for 1 h. The solution was carefully quenched by the addition of water (15 mL), the phases were separated and the aqueous layer was extracted with DCM (3 x 20 mL). The combined organic extracts were dried over Na<sub>2</sub>SO<sub>4</sub>, evaporated and the crude was purified by column chromatography (EA:Hex, 1:4) affording **S3** as an orange crystalline solid (207 mg, 0.98 mmol, 45 %). After isolation, the product was frozen and stored under an atmosphere of nitrogen.

**<sup>1</sup>H-NMR** (CDCl<sub>3</sub>, 400 MHz): δ (ppm) = 7.19 (s, 1H), 6.83 (s, 1H), 3.95 (s, 3H), 3.88 (s, 3H), 3.80 (s, 2H); **<sup>13</sup>C-NMR** (CDCl<sub>3</sub>, 100 MHz): δ (ppm) = 198.6, 156.6, 149.6, 148.0, 123.8, 107.0, 105.6, 56.6, 56.3, 40.1; **R<sub>f</sub>** = 0.36 on 1:4 EA:Hx (blue fluorescence upon illumination with 254/366 nm); **HRMS** (ESI<sup>+</sup>) for C<sub>10</sub>H<sub>11</sub>O<sub>3</sub>S<sup>+</sup> [M+H<sup>+</sup>]: calcd. *m/z* 211.04289, found *m/z* 211.04237.



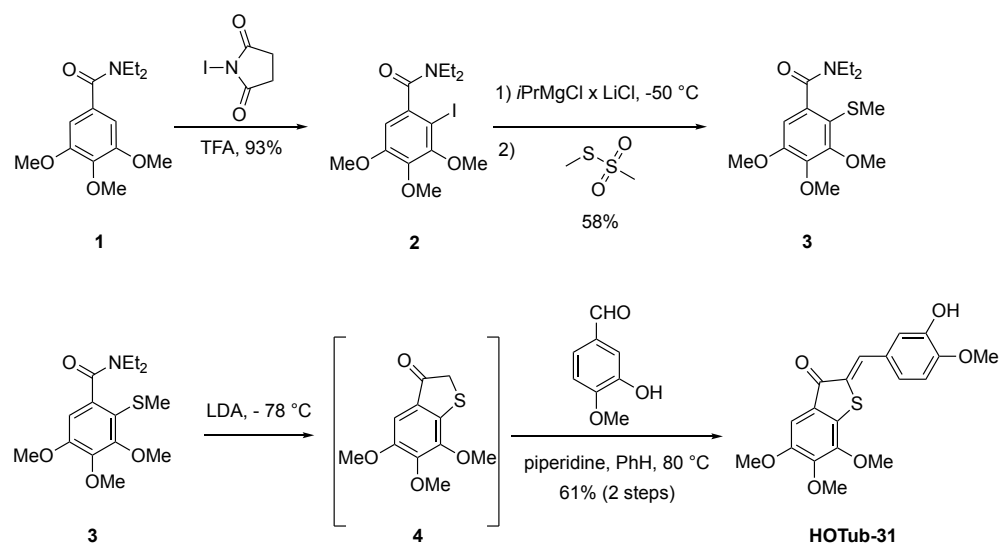
**2-(3-Hydroxy-4-methoxybenzylidene)-5,6-dimethoxybenzo[*b*]thiophen-3(2*H*)-one  
(HOTub-13)**



By Standard Procedure, commercial 3-Hydroxy-4-methoxybenzaldehyde (80 mg, 0.52 mmol, 1.10 eq.) was reacted with **S3** (100 mg, 0.48 mmol, 1.00 eq.) for 2 h. Precipitation by addition of distilled water to a concentrated solution of the crude in DMSO (repeated once) yielded **HOTub-13** as a red solid (141 mg, 0.41 mmol, 86 %).

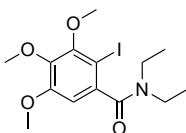
**<sup>1</sup>H-NMR** (CDCl<sub>3</sub>, 400 MHz): δ (ppm) = 7.83 (s, 1H), 7.34 (s, 1H), 7.29 (d, *J* = 2.1 Hz, 1H), 7.21 (dd, *J* = 2.1 / 8.4 Hz, 1H), 6.92 (d, *J* = 8.4 Hz), 6.89 (s, 1H), 5.85 (s, 1H), 3.97 (s, 3H), 3.93 (s, 3H), 3.91 (s, 3H); **<sup>13</sup>C-NMR** (CDCl<sub>3</sub>, 100 MHz): δ (ppm) = 187.6, 155.9, 148.5, 148.3, 146.0, 141.0, 133.4, 129.5, 128.1, 125.0, 123.6, 116.3, 110.9, 107.8, 105.3, 56.6, 56.4, 56.2; **R<sub>f</sub>** = 0.33 on 1:1 EA:Hx; **HRMS** (ESI<sup>+</sup>) for C<sub>18</sub>H<sub>17</sub>O<sub>5</sub>S<sup>+</sup> [M+H<sup>+</sup>]: calcd. *m/z* 345.07967, found *m/z* 345.07902; **HRMS** (ESI<sup>-</sup>) for C<sub>18</sub>H<sub>15</sub>O<sub>5</sub>S<sup>-</sup> [M-H<sup>+</sup>]: calcd. *m/z* 343.06457, found *m/z* 343.06485.

**Synthesis of HOTub-31**



**Scheme S2:** Synthesis of **HOTub-31**

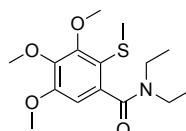
### ***N,N*-Diethyl-2-iodo-3,4,5-trimethoxybenzamide (2)**



To a solution of *N,N*-Diethyl-3,4,5-trimethoxybenzamide (763 mg, 2.85 mmol, 1.00 eq.) in acetonitrile (40 mL) was added *N*-iodosuccinimide (728 mg, 3.14 mmol, 1.10 eq.) and 2,2,2-trifluoroacetic acid (114 mg, 1.00 mmol, 0.08 mL, 0.35 eq.) at room temperature and the reaction mixture was stirred for 2.5 h. The reaction mixture was extracted with Et<sub>2</sub>O (3 × 60 mL) and the combined organic extracts were washed with brine, dried over Na<sub>2</sub>SO<sub>4</sub>, filtered and concentrated under reduced pressure. The crude was purified by column chromatography (EA:Hex, 2:3) to give **2** (1.04 g, 2.65 mmol, 93 %) as a yellow solid.

<sup>1</sup>H-NMR (CDCl<sub>3</sub>, 400 MHz): δ (ppm) = 6.60 (s, 1H), 3.87 (s, 3H), 3.86 (s, 3H), 3.83 (s, 3H), 3.30 – 3.10 (m, 4H), 1.28 (t, *J* = 7.1 Hz, 3H), 1.08 (t, *J* = 7.1 Hz, 3H); <sup>13</sup>C-NMR (CDCl<sub>3</sub>, 100 MHz): δ (ppm) = 169.9, 154.5, 153.6, 142.2, 138.4, 106.6, 80.9, 61.2, 61.1, 56.4, 42.9, 39.0, 14.1, 12.5; *R*<sub>f</sub> = 0.17 on 2:3 EA:Hx; HRMS (EI<sup>+</sup>) for C<sub>14</sub>H<sub>20</sub>INO<sub>4</sub> [M<sup>+</sup>]: calcd. *m/z* 393.0437; found *m/z* 393.0426.

### ***N,N*-Diethyl-3,4,5-trimethoxy-2-(methylthio)benzamide (3)**

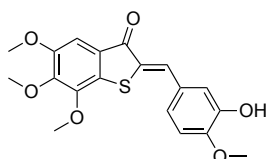


To a solution of **2** (0.27 g, 0.70 mmol, 1.00 eq.) in THF (2 mL) was added Turbo-Grignard (1.1 M in THF, 0.81 mL, 0.91 mmol, 1.30 eq.) dropwise at – 50 °C under an atmosphere of nitrogen. After 5 min, *S*-Methyl methanethiosulfonate (215 mg, 1.70 mmol, 0.16 mL, 2.50 eq.) was added at – 50 °C and the yellow reaction mixture was allowed to warm to –30 °C. After 1 h, the yellow/red reaction mixture was allowed to warm to room temperature, quenched with saturated aqueous NH<sub>4</sub>Cl solution and extracted with ethyl acetate. After washing with brine, drying over Na<sub>2</sub>SO<sub>4</sub>, filtering and concentration under reduced pressure, the crude product was purified by column chromatography (EA:Hx, 2:3) to give **3** (125 mg, 0.40 mmol, 58 %) as a pale yellow solid.

<sup>1</sup>H-NMR (CDCl<sub>3</sub>, 400 MHz): δ (ppm) = 6.52 (s, 1H), 3.95 (s, 3H), 3.85 (s, 3H), 3.83 (s, 3H), 3.79 (m, 1H), 3.34 (dq, *J* = 14.1 / 7.1 Hz, 1H), 3.11 (q, *J* = 7.2 Hz, 2H), 2.35 (s, 3H), 1.26 (t, *J* = 7.1

Hz, 3H), 1.05 (t,  $J = 7.1$  Hz, 3H);  $^{13}\text{C-NMR}$  ( $\text{CDCl}_3$ , 100 MHz):  $\delta$  (ppm) = 169.3, 155.6, 154.5, 142.9, 138.1, 118.2, 105.3, 61.4, 61.1, 56.3, 43.0, 39.0, 19.5, 14.1, 12.6;  $R_f = 0.23$  on 1:1 EA:Hx; **HRMS** ( $\text{EI}^+$ ) for  $\text{C}_{15}\text{H}_{23}\text{NO}_4\text{S}$  [ $\text{M}^+$ ]: calcd.  $m/z$  313.1348; found  $m/z$  313.1343.

**(3-Hydroxy-4-methoxybenzylidene)-4,5,6-trimethoxybenzo[*b*]thiophen-3(2*H*)-one**  
**(HOTub-31)**

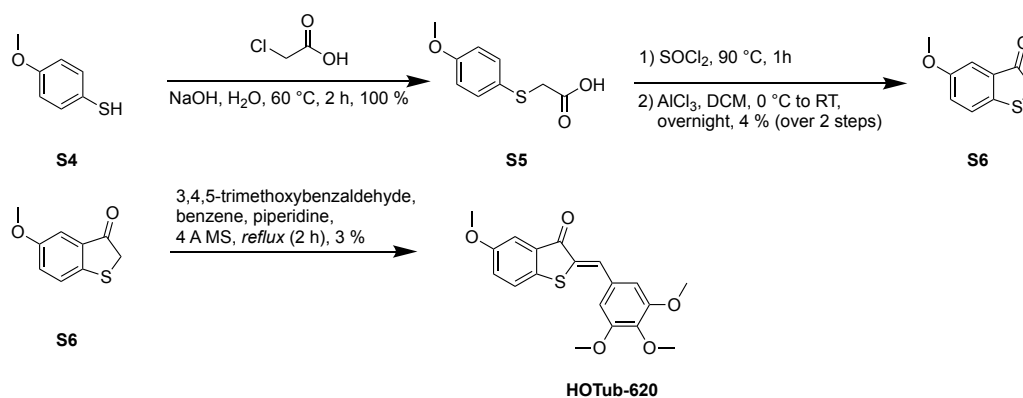


To a solution of *n*BuLi (1.6 M in hexanes, 153 mg, 1.50 mL, 2.39 mmol, 1.50 eq.) in dry THF was added *N,N*-diisopropylamine (403 mg, 3.99 mmol, 0.56 mL, 2.50 eq.) dropwise at  $-78$  °C. The resulting reaction mixture was allowed to warm to  $-30$  °C and stirred for 45 min. prior to the addition of a solution of **3** (500 mg, 1.60 mmol, 1.00 eq.) in THF in the range of  $-78$  to  $-30$  °C. The resulting yellow solution was allowed to warm to rt. After 14 h, the reaction mixture was quenched with saturated aqueous  $\text{NH}_4\text{Cl}$  solution and extracted with ethyl acetate. After washing with brine, drying over  $\text{Na}_2\text{SO}_4$ , filtering and concentration under reduced pressure, the crude product was used without further purification.

The crude thioindoxyl was reacted with commercial isovanillin (170 mg, 1.12 mmol, 0.70 eq.) according to Standard Procedure for 16 h. Purification was accomplished by MPLC (EA:Hx, 2 %:98 %) giving **HO-Tub 31** as a red/brown solid (255 mg, 0.98 mmol, 61 %).

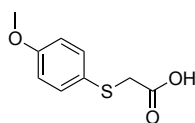
$^1\text{H-NMR}$  ( $\text{CDCl}_3$ , 400 MHz):  $\delta$  (ppm) = 7.86 (s, 1H), 7.36 (d,  $J = 2.2$  Hz, 1H), 7.30 – 7.26 (m, 1H), 7.24 (s, 1H), 6.94 (d,  $J = 8.4$  Hz, 1H), 5.76 (s, 1H), 4.01 (s, 3H), 4.00 (s, 3H), 3.96 (s, 3H), 3.91 (s, 3H);  $^{13}\text{C-NMR}$  ( $\text{CDCl}_3$ , 100 MHz):  $\delta$  (ppm) = 188.0, 153.1, 148.6, 148.3, 147.6, 146.1, 134.1, 133.1, 129.2, 128.1, 126.0, 125.2, 116.5, 110.9, 104.4, 61.4, 61.1, 56.6, 56.2;  $R_f = 0.35$  on 1:1 EA:Hx; **HRMS** ( $\text{ESI}^+$ ) for  $\text{C}_{19}\text{H}_{19}\text{O}_6\text{S}$  [ $\text{M}+\text{H}^+$ ]: calcd.  $m/z$  375.0896, found  $m/z$  375.0897.

## Synthesis of HOTub-620



Scheme S3: Synthesis of HOTub-620

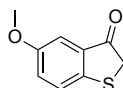
### 2-((4-Methoxyphenyl)thio)acetic acid (S5)



4-Methoxythiophenol (213 mg, 1.52 mmol, 1.00 eq.) was suspended in NaOH (2 M, 5 mL). A solution of chloroacetic acid (179 mg, 1.81 mmol, 1.19 eq.) in water (0.5 mL) was added and the mixture was stirred for 2 h at 60 °C. Na<sub>2</sub>S<sub>2</sub>O<sub>3</sub> solution (1 M, 2 mL) was added and the mixture was stirred for another hour at 60 °C. After acidifying with concentrated HCl to pH 1, it was extracted with EtOAc (3 × 25 mL), the organic layer was washed with brine, dried over Na<sub>2</sub>SO<sub>4</sub> and the solvent was removed under reduced pressure giving **S5** as a yellow solid (302 mg, 1.52 mmol, 100 %).

<sup>1</sup>H-NMR (400 MHz, CDCl<sub>3</sub>): δ (ppm) = 10.80 (br. s, 1H), 7.29 (d, *J* = 8.8 Hz, 2H), 6.70 (d, *J* = 8.8 Hz, 2H), 3.62 (s, 3H), 3.40 (s, 2H) ppm.; <sup>13</sup>C-NMR (100 MHz, CDCl<sub>3</sub>): δ (ppm) = 175.8, 159.9, 134.3, 124.4, 114.8, 55.4, 38.6 ppm; HRMS (ESI<sup>-</sup>) for C<sub>9</sub>H<sub>9</sub>O<sub>3</sub>S<sup>-</sup> = [M-H<sup>+</sup>]: calcd. *m/z* 197.02779, found *m/z* 197.02756.

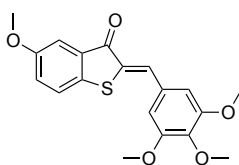
### 5-Methoxybenzo[*b*]thiophen-3(2*H*)-one (S6)



A solution of **S5** (1.34 g, 6.74 mmol, 1.00 eq.) in an excess of SOCl<sub>2</sub> (7 mL) was heated to 90 °C for 1 h. After cooling to room temperature, the solvent was removed under reduced pressure and the residue was dried in high vacuum. The remaining oil was dissolved in DCM (15 ml) and AlCl<sub>3</sub> (1.20 g, 7.50 mmol, 1.11 eq.) was added slowly under cooling. The mixture was stirred overnight at room temperature and then poured into ice water, basified using 2 M NaOH and extracted with EtOAc. After acidifying the solution with conc. HCl it was extracted again with EtOAc. The combined organic extracts were washed with brine, dried over MgSO<sub>4</sub> and the solvent was removed under reduced pressure. The crude product was purified by chromatography (EA:Hx, 1:5→1:2) to yield **S6** (43 mg, 0.24 mmol, 4 %). This product can be further purified by crystallization from absolute EtOH.

<sup>1</sup>H-NMR (400 MHz, CDCl<sub>3</sub>): δ (ppm) = 7.25 (dd, *J* = 8.6 / 0.6 Hz, 1H), 7.17 (d, *J* = 2.6 Hz, 1H), 7.13 (dd, *J* = 8.6 / 2.7 Hz, 1H), 3.78 (s, 2H), 3.76 (s, 3H); <sup>13</sup>C-NMR (100 MHz, CDCl<sub>3</sub>): δ (ppm) = 200.0, 157.7, 146.3, 131.9, 125.6, 125.2, 107.9, 55.7, 40.1; *R*<sub>f</sub> = 0.46 on 1:2 EA:Hx, (blue fluorescence upon illumination with 366 nm).

### 5-Methoxy-2-(3,4,5-trimethoxybenzylidene)benzo[*b*]thiophen-3(2*H*)-one (HOTub-620)

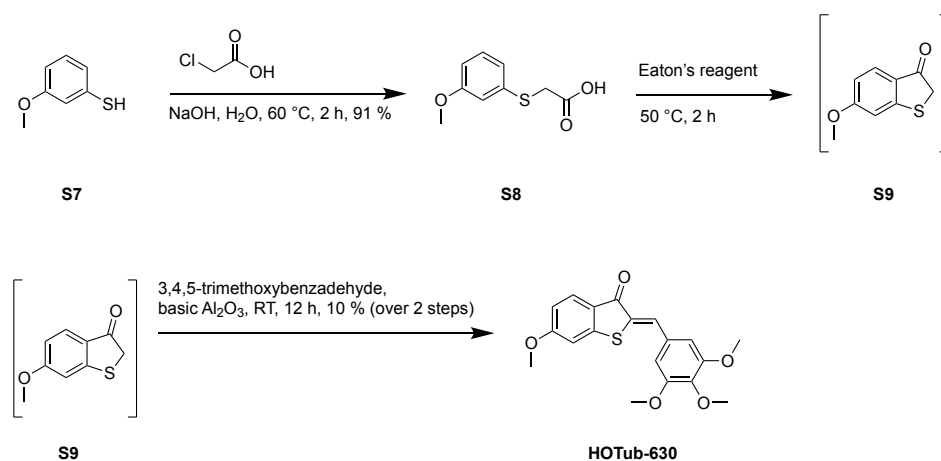


By Standard Procedure, commercial 3,4,5-trimethoxybenzaldehyde (7 mg, 33.3 μmol, 1.00 eq.) was reacted with **S6** (6 mg, 33.3 μmol, 1.00 eq.) and piperidine (0.05 mL) in dry benzene (3 mL) for 2 h at *reflux* and 4 h at room temperature. The crude product was purified by column chromatography (EA:Hx, 1:10 →1:4) and automated flash chromatography (9 %:91 %, EA:Hx) giving **HOTub-620** as orange crystals (0.4 mg, 1,12 μmol, 3 %).

<sup>1</sup>H-NMR (400 MHz, CDCl<sub>3</sub>): δ (ppm) = 7.88 (s, 1H), 7.41 (d, *J* = 2.7 Hz, 1H), 7.38 (d, *J* = 8.6 Hz, 1H), 7.20 (dd, *J* = 8.6 / 2.7 Hz, 1H), 6.95 (s, 2H), 3.94 (s, 6H), 3.92 (s, 3H), 3.86 (s, 3H);

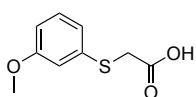
$^{13}\text{C-NMR}$  (100 MHz,  $\text{CDCl}_3$ ):  $\delta$  (ppm) = 188.6, 158.5, 153.6, 140.1, 137.7, 134.1, 131.7, 130.6, 129.9, 124.8, 124.6, 109.1, 108.3, 61.2, 56.3, 55.9;  $R_f$  = 0.47 on 1:2 EA:Hx; **HRMS** (ESI<sup>+</sup>) for  $\text{C}_{19}\text{H}_{18}\text{O}_5\text{S}$  = [M]: calcd.  $m/z$  358.0875, found  $m/z$  358.0852.

### Synthesis of HOTub-630



**Scheme S4:** Synthesis of **HOTub-630**

### 2-((3-Methoxyphenyl)thio)acetic acid (**S8**)

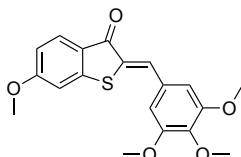


To a suspension of 3-Methoxythiophenol (250 mg, 1.79 mmol, 1.00 eq.) in aqueous NaOH (2 M, 5 mL) was added a solution of chloroacetic acid (201 mg, 2.13 mmol, 1.19 eq.) in water (0.5 mL) and the mixture was stirred for 2 h at 60 °C. Aqueous  $\text{Na}_2\text{S}_2\text{O}_3$  solution (1 M, 2 mL) was added and the mixture was stirred for another hour at 60 °C. After acidifying with concentrated HCl to pH 1, the mixture was extracted with EtOAc (3  $\times$  25 mL), the organic layer was washed with brine, dried over  $\text{Na}_2\text{SO}_4$  and the solvent was removed under reduced pressure giving **S8** as a colourless oil (321 mg, 1.62 mmol, 91 %).

$^1\text{H-NMR}$  (400 MHz,  $\text{CDCl}_3$ ):  $\delta$  (ppm) = 12.80 (br. s, 1H), 7.22 (t,  $J$  = 8.2 Hz, 1H), 6.88 (d,  $J$  = 7.1 Hz, 2H), 6.80 – 6.70 (m, 1H), 3.81 (s, 2H), 3.74 (s, 3H), 3.68 (s, 3H);  $^{13}\text{C-NMR}$  (100 MHz,

CDCl<sub>3</sub>):  $\delta$  (ppm) = 170.9, 148.9, 148.1, 125.8, 122.6, 113.9, 112.3, 55.6, 36.9; **HRMS** (ESI<sup>-</sup>) for C<sub>9</sub>H<sub>9</sub>O<sub>3</sub>S [M-H<sup>+</sup>]: calcd m/z 197.02779, found m/z 197.02756.

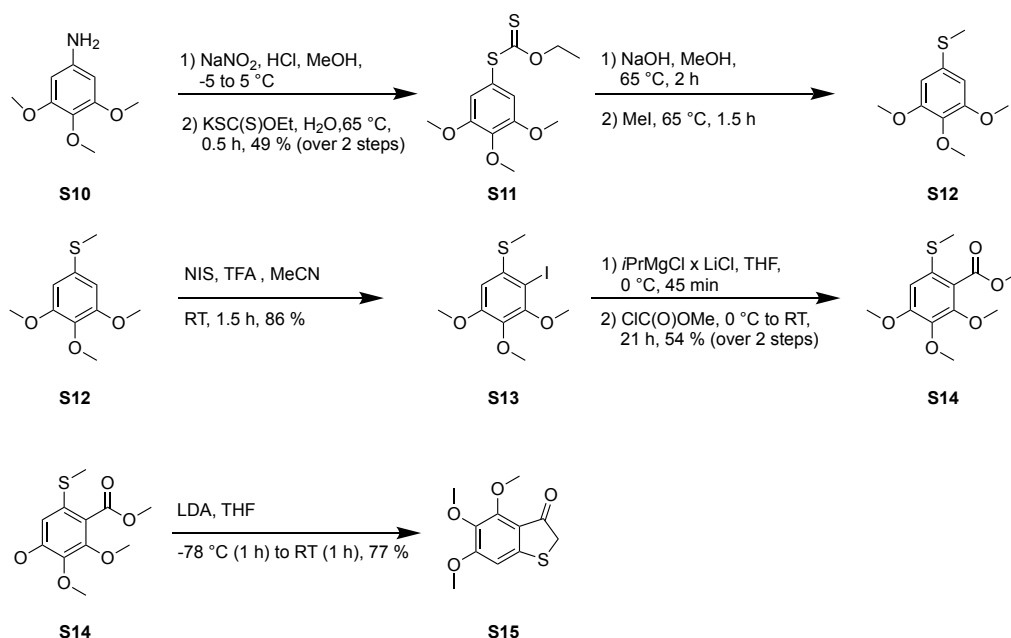
**6-Methoxy-2-(3,4,5-trimethoxybenzylidene)benzo[b]thiophen-3(2H)-one (HOTub-630)**



**S8** (109 mg, 0.55 mmol, 1.00 eq.) was covered with Eaton's reagent and stirred for 2 h at 50 °C. The reaction was quenched by addition of water and the mixture was extracted with DCM (3 × 25 mL). The combined organic layers were washed with a saturated aqueous NaHCO<sub>3</sub> solution (3 × 25 mL) and brine (3 × 25 mL), dried over Na<sub>2</sub>SO<sub>4</sub> and the volume was reduced to 5 – 6 mL. To this solution of the crude thioindoxyl **S9**, basic Al<sub>2</sub>O<sub>3</sub> (200 mg) and 3,4,5-trimethoxybenzaldehyde (22 mg, 0.11 mmol, 0.20 eq.) were added, and the mixture was stirred at room temperature for 12 h after which time the mixture was filtered through a silica gel pad on 1:1 EA:Hx. The solvent was removed under reduced pressure and the crude product was purified by column chromatography (EA:Hx, 1:10 → 1:1.5) and preparative TLC (cHx:CHCl<sub>3</sub>:MeOH, 1:1:0.08) followed by precipitation with water from a solution in acetone (water:acetone, 3:1). After centrifugation, **HOTub-630** was separated mechanically as a pale yellow solid (4 mg, 0.01 mmol, 10 %).

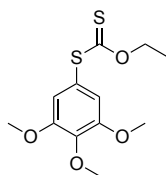
**<sup>1</sup>H-NMR** (400 MHz, CDCl<sub>3</sub>):  $\delta$  (ppm) = 7.88 (d, *J* = 8.6 Hz, 1H), 7.83 (s, 1H), 6.97 (d, *J* = 2.1 Hz, 1H), 6.94 (s, 2H), 6.84 (dd, *J* = 8.6 / 2.1 Hz, 1H), 3.95 (s, 6H), 3.92 (s, 6H); **<sup>13</sup>C-NMR** (100 MHz, CDCl<sub>3</sub>):  $\delta$  (ppm) = 187.0, 165.8, 153.6 (2), 148.8, 139.9, 132.9, 130.1, 130.0, 128.7, 124.1, 113.6, 108.1 (2), 107.7, 61.2, 56.3 (2), 56.0; **R<sub>f</sub>** = 0.43 on 1:2.4, EA:Hx; **HRMS** (EI<sup>+</sup>) for C<sub>19</sub>H<sub>18</sub>O<sub>5</sub>S = [M]: calcd. m/z 358.4080, found m/z 358.0864.

## Synthesis of 4,5,6-trimethoxybenzo[*b*]thiophen-3(2*H*)-one (S15)



Scheme S5: Synthesis of S15

### O-ethyl S-(3,4,5-trimethoxyphenyl) carbonodithioate (S11)



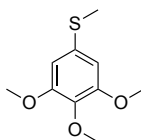
3,4,5-Trimethoxyaniline (750 mg, 4.09 mmol, 1.00 eq.) was dissolved in MeOH (20 mL) and cooled to  $-5^\circ\text{C}$ . An aqueous solution of  $\text{NaNO}_2$  (333 mg, 4.83 mmol, 2M, 2.4 mL, 1.18 eq.) and HCl (900 mg, 24.7 mmol, 12M, 0.75 mL, 6.04 eq.) were added keeping the temperature below  $5^\circ\text{C}$ . The reaction mixture was then slowly added to a solution of potassium ethyl xanthogenate (1.97 g, 12.3 mmol, 3.00 eq.) in water (15 mL) and heated to  $65^\circ\text{C}$  for 0.5 h. The aqueous layer was then extracted with EtOAc (3 x 30 mL) and the combined organic extracts were evaporated. The crude was purified by means of column chromatography (EA:Hex, 1:8). The product can be further purified by recrystallization from *n*-pentane giving



**S11** as a slightly yellow solid (575 mg, 2.00 mmol, 49 %). The experimental data is in full accordance with literature.<sup>[2]</sup>

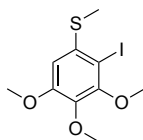
<sup>1</sup>H-NMR (CDCl<sub>3</sub>, 400 MHz): δ (ppm) = 6.72 (s, 2H), 4.61 (q, *J* = 7.1 Hz, 2H), 3.87 (s, 3H), 3.84 (s, 6H), 1.33 (t, *J* = 7.1 Hz, 3H, H<sub>1</sub>); <sup>13</sup>C-NMR (CDCl<sub>3</sub>, 100 MHz): δ (ppm) = 213.4, 153.5, 139.7, 124.7, 112.3, 70.5, 61.1, 56.4, 13.8; *R*<sub>f</sub> = 0.58 on 1:4 EA:Hex; HRMS (EI<sup>+</sup>) for C<sub>12</sub>H<sub>17</sub>O<sub>4</sub>S<sub>2</sub><sup>+</sup> = [M<sup>+</sup>]: calcd. *m/z* 288.0490, found 288.0486, for C<sub>9</sub>H<sub>11</sub>O<sub>3</sub>S = [M-C<sub>3</sub>H<sub>5</sub>OS<sup>+</sup>]: calcd. *m/z* 199.0428, found *m/z* 199.0424.

#### Methyl(3,4,5-trimethoxyphenyl) sulfane (S12)



To a solution of **S11** (2.96 g, 10.3 mmol, 1.00 eq.) in MeOH (30 mL) was added a solution of NaOH (4.42 g, 111 mmol, 10.8 eq.) in water (30 mL) at room temperature. The suspension was heated to 65 °C for 2 h after which time MeI (2.19 g, 15.4 mmol, 0.96 mL, 1.50 eq.) was added dropwise. The reaction mixture was heated to 65 °C for 1.5 h and the solvents were removed under reduced pressure. The residue was treated with water (50 mL) and EtOAc (50 mL), the remaining solid was filtered off and the aqueous phase was extracted with EtOAc (2 x 50 mL). After drying the combined organic extracts over Na<sub>2</sub>SO<sub>4</sub>, the volatiles were removed yielding **S12** as an off-white solid (1.77 g, 8.26 mmol, 80 %), which was pure enough to be used in the next steps without further purification. <sup>1</sup>H-NMR (CDCl<sub>3</sub>, 400 MHz): δ (ppm) = 6.50 (s, 2H), 3.83 (s, 6H), 3.79 (s, 3H), 2.46 (s, 3H); <sup>13</sup>C-NMR (CDCl<sub>3</sub>, 100 MHz): δ (ppm) = 153.6, 136.4, 133.4, 104.9, 61.1, 56.4, 17.2; *R*<sub>f</sub> = 0.50 on 1:4 EA:Hex; HRMS (EI<sup>+</sup>) for C<sub>10</sub>H<sub>14</sub>O<sub>3</sub>S<sup>+</sup> = [M<sup>+</sup>]: calcd. *m/z* 214.0667, found *m/z* 214.0643, for C<sub>9</sub>H<sub>11</sub>O<sub>3</sub>S<sup>+</sup> = [M-CH<sub>3</sub><sup>+</sup>]: calcd. *m/z* 199.0428, found *m/z* 199.0423.

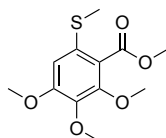
### (2-Iodo-3,4,5-trimethoxyphenyl)(methyl)sulfane (**S13**)



To a solution of **S12** (1.82 g, 8.48 mmol, 1.00 eq.) in acetonitrile (90 mL) were added N-iodosuccinimide (2.10 g, 9.33 mmol, 1.10 eq.) and 2,2,2-trifluoroacetic acid (338 mg, 2.97 mmol, 0.23 mL, 0.35 eq.) at room temperature. The reaction mixture was stirred for 1.5 h in the dark before a saturated aqueous solution of Na<sub>2</sub>S<sub>2</sub>O<sub>3</sub> (90 mL) was added. The solids were filtered off, the acetonitrile was removed under reduced pressure and the remaining aqueous layer was extracted with DCM (3 x 90 mL). The combined organic extracts were dried over Na<sub>2</sub>SO<sub>4</sub>, filtered and evaporated. The crude product was purified by column chromatography (EA:Hx, 1:1) giving **S13** as an off-white solid (2.76 g, 7.26 mmol, 86 %).

<sup>1</sup>H-NMR (CDCl<sub>3</sub>, 400 MHz): δ (ppm) = 6.56 (s, 1H), 3.87 (s, 3H), 3.86 (s, 3H), 3.83 (s, 3H), 2.44 (s, 3H); <sup>13</sup>C-NMR (CDCl<sub>3</sub>, 100 MHz): δ (ppm) = 154.3, 153.7, 139.8, 138.0, 106.0, 85.9, 61.2, 60.9, 56.4, 18.0; R<sub>f</sub> = 0.48 on 1:1 EA:Hex; HRMS (EI<sup>+</sup>) for C<sub>10</sub>H<sub>13</sub>IO<sub>3</sub>S<sup>+</sup> = [M<sup>+</sup>]: calcd. m/z 339.9630, found m/z 339.9610.

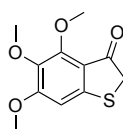
### Methyl 2,3,4-trimethoxy-6-(methylthio)benzoate (**S14**)



A solution of **S13** (340 mg, 1.00 mmol, 1.00 eq.) in dry THF (2 mL) was added to Turbo-Grignard (1.3 M in THF, 1.05 mmol, 0.77 mL, 1.05 eq.) at 0 °C under nitrogen. After complete magnesiation (as indicated *via* LC-MS, 45 min.), freshly distilled methyl chloroformate (bp. 69 °C, 243 mg, 2.50 mmol, 0.20 mL, 2.50 eq.) was added. The ice bath was removed and the reaction mixture was stirred for 21 h at room temperature. A saturated aqueous solution of NH<sub>4</sub>Cl (5 mL) was added and the phases were separated. The aqueous layer was extracted with DCM (3 x 10 mL), dried over Na<sub>2</sub>SO<sub>4</sub> and evaporated. Purification by column chromatography (EA:Hex, 1:10) gave **S14** as an off-white solid (147 mg, 0.54 mmol, 54 %). **S12** was isolated as a side-product (14 mg, 0.07 mmol, 7 %).

**<sup>1</sup>H-NMR** (CDCl<sub>3</sub>, 400 MHz): δ (ppm) = 6.63 (s, 1H), 3.86 (s, 3H), 3.84 (s, 3H), 3.83 (s, 3H), 3.79 (s, 3H) 2.39 (s, 3H); **<sup>13</sup>C-NMR** (CDCl<sub>3</sub>, 100 MHz): δ (ppm) = 166.9, 154.7, 151.2, 140.7, 130.9, 123.2, 108.6, 61.8, 60.9, 56.2, 52.3, 18.3; **R<sub>f</sub>** = 0.10 on 1:10 EA:Hex; **HRMS** (ESI<sup>+</sup>) for C<sub>11</sub>H<sub>13</sub>O<sub>4</sub>S<sup>+</sup> = [M-CH<sub>3</sub>O<sup>+</sup>]: calcd. m/z 241.05291, found m/z 241.05284, for C<sub>12</sub>H<sub>16</sub>O<sub>5</sub>NaS<sup>+</sup> = [M+Na<sup>+</sup>] calcd. m/z 295.06107, found m/z 295.06111.

#### 4,5,6-Trimethoxybenzo[*b*]thiophen-3(2*H*)-one (S15)

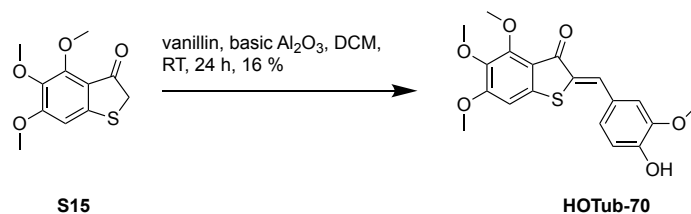


To a freshly prepared solution of LDA in THF was added a solution of **S14** (164 mg, 0.60 mmol, 1.00 eq.) in dry THF (3 mL) at -78 °C and the reaction mixture was stirred for 1 h, then allowed to reach room temperature and stirred at room temperature for 1 h. The reaction was quenched by the addition of a saturated aqueous solution of NH<sub>4</sub>Cl (15 mL), the phases were separated and the aqueous phase was extracted with DCM (4 x 10 mL). The combined organic extracts were dried over Na<sub>2</sub>SO<sub>4</sub>, evaporated and the crude product was purified by column chromatography (EA:Hex, 1:4) yielding **S15** as a yellow solid (111 mg, 0.46 mmol, 77 %). After isolation, the product was frozen and stored under an atmosphere of nitrogen.

LDA was prepared by adding *n*BuLi (2.5 M in THF, 596 mg, 0.80 mL, 1.99 mmol, 3.31 eq.) to a solution of freshly distilled DIPA (219 mg, 0.31 mL, 2.17 mmol, 3.60 eq.) in dry THF (3 mL) at -78 °C and stirring the solution for 15 min.

**<sup>1</sup>H-NMR** (CDCl<sub>3</sub>, 400 MHz): δ (ppm) = 6.59 (s, 1H), 3.97 (s, 3H), 3.89 (s, 3H), 3.79 (s, 3H), 3.74 (s, 2H); **<sup>13</sup>C-NMR** (CDCl<sub>3</sub>, 100 MHz): δ (ppm) = 196.5, 160.6, 154.0, 152.4, 139.3, 117.2, 101.9, 62.0, 61.5, 56.5, 40.3; **R<sub>f</sub>** = 0.32 on 1:4 EA:Hex (blue fluorescence upon illumination with 254 nm); **HRMS** (ESI<sup>+</sup>) for C<sub>11</sub>H<sub>13</sub>O<sub>4</sub>S<sup>+</sup> [M+H<sup>+</sup>]: calcd. m/z 241.05291, found m/z 241.05281, for C<sub>11</sub>H<sub>12</sub>O<sub>4</sub>NaS<sup>+</sup> = [M+Na<sup>+</sup>]: calcd. m/z 263.03485, found m/z 263.03485.

## Synthesis of HOTub-70

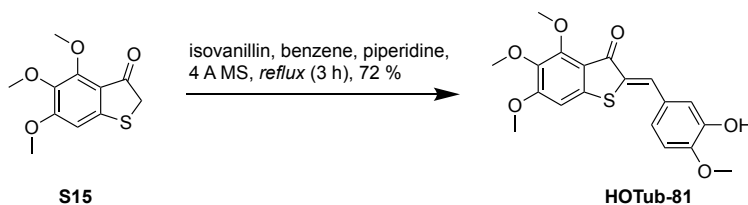


Scheme S6: Synthesis of **HOTub-70**

**S15** (46 mg, 0.19 mmol, 1.00 eq.) was dissolved in DCM (5 mL), then vanillin (23 mg, 0.15 mmol, 0.80 eq.) and basic aluminium oxide (200 mg) were added. After stirring at room temperature for one day, the formation of yellow hemithioindigo could be observed. The suspension was filled into a narrow, sand filled column, and the hemithioindigo was desorbed by rinsing the aluminium oxide with acetone, DCM and MeOH, until the solvents were colourless. The mixture was then dried over Na<sub>2</sub>SO<sub>4</sub> and evaporated. The crude product was dissolved in CHCl<sub>3</sub> and washed with a saturated solution of Na<sub>2</sub>SO<sub>3</sub> in 50 % EtOH (3 x 10 mL), 50 % EtOH (2 x 10 mL) and brine (1 x 10 mL) to remove residual aldehyde. After drying over Na<sub>2</sub>SO<sub>4</sub>, the product was purified via column chromatography yielding **HOTub-70** as yellow crystals (11 mg, 0.03 mmol, 16 %).

**<sup>1</sup>H NMR** (400 MHz, CDCl<sub>3</sub>): δ (ppm) = 7.72 (s, 1H), 7.18 (dd, *J* = 8.3 / 2.0 Hz, 2H), 7.11 (d, *J* = 2.0 Hz, 1H), 6.94 (d, *J* = 8.3 Hz, 1H), 6.67 (s, 1H), 5.90 (s, 1H), 4.00 (s, 3H), 3.91 (s, 3H), 3.90 (s, 3H), 3.80 (s, 3H); **<sup>13</sup>C NMR** (101 MHz, CDCl<sub>3</sub>): δ (ppm) = 185.5, 159.9, 154.7, 147.5, 146.7, 143.7, 140.1, 132.4, 128.5, 127.1, 125.7, 117.2, 115.1, 112.7, 101.7, 62.2, 61.6, 56.5, 56.0; **HRMS** (ESI<sup>+</sup>) for C<sub>19</sub>H<sub>19</sub>O<sub>6</sub>S<sup>+</sup> = [M+H<sup>+</sup>]: calcd *m/z* 375.08969, found *m/z* 375.08930.

## Synthesis of HOTub-81



Scheme S7: Synthesis of **HOTub-81**

By Standard Procedure, commercial 3-Hydroxy-4-methoxybenzaldehyde (44 mg, 0.29 mmol, 0.87 eq.) was reacted with **S15** (80 mg, 0.33 mmol, 1.00 eq.) for 3 h. The crude was purified by column chromatography (EA:Hx, 1:2 →3:1) giving **HOTub-81** as a red solid (78 mg, 0.21 mmol, 72 %).

**<sup>1</sup>H-NMR** (CDCl<sub>3</sub>, 400 MHz): δ (ppm) = 7.75 (s, 1H), 7.27 (d, *J* = 2.1 Hz, 1H), 7.18 (dd, *J* = 2.1 / 8.0 Hz, 1H), 6.91 (d, *J* = 8.4 Hz, 1H), 6.70 (s, 1H), 5.69 (s, 1H), 4.04 (s, 3H), 3.94 (s, 3H), 3.93 (s, 3H), 3.85 (s, 3H); **<sup>13</sup>C-NMR** (CDCl<sub>3</sub>, 100 MHz): δ (ppm) = 185.7, 160.0, 154.8, 148.2, 146.0, 144.0, 140.2, 132.2, 129.3, 128.2, 124.8, 117.2, 116.1, 110.9, 101.8, 62.3, 61.7, 56.6, 56.2; **R<sub>f</sub>** = 0.24 on 1:2 EA:Hx; **HRMS** (ESI<sup>+</sup>) for C<sub>19</sub>H<sub>19</sub>O<sub>6</sub>S<sup>+</sup> [M+H<sup>+</sup>]: calcd. *m/z* 375.08969, found *m/z* 375.09004; **HRMS** (ESI<sup>-</sup>) for C<sub>19</sub>H<sub>17</sub>O<sub>6</sub>S<sup>-</sup> [M-H<sup>+</sup>]: calcd. *m/z* 373.07513, found *m/z* 373.07548.

### Determination of the E/Z-ratio in the photostationary state

For the determination of E/Z ratio in the photostationary state, solutions of **HOTub-31** (1 mM, 0.65 mL in d<sub>6</sub>-DMSO) were prepared. To adapt the dark state, the vials were wrapped with aluminium foil and kept at 60 °C for 14 h. After cooling to room temperature, a <sup>1</sup>H-NMR spectrum (500 MHz, 32 scans) was recorded. Subsequently, the samples were transferred to a wide-necked vial, illuminated with a 450 nm LED for 2 min and a second <sup>1</sup>H-NMR spectrum was recorded. This procedure was repeated with a 505 nm LED. The ratio of the two photosomers was determined by comparison of the integrals at 3.89 ppm (Z- isomer) and 3.90 ppm (E- isomer). At 450 nm, the PSS is comprised of 65 % E-isomer and 35 % Z-isomer, while at 505 nm the Z-isomer (74 %) is the dominating species.

In order to assess the influence of thermal relaxation under these measurement conditions, a sample was irradiated with 450 nm for 5 min and then split into two separate NMR tubes. The first tube was measured subsequently after irradiation, while the second tube was wrapped with aluminium foil and kept at room temperature for 20 min and a <sup>1</sup>H-NMR spectrum was recorded. No significant differences were observed and we concluded that relaxation under these conditions was negligible.

UV-vis spectra were recorded in mixtures of DMSO and PBS (3:1 v:v) at 150 μM, covering the range from 340 to 600 nm. The samples were illuminated with 3 W (350 mA) Epistar LEDs (eBay *suiyanr*) shining through the optical beam of a quartz microcuvette, with second illumination periods at the same wavelength used to verify that PSS had indeed been reached (no evolution of the spectrum). Less than 30 s illumination was required to reach PSSs.

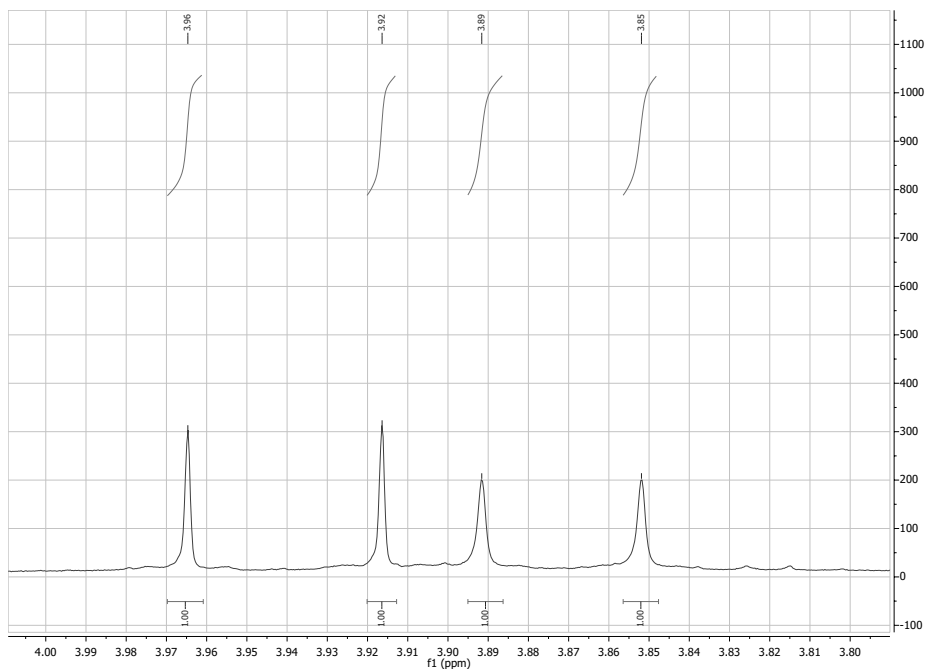


**Figure S1:** Section of the  $^1\text{H-NMR}$  spectrum of (*all-Z*)-HOTub-31 in the dark adapted state. Note that for easier comparison each signal of the methoxy groups is calibrated to 1.

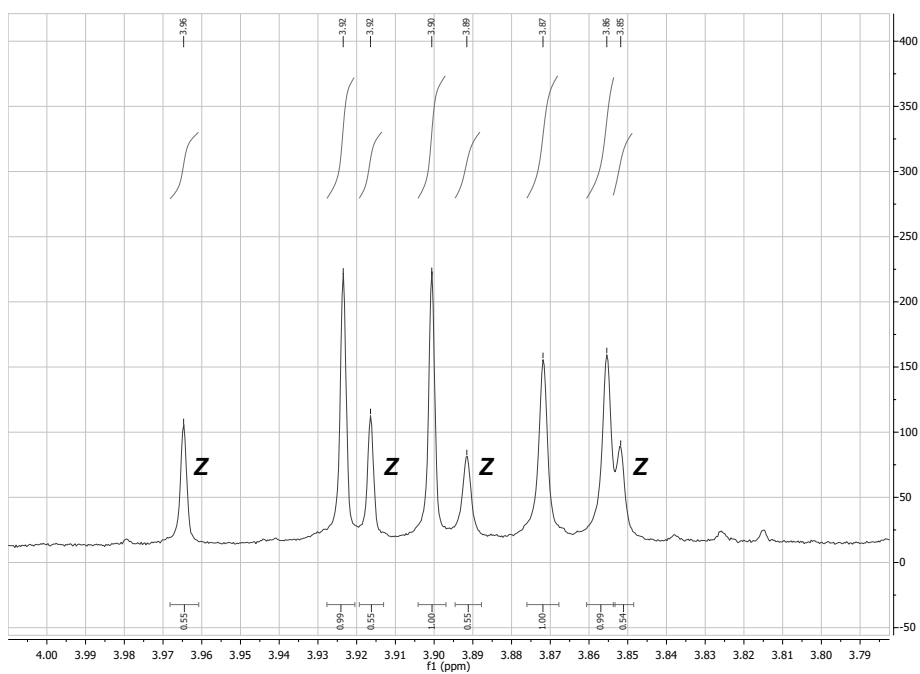


**Figure S2:** Section of the  $^1\text{H-NMR}$  spectrum of HOTub-31 in the PSS at 450 nm

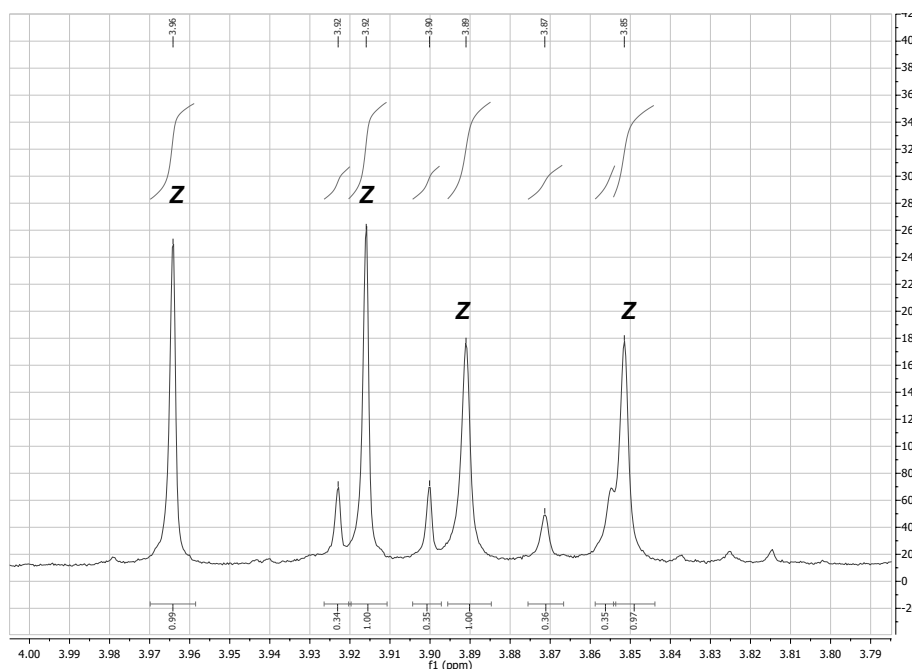


**Figure S3:**  $^1\text{H}$ -NMR spectrum of **HOTub-31** in the PSS at 505 nm

### ***in cellulo* biology assays**

**General Cell Culture:** HeLa cells were maintained under standard cell culture conditions. Compounds were applied using a minimum of co-solvent, typically 1 % DMSO. Cells were incubated in lightproof boxes or under pulsed illumination using a home-made LED lighting system as described before<sup>[3]</sup>.

**MTT assay:** Mitochondrial dehydrogenase activity in HeLa cell lines was quantified by spectrophotometrically measuring the reduction of 3-(4,5-dimethylthiazol-2-yl)-2,5-diphenyl tetrazolium bromide (MTT) to formazan, as previously described.<sup>[3]</sup> Cells were seeded on 96-well microtitre plates. After 24 h, cells were treated with **HOTubs**, shielded from ambient light with light-proof boxes, and exposed to the appropriate light regimes (100 ms on every 60 s). Following 48 h of treatment, cells were incubated with 0.5 mg/mL MTT for 3 hours at 37 °C. The formazan crystals were dissolved in DMSO, and absorbance at 570 nm was measured using a FLUOstar Omega microplate reader (BMG Labtech). Results represent mean and SD, which are proportional to the cell number.

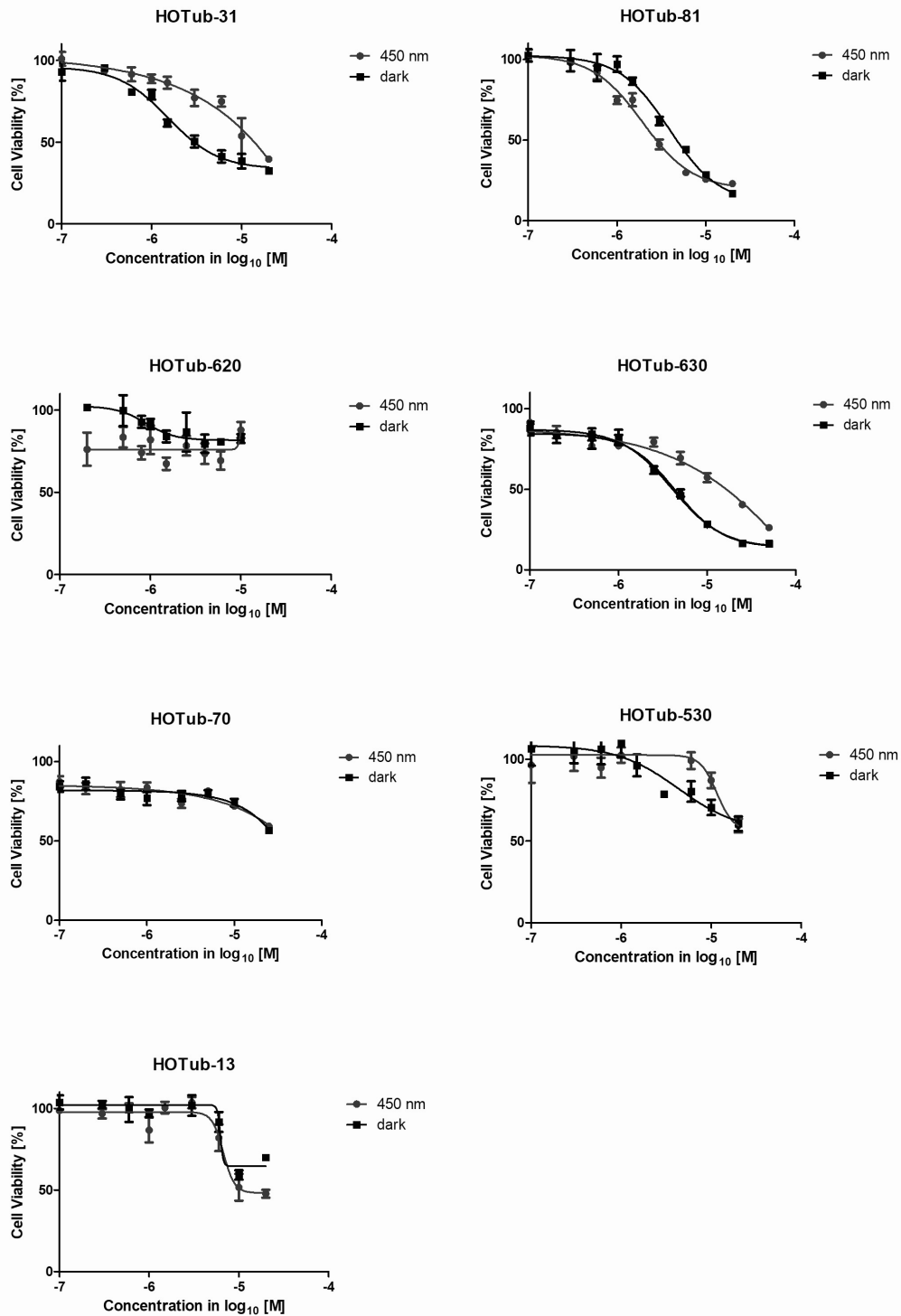


**Figure S4:** Representative results from MTT assays for HOTubs



**Cell cycle analysis:** Following treatment with **HOTubs** under the indicated light regime, cells were harvested and fixed in 70 % ethanol on ice and incubated in a staining solution [2 % DNase-free RNase A 10 mg/mL, 0.1 % Triton X-100 and 1 mg/mL propidium iodide (PI)] for 15 min at 37 °C. Following the PI staining cells were analysed by flow cytometry using a LSR Fortessa- BD company (FACS Core Facility – Gene Centre Munich, Munich, Germany) run by BD FACSDiva 8.0.1 software. The cell cycle analysis was subsequently performed using FlowJo-V10 software (Tree Star Inc., Ashland, OR, USA). Cells with subdiploid DNA content (inferior to G1 phase content) were considered as apoptotic in accordance with *Nicoletti et al.*<sup>[4]</sup> Results represent mean and SD calculated for triplicates from one representative experiment.

**Fixed cell imaging by confocal microscopy:** For fixed cell imaging, HeLa cells were seeded directly on glass coverslips in 24-well plates and treated with **HOTub**, either in the dark or under illumination by the LED array system using 410 nm or 450 nm LEDs and pulsing of 75 ms every 15 s or 100 ms every 60 s for 24 hours. Then the coverslips were washed with extraction buffer (80 mM PIPES pH 6.8; 1 mM MgCl<sub>2</sub>, 5 mM ethylene glycol tetra-acetic acid (EGTA) dipotassium salt and 0.5 % Triton X- 100) for 30 s at 37 °C to remove monomeric and dimeric tubulin subunits and fixed for 10 min with a final concentration of 0.5 % glutaraldehyde or else 6 min in ice-cold methanol; the glutaraldehyde-fixed cells were then quenched for 7 min with 0.1 % NaBH<sub>4</sub> in PBS. Coverslips were washed with PBS twice and then blocked with PBS containing 10 % FCS and 0.3% Tween 20 for 30 min at room temperature. For immunofluorescence staining of microtubules, the cells were treated with primary antibody (rabbit alpha-tubulin AB (Abcam ab18251), 1:400 dilution in PBS/10 %FCS) for one hour and then washed with PBS before application of the secondary antibody (donkey anti-rabbit Alexa Fluor 488 (Abcam ab150073), 1:400 dilution in PBS/10 %FCS) for one hour. The coverslips were mounted on microscopy glass slides using Roti®-Mount FluorCare DAPI (Carl Roth) and then imaged with a Zeiss LSM 510, LSM 710 or SP5 confocal microscope.

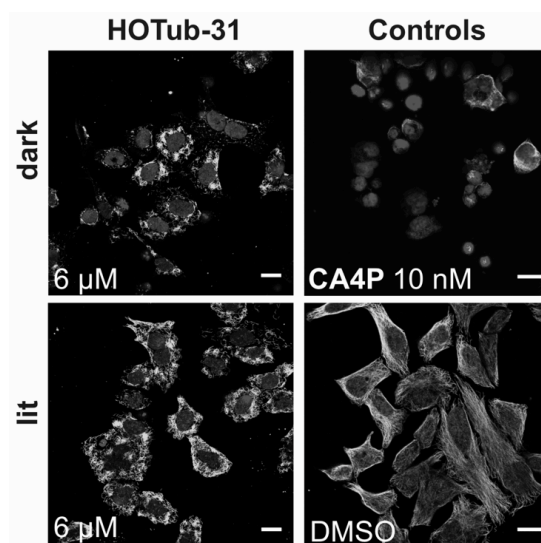


**Figure S5:** Extended immunofluorescence results from **HOTub-31** shows the dark-activity of this compound in more detail. Substantially greater microtubule depolymerisation is evident under dark conditions as compared to lit incubation, despite the lit condition's disruption of network integrity due to residual inhibition (likely from residual Z-**HOTub-31**).

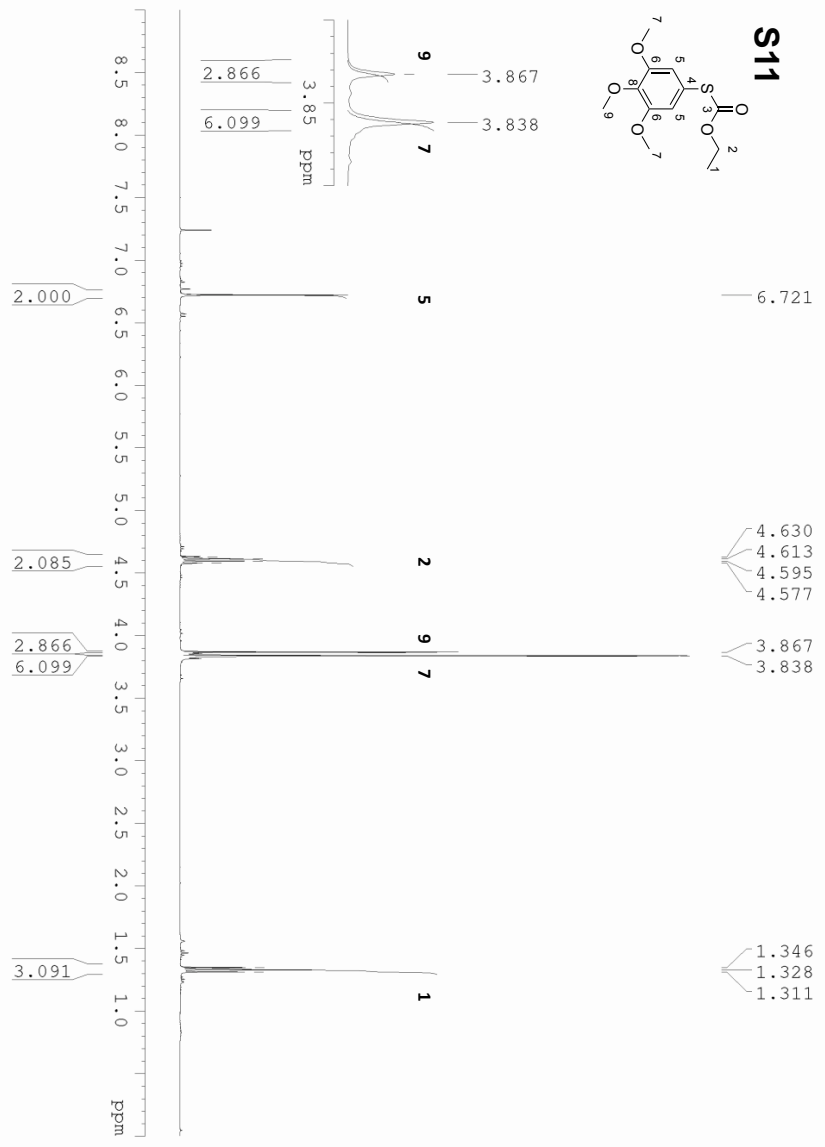
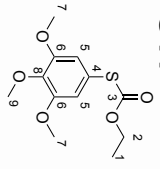
### Supplemental References

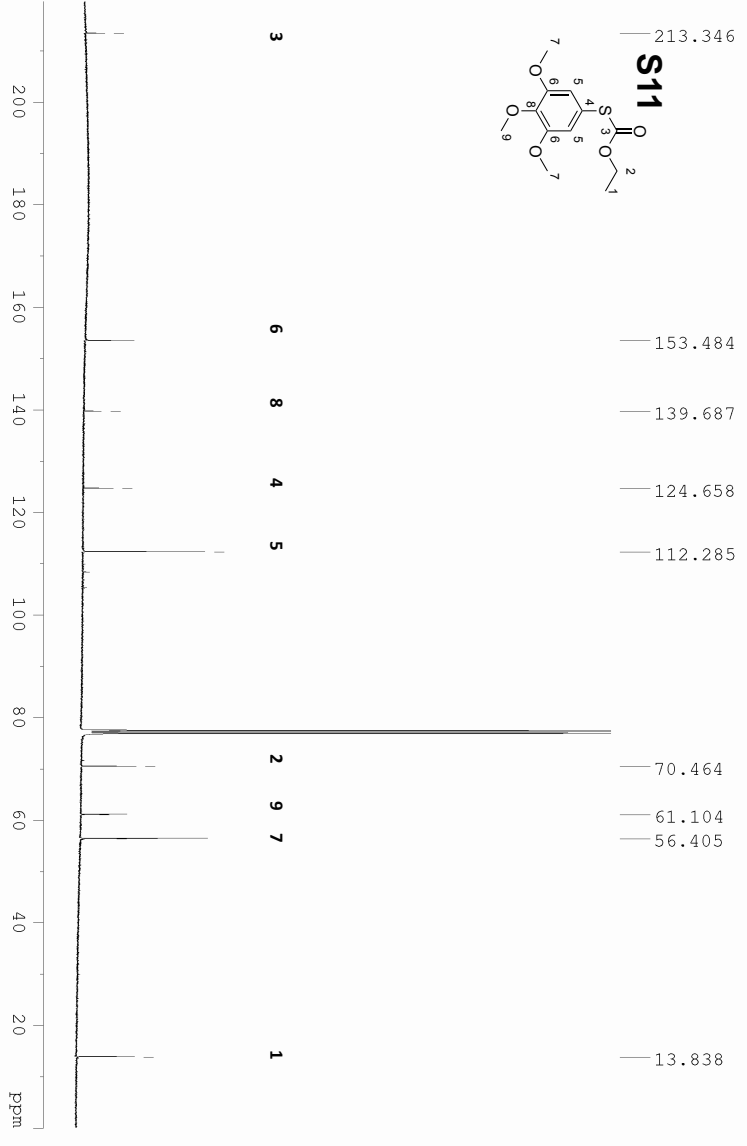
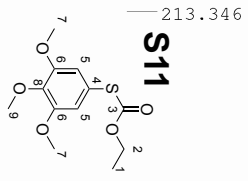
- [1] H. E. Gottlieb, V. Kotlyar, A. Nudelman, *J. Org. Chem.* **1997**, *62*, 7512-7515.
- [2] S. Kitzig, K. Ruck-Braun, *J Pept Sci* **2017**, *23*, 567-573.
- [3] M. Borowiak, W. Nahaboo, M. Reynders, K. Nekolla, P. Jalinot, J. Hasserodt, M. Rehberg, M. Delattre, S. Zahler, A. Vollmar, D. Trauner, O. Thorn-Seshold, *Cell* **2015**, *162*, 403-411.
- [4] I. Nicoletti, G. Migliorati, M. C. Pagliacci, F. Grignani, C. Riccardi, *J Immunol Methods* **1991**, *139*, 271-279.

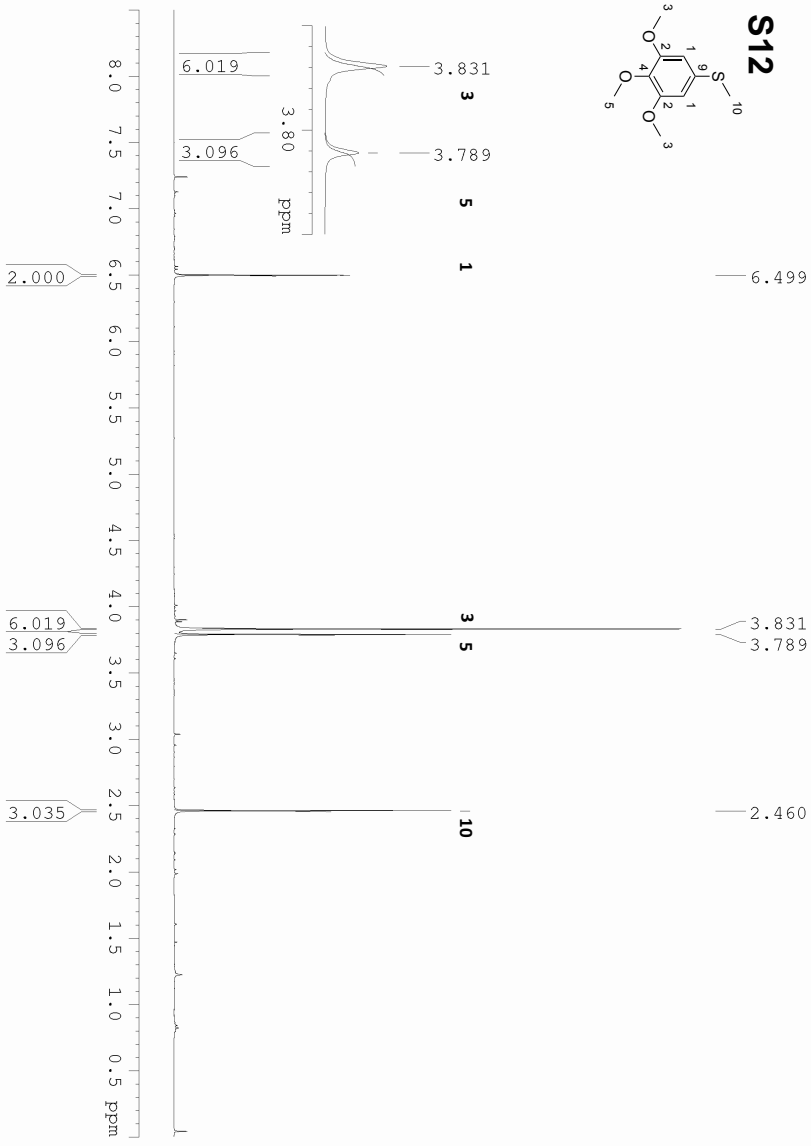
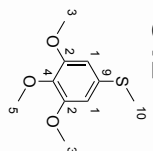
### NMR spectra

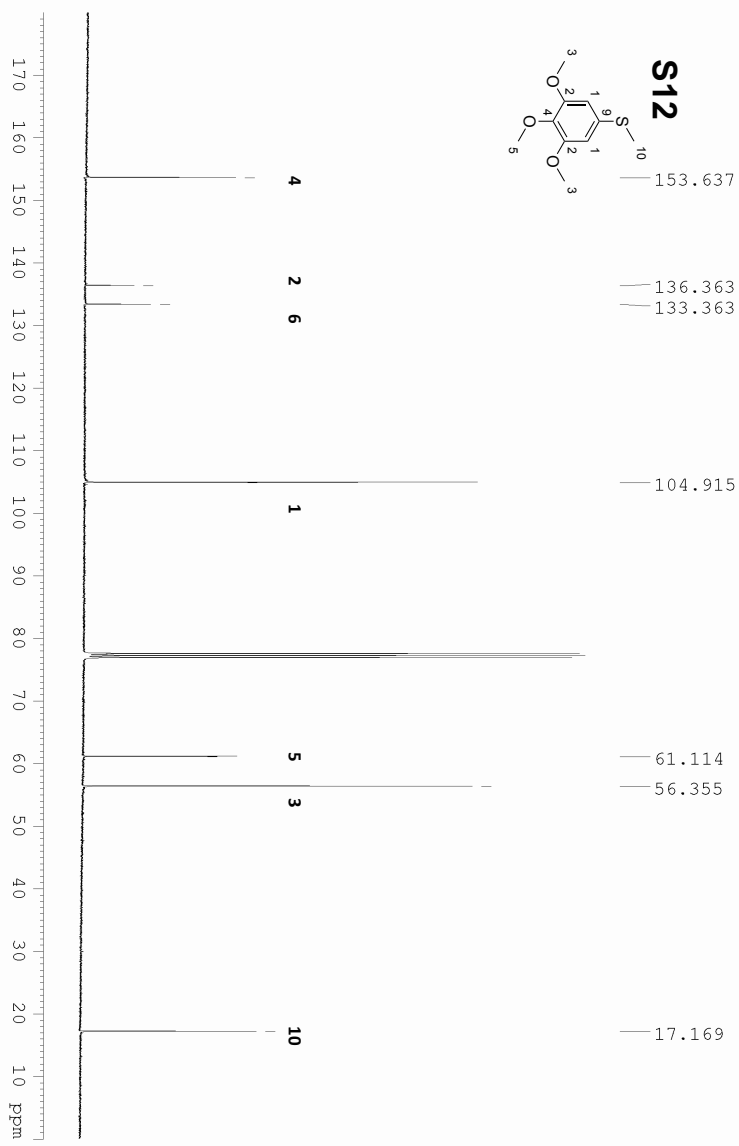
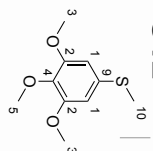
On the following pages, NMR spectra of intermediates towards and final products of the most bioactive compounds **HOTub-81** and **HOTub-81** are shown, as representative examples for all **HOTub** syntheses.

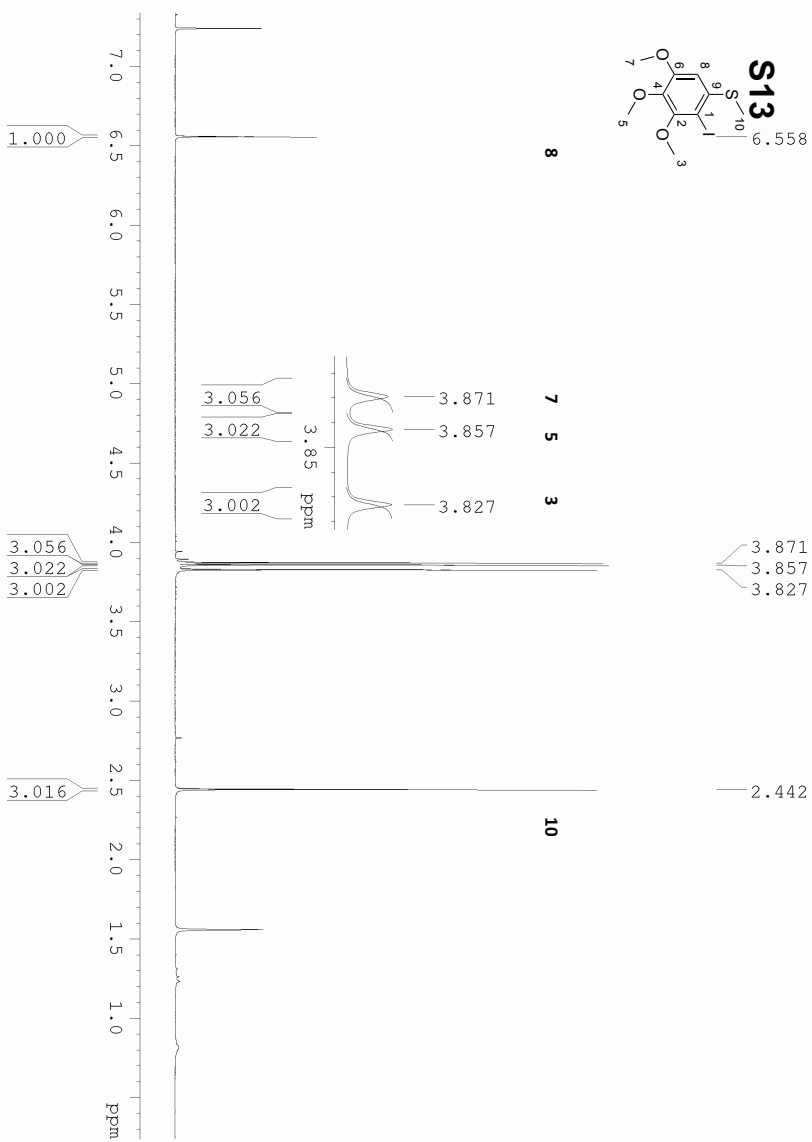
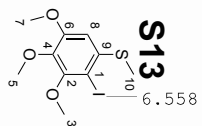
S11

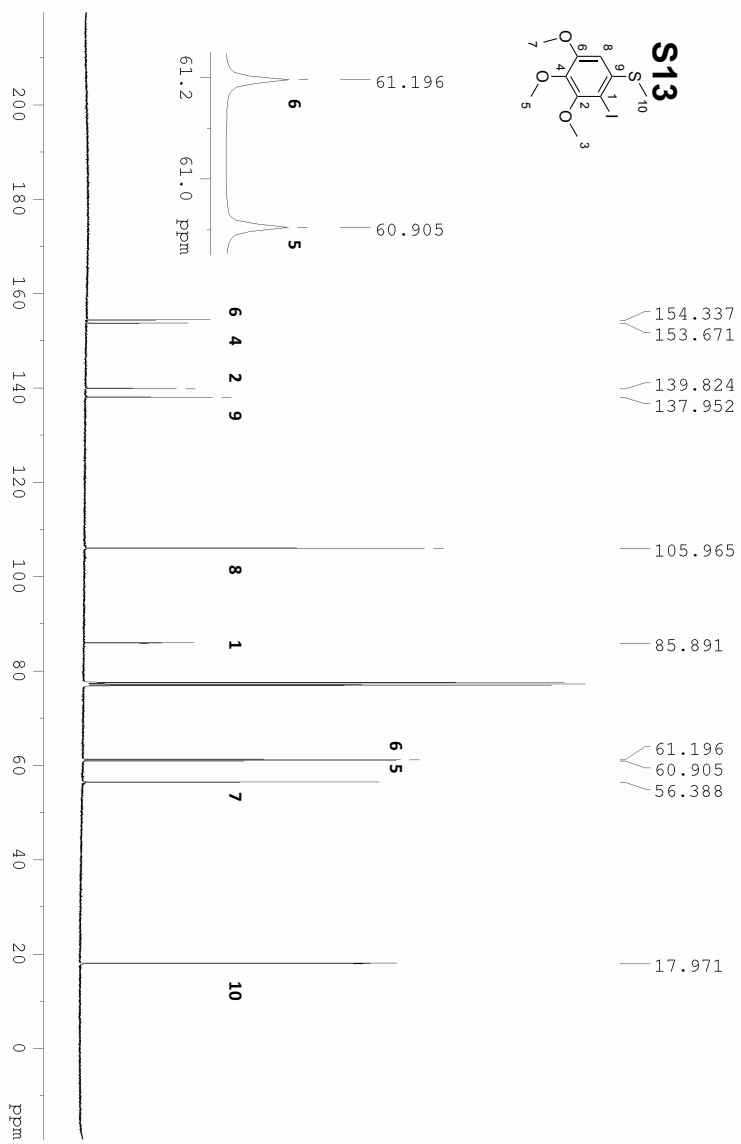
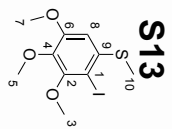




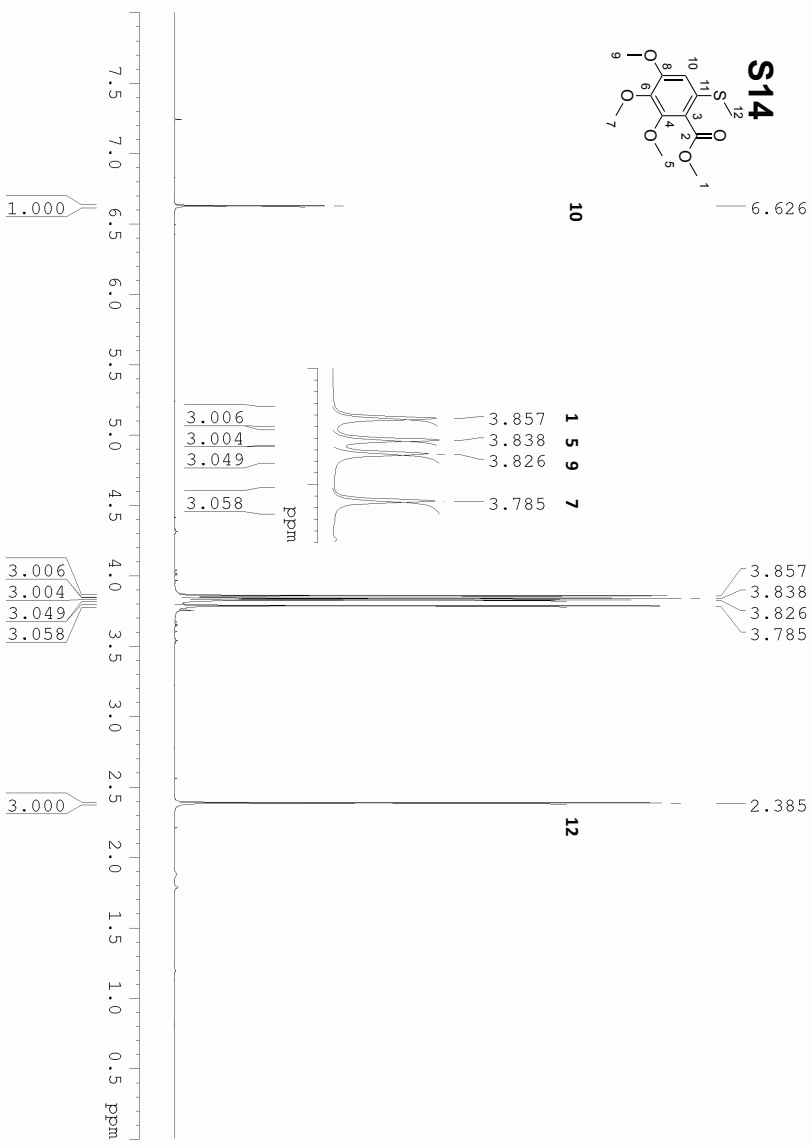
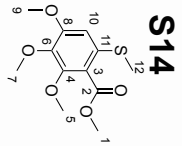


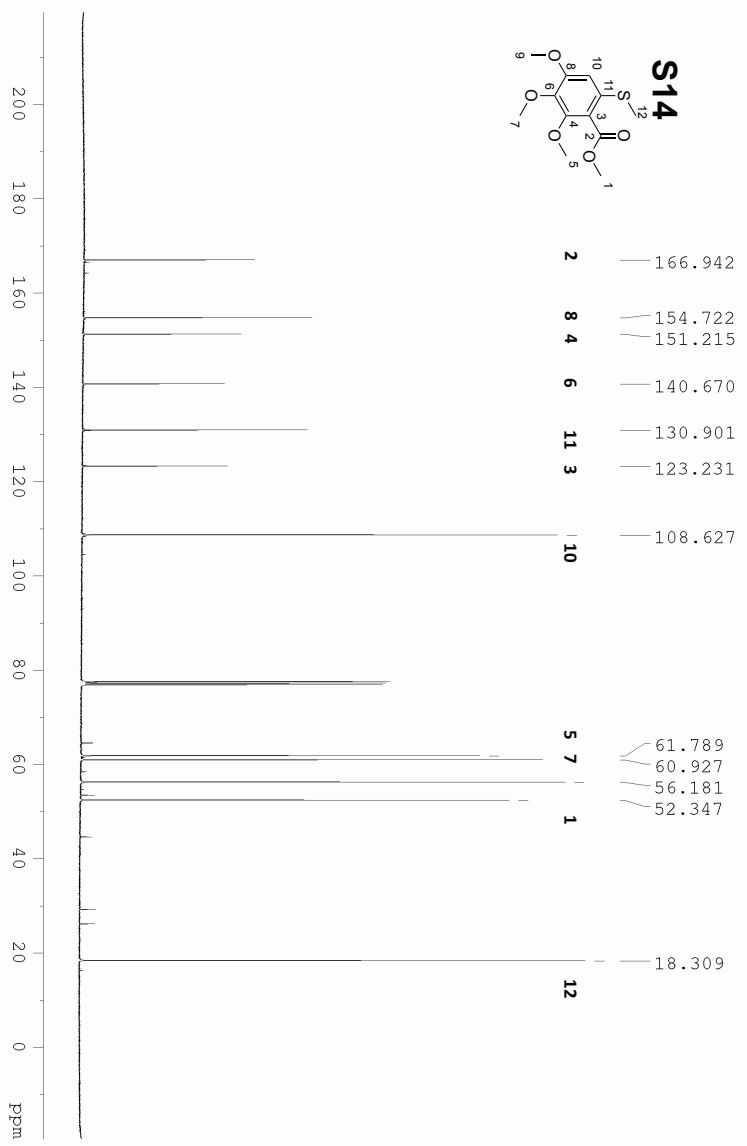
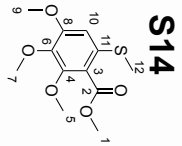


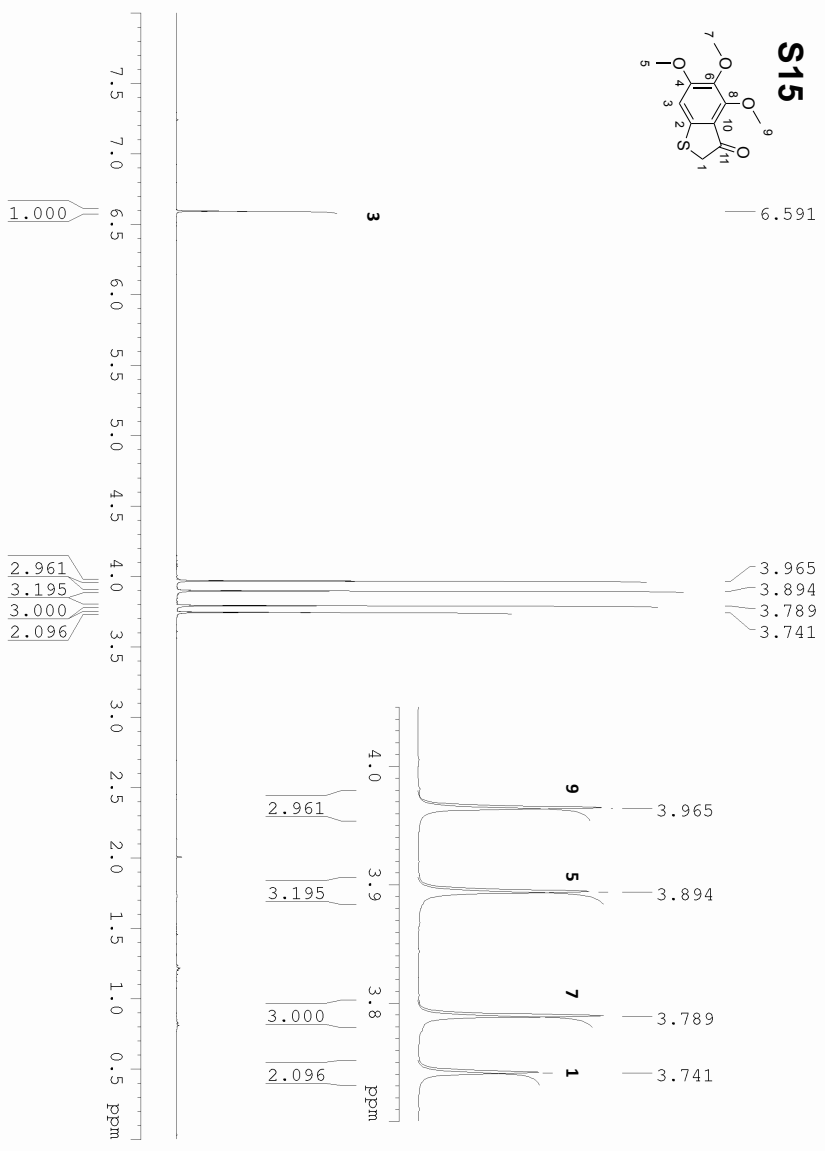
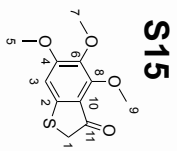


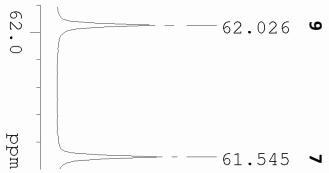
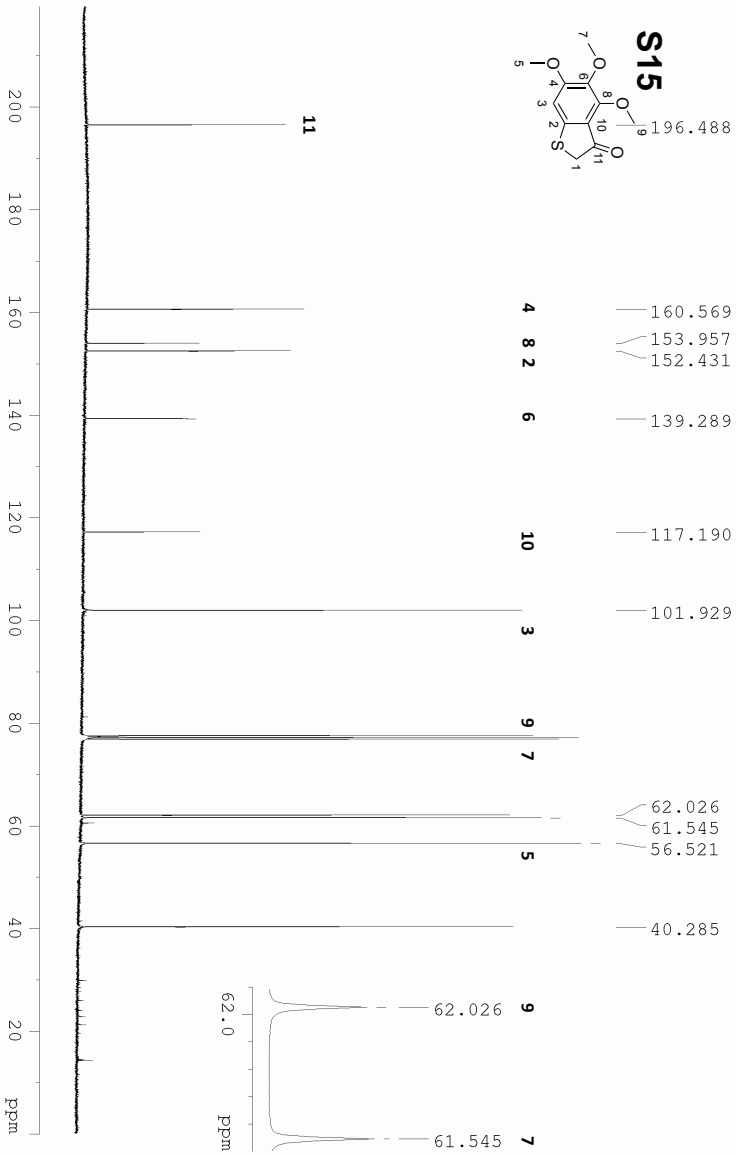
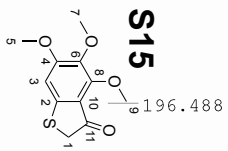


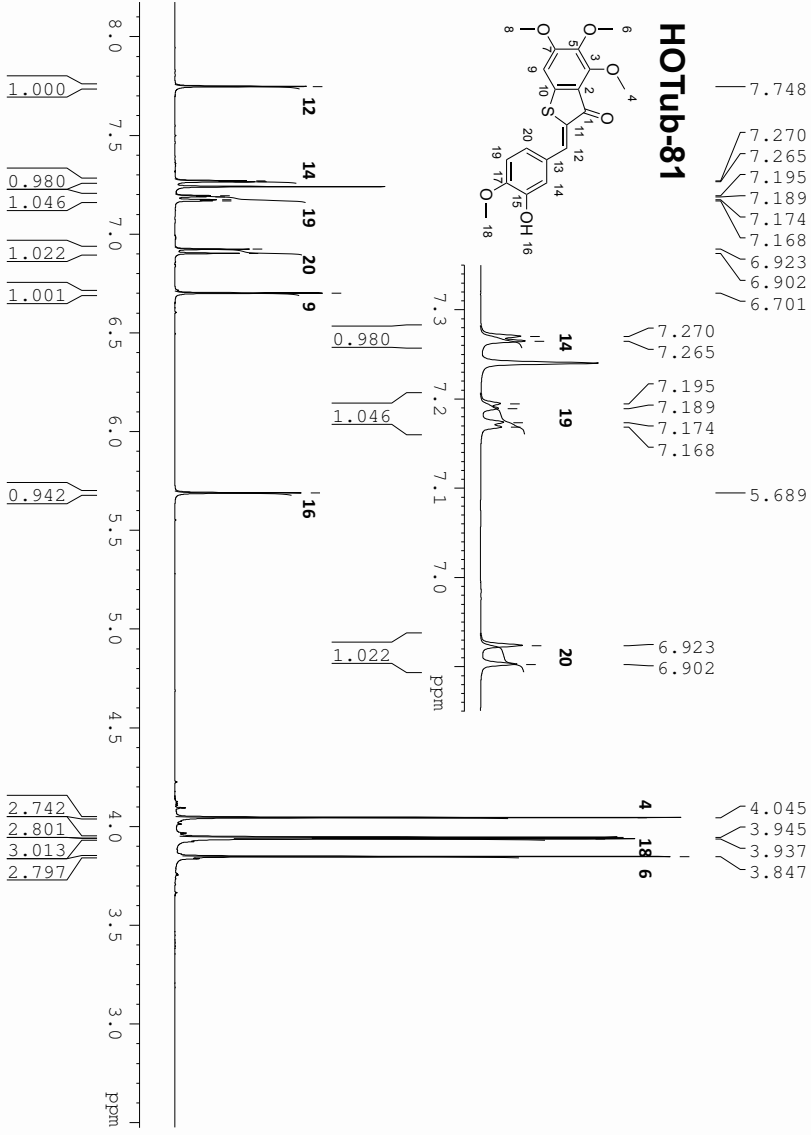


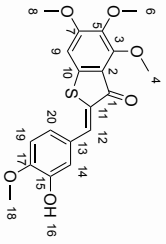






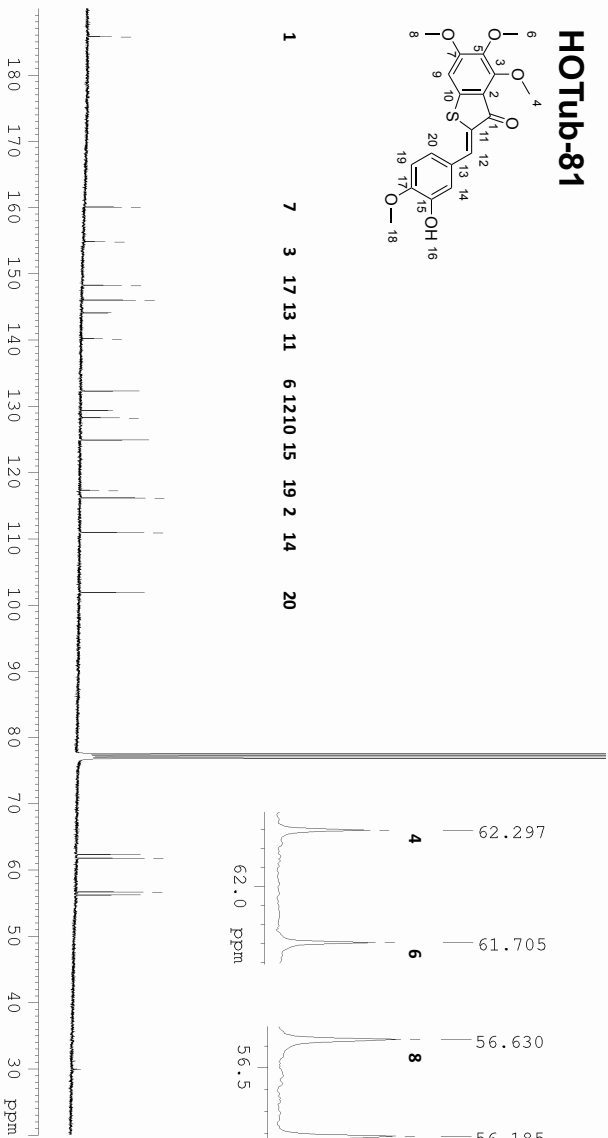




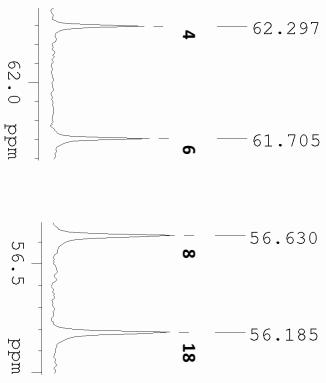


- 185.733
- 160.023
- 154.793
- ↘ 148.180
- ↘ 145.972
- ↘ 144.041
- ↘ 140.150
- ↘ 132.244
- ↘ 129.327
- ↘ 128.195
- ↘ 124.848
- ↘ 117.242
- ↘ 116.115
- 110.885
- 101.837

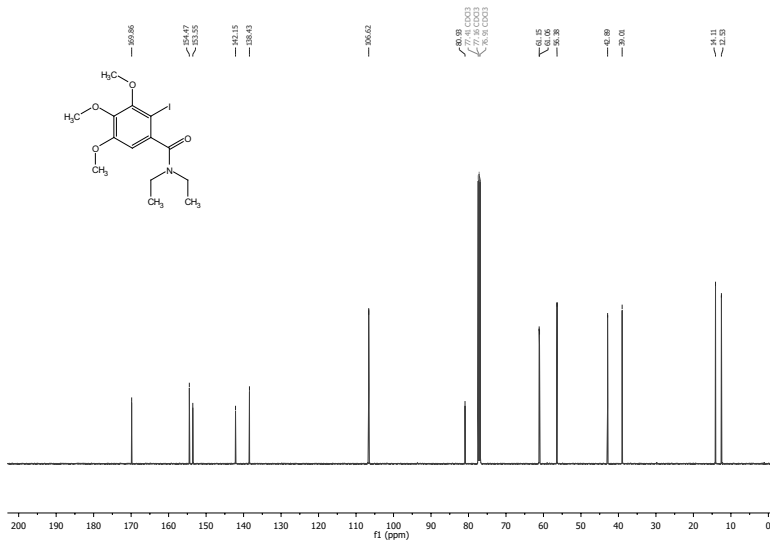
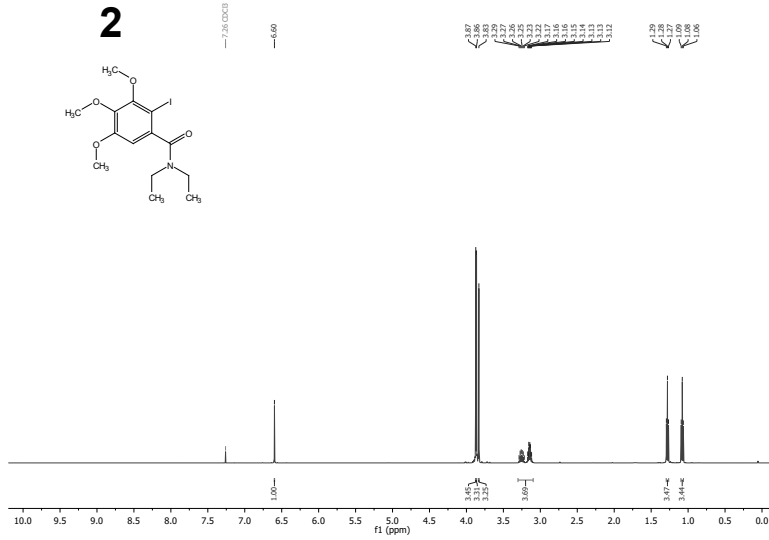
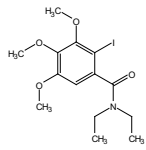
- 1
- 7
- 3
- 17
- 13
- 11
- 6
- 12
- 10
- 15
- 19
- 2
- 14
- 20



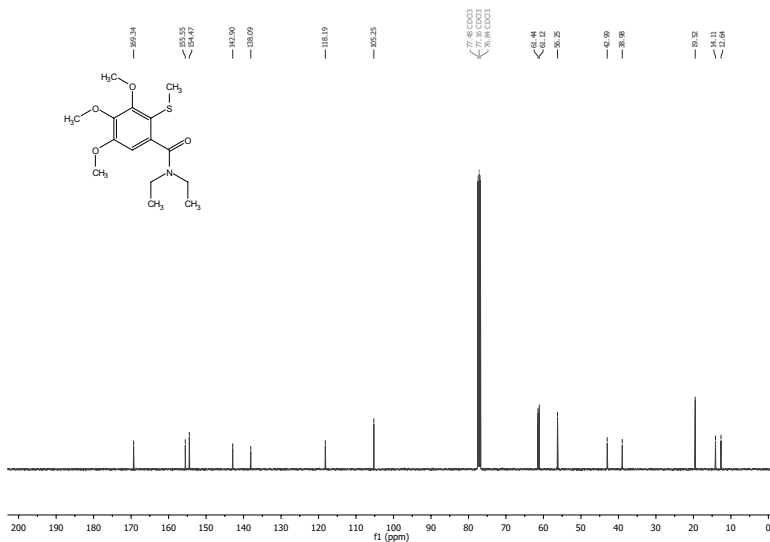
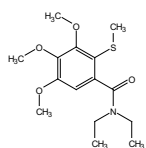
- ↘ 62.297
- ↘ 61.705
- ↘ 56.630
- ↘ 56.185



2

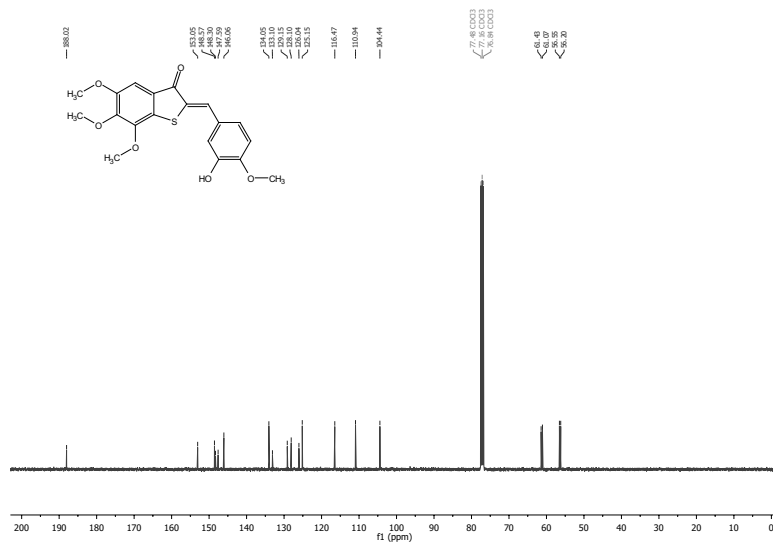
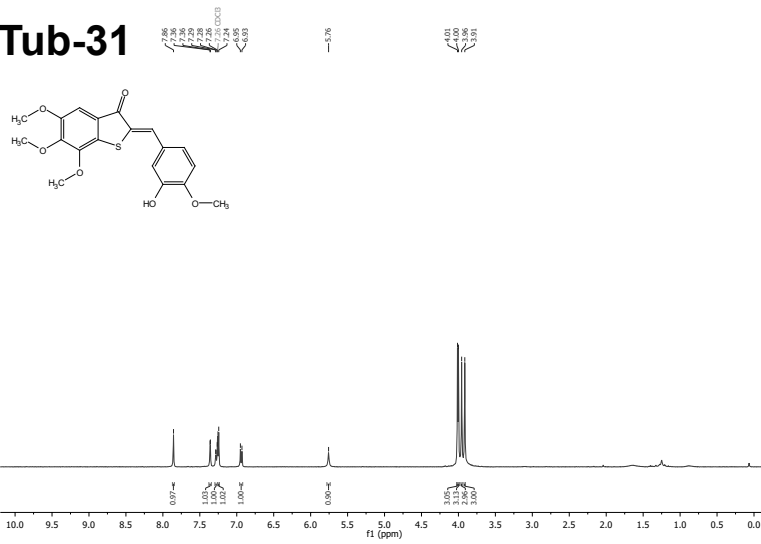


3





# HOTub-31



### Chapter 4.3 Hemithioindigo HITubs

#### Licence

Reprinted with permission from: Alexander Sailer, Franziska Ermer, Yvonne Kraus, Rebekkah Bingham, Ferdinand Lutter, Julia Ahlfeld and Oliver Thorn-Seshold, Potent hemithioindigo-based antimicrotubule photocontrol the microtubule cytoskeleton in cellulose, *Beilstein Journal of Organic Chemistry* **2020**, *16*, 125. Copyright Sailer et al.; licensee Beilstein Institut.



## Supporting Information

for

### **Potent hemithioindigo-based antimetotics photocontrol the microtubule cytoskeleton in cellulo**

Alexander Sailer, Franziska Ermer, Yvonne Kraus, Rebekkah Bingham,  
Ferdinand H. Lutter, Julia Ahlfeld and Oliver Thorn-Seshold

*Beilstein J. Org. Chem.* **2020**, *16*, 125–134. doi:10.3762/bjoc.16.14

**Full experimental protocols for chemical syntheses,  
photocharacterisation, biochemistry, and cell biology,  
including NMR spectra**

**Authorship Statement:** Following the ICMJE guidelines, the authors declare their roles in the present work as follows: A.S. performed chemical synthesis, photocharacterisation and coordinated data assembly, F.E. performed in vitro studies, Y.K. performed in cellulose studies, R.B. performed in vitro tubulin polymerisation assays, F.H.L. performed chemical synthesis, J.A. performed in cellulose studies and coordinated data interpretation and assembly. O.T.-S. designed the concept and experiments, supervised all experiments, coordinated all data and wrote the manuscript with input from all authors.

## **Table of Contents**

<b>Part A: Chemical syntheses .....</b>	<b>S3</b>
Conventions .....	S3
Standard procedures .....	S4
Synthesis of HITub-3 .....	S6
Synthesis of HITub-4 .....	S8
Synthesis of HITub-2 and HITub-5 .....	S10
Synthesis of HITub-1 .....	S11
Synthesis of HITub-7 .....	S13
Synthesis of HITub-6 .....	S14
<b>Part B: Photocharacterisation in vitro .....</b>	<b>S17</b>
UV-vis spectrophotometry of bulk samples .....	S17
PSS spectra of the HITubs .....	S17
Solvent- and pH-dependency of photoisomerisability and relaxation rate .....	S18
<b>Part C: Biochemistry and cellular biology .....</b>	<b>S21</b>
Resazurin antiproliferation assays .....	S22
In vitro tubulin polymerisation assay .....	S22
Immunofluorescence imaging of microtubule network structure .....	S23
Cell cycle analysis .....	S24
<b>Supplemental references .....</b>	<b>S25</b>
<b>Part D: NMR spectra .....</b>	<b>S26</b>

## **Part A: Chemical syntheses**

### **Conventions**

Hemithioindigo geometry and nomenclature: Hemithioindigos (HTIs) are drawn by default in their *Z*-isomeric form. However, this should be understood to imply either or both of the *E* & *Z* forms constituting a given sample depending on light exposure, therefore by default they are also named without *E/Z*-designations.

Abbreviations: The following abbreviations are used: *sec*Bu – *secondary* butyl, Bu – butyl, calcd. – calculated, cHx – cyclohexane, DCM – dichloromethane, DIPA – *N*-(propan-2-yl)propan-2-amine, DMSO – dimethyl sulfoxide, EA / EtOAc – ethyl acetate, EtOH – ethanol, Hx – distilled isohexanes, HRMS – high-resolution mass spectrometry, LDA – lithium diisopropylamide, MeCN – acetonitrile, *n*-Bu – *normal* butyl, MS – molecular sieves, NIS – *N*-iodosuccinimide, TFA – trifluoroacetic acid, THF – tetrahydrofuran, TMEDA – tetramethylethylenediamine,.

Automated flash chromatography: Automated flash chromatography was performed on a Biotage Isolera One instrument using 254 nm as detection wavelength and eluting with mixtures of ethyl acetate and isohexanes.

Reagents and conditions: Unless stated otherwise: (1) all reactions and characterisations were performed with unpurified, undried, non-degassed solvents and reagents, used as obtained, under closed air atmosphere without special precautions unless stated otherwise. The use of dry solvents in this context is to be understood as using anhydrous solvents bought from Acros Organics which were stored and handled under an atmosphere of nitrogen; (2) “hexane” used for chromatography was distilled from commercial crude isohexane fraction on rotavap; (3) when not specified, “column” and “chromatography” refer to flash column chromatography performed on Merck silica gel Si-60 (40–63 μm); (4) procedures and yields are unoptimised; (5) yields refer to isolated chromatographically and spectroscopically pure materials (6) all eluent and solvent mixtures are given as volume ratios unless otherwise specified, thus “1:1 EA:Hx” indicates a 1:1 mixture (by volume) of ethyl acetate and hexanes.

Thin-layer chromatography (TLC) was run on 0.25 mm Merck silica gel plates (60, F-254). UV light (254 nm) was used as a visualising agent.  $R_f$  values were usually determined in ethyl acetate : hexane (EA:Hx) eluents. TLC characterisations are thus abbreviated as per ( $R_f = 0.09$  on EA:Hx, 6:1).

NMR: Standard NMR characterisation was by 1D  $^1\text{H}$ - and  $^{13}\text{C}$ -NMR spectra, with COSY, HSQC, HMBC or heteronuclear NMR performed as needed. Known compounds were checked against literature data and their spectral analysis is not detailed unless necessary. The default spectrometer used was a Bruker Ascend 400 (400 MHz & 100 MHz for  $^1\text{H}$  and  $^{13}\text{C}$

respectively); NMR solvents are given individually for each compound. For determination of the composition of the photostationary states (450 and 505 nm), a Bruker Avance III HD (500 MHz) equipped with CryoProbe™ Prodigy broadband probe was used.

Chemical shifts ( $\delta$ ) are reported in ppm calibrated to residual non-perdeuterated solvent as an internal reference[1]. The following peak descriptions are used: singlet (s), doublet (d), triplet (t), quartet (q), multiplet (m), broad (br.).

Mass Spectra: HRMS was carried out by the Zentrale Analytik of the LMU, Munich using ESI or EI ionisation as specified.

### **Standard procedures**

Where standard procedures were used in synthesis, unless stated otherwise, the amounts of reactants/reagents employed were implicitly adjusted to maintain the same molar ratios as in the given procedure, and no other alterations from the standard procedure (e.g., reaction time, extraction solvent, temperature) were made, unless stated otherwise.

#### **Standard procedure A: amidation of benzoic acids**

The carboxylic acid was dissolved in an excess of thionyl chloride under an atmosphere of nitrogen and heated to reflux for 3 h. The volatiles were removed under reduced pressure using an external cooling trap, the oily residue was dried in high vacuum and dissolved in dry THF. The solution was cooled to 0 °C and diethylamine (3.00 equiv) was added dropwise via syringe under a stream of nitrogen (a second needle was used as overpressure valve to remove HCl). After complete addition, the cooling bath was removed and the reaction mixture was stirred overnight at room temperature. Water was added carefully, the phases were separated and the aqueous phase was extracted with EtOAc. The combined organic extracts were washed with HCl (2 M, 2 times) and NaOH (2 M, 2 times) to remove residual amine and benzoic acid, respectively. After washing with brine (2 times), the combined organic extracts were dried over Na<sub>2</sub>SO<sub>4</sub>, evaporated and purified by flash chromatography to yield the benzamide.

#### **Standard procedure B: directed *ortho* metalation and thiomethylation**

*TMEDA was distilled over KOH pellets under an atmosphere of nitrogen (bp. 123 °C; ambient pressure) and stored under nitrogen.* To a solution of TMEDA (1.20 or 2.50 equiv) in dry THF was added *sec*BuLi (1.4 M in cyclohexane, 1.2 or 2.5 equiv) at -78 °C and the bright yellow reaction mixture was stirred for 15 min. prior to dropwise addition of a solution of the benzamide (1.00 equiv) in dry THF. The colourless solution was kept at -78 °C for further 15 min. and a solution of dimethyl disulfide (2.00 equiv) in dry THF was added dropwise. After 15 min. the reaction mixture was allowed to warm to room temperature and stirred for the time indicated. The reaction was quenched by the careful addition of a saturated aqueous solution

of  $\text{NH}_4\text{Cl}$ , the phases were separated and the aqueous phase was extracted with EtOAc (3 times). The combined organic extracts were washed with brine (3 times), dried over  $\text{Na}_2\text{SO}_4$  and evaporated. The crude was purified as stated to yield the *ortho*-thiomethyl benzamide.

**Standard procedure C: base-mediated cyclisations of *ortho*-thiomethyl benzamides**

LDA was prepared fresh by adding *n*-BuLi (2.50 M in cyclohexane) to a solution of DIPA in dry THF. To a solution of LDA (1.50–4.30 equiv) in dry THF was added the *ortho*-thiomethyl benzamide (1.00 equiv) at  $-78\text{ }^\circ\text{C}$  and the reaction mixture was stirred at this temperature for 1–1.25 h, then allowed to warm to room temperature and stirred for another hour. The reaction was quenched by the careful addition of a saturated aqueous solution of  $\text{NH}_4\text{Cl}$ , the phases were separated and the aqueous phase was extracted with DCM. The combined organic extracts were dried over  $\text{Na}_2\text{SO}_4$  and evaporated. Purification was accomplished by (automated) flash chromatography to yield the thioindoxyl.

**Standard procedure D: formation of HTIs via piperidine catalysed aldol condensations**

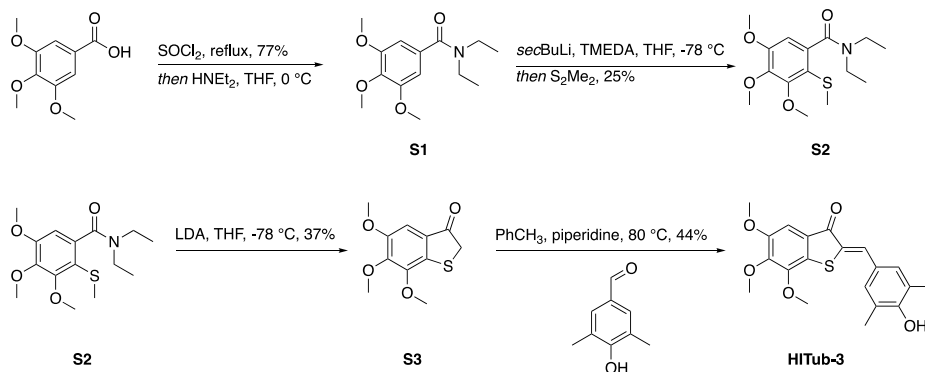
An oven dried Schlenk flask was charged with the thioindoxyl (1.00 equiv), the aldehyde (equivalents are given individually) and molecular sieves (4 Å) under an atmosphere of nitrogen. Dry benzene or toluene and piperidine (few drops) were added and the solution was heated to  $80\text{ }^\circ\text{C}$  for the time indicated individually. After cooling to room temperature, a saturated aqueous solution of  $\text{NH}_4\text{Cl}$  was added, the phases were separated and the aqueous layer was extracted with DCM. The combined organic extracts were dried over  $\text{Na}_2\text{SO}_4$  and evaporated. Purification was accomplished as stated to yield the hemithioindigo.

**Standard procedure E: formation of HTIs via dehydrative ring closure**

The (phenylthio)acetic acid (1.00 equiv) was suspended in an excess of Eaton's reagent ( $\text{P}_2\text{O}_5$  in methanesulfonic acid) and stirred for 2 h at  $50\text{ }^\circ\text{C}$ . The reaction was quenched by addition of water and the mixture was extracted with DCM. The combined organic layers were washed with a saturated aqueous solution of  $\text{NaHCO}_3$  (3 times), brine, dried over  $\text{Na}_2\text{SO}_4$  and the volume was reduced to 5–6 mL. To this solution of thioindoxyl was added basic  $\text{Al}_2\text{O}_3$  and the corresponding aldehyde (typically 0.25–0.45 equiv; as stated) and the mixture was stirred at ambient temperature. After completion of the reaction (detected by TLC), the mixture was filtered through a silica gel pad on 1:1 EA:Hx and the solvent was removed under reduced pressure. Purification was accomplished by flash chromatography, preparative thin-layer chromatography or precipitation as stated to yield the hemithioindigo.

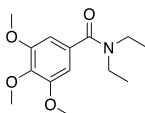


### Synthesis of HITub-3



Scheme S1: Synthesis of **HITub-3**.

#### *N,N*-Diethyl-3,4,5-trimethoxybenzamide (**S1**)

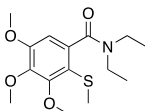


By standard procedure A, reacting commercially available 3,4,5-trimethoxybenzoic acid (1.00 g, 4.71 mmol, 1.00 equiv) with excess thionyl chloride (5 mL) followed by treatment of the acid chloride with diethylamine (1.03 g, 14.1 mmol, 1.46 mL, 3.00 equiv) in dry THF (20 mL). Purification by means of flash chromatography (EA:Hx, 1:1 → 3:1) afforded amide **S1** (969 mg, 3.62 mmol, 77%) as colorless oil that solidified upon standing.

The spectral data match the literature[2].

**<sup>1</sup>H-NMR** ( $\text{CDCl}_3$ , 400 MHz):  $\delta$  (ppm) = 6.56 (pseudo d, 2H), 3.84 (pseudo d, 6H), 3.82 (pseudo d, 3H), 3.50 (br. pseudo s, 2H), 3.27 (br. pseudo s, 2H), 1.20 – 1.13 (br. m, 6H, H); **<sup>13</sup>C-NMR** ( $\text{CDCl}_3$ , 100 MHz):  $\delta$  (ppm) = 171.1, 153.4, 138.7, 132.8, 130.0, 103.6, 61.0, 56.3, 43.4, 39.4, 14.5, 13.0;  $R_f$  = 0.20 on EA:Hx, 1:1; ESI<sup>+</sup> **HRMS** for  $\text{C}_{14}\text{H}_{22}\text{NO}_4^+$ : calcd.  $m/z$  268.15433, found  $m/z$  268.15450; for  $\text{C}_{14}\text{H}_{21}\text{NO}_4\text{Na}^+$ : calcd.  $m/z$  290.13628, found  $m/z$  290.13640.

#### *N,N*-diethyl-3,4,5-trimethoxy-2-(methylthio)benzamide (**S2**)



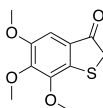
By standard procedure B, reacting amide **S1** (640 mg, 2.39 mmol, 1.00 equiv) with  $\text{secBuLi}$  (3.21 g, 5.99 mmol, 4.28 mL, 2.50 equiv) and TMEDA (696 mg, 5.99 mmol, 0.90 mL, 2.50 equiv) followed by quenching with dimethyl disulfide (451 mg, 4.79 mmol, 0.43 mL,

2.00 equiv) in dry THF (20 mL) overnight. Purification was accomplished by flash chromatography (EA:Hx, 1:1) and automated flash chromatography (EA:Hx, 5 → 60%) affording **S2** as a colorless oil (184 mg, 0.59 mmol, 25%).

The analytical data is in good agreement with our previously published data[3].

**<sup>1</sup>H-NMR** (CDCl<sub>3</sub>, 400 MHz): δ (ppm) = 6.39 (s, 1H), 3.81 (s, 3H), 3.72 (s, 3H), 3.70 (s, 3H), 3.66 – 3.59 (m, 1H), 3.25 – 3.17 (m, 1H), 3.01 – 2.96 (q, *J* = 7.1 Hz, 2H), 2.21 (s, 3H), 1.12 (t, *J* = 7.1 Hz, 3H), 0.92 (t, *J* = 7.1 Hz, 3H); **<sup>13</sup>C-NMR** (CDCl<sub>3</sub>, 100 MHz): δ (ppm) = 168.8, 155.1, 154.1, 142.4, 138.0, 117.7, 104.8, 61.0, 60.7, 55.9, 42.6, 38.5, 19.1, 13.8, 12.3; **R<sub>f</sub>** = 0.36 on EA:Hx, 1:1; ESI<sup>+</sup> **HRMS** for C<sub>15</sub>H<sub>23</sub>NO<sub>4</sub>SNa<sup>+</sup>: calcd. *m/z* 336.12400, found *m/z* 336.12402.

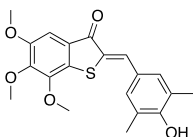
### 5,6,7-Trimethoxybenzo[*b*]thiophen-3(2*H*)-one (**S3**)



By standard procedure C, **S2** (25 mg, 79.8 μmol, 1.00 equiv) was reacted with LDA (prepared from *n*-BuLi (36 mg, 120 μmol, 0.05 mL, 1.50 equiv) and DIPA (20 mg, 200 μmol, 0.03 mL, 2.50 equiv)). After stirring for 1 h at -78 °C and 1 h at ambient temperature, the mixture was worked up and the crude product was purified by automated flash chromatography (EA:Hx, 5 → 40%) affording thioindoxyl **S3** (7 mg, 29.1 μmol, 37%) as a pale yellow crystalline solid. Due to limited chemical stability of electron-rich thioindoxyls under air, the product was immediately condensed with the respective aldehyde after spectroscopic characterisation.

**<sup>1</sup>H-NMR** (CDCl<sub>3</sub>, 400 MHz): δ (ppm) = 7.05 (s, 1H), 3.97 (s, 3H), 3.95 (s, 3H), 3.86 (s, 3H), 3.75 (s, 2H); **<sup>13</sup>C-NMR** (CDCl<sub>3</sub>, 100 MHz): δ (ppm) = 199.3, 152.6, 148.9, 147.8, 141.7, 126.2, 103.4, 61.4, 60.8, 56.5, 39.5; **R<sub>f</sub>** = 0.36 (blue fluorescence under illumination with 366 nm) on EA:Hx, 1:4.

### 2-(4-Hydroxy-3,5-dimethylbenzylidene)-5,6,7-trimethoxybenzo[*b*]thiophen-3(2*H*)-one (**HITub-3**)

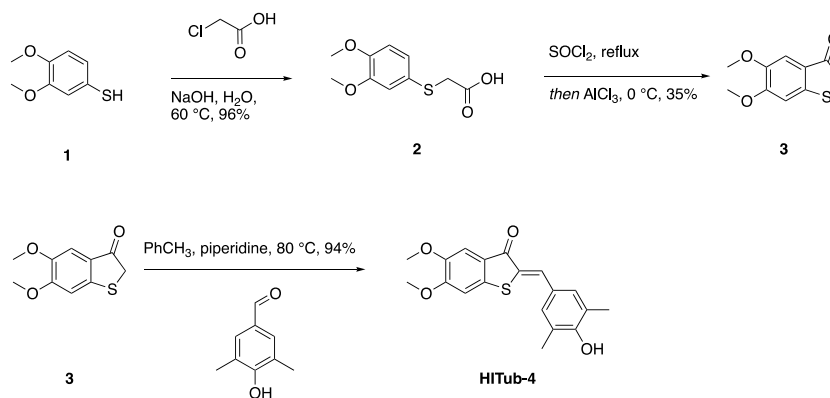


By standard procedure D, thioindoxyl **S3** (5 mg, 20.8 μmol, 1.00 equiv) was reacted with commercially available 3,5-dimethyl-4-hydroxybenzaldehyde (4 mg, 27.1 μmol, 1.30 equiv) in

dry toluene (3 mL) for 2.5 h at 80 °C then 1 h at 25 °C. Automated flash chromatography (EA:Hx, 5 → 40%) yielded **HITub-3** as an orange solid (3.4 mg, 9.1 μmol, 44%).

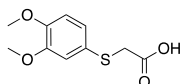
**<sup>1</sup>H-NMR** (CDCl<sub>3</sub>, 400 MHz): δ (ppm) = 7.84 (s, 1H), 7.38 (s, 2H), 7.23 (s, 1H), 5.08 (br. s, 1H), 4.01 (s, 3H), 3.98 (s, 3H), 3.90 (s, 3H), 2.30 (s, 6H); **<sup>13</sup>C-NMR** (CDCl<sub>3</sub>, 100 MHz): δ (ppm) = 188.1, 154.7, 153.0, 148.1, 147.6, 134.6, 133.0, 132.3, 128.0, 126.7, 126.2, 124.0, 104.4, 61.4, 61.2, 56.5, 16.1; **R<sub>f</sub>** = 0.27 on EA:Hx, 1:4; ESI<sup>+</sup> **HRMS** for C<sub>21</sub>H<sub>23</sub>O<sub>5</sub>S<sup>+</sup>: calcd. m/z 373.11042, found m/z 373.11008; ESI<sup>-</sup> **HRMS** for C<sub>21</sub>H<sub>22</sub>O<sub>5</sub>S<sup>-</sup>: calcd. m/z 371.09587, found m/z 371.09597.

### Synthesis of HITub-4



Scheme S2: Synthesis of **HITub-4**.

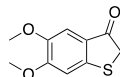
### 2-((3,4-Dimethoxyphenyl)thio)acetic acid (2)



Acetic acid derivative **2** was prepared starting from commercially available thiol **1** following our previously published procedure; spectral data are in good agreement with our previously published data[3].

**<sup>1</sup>H-NMR** (DMSO-d<sub>6</sub>, 400 MHz): δ (ppm) = 12.67 (s, 1H), 7.00 (d, *J* = 1.7 Hz, 1H), 6.94 (dd, *J* = 1.7 & 8.3 Hz, 1H), 6.90 (d, *J* = 8.3 Hz, 1H), 3.74 (s, 3H), 3.73 (s, 3H), 3.67 (s, 2H); **<sup>13</sup>C-NMR** (DMSO-d<sub>6</sub>, 100 MHz): δ (ppm) = 161.3, 139.2, 138.5, 116.2, 112.9, 104.2, 102.6, 45.9, 45.8, 27.3; ESI<sup>-</sup> **HRMS** for C<sub>10</sub>H<sub>11</sub>O<sub>4</sub>S<sup>-</sup>: calcd. m/z 227.03780, found m/z 227.03844.

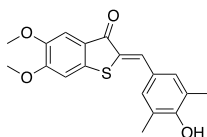
### 5,6-Dimethoxybenzo[*b*]thiophen-3(2*H*)-one (3)



Thioindoxyl **3** was prepared following our previously reported procedure and all spectral data are in good agreement with our previously published data[3].

**<sup>1</sup>H-NMR** (CDCl<sub>3</sub>, 400 MHz): δ (ppm) = 7.17 (s, 1H), 6.82 (s, 1H), 3.94 (s, 3H), 3.87 (s, 3H), 3.79 (s, 2H); **<sup>13</sup>C-NMR** (CDCl<sub>3</sub>, 100 MHz): δ (ppm) = 198.6, 156.5, 149.6, 147.9, 123.7, 106.9, 105.6, 56.6, 56.3, 40.1; **R<sub>f</sub>** = 0.33 on EA:Hx, 1:4 (blue fluorescence under illumination with 254 / 366 nm); **EI HRMS** for C<sub>10</sub>H<sub>10</sub>O<sub>3</sub>S: calcd. m/z 210.0345, found m/z 210.1287.

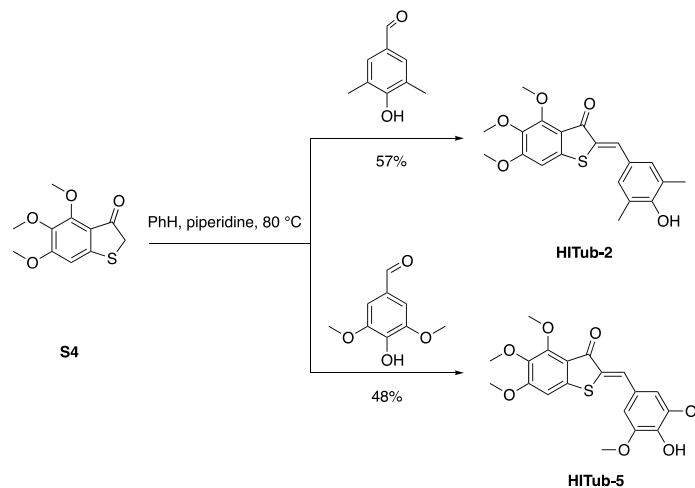
### 2-(4-Hydroxy-3,5-dimethylbenzylidene)-5,6-dimethoxybenzo[*b*]thiophen-3(2*H*)-one (HITub-4)



By standard procedure D, reacting thioindoxyl **3** (325 mg, 1.55 mmol, 1.00 equiv) with commercially available 3,5-dimethyl-4-hydroxybenzaldehyde (255 mg, 1.70 mmol, 1.10 equiv) in dry toluene (20 mL) for 2 h at 80 °C and overnight at room temperature. The crude product was dissolved in DMSO, water was added, the suspension was centrifuged and the supernatant was pipetted off (repeated once). The residue was dissolved in DCM, washed with water and dried over Na<sub>2</sub>SO<sub>4</sub>. The volatiles were removed in vacuo and the remaining solid was lyophilised to yield **HITub-4** as red solid (500 mg, 1.46 mmol, 94%).

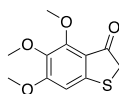
**<sup>1</sup>H-NMR** (DMSO-*d*<sub>6</sub>, 400 MHz): δ (ppm) = 9.19 (s, 1H), 7.71 (s, 1H), 7.40 (s, 1H), 7.38 (s, 2H), 7.27 (s, 1H), 3.90 (s, 3H), 3.83 (s, 3H), 2.23 (s, 6H); **<sup>13</sup>C-NMR** (DMSO-*d*<sub>6</sub>, 100 MHz): δ (ppm) = 186.0, 156.2, 155.8, 148.1, 139.7, 132.9, 131.8, 127.1, 125.1, 124.9, 122.5, 107.2, 106.4, 56.4, 55.8, 16.8; **R<sub>f</sub>** = 0.41 on EA:Hx, 1:2; **ESI<sup>+</sup> HRMS** for C<sub>19</sub>H<sub>17</sub>O<sub>4</sub>S: calcd. m/z 341.08530, found m/z 341.08545.

### Synthesis of HITub-2 and HITub-5



Scheme S3: Synthesis of **HITub-2** and **HITub-5**.

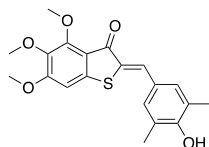
### 4,5,6-Trimethoxybenzo[*b*]thiophen-3(2*H*)-one (S4)



**S4** was prepared following our previously reported procedure and all spectral data are in good agreement with our previously published data[3].

**<sup>1</sup>H-NMR** (CDCl<sub>3</sub>, 400 MHz): δ (ppm) = 6.59 (s, 1H), 3.97 (s, 3H), 3.89 (s, 3H), 3.79 (s, 3H), 3.74 (s, 2H); **<sup>13</sup>C-NMR** (CDCl<sub>3</sub>, 100 MHz): δ (ppm) = 196.5, 160.6, 154.0, 152.4, 139.3, 117.2, 101.9, 62.0, 61.5, 56.5, 40.3; **R<sub>f</sub>** = 0.32 on EA:Hx, 1:4 (blue fluorescence under illumination with 254 nm); ESI<sup>+</sup> **HRMS** for C<sub>11</sub>H<sub>13</sub>O<sub>4</sub>S<sup>+</sup>: calcd. m/z 241.05291, found m/z 241.05281, for C<sub>11</sub>H<sub>12</sub>O<sub>4</sub>NaS<sup>+</sup>: calcd. m/z 263.03485, found m/z 263.03485.

### 2-(4-Hydroxy-3,5-dimethylbenzylidene)-4,5,6-trimethoxybenzo[*b*]thiophen-3(2*H*)-one (HITub-2)

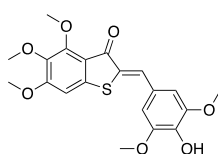


By standard procedure D, thioindoxyl **S5** (50 mg, 0.21 mmol, 1.00 equiv) was reacted with commercially available 3,5-dimethyl-4-hydroxybenzaldehyde (31 mg, 0.21 mmol, 1.00 equiv)

in dry benzene (20 mL) for 2 h at 80 °C. The crude product was dissolved in DMSO, water was added, the suspension was centrifuged and the supernatant was pipetted off (repeated once) yielding **HITub-2** as orange solid (44 mg, 0.12 mmol, 57%).

**<sup>1</sup>H-NMR** (CDCl<sub>3</sub>, 400 MHz): δ (ppm) = 7.74 (s, 1H), 7.31 (s, 2H), 6.71 (s, 1H), 5.05 (br. s, 1H), 4.05 (s, 3H), 3.94 (s, 3H), 3.85 (s, 3H), 2.29 (s, 6H); **<sup>13</sup>C-NMR** (CDCl<sub>3</sub>, 100 MHz): δ (ppm) = 185.8, 159.9, 154.7, 154.3, 144.0, 140.1, 132.7, 132.0, 128.3, 126.8, 123.9, 117.4, 101.7, 62.3, 61.7, 56.6, 16.1; **R<sub>f</sub>** = 0.39 on Hx:DCM:MeOH, 1:1:0.04; ESI<sup>+</sup> **HRMS** for C<sub>20</sub>H<sub>21</sub>O<sub>5</sub>S<sup>+</sup>: calcd. m/z 373.11042, found m/z 373.11050, ESI<sup>-</sup> **HRMS** for C<sub>20</sub>H<sub>19</sub>O<sub>7</sub>S<sup>-</sup>: calcd. m/z 371.09587, found m/z 371.09634.

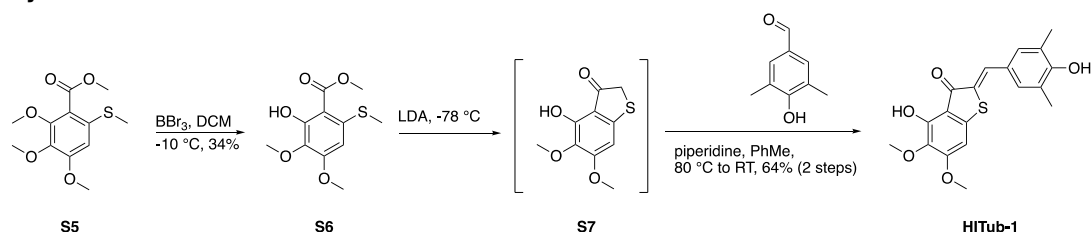
**2-(4-Hydroxy-3,5-dimethoxybenzylidene)-4,5,6-trimethoxybenzo[*b*]thiophen-3(2*H*)-one (HITub-5)**



By standard procedure D, thioindoxyl **S5** (15 mg, 0.06 mmol, 1.00 equiv) was reacted with commercially available 3,5-dimethoxy-4-hydroxybenzaldehyde (14 mg, 0.07 mmol, 1.2 equiv) in dry benzene (5 mL) for 3.5 h at 80 °C. The crude was purified by flash chromatography (Hx:DCM:MeOH, 1:1:0.04) to give **HITub-5** (12 mg, 0.03 mmol, 48%).

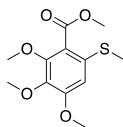
**<sup>1</sup>H-NMR** (CDCl<sub>3</sub>, 400 MHz): δ (ppm) = 7.75 (s, 1H), 6.91 (s, 2H), 6.72 (s, 1H), 5.83 (s, 1H), 4.06 (s, 3H), 3.95 (s, 6H), 3.94 (s, 3H), 3.85 (s, 3H); **<sup>13</sup>C-NMR** (CDCl<sub>3</sub>, 100 MHz): δ (ppm) = 185.5, 160.1, 154.8, 147.4, 143.7, 140.2, 136.9, 132.7, 129.0, 126.2, 117.3, 108.0, 101.8, 62.3, 61.7, 56.6, 56.5; **R<sub>f</sub>** = 0.39 on Hx:DCM:MeOH, 1:1:0.04; ESI<sup>+</sup> **HRMS** for C<sub>20</sub>H<sub>21</sub>O<sub>7</sub>S<sup>+</sup>: calcd. m/z 405.10080, found m/z 405.10015; ESI<sup>-</sup> **HRMS** for C<sub>20</sub>H<sub>19</sub>O<sub>7</sub>S<sup>-</sup>: calcd. m/z 403.08570, found m/z 403.08616.

**Synthesis of HITub-1**



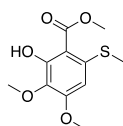
Scheme S4: Synthesis of **HITub-1**.

### Methyl 2,3,4-trimethoxy-6-(methylthio)benzoate (**S5**)



**S5** was prepared following our previously reported procedure with all spectroscopical data matching the literature.[3]

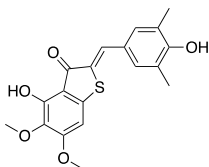
### Methyl 2-hydroxy-3,4-dimethoxy-6-(methylthio)benzoate (**S6**)



To a solution of **S5** (50 mg, 0.18 mmol, 1.00 equiv) in dry DCM (2 mL) was added  $\text{BBr}_3$  (1 M in DCM, 0.20 mmol, 0.20 mL, 1.10 equiv) at  $-10\text{ }^\circ\text{C}$  and the mixture was stirred for 30 min prior to quenching by the addition of an aqueous saturated solution of  $\text{NaHCO}_3$ . After acidification with HCl (2 M) the layers were separated and the aqueous phase was extracted with DCM. The combined organic layers were dried over  $\text{Na}_2\text{SO}_4$  and evaporated. The crude was purified by flash chromatography (EA:Hx, 1:4) giving pure **S6** as a white solid (16 mg, 0.06 mmol, 34%).

$^1\text{H-NMR}$  ( $\text{CDCl}_3$ , 400 MHz):  $\delta$  (ppm) = 11.61 (s, 1H), 6.23 (s, 1H), 3.96 (s, 3H), 3.92 (s, 3H), 3.82 (s, 3H), 2.41 (s, 3H);  $^{13}\text{C-NMR}$  ( $\text{CDCl}_3$ , 100 MHz):  $\delta$  (ppm) = 170.9, 157.8, 156.7, 139.8, 133.6, 105.0, 99.9, 60.8, 56.0, 52.1, 16.6;  $R_f$  = 0.34 on EA:Hx, 1:4; ESI $^+$  HRMS for  $\text{C}_{11}\text{H}_{13}\text{O}_5\text{S}^-$ : calcd.  $m/z$  257.04892, found  $m/z$  257.04937.

### 4-Hydroxy-2-(4-hydroxy-3,5-dimethylbenzylidene)-5,6-dimethoxybenzo[b]thiophen-3(2H)-one (HITub-1)



By standard procedure C, **S6** (18 mg, 0.07 mmol, 1.00 equiv) was reacted with LDA (prepared from *n*-BuLi ((2.5 M in hexane, 19 mg, 0.30 mmol, 0.12 mL, 4.33 equiv) and DIPA (32 mg, 0.32

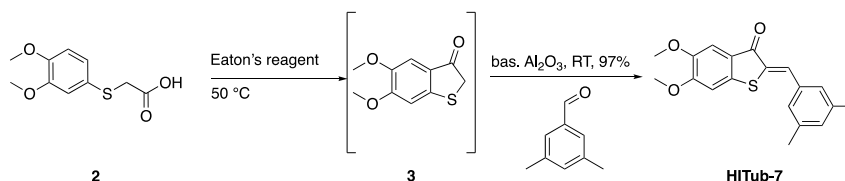
mmol, 0.04 mL, 4.60 equiv)). After stirring for 1 h at  $-78\text{ }^{\circ}\text{C}$  and 1 h at  $25\text{ }^{\circ}\text{C}$ , the mixture was worked up yielding crude **S7**.

An analytically pure sample of thioindoxyl **S7** can be obtained by purification of the crude by automated flash chromatography (EA:Hx, 5  $\rightarrow$  100%) and was characterised as follows:  **$^1\text{H-NMR}$**  ( $\text{CDCl}_3$ , 400 MHz):  $\delta$  (ppm) = 9.81 (s, 1H), 6.46 (s, 1H), 3.92 (s, 3H), 3.85 (s, 2H), 3.84 (s, 3H);  **$^{13}\text{C-NMR}$**  ( $\text{CDCl}_3$ , 100 MHz):  $\delta$  (ppm) = 201.8, 161.7, 153.0, 150.5, 132.9, 112.4, 98.7, 61.1, 56.7, 40.5;  $R_f$  = 0.37 on EA:Hx, 1:4; ESI<sup>+</sup> **HRMS** for  $\text{C}_{10}\text{H}_{11}\text{O}_4\text{S}^+$ : calcd.  $m/z$  227.03726, found  $m/z$  227.03743; ESI<sup>-</sup> **HRMS** for  $\text{C}_{10}\text{H}_9\text{O}_4\text{S}^-$ : calcd.  $m/z$  225.02270, found  $m/z$  225.02256.

Due to partial decomposition during chromatography it is however more practical to use crude **S7** in the following step. By standard procedure D, crude **S7** was reacted with commercially available 3,5-dimethyl-4-hydroxybenzaldehyde (11 mg, 0.07 mmol, 1.00 equiv) in dry toluene (5 mL) for 1h at  $80\text{ }^{\circ}\text{C}$  and overnight at room temperature. After work-up, the crude product was purified by precipitation with water from a concentrated DMSO solution (repeated once) to afford **HITub-1** as an orange-brown solid (16 mg, 0.04 mmol, 64% over two steps).

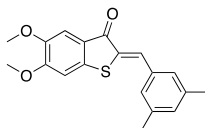
**$^1\text{H-NMR}$**  ( $\text{DMSO-d}_6$ , 400 MHz):  $\delta$  (ppm) = 10.14 (s, 1H), 9.22 (s, 1H), 7.65 (s, 1H), 7.36 (s, 2H), 7.00 (s, 1H), 3.90 (s, 3H), 3.70 (s, 3H), 2.23 (s, 6H);  **$^{13}\text{C-NMR}$**  ( $\text{DMSO-d}_6$ , 100 MHz):  $\delta$  (ppm) = 187.8, 170.6, 170.2, 160.5, 156.7, 152.8, 141.8, 133.8, 132.7, 132.2, 127.4, 125.6, 125.2, 111.9, 99.9, 60.8, 57.1, 17.2;  $R_f$  = 0.35 on DCM + 1% MeOH; **HRMS** for  $\text{C}_{19}\text{H}_{19}\text{O}_5\text{S}^+$ : calcd.  $m/z$  359.09477, found  $m/z$  359.09522; **HRMS** for  $\text{C}_{19}\text{H}_{17}\text{O}_5\text{S}^-$ : calcd.  $m/z$  357.08022, found  $m/z$  357.08054.

### Synthesis of HITub-7



Scheme S5: Synthesis of **HITub-7**.

### 2-(3,5-Dimethylbenzylidene)-5,6-dimethoxybenzo[*b*]thiophen-3(2*H*)-one (HITub-7)

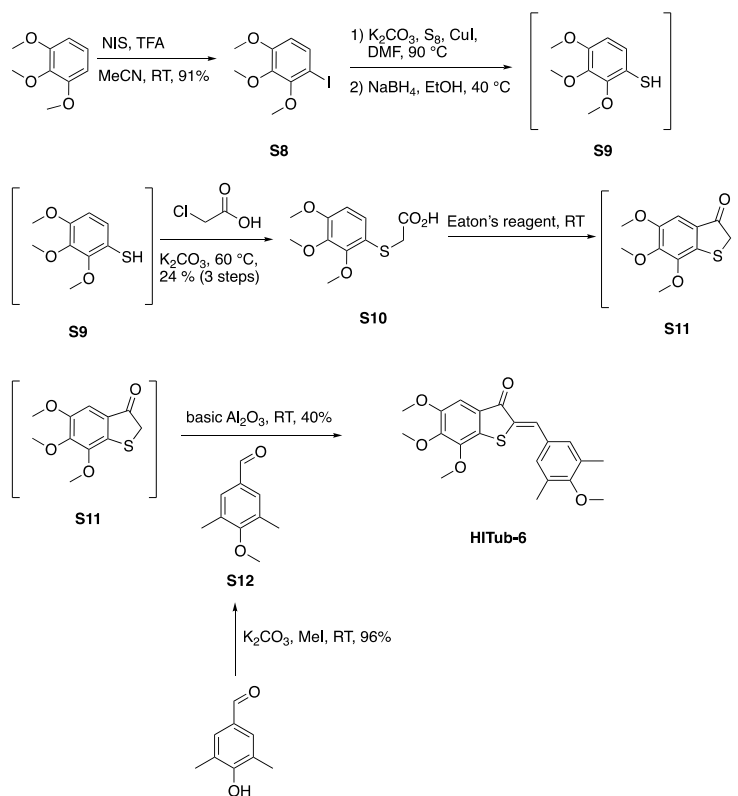




By standard procedure E, **2** (300 mg, 1.31 mmol, 4.00 equiv) was stirred with Eaton's reagent for 2 h. After extraction, commercially available 3,5-dimethylbenzaldehyde (44 mg, 0.33 mmol, 1.00 equiv) and basic Al<sub>2</sub>O<sub>3</sub> were added to crude **3**. The mixture was stirred for 12 h and after work-up the crude product was purified by chromatography (EA:Hx, 1:10 → 1:4) to yield **HITub-7** (104 mg, 0.32 mmol, 97%).

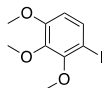
<sup>1</sup>H-NMR (CDCl<sub>3</sub>, 400 MHz): δ (ppm) = 7.86 (s, 1H), 7.36 (s, 1H), 7.30 (s, 2H), 7.03 (s, 1H), 6.91 (s, 1H), 3.97 (s, 3H), 3.92 (s, 3H), 2.36 (s, 6H); <sup>13</sup>C-NMR (CDCl<sub>3</sub>, 100 MHz): δ (ppm) = 187.6, 156.1, 148.4, 141.2, 138.7, 134.4, 133.6, 132.1, 130.9, 128.9, 123.5, 107.9, 105.3, 56.6, 56.4, 21.5; **R<sub>f</sub>** = 0.38 on EA:Hx, 1:2.4; EI **HRMS** for C<sub>19</sub>H<sub>18</sub>O<sub>3</sub>S: calcd. m/z 326.4100, found m/z 326.0966.

### Synthesis of HITub-6



Scheme S6: Synthesis of **HITub-6**.

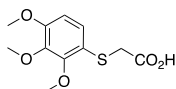
### 1-Iodo-2,3,4-trimethoxybenzene (**S8**)



The compound was prepared following a procedure published by Castanet et al.[4] and the spectral data are in good agreement with literature.[5]

**<sup>1</sup>H-NMR** (CDCl<sub>3</sub>, 400 MHz): δ (ppm) = 7.42 (d, *J* = 8.8 Hz, 1H), 6.50 (d, *J* = 8.8 Hz, 1H), 3.88 (s, 3H), 3.86 (s, 3H), 3.87 (s, 3H) 3.85 (s, 3H); **<sup>13</sup>C-NMR** (CDCl<sub>3</sub>, 100 MHz): δ (ppm) = 154.5, 153.5, 142.8, 132.7, 109.9, 81.5, 61.2, 61.0, 56.3; **R<sub>f</sub>** = 0.52 on EA:Hx, 1:5.

### 2-((2,3,4-Trimethoxyphenyl)thio)acetic acid (**S10**)

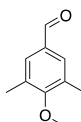


An oven-dried Schlenk tube was filled with **S8** (1.95 g, 6.61 mmol, 1.00 equiv), sulphur powder (701 mg, 21.9 mmol, 3.31 equiv), CuI (136 mg, 0.72 mmol, 0.11 equiv) and K<sub>2</sub>CO<sub>3</sub> (1.80 g, 13.0 mmol, 1.97 equiv). After addition of DMF (15 mL), the tube was evacuated carefully and refilled with nitrogen. The mixture was stirred for 12 h at 90 °C. Under cooling with ice-water, ground NaBH<sub>4</sub> (891 mg, 23.6 mmol, 3.57 equiv) was added and the mixture was stirred for 5 h at 40 °C. After addition of EtOH (5 mL), the mixture was stirred for another 4 h at this temperature. Chloroacetic acid (1.50 g, 15.9 mmol, 2.41 equiv) and K<sub>2</sub>CO<sub>3</sub> (0.51 g, 3.69 mmol, 0.56 equiv) were added and the reaction mixture was heated up to 60 °C for 5 h. After addition of water (5 mL), the reaction mixture was stirred for 4 d at ambient temperature. Water (400 mL) was added and it was extracted with EtOAc (3 × 50 mL). The combined organic layers were washed with Na<sub>2</sub>S<sub>2</sub>O<sub>3</sub> solution (1 M, 3 × 25 mL), brine (25 mL) and dried over Na<sub>2</sub>SO<sub>4</sub>. The solvent was evaporated under reduced pressure to yield 1.49 g of crude acid **S10**. By checking with LC-MS, desired product **S10** as well as the corresponding thiol **S9** were detected. Therefore, the alkylation procedure was repeated. The crude product was suspended in NaOH (2 M, 30 mL) and a solution of chloroacetic acid (813 mg, 8.60 mmol) in water (3 mL) was added and the reaction mixture was stirred at 60 °C for 2 h. Na<sub>2</sub>S<sub>2</sub>O<sub>3</sub> solution (1 M, 2 mL) was added and the mixture was stirred for another hour at 60 °C. After acidifying with concentrated HCl to pH 1, it was extracted with EtOAc (3 × 25 mL), the organic layer was washed with brine, dried over Na<sub>2</sub>SO<sub>4</sub> and the solvent was removed under reduced pressure. The residue was purified by chromatography (EA:Hx:MeOH, 1:1:0 → 1:1:1) to yield **S10** as a pale yellow oil (413 mg, 1.60 mmol, 24% over 3 steps).

**<sup>1</sup>H-NMR** (CDCl<sub>3</sub>, 400 MHz): δ (ppm) = 7.14 (d, *J* = 8.7 Hz, 1H), 6.63 (d, *J* = 8.7 Hz, 1H), 3.94 (s, 3H), 3.86 (s, 3H), 3.85 (s, 3H), 3.59 (s, 2H); **<sup>13</sup>C-NMR** (CDCl<sub>3</sub>, 100 MHz): δ (ppm) = 175.3,

154.5, 153.6, 142.8, 128.0, 119.0, 107.8, 61.3, 61.1, 56.2, 37.0;  $R_f$  = 0.68 on EA:Hx:MeOH, 1:1:1; ESI<sup>+</sup> HRMS for C<sub>11</sub>H<sub>15</sub>O<sub>5</sub>S<sup>+</sup>: calcd. m/z 259.29545, found m/z 259.06355.

#### 4-Methoxy-3,5-dimethylbenzaldehyde (**S12**)



4-Hydroxy-3,5-dimethylbenzaldehyde (600 mg, 3.99 mmol, 1.00 equiv) and an excess of K<sub>2</sub>CO<sub>3</sub> were suspended in dry acetone. Iodomethane (1 mL, 16.00 mmol, 4.01 equiv) was added and the reaction mixture was stirred for 12 h at ambient temperature. The solvent was removed under reduced pressure. After addition of water (20 mL), the mixture was extracted with ethyl acetate (3 × 30mL), the combined organic layers were washed with brine, dried over Na<sub>2</sub>SO<sub>4</sub> and the solvent was removed under reduced pressure to yield **S12** as a colourless oil (630 mg, 3.84 mmol, 96%)

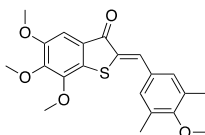
The spectral data match the literature.[5]

<sup>1</sup>H-NMR (CDCl<sub>3</sub>, 400 MHz): δ (ppm) = 9.87 (s, 1H), 7.55 (s, 2H), 3.77 (s, 3H), 2.34 (s, 6H);

<sup>13</sup>C-NMR (CDCl<sub>3</sub>, 100 MHz): δ (ppm) = 191.8, 162.5, 132.2, 132.1, 130.8, 59.8;

$R_f$  = 0.29 on EA:Hx, 1:2.4.

#### 5,6,7-Trimethoxy-2-(4-methoxy-3,5-dimethylbenzylidene)benzo[*b*]thiophen-3(2*H*)-one (**HITub-6**)



By Standard Procedure E, acid **S10** (75 mg, 0.29 mmol, 4.75 equiv) was stirred with Eaton's reagent for 1 h. After extraction, aldehyde **S12** (10.0 mg, 0.06 mmol, 1.00 equiv) was added to crude **S11**. The mixture was stirred for 12 h. The crude product was purified by chromatography (EA:Hx, 1:10 → 1:2.4) to yield **HITub-6** as a yellow solid (8.8 mg, 0.02 mmol, 40%).

<sup>1</sup>H-NMR (CDCl<sub>3</sub>, 400 MHz): δ (ppm) = 7.84 (s, 1H), 7.39 (s, 2H), 7.23 (s, 1H), 4.01 (s, 3H), 3.99 (s, 3H), 3.90 (s, 3H), 3.75 (s, 3H), 2.34 (s, 6H); <sup>13</sup>C-NMR (CDCl<sub>3</sub>, 100 MHz): δ

(ppm) = 188.1, 159.1, 153.1, 148.3, 147.6, 134.0, 133.1, 132.1, 132.0, 130.1, 129.5, 126.0, 104.4, 61.4, 61.2, 59.9, 56.6, 16.4;  $R_f$  = 0.36 on EA:Hx, 1:2.4; EI HRMS for C<sub>21</sub>H<sub>22</sub>O<sub>5</sub>S: calcd. m/z 386.4620 m/z, found m/z 386.1187.

## **Part B: photocharacterisation in vitro**

### **UV-vis spectrophotometry of bulk samples**

Absorption spectra in cuvette ("UV-vis") were acquired on a Varian CaryScan 60 (1 cm pathlength). For photoisomerisation measurements, Hellma microcuvettes (108-002-10-40) taking 500  $\mu$ L volume to top of optical window were used with test solution such that the vertical pathlength of the isomerisation light is less than 7 mm to the bottom of the cuvette window. Measurements were performed as stated individually. All photoisomerisations and relaxation rate measurements were performed at room temperature. "Star" LEDs (H2A1-models at 375, 450, 505, 515 and 530 nm from Roithner Lasertechnik) were used for photoisomerisations in the cuvette that were also predictive of what would be obtained in LED-illuminated cell culture. For all photoswitching studies the samples were illuminated by shining through the optical beam of the microcuvette, with additional illumination periods at the same wavelength used to verify that PSS had indeed been reached (no further evolution of the spectrum).

### **PSS spectra of the HITubs**

**HITubs** show reliable and robust reversible switching in polar aprotic solvents. Samples containing 100% *Z* isomer (from incubation in the dark at 60 °C, Figures S1 and 3) are photoswitched to a PSS with a majority of *E* isomer after saturating illumination with 450 nm; subsequent illumination with 530 nm photoisomerizes back to a PSS favouring the *Z* isomer (typically almost 100% reached). We observed that **HITub-1** could be photoswitched in slightly acidified DMSO (Figure S1a) but did not show bulk photoswitching in neutral DMSO presumably due to pH-dependent fast relaxation as discussed below.

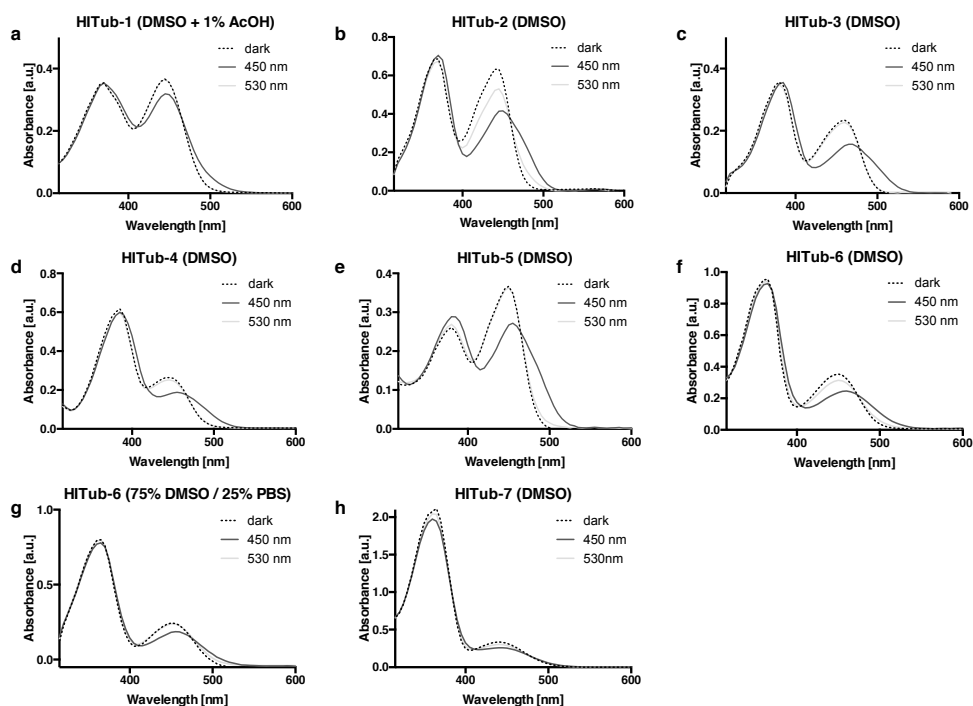


Figure S1: PSS absorption spectra of the **HITubs** at a concentration of 25  $\mu\text{M}$  after incubation at 60  $^{\circ}\text{C}$  in the dark and after saturating illumination with 450 and 530 nm, respectively. All spectra in DMSO unless stated otherwise.

### Solvent- and pH-dependency of photoisomerisability and relaxation rate

Addition of acid does not alter the absorption spectra or photoswitchability of **HITub-4** (Figure S2a,b). Under basic conditions however a significant hyperchromic and bathochromic shift of the absorption maximum (and to abolition of photoswitchability) is observed (Figure S2c,d). This is equally true for all **HITubs** bearing a *para*-hydroxy group on the stilbene moiety (data only shown for **HITub-4**; Figure S2c,d). We presume this results from deprotonation of the *p*-hydroxy group and resonance that substantially favours a quinoidal species, in which the photoswitchable C=C double bond of the hemithioindigo form is now tautomerised to a single bond, leading to free rotation and preventing photoswitchability. In neutral or acidic aqueous media, where the presumed quinoidal form is not present (Figure S2e-f), still no bulk photoisomerisation was observed under the applied conditions, which we presume is caused by very fast relaxation to the thermodynamically preferred *Z* isomer in aqueous media.[6]

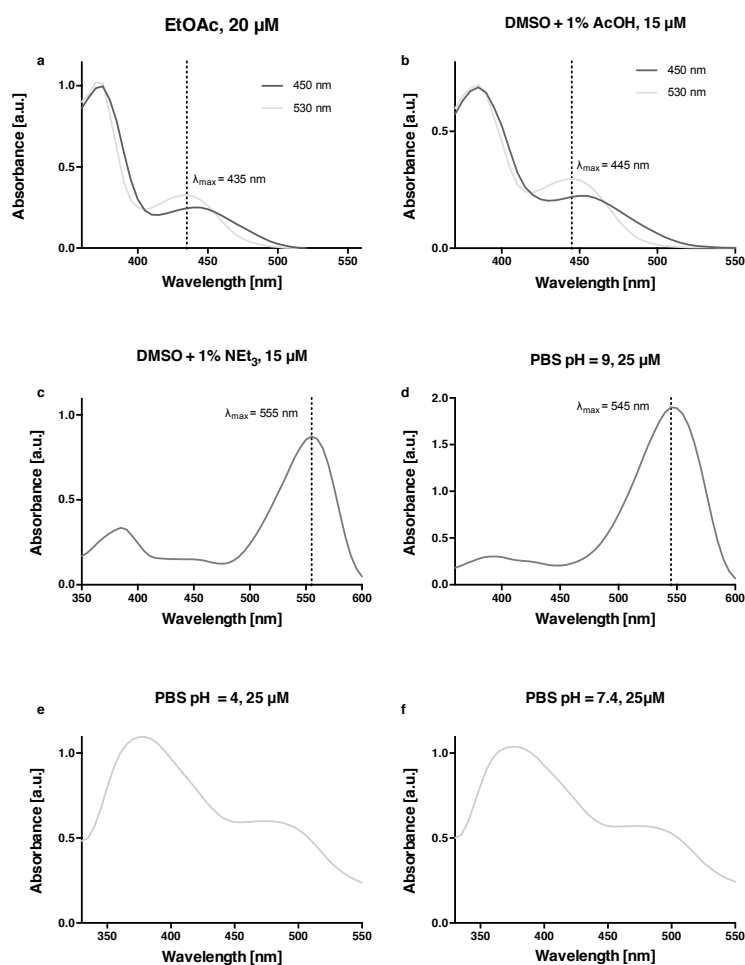


Figure S2: (a, b) Absorption spectra of **HITub-4** after saturating illumination with 450 (blue) and 530 nm (green) in neutral or acidified polar aprotic solvents, see also Fig S1d. (c) **HITub-4** photoswitchability could not be observed in basified aprotic media. (d – f) **HITub-4** photoswitchability could not be observed in aqueous media mixtures (75% DMSO / 25% PBS at the indicated pH).

The thermal relaxation half-life of **HITub-4** was measured at around 40 s in neutral polar aprotic solvents DMSO and EtOAc (Figure 3d and S3a) and was only slightly faster in acidified DMSO (Figure S3b). To bridge the gap towards determining a half-life in aqueous media, we measured relaxation in polar protic EtOH (Figure S3c) where the *E*-**HITub-4** thermal half-life is decreased to around 800 ms. In order to compare its performance to that of a similar *para*-hydroxy-substituted azobenzene, we attempted cuvette measurements of the thermal half-life of 4'-hydroxy-3,4,5-trimethoxyazobenzene (prepared according to literature [7]). However, neither in water nor even in DMSO could we observe that azobenzene's bulk photoisomerisation in cuvette, i.e. any spectral reversion was complete in < 12.5 ms (data not

shown) although we presume its half-life is orders of magnitude smaller as literature suggests [8]. Therefore, we concluded that the use of the HTI scaffold in this way can significantly slows spontaneous relaxation of resonance- or tautomerism-capable substituents as compared to cognate azobenzenes, and we considered there would be a chance to observe HTI isomer-dependent bioactivity in the heterogeneous cellular milieu when we applied photoswitching pulses faster than the timescale of spontaneous relaxation in aprotic media.

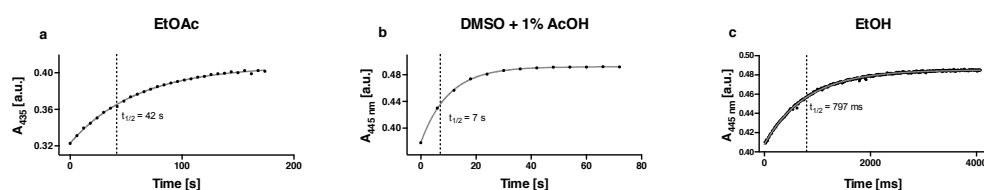


Figure S3: Thermal relaxation of **HITub-4** at 25 °C (a) in EtOAc, (b) in acidified DMSO and (c) in EtOH.

In these experiments, the bulk photoswitchability of *para*-hydroxy **HITub-4** was therefore confirmed in aprotic media, although not observed in protic cosolvent-aqueous media. This later seemed paradoxical when faced with its clearly photoswitchable cellular bioactivity profile. However, we note that (1) the ca. 3–4 fold biological photoswitchability index (difference between 450 nm-lit and dark-state bioactivity) of **HITub-4** and of other *para*-hydroxy **HITubs** matches closely the ca. 3.3-fold cell-free change of bioactive *Z*-isomer concentration going from dark/530 nm (100% / > 98% *Z*) to 450 nm (ca. 32% *E*) conditions, seen in PSS measurements in aprotic media; (2) these biological and concentration indices are identical to those measured for non-*para*-hydroxy **HOTubs**[3] that are metastable in aqueous media; (3) the solubility of **HITub-4** in pure water is very low (approx. 60 nM in distilled water, unpublished data) and it is rapidly extracted from aqueous phase into organic solvent (the limitations associated to hydrophobicity / poor solubility for further studies, such as in vivo work, are common for the vast majority of microtubule modulators of this binding site class and can be overcome by introducing water-soluble prodrug designs as we have previously shown for azocombretastatins [9]).

We theorise therefore that (a) *para*-hydroxy **HITubs** are *not* photoswitched in extracellular aqueous solution but remain as *Z* isomers there; (b) **HITubs** accumulate mainly in aprotic environments in the cell, presumably lipid membranes and vesicles, slowly exchanging across intervening (unfavoured) aqueous environments and thereby also partitioning onto hydrophobic domains of carrier protein (including binding to the colchicine site of tubulin, for active compounds); (c) under biological assay conditions the overall (*Z* + *E*) **HITub** concentration in cellular lipid environments reaches equilibrium with the extracellular applied concentration, and due to the unfavoured partitioning into water, the lipid cellular environments act as a barrier to isomer-specific equilibration of *Z*-**HITub** concentration across the membrane

between extracellular and intracellular aqueous environments; therefore (d) the *para*-hydroxy **HITub** located in aprotic environments can be photoswitched to reach its PSS there (e.g., 70:30 *E:Z* under 450 nm) while the aqueous intracellular *Z*-**HITub** concentration quickly equilibrates with this new reservoir concentration of *Z*-**HITub**. Thereby changes to the lipid reservoir *E:Z* ratio of the **HITub** (by photoequilibration) modify the intracellularly-available *Z*-**HITub** concentration that can bind tubulin, independent of the speed of *E* to *Z* relaxation in aqueous media. We have not found similar analyses in the literature of photopharmaceuticals, but we believe this principle may be found to apply in the case of other stable-isomer-active fast-relaxing photopharmaceuticals.[10]

### **Part C: Biochemistry and cellular biology**

**General cell culture:** HeLa cells were maintained under standard cell culture conditions in Dulbecco's modified Eagle's medium (DMEM; PAN-Biotech: P04-035550) supplemented with 10% fetal calf serum (FCS), 100 U/mL penicillin and 100 U/mL streptomycin. Cells were grown and incubated at 37 °C in a 5% CO<sub>2</sub> atmosphere. Cells were typically transferred to phenol red free medium prior to assays (DMEM; PAN-Biotech: P04-03591). Compounds were applied using a minimum of co-solvent, typically 1% DMSO and were added via a D300e digital dispenser (Tecan). For assays, cells were either incubated under dark conditions (indicating that compounds were set to the all-*Z* state by thermal relaxation of the DMSO stocks at 60 °C overnight, applied while working under red-light conditions and then incubated in lightproof boxes) or lit conditions (under pulsed illumination at 450 or 530 nm using a home-made LED lighting system). "Lit" timing conditions were 75 ms pulses applied every 15 s. We controlled for unspecific phototoxicity induced by the illumination setup by including an untreated and illuminated sample in every cellular assay.

**Resazurin assay:** Mitochondrial diaphorase activity in HeLa cell lines was quantified by spectrophotometrically measuring the reduction of resazurin (7-hydroxy-3*H*-phenoxazin-3-one 10-oxide) to resorufin. 5,000 cells/well were seeded on 96-well microtitre plates. After 24 h, cells were treated with **HITubs**, shielded from ambient light with light-proof boxes, and exposed to the appropriate light regimes. Following 45 h of treatment, cells were incubated with 20 µL of 0.15 mg/mL resazurin per well for 3 hours at 37°C. The resorufin fluorescence (excitation 544 nm, emission 590 nm) was measured using a FLUOstar Omega microplate reader (BMG Labtech). Results are represented as percent of untreated control (reading zero was assumed to correspond to zero viable cells) and represented as mean of at least three independent experiments with SD.

**Cell cycle analysis:** Following 24 h of treatment with **HITubs** under the indicated light regime, cells were harvested and fixed in ice-cold 70% ethanol and incubated in a staining solution [2% DNase-free RNase A 10 mg/mL, 0.1 % Triton X-100 and 2 mg/mL propidium iodide (PI)]



for 30 min at 37 °C. Following the PI staining, cells were analyzed by flow cytometry using an LSR Fortessa (Becton Dickinson) run by BD FACSDiva 8.0.1 software. The cell cycle analysis was subsequently performed using FlowJo-V10 software (Tree Star Inc.). Results from one representative experiment are shown as a histogram. Quantification from gating on the respective histograms is shown as percent of live/singlet/PI-positive parent population per cell cycle phase across different concentrations of the compound. Every experiment was performed independently and in technical triplicates at least three times with a mean of 14,000 PI-positive singlet cells analyzed per replicate.

### Resazurin antiproliferation assays

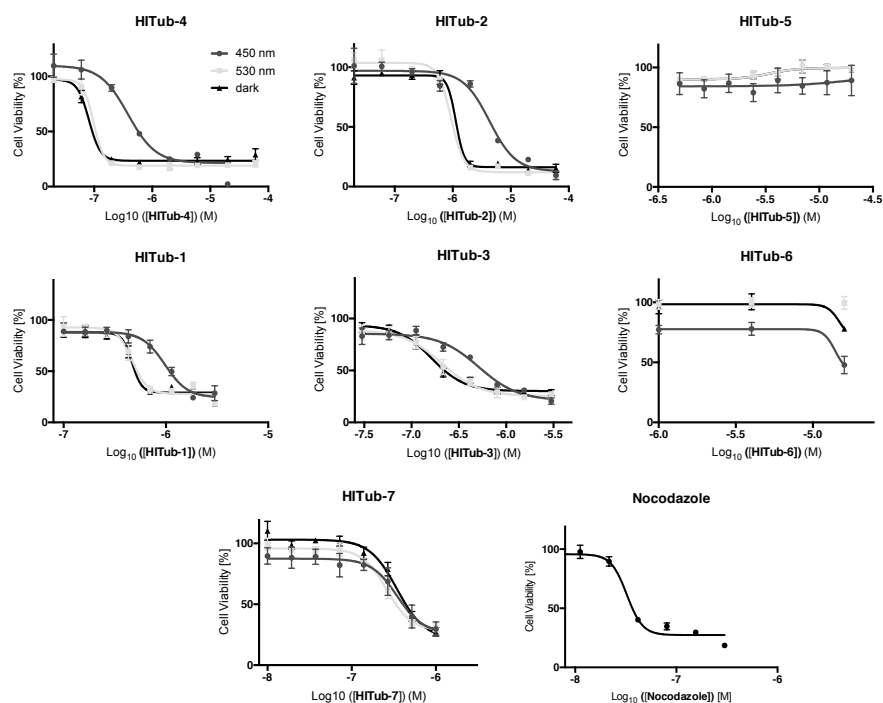


Figure S4: Representative results from Resazurin assays for **HITubs**. HeLa cells were treated with the compounds for 48 h under dark or lit (530 nm, 450 nm) conditions. Nocodazole was used as a positive reference to show antiproliferative effect in cells via microtubule depolymerisation leading towards cell death.

### In vitro tubulin polymerisation assay

A **HITub-4** DMSO stock was diluted using 10% DMSO in BRB80 to reach 0.5 mM. This was mixed 1:1 with 100 mM GTP solution (in water) at room temperature. 4  $\mu$ L of this mixture were spiked into ice-cold MAP-rich tubulin in BRB80 buffer (96  $\mu$ L, 2 mg/mL). The sample was transferred to a quartz microcuvette held at 37 °C in a UV-vis spectrophotometer, and was then monitored for absorbance (= turbidity) changes due to polymerisation over 20 min. A Cary 60 UV-vis spectrophotometer (Agilent Technologies) run by Cary WinUV software (version 5.0.0.999, Agilent Technologies) was used with temperature control achieved by a Cary single

cell Peltier accessory (Agilent Technologies). Absorbance data were acquired every 15 s. Generated data were processed and visualised using GraphPad Prism 6 software. Curve heights were adjusted to 0 at time zero, to account for differences in sample preparation. Since **HITub-4** cannot be isomerised in this monophasic cell-free solvent system, we did not expect to be able to observe a difference between **HITub-4** antipolymerisation activity in the dark or after 450 nm illumination, and indeed this was shown experimentally; therefore, only dark data (indicating strong polymerisation inhibition) are shown (Figure S5). We left it to cellular assays (complex multiphasic environment) to test isomer-dependent differences in bioactivity.

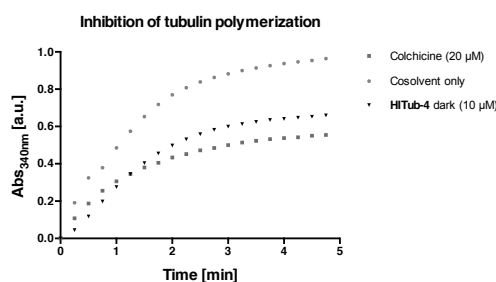


Figure S5: **HITub-4** shows *in vitro* inhibition of tubulin polymerisation (black triangle). Turbidimetric *in vitro* polymerisation assay; greater absorbance corresponds to a greater degree of polymerisation.

### Immunofluorescence imaging of microtubule network structure

For fixed cell imaging (Figure 5, Figure S6), HeLa cells were seeded directly on glass coverslips in 24-well plates and treated with **HITubs**, either in the dark (all-*Z*) or under illumination by the LED array system using 450 nm LEDs (max. 70% *E*) pulsed at 75 ms “on” every 15 s, for 24 h. Then the coverslips were washed with extraction buffer (80 mM PIPES pH 6.8; 1 mM MgCl<sub>2</sub>, 5 mM ethylene glycol tetra-acetic acid (EGTA) dipotassium salt and 0.5% Triton X-100) for 30 s at 37°C to remove monomeric and dimeric tubulin subunits and fixed for 10 min with a final concentration of 0.5% glutaraldehyde or else 6 min in ice-cold methanol; the glutaraldehyde-fixed cells were then quenched for 7 min with 0.1% NaBH<sub>4</sub> in PBS. Coverslips were washed with PBS twice and then blocked with PBS containing 10% FCS and 0.3% Tween-20 for 30 min at room temperature. For immunofluorescence staining of microtubules, the cells were treated with primary antibody (rabbit anti-alpha-tubulin; abcam ab18251; 1:400 in blocking buffer) for 1 h and then washed with PBS before application of the secondary antibody (donkey anti-rabbit Alexa Fluor 488; abcam ab150073; 1:400 in blocking buffer) for 1 h. The coverslips were mounted on microscopy glass slides using Roti®-Mount FluorCare DAPI (Carl Roth) and imaged with a Zeiss LSM 510, LSM 710 or SP5 confocal microscope. Image processing was performed using FIJI image analysis platform[11].

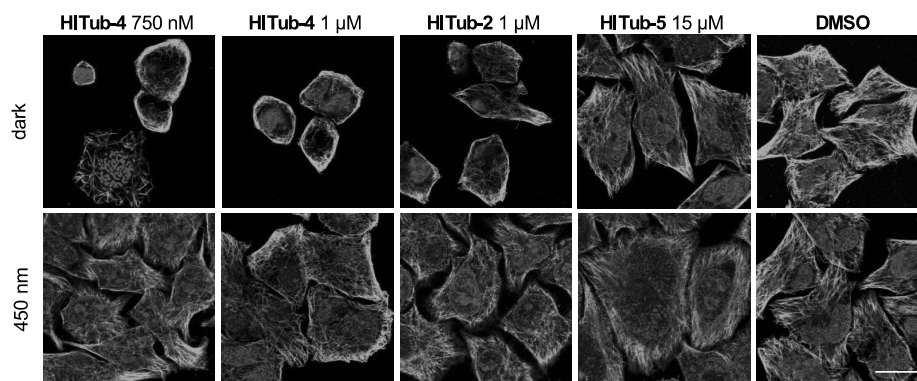


Figure S6: Immunofluorescence imaging of cells treated under lit/dark conditions with **HITub-4**, **HITub-2** and **HITub-5**, or the corresponding DMSO cosolvent controls. Microtubules of HeLa cells were immunostained with anti- $\alpha$ -tubulin (green), nuclei stained with DAPI (blue), scale bar = 20  $\mu$ m; some images were shown in Figure 5.

### Cell cycle analysis

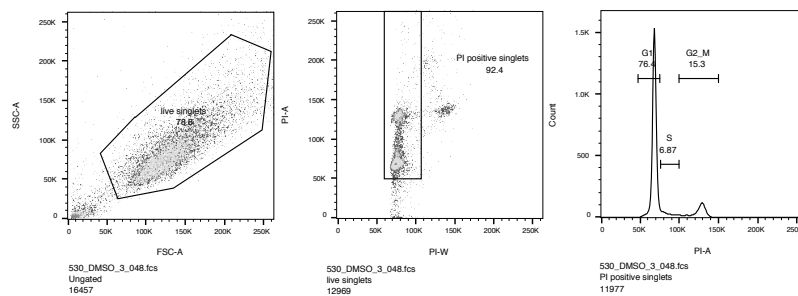


Figure S7: Representative gating strategy applied to all datasets from flow cytometric cell cycle analysis. Live singlets were determined from SSC/FSC plot, PI-positive singlets (mean of 14,000 per replicate) were then plotted as histogram and cell cycle phase gates were set to accommodate for minimal peak shifts across all samples.

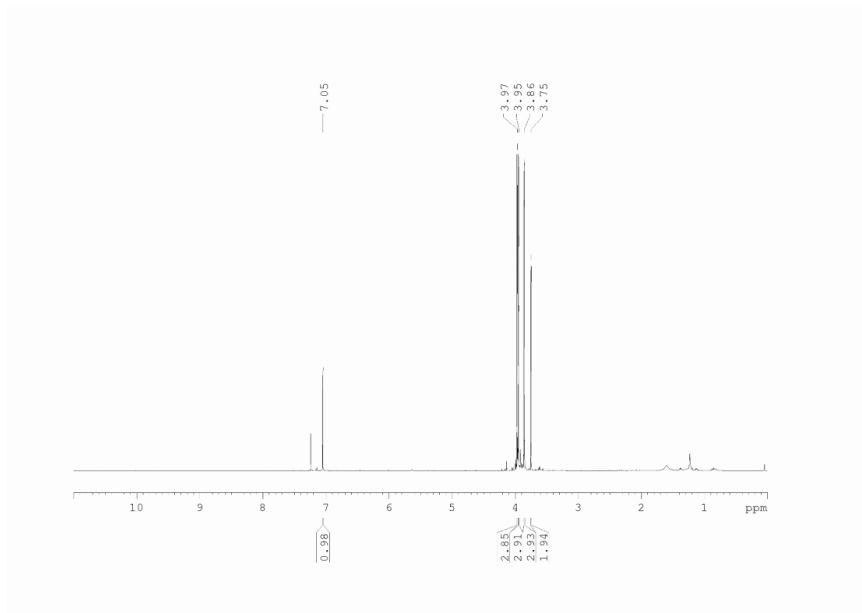
## **Supplemental references**

1. Gottlieb, H. E.; Kotlyar, V.; Nudelman, A. *J. Org. Chem.* **1997**, *62* (21), 7512-7515.
2. Suresh Kumar, A.; Thulasiram, B.; Bala Laxmi, S.; Rawat, V. S.; Sreedhar, B. *Tetrahedron* **2014**, *70* (36), 6059-6067.
3. Sailer, A.; Ermer, F.; Kraus, Y.; Lutter, F. H.; Donau, C.; Bremerich, M.; Ahlfeld, J.; Thorn-Seshold, O. *Chembiochem* **2019**, *20* (10), 1305-1314.
4. Castanet, A.-S.; Colobert, F.; Broutin, P.-E. *Tetrahedron Lett.* **2002**, *43* (29), 5047-5048.
5. Orito, K.; Hatakeyama, T.; Takeo, M.; Suginome, H. *Synthesis* **1995**, *1995* (10), 1273-1277.
6. Kink, F.; Collado, M. P.; Wiedbrauk, S.; Mayer, P.; Dube, H. *Chemistry* **2017**, *23* (26), 6237-6243.
7. Sutariya, P. G.; Modi, N. R.; Pandya, A.; Rana, V. A.; Menon, S. K. *RSC Advances* **2013**, *3* (13).
8. Garcia-Amorós, J.; Sánchez-Ferrer, A.; Massad, W. A.; Nonell, S.; Velasco, D. *Phys. Chem. Chem. Phys.* **2010**, *12* (40), 13238-13242, 10.1039/C004340K.
9. Borowiak, M.; Nahaboo, W.; Reynders, M.; Nekolla, K.; Jalinot, P.; Hasserodt, J.; Rehberg, M.; Delattre, M.; Zahler, S.; Vollmar, A.; Trauner, D.; Thorn-Seshold, O. *Cell* **2015**, *162* (2), 403-411.
10. Eisel, B.; Hartrampf, F. W. W.; Meier, T.; Trauner, D. *FEBS Lett* **2018**, *592* (3), 343-355.
11. Schindelin, J.; Arganda-Carreras, I.; Frise, E.; Kaynig, V.; Longair, M.; Pietzsch, T.; Preibisch, S.; Rueden, C.; Saalfeld, S.; Schmid, B.; Tinevez, J. Y.; White, D. J.; Hartenstein, V.; Eliceiri, K.; Tomancak, P.; Cardona, A. *Nat Methods* **2012**, *9* (7), 676-82.

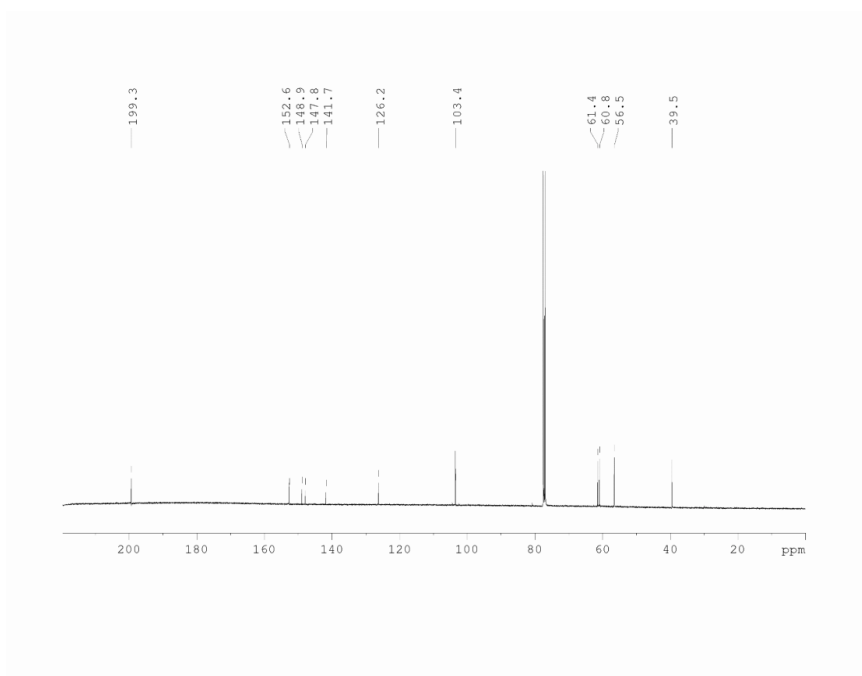
## Part D: NMR spectra

### 5,6,7-Trimethoxybenzo[*b*]thiophen-3(2*H*)-one (S3)

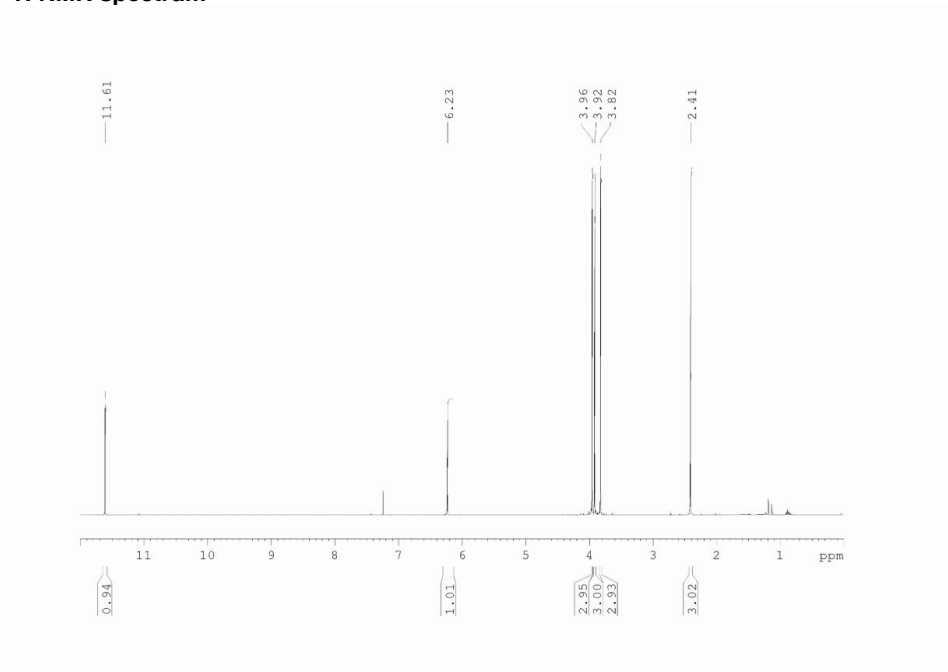
#### <sup>1</sup>H-NMR spectrum



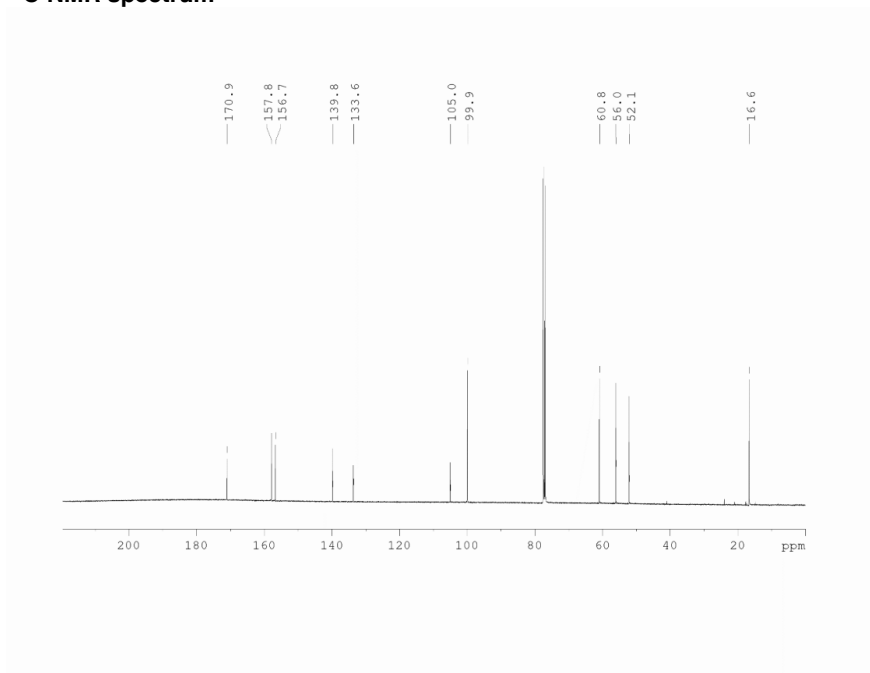
#### <sup>13</sup>C-NMR spectrum



**Methyl 2-hydroxy-3,4-dimethoxy-6-(methylthio)benzoate (S6)**  
**<sup>1</sup>H NMR spectrum**

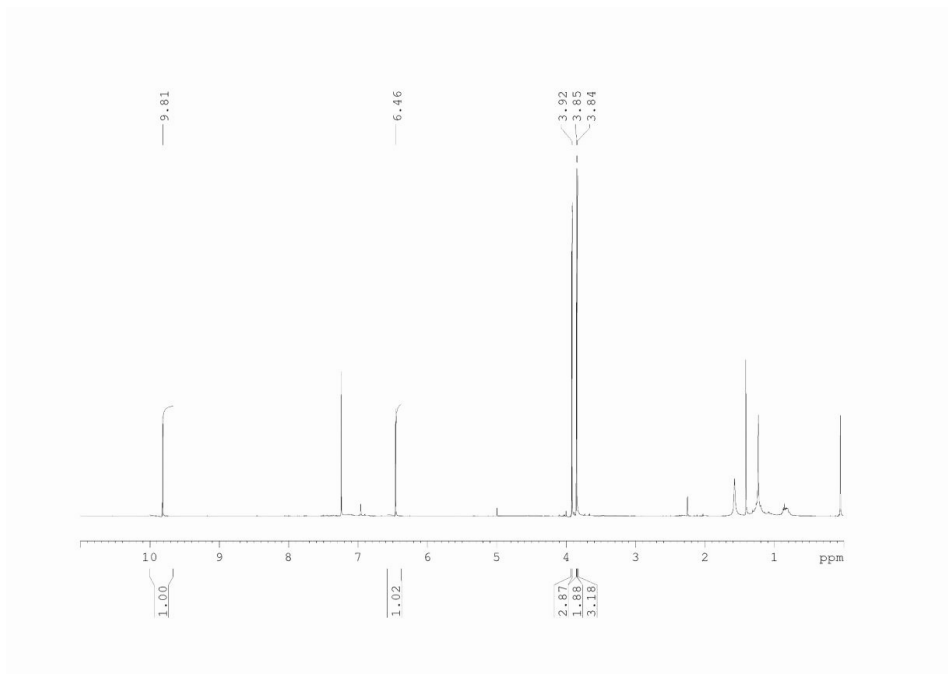


**<sup>13</sup>C NMR spectrum**

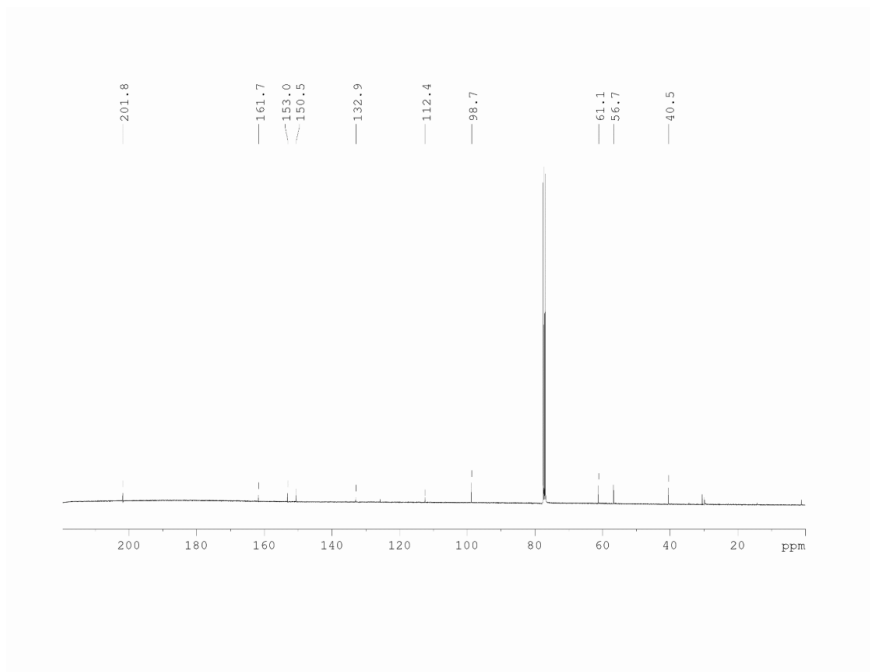


4-Hydroxy-5,6-dimethoxybenzo[*b*]thiophen-3(2*H*)-one (S7)

<sup>1</sup>H NMR spectrum

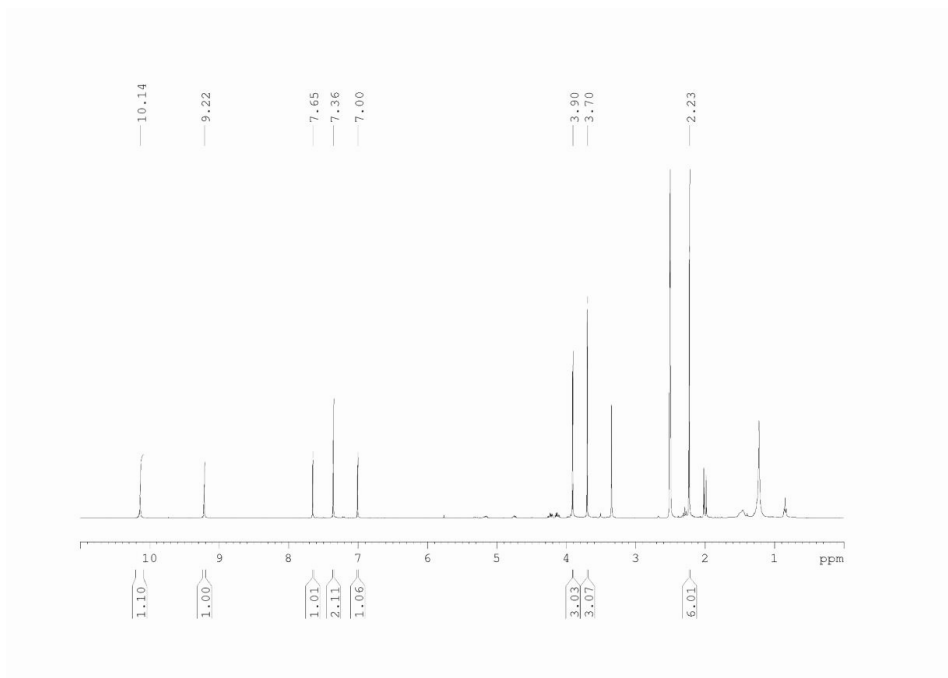


<sup>13</sup>C NMR spectrum

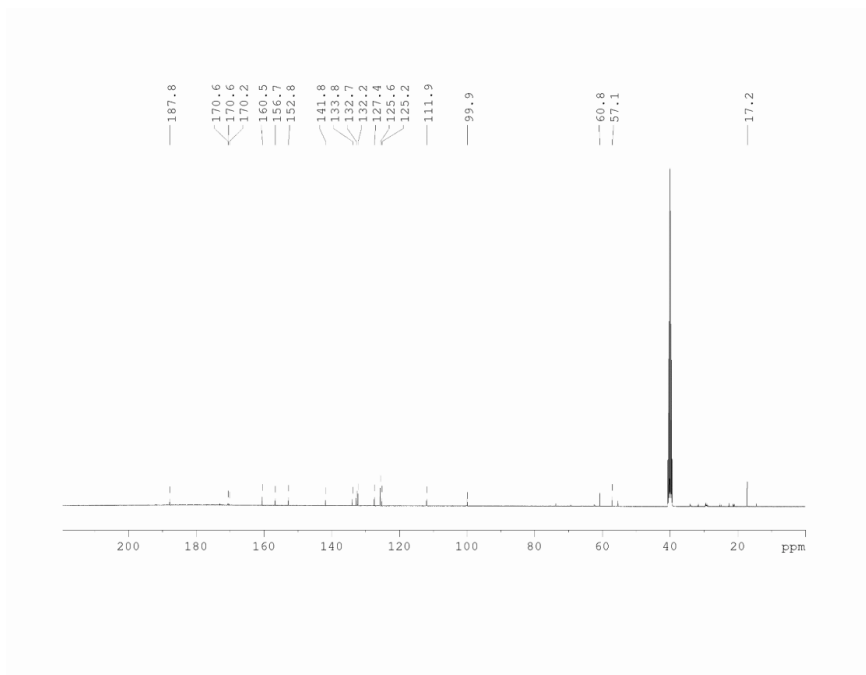


**4-Hydroxy-2-(4-hydroxy-3,5-dimethylbenzylidene)-5,6-dimethoxybenzo[b]thiophen-3(2H)-one (HITub-1)**

**<sup>1</sup>H NMR spectrum**



**<sup>13</sup>C NMR spectrum**





## **Supplementary Information Chapter 5: Photopharmaceutical Microtubule Stabilisers**

Licence

Reprinted with permission from: Adrian Müller-Deku, Joyce Meiring, Christina Loy, Yvonne Kraus, Constanze Heise, Rebekkah Bingham, Klara Jansen, Xiaoyi Qu, Francesca Bartolini, Lukas Kapitein, Anna Akhmanova, Julia Ahlfeld, Dirk Trauner & Oliver Thorn-Seshold, Photoswitchable paclitaxel-based microtubule stabilisers allow optical control over the microtubule cytoskeleton, *Nature Communications* **2020**, *11*, 4640. *Copyright by the author(s)*.

## **Supporting Information to:**

# **Photoswitchable microtubule stabilisers optically control tubulin cytoskeleton structure and function**

Adrian Müller-Deku<sup>1</sup>, Kristina Loy<sup>1</sup>, Yvonne Kraus<sup>1</sup>, Constanze Heise<sup>1</sup>, Rebekkah Bingham<sup>1</sup>, Julia Ahlfeld<sup>1</sup>, Dirk Trauner<sup>2,\*</sup>, Oliver Thorn-Seshold<sup>1,\*,#</sup>

1: Department of Pharmacy, Ludwig-Maximilians University, Butenandtstrasse 7, Munich 81377, Germany; 2: Department of Chemistry, New York University, 100 Washington Square East, New York NY 10003, United States of America.

\* Senior Authors

# Correspondence and requests for materials to O.T.-S. (oliver.thorn-seshold@cup.lmu.de)

ORCID: J.A. 0000-0002-4879-4159; D.T. 0000-0002-6782-6056;

O.T.-S. 0000-0003-3981-651X

## **Table of Contents**

<b>Part A: Chemistry</b> .....	<b>2</b>
Conventions.....	2
Standard Procedures.....	3
Azobenzene carboxylic acids.....	5
AzTaxes.....	13
Water-soluble model photoswitch carboxamides.....	23
Discussion of arylazopyrazole-dextran heterodimerisation (Liu et al., 2018).....	24
<b>Part B: Photocharacterisation <i>in vitro</i></b> .....	<b>25</b>
Materials and Methods.....	25
Thermally reversible and photoreversible photoisomerisation.....	25
Photostationary state (PSS) equilibria.....	27
PSS analysis.....	27
<b>Part C: Biochemistry: tubulin polymerisation <i>in vitro</i></b> .....	<b>29</b>
<b>Part D: Cell Biology</b> .....	<b>30</b>
Cell assay methods.....	30
Resazurin viability assay results for all compounds.....	32
FACS cell cycle analysis.....	33
Immunofluorescence imaging of microtubule network structure.....	33
<b>Supporting Information Bibliography</b> .....	<b>35</b>
<b>Part F: NMR Spectra</b> .....	<b>37</b>

## Part A: Chemistry

### **Conventions**

#### Abbreviations:

The following abbreviations are used: Boc – *tert*-butoxycarbonyl; brsm – based on recovered starting material; DCM: dichloromethane; DIPEA: diisopropylethylamine; DMF: dimethylformamide; DMSO: dimethylsulfoxide; EA: ethyl acetate; EDCI: 1-Ethyl-3-(3-dimethylaminopropyl)carbodiimide; Hex: distilled isohexane; HOBt: 1-hydroxybenzotriazole; Me: methyl; TFA: trifluoroacetic acid; PBS – phosphate buffered saline; T3P: propylphosphonic anhydride; wt% - percentage by weight.

#### Safety Hazards:

No remarkable safety hazards were encountered.

#### Reagents and Conditions:

Unless stated otherwise, (1) all reactions and characterisations were performed with unpurified, undried, non-degassed solvents and reagents, used as obtained, under closed air atmosphere without special precautions; (2) “hexane” used for chromatography was distilled from commercial crude isohexane fraction by rotary evaporation; (3) “column” and “chromatography” refer to manual flash column chromatography on Merck silica gel Si-60 (40–63  $\mu\text{m}$ ) unless otherwise specified; (4) procedures and yields are unoptimised; (5) yields refer to isolated chromatographically and spectroscopically pure materials; (6) all eluent and solvent mixtures are given as volume ratios unless otherwise specified, thus “1:1 Hex:EA” indicates a 1:1 mixture (by volume) of hexanes and ethyl acetate; (7) chromatography eluents e.g. “3:1  $\rightarrow$  1:1” indicate a stepwise or continual gradient of eluent composition.

#### Thin-layer chromatography (TLC):

TLC was run on 0.25 mm Merck silica gel plates (60, F-254), typically with Hex:EA eluents. All compounds carrying an azobenzene need no visualization on the TLC-plate but are clearly visible as colored spots (color range yellow to red). The presence of an azobenzene can be verified by exposure of the colored spot to TFA vapors, which transiently changes the color to shades of purple according to basicity. For further visualization UV light (254 nm) was used. TLC characterizations are abbreviated as  $R_f = 0.64$  (UV 254 nm, Hex:EA = 1:1).

#### Nuclear magnetic resonance spectroscopy (NMR):

Standard NMR characterisation was by  $^1\text{H}$ - and  $^{13}\text{C}$ -NMR spectra on an Avance III HD 400 MHz Bruker BioSpin or Bruker Ascend 400, or Avance III HD 500 MHz Bruker BioSpin ( $^1\text{H}$ : 400 MHz and 500 MHz,  $^{13}\text{C}$ : 101 MHz and 126 MHz). Chemical shifts ( $\delta$ ) are reported in ppm calibrated to residual non-perdeuterated solvent as an internal reference<sup>1</sup>. Peak descriptions singlet (s), doublet (d), triplet (t), quartet (q), multiplet (m) and broad (br) are used. Apparent multiplicities (resolved by 2D experiments or determined by complete spectral

assignment) are denoted by a tilde, eg. "appears as a triplet with apparent coupling constant  $J = 3$  Hz" is denoted ( $\sim t$ , 3 Hz). NMR spectra are given in Part F.

#### High resolution mass spectrometry (HRMS):

HRMS was performed by electron impact (EI) at 70 eV with a Thermo Finnigan MAT 95 or a Jeol GCmate II spectrometer; or electrospray ionization (ESI) with a Thermo Finnigan LTQ FT Ultra Fourier Transform Ion Cyclotron resonance mass spectrometer; as specified.

#### High-performance liquid chromatography coupled to mass spectrometry (LCMS):

Analytical high-performance liquid chromatography (HPLC) was performed on an Agilent 1100 SL coupled HPLC system with (a) a binary pump to deliver H<sub>2</sub>O:MeCN eluent mixtures containing 0.1% formic acid at a 0.4 mL/min flow rate, (b) Thermo Scientific Hypersil GOLD™ C18 column (1.9  $\mu$ m; 3  $\times$  50 mm) maintained at 25 °C, whereby the solvent front eluted at  $t_{ret} = 0.5$  min, (c) an Agilent 1100 series diode array detector, (d) a Bruker HCT Ultra mass spectrometer. Typical run conditions were a linear gradient of H<sub>2</sub>O:MeCN eluent composition from 90:10 through to 1:99, applied during the separation phase (first 5 min), then 0:100 for 2 min for flushing; the column was (re)equilibrated with 90:10 eluent mixture for 2 min before each run. Ion peaks from (positive/negative mode) are reported as (+/-) with units Th (m/z). Thus "LCMS(+):  $t_{ret} = 5.60$  &  $5.82$  min, each 419 Th = [MH]<sup>+</sup>" indicates LCMS under the standard run conditions with ESI ionisation giving two positive ion peaks eluting at 5.60 and 5.82 min retention times, each at  $m/z = 419$  Th, attributed as the protonated molecular ion. Unless stated otherwise, all reported peaks in the positive mode were [MH]<sup>+</sup> peaks.

#### **Standard Procedures**

Where Standard Procedures were used in synthesis, unless stated otherwise, the amounts of reactants/reagents employed were implicitly adjusted to maintain the same molar ratios as in the given Procedure, and no other alterations from the Standard Procedure (eg. reaction time, extraction solvent, temperature) were made, unless stated otherwise.

#### Standard Procedure A: Azo coupling with a phenol partner

A flask was charged with the aniline coupling partner (1.0 eq) and MeOH (3 mL/mmol). Aqueous HCl (2 M, 6.0 eq) was added. The reaction mixture was cooled to 0 °C and a 2 M aqueous solution of NaNO<sub>2</sub> (1.1 eq) was added dropwise. It was allowed to stir for 30 min. A solution of the phenol coupling partner (1.1 eq) in MeOH (4 mL/mmol) and 0.5 M aqueous HK<sub>2</sub>PO<sub>4</sub> (4 mL/mmol) was prepared at 0 °C. The diazonium solution was added dropwise onto the phenol mixture. The pH was maintained between 9-10 by adding aq. KOH (1 M). Upon completion of the addition the reaction mixture was allowed to stir for 1 h in the cold. The reaction progress was monitored by LCMS/TLC analysis. The reaction was quenched by the adjustment of the pH to pH 4-6 with 2 M aqueous HCl and extracted with EA (3  $\times$  20 mL/mmol). The combined organic phases were dried with Na<sub>2</sub>SO<sub>4</sub>, filtrated and concentrated. The crude product was purified by flash chromatography using a Hex:EA gradient.

Standard Procedure B: Azo coupling with a dialkylaniline partner

A flask was charged with the aniline coupling partner (1.0 eq) and MeOH (3 mL/mmol). Aqueous HCl (2 M, 6.0 eq) was added. The reaction mixture was cooled to 0 °C and a 2 M aqueous solution of NaNO<sub>2</sub> (1.1 eq) was added dropwise. It was allowed to stir for 30 min. Acetic acid (3 mL/mmol) followed by the dialkylaniline coupling partner (1.5 eq) were added neat. Sodium acetate (10.0 eq) was added portionwise. Upon completion of the addition the reaction mixture was allowed to stir for 1 h in the cold. The reaction progress was monitored by LCMS/TLC analysis. The reaction was quenched by neutralization with KOH solution (1 M) and extracted with EA (3 × 20 mL/mmol). The combined organic phases were dried with Na<sub>2</sub>SO<sub>4</sub>, filtrated and concentrated. The crude product was purified by flash chromatography using a Hex:EA gradient.

Standard Procedure C: Methylation of a *para*-hydroxy azobenzene

A flask was charged with the respective azobenzene compound and acetone (5 mL/mmol) was added. Potassium carbonate (5.0 eq) was added. Iodomethane (3.00 eq) was added dropwise. The reaction mixture was heated to 50 °C for typically 5 h. The reaction progress was monitored by LCMS/TLC analysis. The reaction was quenched by the addition of water (20 mL/mmol) and extracted with EA (3 × 20 mL/mmol). The combined organic phases were dried with Na<sub>2</sub>SO<sub>4</sub>, filtrated and concentrated. The crude product was purified by flash chromatography on silica using a Hex:EA gradient.

Standard Procedure D: Hydrolysis of an azobenzenecarboxylate ester

A flask was charged with the respective azobenzenecarboxylate ester and MeOH (5 mL/mmol) was added. Potassium hydroxide (5.0 eq) was added neat. The reaction mixture was heated to 65 °C for 12 h. The reaction progress was monitored by LCMS/TLC analysis. Upon completion the reaction was quenched with water (20 mL/mmol), neutralized with 2 M aqueous KOH and extracted with EA (3 × 20 mL/mmol). The combined organic phases were dried with Na<sub>2</sub>SO<sub>4</sub>, filtrated and concentrated. Typically, no further purification was needed.

Standard Procedure E: Docetaxel deprotection and amide coupling

A flask was charged with docetaxel (16 mg, 20 μmol, 1.0 eq) and DCM (2 mL) and the solution stirred at 0 °C for 2 min. TFA (2 mL) was added and the mixture stirred at 0 °C for 1 hour. The solution was added into rapidly stirred sat. aq. NaHCO<sub>3</sub> (15 mL). Solid NaHCO<sub>3</sub> was added until all TFA was neutralized. The mixture was extracted with DCM (3 × 10 mL). The combined organic layers were washed with sat. aq. NaHCO<sub>3</sub> (10 mL), brine (10 mL), dried on Na<sub>2</sub>SO<sub>4</sub>, filtered and concentrated to a colourless crude foam (typically 10 mg, 15 μmol, 71%; LCMS(+): t<sub>ret</sub> = 4.71 min, 708 Th = [MH]<sup>+</sup>). The crude was dissolved in HPLC-grade DMF (2 mL). The azobenzene carboxylic acid (1.2 eq.) was dissolved in HPLC-grade DMF (1 mL), HOBt-H<sub>2</sub>O (2.5 eq) and EDCI (2.25 eq) were added and the solution stirred at room temperature for 5 min. A DMF (1 mL) solution of DIPEA (4.0 eq) was added dropwise and stirring continued for 10 min. The solution of crude deprotected docetaxel was added and the solution stirred for

12 h at room temperature, then poured into 10% aq. NaHCO<sub>3</sub> (20 mL) and extracted with DCM (3 × 10 mL). The combined organic layers were washed with sat. aq. NaHCO<sub>3</sub> (10 mL), sat. aq. LiCl (10 mL), brine (10 mL), dried on Na<sub>2</sub>SO<sub>4</sub>, filtered and concentrated to a yellow solid. Chromatography on silica with a iHex:EA= 7:3→1:1 then DCM:MeOH= 1:0→9:1 gradient couple typically separated the product fractions. These were combined, concentrated, and dried under high vacuum.

#### Standard Procedure F: Preparation of soluble azo derivatives for photocharacterization

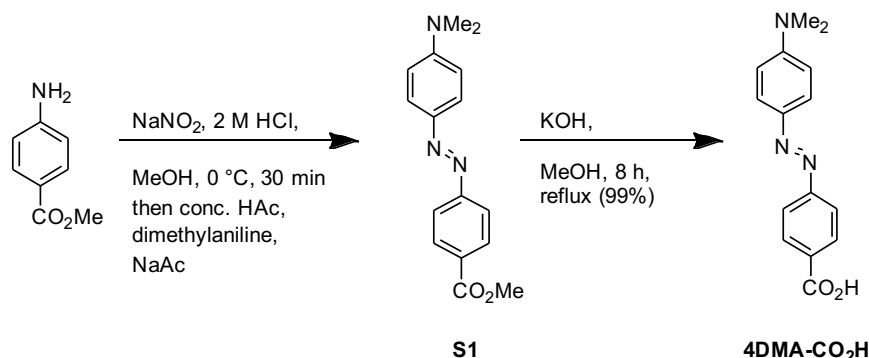
A flask was charged with the azobenzene carboxylic acid (1.0 eq) and DMF (25 mL/mmol) was added. Triethylamine (10.0 eq) was added. Diethanolamine (2.0 eq) dissolved in DMF (0.65 mL/mmol) was added to the reaction mixture. T3P (2.0 eq, ≥50 wt. % in EA) was added and the resulting solution was allowed to stir for 16 h at 25 °C. Progress of the reaction was monitored by LCMS. Upon completion the DMF was removed *in vacuo* and the crude product was purified by flash chromatography on silica using a DCM:MeOH gradient.

#### **Azobenzene carboxylic acids**

##### **4-(phenyldiazenyl)benzoic acid (4H-CO<sub>2</sub>H)**

Commercially available (CAS 1562-93-2).

##### **4-((4-(dimethylamino)phenyl)diazenyl)benzoic acid (4DMA-CO<sub>2</sub>H)**

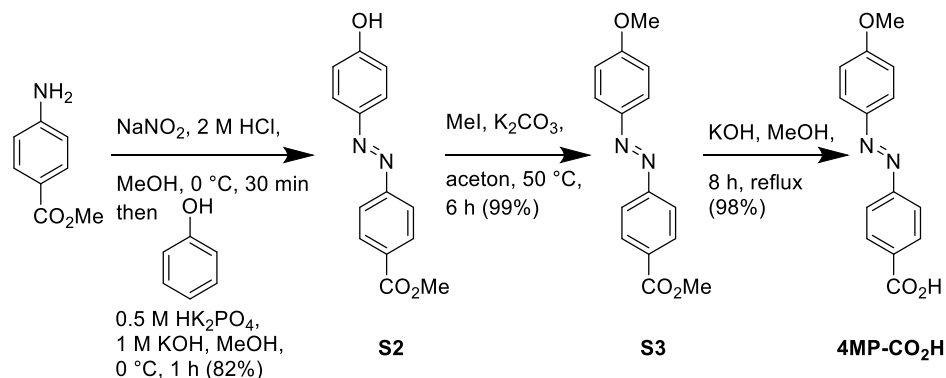


By standard procedure B, commercially available methyl 4-aminobenzoate (302 mg, 2.0 mmol, 1.0 eq) was reacted with dimethylaniline (364 mg, 3.0 mmol, 1.5 eq). After purification by flash chromatography (EA:iHex, 9:1 → 8:2) the desired product **methyl 4-((4-(dimethylamino)phenyl)diazenyl)benzoate (S1)** (224 mg, 0.80 mmol, 40%) was obtained as red solid. Spectral data matches literature<sup>2</sup>: <sup>1</sup>H NMR (400 MHz, chloroform-*d*) δ (ppm) = 8.19 – 8.10 (m, 2H), 7.96 – 7.82 (m, 4H), 6.79 – 6.73 (m, 2H), 3.94 (s, 3H), 3.11 (s, 6H). <sup>13</sup>C NMR (101 MHz, chloroform-*d*) δ (ppm) = 167.1, 156.3, 153.2, 144.0, 130.8, 130.4, 125.8, 122.3, 111.7, 52.5, 40.6. **LCMS(+)**: *t*<sub>ret</sub> = 4.7 min, 284 Th = [MH]<sup>+</sup>. **HRMS (EI)**: calc. for [C<sub>16</sub>H<sub>17</sub>O<sub>2</sub>N<sub>3</sub>]<sup>+</sup> = [M]<sup>+</sup>: 283.1321; found: 283.1314.

By standard procedure D, **S1** (100 mg, 0.35 mmol, 1.0 eq) was reacted to the desired product **4DMA-CO<sub>2</sub>H** (93 mg, 0.40 mmol, 98%) which was obtained as a red solid. Spectral data

matches literature<sup>2</sup>: **<sup>1</sup>H NMR** (400 MHz, DMSO-*d*<sub>6</sub>)  $\delta$  (ppm) = 8.13 – 8.02 (m, 2H), 7.89 – 7.78 (m, 4H), 6.92 – 6.79 (m, 2H), 3.08 (s, 6H). **<sup>13</sup>C NMR** (101 MHz, DMSO)  $\delta$  (ppm) = 166.9, 155.1, 153.0, 142.7, 130.9, 130.5, 125.3, 121.7, 111.6, 39.8. **LCMS(+)**:  $t_{\text{ret}}$  = 4.7 min, 270 Th = [MH]<sup>+</sup>. **HRMS (EI)**: calc. for [C<sub>15</sub>H<sub>15</sub>O<sub>2</sub>N<sub>3</sub>]<sup>+</sup> = [M]<sup>+</sup>: 269.1164; found: 269.1158.

#### 4-((4-methoxyphenyl)diazenyl)benzoic acid (4MP-CO<sub>2</sub>H)



By standard procedure A, commercially available methyl 4-amino benzoate (302 mg, 2.0 mmol, 1.0 eq) was reacted with phenol (207 mg, 2.2 mmol, 1.1 eq). After purification by means of flash chromatography (EA:iHex, 8:2 → 1:1) the desired product **methyl 4-((4-hydroxyphenyl)diazenyl)benzoate (S2)** (421 mg, 1.6 mmol, 82%) was obtained as an orange solid. Spectral data matches literature<sup>3</sup>: **<sup>1</sup>H NMR** (400 MHz, DMSO-*d*<sub>6</sub>)  $\delta$  (ppm) = 8.17 – 8.08 (m, 2H), 7.93 – 7.88 (m, 2H), 7.88 – 7.80 (m, 2H), 7.00 – 6.93 (m, 2H), 3.89 (s, 3H). **<sup>13</sup>C NMR** (101 MHz, DMSO-*d*<sub>6</sub>)  $\delta$  (ppm) = 165.7, 161.8, 154.8, 145.3, 130.6, 130.5, 125.4, 122.3, 116.1, 52.4. **LCMS(+)**:  $t_{\text{ret}}$  = 5.0 min, 257 Th = [MH]<sup>+</sup>. **HRMS (EI)**: calc. for [C<sub>16</sub>H<sub>17</sub>O<sub>2</sub>N<sub>3</sub>]<sup>+</sup> = [M]<sup>+</sup>: 256.0848; found: 256.0843.

By standard procedure C, **S2** (410 mg, 1.6 mmol, 1.0 eq) was reacted with methyl iodide (681 mg, 4.8 mmol, 3.0 eq). After purification by means of flash chromatography (EA:iHex, 9:1 → 7:3) the desired product **methyl 4-((4-methoxyphenyl)diazenyl)benzoate (S3)** (431 mg, 1.6 mmol, 99%) was obtained as an orange solid. Spectral data matches literature<sup>4</sup>: **<sup>1</sup>H NMR** (400 MHz, chloroform-*d*)  $\delta$  (ppm) = 8.21 – 8.14 (m, 2H), 7.95 (d, *J* = 9.0 Hz, 2H), 7.91 (d, *J* = 8.7 Hz, 2H), 7.03 (d, *J* = 9.0 Hz, 2H), 3.95 (s, 3H), 3.91 (s, 3H). **<sup>13</sup>C NMR** (101 MHz, chloroform-*d*)  $\delta$  (ppm) = 166.8, 162.8, 155.5, 147.2, 131.3, 130.7, 125.3, 122.5, 114.5, 55.8, 52.4. **LCMS(+)**:  $t_{\text{ret}}$  = 6.0 min, 271 Th = [MH]<sup>+</sup>. **HRMS (EI)**: calc. for [C<sub>15</sub>H<sub>14</sub>N<sub>2</sub>O<sub>3</sub>]<sup>+</sup> = [M]<sup>+</sup>: 270.1004; found: 270.0998.

By standard procedure D, **S3** (100 mg, 0.35 mmol, 1.0 eq) was reacted to the desired product **4-((4-(dimethylamino)phenyl)diazenyl)benzoic acid (4MP-CO<sub>2</sub>H)** (93 mg, 0.40 mmol, 98%) was obtained as orange solid. Spectral data matches literature<sup>5</sup>: **<sup>1</sup>H NMR** (400 MHz, DMSO-*d*<sub>6</sub>)  $\delta$  (ppm) = 8.03 (d, *J* = 8.4 Hz, 2H), 7.91 (d, *J* = 9.0 Hz, 2H), 7.79 (d, *J* = 8.4 Hz, 2H), 7.14 (d, *J* = 9.0 Hz, 2H), 3.87 (s, 3H). **<sup>13</sup>C NMR** (101 MHz, DMSO)  $\delta$  166.8, 162.6, 154.4,



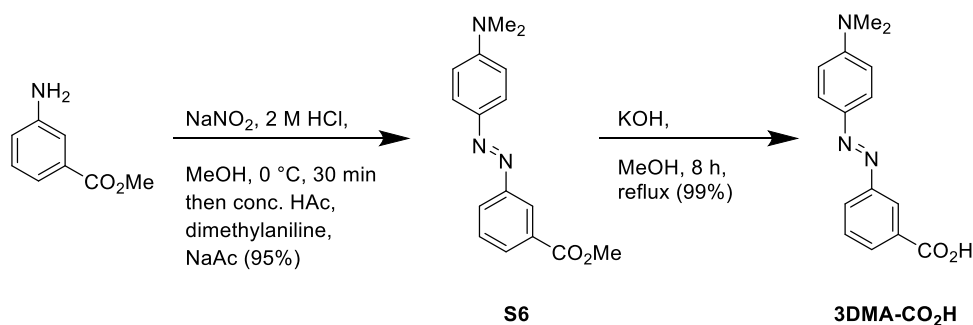


orange solid. **<sup>1</sup>H NMR** (400 MHz, chloroform-*d*)  $\delta$  (ppm) = 8.53 (t,  $J$  = 1.9 Hz, 1H), 8.12 (dt,  $J$  = 7.8, 1.4 Hz, 1H), 8.07 (ddd,  $J$  = 8.0, 2.0, 1.1 Hz, 1H), 7.94 – 7.88 (m, 2H), 7.58 (t,  $J$  = 7.8 Hz, 1H), 7.01 – 6.94 (m, 2H), 3.97 (s, 3H). **<sup>13</sup>C NMR** (101 MHz, chloroform-*d*)  $\delta$  (ppm) = 166.9, 158.9, 152.8, 147.2, 131.4, 131.3, 129.3, 126.9, 125.5, 123.9, 116.0, 77.4, 52.5. **LCMS(+)**:  $t_{\text{ret}}$  = 5.0 min, 257 Th = [MH]<sup>+</sup>, **HRMS (EI)**: calc. for [C<sub>14</sub>H<sub>12</sub>O<sub>3</sub>N<sub>2</sub>]<sup>+</sup> = [M]<sup>+</sup>: 256.0848; found: 256.0850.

By standard procedure C, **S4** (440 mg, 1.7 mmol, 1.0 eq) was reacted with methyl iodide (731 mg, 5.2 mmol, 3.0 eq). After purification by means of flash chromatography (EA:iHex, 9:1 → 7:3) the desired product **methyl 3-((4-methoxyphenyl)diazenyl)benzoate (S5)** (454 mg, 1.7 mmol, 98%) was obtained as an orange solid. **<sup>1</sup>H NMR** (400 MHz, chloroform-*d*)  $\delta$  (ppm) = 8.56 – 8.50 (m, 1H), 8.11 (ddd,  $J$  = 7.7, 1.7, 1.2 Hz, 1H), 8.06 (ddd,  $J$  = 8.0, 2.1, 1.2 Hz, 1H), 8.00 – 7.91 (m, 2H), 7.58 (td,  $J$  = 7.8, 0.5 Hz, 1H), 7.07 – 6.98 (m, 2H), 3.97 (s, 3H), 3.90 (s, 3H). **<sup>13</sup>C NMR** (101 MHz, chloroform-*d*)  $\delta$  (ppm) = 166.7, 162.4, 152.8, 146.9, 131.2, 131.1, 129.1, 126.8, 125.0, 123.7, 114.3, 55.6, 52.3. **LCMS(+)**:  $t_{\text{ret}}$  = 5.9 min, 271 Th = [MH]<sup>+</sup>. **HRMS (EI)**: calc. for [C<sub>15</sub>H<sub>14</sub>N<sub>2</sub>O<sub>3</sub>]<sup>+</sup> = [M]<sup>+</sup>: 270.1004; found: 270.0998.

By standard procedure D, **S5** (430 mg, 1.6 mmol, 1.0 eq) was reacted to the desired product **3-((4-methoxyphenyl)diazenyl)benzoic acid (3MP-CO<sub>2</sub>H)** (399 mg, 1.6 mmol, 98%) was obtained as orange solid. **<sup>1</sup>H NMR** (400 MHz, methanol-*d*<sub>4</sub>)  $\delta$  (ppm) = 10.02 (t,  $J$  = 1.8 Hz, 1H), 9.67 (dt,  $J$  = 7.7, 1.4 Hz, 1H), 9.63 (ddd,  $J$  = 8.0, 2.1, 1.2 Hz, 1H), 9.53 – 9.47 (m, 2H), 9.19 (t,  $J$  = 7.8 Hz, 1H), 8.67 – 8.62 (m, 2H), 5.46 (s, 3H). **<sup>13</sup>C NMR** (101 MHz, methanol-*d*<sub>4</sub>)  $\delta$  (ppm) = 167.79, 162.82, 152.72, 146.72, 131.84, 130.89, 129.00, 126.32, 124.62, 123.06, 114.04, 54.76. **LCMS(+)**:  $t_{\text{ret}}$  = 5.2 min, 257 Th = [MH]<sup>+</sup>. **HRMS (EI)**: calc. for [C<sub>14</sub>H<sub>12</sub>O<sub>3</sub>N<sub>2</sub>]<sup>+</sup> = [M]<sup>+</sup>: 256.0848; found: 256.0842.

### 3-((4-(dimethylamino)phenyl)diazenyl)benzoic acid (3DMA-CO<sub>2</sub>H)

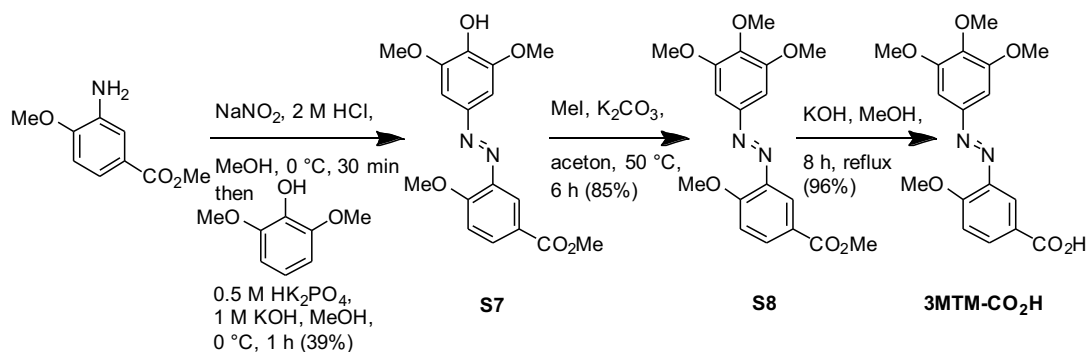


By standard procedure B, commercially available methyl 3-amino benzoate (302 mg, 2.0 mmol, 1.00 eq) was reacted with dimethylaniline (364 mg, 3.0 mmol, 1.5 eq). After purification by means of flash chromatography (EA:iHex, 9:1 → 8:2) the desired product **methyl 3-((4-(dimethylamino)phenyl)diazenyl)benzoate (S6)** (539 mg, 1.9 mmol, 95%) was obtained as red solid. Spectral data matches literature<sup>7</sup>: **<sup>1</sup>H NMR** (500 MHz, chloroform-*d*)  $\delta$  (ppm) = 8.49 (t,  $J$  = 1.8 Hz, 1H), 8.04 (tdd,  $J$  = 7.3, 2.4, 1.2 Hz, 2H), 7.92 (d,  $J$  = 9.1 Hz, 2H), 7.54 (t,  $J$  = 7.8 Hz, 1H), 6.78 (d,  $J$  = 9.0 Hz, 2H), 3.96 (s, 3H), 3.11 (s, 6H). **<sup>13</sup>C NMR** (126 MHz,

chloroform-*d*)  $\delta$  (ppm) = 166.9, 153.1, 152.7, 143.5, 131.1, 130.1, 129.0, 126.4, 125.4, 123.4, 111.7, 52.3, 40.4. **LCMS(+)**:  $t_{\text{ret}}$  = 6.0 min, 284 Th =  $[\text{MH}]^+$ . **HRMS (EI)**: calc. for  $[\text{C}_{16}\text{H}_{17}\text{O}_2\text{N}_3]^+ = [\text{M}]^+$ : 283.1321; found: 283.1315.

By standard procedure D, **S6** (100 mg, 0.35 mmol, 1.0 eq) was reacted to the desired product **3-((4-(dimethylamino)phenyl)diazenyl)benzoic acid (3DMA-CO<sub>2</sub>H)** (93 mg, 0.35 mmol, 98%) was obtained as red solid. Spectral data matches literature<sup>8</sup>: **<sup>1</sup>H NMR** (500 MHz, methanol-*d*<sub>4</sub>)  $\delta$  (ppm) = 8.41 (t,  $J$  = 1.8 Hz, 1H), 8.04 (dt,  $J$  = 7.7, 1.4 Hz, 1H), 8.02 – 7.99 (m, 1H), 7.89 – 7.84 (m, 2H), 7.59 (t,  $J$  = 7.8 Hz, 1H), 6.87 – 6.82 (m, 2H), 3.10 (s, 6H). **<sup>13</sup>C NMR** (126 MHz, methanol-*d*<sub>4</sub>)  $\delta$  (ppm) = 169.6, 154.8, 154.7, 144.8, 133.3, 131.4, 130.4, 127.5, 126.4, 124.2, 112.8, 40.5. **LCMS(+)**:  $t_{\text{ret}}$  = 6.2 min, 270 Th =  $[\text{MH}]^+$ . **HRMS (EI)**: calc. for  $[\text{C}_{16}\text{H}_{17}\text{O}_2\text{N}_3]^+ = [\text{M}]^+$ : 269.1164; found: 269.1159.

#### 4-methoxy-3-((3,4,5-trimethoxyphenyl)diazenyl)benzoic acid (3MTM-CO<sub>2</sub>H)



By standard procedure A, commercially available methyl 3-amino 4-methoxybenzoate (181 mg, 1.0 mmol, 1.0 eq) was reacted with 2,6-dimethoxyphenol (185 mg, 1.2 mmol, 1.2 eq). After purification by means of flash chromatography (EA:iHex, 9:1 → 1:1) the desired product **methyl 3-((4-hydroxy-3,5-dimethoxyphenyl)diazenyl)-4-methoxybenzoate (S7)** (136 mg, 0.39 mmol, 39%) was obtained as a yellow solid. **<sup>1</sup>H NMR** (400 MHz, chloroform-*d*)  $\delta$  (ppm) = 8.28 (d,  $J$  = 2.2 Hz, 1H), 8.12 (dd,  $J$  = 8.7, 2.2 Hz, 1H), 7.32 (s, 2H), 7.12 (d,  $J$  = 8.7 Hz, 1H), 5.88 (s, 1H), 4.08 (s, 3H), 4.01 (s, 6H), 3.92 (s, 3H). **<sup>13</sup>C NMR** (101 MHz, chloroform-*d*)  $\delta$  (ppm) = 166.8, 159.9, 147.4, 146.2, 142.0, 138.4, 133.2, 123.1, 119.0, 112.2, 101.1, 56.7, 56.6, 52.3. **LCMS(+)**:  $t_{\text{ret}}$  = 4.5 min, 347 Th =  $[\text{MH}]^+$ . **HRMS (EI)**: calc. for  $[\text{C}_{17}\text{H}_{18}\text{N}_2\text{O}_6]^+ = [\text{M}]^+$ : 346.1165; found: 346.1160.

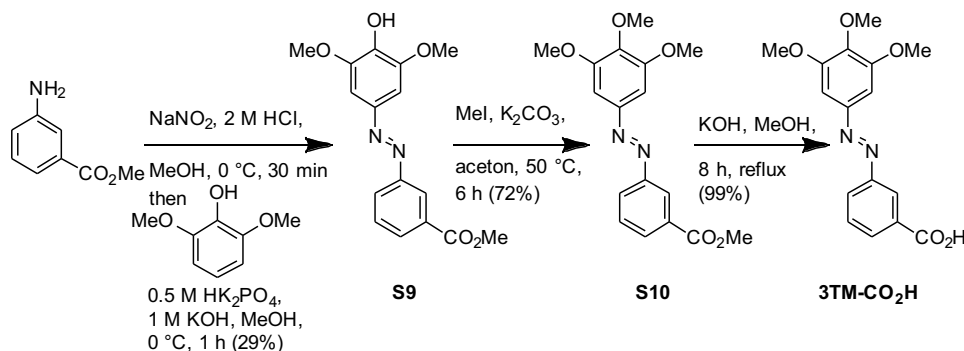
By standard procedure C, **S7** (136 mg, 0.39 mmol, 1.0 eq) was reacted with methyl iodide (111 mg, 0.79 mmol, 2.0 eq). After purification by means of flash chromatography (EA:iHex, 9:1 → 1:1) the desired product **methyl 4-methoxy-3-((3,4,5-trimethoxyphenyl)diazenyl)benzoate (S8)** (120 mg, 0.33 mmol, 85%) was obtained as an orange solid. **<sup>1</sup>H NMR** (400 MHz, chloroform-*d*)  $\delta$  (ppm) = 8.27 (d,  $J$  = 2.2 Hz, 1H), 8.14 (dd,  $J$  = 8.7, 2.2 Hz, 1H), 7.27 (s, 2H), 7.12 (d,  $J$  = 8.8 Hz, 1H), 4.08 (s, 3H), 3.97 (s, 6H), 3.94 (s, 3H), 3.92 (s, 3H). **<sup>13</sup>C NMR** (101 MHz, chloroform-*d*)  $\delta$  (ppm) = 166.6, 159.9, 153.5, 148.9,

141.8, 141.0, 133.4, 122.9, 118.8, 112.1, 100.8, 61.1, 56.4, 56.3, 52.1. **LCMS(+)**:  $t_{\text{ret}} = 4.9$  min, 361 Th =  $[\text{MH}]^+$ . **HRMS (EI)**: calc. for  $[\text{C}_{18}\text{H}_{20}\text{N}_2\text{O}_6]^+ = [\text{M}]^+$ : 360.1321; found: 360.1314.

By standard procedure D, **S9** (110 mg, 0.32 mmol, 1.0 eq) was reacted to the desired product **4-methoxy-3-((3,4,5-trimethoxyphenyl)diazenyl)benzoic acid (3MTM-CO<sub>2</sub>H)** (102 mg, 0.30 mmol, 96%) was obtained as yellow solid.

**<sup>1</sup>H NMR** (400 MHz, DMSO-*d*<sub>6</sub>)  $\delta$  (ppm) = 8.11 – 8.05 (m, 2H), 7.38 (d,  $J = 9.4$  Hz, 1H), 7.26 (s, 2H), 4.04 (s, 3H), 3.89 (s, 6H), 3.77 (s, 3H). **<sup>13</sup>C NMR** (101 MHz, DMSO-*d*<sub>6</sub>)  $\delta$  (ppm) = 167.2, 160.1, 153.8, 148.6, 141.2, 140.9, 134.8, 134.0, 123.5, 118.1, 113.8, 101.0, 60.8, 57.0, 56.5. **LCMS(+)**:  $t_{\text{ret}} = 4.3$  min, 347 Th =  $[\text{MH}]^+$ . **HRMS (EI)**: calc. for  $[\text{C}_{18}\text{H}_{20}\text{N}_2\text{O}_6]^+ = [\text{M}]^+$ : 346.1165; found: 346.1157.

### 3-((3,4,5-trimethoxyphenyl)diazenyl)benzoic acid (3TM-CO<sub>2</sub>H)

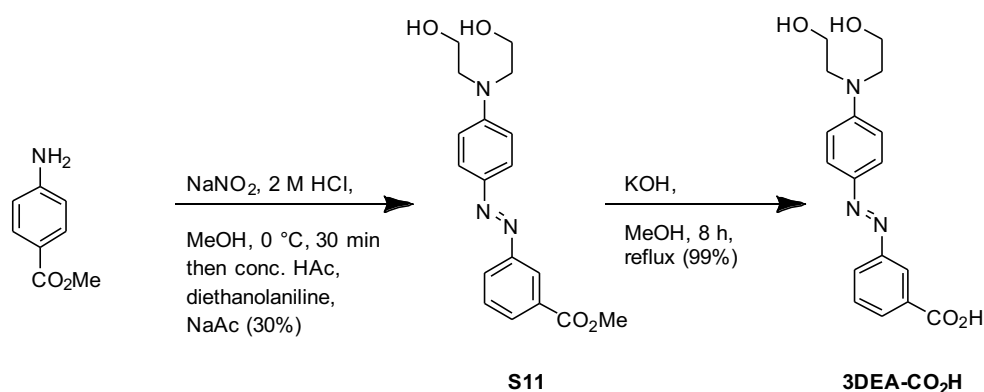


By standard procedure A, commercially available methyl 3-amino benzoate (151 mg, 1 mmol, 1.00 eq) was reacted with 2,6-dimethoxyphenol (185 mg, 1.1 mmol, 1.1 eq). After purification by means of flash chromatography (EA:iHex, 9:1 → 6:4) the desired product **methyl 3-((4-hydroxy-3,5-dimethoxyphenyl)diazenyl)benzoate (S9)** (229 mg, 0.72 mmol, 73%) was obtained as an orange solid. **<sup>1</sup>H NMR** (400 MHz, chloroform-*d*)  $\delta$  (ppm) = 8.46 (t,  $J = 1.7$  Hz, 1H), 8.05 (ddd,  $J = 7.7, 1.7, 1.2$  Hz, 1H), 7.99 (ddd,  $J = 8.0, 2.1, 1.2$  Hz, 1H), 7.51 (td,  $J = 7.8, 0.5$  Hz, 1H), 7.18 (s, 1H), 5.81 (s, 1H), 3.94 (s, 6H), 3.90 (s, 3H). **<sup>13</sup>C NMR** (101 MHz, chloroform-*d*)  $\delta$  (ppm) = 166.8, 152.8, 147.4, 138.5, 131.5, 131.3, 129.3, 126.9, 123.9, 100.9, 56.6, 52.5. **LCMS(+)**:  $t_{\text{ret}} = 4.9$  min, 317 Th =  $[\text{MH}]^+$ . **HRMS (EI)**: calc. for  $[\text{C}_{16}\text{H}_{16}\text{O}_5\text{N}_2]^+ = [\text{M}]^+$ : 316.1059; found: 316.1050.

By standard procedure C, **S9** (221 mg, 0.70 mmol, 1.0 eq) was reacted with methyl iodide (198 mg, 1.4 mmol, 2.0 eq). After purification by means of flash chromatography (EA:iHex, 9:1 → 7:3) the desired product **methyl 3-((3,4,5-trimethoxyphenyl)diazenyl)benzoate (S10)** (174 mg, 0.53 mmol, 72%) was obtained as a yellow solid. **<sup>1</sup>H NMR** (400 MHz, chloroform-*d*)  $\delta$  (ppm) = 8.55 (t,  $J = 1.6$  Hz, 1H), 8.14 (ddd,  $J = 7.7, 1.7, 1.2$  Hz, 1H), 8.09 (ddd,  $J = 7.9, 2.1, 1.2$  Hz, 1H), 7.60 (td,  $J = 7.8, 0.5$  Hz, 1H), 7.29 (s, 2H), 3.98 (s, 6H), 3.98 (s, 3H), 3.95 (s, 3H). **<sup>13</sup>C NMR** (101 MHz, chloroform-*d*)  $\delta$  (ppm) = 166.7, 153.7, 152.7, 148.5, 141.2, 131.6, 131.5, 129.4, 127.0, 124.1, 100.8, 61.2, 56.4, 52.5. **LCMS(+)**:  $t_{\text{ret}} = 5.7$  min, 331 Th =  $[\text{MH}]^+$ . **HRMS (EI)**: calc. for  $[\text{C}_{17}\text{H}_{18}\text{O}_5\text{N}_2]^+ = [\text{M}]^+$ : 330.1216; found: 330.1206.

By standard procedure D, **S10** (174 mg, 0.53 mmol, 1.0 eq) was reacted to the desired product **3-((3,4,5-trimethoxyphenyl)diazenyl)benzoic acid (3TM-CO<sub>2</sub>H)** (167 mg, 0.53 mmol, 99%) was obtained as yellow solid. <sup>1</sup>H NMR (500 MHz, methanol-*d*<sub>4</sub>) δ (ppm) = 8.53 (t, *J* = 1.8 Hz, 1H), 8.17 (dt, *J* = 7.7, 1.4 Hz, 1H), 8.13 (ddd, *J* = 7.9, 2.1, 1.2 Hz, 1H), 7.67 (t, *J* = 7.8 Hz, 1H), 7.38 (s, 2H), 3.98 (s, 6H), 3.89 (s, 3H). <sup>13</sup>C NMR (126 MHz, methanol-*d*<sub>4</sub>) δ (ppm) = 168.3, 153.6, 152.4, 148.4, 140.9, 132.8, 131.4, 129.0, 126.3, 123.2, 100.4, 59.9, 55.3, 55.2. **LCMS(+)**: *t*<sub>ret</sub> = 4.6 min, 317 Th = [MH]<sup>+</sup>. **HRMS (EI)**: calc. for [C<sub>16</sub>H<sub>16</sub>O<sub>5</sub>N<sub>2</sub>]<sup>+</sup> = [M]<sup>+</sup>: 316.1043; found: 316.1059.

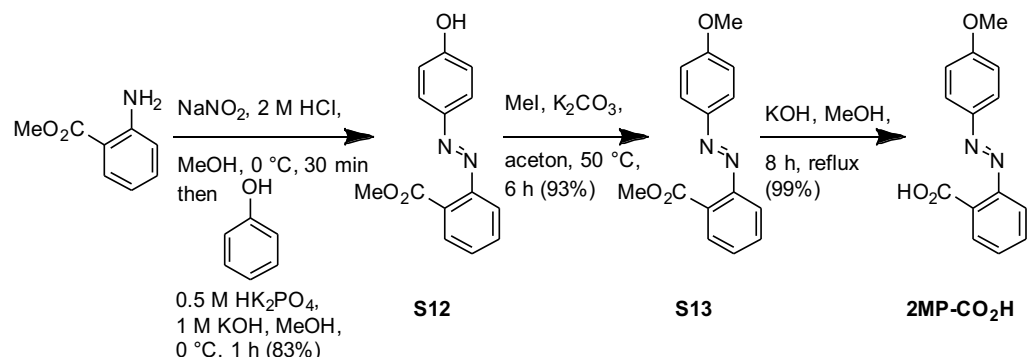
**3-((4-(bis(2-hydroxyethyl)amino)phenyl)diazenyl)benzoic acid (3DEA-CO<sub>2</sub>H)**



By standard procedure B, commercially available methyl 3-amino benzoate (302 mg, 2 mmol, 1.00 eq) was reacted with diethanolamine (544 mg, 3 mmol, 1.50 eq). After purification by means of flash chromatography (DCM:MeOH, 95:5) the desired product **methyl 3-((4-(bis(2-hydroxyethyl)amino)phenyl)diazenyl)benzoate (S11)** (200 mg, 0.58 mmol, 29%) was obtained as red solid. <sup>1</sup>H NMR (400 MHz, chloroform-*d*) δ 8.49 (t, *J* = 1.8 Hz, 1H), 8.04 (tdd, *J* = 7.9, 2.4, 1.2 Hz, 2H), 7.89 (d, *J* = 8.7 Hz, 2H), 7.54 (t, *J* = 7.9 Hz, 1H), 6.80 (d, *J* = 8.9 Hz, 2H), 3.95 (d, *J* = 4.3 Hz, 7H), 3.82 (d, *J* = 18.8 Hz, 2H), 3.73 (t, *J* = 4.9 Hz, 4H). <sup>13</sup>C NMR (101 MHz, MeOD-*d*<sub>4</sub>) δ (ppm) = 168.3, 152.9, 132.6, 131.1, 130.6, 127.8, 126.7, 123.8, 113.0, 60.4, 55.2, 53.0. **LCMS(+)**: *t*<sub>ret</sub> = 4.3 min, 344 Th = [MH]<sup>+</sup>. **HRMS (EI)**: calc. for [C<sub>18</sub>H<sub>21</sub>N<sub>3</sub>O<sub>4</sub>]<sup>+</sup> = [M]<sup>+</sup>: 343.1532; found: 343.1529.

By standard procedure D, **S11** (200 mg, 0.58 mmol, 1.0 eq) was reacted to the desired product **3-((4-(bis(2-hydroxyethyl)amino)phenyl)diazenyl)benzoic acid (3DEA-CO<sub>2</sub>H)** (154 mg, 0.47 mmol, 80%) was obtained as yellow solid. The compound has been reported<sup>9</sup> but no spectral data for comparison was available, so we report it here: <sup>1</sup>H NMR (400 MHz, DMSO-*d*<sub>6</sub>) δ (ppm) = 7.95 – 7.89 (m, 4H), 7.61 (dt, *J* = 6.4, 1.9 Hz, 5H), 4.83 (d, *J* = 21.9 Hz, 2H), 3.64 (s, 2H), 3.56 (d, *J* = 6.0 Hz, 2H), 3.47 (s, 3H). <sup>13</sup>C NMR (101 MHz, DMSO-*d*<sub>6</sub>) δ 170.3, 151.9, 151.7, 140.0, 131.8, 130.7, 129.6, 128.1, 122.7, 122.5, 58.5, 58.5, 51.6, 47.4. **LCMS(+)**: *t*<sub>ret</sub> = 3.6 min, 330 Th = [MH]<sup>+</sup>. **HRMS (EI)**: calc. for [C<sub>17</sub>H<sub>19</sub>N<sub>3</sub>O<sub>4</sub>]<sup>+</sup> = [M]<sup>+</sup>: 329.1576; found: 329.1362.

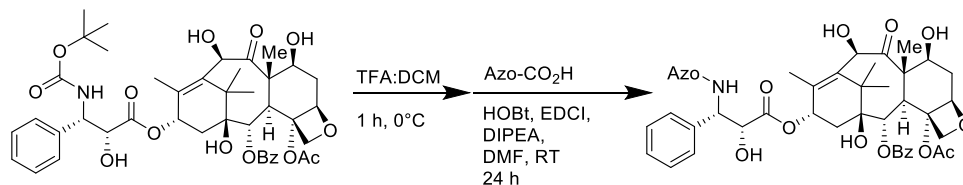
**2-((4-methoxyphenyl)diazenyl)benzoic acid (2MP-CO<sub>2</sub>H)**



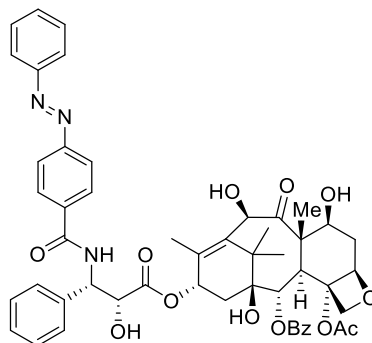
By standard procedure A, commercially available methyl 2-amino benzoate (302 mg, 2.0 mmol, 1.0 eq) was reacted with phenol (207 mg, 2.2 mmol, 1.1 eq). After purification by means of flash chromatography (EA:iHex, 9:1 → 7:3) the desired product **methyl 2-((4-hydroxyphenyl)diazenyl)benzoate (S12)** (423 mg, 1.8 mmol, 83%) was obtained as an orange solid. The compound has been reported but no spectral data for comparison were available so these are given here<sup>10</sup>: **<sup>1</sup>H NMR** (400 MHz, DMSO-*d*<sub>6</sub>) δ 7.79 – 7.75 (m, 2H), 7.74 (dd, *J* = 7.5, 1.4 Hz, 1H), 7.69 (ddd, *J* = 8.6, 7.1, 1.5 Hz, 1H), 7.63 (dd, *J* = 8.1, 1.4 Hz, 1H), 7.56 (td, *J* = 7.3, 1.5 Hz, 1H), 7.01 – 6.92 (m, 2H), 3.81 (s, 3H). **<sup>13</sup>C NMR** (101 MHz, DMSO-*d*<sub>6</sub>) δ (ppm) = 168.2, 161.9, 151.2, 145.7, 132.4, 130.1, 129.6, 128.8, 125.6, 119.8, 116.5, 52.7. **LCMS(+)**: *t*<sub>ret</sub> = 4.5 min, 257 Th = [MH]<sup>+</sup>. **HRMS (EI)**: calc. for [C<sub>14</sub>H<sub>12</sub>N<sub>2</sub>O<sub>3</sub>]<sup>+</sup> = [M]<sup>+</sup>: 256.0848; found: 256.0838.

By standard procedure C, **S12** (402 mg, 1.57 mmol, 1.0 eq) was reacted with methyl iodide (668 mg, 4.7 mmol, 3.0 eq). After purification by means of flash chromatography (EA:iHex, 8:2) the desired product **methyl 2-((4-methoxyphenyl)diazenyl)benzoate (S13)** (394 mg, 0.53 mmol, 93%) was obtained as a yellow solid. The compound has been reported<sup>11</sup> but no spectral data for comparison were available so these are given here: **<sup>1</sup>H NMR** (400 MHz, chloroform-*d*) δ (ppm) = 7.97 – 7.87 (m, 2H), 7.80 (ddd, *J* = 7.7, 1.4, 0.5 Hz, 1H), 7.64 – 7.54 (m, 2H), 7.45 (ddd, *J* = 7.7, 7.0, 1.6 Hz, 1H), 7.05 – 6.98 (m, 2H), 3.90 (d, *J* = 2.3 Hz, 6H). **<sup>13</sup>C NMR** (101 MHz, chloroform-*d*) δ (ppm) = 168.2, 162.5, 152.1, 147.1, 131.9, 129.7, 129.2, 128.4, 125.2, 119.0, 114.3, 55.6, 52.3. **LCMS(+)**: *t*<sub>ret</sub> = 5.4 min, 271 Th = [MH]<sup>+</sup>. **HRMS (EI)**: calc. for [C<sub>15</sub>H<sub>14</sub>N<sub>2</sub>O<sub>3</sub>]<sup>+</sup> = [M]<sup>+</sup>: 270.1004; found: 270.1003.

By standard procedure D, **S13** (385 mg, 0.53 mmol, 1.0 eq) was reacted to the desired product **2-((4-methoxyphenyl)diazenyl)benzoic acid (2MP-CO<sub>2</sub>H)** (363 mg, 0.53 mmol, 99%) was obtained as yellow solid. Spectral data matches literature<sup>12</sup>: **<sup>1</sup>H NMR** (400 MHz, chloroform-*d*) δ (ppm) = 7.93 – 7.89 (m, 2H), 7.88 (dd, *J* = 7.7, 1.5 Hz, 1H), 7.71 (dd, *J* = 8.0, 1.3 Hz, 1H), 7.66 – 7.59 (m, 1H), 7.54 (td, *J* = 7.5, 1.3 Hz, 1H), 7.12 – 7.07 (m, 2H), 3.90 (s, 3H). **<sup>13</sup>C NMR** (101 MHz, chloroform-*d*) δ (ppm) = 170.0, 163.2, 150.9, 146.7, 131.6, 130.1, 129.7, 129.5, 125.0, 117.3, 114.2, 54.8. **LCMS(+)**: *t*<sub>ret</sub> = 4.9 min, 257 Th = [MH]<sup>+</sup>. **HRMS (EI)**: calc. for [C<sub>14</sub>H<sub>12</sub>O<sub>3</sub>N<sub>2</sub>]<sup>+</sup> = [M]<sup>+</sup>: 256.0847.

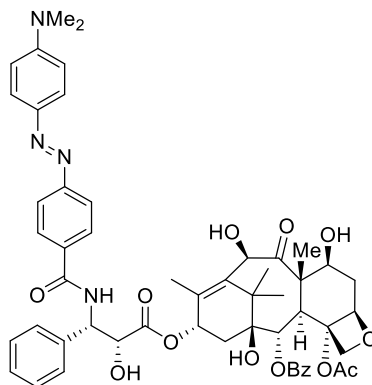
**AzTaxes**

**(2aR,4S,4aS,6R,9S,11S,12S,12aR,12bS)-12b-acetoxy-4,6,11-trihydroxy-9-(((2R,3S)-2-hydroxy-3-phenyl-3-(4-(phenyldiazenyl)benzamido)propanoyl)oxy)-4a,8,13,13-tetramethyl-5-oxo-2a,3,4,4a,5,6,9,10,11,12,12a,12b-dodecahydro-1H-7,11-methanocyclodeca[3,4]benzo[1,2-b]oxet-12-yl benzoate (AzTax4H)**

**AzTax4H**

By Standard Procedure E, docetaxel (25 mg, 31  $\mu$ mol) was deprotected with TFA-DCM and the crude foam reacted with **4H-CO<sub>2</sub>H** (7.5 mg, 33  $\mu$ mol), DIPEA (11 mg, 86  $\mu$ mol), EDCI (10.7 mg, 56  $\mu$ mol), and HOBT.H<sub>2</sub>O (6.5 mg, 42  $\mu$ mol) to yield a yellow crude solid. Chromatography on 5:1:0→1:1:0→1:1:0.2 iHex:EA:MeOH returned **AzTax4H** as a yellow solid (22 mg, 24  $\mu$ mol, 76 %). **<sup>1</sup>H NMR** (400 MHz, chloroform-*d*)  $\delta$  (ppm) = 8.16 – 8.09 (m, 2H), 7.95 – 7.91 (m, 2H), 7.68 – 7.31 (m, 14H), 7.28 (s, 1H), 6.24 – 6.17 (m, 1H), 5.79 (dd, *J* = 8.9, 2.8 Hz, 1H), 5.67 (d, *J* = 6.9 Hz, 1H), 5.18 (d, *J* = 4.9 Hz, 1H), 4.93 (dd, *J* = 9.6, 2.2 Hz, 1H), 4.80 (d, *J* = 2.9 Hz, 1H), 4.31 (d, *J* = 8.4 Hz, 1H), 4.24 – 4.16 (m, 2H), 3.89 (d, *J* = 7.2 Hz, 1H), 2.61 – 2.50 (m, 1H), 2.38 (s, 3H), 2.29 (dd, *J* = 9.0, 3.9 Hz, 2H), 1.89 – 1.79 (m, 2H), 1.78 – 1.73 (m, 6H), 1.72 – 1.68 (m, 1H), 1.20 (d, *J* = 6.4 Hz, 4H), 1.11 (s, 4H). **<sup>13</sup>C NMR** (101 MHz, chloroform-*d*)  $\delta$  (ppm) = 211.2, 172.5, 170.5, 167.0, 166.3, 154.5, 152.5, 138.1, 137.8, 136.1, 135.3, 133.8, 131.7, 130.2, 129.2, 129.1, 129.0, 128.8, 128.4, 128.1, 127.1, 123.1, 123.0, 84.1, 81.1, 78.7, 77.2, 74.7, 74.5, 73.2, 72.4, 72.0, 57.7, 55.2, 46.5, 43.0, 37.0, 35.9, 26.6, 22.6, 20.6, 14.4, 9.9. **LCMS(+)**:  $t_{\text{ret}}$  = 7.26 & 8.25 min, each 916 Th = [MH]<sup>+</sup>, *Z* & *E* isomers respectively. **HRMS (ESI+)** calcd for [C<sub>51</sub>H<sub>54</sub>N<sub>3</sub>O<sub>13</sub>]<sup>+</sup> = [MH]<sup>+</sup>: *m/z* 916.36566, found 916.36715.

**(2aR,4S,4aS,6R,9S,11S,12S,12aR,12bS)-12b-acetoxy-9-(((2R,3S)-3-(4-((4-(dimethylamino)phenyl)diazonyl)benzamido)-2-hydroxy-3-phenylpropanoyl)oxy)-4,6,11-trihydroxy-4a,8,13,13-tetramethyl-5-oxo-2a,3,4,4a,5,6,9,10,11,12,12a,12b-dodecahydro-1H-7,11-methanocyclodeca[3,4]benzo[1,2-b]oxet-12-yl benzoate (AzTax4DMA)**

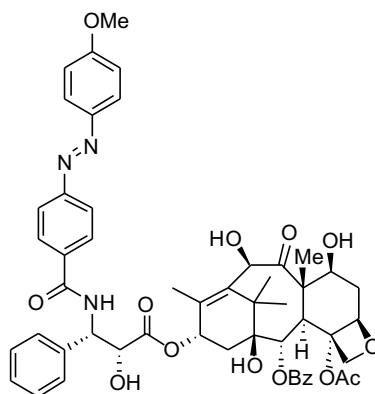


#### AzTax4DMA

By Standard Procedure E, docetaxel (23 mg, 28  $\mu$ mol) was deprotected with TFA-DCM and the crude foam (20 mg) reacted with **4DMA-CO<sub>2</sub>H** (11 mg, 41  $\mu$ mol), Hünig base (11.1 mg, 85  $\mu$ mol), EDCI (8.6 mg, 45  $\mu$ mol), and HOBt·H<sub>2</sub>O (6.9 mg, 45  $\mu$ mol) to yield a yellow crude solid. Chromatography on 5:1:0→1:1:0→1:1:0.08 iHex:EA:MeOH returned **AzTax4DMA** as a yellow solid (13.8 mg, 14.4  $\mu$ mol, 51%).

**<sup>1</sup>H NMR** (400 MHz, chloroform-*d*)  $\delta$  (ppm) = 9.07 (d, *J* = 8.4 Hz, 1H), 8.05 (d, *J* = 8.6 Hz, 2H), 7.97 (d, *J* = 7.5 Hz, 2H), 7.86 (d, *J* = 8.4 Hz, 2H), 7.84 (d, *J* = 9.0 Hz, 2H), 7.78 – 7.68 (m, 1H), 7.69 – 7.59 (m ~t, *J* = 7.7 Hz, 2H), 7.46 – 7.41 (m, 2H), 7.43 – 7.38 (m, 2H), 7.23 (tt, *J* = 5.7, 2.9 Hz, 1H), 6.85 (d, *J* = 9.3 Hz, 2H), 6.23 (d, *J* = 7.8 Hz, 1H), 5.91 (t, *J* = 9.0 Hz, 1H), 5.39 (t, *J* = 8.6 Hz, 1H), 5.39 (d, *J* = 6.5 Hz), 5.09 (d, *J* = 2.6 Hz), 5.03 (d, *J* = 7.2 Hz, 1H), 4.98 (d, *J* = 2.4 Hz, 1H), 4.92 (dd, *J* = 9.7, 2.2 Hz, 1H), 4.57 (s, 1H), 4.59 (~t, *J* = 7.8 Hz, 1H), 4.11 – 3.96 (m, 3H, H10), 3.67 (d, *J* = 7.1 Hz, 1H), 3.09 (s, 6H), 2.35 – 2.25 (m, 1H), 2.23 (s, 3H), 1.90 – 1.81 (m, 1H), 1.73 – 1.65 (m, 1H), 1.74 (s, 3H), 1.72 – 1.63 (m, 1H), 1.53 (s, 3H), 1.01 (s, 3H), 0.98 (s, 3H) ppm. **<sup>13</sup>C NMR** (101 MHz, chloroform-*d*)  $\delta$  (ppm) = 209.7, 173.2, 170.2, 166.1, 165.7, 154.6, 153.3, 143.1, 139.7, 137.3, 136.2, 135.1, 133.9, 130.5, 130.0, 129.2, 129.0, 128.8, 128.0, 127.9, 125.6, 122.0, 112.0, 84.2, 80.7, 77.3, 75.9, 75.2, 74.2, 74.1, 71.3, 70.2, 57.4, 57.1, 46.4, 43.4, 40.6, 36.9, 35.4, 23.0, 21.5, 14.1, 10.3. **LCMS(+)**: *t*<sub>ret</sub> = 8.39 min, 959 Th = [MH]<sup>+</sup>, E isomer only. **HRMS (ESI+)** calcd for [C<sub>53</sub>H<sub>59</sub>N<sub>4</sub>O<sub>13</sub>]<sup>+</sup> = [MH]<sup>+</sup>: *m/z* 959.40786, found 959.40758.

(2aR,4S,4aS,6R,9S,11S,12S,12aR,12bS)-12b-acetoxy-4,6,11-trihydroxy-9-(((2R,3S)-2-hydroxy-3-(4-(4-methoxyphenyl)diazenyl)benzamido)-3-phenylpropanoyloxy)-4a,8,13,13-tetramethyl-5-oxo-2a,3,4,4a,5,6,9,10,11,12,12a,12b-dodecahydro-1H-7,11-methanocyclodeca[3,4]benzo[1,2-b]oxet-12-yl benzoate (**AzTax4MP**)



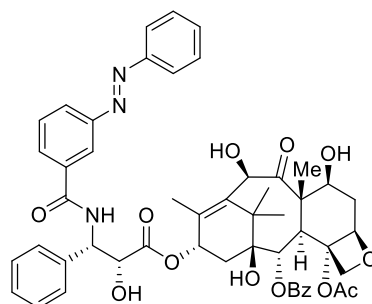
**AzTax4MP**

By Standard Procedure E, docetaxel (20 mg, 24  $\mu\text{mol}$ ) was deprotected with TFA-DCM and the crude foam (17 mg) reacted with **4MP-CO<sub>2</sub>H** (8 mg, 28  $\mu\text{mol}$ , 1.2 eq), Hünig base (12 mg, 96  $\mu\text{mol}$ , 4.0 eq), EDCI (7 mg, 36  $\mu\text{mol}$ ), and HOBt-H<sub>2</sub>O (7 mg, 85 %wt, 39  $\mu\text{mol}$ , 1.6 eq) to yield a yellow crude solid. Chromatography on (iHex:EA 7:3→1:1; DCM:MeOH 99:1→95:5) returned **AzTax4MP** as a yellow solid (10 mg, 10.4  $\mu\text{mol}$ , 41%). LCMS method was

**<sup>1</sup>H NMR** (400 MHz, chloroform-*d*)  $\delta$  (ppm) = 8.09 – 8.03 (m, 2H), 7.89 – 7.83 (m, 2H), 7.81 (d,  $J$  = 1.3 Hz, 3H), 7.58 – 7.51 (m, 1H), 7.49 – 7.39 (m, 4H), 7.39 – 7.32 (m, 2H), 7.32 – 7.25 (m, 1H), 7.12 (d,  $J$  = 9.0 Hz, 1H), 6.98 – 6.91 (m, 2H), 6.19 – 6.08 (m, 1H), 5.73 (dd,  $J$  = 9.0, 2.8 Hz, 1H), 5.61 (d,  $J$  = 7.0 Hz, 1H), 5.11 (d,  $J$  = 1.6 Hz, 1H), 4.91 – 4.83 (m, 1H), 4.73 (dd,  $J$  = 5.1, 2.8 Hz, 1H), 4.25 (d,  $J$  = 8.5 Hz, 1H), 4.19 – 4.10 (m, 3H), 3.83 (s, 4H), 3.55 (d,  $J$  = 5.3 Hz, 1H), 2.51 (ddd,  $J$  = 14.3, 9.6, 6.5 Hz, 1H), 2.32 (s, 3H), 2.23 (dd,  $J$  = 8.9, 5.1 Hz, 2H), 1.83 – 1.66 (m, 8H), 1.14 (s, 3H), 1.05 (s, 3H), 0.84 – 0.74 (m, 1H). **<sup>13</sup>C NMR** (101 MHz, chloroform-*d*)  $\delta$  (ppm) = 211.4, 172.7, 170.6, 167.1, 166.6, 162.8, 154.9, 147.1, 138.2, 138.0, 136.3, 134.8, 133.9, 130.3, 129.3, 129.2, 128.9, 128.5, 128.2, 127.2, 125.3, 122.9, 114.5, 84.3, 81.3, 78.9, 74.9, 74.7, 73.4, 72.6, 72.2, 57.8, 55.8, 55.3, 46.6, 43.2, 37.2, 36.1, 26.7, 22.7, 20.7, 14.5, 10.0. **LCMS(+)**:  $t_{\text{ret}}$  = 8.4 min, 946 Th = [MH]<sup>+</sup> **HRMS (ESI+)** calcd for [C<sub>52</sub>H<sub>56</sub>N<sub>3</sub>O<sub>14</sub>]<sup>+</sup> = [MH]<sup>+</sup>:  $m/z$  946.37568, found 946.37796.



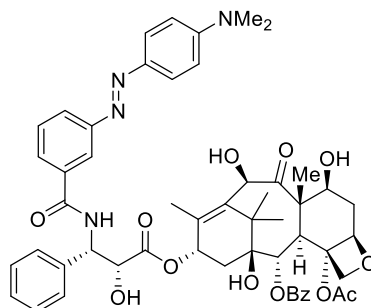
**(2aR,4S,4aS,6R,9S,11S,12S,12aR,12bS)-12b-acetoxy-4,6,11-trihydroxy-9-(((2R,3S)-2-hydroxy-3-phenyl-3-(3-(phenyldiazenyl)benzamido)propanoyl)oxy)-4a,8,13,13-tetramethyl-5-oxo-2a,3,4,4a,5,6,9,10,11,12,12a,12b-dodecahydro-1H-7,11-methanocyclodeca[3,4]benzo[1,2-b]oxet-12-yl benzoate (AzTax3H)**

**3H**

By Standard Procedure E, docetaxel (40 mg, 50  $\mu\text{mol}$ ) was deprotected with TFA-DCM and the crude foam (32 mg) reacted with **3H-CO<sub>2</sub>H** (5.3 mg, 23  $\mu\text{mol}$ ), Hünig base (6.3 mg, 49  $\mu\text{mol}$ ), EDCI (5.1 mg, 26  $\mu\text{mol}$ ), and HOBt·H<sub>2</sub>O (4.1 mg, 27  $\mu\text{mol}$ ) to yield a yellow crude solid (31 mg). Chromatography on 5:1:0→1:1:0→1:1:0.1 iHex:EA:MeOH returned **AzTax3H** as a yellow solid (12.2 mg, 13.3  $\mu\text{mol}$ , 58%).

**<sup>1</sup>H NMR** (400 MHz, DMSO-*d*<sub>6</sub>)  $\delta$  (ppm) = 9.24 (d, *J* = 8.5 Hz, 1H), 8.44 (t, *J* = 1.9 Hz, 1H), 8.08 (t, *J* = 7.1 Hz, 2H), 8.00 – 7.92 (m, 4H), 7.77 – 7.69 (m, 2H), 7.64 (ddd, *J* = 7.9, 6.2, 2.1 Hz, 5H), 7.44 – 7.39 (m, 3H), 6.91 – 6.83 (m, 1H), 6.26 (d, *J* = 7.7 Hz, 1H), 5.96 – 5.88 (m, 1H), 5.45 – 5.38 (m, 2H), 5.09 (s, 1H), 5.05 – 4.94 (m, 2H), 4.91 (dd, *J* = 9.7, 2.2 Hz, 2H), 4.57 (d, *J* = 2.3 Hz, 1H), 4.08 – 3.95 (m, 4H), 3.72 – 3.62 (m, 1H), 2.21 (s, 3H), 2.09 (s, 1H), 1.75 (d, *J* = 1.4 Hz, 3H), 1.53 (s, 4H). **<sup>13</sup>C NMR** (101 MHz, DMSO-*d*<sub>6</sub>)  $\delta$  (ppm) = 209.7, 173.2, 170.2, 165.9, 165.7, 153.8, 153.8, 152.3, 152.2, 139.5, 137.3, 136.2, 136.2, 133.9, 132.4, 130.8, 130.5, 130.1, 130.1, 130.0, 129.4, 129.1, 128.8, 128.0, 125.2, 123.1, 122.3, 120.4, 84.2, 83.4, 83.0, 80.9, 80.7, 77.3, 75.2, 74.2, 74.1, 71.3, 70.2, 57.4, 43.4, 41.2, 33.9, 28.7, 24.6, 21.5, 17.9, 17.2, 15.1, 14.1, 10.3, 8.3. **HRMS (ESI+)** calcd for [C<sub>51</sub>H<sub>54</sub>N<sub>3</sub>O<sub>13</sub>]<sup>+</sup> = [MH]<sup>+</sup>: *m/z* 916.36566, found 916.36526.

**(2aR,4S,4aS,6R,9S,11S,12S,12aR,12bS)-12b-acetoxy-9-(((2R,3S)-3-(3-((4-(dimethylamino)phenyl)diazenyl)benzamido)-2-hydroxy-3-phenylpropanoyl)oxy)-4,6,11-trihydroxy-4a,8,13,13-tetramethyl-5-oxo-2a,3,4,4a,5,6,9,10,11,12,12a,12b-dodecahydro-1H-7,11-methanocyclodeca[3,4]benzo[1,2-b]oxet-12-yl benzoate (AzTax3DMA)**

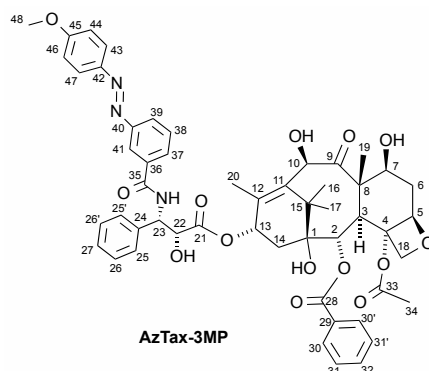


**AzTax3DMA**

By Standard Procedure E, docetaxel (20 mg, 24  $\mu\text{mol}$ ) was deprotected with TFA-DCM and the crude foam (17 mg) reacted with **3DMA-CO<sub>2</sub>H** (8 mg, 28  $\mu\text{mol}$ , 1.2 eq), Hünig base (12 mg, 96  $\mu\text{mol}$ , 4.0 eq), EDCI (7 mg, 36  $\mu\text{mol}$ ), and HOBt·H<sub>2</sub>O (7 mg, 85 %wt, 39  $\mu\text{mol}$ , 1.6 eq) to yield a yellow crude solid. Chromatography on (iHex:EA 7:3→1:1; DCM:MeOH 99:1→95:5) returned **AzTax3DMA** as a yellow solid (8 mg, 8.3  $\mu\text{mol}$ , 35%).

**<sup>1</sup>H NMR** (400 MHz, chloroform-*d*)  $\delta$  (ppm) = 8.17 – 8.10 (m, 3H), 7.98 – 7.92 (m, 1H), 7.89 – 7.82 (m, 2H), 7.79 (dt, *J* = 8.0, 1.3 Hz, 1H), 7.62 – 7.55 (m, 1H), 7.54 – 7.46 (m, 5H), 7.46 – 7.39 (m, 2H), 7.38 – 7.33 (m, 1H), 7.18 (d, *J* = 9.0 Hz, 1H), 6.79 – 6.71 (m, 2H), 6.23 (t, *J* = 8.9 Hz, 1H), 5.85 – 5.79 (m, 1H), 5.69 (d, *J* = 7.1 Hz, 1H), 5.17 (s, 1H), 4.97 – 4.90 (m, 1H), 4.80 (s, 1H), 4.31 (d, *J* = 8.5 Hz, 1H), 4.27 – 4.14 (m, 3H), 3.91 (d, *J* = 7.1 Hz, 1H), 3.65 (s, 1H), 3.10 (s, 6H), 2.57 (ddd, *J* = 15.2, 9.6, 6.5 Hz, 1H), 2.40 (s, 3H), 2.37 – 2.23 (m, 2H), 1.91 – 1.83 (m, 1H), 1.80 (d, *J* = 1.4 Hz, 3H), 1.76 (s, 3H), 1.58 (s, 1H), 1.22 (s, 3H), 1.12 (s, 3H), 0.88 (dd, *J* = 12.4, 8.0 Hz, 1H). **<sup>13</sup>C NMR** (101 MHz, chloroform-*d*)  $\delta$  (ppm) = 211.4, 172.6, 170.5, 167.0, 166.8, 153.2, 152.8, 143.4, 138.2, 137.9, 136.1, 134.5, 133.7, 130.2, 129.5, 129.2, 129.0, 128.8, 128.4, 128.0, 127.1, 125.5, 125.3, 120.4, 111.5, 84.1, 81.1, 78.8, 74.8, 74.5, 73.3, 72.5, 72.0, 57.7, 55.1, 46.5, 43.1, 40.3, 37.1, 36.0, 26.6, 22.6, 20.6, 14.4, 9.9. **LCMS(+)**:  $t_{\text{ret}}$  = 8.7 min, 959 Th = [M]<sup>+</sup>. **HRMS (ESI+)** calcd for [C<sub>53</sub>H<sub>59</sub>N<sub>4</sub>O<sub>13</sub>]<sup>+</sup> = [MH]<sup>+</sup>: *m/z* 959.40731, found 959.40885.

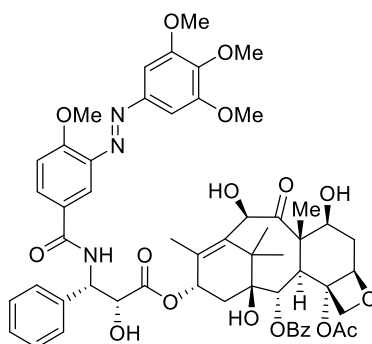
(2a*R*,4*S*,4a*S*,6*R*,9*S*,11*S*,12*S*,12a*R*,12b*S*)-12b-acetoxy-4,6,11-trihydroxy-9-(((2*R*,3*S*)-2-hydroxy-3-(3-((*E*)-(4-methoxyphenyl)diazenyl)benzamido)-3-phenylpropanoyl)oxy)-4a,8,13,13-tetramethyl-5-oxo-2a,3,4,4a,5,6,9,10,11,12,12a,12b-dodecahydro-1*H*-7,11-methanocyclodeca[3,4]benzo[1,2-*b*]oxet-12-yl benzoate (**AzTax3MP**)



By Standard Procedure E, docetaxel (21 mg, 26  $\mu\text{mol}$ ) was deprotected with TFA-DCM and the crude foam reacted with **3MP-CO<sub>2</sub>H** (7.3 mg, 28  $\mu\text{mol}$ ), Hünig base (9.4 mg, 73  $\mu\text{mol}$ ), EDCI (7.1 mg, 37  $\mu\text{mol}$ ), and HOBt·H<sub>2</sub>O (5.5 mg, 36  $\mu\text{mol}$ ) to yield a yellow crude solid. Chromatography on 5:1:0→1:1:0→1:1:0.2 iHex:EA:MeOH returned **AzTax3MP** as a yellow solid (20 mg, 21  $\mu\text{mol}$ , 81%).

**<sup>1</sup>H NMR** (400 MHz, DMSO-*d*<sub>6</sub>)  $\delta$  (ppm) = 8.13 (~t, *J* = 1.8 Hz, 1H), 8.05 (d, *J* = 7.8 Hz, 2H), 7.92 (d, *J* = 7.0 Hz, 1H), 7.83 (d, *J* = 9.0 Hz, 2H), 7.77 (d, *J* = 7.7 Hz, 1H), 7.51 (~t, *J* = 7.5 Hz, 1H), 7.45 (t, *J* = 7.6 Hz, 1H), 7.48 – 7.34 (m, 2H), 7.43 – 7.39 (m, 2H), 7.35 (~t, *J* = 7.5 Hz, 2H), 7.27 (t, *J* = 7.4 Hz, 1H), 6.94 (d, *J* = 9.0 Hz, 2H), 6.15 (t, *J* = 8.7 Hz, 1H), 5.75 (dd, *J* = 8.9, 2.8 Hz, 1H), 5.61 (d, *J* = 7.0 Hz, 1H), 5.11 (s, 1H), 4.86 (~d, *J* = 9.5 Hz, 1H), 4.73 (d, *J* = 2.8 Hz, 1H), 4.24 (d, *J* = 8.5 Hz, 1H), 4.16–4.09 (m, 2H), 3.82 (s, 3H), 3.85 – 3.80 (m overlapped, 1H), 2.56 – 2.43 (m, 1H), 2.32 (s, 3H), 2.27 – 2.19 (m, 1H), 1.89 – 1.72 (m, 1H), 1.72 – 1.64 (m, 1H), 1.71 (s, 3H), 1.68 (s, 3H, 3H<sub>19</sub>), 1.13 (s, 3H), 1.04 (s, 3H). **<sup>13</sup>C NMR** (101 MHz, DMSO-*d*<sub>6</sub>)  $\delta$  (ppm) = 211.3 (C<sub>9</sub>), 172.6 (C<sub>21</sub>), 170.5 (C<sub>33</sub>), 166.9 (C<sub>35</sub>), 166.6 (C<sub>28</sub>), 162.5 (C<sub>45</sub>), 152.7 (C<sub>40</sub>), 146.7 (C<sub>42</sub>), 138.1 (C<sub>12</sub>), 137.9 (C<sub>11</sub>), 136.1 (C<sub>36</sub>), 134.7 (C<sub>24</sub>), 133.7 (C<sub>32</sub>), 130.2 (C<sub>30</sub> & C<sub>30'</sub>), 129.5 (C<sub>29</sub>), 129.1 (C<sub>37</sub>), 129.0 (C<sub>31</sub> & C<sub>31'</sub>), 128.9 (C<sub>38</sub>), 128.7 (C<sub>26</sub> & C<sub>26'</sub>), 128.4 (C<sub>27</sub>), 127.1 (25 & 25'), 125.8 (C<sub>39</sub>), 125.1 (C<sub>43</sub> & C<sub>47</sub>), 121.0 (C<sub>41</sub>), 114.3 (C<sub>44</sub> & C<sub>46</sub>), 84.2 (C<sub>5</sub>), 81.1 (C<sub>4</sub>), 78.7 (C<sub>1</sub>), 77.2 (C<sub>18</sub>), 74.8 (C<sub>2</sub>), 74.5 (C<sub>7</sub>), 73.2 (C<sub>22</sub>), 72.4 (C<sub>10</sub>), 72.0 (C<sub>13</sub>), 57.7 (C<sub>48</sub>), 55.6 (C<sub>23</sub>), 55.2 (C<sub>8</sub>), 46.5 (C<sub>3</sub>), 43.0 (C<sub>15</sub>), 37.0 (C<sub>6</sub>), 36.0 (C<sub>14</sub>), 26.6 (C<sub>34</sub>), 22.6 (C<sub>16</sub>), 20.6 (C<sub>17</sub>), 14.4 (C<sub>20</sub>), 9.9 (C<sub>19</sub>). **LCMS(+)**: *t*<sub>ret</sub> = 7.20 & 8.21 min, each 946 Th = [MH]<sup>+</sup>, Z & E isomers respectively. **HRMS (ESI+)** calcd for [C<sub>52</sub>H<sub>56</sub>N<sub>3</sub>O<sub>14</sub>]<sup>+</sup> = [MH]<sup>+</sup>: *m/z* 946.37623, found 946.37733.

**(2aR,4S,4aS,6R,9S,11S,12S,12aR,12bS)-12b-acetoxy-4,6,11-trihydroxy-9-(((2R,3S)-2-hydroxy-3-(4-methoxy-3-((3,4,5-trimethoxyphenyl)diazenyl)benzamido)-3-phenylpropanoyl)oxy)-4a,8,13,13-tetramethyl-5-oxo-2a,3,4,4a,5,6,9,10,11,12,12a,12b-dodecahydro-1H-7,11-methanocyclodeca[3,4]benzo[1,2-b]oxet-12-yl benzoate (AzTax3MTM)**

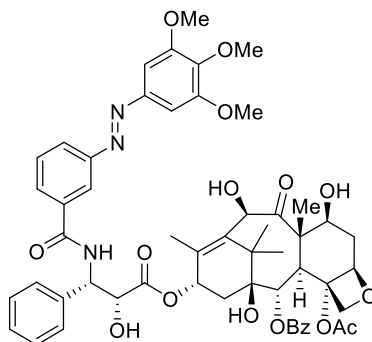


**AzTax3MTM**

By Standard Procedure E, docetaxel (20 mg, 24  $\mu\text{mol}$ ) was deprotected with TFA-DCM and the crude foam (17 mg) reacted with **3MTM-CO<sub>2</sub>H** (8 mg, 28  $\mu\text{mol}$ , 1.2 eq), Hünig base (12 mg, 96  $\mu\text{mol}$ , 4.0 eq), EDCI (7 mg, 36  $\mu\text{mol}$ ), and HOBt·H<sub>2</sub>O (7 mg, 85 %wt, 39  $\mu\text{mol}$ , 1.6 eq) to yield a yellow crude solid. Chromatography on (iHex:EA 7:3→1:1; DCM:MeOH 99:1→95:5) returned **AzTax3MTM** as a yellow solid (8 mg, 8.3  $\mu\text{mol}$ , 35%).

**<sup>1</sup>H NMR** (400 MHz, chloroform-*d*)  $\delta$  (ppm) = 8.14 – 8.06 (m, 3H), 7.94 – 7.87 (m, 2H), 7.58 – 7.52 (m, 1H), 7.48 (td,  $J$  = 8.6, 8.1, 1.6 Hz, 4H), 7.43 (t,  $J$  = 1.7 Hz, 1H), 7.42 – 7.39 (m, 2H), 7.39 – 7.32 (m, 2H), 7.19 (s, 2H), 7.13 – 7.09 (m, 1H), 7.07 (d,  $J$  = 8.7 Hz, 1H), 6.26 – 6.18 (m, 1H), 5.82 (dd,  $J$  = 9.0, 2.7 Hz, 1H), 5.69 (d,  $J$  = 7.0 Hz, 1H), 5.17 (s, 1H), 4.92 (d,  $J$  = 8.8 Hz, 1H), 4.81 (d,  $J$  = 2.6 Hz, 1H), 4.30 (d,  $J$  = 8.4 Hz, 1H), 4.24 – 4.19 (m, 3H), 4.03 (s, 3H), 3.97 (q,  $J$  = 2.2, 1.6 Hz, 2H), 3.94 (s, 6H), 3.93 (s, 3H), 2.56 (ddd,  $J$  = 14.2, 9.5, 6.6 Hz, 2H), 2.40 (s, 3H), 2.29 – 2.19 (m, 2H), 1.89 – 1.84 (m, 3H), 1.80 (d,  $J$  = 1.4 Hz, 3H), 1.76 (s, 3H), 1.21 (s, 3H), 1.11 (s, 3H). **<sup>13</sup>C NMR** (101 MHz, CDCl<sub>3</sub>)  $\delta$  (ppm) = 211.4, 172.7, 170.7, 167.0, 166.3, 162.8, 159.3, 153.6, 148.9, 141.8, 141.2, 138.2, 138.1, 136.2, 133.8, 131.2, 130.3, 129.3, 129.1, 128.8, 128.4, 127.2, 126.1, 116.0, 112.6, 101.0, 84.3, 81.2, 78.8, 75.0, 74.6, 73.4, 72.6, 72.1, 61.2, 57.8, 56.6, 56.4, 55.2, 46.6, 43.2, 37.1, 36.7, 36.3, 31.6, 29.8, 26.7, 22.7, 20.8, 14.5, 10.0.

**(2aR,4S,4aS,6R,9S,11S,12S,12aR,12bS)-12b-acetoxy-4,6,11-trihydroxy-9-(((2R,3S)-2-hydroxy-3-phenyl-3-((3,4,5-trimethoxyphenyl)diazenyl)benzamido)propanoyl)oxy)-4a,8,13,13-tetramethyl-5-oxo-2a,3,4,4a,5,6,9,10,11,12,12a,12b-dodecahydro-1H-7,11-methanocyclodeca[3,4]benzo[1,2-b]oxet-12-yl benzoate (AzTax3TM)**

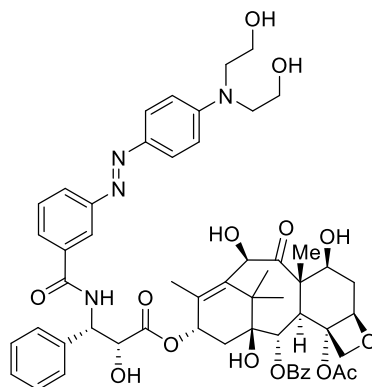


#### AzTax3TM

By Standard Procedure E, docetaxel (20 mg, 24  $\mu\text{mol}$ ) was deprotected with TFA-DCM and the crude foam (17 mg) reacted with **3TM-CO<sub>2</sub>H** (10 mg, 29  $\mu\text{mol}$ , 1.2 eq), Hünig base (12 mg, 96  $\mu\text{mol}$ , 4.0 eq), EDCI (7 mg, 36  $\mu\text{mol}$ ), and HOBt·H<sub>2</sub>O (7 mg, 85 %wt, 39  $\mu\text{mol}$ , 1.6 eq) to yield a yellow crude solid. Chromatography on (iHex:EA 7:3→1:1; DCM:MeOH 99:1→96:4) returned **AzTax3TM** as a yellow solid (9 mg, 9.0  $\mu\text{mol}$ , 37%).

**<sup>1</sup>H NMR** (400 MHz, chloroform-d)  $\delta$  (ppm) = 8.22 (t,  $J$  = 1.9 Hz, 1H), 8.15 – 8.10 (m, 2H), 8.04 – 7.99 (m, 1H), 7.87 (dt,  $J$  = 7.9, 1.3 Hz, 1H), 7.62 – 7.54 (m, 2H), 7.54 – 7.48 (m, 4H), 7.47 – 7.44 (m, 1H), 7.44 – 7.39 (m, 2H), 7.39 – 7.35 (m, 1H), 7.24 (s, 2H), 7.20 (dd,  $J$  = 8.7, 3.9 Hz, 1H), 6.26 – 6.20 (m, 1H), 5.84 (dd,  $J$  = 9.0, 2.6 Hz, 1H), 5.69 (d,  $J$  = 7.1 Hz, 1H), 5.17 (d,  $J$  = 4.7 Hz, 1H), 4.97 – 4.90 (m, 1H), 4.82 (s, 1H), 4.31 (d,  $J$  = 8.5 Hz, 1H), 4.22 (d,  $J$  = 8.2 Hz, 3H), 3.96 (s, 6H), 3.94 (s, 3H), 3.93 – 3.87 (m, 2H), 3.69 – 3.60 (m, 2H), 3.58 (s, 1H), 2.57 (ddd,  $J$  = 15.7, 9.7, 6.5 Hz, 1H), 2.40 (s, 3H), 2.37 – 2.21 (m, 3H), 1.86 (d,  $J$  = 12.4 Hz, 2H), 1.80 (d,  $J$  = 1.4 Hz, 2H), 1.76 (s, 3H), 1.21 (s, 4H), 1.12 (s, 3H), 0.93 – 0.80 (m, 2H). **<sup>13</sup>C NMR** (101 MHz, chloroform-d)  $\delta$  (ppm) = 211.3, 172.6, 170.5, 167.0, 166.4, 152.5, 148.2, 141.2, 138.1, 137.9, 136.2, 134.7, 133.7, 130.2, 129.6, 129.2, 129.2, 129.1, 128.7, 128.4, 127.1, 126.0, 121.0, 100.8, 84.1, 81.1, 78.8, 74.8, 74.5, 73.1, 72.5, 72.0, 61.1, 57.7, 56.3, 55.1, 46.5, 43.1, 37.0, 36.0, 29.7, 26.6, 22.6, 20.6, 14.4, 9.9. **LCMS(+)**:  $t_{\text{ret}}$  = 8.2 min, 1006 Th = [M]<sup>+</sup>. **HRMS (ESI+)** calcd for [C<sub>55</sub>H<sub>59</sub>N<sub>3</sub>O<sub>16</sub>]<sup>+</sup> = [MH]<sup>+</sup>:  $m/z$  1006.39681, found 1006.39929.

(2aR,4S,4aS,6R,9S,11S,12S,12aR,12bS)-12b-acetoxy-9-(((2R,3S)-3-(3-((4-(bis(2-hydroxyethyl)amino)phenyl)diazenyl)benzamido)-2-hydroxy-3-phenylpropanoyl)oxy)-4,6,11-trihydroxy-4a,8,13,13-tetramethyl-5-oxo-2a,3,4,4a,5,6,9,10,11,12,12a,12b-dodecahydro-1H-7,11-methanocyclodeca[3,4]benzo[1,2-b]oxet-12-yl benzoate (AzTax3DEA)

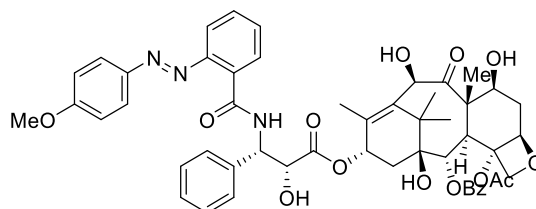


**AzTax3DEA**

By Standard Procedure E, docetaxel (20 mg, 24  $\mu\text{mol}$ ) was deprotected with TFA-DCM and the crude foam (17 mg) reacted with **3DEA-CO<sub>2</sub>H** (10 mg, 29  $\mu\text{mol}$ , 1.2 eq), Hünig base (12 mg, 96  $\mu\text{mol}$ , 4.0 eq), EDCI (7 mg, 36  $\mu\text{mol}$ ), and HOBt·H<sub>2</sub>O (7 mg, 85 %wt, 39  $\mu\text{mol}$ , 1.6 eq) to yield a yellow crude solid. Chromatography on (DCM:MeOH 98:2→92:8) returned **AzTax3DEA** as a yellow solid (12 mg, 11.8  $\mu\text{mol}$ , 49%).

**<sup>1</sup>H NMR** (400 MHz, methanol-*d*<sub>4</sub>)  $\delta$  (ppm) = 8.29 (t,  $J$  = 1.8 Hz, 1H), 8.12 (d,  $J$  = 1.2 Hz, 1H), 8.10 (d,  $J$  = 1.5 Hz, 1H), 7.96 (ddd,  $J$  = 8.0, 2.0, 1.1 Hz, 1H), 7.89 (dt,  $J$  = 7.8, 1.4 Hz, 1H), 7.85 – 7.81 (m, 2H), 7.68 – 7.62 (m, 1H), 7.61 – 7.55 (m, 3H), 7.55 – 7.52 (m, 1H), 7.50 (d,  $J$  = 1.2 Hz, 1H), 7.43 (t,  $J$  = 7.8 Hz, 2H), 7.33 – 7.27 (m, 1H), 6.89 (d,  $J$  = 9.3 Hz, 2H), 6.27 – 6.17 (m, 1H), 5.69 (d,  $J$  = 5.3 Hz, 1H), 5.64 (d,  $J$  = 7.2 Hz, 1H), 5.25 (s, 1H), 4.99 – 4.94 (m, 1H), 4.76 (d,  $J$  = 5.4 Hz, 1H), 4.58 (s, 1H), 4.20 (td,  $J$  = 8.6, 5.9 Hz, 3H), 3.88 (d,  $J$  = 7.2 Hz, 1H), 3.79 (t,  $J$  = 5.9 Hz, 4H), 3.68 (t,  $J$  = 5.9 Hz, 4H), 2.48 – 2.40 (m, 1H), 2.39 (s, 3H), 2.30 – 2.18 (m, 2H), 1.96 (dd,  $J$  = 15.5, 8.8 Hz, 1H), 1.89 (d,  $J$  = 1.4 Hz, 3H), 1.82 (td,  $J$  = 12.6, 11.3, 2.6 Hz, 1H), 1.69 (s, 3H), 1.16 (s, 3H), 1.11 (s, 3H). **<sup>13</sup>C NMR** (101 MHz, methanol-*d*<sub>4</sub>)  $\delta$  (ppm) = 209.7, 173.1, 170.5, 170.0, 168.3, 166.3, 153.2, 151.2, 143.3, 137.8, 136.6, 130.1, 129.8, 129.0, 128.4, 128.3, 127.8, 127.6, 127.1, 125.0, 120.5, 111.4, 84.6, 80.9, 77.8, 76.2, 75.1, 74.2, 73.6, 71.2, 71.1, 58.9, 57.5, 56.5, 53.6, 46.4, 43.1, 36.1, 35.5, 25.6, 21.9, 13.0, 9.1. **LCMS(+)**:  $t_{\text{ret}}$  = 7.3 min, 1019 Th = [M]<sup>+</sup>.

**(2aR,4S,4aS,6R,9S,11S,12S,12aR,12bS)-12b-acetoxy-4,6,11-trihydroxy-9-(((2R,3S)-2-hydroxy-3-(2-((4-methoxyphenyl)diazanyl)benzamido)-3-phenylpropanoyl)oxy)-4a,8,13,13-tetramethyl-5-oxo-2a,3,4,4a,5,6,9,10,11,12,12a,12b-dodecahydro-1H-7,11-methanocyclodeca[3,4]benzo[1,2-b]oxet-12-yl benzoate (AzTax2MP)**

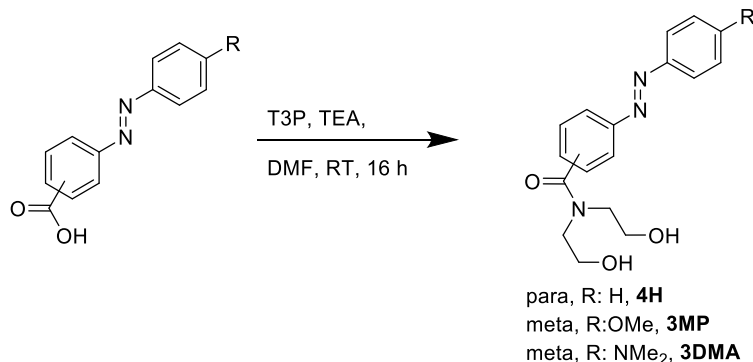


**AzTax2MP**

By Standard Procedure E, docetaxel (20 mg, 24  $\mu\text{mol}$ ) was deprotected with TFA-DCM and the crude foam (17 mg) was dissolved in 2 mL DMF. **4MP-CO<sub>2</sub>H** (8 mg, 28  $\mu\text{mol}$ , 1.2 eq) was added to the reaction mixture. Triethylamine (24 mg, 240  $\mu\text{mol}$ , 10 eq) was added. T3P (26 mg, 50 wt% in EA, 40  $\mu\text{M}$ , 1.7 eq) was added. The resulting organic solution was stirred at room temperature for 16 h. Upon completion the DMF was removed *in vacuo* and the resulting yellow crude product was purified by means of flash chromatography on silica (iHex:EA 7:3→1:1; DCM:MeOH 99:1→95:5). **AzTax2MP** was obtained as a yellow solid (10 mg, 10.4  $\mu\text{mol}$ , 41%).

**<sup>1</sup>H NMR** (400 MHz, chloroform-*d*)  $\delta$  (ppm) = 9.69 (d,  $J$  = 8.6 Hz, 1H), 8.28 (dd,  $J$  = 7.9, 1.6 Hz, 1H), 8.20 – 8.12 (m, 2H), 7.85 – 7.80 (m, 2H), 7.78 (dd,  $J$  = 8.2, 1.3 Hz, 1H), 7.66 – 7.60 (m, 1H), 7.56 – 7.47 (m, 5H), 7.42 (td,  $J$  = 7.6, 1.3 Hz, 1H), 7.38 – 7.30 (m, 3H), 6.96 (d,  $J$  = 9.0 Hz, 2H), 6.22 (d,  $J$  = 8.8 Hz, 1H), 5.95 (dd,  $J$  = 8.7, 2.5 Hz, 1H), 5.68 (d,  $J$  = 7.0 Hz, 1H), 5.16 – 5.12 (m, 1H), 4.94 (d,  $J$  = 9.4 Hz, 1H), 4.77 (dd,  $J$  = 4.9, 2.5 Hz, 1H), 4.33 (d,  $J$  = 8.5 Hz, 1H), 4.25 – 4.16 (m, 3H), 3.89 (s, 4H), 3.69 (d,  $J$  = 7.6 Hz, 2H), 2.58 (t,  $J$  = 15.2 Hz, 2H), 2.42 (s, 3H), 2.40 – 2.22 (m, 3H), 1.86 (d,  $J$  = 14.3 Hz, 2H), 1.80 (d,  $J$  = 1.4 Hz, 3H), 1.77 (d,  $J$  = 5.5 Hz, 3H), 1.51 (s, 2H), 1.19 (s, 3H), 1.11 (s, 3H), 0.95 – 0.81 (m, 2H).

**<sup>13</sup>C NMR** (101 MHz, chloroform-*d*)  $\delta$  (ppm) = 172.5, 170.5, 167.0, 165.9, 163.2, 150.1, 146.7, 138.7, 138.5, 135.9, 133.7, 132.2, 131.9, 130.7, 130.3, 129.4, 129.3, 128.9, 128.8, 128.3, 128.3, 128.0, 127.2, 126.8, 125.8, 116.1, 114.6, 84.1, 81.1, 78.8, 74.8, 74.6, 73.8, 72.3, 72.1, 57.7, 55.7, 46.5, 43.0, 37.0, 36.0, 29.7, 26.5, 22.7, 20.6, 14.6, 9.9. **LCMS(+)**:  $t_{\text{ret}}$  = 8.7 min, 946 Th =  $[\text{MH}]^+$ , **HRMS (ESI+)** calcd for  $[\text{C}_{52}\text{H}_{55}\text{N}_3\text{O}_{14}]^+$  =  $[\text{MH}]^+$ :  $m/z$  946.37740, found 946.37568.

**Water-soluble model photoswitch carboxamides*****N,N*-bis(2-hydroxyethyl)-4-(phenyldiazenyl)benzamide (4H)**

By standard procedure F, Commercial compound **4H-CO<sub>2</sub>H** (20 mg, 0.089 mmol, 1.0 eq) was reacted with diethanolamine (19 mg, 0.18 mmol, 2.0 eq). After purification by means of flash chromatography (DCM:MeOH, 100:0→98:2) the desired product ***N,N*-bis(2-hydroxyethyl)-4-(phenyldiazenyl)benzamide (4H)**. <sup>1</sup>H NMR (400 MHz, methanol-*d*<sub>4</sub>) δ (ppm) = 8.01 – 7.97 (m, 2H), 7.97 – 7.92 (m, 2H), 7.68 – 7.63 (m, 2H), 7.60 – 7.51 (m, 3H), 3.87 (t, *J* = 5.5 Hz, 2H), 3.74 (t, *J* = 5.6 Hz, 2H), 3.64 (t, *J* = 5.6 Hz, 2H), 3.54 (t, *J* = 5.7 Hz, 2H). <sup>13</sup>C NMR (101 MHz, DMSO-*d*<sub>6</sub>) δ (ppm) = 170.3, 151.9, 151.7, 140.0, 131.8, 130.7, 129.6, 128.1, 122.7, 122.5, 58.5, 58.5, 51.6, 47.4. **LCMS(+)**: *t*<sub>ret</sub> = 3.8 min, 314 Th = [MH]<sup>+</sup>. **HRMS (EI)**: calc. for C<sub>17</sub>H<sub>19</sub>N<sub>3</sub>O<sub>3</sub><sup>+</sup> [M]<sup>+</sup>: 313.1426; found: 343.1409.

***3*-((4-(dimethylamino)phenyl)diazenyl)-*N,N*-bis(2-hydroxyethyl)benzamide (3DMA)**

By standard procedure F, **3DMA-CO<sub>2</sub>H** (20 mg, 0.074 mmol, 1.0 eq) was reacted with diethanolamine (16 mg, 0.15 mmol, 2.0 eq). After purification by means of flash chromatography (DCM:MeOH, 98:2→96:4) the desired product ***3*-((4-(dimethylamino)phenyl)diazenyl)-*N,N*-bis(2-hydroxyethyl)benzamide (3DMA)** (16 mg, 0.045 mmol, 60%) was obtained as a yellow solid. <sup>1</sup>H NMR (500 MHz, methanol-*d*<sub>4</sub>) δ (ppm) = 7.92 – 7.81 (m, 4H), 7.57 (dd, *J* = 8.5, 7.6 Hz, 1H), 7.48 (dt, *J* = 7.5, 1.4 Hz, 1H), 6.86 – 6.81 (m, 2H), 3.88 (t, *J* = 5.7 Hz, 2H), 3.74 (t, *J* = 5.7 Hz, 2H), 3.64 (t, *J* = 5.8 Hz, 2H), 3.54 (t, *J* = 5.7 Hz, 2H), 3.10 (s, 6H). <sup>13</sup>C NMR (126 MHz, methanol-*d*<sub>4</sub>) δ (ppm) = 173.1, 165.0, 153.1, 153.0, 143.3, 137.5, 129.0, 127.2, 124.8, 123.0, 119.8, 111.2, 59.2, 59.0, 52.3, 39.0. **LCMS(+)**: *t*<sub>ret</sub> = 4.0 min, 357 Th = [MH]<sup>+</sup>. **HRMS (EI)**: calc. for C<sub>14</sub>H<sub>12</sub>O<sub>3</sub>N<sub>2</sub><sup>+</sup> [M]<sup>+</sup>: 356.1848; found: 356.1839.

***N,N*-bis(2-hydroxyethyl)-3-((4-methoxyphenyl)diazenyl)benzamide (3MP)**

By standard procedure F, **3MP-CO<sub>2</sub>H** (20 mg, 0.078 mmol, 1.0 eq) was reacted with diethanolamine (16 mg, 0.16 mmol, 2.0 eq). After purification by means of flash chromatography (DCM:MeOH, 98:2→95:5) the desired product ***N,N*-bis(2-hydroxyethyl)-3-((4-methoxyphenyl)diazenyl)benzamide (3MP)** (17 mg, 0.050 mmol, 64%) was obtained as



a yellow solid. **<sup>1</sup>H NMR** (400 MHz, methanol-*d*<sub>4</sub>)  $\delta$  (ppm) = 7.97 – 7.90 (m, 4H), 7.64 – 7.58 (m, 1H), 7.56 (dt, *J* = 7.6, 1.5 Hz, 1H), 7.12 – 7.04 (m, 2H), 3.89 (s, 5H), 3.74 (t, *J* = 5.7 Hz, 2H), 3.64 (t, *J* = 5.7 Hz, 2H), 3.53 (t, *J* = 5.7 Hz, 2H). **<sup>13</sup>C NMR** (101 MHz, methanol-*d*<sub>4</sub>)  $\delta$  (ppm) = 172.1, 162.0, 151.7, 145.9, 136.8, 128.4, 127.6, 123.8, 122.6, 119.5, 113.2, 58.4, 58.1, 54.0, 51.5. **LCMS(+)**: *t*<sub>ret</sub> = 3.6 min, 344 Th = [MH]<sup>+</sup>. **HRMS (EI)**: calc. for C<sub>14</sub>H<sub>12</sub>O<sub>3</sub>N<sub>2</sub><sup>+</sup> [M]<sup>+</sup>: 343.1532; found: 343.1522.

### ***Discussion of arylazopyrazole-dextran heterodimerisation (Liu et al., 2018)***

As far as we are aware, Liu and coworkers (Angewandte 2018)<sup>13</sup> disclosed the only work in the direction of optically-localisable microtubule stabilisation. They aimed to use the known photoswitchability of host-guest interactions between beta-cyclodextran and <sup>1</sup>arylazopyrazoles (*trans*-arylazopyrazole:dextran binding constant up to 2300 M<sup>-1</sup> while the *cis*- is essentially nonbinding)<sup>14</sup> to aim at photoswitchably reversible, noncovalent heterodimerisation of two paclitaxel conjugates each applied to cells at 100 nM. Their hypothesis (as Fig 1<sup>13</sup>) is that the heterodimer (max taxol-to-taxol distance approx 2 nm) should allow crosslinking binding to two microtubules (minimum taxol-to-taxol distance ca. 7 nm), but this is to our mind geometrically unlikely since taxol's binding site is on the luminal (inner) face of the microtubules<sup>15</sup> and crosslinked binding would require the linker to penetrate directly through both protein walls, as well as stretching substantially beyond its limit end-to-end distance and reorienting taxol away from its usual binding structure. It is also noteworthy that the maximum concentration of heterodimer in free solution that could be predicted from this approach using the literature binding constant is only ca. 23 pM; and that the separated monomeric paclitaxel halves counterintuitively do not appear to hyperpolymerise microtubule structure *in cellulo* (as Fig 4<sup>13</sup>) which may reflect poor potency when the 2'-hydroxyl group, usually thought necessary for binding as it is oriented into the protein, is masked with large although potentially enzymatically cleavable esters. Nevertheless, the authors reported that the combination of the two heterodimeriser halves isomer-dependently alters the proportion of subG1-phase (dying) cells in a treated sample from 8% to 12% (error bars  $\pm$  2%; as Fig S14<sup>13</sup>); but this approach has not been shown to allow *in cellulo* photoswitchability of effect, nor an apparent switch-on/switch-off of bioactivity. To our mind it cannot be excluded that the relatively modest isomer-dependency of cellular effect results from slightly improved dextran trafficking of the *trans*-conjugate and also invokes intracellular ester hydrolysis; nor that the differences of cell-free MT aggregate shapes (as Fig 2<sup>13</sup>), if such are reproducible and significant, could arise from the differential solubilities of the species employed. The choice of a ~4 kDa construct design with two applied drugs also seems to leave room for reagent design improvement.

## Part B: Photocharacterisation *in vitro*

### **Materials and Methods**

#### **HPLC for UV-Vis spectroscopy on separated isomers**

During HPLC (as in Part A), the diode array detector was used to acquire peak spectra of separated photoswitch isomers over the range 200–550 nm, manually baselining across each elution peak of interest to correct for eluent composition effects.

#### **UV-Vis spectrophotometry to monitor photoswitching and relaxation in bulk samples**

Absorption spectra in cuvette ("UV-Vis") were acquired on a Varian CaryScan 60 (1 cm pathlength). For photoisomerisation measurements, Hellma microcuvettes (108-002-10-40) taking 500  $\mu$ L volume to top of optical window were used with test solution such that the vertical pathlength of the isomerization light is less than 7 mm to the bottom of the cuvette, with the default test solution concentrations of 25  $\mu$ M. Measurements on soluble photoswitches were performed by default in PBS at pH  $\sim$ 7.4 with 1% of DMSO to better mimic the intracellular environment during cell culture conditions (with 1% DMSO). Photoisomerisations and relaxation rate measurements were performed at room temperature. "Star" LEDs (H2A1-models spanning 360–590 nm from Roithner Lasertechnik) were used for photoisomerisations in the cuvette that were also predictive of what would be obtained in LED-illuminated cell culture.

The **AzTaxes** were not reliably soluble enough to be assayed in physiologically relevant aqueous media ( $\sim$ 1% DMSO max, aqueous buffer) at  $\sim$ 50  $\mu$ M as is necessary for long-term UV-Vis based studies on our setup. Therefore the spectra of the excellently water-soluble diethanolamide model photoswitches were instead acquired, in physiologically relevant aqueous media (PBS with  $<$ 1% DMSO), to give the closest approximation of the PSSs to be expected in cell assays with the cognate series of **AzTaxes**. Their absorption spectra at the photostationary states (PSSs) under illumination at different biocompatible and photoswitching-relevant wavelengths, were measured. Note that "dark" represents a solution quantitatively relaxed to all-*E* by warming overnight to 60 °C.

#### **Thermally reversible and photoreversible photoisomerisation**

Azobenzenes photoswitches featuring *para*-dialkylamino groups (**3DMA**, **3DEA**, **4DMA**) did not appear to undergo bulk photoisomerisation in homogeneous aqueous physiological media (1 cm UV-Vis cuvette measurement, 25  $\mu$ M, PBS pH  $\sim$ 7.4,  $<$ 1% DMSO, 37 °C, detection limit for photoisomerisation implies maintenance of PSS with ca. 2% *Z* isomer) which literature suggests is caused by fast (half-life  $<$  ms range) spontaneous ("thermal"), quantitative, unidirectional *Z*→*E* relaxation in this solvent<sup>16</sup>. All other azobenzenes were photoreversibly isomerisable in this homogeneous aqueous physiological media, which literature supports for azobenzenes not featuring strong resonance donor groups in *para* to the diazene<sup>17</sup>; results are shown for representative photoswitch **3MP** (Fig S1).

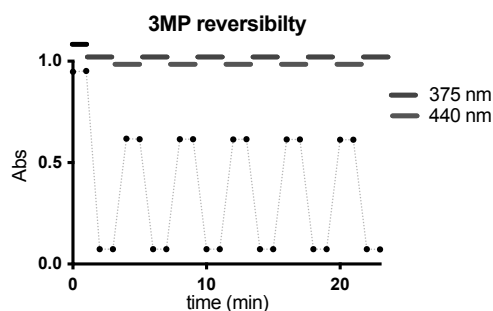


Figure S1: Photoisomerisations in homogeneous aqueous physiological media (PBS pH ~7.4, <1% DMSO, 37 °C) are perfectly photoreversible over many cycles, with no signs of degradation, implying robust and reproducible photoswitching can be possible under biological conditions.

We have previously observed however that non-azobenzene photoswitches that were not bulk-photoswitchable in homogeneous aqueous physiological media, can reliably display photoswitchability of bioactivity when used in the heterogeneous context of cell biology.<sup>18</sup> There are also reports of light-dependent activity for very fast-relaxing azobenzene photopharmaceuticals intended to address intracellular protein targets located in aqueous environments<sup>19</sup>; although, as far as we are aware, those fast-relaxing azobenzenes required illumination with such high photon flux to trigger irreversible bioactivity, that it is conceivable (given e.g. the mismatch between the *trans*-active structure-activity relationship expected, and the experimental *cis*-active result, as well as non-photoreversibility of biological effect) that transient photoisomerisation could to some extent be followed by glutathione (GSH) degradation of the more GSH-sensitive *cis*-azobenzene isomer<sup>20</sup>, yielding a range of undefined, non-photoswitchable byproducts presumably including the diazene scission product aniline, several of which could be expected to be potent, photoirreversible, and biologically essentially irreversible enzyme-inhibiting species. In this work we therefore determined that biological evaluations for fast-relaxing **AzTax** conjugates would proceed with very limited photon flux, applied from short and low-intensity LED pulses, which we estimate to be insufficient<sup>21-23</sup> to give confounding results. Assuming that biological photoswitchability for these species can only arise by their biolocalisation in relatively hydrophobic environments (membranes, lipid vesicles, adsorbed onto proteins) which allow greater thermal stability of the metastable isomer, we therefore measured all photoproperties of the *para*-dialkylaminoazobenzenes in ethyl acetate solution, which we consider to be a reasonable mimic of an aprotic, moderately polar environment. We observed that this allowed **3DMA** to exhibit fully photoreversible isomerisations (Fig S2) which gave hope that *para*-dialkylaminoazobenzene **AzTaxes** might prove to display photoswitchable bioactivity *in cellulo*. We also monitored the rate of spontaneous ("thermal"), quantitative, unidirectional *Z*→*E* relaxation of all azobenzenes. The photoswitches used in this study could be split in two groups according to their performance as relevant to conditions for biological use: (1) The *para*-dialkylamino switches had *cis*-half-life  $t_{1/2} \sim 11$  min in EtOAc (although no switching was observed in water); whereas (2) *para*-alkoxy and *para*-unsubstituted azobenzenes showed relaxation that is much slower (in PBS with < 1% DMSO at 37 °C) than the typical 1-to-60 min

timescale that biological assays would require for delivering functional reversibility; these would therefore require active  $Z \rightarrow E$  photoisomerisation and/or diffusion-based reduction of localised  $Z$  isomer concentration in order to display biological reversibility. *Para*-alkoxy compounds displayed  $t_{1/2}$  (half-life) values on the order of 10 h - 5 days (representative **3MP** had  $t_{1/2} \sim 24$  h); unsubstituted compounds displayed  $t_{1/2}$  values substantially above 1 day (representative **4H** had  $t_{1/2} \gg 24$  h (estimated by exponential decay fit to be ca. 1200 h)). Note however that it is not important for this reagent development research to know precisely the values of the switches' half-lives in homogeneous media *in cuvette*: they are however either far below, or else far above, the biological timescale and can be simply treated accordingly.

### Photostationary state (PSS) equilibria

PSSs were measured. Results for three compounds representative of the three electronic classes of azobenzenes (**3MP** for *p*-OMe, **3DMA** for *p*-NR<sub>2</sub>, **4H** for *p*-unsubstituted switches) are shown in Fig S2.

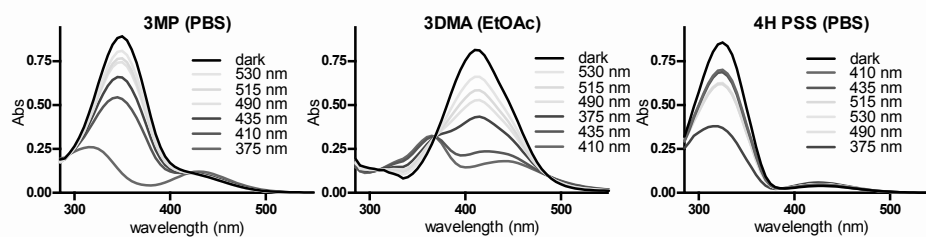


Figure S2: PSS spectra for photoswitches representative of the three structural classes explored in this work.

### PSS analysis

For photopharmaceutical assays in biology it is helpful to anticipate the  $E/Z$  ratio at any wavelength's photostationary state (PSS), to choose optimal wavelengths for illumination during biological assays or to understand the limits of what is possible on a given setup: e.g. on a microscope with laser lines 405 nm, 488 nm and 515 nm, what dynamic range of photoswitchability is possible by establishing localised PSSs (inside a single cell) that alternate between 405 nm and 515 nm? Ideally, 405 nm would establish a PSS with 100% of one isomer (e.g.  $Z$ ), and 515 nm would establish a PSS with 100% of the other isomer, implying a 100% dynamic range of isomer photoswitchability; and ideally, one isomer (e.g.  $Z$ ) would be bioactive while the other isomer would be entirely biologically inactive, therefore that 405 nm / 515 nm photoswitching would also allow 100% dynamic range of biological photoswitchability. However, no azobenzenes have ever been shown to enable 100% dynamic range of isomer photoswitchability, and anyway as far as we are aware only **PSTs**<sup>23</sup> feature one isomer that is entirely biologically inactive. Therefore it is impossible that any azobenzene-based photopharmaceutical according to current designs features 100% dynamic range of biological photoswitchability. Analysing PSS ratios *in cuvette* can extract the isomer photoswitchability, and analysing bioactivity determinations under those same PSSs

in light of the isomer photoswitchabilities can determine the isomer *bioactivity differentials*; both analyses are needed to be able to gauge the dynamic range of biological photoswitchability that is theoretically obtainable under any arbitrary wavelength.

We have previously published a workflow<sup>20</sup> to estimate PSS at any wavelength in biological media, based on acquiring separated *E* and *Z* isomer spectra by LCMS-UV, and relying on isosbestic point determination in physiological media. In brief, to determine the ratios of *E* and *Z* isomers in PSS equilibria, the UV/Vis spectra of the HPLC-separated isomers are measured by inline DAD, extracted, scaled relative to each other using the isosbestic point determined from UV-Vis studies in biological media, then fitted as a linear combination to the measured PSS absorption spectra, with the linear combination coefficients then being the PSS fractions of each isomer.

However, in this research, the isolated *E* and *Z* spectra of the amides in LCMS eluent did not match up to their dark (all-*E*) and illuminated (mostly-*Z*) spectra as recorded in PBS buffer. The  $n \rightarrow \pi^*$  band notably showed lower intensity in the LCMS spectra which we attribute to influence of solvent, as the acidic acetonitrile/water eluent provides a different environment for the azobenzene than the neutral aqueous PBS buffer. We decided that results from measurements in PBS buffer however provide far more useful information for biology, than would performing PSS measurements in the HPLC solvent system, so we changed to a different "envelope" method that establishes entirely robust and assumption-free upper and lower bounds for the true PSS ratios. Since these bounds are often remarkably close to each other the method can allow remarkably precise, assumption-free estimation of the PSS isomer ratios in biological media, and also gives a maximum possible error of that PSS which it is useful to know.

#### Envelope Method

(0) The absorption spectrum of a fully-relaxed sample (60 °C overnight relaxation) is acquired and assumed to be the all-*E* spectrum. This step can also be checked by NMR (in contrast, we consider that establishing illuminated PSSs by NMR is not a straightforward approach due to (a) Lambert-Beer shielding at relatively high concentrations plus high reflection from the tube surface making establishment of many PSSs in many NMR tubes a very timeconsuming process; and (b) need for deuterated biological buffers).

(1) *Upper Bounds*: The *relative completeness* of photoreversions towards the all-*trans* state under different illuminations was examined first. For each PSS wavelength, the "relative completeness fraction" RCF( $\lambda$ ) calculated as the ratio  $[[P(\lambda)-MC(\lambda)],[D(\lambda)-MC(\lambda)]]$ , where  $P(\lambda)$  is the PSS absorption spectrum being evaluated,  $MC(\lambda)$  is the PSS absorption spectrum under the wavelength giving the most-*cis*-containing PSS, and  $D(\lambda)$  is the all-*trans* absorption spectrum, was calculated. This "relative completeness fraction" was calculated across the data range where the variation in absorbances with different PSSs is strongest (typically 370-420 nm), then the data were averaged to give the mean, and their standard deviation determined as a measure of the error in this fitting method. These completeness fraction

values are, by definition, lower bounds for the PSS values of *E*-content, so **[1-RCF( $\lambda$ )] determines robust upper bounds** for the PSS values of *Z*-content.

(2) *Lower Bounds*: **Lower bounds** for the PSS *Z*-content values may separately be obtained by assuming the absorption of the *cis* isomer is zero at a single wavelength  $\lambda_{\text{strong}}$  (the wavelength with the largest fold differential of extinction coefficients between *cis* and *trans* forms) and then tabulating  $A(\lambda_{\text{strong, PSS}})/A(\lambda_{\text{strong, all-trans}})$ . Typically,  $\lambda_{\text{strong}}$  is approx. 385 nm.

(3) *Envelope*: The interval from lower to upper bound is an assumption-free bounded range for the true PSS at any measured wavelength. This will be seen to be more than sufficient to give a PSS range with typically only  $\pm 5$ -10% possible error at the wavelengths of most interest to this study. We here represent the envelope midpoint as the fitted "PSS %Z", and give the half-width of the envelope (100% CI) as the possible error " $\pm$  %" (Table S1).

$\lambda$ (nm)	3MP		4H		3DMA (in EA)	
	PSS %Z	+/- %	PSS %Z	+/- %	PSS %Z	+/- %
375	96%	4%	80%	20%	53%	5%
410	44%	2%	26%	6%	91%	9%
435	29%	1%	28%	7%	80%	8%
490	18%	1%	39%	10%	39%	4%
515	16%	1%	39%	9%	32%	3%
530	11%	1%	38%	9%	21%	2%

Table S1 - Estimated PSSs from the envelope method and maximum error in the estimated PSSs, for the three different families of azobenzene photoswitches used in this study (*p*-OMe, *p*-unsubstituted, *p*-NR<sub>2</sub>).

### Part C: Biochemistry: tubulin polymerisation *in vitro*

99% tubulin from porcine brain was obtained from Cytoskeleton Inc. (cat. #T240). The polymerisation reaction was performed at 5 mg/mL tubulin, in polymerisation buffer BRB80 (80 mM piperazine-N,N'-bis(2-ethanesulfonic acid) (PIPES) pH = 6.9; 0.5 mM EGTA; 2 mM MgCl<sub>2</sub>), in a cuvette (120  $\mu$ L final volume, 1 cm path length) in a Varian CaryScan 60 with Peltier cell temperature control unit maintained at 37 °C; with glycerol (10  $\mu$ L). Tubulin was incubated at 37 °C with "pre-lit"- [360 nm-pre-illuminated; mostly-*Z*-] or dark- [all-*E*] **AzTax3MP**, or docetaxel (final inhibitor concentration 10  $\mu$ M), or without inhibitor ("cosolvent" control), in buffer with 3% DMSO and 1 mM GTP, and the change in absorbance at 340 nm was monitored, scanning at 15 s intervals<sup>24</sup>. Docetaxel showed the strongest microtubule hyperpolymerisation effect; pre-lit **AzTax3MP** had ca. 2/3 of docetaxel's hyperpolymerising potency compared to cosolvent-only control; all-*E* **AzTax3MP** had had ca. 1/3 of docetaxel's potency (Fig 2d).

## Part D: Cell Biology

### **Cell assay methods**

#### **General cell culture**

HeLa cells were maintained under standard cell culture conditions in Dulbecco's modified Eagle's medium (DMEM; PAN-Biotech: P04-035550) supplemented with 10% fetal calf serum (FCS), 100 U/mL penicillin and 100 U/mL streptomycin. Cells were grown and incubated at 37 °C in a 5% CO<sub>2</sub> atmosphere. Cells were cultured in phenol red free medium prior to assays (DMEM; PAN-Biotech: P04-03591). Compounds and cosolvent (DMSO; 1% final concentration) were added *via* a D300e digital dispenser (Tecan); all photoswitches were added in their all-*E* state (thermal relaxation of the DMSO stocks at 60 °C overnight, applied under light exclusion conditions). Cells were either incubated under "lit" or "dark" conditions; "lit" indicates a pulsed illumination protocol applied by multi-LED arrays to create, *in situ* in cells, the wavelength-dependent PSS isomer ratio of the compounds, and then maintain it throughout the experiment, as described previously.<sup>20,22</sup> Typical "lit" timing conditions were 75 ms pulses applied every 15 s. "Dark" indicates that compounds were applied while working, sterile, under red-light conditions, and cells were then incubated in light-proof boxes to shield from ambient light, thereby maintaining the all-*E*-isomer population throughout the experiment.

#### **Resazurin antiproliferation assay**

Cells were seeded in 96-well plates at 5,000 cells/well and left to adhere for 24 h before treating with various concentrations of different compounds. *E*-**AzTax** were added and incubated under the indicated lighting conditions for 48 h (final well volume 100  $\mu$ L, 1% DMSO; three technical replicates); the "cosolvent control" ("ctrl") indicates treatment with DMSO only. Cell viability was measured by addition of resazurin, which is reduced to resorufin under metabolic activity in live cells. Fluorescence of the resorufin product was measured using a FLUOstar Omega microplate reader (BMG Labtech) at 544/590 nm (ex/em). Fluorescence data was averaged over technical replicates, then normalized to viable cell count from cosolvent control cells (%control) as 100%, where 0% viability was assumed to correspond to zero. Three independent experiments were performed and data is shown as mean $\pm$ SD; data were plotted against the log of **AzTax** concentration ( $\log_{10}([\text{AzTax}] \text{ (M)})$ ).

#### **Cell cycle analysis**

HeLas were seeded in 6 well plates (300,000/well) 24 h prior to treatment. **AzTax3MP** and **AzTax4DMA** were added to the wells and cells were incubated either under "dark" or "lit" regimens. 0.1  $\mu$ M Docetaxel served as positive control and 1% DMSO as cosolvent control. Cells were harvested 24 h later and fixed overnight in 70% ice cold ethanol. After 12 h, cells were washed and re-hydrated for 15 min in PBS before staining with propidium iodide ("PI", 200  $\mu$ g/mL in 0.1 % Triton X-100 containing 200  $\mu$ g/mL DNase-free RNase (Thermo Fischer Scientific EN0531) for 30 min at RT. Flow cytometry was done with an LSR Fortessa (BD Biosciences) run by BD FACSDiva 8.0.1 software and at least 10,000 individual PI-positive

cells per condition were collected. FlowJo software (BD Biosciences) was used for gating, first selecting alive cells, then single cells and then setting gates in the PI channel that correspond to less than two sets of chromosomes (subG1), two sets of chromosomes (G1), more than two and less than four (S) and four sets of chromosomes (G2/M). Results plotted as % of parent gate and are given as the mean $\pm$ SD of at least three biological replicates.

#### **Immunofluorescence staining**

For visualization of polymerized tubulin and DNA cells were seeded on glass coverslips in 24 well plates (50,000 cells/well) 24 h prior to treatment. **AzTax3MP**, DMSO or 0.1  $\mu$ M docetaxel was applied the next day (concentration range **AzTax3MP**: 0.1  $\mu$ M-3  $\mu$ M, all wells with 1% DMSO) and cells were incubated either in the dark or with the regular illumination protocol. The next day medium was removed, Cells were washed with pre-warmed (37 °C) MTSB buffer (80 mM PIPES, pH 6.8; 1 mM MgCl<sub>2</sub>, 5 mM ethylene glycol tetraacetic acid (EGTA) dipotassium salt; 0.5% Triton X-100) for 30 s to remove tubulin monomers then fixed with 0.5% glutaraldehyde for 10 min. After quenching with 0.1% NaBH<sub>4</sub> cells were blocked for 30 min in PBS containing 30% FCS before incubation with anti- $\alpha$ -tubulin primary antibody (1:400 rabbit Abcam ab18251) for 1 h. Secondary antibody was donkey-anti-rabbit Alexa488 (Thermo Fisher Scientific A21206; 1:400 in PBS + 10% FCS). Coverslips were then mounted on slides with Roti-Mount FluorCare DAPI (Carl Roth) and left to dry. Confocal images were acquired on a Leica SP8 with a 405 nm laser and a white light laser, using a 63 $\times$  glycerol objective. Confocal stacks (0.33  $\mu$ m step size) were z-projected and gamma adjusted for better visualization in Fiji/ImageJ.



### Resazurin viability assay results for all compounds

Results for all compounds are shown in Fig S3. The results of the resazurin assays can be correlated with the compounds' structures. The important parameters are the general potency of the compound (roughly, the average IC<sub>50</sub> of the lit and dark states) and the dynamic range (difference of IC<sub>50</sub> dark vs lit).

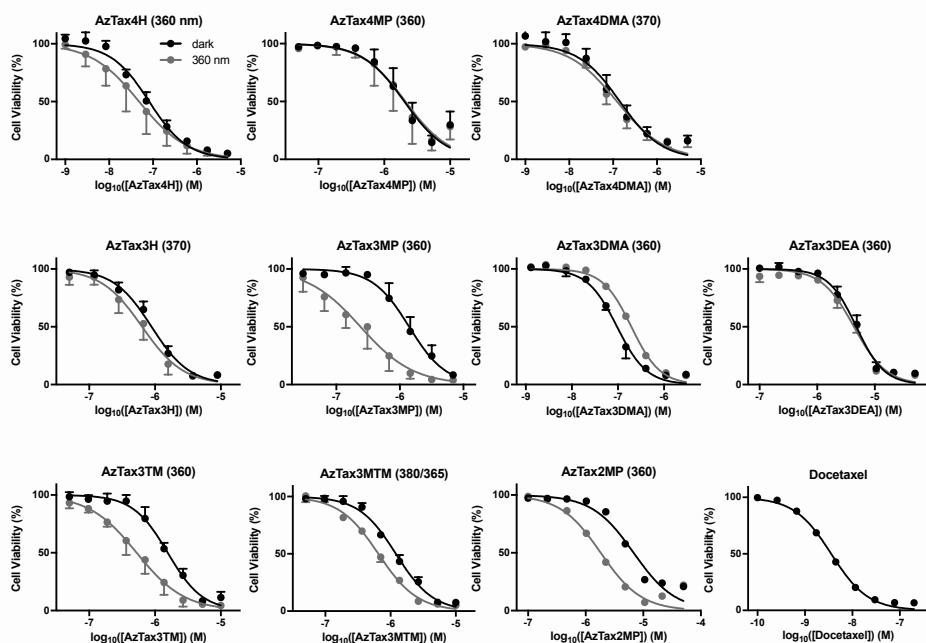


Figure S3: resazurin viability assay results for all compounds. The wavelength/s (in nm) used for the "lit" experiments (shown as purple curves) are given in brackets after each graph title, as different wavelengths were used for the assays. The "dark" experiments are depicted in black.

The first structural element to be examined is the attachment point of the azobenzene to the taxane scaffold. The number in the compound name specifies the attachment relative to the diazene bridge (2 = *ortho*, 3 = *meta*, 4 = *para*). It can be generalized that no *para* connected compound showed significant lit vs. dark difference of IC<sub>50</sub>. *Meta* connected compounds show the highest dynamic range, and attachment in *ortho* reduced the overall potency significantly. The second structural element examined is the substitution on the azobenzenes. Unsubstituted compounds **AzTax4H** and **AzTax3H** show no significant toxicity change upon illumination, although **AzTax4H** is an order of magnitude more toxic than **AzTax3H**. Alkylated *para*-amino compounds with fast relaxation times also show no strong difference between dark and lit experiments; **AzTax4DMA** and **AzTax3DMA** are approximately equally toxic and **AzTax3DMA** is the only compound that appears to show a higher toxicity under dark conditions, while more polar **AzTax3DEA** shows substantially lower toxicity than either dimethylamino compound. The last group of **AzTax** compounds are variously methoxylated. **AzTax4MP** shows no difference in IC<sub>50</sub> upon irradiation. The *meta* connected **AzTax3MP** shows the highest dynamic range as well as satisfactory toxicity. The two derivatives

**AzTax3TM** and **AzTax3MTM** have roughly the same cytotoxicities but more moderate dynamic range. **AzTax2MP** shows a drop in toxicity while displaying higher toxicity under illuminated conditions.

### FACS cell cycle analysis

Results of cell cycle analysis for **AzTax3MP** were shown in Fig 3b-c. Docetaxel and DMSO and lighting controls are shown in Fig S4a; results for non-photoswitchable yet cytotoxic control compound **AzTax4DMA** are shown in Fig S4b; and gating strategy is depicted in Fig S4c. Lighting and cosolvent cause no change to cell cycle repartition; **AzTax4DMA** (whose short aqueous *cis*-half-life should prevent any light-dependent bioactivity being visible) shows no light-dependent effects, and it also dose-dependently recapitulates the cell cycle repartition seen for positive control docetaxel.

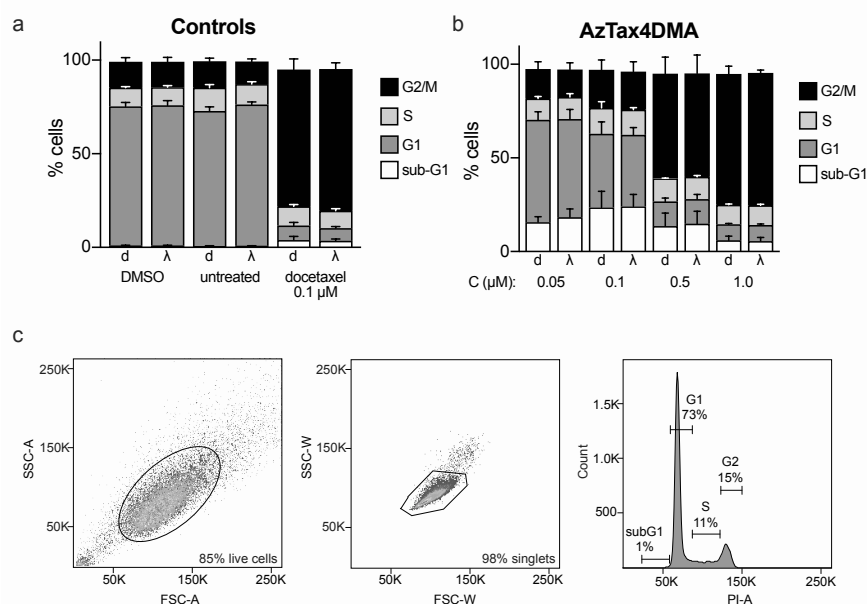


Figure S4: Controls for cell cycle repartition. **a** Controls without ("untreated") and with ("DMSO") cosolvent show no cosolvent-induced change of cell cycle repartition; positive control docetaxel gives strong G2/M arrest; and none of these controls show light-dependency of cell cycle repartition. **b** Non-photoswitchable **AzTax4DMA** shows no light-dependency of cell cycle repartition, but does show dose-dependent G2/M arrest (compare Fig 3c). **c** Gating strategy for the FACS cell cycle analyses.

### Immunofluorescence imaging of microtubule network structure

**AzTax3MP** caused light- and dose-dependent disruption of microtubule structure, as well as cell toxicity (visible as the density of cells) (Fig 3a, Fig S5). At 0.1 μM, disorganisation of the MT network is evident under lit conditions but no change is seen under dark conditions. By 0.5 μM, **AzTax3MP** causes extensive mitotic arrest under lit, but not dark, conditions. At 1 μM, under lit conditions only a minor population of adherent cells persists (although the latter have severe MT organisational defects and multinucleation) and mitotic spindle defects are visible (see arrows and inset), while under dark conditions cells mainly escape mitotic arrest (albeit

with nuclear defects) and no mitotic arrests are visible. Nuclei are especially fragmented and highly condensed under lit treatment. Fantastically disrupted microtubule patterns are seen with higher doses of lit **AzTax3MP** and some cells appear to have no remaining microtubule structures, perhaps since non-microtubular tubulin aggregates (expected at high doses of MT stabiliser, as seen in the cell-free polymerisation assay) are removed during the wash steps of the staining process; under dark conditions, mitotic arrests are seen and nuclear disorganisation becomes severe although the MT networks persist, in a disorganised state.

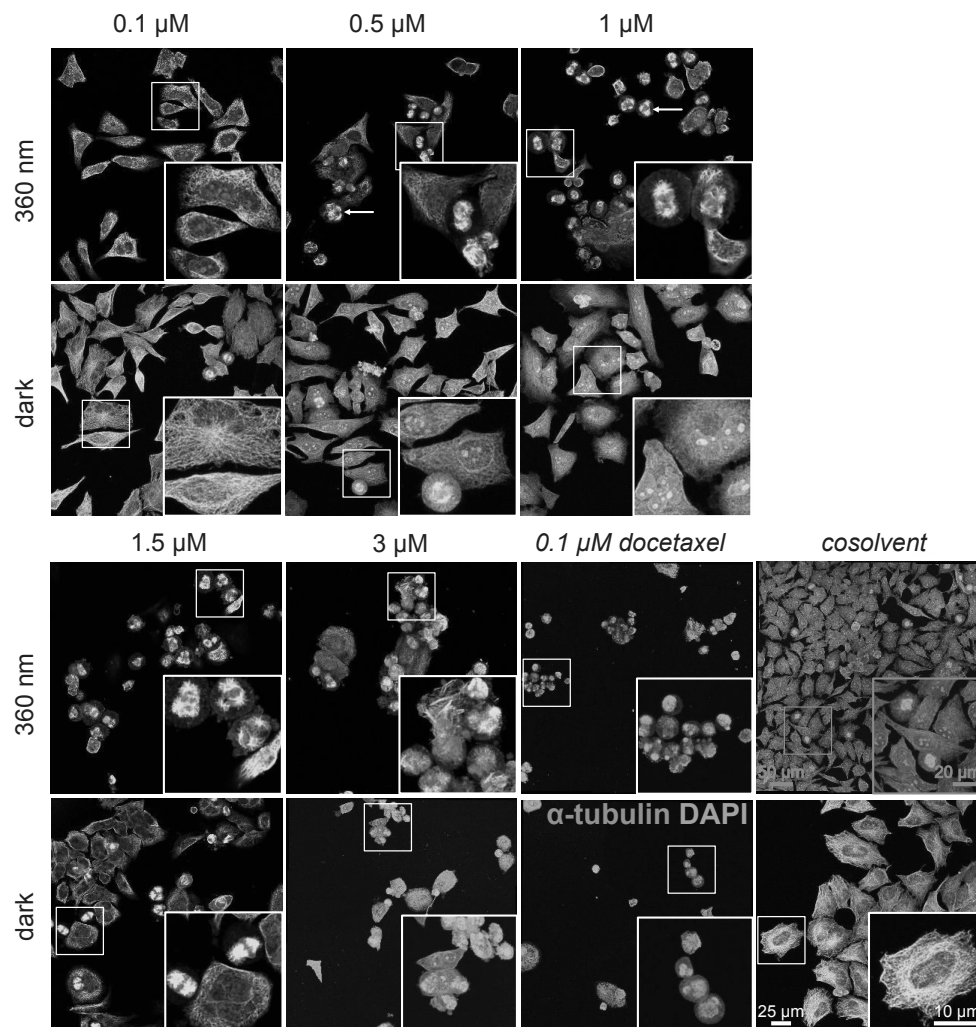
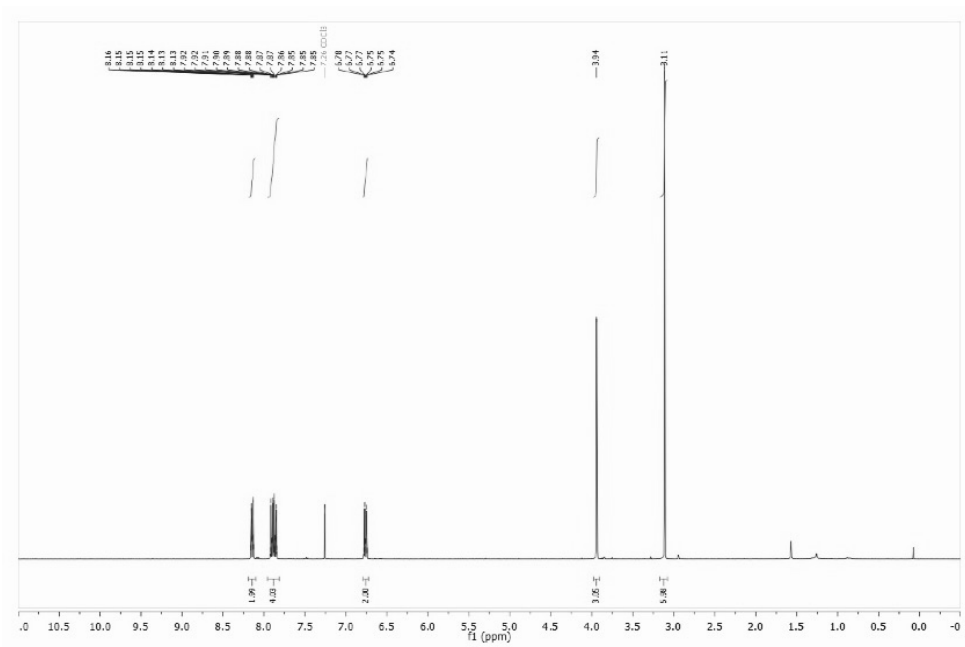
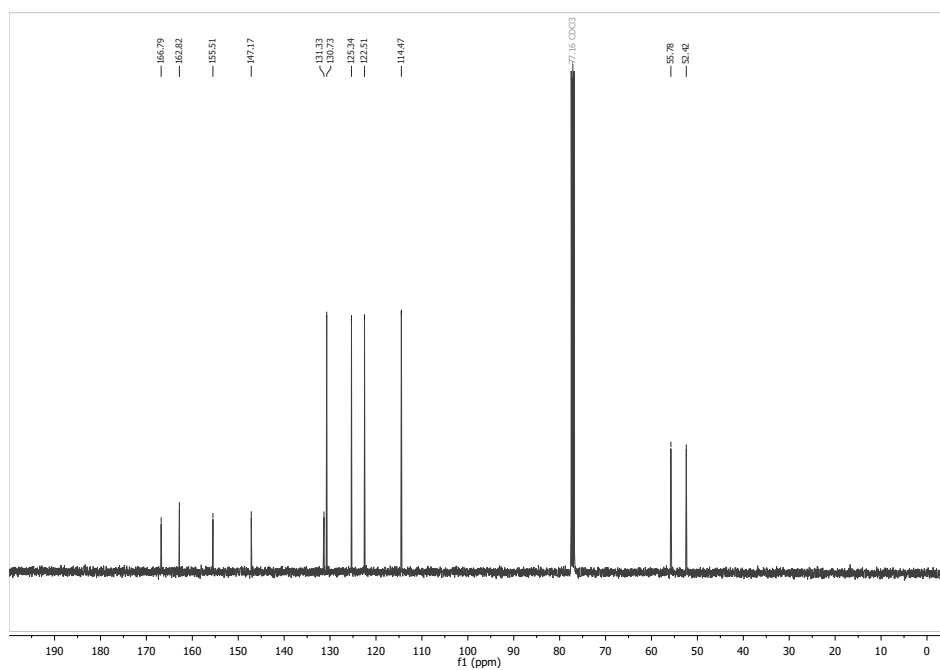


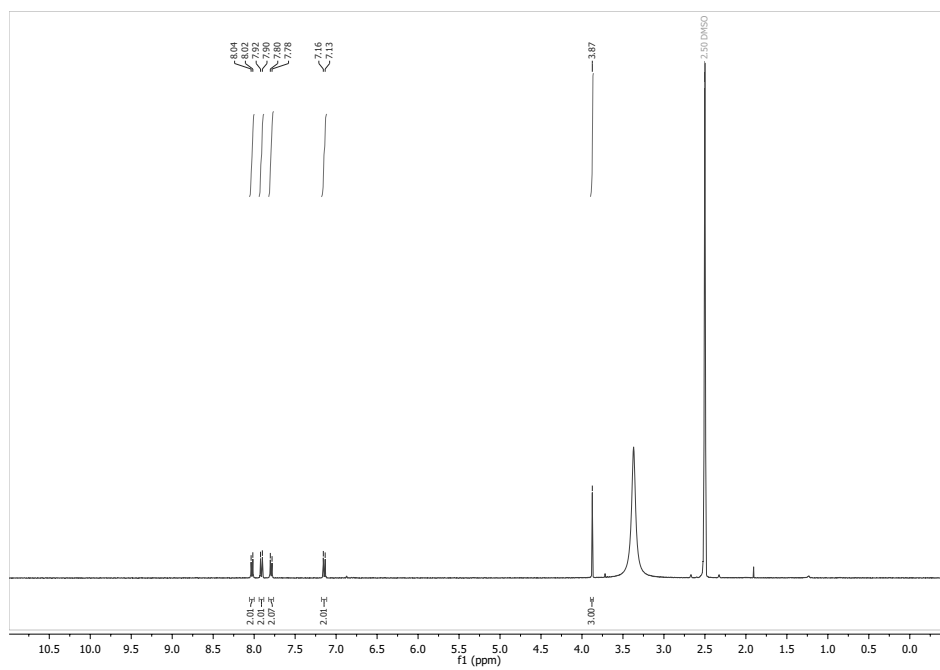
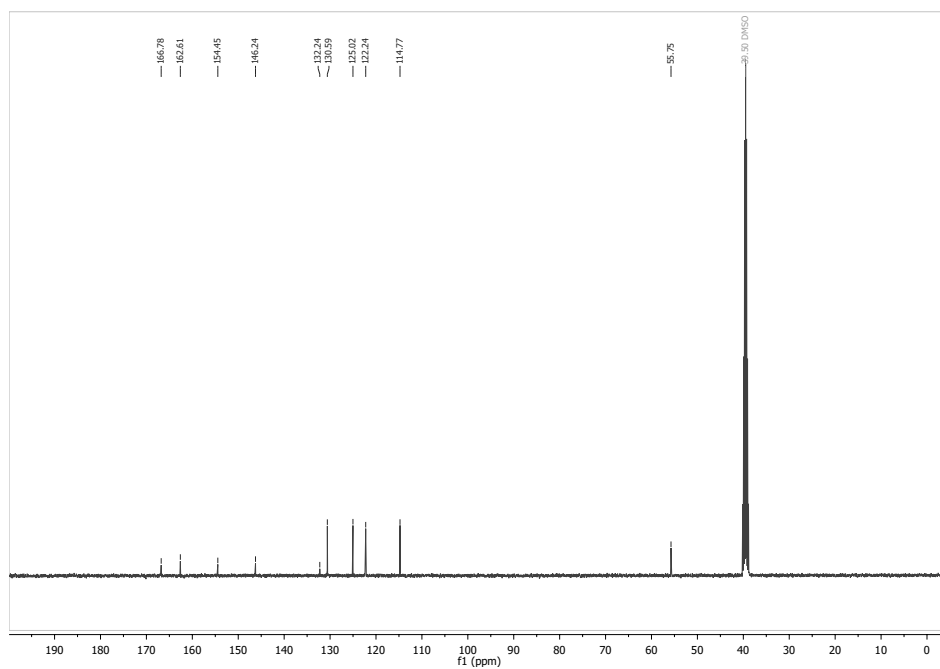
Figure S5 (expanded from data shown in Fig 3a): Immunofluorescence imaging of cells treated under lit/dark conditions with **AzTax3MP**, docetaxel (positive control), or 1% DMSO only (negative control) (HeLa cells, MTs immunostained with anti- $\alpha$ -tubulin (green), nuclei stained with DAPI (blue), 25  $\mu\text{m}$  scale for overviews, 10  $\mu\text{m}$  scale for insets (white) except for the orange-indicated cosolvent control panel (50  $\mu\text{m}$  / 20  $\mu\text{m}$  for better overview).

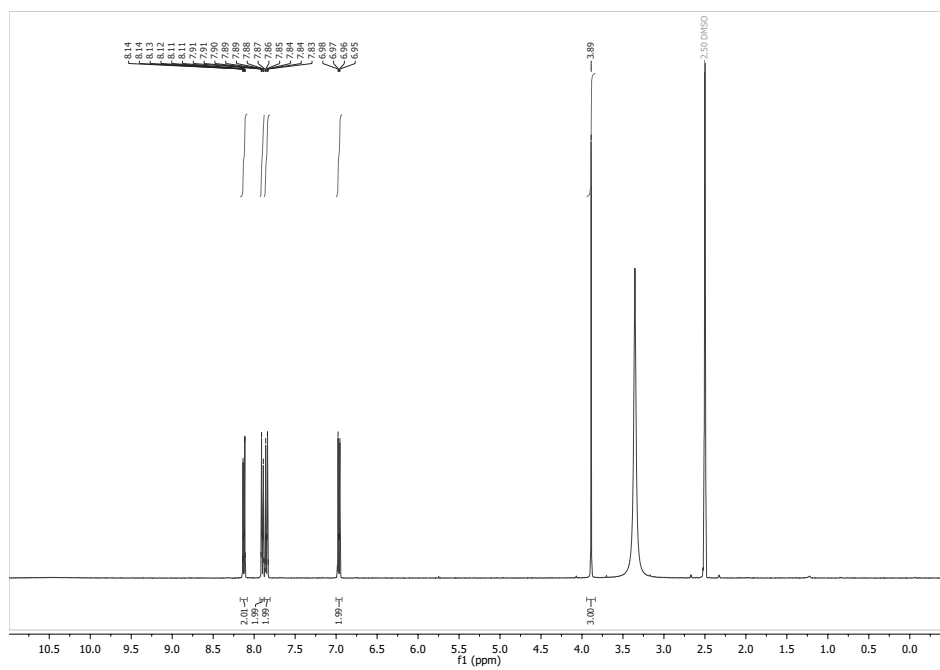
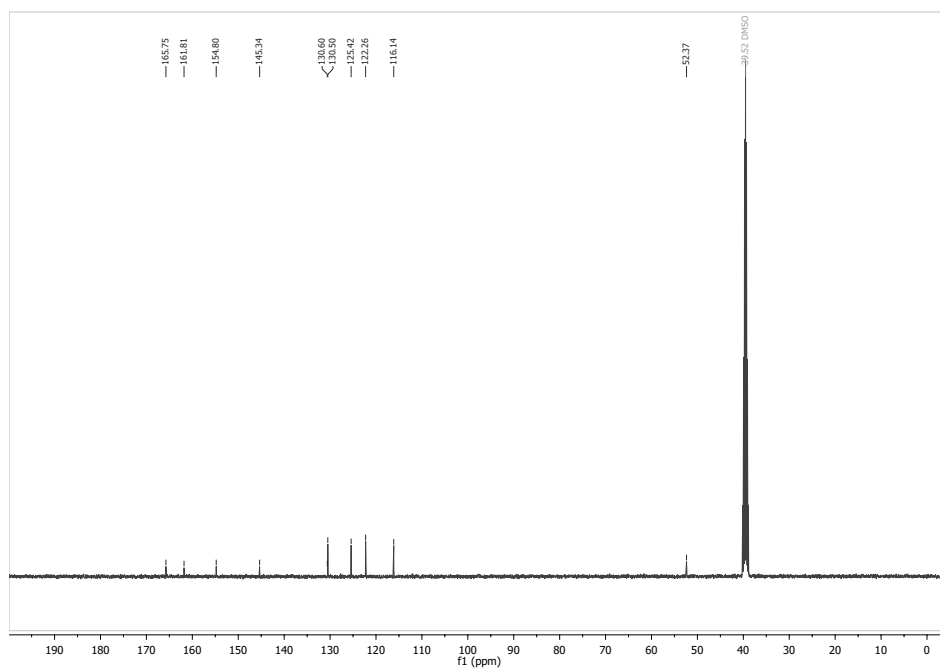
## Supporting Information Bibliography

- (1) Gottlieb, H. E.; Kotlyar, V.; Nudelman, A. NMR Chemical Shifts of Common Laboratory Solvents as Trace Impurities. *J. Org. Chem.* **1997**, *62* (21), 7512–7515. <https://doi.org/10.1021/jo971176v>.
- (2) McNamara, W. R.; Milot, R. L.; Song, H.; Snoeberger III, R. C.; Batista, V. S.; Schmuttenmaer, C. A.; Brudvig, G. W.; Crabtree, R. H. Water-Stable, Hydroxamate Anchors for Functionalization of TiO<sub>2</sub> Surfaces with Ultrafast Interfacial Electron Transfer. *Energy Environ. Sci.* **2010**, *3* (7), 917–923. <https://doi.org/10.1039/C001065K>.
- (3) Palmer, L. C.; Leung, C.-Y.; Kewalramani, S.; Kumthekar, R.; Newcomb, C. J.; Olvera de la Cruz, M.; Bedzyk, M. J.; Stupp, S. I. Long-Range Ordering of Highly Charged Self-Assembled Nanofilaments. *J. Am. Chem. Soc.* **2014**, *136* (41), 14377–14380. <https://doi.org/10.1021/ja5082519>.
- (4) Lim, Y.-K.; Lee, K.-S.; Cho, C.-G. Novel Route to Azobenzenes via Pd-Catalyzed Coupling Reactions of Aryl Hydrazides with Aryl Halides, Followed by Direct Oxidations. *Org. Lett.* **2003**, *5* (7), 979–982. <https://doi.org/10.1021/ol027311u>.
- (5) Kreger, K.; Wolfer, P.; Audorff, H.; Kador, L.; Stingelin-Stutzmann, N.; Smith, P.; Schmidt, H.-W. Stable Holographic Gratings with Small-Molecular Trisazobenzene Derivatives. *J. Am. Chem. Soc.* **2010**, *132* (2), 509–516. <https://doi.org/10.1021/ja9091038>.
- (6) Fatás, P.; Longo, E.; Rastrelli, F.; Crisma, M.; Toniolo, C.; Jiménez, A. I.; Cativiela, C.; Moretto, A. Bis(Azobenzene)-Based Photoswitchable, Prochiral, *Ca*-Tetrasubstituted  $\alpha$ -Amino Acids for Nanomaterials Applications. *Chemistry – A European Journal* **2011**, *17* (45), 12606–12611. <https://doi.org/10.1002/chem.201102609>.
- (7) Stawski, P.; Sumser, M.; Trauner, D. A Photochromic Agonist of AMPA Receptors. *Angewandte Chemie International Edition* **2012**, *51* (23), 5748–5751. <https://doi.org/10.1002/anie.201109265>.
- (8) Wang, Y.-T.; Zhang, Y.; Gong, H.; Sun, R.; Mao, W.; Wang, D.-H.; Chen, Y. A Colorimetric Pb<sup>2+</sup> Chemosensor: Rapid Naked-Eye Detection, High Selectivity, Theoretical Insights, and Applications. *Journal of Photochemistry and Photobiology A: Chemistry* **2018**, *355*, 101–108. <https://doi.org/10.1016/j.jphotochem.2017.10.027>.
- (9) Štastná, M.; Trávníček, M.; Šlais, K. New Azo Dyes as Colored Isoelectric Point Markers for Isoelectric Focusing in Acidic pH Region. *Electrophoresis* **2005**, *26* (1), 53–59. <https://doi.org/10.1002/elps.200406088>.
- (10) Leriche, G.; Budin, G.; Brino, L.; Wagner, A. Optimization of the Azobenzene Scaffold for Reductive Cleavage by Dithionite; Development of an Azobenzene Cleavable Linker for Proteomic Applications. *European Journal of Organic Chemistry* **2010**, *2010* (23), 4360–4364. <https://doi.org/10.1002/ejoc.201000546>.
- (11) Berwick, M. A.; Rondeau, R. E. Oxidation of O-Substituted Azobenzenes as Followed by Tris(1,1,1,2,2,3,3-Heptafluoro-7,7-Dimethyl-4,6-Octanedionato(Europium) Proton Magnetic Resonance Spectral Clarification. Regioselective Routes to Azoxybenzenes. *J. Org. Chem.* **1972**, *37* (15), 2409–2413. <https://doi.org/10.1021/jo00980a012>.
- (12) Farrera, J.-A.; Canal, I.; Hidalgo-Fernández, P.; Pérez-García, M. L.; Huertas, O.; Luque, F. J. Towards a Tunable Tautomeric Switch in Azobenzene Biomimetics: Implications for the Binding Affinity of 2-(4'-Hydroxyphenylazo)Benzoic Acid to Streptavidin. *Chemistry – A European Journal* **2008**, *14* (7), 2277–2285. <https://doi.org/10.1002/chem.200701407>.
- (13) Zhang, Y.-M.; Zhang, N.-Y.; Xiao, K.; Yu, Q.; Liu, Y. Photo-Controlled Reversible Microtubule Assembly Mediated by Paclitaxel-Modified Cyclodextrin. *Angewandte Chemie International Edition* **2018**, *57* (28), 8649–8653. <https://doi.org/10.1002/anie.201804620>.
- (14) Stricker, L.; Fritz, E.-C.; Peterlechner, M.; Doltsinis, N. L.; Ravoo, B. J. Arylazopyrazoles as Light-Responsive Molecular Switches in Cyclodextrin-Based Supramolecular Systems. *J. Am. Chem. Soc.* **2016**, *138* (13), 4547–4554. <https://doi.org/10.1021/jacs.6b00484>.
- (15) Alushin, G. M.; Lander, G. C.; Kellogg, E. H.; Zhang, R.; Baker, D.; Nogales, E. High-Resolution Microtubule Structures Reveal the Structural Transitions in  $\beta$ -Tubulin upon GTP Hydrolysis. *Cell* **2014**, *157* (5), 1117–1129. <https://doi.org/10.1016/j.cell.2014.03.053>.
- (16) Dunn, N. J.; Humphries, W. H.; Offenbacher, A. R.; King, T. L.; Gray, J. A. pH-Dependent Cis  $\rightarrow$  Trans Isomerization Rates for Azobenzene Dyes in Aqueous Solution. *J. Phys. Chem. A* **2009**, *113* (47), 13144–13151. <https://doi.org/10.1021/jp903102u>.
- (17) Hüll, K.; Morstein, J.; Trauner, D. In Vivo Photopharmacology. *Chemical Reviews* **2018**, *118* (21), 10710–10747. <https://doi.org/10.1021/acs.chemrev.8b00037>.
- (18) Alexander Sailer; Franziska Ermer; Yvonne Kraus; Rebekkah Bingham; Ferdinand H. Lutter; Julia Ahlfeld; Oliver Thorn-Seshold. Potent Hemithioindigo-Based Antimitotics Photocontrol the Microtubule Cytoskeleton in Cellulo. *ChemRxiv* **2019**. <https://doi.org/10.26434/chemrxiv.9176747.v1>.

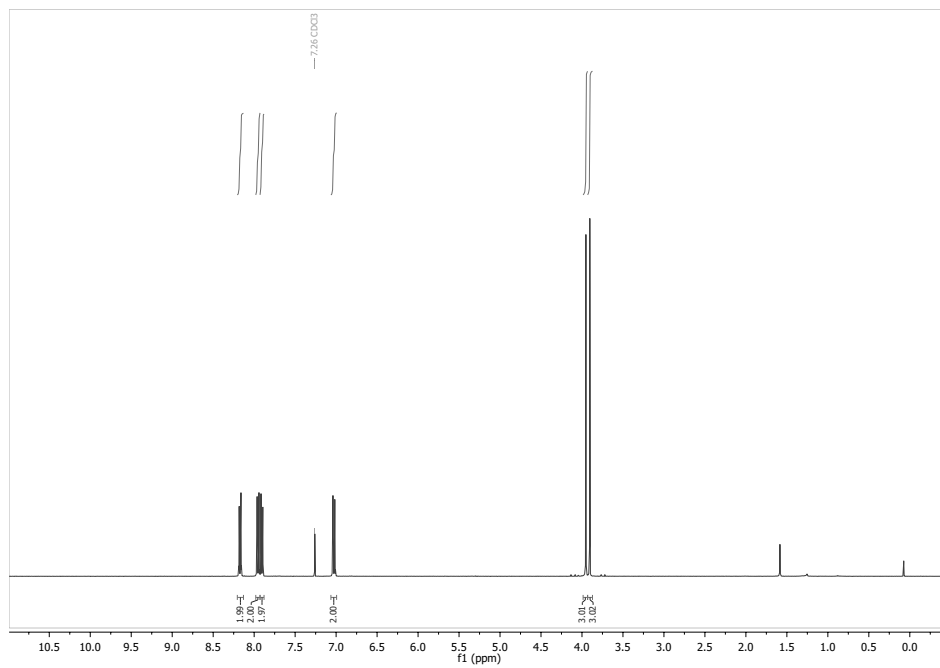
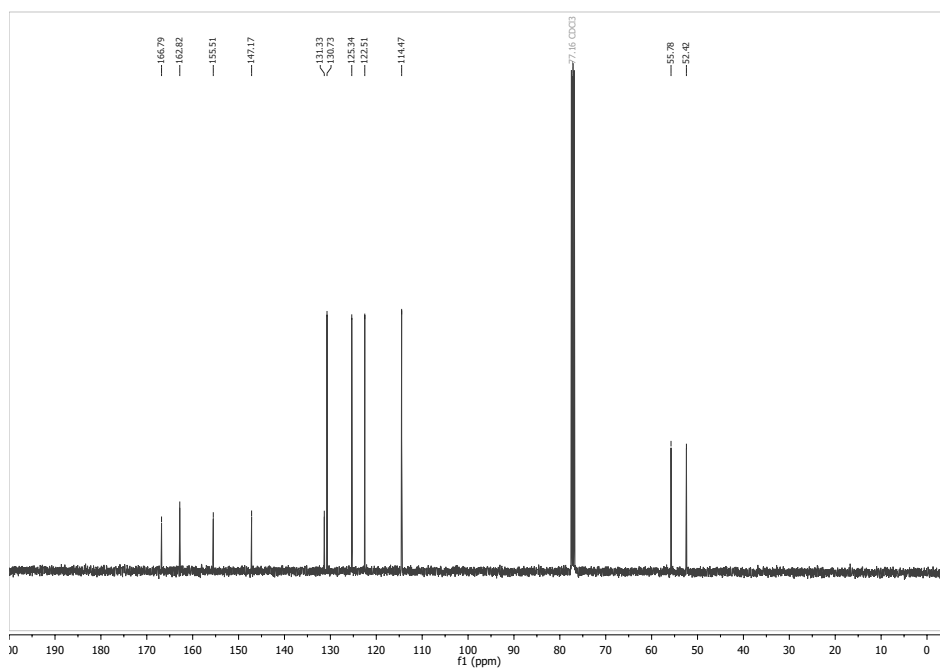
- (19) Reis, S. A.; Ghosh, B.; Hendricks, J. A.; Szantai-Kis, D. M.; Törk, L.; Ross, K. N.; Lamb, J.; Read-Button, W.; Zheng, B.; Wang, H.; et al. Light-Controlled Modulation of Gene Expression by Chemical Optoepigenetic Probes. *Nature Chemical Biology* **2016**, *12*, 317. <https://doi.org/10.1038/nchembio.2042>.
- (20) Gao, L.; Kraus, Y.; Wranik, M.; Weinert, T.; Pritzl, S. D.; Meiring, J. C. M.; Bingham, R.; Olieric, N.; Akhmanova, A.; Lohmüller, T.; et al. Photoswitchable Microtubule Inhibitors Enabling Robust, GFP-Orthogonal Optical Control over the Tubulin Cytoskeleton. *bioRxiv* **2019**, 716233. <https://doi.org/10.1101/716233>.
- (21) Kopf, A.; Renkawitz, J.; Hauschild, R.; Girkontaite, I.; Tedford, K.; Merrin, J.; Thorn-Seshold, O.; Trauner, D.; Häcker, H.; Fischer, K.-D.; et al. Microtubules Control Cellular Shape and Coherence in Amoeboid Migrating Cells. *bioRxiv* **2019**, 609420. <https://doi.org/10.1101/609420>.
- (22) Sailer, A.; Ermer, F.; Kraus, Y.; Lutter, F.; Donau, C.; Bremerich, M.; Ahlfeld, J.; Thorn-Seshold, O. Hemithioindigos as Desymmetrised Molecular Switch Scaffolds: Design Control over the Isomer-Dependency of Potent Photoswitchable Antimitotic Bioactivity in Cellulo. *ChemBioChem* **2019**, *20*, 1305–1314. <https://doi.org/10.1002/cbic.201800752>.
- (23) Borowiak, M.; Nahaboo, W.; Reynders, M.; Nekolla, K.; Jalinot, P.; Hasserodt, J.; Rehberg, M.; Delattre, M.; Zahler, S.; Vollmar, A.; et al. Photoswitchable Inhibitors of Microtubule Dynamics Optically Control Mitosis and Cell Death. *Cell* **2015**, *162* (2), 403–411. <https://doi.org/10.1016/j.cell.2015.06.049>.
- (24) Lin, C. M.; Singh, S. B.; Chu, P. S.; Dempsy, R. O.; Schmidt, J. M.; Pettit, G. R.; Hamel, E. Interactions of Tubulin with Potent Natural and Synthetic Analogs of the Antimitotic Agent Combretastatin: A Structure-Activity Study. *Molecular Pharmacology* **1988**, *34* (2), 200–208.

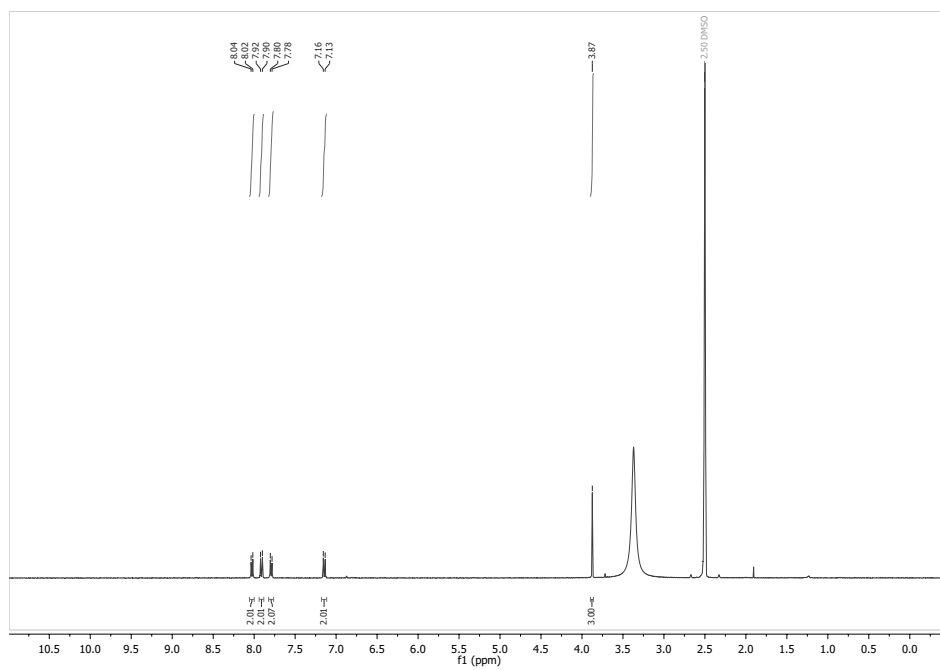
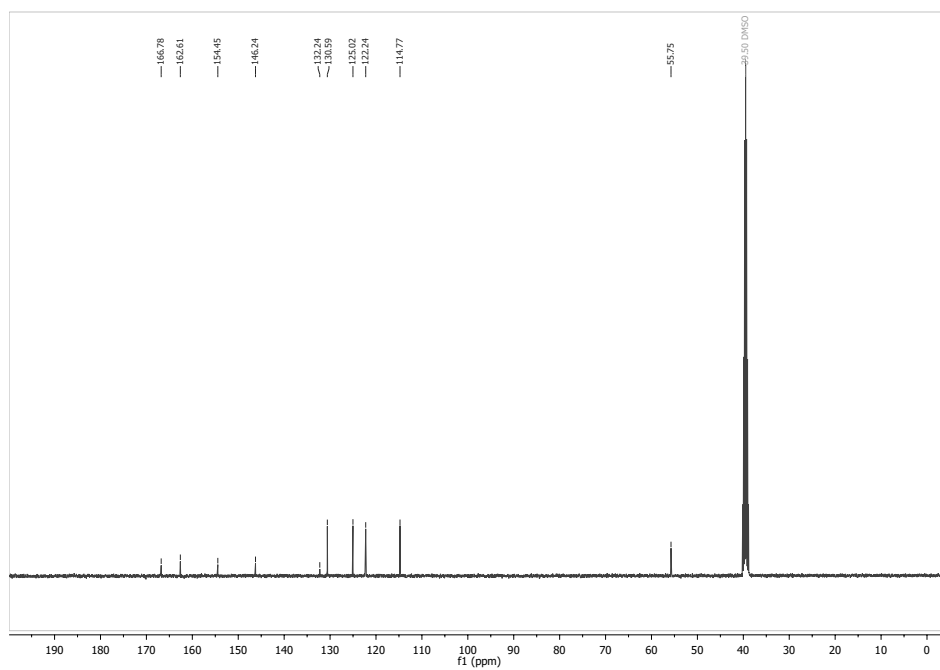
**Part F: NMR Spectra****methyl 4-((4-(dimethylamino)phenyl)diazenyl)benzoate (S1) : <sup>1</sup>H-NMR****<sup>13</sup>C-NMR**

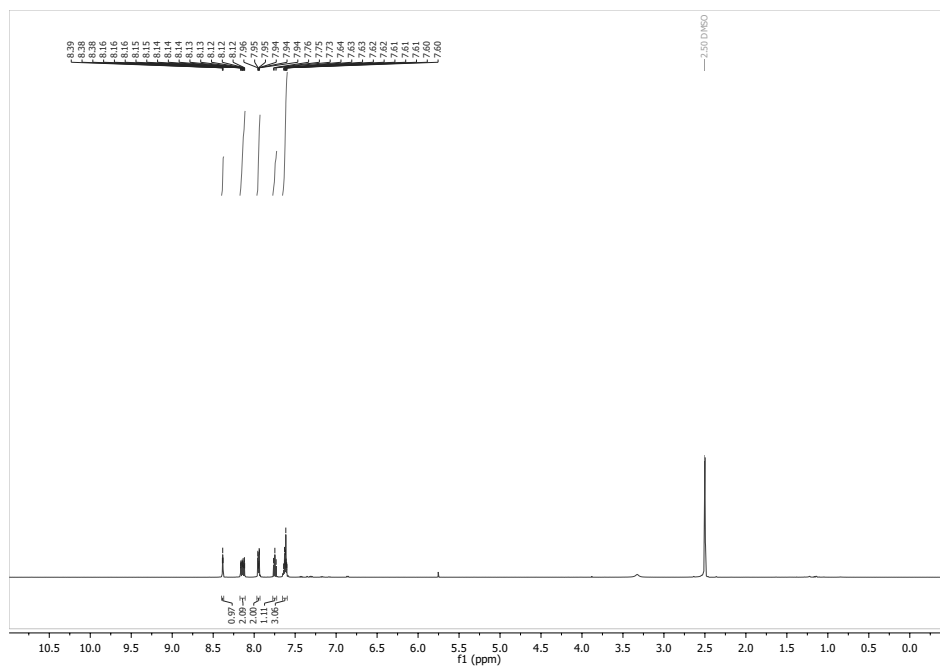
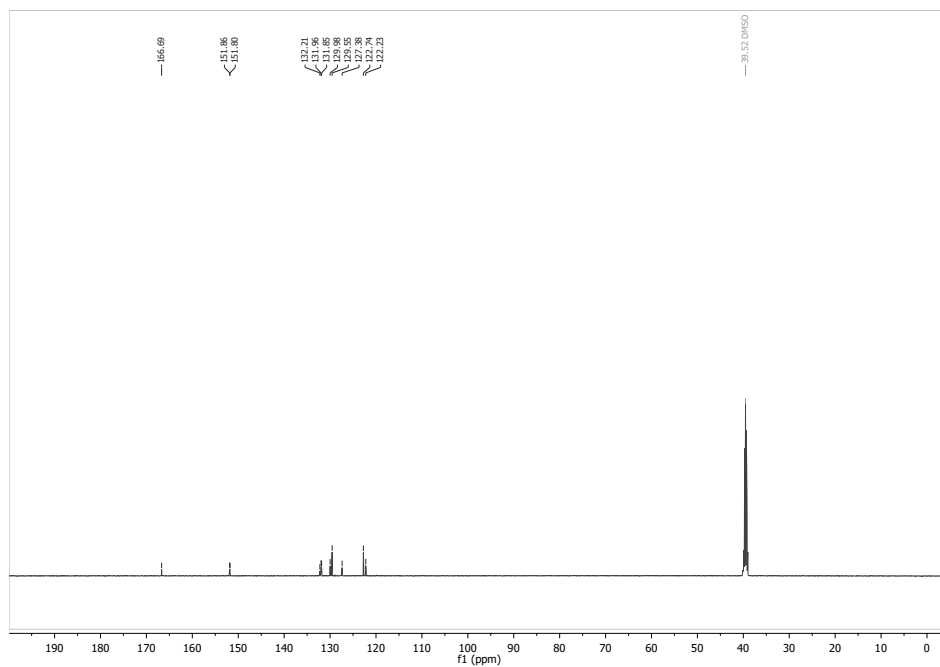
4-((4-(dimethylamino)phenyl)diazenyl)benzoic acid (4DMA-CO<sub>2</sub>H): <sup>1</sup>H-NMR<sup>13</sup>C-NMR

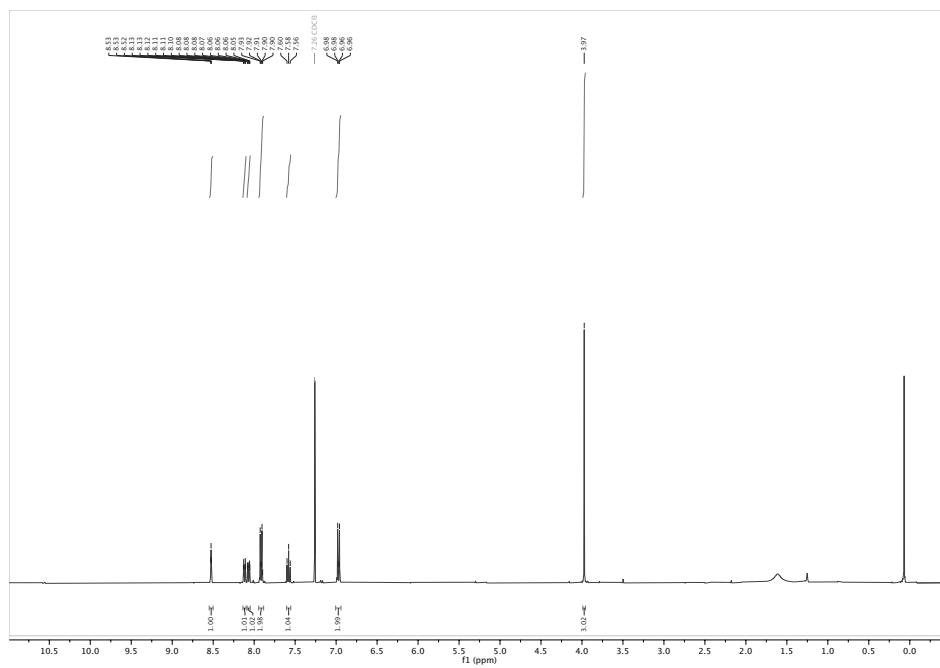
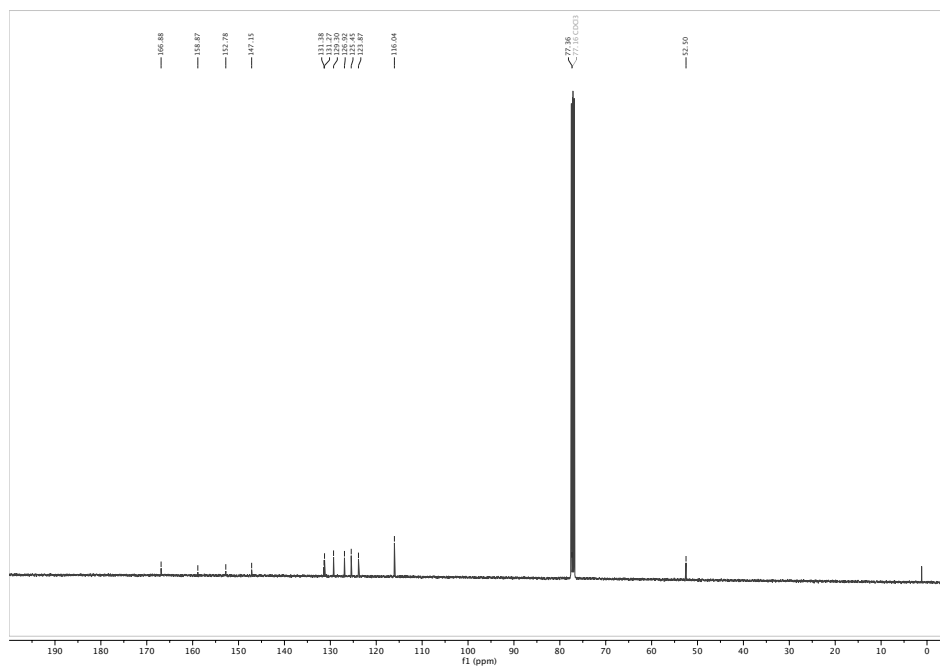
methyl 4-((4-hydroxyphenyl)diazenyl)benzoate (S2) <sup>1</sup>H-NMR<sup>13</sup>C-NMR



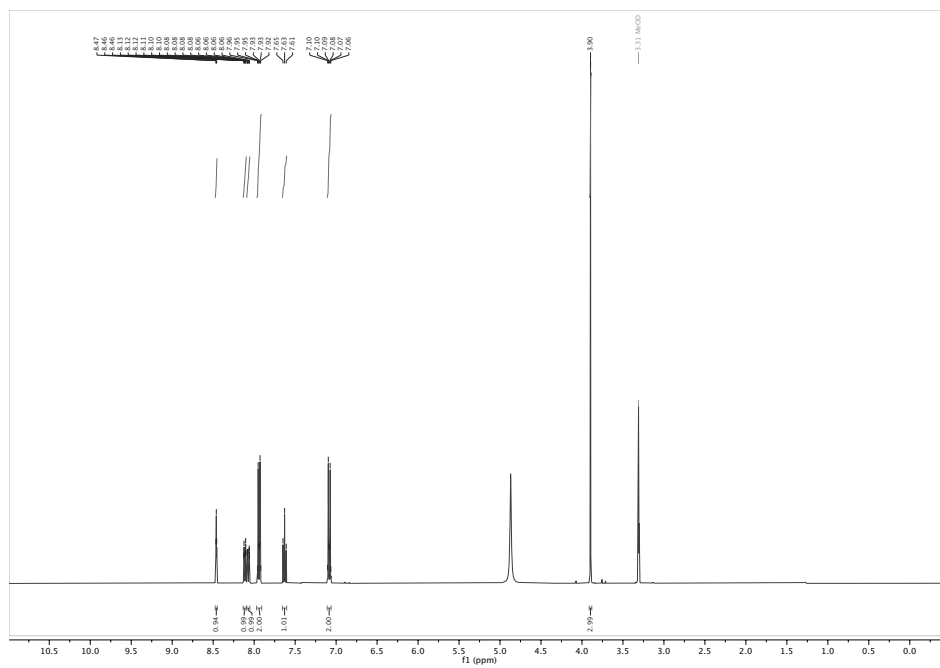
methyl 4-((4-methoxyphenyl)diazenyl)benzoate (S3) <sup>1</sup>H-NMR<sup>13</sup>C-NMR

4-((4-methoxyphenyl)diazenyl)benzoic acid (4MP-CO<sub>2</sub>H): <sup>1</sup>H-NMR<sup>13</sup>C-NMR

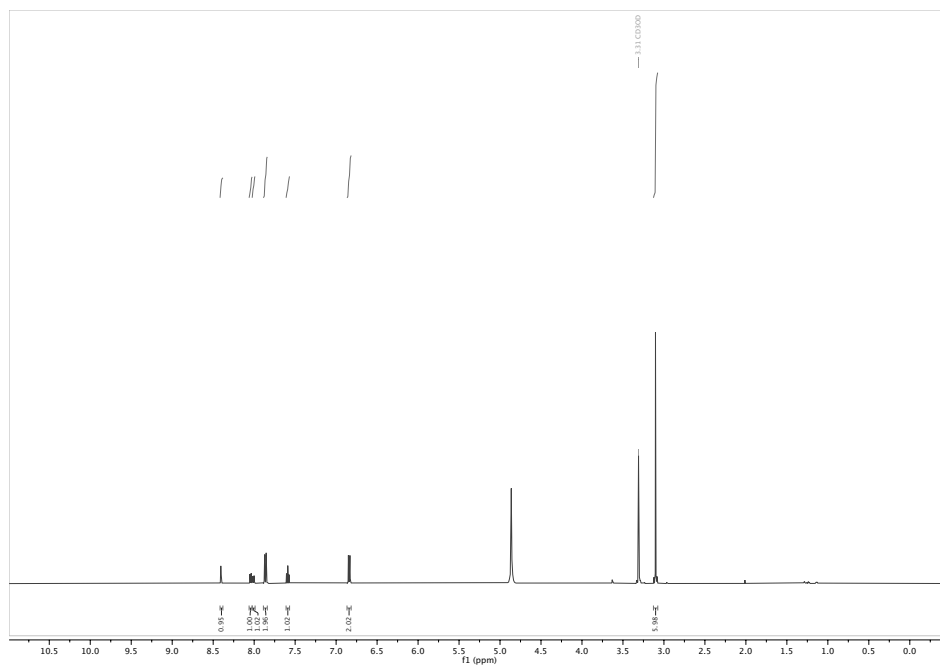
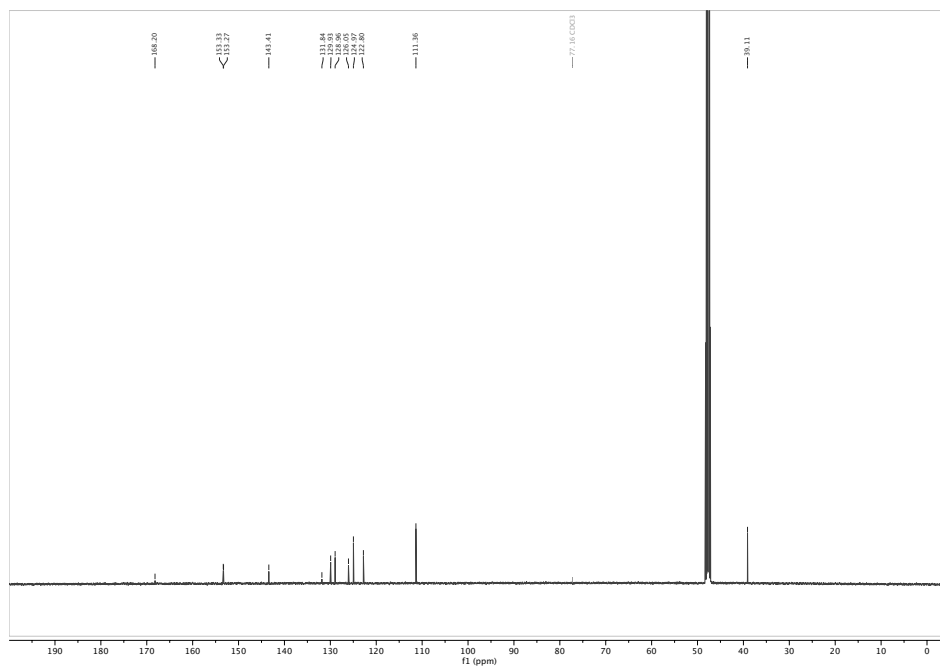
**3-(phenyldiazenyl)benzoic acid (3H-CO<sub>2</sub>H): <sup>1</sup>H-NMR****<sup>13</sup>C-NMR**

methyl 3-((4-hydroxyphenyl)diazenyl)benzoate (S4):  $^1\text{H-NMR}$  $^{13}\text{C-NMR}$ 

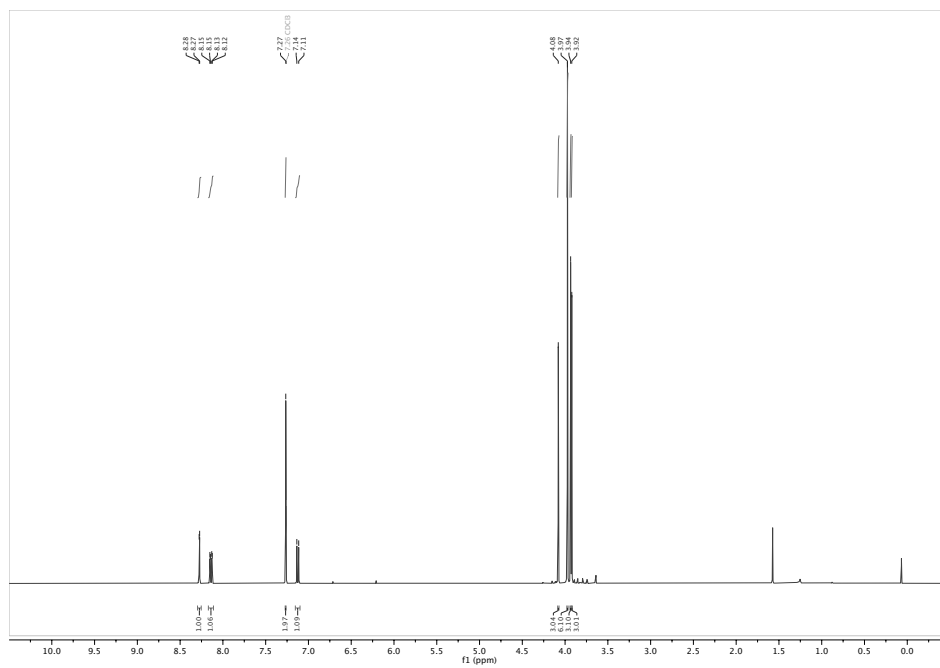
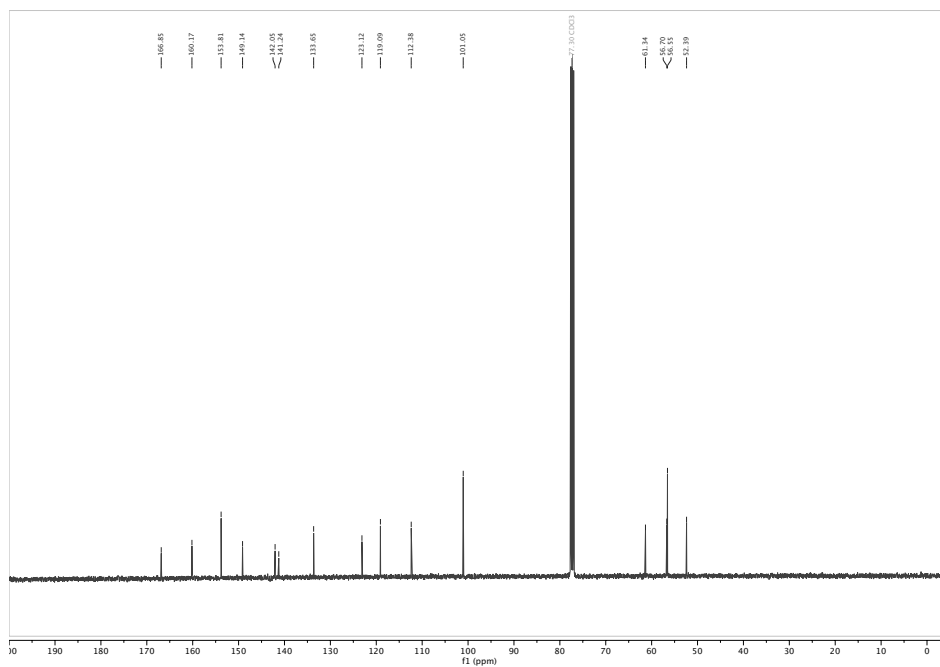


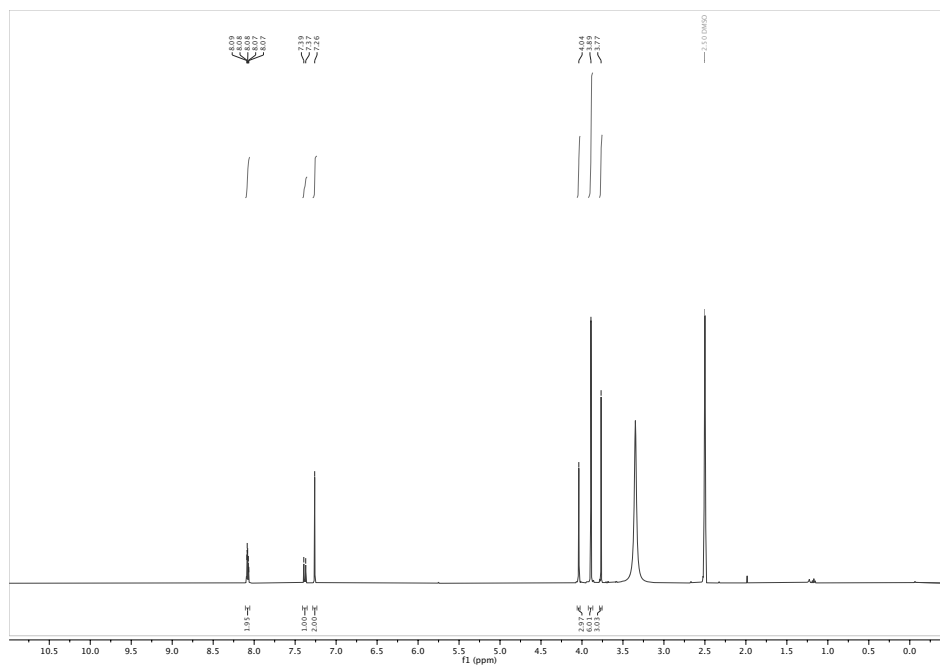
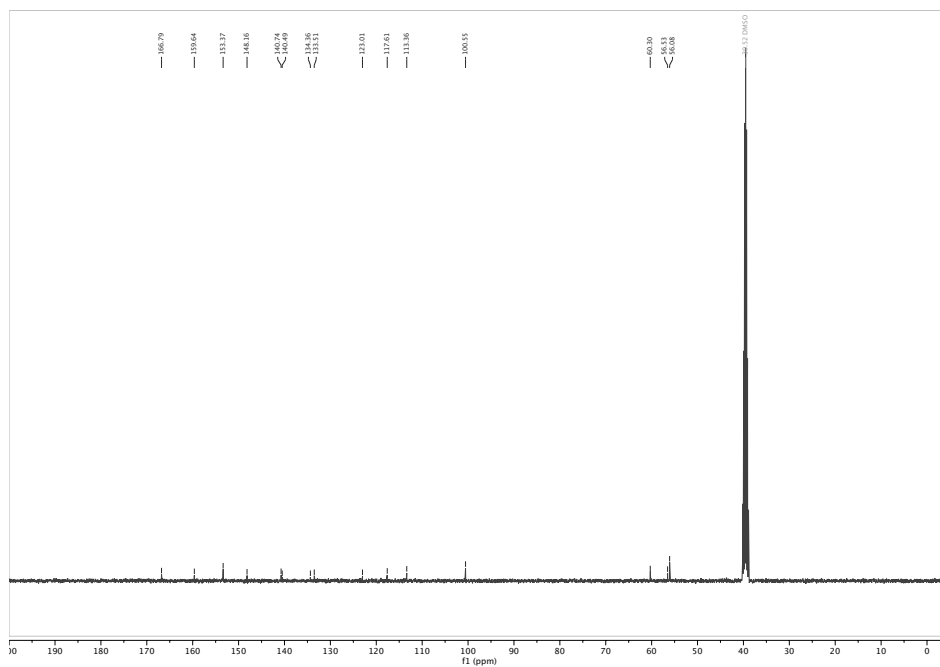
**3-((4-methoxyphenyl)diazenyl)benzoic acid (3MP-CO<sub>2</sub>H): <sup>1</sup>H-NMR**



**3-((4-(dimethylamino)phenyl)diazenyl)benzoic acid (3DMA-CO<sub>2</sub>H): <sup>1</sup>H-NMR****<sup>13</sup>C-NMR**

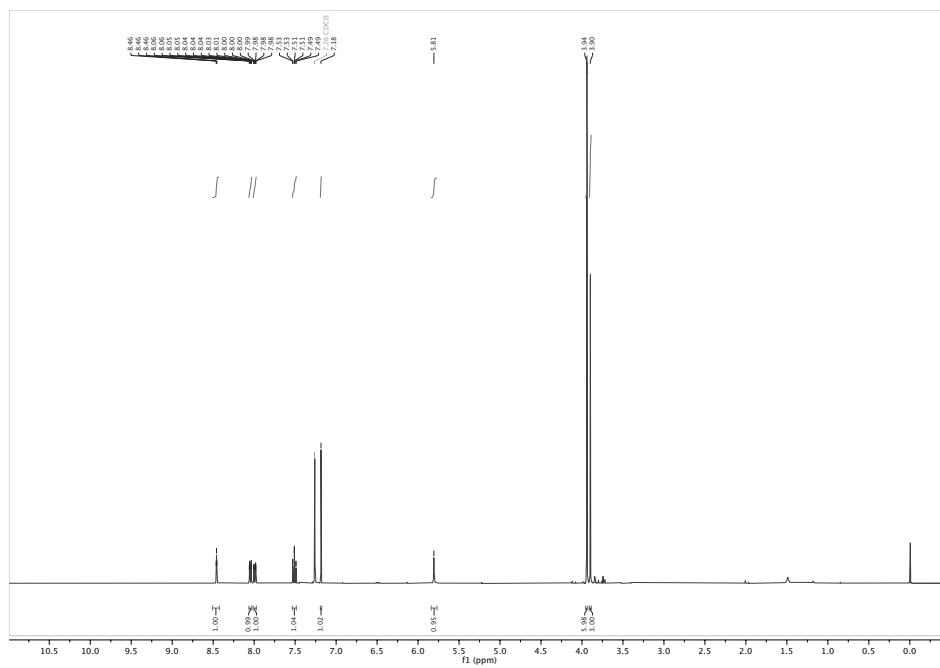


methyl 3-((4-hydroxy-3,5-dimethoxyphenyl)diazenyl)-4-methoxybenzoate (S7): <sup>1</sup>H-NMR<sup>13</sup>C-NMR

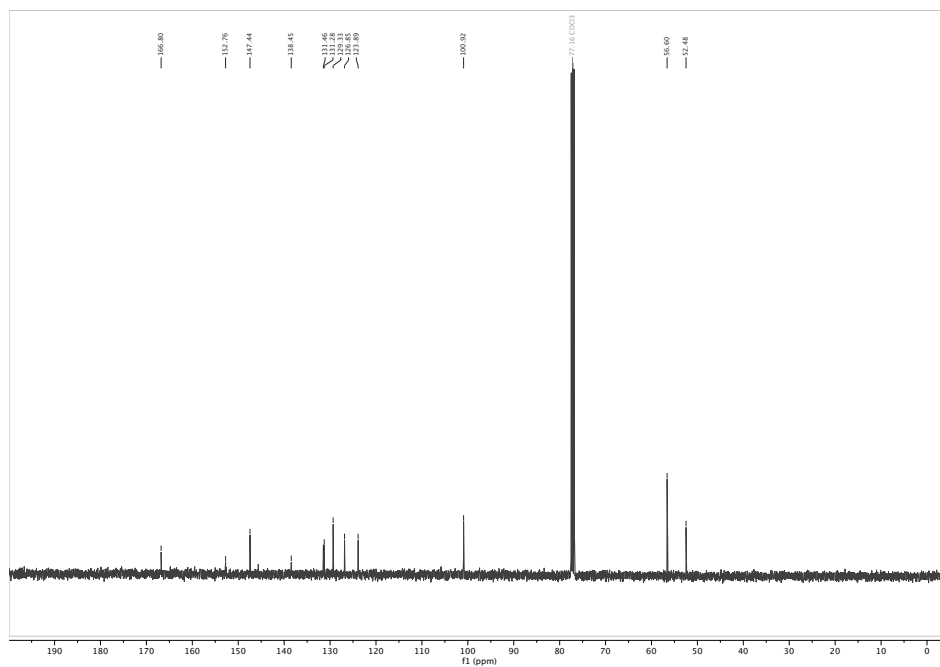
methyl 4-methoxy-3-((3,4,5-trimethoxyphenyl)diazenyl)benzoate (S8): <sup>1</sup>H-NMR<sup>13</sup>C-NMR

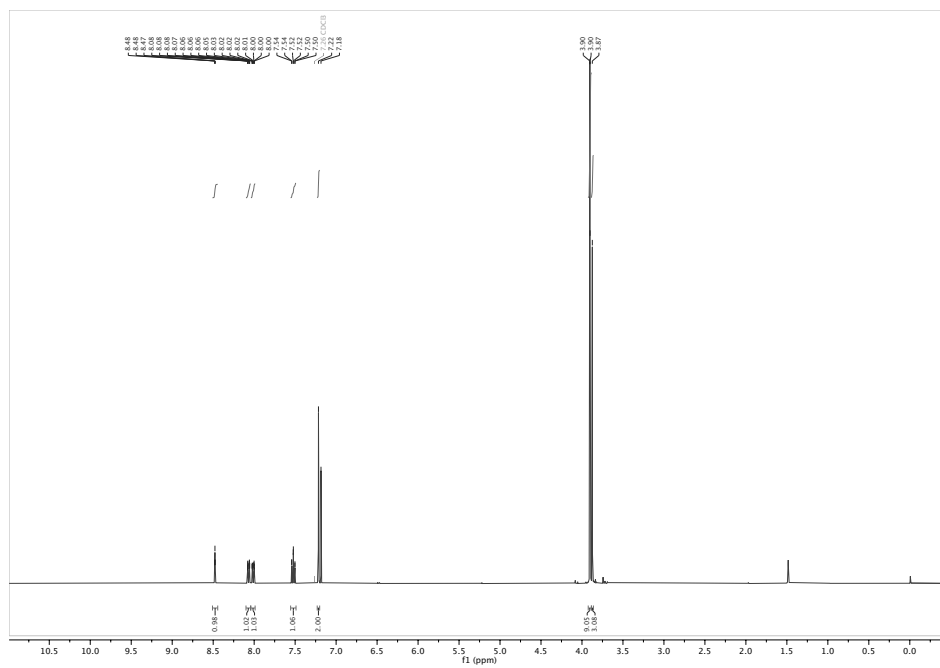
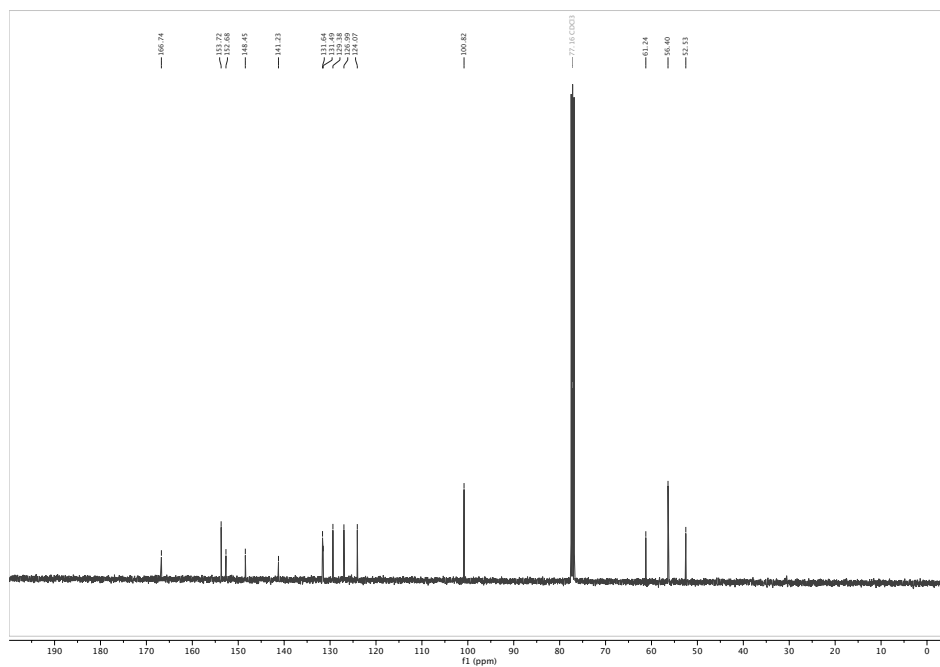
S50

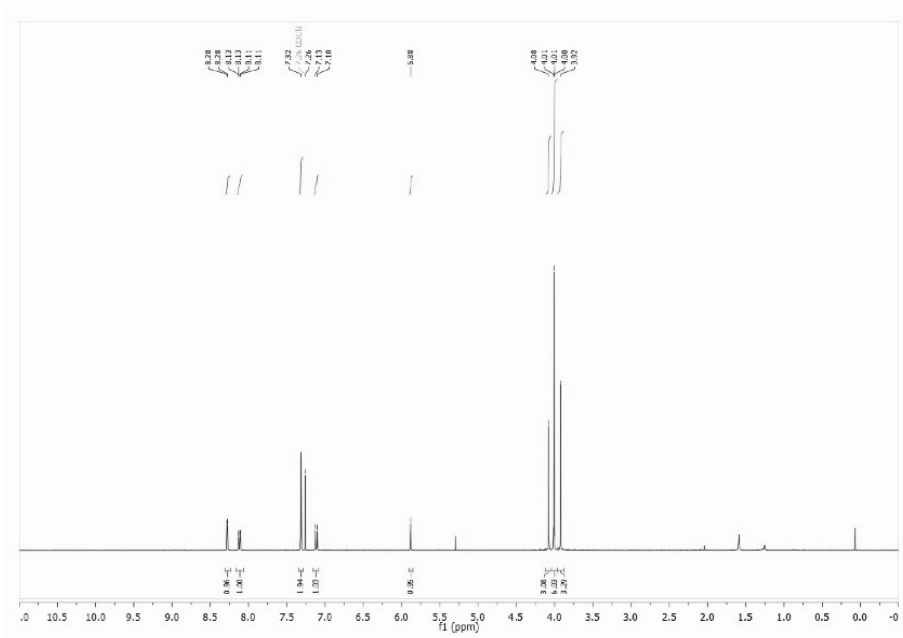
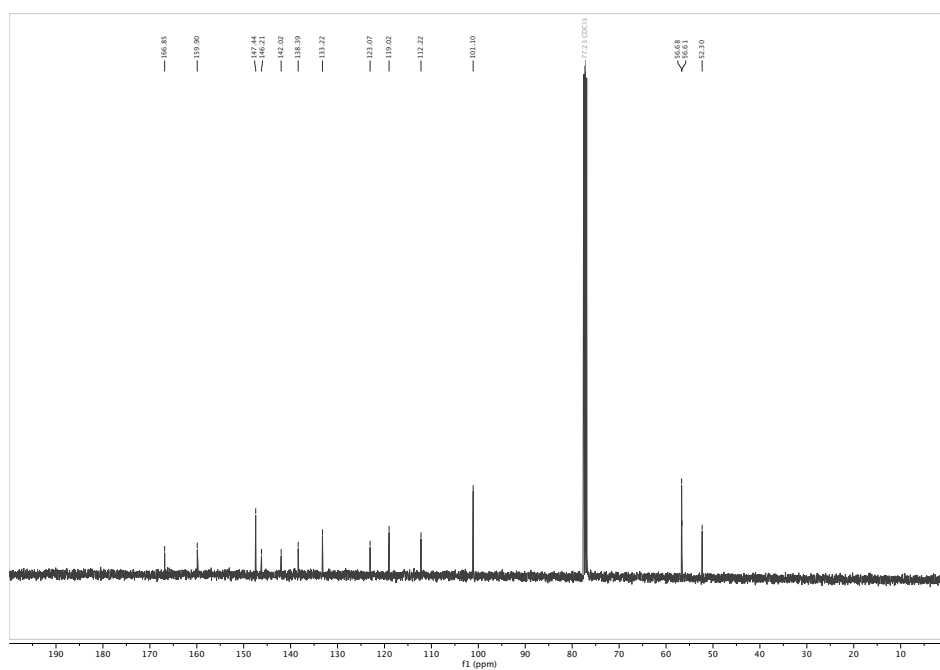
**4-methoxy-3-((3,4,5-trimethoxyphenyl)diazenyl)benzoic acid (3MTM-CO<sub>2</sub>H): <sup>1</sup>H-NMR**

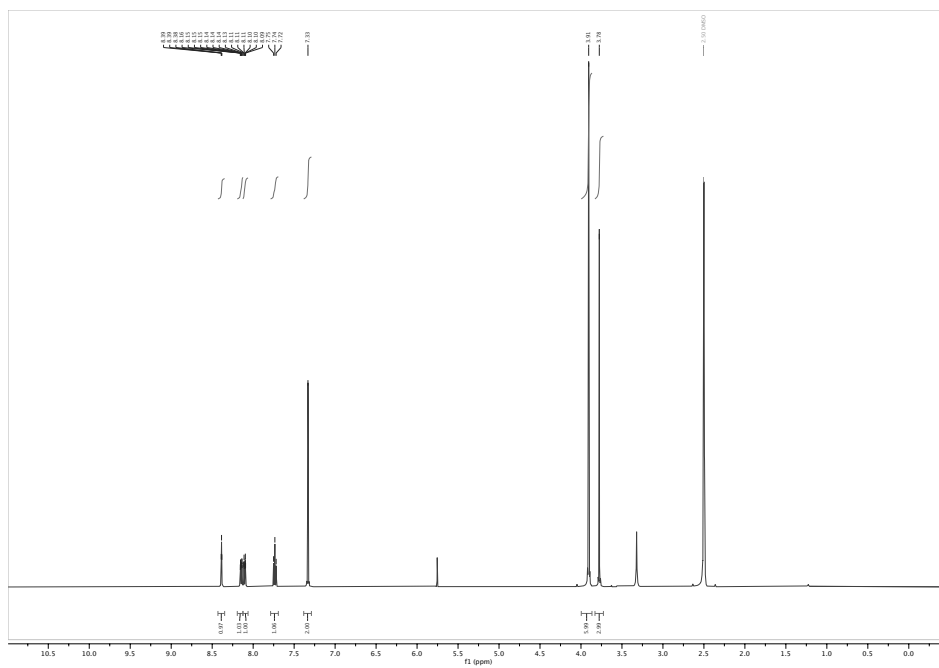
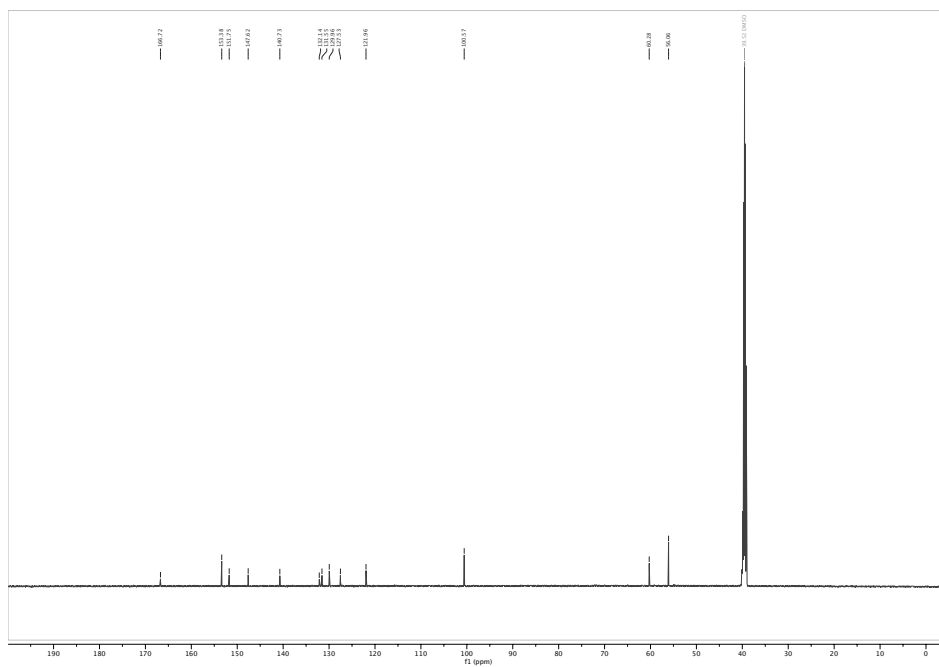


**<sup>13</sup>C-NMR**

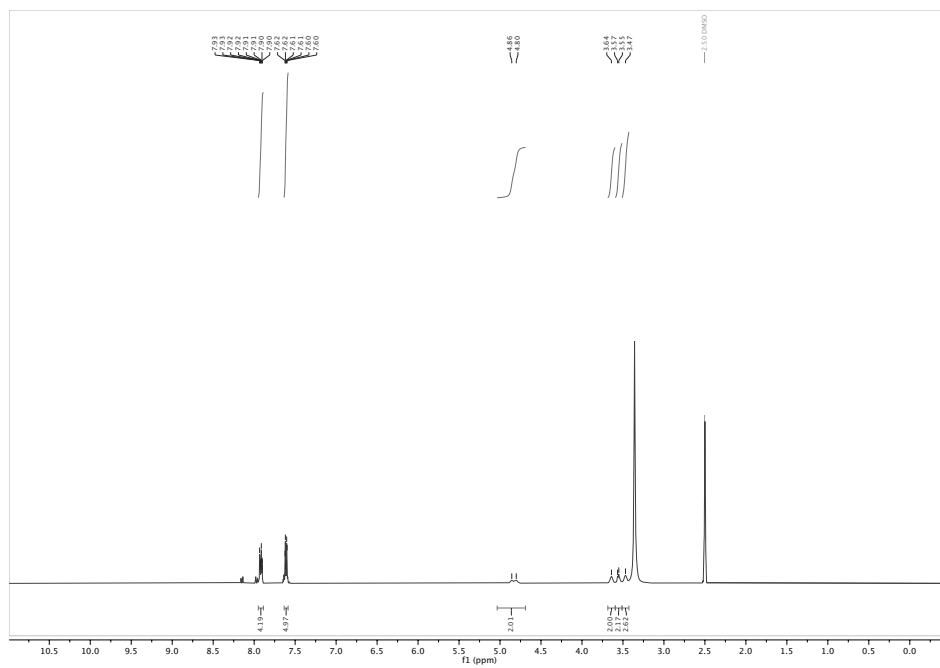
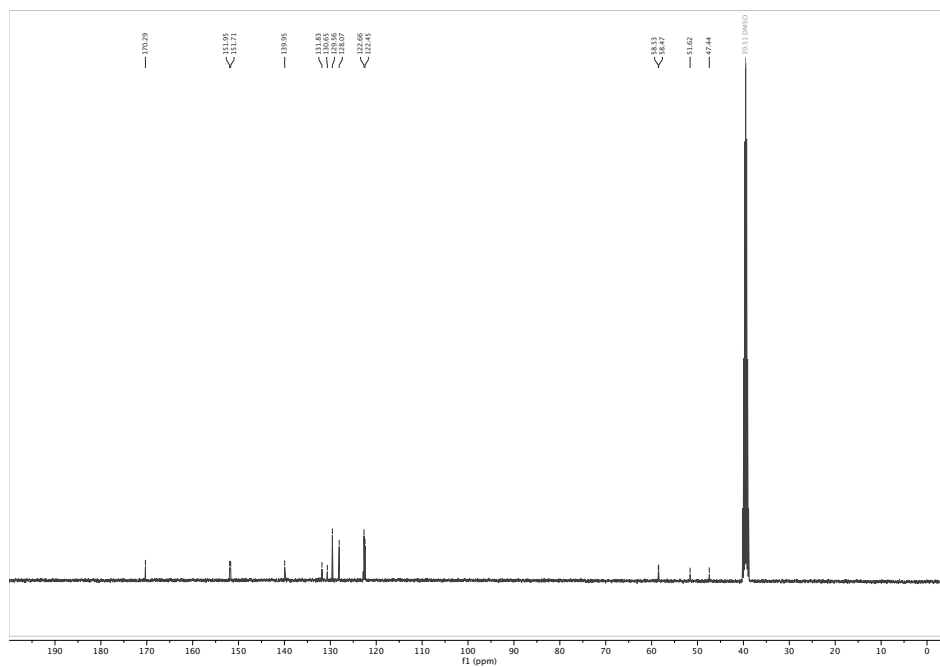


**Methyl 3-((4-hydroxy-3,5-dimethoxyphenyl)diazenyl)benzoate (S9): <sup>1</sup>H-NMR****<sup>13</sup>C-NMR**

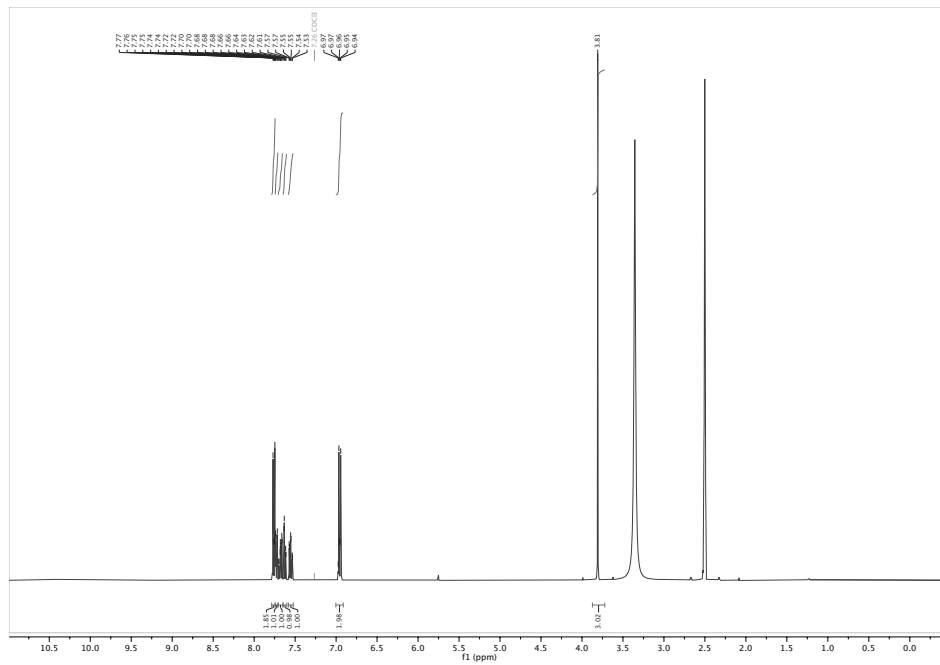
methyl 3-((3,4,5-trimethoxyphenyl)diazenyl)benzoate (S10):  $^1\text{H-NMR}$  $^{13}\text{C-NMR}$ 

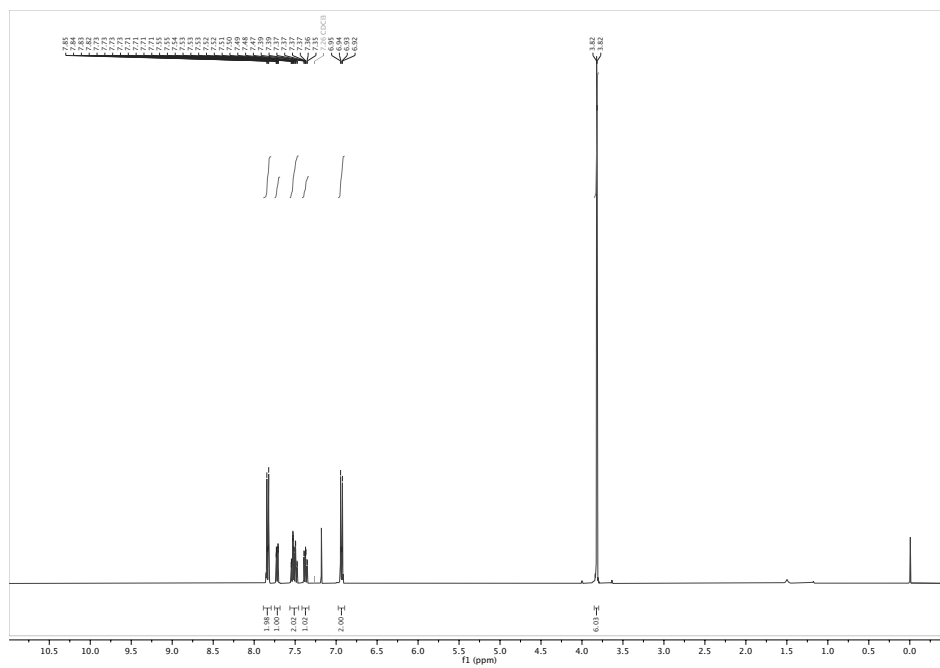
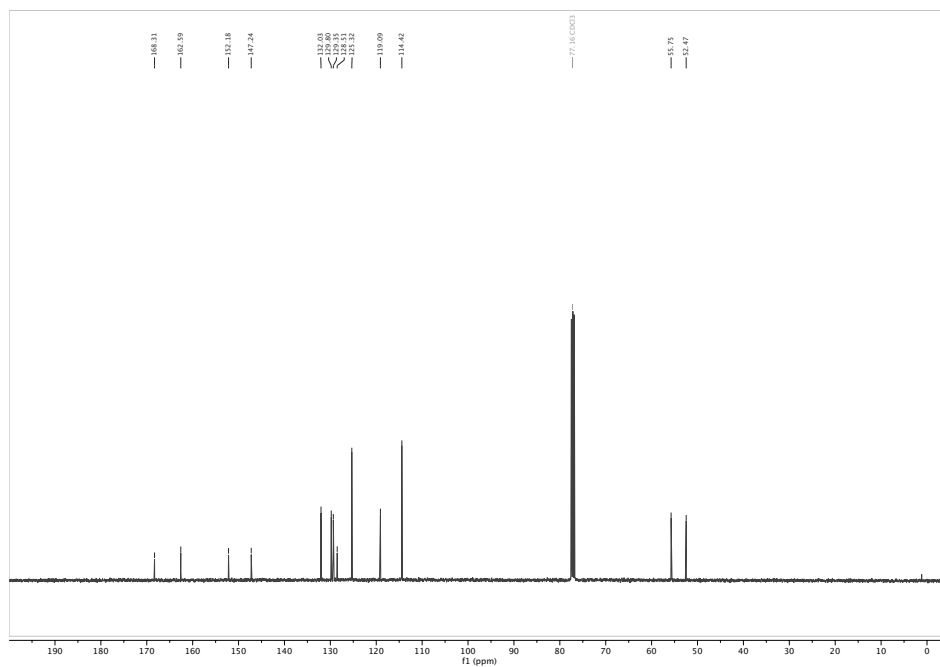
**3-((3,4,5-trimethoxyphenyl)diazenyl)benzoic acid (3TM-CO<sub>2</sub>H): <sup>1</sup>H-NMR****<sup>13</sup>C-NMR**

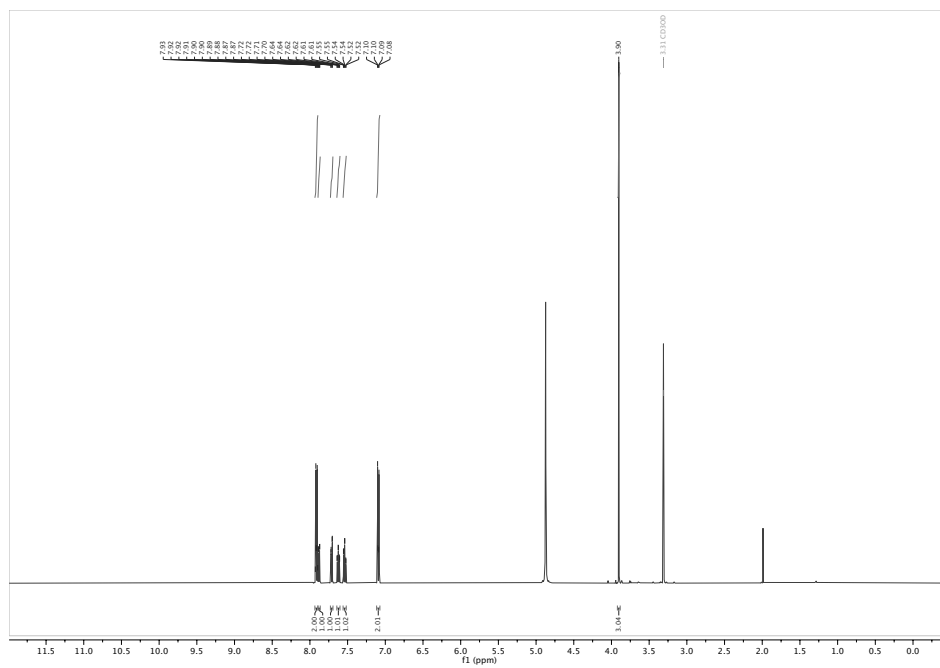
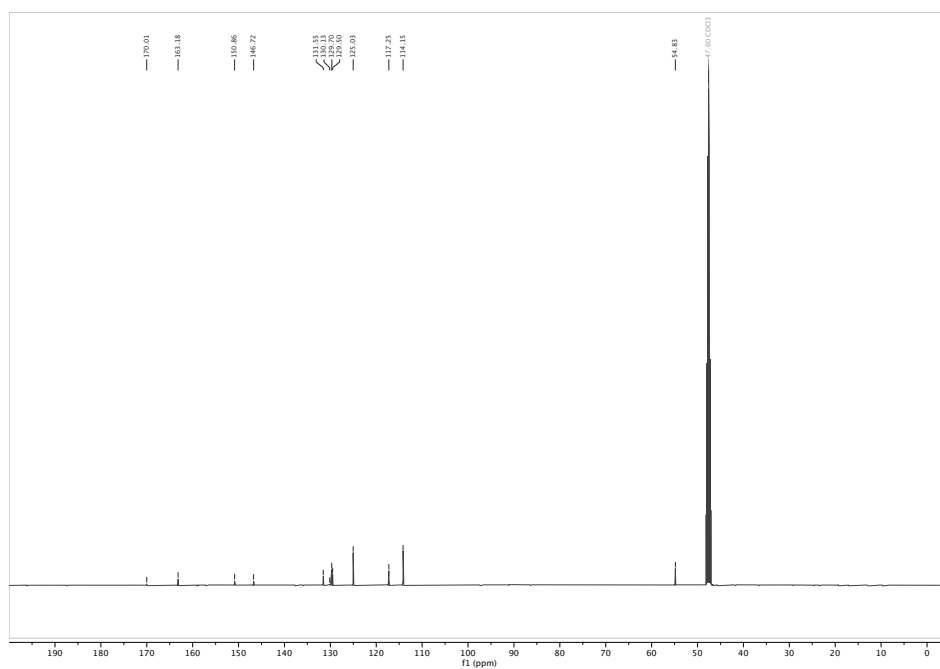


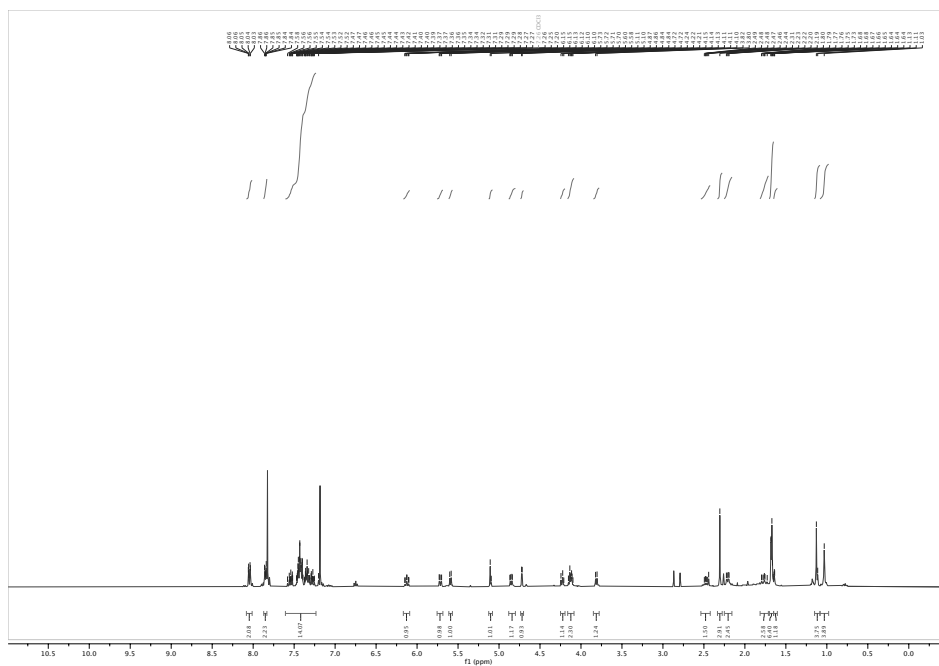
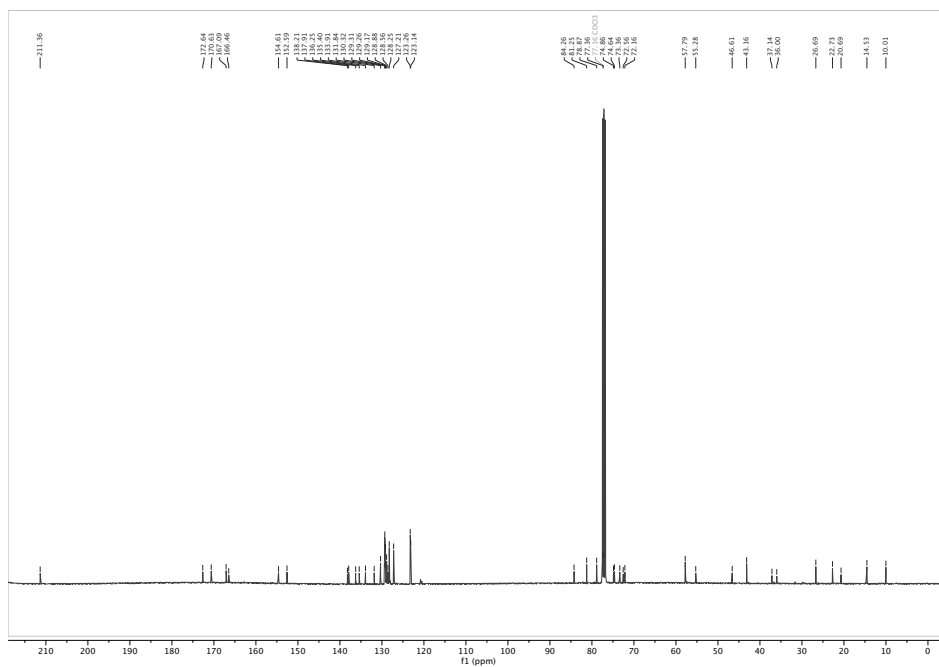
**3-((4-(bis(2-hydroxyethyl)amino)phenyl)diazenyl)benzoic acid (3DEA-CO<sub>2</sub>H): <sup>1</sup>H-NMR****<sup>13</sup>C-NMR**

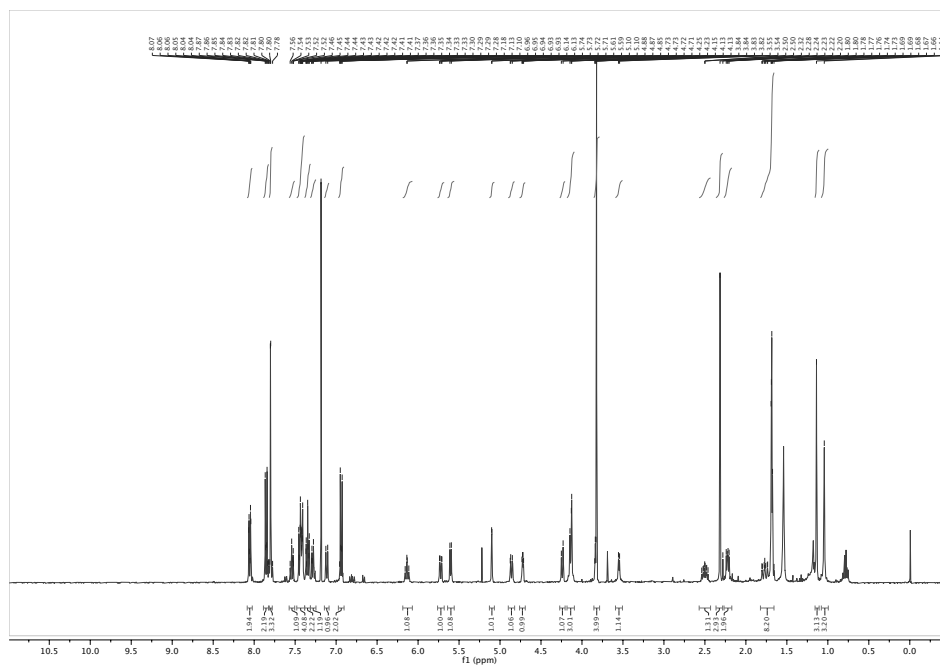
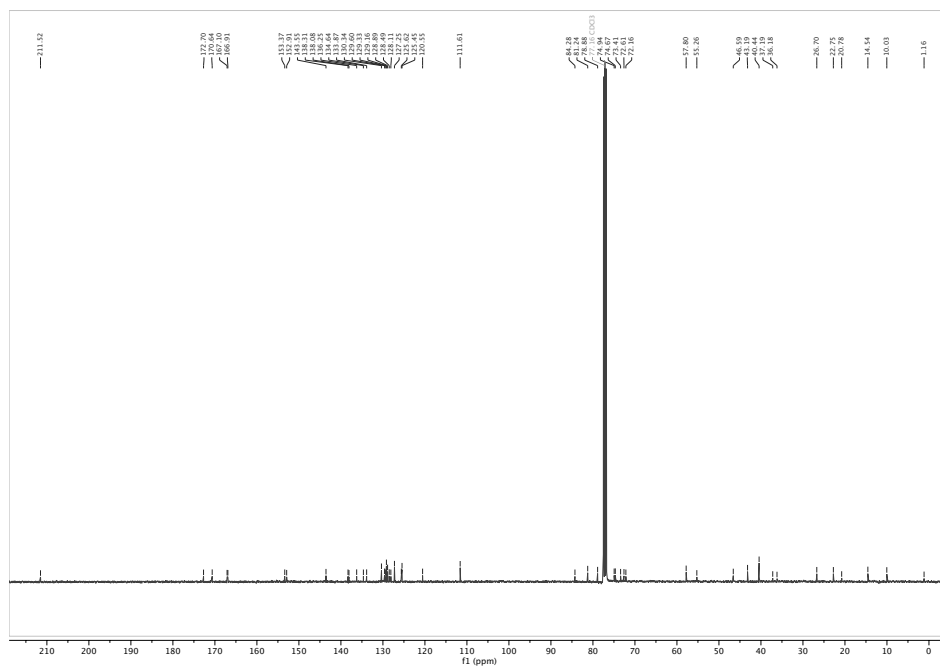


methyl 2-((4-hydroxyphenyl)diazenyl)benzoate (S12):  $^1\text{H-NMR}$ 

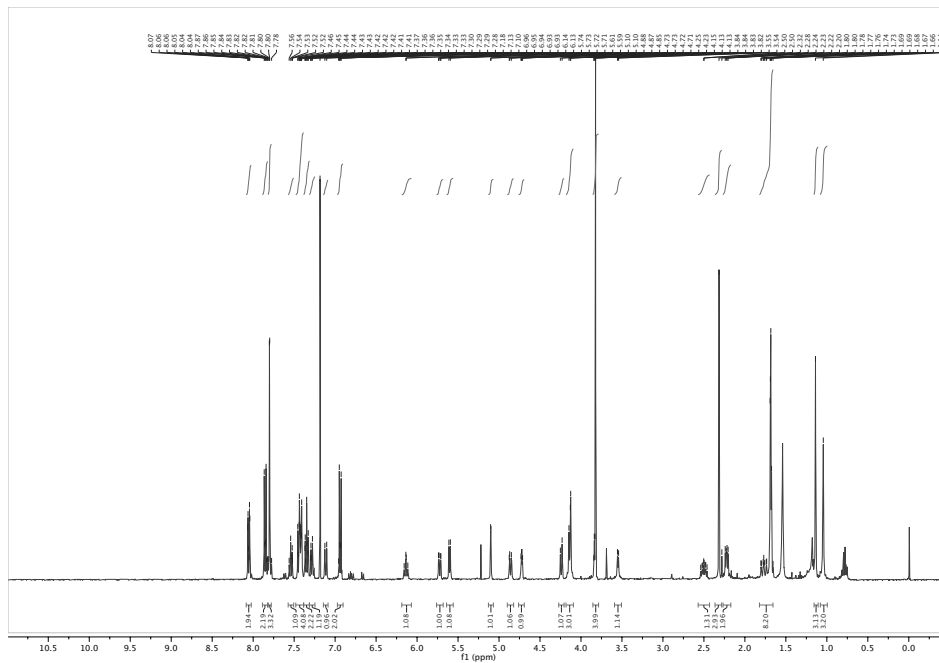
methyl 2-((4-methoxyphenyl)diazenyl)benzoate (S13): <sup>1</sup>H-NMR<sup>13</sup>C-NMR

2-((4-methoxyphenyl)diazenyl)benzoic acid (2MP-CO<sub>2</sub>H): <sup>1</sup>H-NMR<sup>13</sup>C-NMR

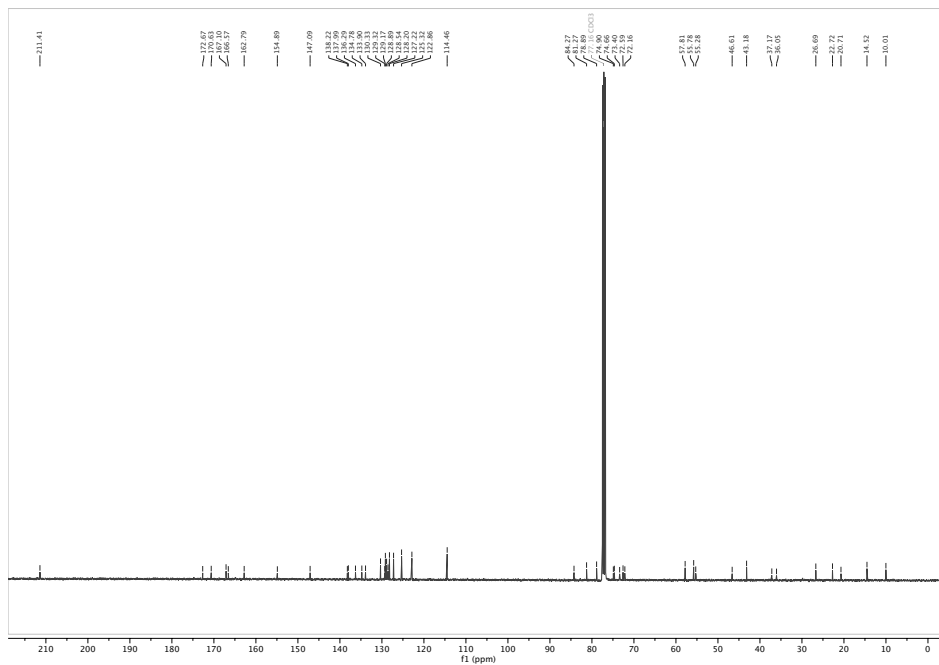
AzTax4H: <sup>1</sup>H-NMR<sup>13</sup>C-NMR

AzTax4DMA: <sup>1</sup>H-NMR<sup>13</sup>C-NMR

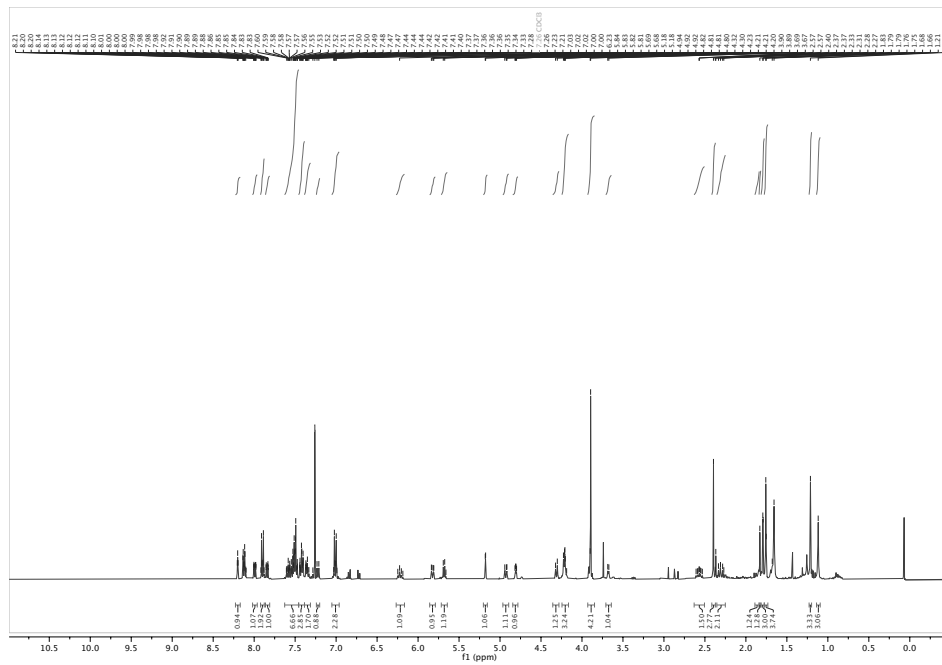
AzTax4MP: <sup>1</sup>H-NMR



<sup>13</sup>C-NMR

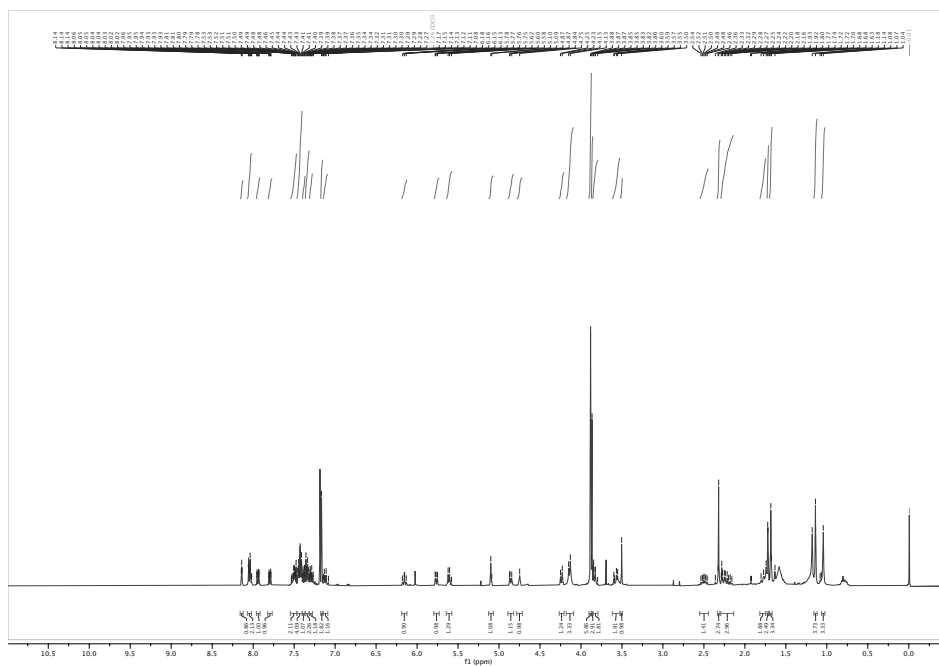
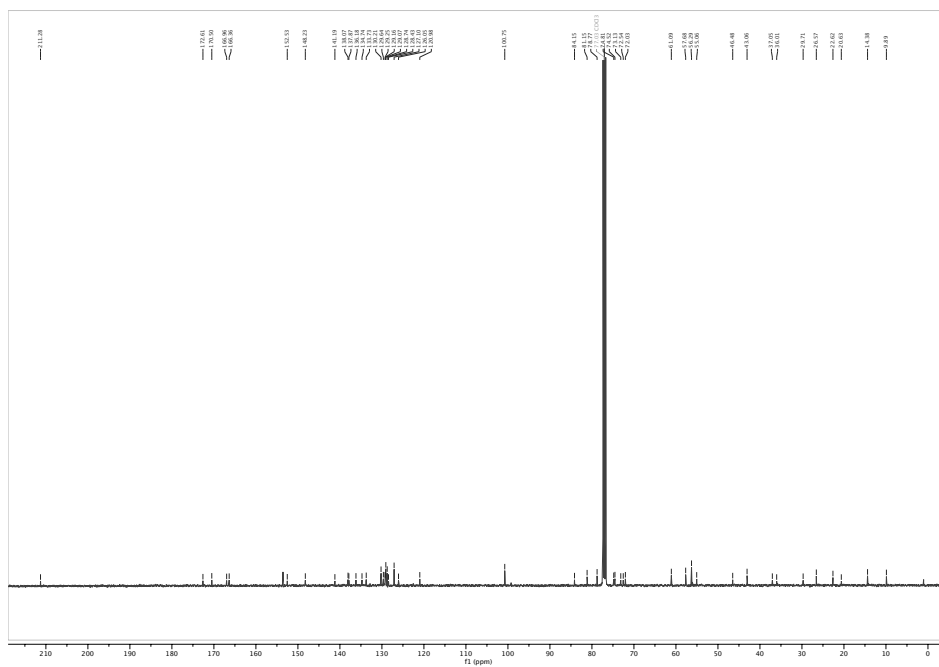


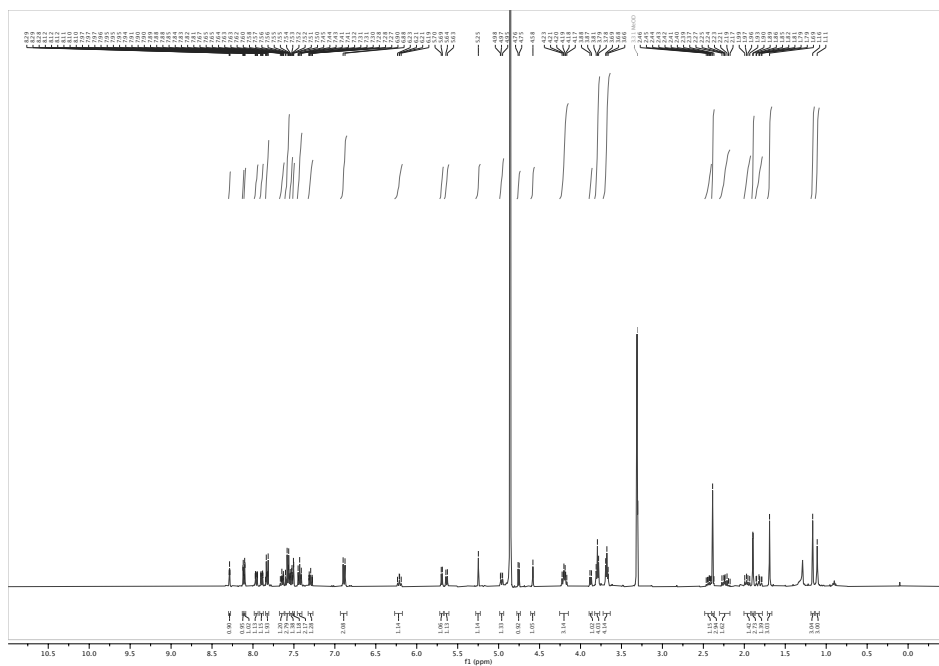
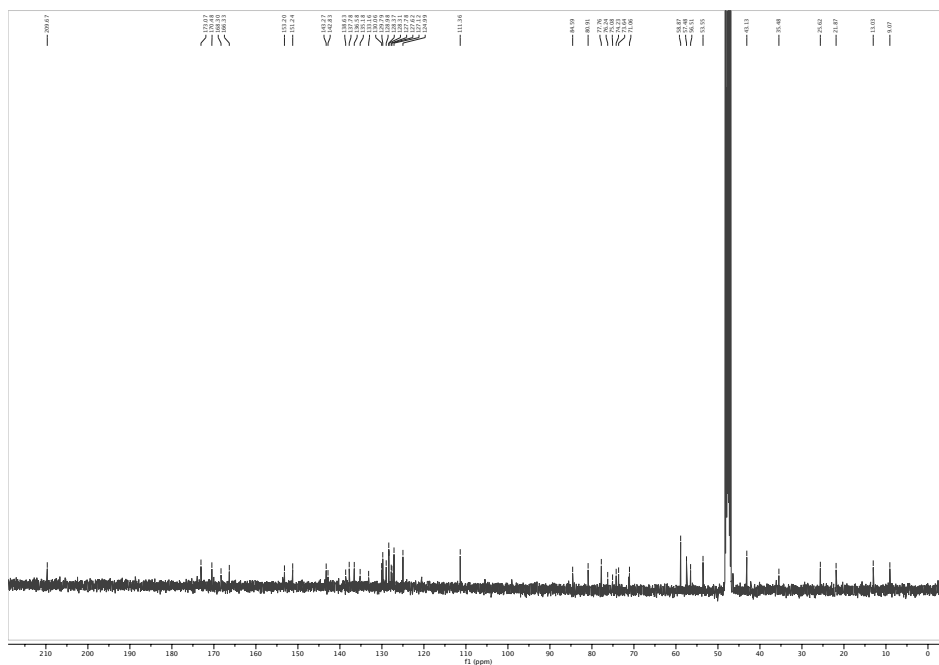


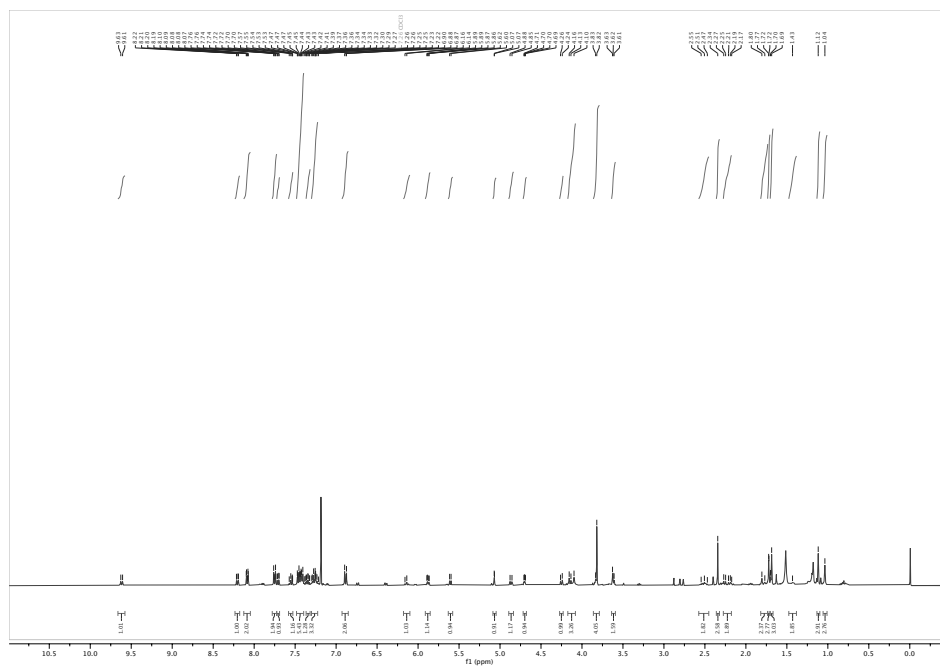
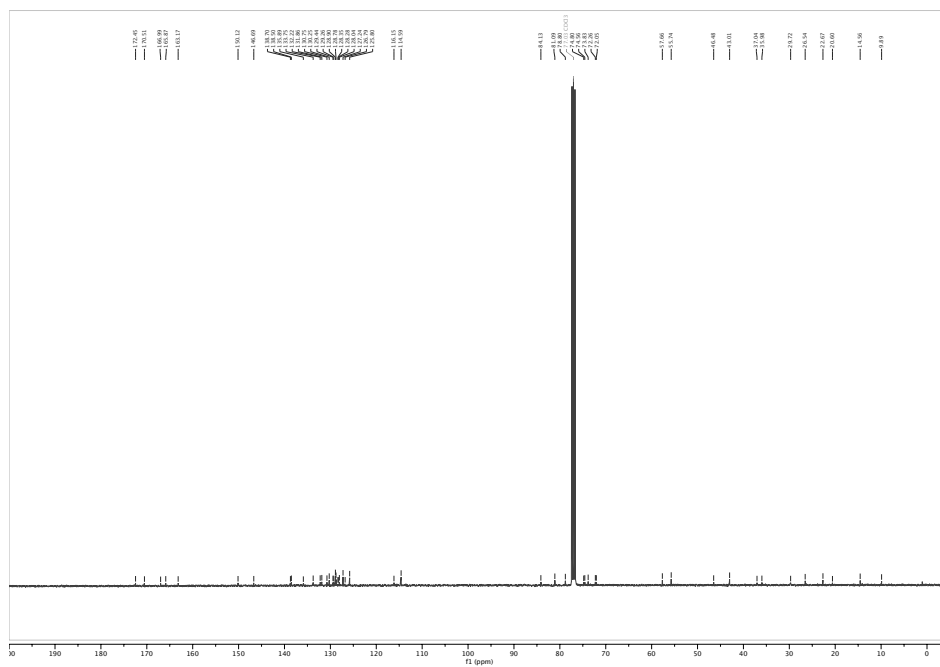
AzTax3MP: <sup>1</sup>H-NMR

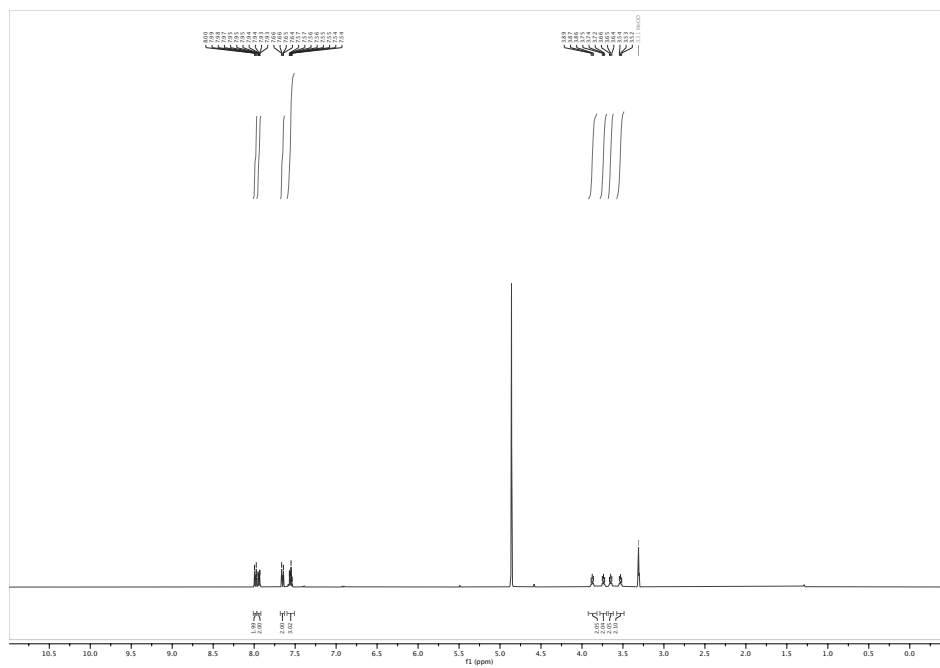
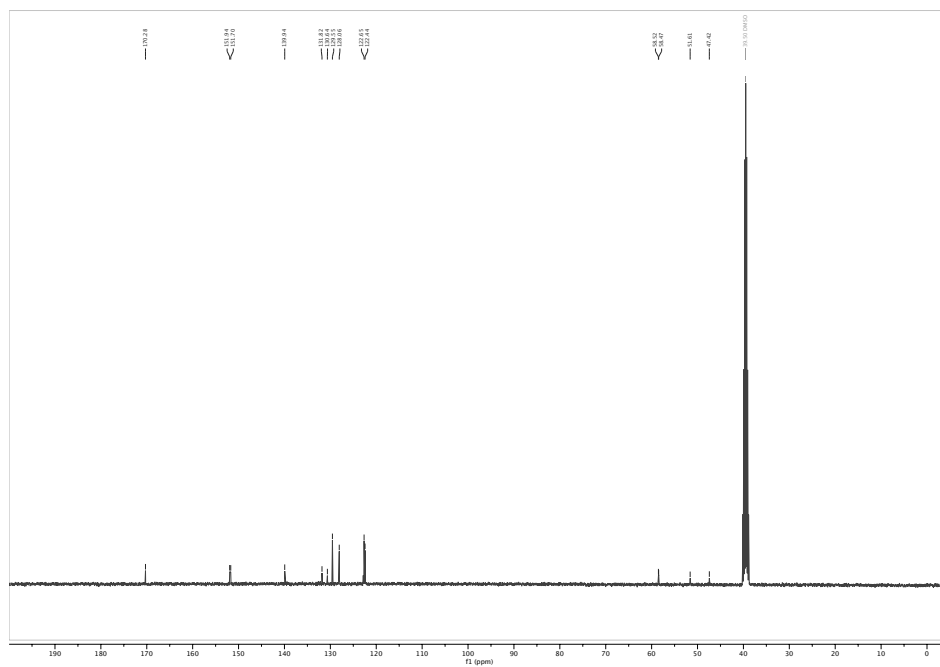


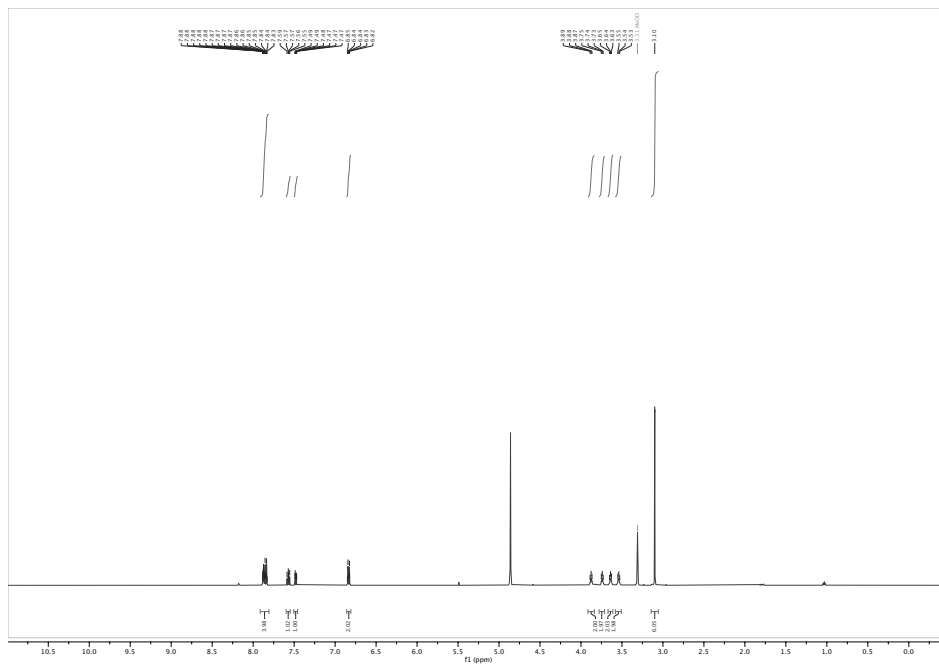
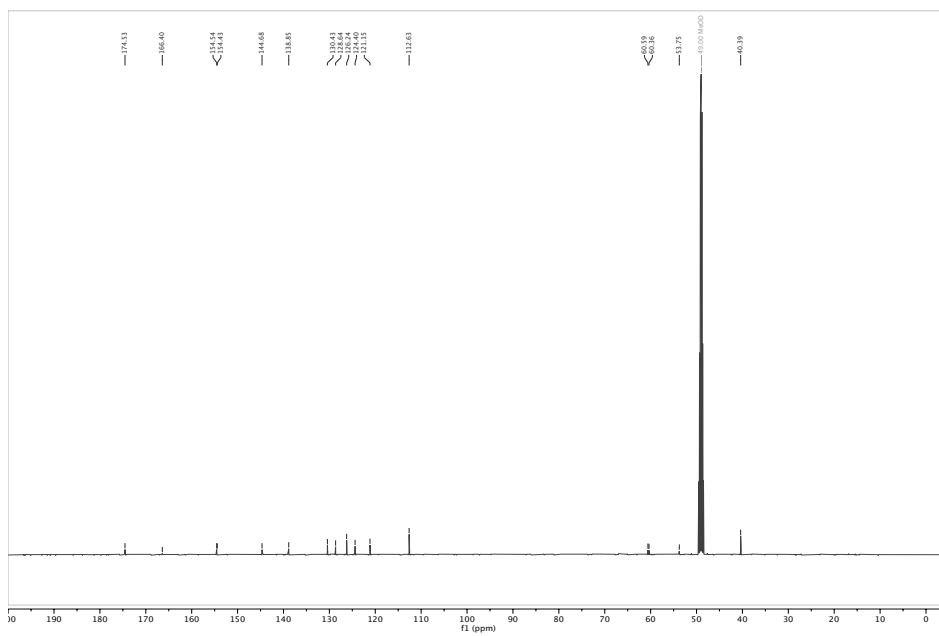


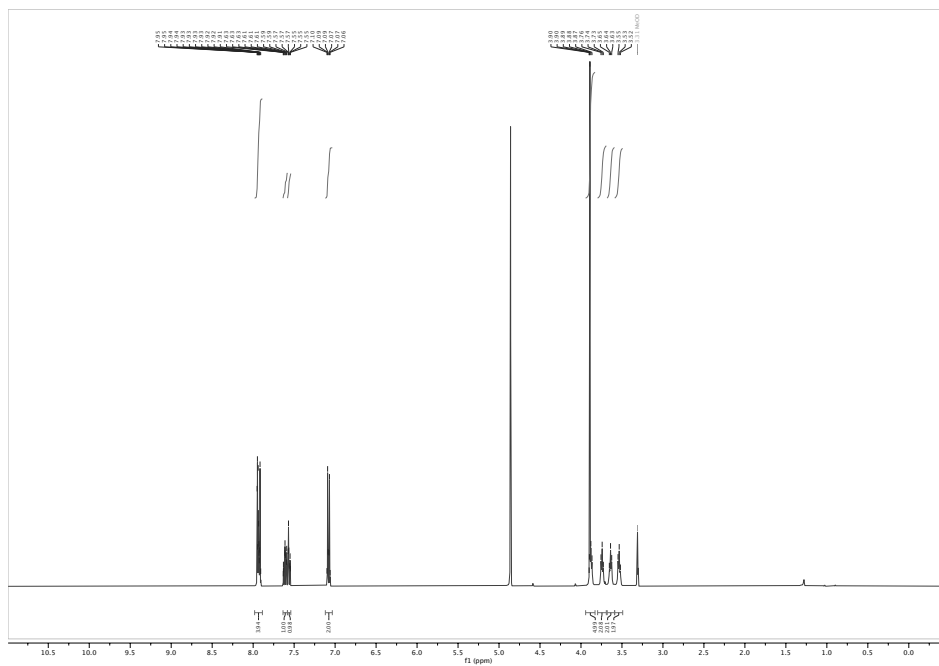
AzTax3TM: <sup>1</sup>H-NMR<sup>13</sup>C-NMR

AzTax3DEA: <sup>1</sup>H-NMR<sup>13</sup>C-NMR

AzTax2MP: <sup>1</sup>H-NMR<sup>13</sup>C-NMR

***N,N*-bis(2-hydroxyethyl)-4-(phenyldiazenyl)benzamide (4H): <sup>1</sup>H-NMR****<sup>13</sup>C-NMR**

**3-((4-(dimethylamino)phenyl)diazenyl)-*N,N*-bis(2-hydroxyethyl)benzamide (3DMA): <sup>1</sup>H NMR****<sup>13</sup>C-NMR**

***N,N*-bis(2-hydroxyethyl)-3-((4-methoxyphenyl)diazenyl)benzamide (3MP): <sup>1</sup>H-NMR****<sup>13</sup>C-NMR**